Proceedings

11th International INQUA Workshop on Paleoseismology, Active Tectonics and Archaeoseismology ("PATA Days")

25 - 30 September 2022, Aix-En-Provence, FRANCE

Editors : Stéphane Baize (IRSN) and Magali Rizza (CEREGE, Aix-En-Provence)

This event was hosted at the Holiday Resort "Village Pierre et Vacances de Pont-Royal-En-Provence", in Mallemort, France. This event was supported by: INQUA Focus Group n°2008F TPPT (Terrestrial Processes Perturbed by Tectonics). More information on the event and field trip guides here: https://patadays-2022.sciencesconf.org/

PATA Days are a conference series dedicated to Paleoseismology, Active Tectonics, and Archaeoseismology. The meetings started in 2009 and are held in varying locations every year. More information is available at https://www.inqua.org/commissions/terpro/ifg.

PATA days 2022 Organizing Committee: Magali Rizza (CEREGE, Aix-Marseille Université), Stéphane Baize (IRSN), Jean-François Ritz (GM), Christian Sue (ISTERRE, UGA), Hervé Jomard (IRSN), Yann Klinger (IPGP), Laurent Bollinger (CEA), Laurence Audin (ISTERRE, UGA), Frédérique Leclerc (Géoazur, Université Côte d'Azur), Anne-Sophie Mériaux (EOST), Oona Scotti (IRSN)

Programme Of The Workshop

Sunday Sept. 25th

1 pm - 7 pm	Registration	
8:30 pm	Dinner	

Monday Sept. 26th

8am - 6 pm	Field trips	Group 1 : 1909 Lambesc earthquake Group 2 : 2019 Le Teil Earthquake
8:30 pm	Dinner	

Tuesday Sept. 27th

	Session "Earthquake of plate interiors"	
8 - 10 am	Flash presentations and Talks	Room : Pont-Royal 1
10 - 11 am	Posters and coffee break	Room : Pont-Royal 2
11 - 12:15 am	Talks	Pont-Royal 1
12:15 - 2 pm	Lunch	
	Session "Archeoseismology and Historical Earthquakes"	
2 - 4 pm	Flash presentations and Talks	Pont-Royal 1
4 - 5 pm	Posters and coffee break	Pont-Royal 2
5 - 6 pm	Talks and flash presentations	Pont-Royal 1
6:30 - 7:30 pm	EDITH Project	Pont-Royal 1
8:30 pm	Dinner	

Wednesday Sept. 28th

	Session "Earthquake Geology and General Contributions"	
8 - 10 am	Flash presentations and Talks	Pont-Royal 1
10 - 11 am	Posters and coffee break	Pont-Royal 2
11 - 12:15 am	Talks	Pont-Royal 1
12:15 - 2 pm	Lunch	
	Session "Advances and Challenges in Quaternary Geochronology"	
2 - 4 pm	Flash presentations and Talks	Pont-Royal 1
4 - 5 pm	Posters and coffee break	Pont-Royal 2
5 - 6 pm	Talks and flash presentations	Pont-Royal 1
6:30 - 7:30 pm	EDITH Project	Pont-Royal 1
8:30 pm	Dinner	

Thursday Sept. 29th

"Advances in earthquake geology techniques (onland and offshore)"		
8 - 10 am	Flash presentations and Talks	Pont-Royal 1
10 - 11 am	Posters and coffee break	Pont-Royal 2
11 - 12:15 am	Talks	Pont-Royal 1
12:15 - 2 pm	Lunch	
Session "Contribution to seismic hazard analysis"		
2 - 4 pm	Talks	Pont-Royal 1
4 - 5:30 pm	Posters and coffee break	Pont-Royal 2
5:45 - 6:15 pm	Le Teil earthquake	Pont-Royal 1
6:15 - 6:45 pm	Best Student Poster and Talk Award	
8h30 pm	Dinner	

Friday Sept. 30th

8 am - 6 pm	**Field trips**	**Group 1 : 2019 Le Teil Earthquake** **Group 2 : 1909 Lambesc earthquake**

Oct. 01st to 03rd

Extra Field trip "Internal Alps tectonics and gravitational controls"

Programme Of Scientific Sessions

International Workshop on Paleoseismology, Active Tectonics, and Archaeoseismology

Tuesday, September 27

Time	Duration	Title	Speaker
8:00 AM	30 mn	**Poster - Flash presentations #1**	
8:15 AM			
Session "Earthquake of Plate Interiors"			
8:30 AM	15 mn	Surface rupture of the 2020 Mw 5.1 Sparta, North Carolina, USA Earthquake and evidence of an active structure with recurrent Quaternary deformation	Figueiredo P.
8:45 AM	15 mn	Paleoearthquake rupture scenarios and the role of fault geometrical complexity on the Yangsan Fault, SE Korea	Kim T.
9:00 AM	15 mn	Paleoearthquakes Constrained by 2D and 3D Paleoseismic trenching: A case study along the Yangsan Fault, South Korea	Naik Sambit P.
9:15 AM	15 mn	Cumulative and coseismic slip observed on the intracontinental Petrinja-Pokupsko Fault, source of the Mw 6.4 2020 Petrinja earthquake (Croatia): Insights from morphotectonic, paleoseismologic and geodetic data	Henriquet M.
9:30 AM	15 mn	Paleoseismic characterization of the eastern Rhine Graben Boundary Fault (RGFB), Southern Germany	Pena-Castellnou S.
9:45 AM	15 mn	The silent and slow active faults of Germany: results from paleoseismological trenching	Reicherter K.
10:00 AM	60 mn	Coffee Break and **POSTERS**	
10:15 AM			
10:30 AM			
10:45 AM			
11:00 AM	15 mn	Characterizating the Quaternary activity of the NE termination of the Cévennes Fault System and origin of the movement	Cathelin N.
11:15 AM	15 mn	Was the XXth century earthquake cluster in Mongolia a coincidence?	Klinger Y.
11:30 AM	15 mn	Slip distribution and segmentation of the Ar-Hötöl surface rupture along the Khovd Fault (Mongolian Alay)	Ferry M.
11:45 AM	15 mn	Earthquake Ruptures and Seismotectonics of the NE Tien Shan	Tsai C-H.
12:00 PM	15 mn	Spatial and temporal variations in slip rate across extensional fault networks	Mildon Z.
12:15 PM		LUNCH	
12:30 PM			
1:00 PM			
1:30 PM			

2:00 PM	30 mn	**Poster - Flash presentations #2**	
2:15 PM			
Session "Archeoseismology and Historical Earthquakes"			
2:30 PM	15 mn	From stratigraphic analysis to Finite Element models in the archaeoseismic study of the Ronta bell tower	Montabert A.
2:45 PM	15 mn	Qualitative and quantitative assessment of a lake sensitivity to paleoseismic events in the NW Alps	Banjan M.
3:00 PM	15 mn	The twisted gate - repeated destructive earthquakes in Cluj-Napoca, Transilvania	Kazmer, M.
3:15 PM	15 mn	Assessing historical earthquake sequences with Coulomb stress models	Diercks M.
3:30 PM	15 mn	Did a 3,800 years old ~Mw9.5 earthquake trigger major social disruption in the Atacama Desert?: Geoarchaeological evidence	Easton Vargas G.
3:45 PM	15 mn	Surface expression of historical earthquakes in central and eastern Nepal	Bollinger L.
4:00 PM	60 mn	Coffee Break and **POSTERS**	
4:15 PM			
4:30 PM			
4:45 PM			
5:00 PM	15 mn	Investigating Holocene earthquakes along an Oceanic Transform Fault: the Húsavík-Flatey Fault in northern Iceland	Matrau R.
5:15 PM	15 mn	Paleo-tsunami records response to submarine volcano activities in Korea	Lee H.
5:30 PM	30 mn	**Poster - Flash presentations #3**	
5:45 PM			
6:00 PM			
6:15 PM			
6:30 PM		**EDITH workshop « Hands-on workshop on Artificial Intelligence in Geosciences" , lead by Dr. Anika Braun.**	
6:45 PM			
7:00 PM			
7:30 PM			
8:00 PM			
8:30 PM	DINNER		
9:00 PM			
9:30 PM			
10:00 PM			

POSTER Flash Presentations #1

Baize Stéphane	New perspectives in studying active faults in metropolitan France
Kim Chang-Min	Long-term weakening and short-term rupture propagation processes of the intraplate Yangsan Fault, SE Korea, using low-angle borehole drilling
Kim Dong-Eun	Tectonic geomorphology of the Yangsan fault: regional implications for active tectonics in the intraplate region
Lefevre Marthe	Quantifying fault activity over different time scales in the Lower Rhine Graben, towards a new fault database for seismic hazard assessment.
Marconato Leo	Insights on fault reactivation during the 2019 November 11, Mw 4.9 Le Teil earthquake in southeastern France, from a joint 3-D geological model and InSAR time-series analysis
Park Kiwoong	Paleoseismic characteristics based on geomorphological and structural geological analysis for the central part of the Ulsan fault zone, SE Korea
Perrin Clement	Looking for quaternary fault activities in the Armorican Massif (R8 FACT region): preliminary results of a geophysical analysis along the Southern Armorican Shear Zone.
Audin Laurence	M>7.5 Earthquake on the Pallatanga Fault evidenced by archeoseismic damage and secondary landslides in Riobamba region of Ecuador
Duperret Anne	A paleoseismic attempt using archeoseismology in a region of low intraplate seismicity in the Chalk of the Paris Basin, Normandy, France. Is the FÃ©camp-Lillebonne fault always active ?
Gaidzik Krzysztof	Historical earthquakes in Lower Silesian Block - an archeoseismological approach
Marshall Neill	Re-evaluating the 1948 Ashgabat earthquake, Turkmenistan. Evidence for a multi-fault rupture?
Kázmér Miklós	Coherent toppled walls - an archaeoseismological assessment
Ramirez-Herrera Maria-Teresa	The largest earthquake and tsunami of the last five centuries in Mexico uncovered in historical and geological records

POSTER Flash Presentations #2

Alvarado Alexandra	Evidence of progradation of the reverse fault system of Quito towards a transpressive fault system
Alvarellos Victoria	From emergent to blind: The Active Andean Thrust Front in the Southern Precordillera, Argentina
Arora Shreya	Estimation of the slip rate along the un-ruptured fault segment of the M7.2 1896 Rikuu earthquake, northeast Japan.
Azuma Takashi	Vertical slip-rate on the Shibetsu fault zone in the most eastern part of Hokkaido, Japan
Goswami Chandreyee	The Uplift History along the Mishmi Thrust within the Eastern Himalayan Syntaxis during Neogene and Quaternary time
Cheon Youngbeom	Near-surface upward termination of the contractional strike-slip ruptures: Evidence from paleoearthquakes of the Yangsan Fault in SE Korea
Cinti Francesca Romana	Analysis of trenching records in central Apennines: from data uncertainties to earthquake recurrence estimates and rupture scenarios
Debaecker Sophie	Studying seismic supercycles through coral microatolls: the study case of Ishigaki island, Japan.
Gomez-Novell Octavi	Geomorphological evidence of Quaternary activity in the Amarguillo Fault, a transtensional structure within the Alhama de Murcia Fault system (SE Spain)
Gwon Ohsang	Paleoseismic characteristics along the southern Ulsan Fault Zone, SE Korea

Jomard Hervé	Interactions between active tectonics and gravitational deformation along the Billecocha fault system (Northern Ecuador): insights from morphological and paleoseismological investigations
Kim Young-Seog	New suggestion for the regulation of safe separation distance from active faults based on damage characteristics
Koehler Richard	Quaternary mapping and paleoseismic trenching of the Bonham Ranch fault: An active structure along the Walker Lane/Basin and Range transition zone, Nevada USA
Lei Shengxue	Seismogenic structure of the 1976 Ninghe (North China) Ms6.9 earthquake and its tectonic implications
Livio Franz	Seeking seismogenic sources for paleoearthquakes in the Alps: clues from a DSGSD in the Italian Southern Alps.
Maslac Josipa	Structural architecture and kinematic properties of faults in the Dubrovnik area and its hinterland (Croatia, Bosnia and Herzegovina, Montenegro)

POSTER Flash Presentations #3

Molins Vigata Julia	Geological, geomorphological, geophysical and paleoseismic exploration along the Palomares Fault (southeast Iberian Peninsula)
Niemi Tina	A New Look at the Ground Rupture of the Motagua Fault in the 1976 Guatemalan Earthquake along the Caribbean-North American Plate Boundary
Olle Marc	New paleoseismic data for the characterization of a complete transect in the Alhama de Murcia Fault (SE Spain)
Pamumpuni Astyka	Paleoseismological investigation in a remote region of Kalimantan, Indonesia
Pierce Ian	Trenching the Greater Caucasus Frontal Thrusts
Pizza Marco	LIKELIHOOD OF PRIMARY SURFACE FAULTING: A SEQUEL
Rodriguez Piceda Constanza	Contributions of lithospheric strength, mantle hydration and slab flexure to seismic localization in the southern Central Andes
Sue Christian	Tectonic Transfer from the Western Alpine Front to the French Rhône Valley in its 3D-Structural Context
Tringali Giorgio	Sites selection for creepmeter fault monitoring in a complex volcano-tectonic framework: the Mt. Etna eastern flank as an example
Vega Ruiz Ambrosio	Late Cenozoic reactivation of trench-parallel strike-slip system and tectonic forcing of drainages close to the Oroclinal Bend, Andean forearc of N-Chile
Walker Richard	Active faulting, earthquakes, and geomorphology of the Main Kopetdag fault, Turkmenistan
Han LongFei	Impact of geometrical complexity on start and propagation of strike-slip earthquakes: The case of the 2021 M*w*7.4 Madoi earthquake, China
Pinzon Nicolas	Paleoseismology along the Aksay segment of the Altyn Tagh fault, China
Petra Stepancikova	Stress field changes in Central Europe since Late Miocene to date as determined from volcanic rocks and extensometric measurements in the Bohemian Massif, Central Europe

Wednesday, September 28

Time	Duration	Title	Speaker
8:00 AM	15 mn	**Poster - Flash presentations #4**	
		Session " Earthquakes Geology and General Contributions"	
8:15 AM	15 mn	Neotectonic of Papua, Indonesia	Pamumpuni A.
8:30 AM	15 mn	Paleoseismological trenching and tectonic geomorphology reveal an active fault with evidence for repeated large Holocene earthquakes in Papua New Guinea	Whitney B.
8:45 AM	15 mn	First palaeoseismological constraints on the Anghiari normal fault (Upper Tiber Valley, Northern Apennines)	Testa A.
9:00 AM	15 mn	Capable or not? The intriguing case of the Pescopagano fault in the area of the 1980, Mw 6.9 Irpinia earthquake, southern Italy	Ferranti L.
9:15 AM	15 mn	Quantifying the slip over various time scales on active normal faults in the Apennines (Italy): challenges on the Liri fault from paleoearthquakes to long-term slip rate	Riesner M.
9:30 AM	15 mn	Paleoseismological surveys for the identification of capable faults in urban areas: the case of the Mt. Marine Fault (Central Apennines, Italy)	Iezzi F.
9:45 AM	15 mn	Where are seismites formed? New insights from lacustrine sediments with implications for palaeoseismology	Marco S.
10:00 AM	60 mn	Coffee Break and **POSTERS**	
10:15 AM			
10:30 AM			
10:45 AM			
11:00 AM	15 mn	Mendocino Triple Junction, Humboldt County, California: Terraces and Tectonics in the latest Quaternary	Patton J.
11:15 AM	15 mn	Paleoseismic study of the Elk Lake fault: A newly identified Holocene-active fault in the northern Cascadia forearc near Victoria, British Columbia, Canada	Harrichlausen N.
11:30 AM	15 mn	Seismogenic faults, seismo-lineaments, and related thermal waters in the Colca basin, S Peru	Gaidzik K.
11:45 AM	15 mn	Architecture, upper crustal extension, and collapse of a continental shelf raised at an accelerated rate during the Quaternary, northern Chile	Gonzales-Alfaro J
12:00 PM	15 mn	Major California faults are smooth across multiple scales at seismogenic depth	Lomax A.
12:15 PM		LUNCH	
12:30 PM			
1:00 PM			
1:30 PM			

2:00 PM	30 mn	**Poster - Flash presentations #5**	
2:15 PM			
Session "Advances and Challenges in Dating"			
2:30 PM	30 mn	Luminescence and ESR dating for palaeoseismology and active tectonics : limits and future possibilities	Tsukamoto S.
2:45 PM			
3:00 PM	15 mn	Inheritance of Detrital Charcoal: Implications for Age Estimates on Paleoearthquakes	Rockwell T.
3:15 PM	15 mn	Assumptions and limitations in interpreting 10Be and 26Al cosmogenic isotope surface and sub-surface data	Van Der Woerd J.
3:30 PM	15 mn	2022 updates regarding slip rates along Patagonia's fastest slipping strike strip faults: the Magallanes Fault (MF) and Liquiñe-Ofqui fault zone (LOFZ)	De Pascale G.
3:45 PM	15 mn	Quaternary faults reactivation in the Northern Calcareous Alps (Austria): kinematics and timing inferred from caves passage offsets	Szczygiel J.
4:00 PM	60 mn	Coffee Break and **POSTERS**	
4:15 PM			
4:30 PM			
4:45 PM			
5:00 PM	15 mn	Climate and tectonic forcings driving the coastal landscape evolution: clues form late quaternary fan lobes in Kachchh region (NW India)	Srivastava E.
5:15 PM	15 mn	Luminescence dating of the dammed lake formed by the catastrophic Beshkiol landslide along the Naryn River (Tien Shan)	Losen J.
5:30 PM	15 mn	Episodic deformation in the western Transverse Ranges of California during the past 125 kyr	Onderdonk N.
5:45 PM	15 mn	A new long-term slip-rate on the Banning Fault to help untangle the deformation pattern of southern California	Meriaux A-S.
6:00 PM			
6:15 PM			
6:30 PM		**EDITH workshop « Hands-on workshop on Artificial Intelligence in Geosciences" , lead by Dr. Anika Braun.**	
6:45 PM			
7:00 PM			
7:30 PM			
8:00 PM			
8:30 PM	DINNER		
9:00 PM			
9:30 PM			
10:00 PM			

POSTER Flash Presentations #4

Figueiredo Paula	Late Pleistocene and Holocene paleoseismology and deformation rates of the Pleasant Valley Fault (Nevada, USA)
Guzman Oswaldo	Combining ESR and 10Be dating of fluvial terraces of the Santo Domingo River on the Southeastern of MÃ©rida Andes, Venezuela: Methodology and tectonic implications.
Choi J-H	Constraint of Quaternary fault activity using quartz OSL and detrital zircon U-Pb ages
Arrowsmith Ramon	Robotic mapping, machine learning, and particle dynamics for earthquake geology
Benites Belen	Analysis of geomorphological index for the characterization of the neotectonic activity of the Tena Fault in the Amazon foothills
Buck Jason	Benefits and techniques for using digital photography and structure from motion software in paleoseismic field studies with an emphasis on low-cost methods.
Choi Yire	Introduction to the mapping and quantitative analysis of surface ruptures using deep learning and satellite

POSTER Flash Presentations #5

Cornejo Carolina	First paleosismology analysis in Ecuadorian Amazon piedmont: implication for seismic risk analysis.
Gruetzner Christoph	Remote sensing of active tectonics in the Eastern and Southern Alps
Kaci Tassadit	Seismotectonic activity in the NW Cotentin Peninsula (Normandy, France). The input of offshore high-resolution data.
Leclerc Frederique	Unravelling the recent rupture history of a submarine active fault using video-derived photogrammetry acquired with underwater vehicles
Marliyani Gayatri	Measuring spatial anomalies of radon to explore their usability to study active fault zone in Ambarawa, Central Java, Indonesia
Palagonia Sylvain	Can high-resolution seismic profiles be interpreted similarly to paleoseismological trenches in order to reconstruct the past rupture history of submarine faults?
Perea Manera Hector	High-Resolution multichannel seismic reflection experiment with active tectonics objectives: Defining the deep geometry of the faults bounding the Guadalentin Depression (SE Iberia)
Pousse Lea	Characterization of normal fault scarp using convolutional neural network: application to Mexico
Vassallo Riccardo	Numerical 3D back-slip reconstructions from high-resolution imagery of Western Alps active faults
De Sigoyer Julia	Active Subaquatic Fault Segments in Lake Iznik along the Middle Strand of the North Anatolian Fault, and paleoseismicty of the NAF, NW Turkey

Thursday, September 29

Time	Duration	Title	Speaker
8:00 AM	30 mn	**Poster - Flash presentations #6**	
8:15 AM			
Session "Advances in earthquake geology techniques (onland and offshore)"			
8:30 AM	15 mn	Horizontal offset measurements along the surface rupture of the 1995 Kobe earthquake from aerial photo correlation using MicMac	Choi J-H.
8:45 AM	15 mn	Styles of Quaternary deformation along the south-central Chilean forearc revealed by LiDAR	Melnick D.
9:00 AM	15 mn	Segmentation of the Trévaresse thrust system (Provence) from airborne LiDAR topography and field mapping. Implications for paleosismic investigations on the Lambesc 1909 earthquake.	Rizza M.
9:15 AM	15 mn	Predicting spatial patterns of landslides induced by the 2010 and 2021 Haiti earthquakes with machine learning methods	Braun A.
9:30 AM	15 mn	Advantages of retrodeforming trench logs	McCalpin J.
9:45 AM	15 mn	3D paleoseismic trenching combined with 3D geophysics	Stepancikova P.
10:00 AM	60 mn	Coffee Break and **POSTERS**	
10:15 AM			
10:30 AM			
10:45 AM			
11:00 AM	15 mn	3D geological model of the northeastern part of the Cevennes Fault System (CFS) (France)	Thomasset C.
11:15 AM	15 mn	Effects of sampling biases in extracting throw measurements along complex fault geometries from seismic reflection datasets	Andrews B.
11:30 AM	15 mn	Factors Affecting Deposition of Turbidite-Homogenite Units in Kumburgaz Basin, Sea of Marmara	Henri P.
11:45 AM	15 mn	Unveiling the Upper Quaternary earthquake history on a large submarine strike-slip fault: The Yusuf Fault System (Alboran Sea)	Perea Manera H.
12:00 PM	15 mn	The IPOC Creepemter Array in Northern Chile: Potential for a future natural fault observatory	Victor P.
12:15 PM		LUNCH	
12:30 PM			
1:00 PM			
1:30 PM			

Session "Contributions to seismic hazard analysis"			
2:00 PM	15 mn	Collisional (Indenter) Tectonics of the Santa Ana Mountains and the Southern Los Angeles Basin, Orange County, California	Gath E.
2:15 PM	15 mn	The Tien Shan Active Fault Database; a new collaborative compilation for multi-use purposes	King T.
2:30 PM	15 mn	Characteristics of secondary (distributed) ruptures of normal and reverse surface faulting earthquakes: implications for fault displacement hazard analysis	Boncio P.
2:45 PM	15 mn	Recurrence period of large earthquakes at the western Alps-Mediteranean sea junction : from geological observations and modeling of the seismicity rate	Larroque C.
3:00 PM	15 mn	Speleoseismology as a tool to validate and constrain seismic hazard models: examples from Central and Southern Apennines in Italy.	Pace B.
3:15 PM	15 mn	Probabilistic assessment of the seismic source of subaqueous mass transport deposits, with application to AysÃ©n Fjord, southern Chile	Vanneste K.
3:30 PM	15 mn	Why do seismic hazard maps overpredict historically observed shaking?	Gallahue M.
3:45 PM	15 mn	Outreach on Earthquake Geology as a tool to increase social seismic awareness	Ortuño M.
4:00 PM	60 mn	Coffee Break and **POSTERS**	
4:15 PM			
4:30 PM			
4:45 PM			
5:00 PM	45 mn	**POSTERS**	
5:15 PM			
5:30 PM			
5:45 PM	30 mn	Le Teil Earthquake	Ritz J-F & Baize S.
6:00 PM			
6:15 PM			
6:30 PM			
6:45 PM			
7:00 PM			
7:30 PM		APERITIF	
8:00 PM			
8:30 PM		DINNER	
9:00 PM			
9:30 PM			
10:00 PM			

POSTER Flash Presentations #6

Campos Corina	Identification and measurement of the co-seismic fault offset along the North Anatolian Fault in the Central Basin through the co-seismic sedimentary episodes
Damon Adrien	Impact of far-field Western Europe GIA on potential fault reactivation in the intraplate Paris Basin
Delogkos Efstratios	Impact of variable fault geometries and slip rates on earthquake catalogues from physics-based simulators for the Cape Egmont Fault, New Zealand
Le Roux-Mallouf Romain	Magnitude 9 along the Himalayan arc during the medieval period ?
Manchuel Kevin	Characterization of active faults in intraplate domains: benefits from the use of multi-scale seismic reflection data
Ramel Fabien	Fault-based seismic hazard assessment for the city of Guadalajara, Central Mexico

Table Of Contents - Extended Abstracts

Extended Abstracts

From emergent to blind: The Active Andean Thrust Front in the Southern Precordillera, Argentina

Alvarellos, Victoria (1), Costa, Carlos (2), Richard, Andrés (3), Sagripanti, Lucía (1,4), Folguera, Andrés (1,4)

(1) Instituto de Estudios Andinos "Don Pablo Groeber" (IDEAN), CONICET-Universidad de Buenos Aires, Buenos Aires, Argentina.
(2) Universidad Nacional de San Luis, San Luis, Argentina
(3) Universidad Nacional de San Luis-CONICET, San Luis, Argentina
(4) Facultad de Ciencias Exactas y Naturales, Universidad de Buenos Aires, Buenos Aires, Argentina.

Abstract: *At the southern Pampean flat-slab, Quaternary active deformation is concentrated on the easternmost thrusts of the Southern Precordillera along the Las Peñas-Las Higueras range (32° 10'-32° 45'S). The Las Peñas thrust bounds this range and propagates in the piedmont through splays successively incorporated into the hanging wall. At the southern range end, the thrust front corresponds to a transposed east-verging south-plunging anticline. Our study area comprises the section where the emergent Las Peñas thrust transitions to a blind anticline. Retrodeformation of geometric markers, such as alluvial surfaces and key strata layers, allowed the estimation of shortening rates which vary from 0.08mm/a to 1.38mm/a. This may be due to the thrust passage from emergent to blind and/or to Spatio-temporal complexities of the thrust kinematics. However, more data is needed to unveil this matter.*

Keywords: *Active Tectonics; Orogenic front; Andean thrusts; Southern Precordillera Argentina; Blind thrusts.*

INTRODUCTION

The southern sector of the subhorizontal subduction segment (27°-33°S) of the Central Andes concentrates the Quaternary thrust deformation on the eastern margin of the Precordillera, where crustal seismicity has generated the most destructive earthquakes in the country in the last two centuries.

The Southern Precordillera is characterized by NNW-strike thrusts with east vergence, resulting from the Neogene inversion of ancient Triassic normal faults (Ramos and Kay, 1991; Cortés et al., 2006; Giambiagi et al., 2011). Within this domain, the Las Peñas-Las Higueras range (32° 10'-32° 45'S) concentrates the frontal Andean deformation zone (Fig. 1), which exhibits one of the clearest and most continuous exposures of the Quaternary thrust front (Costa et al., 2000, 2014, 2019). This mountain range comprises two large thrust systems: the Las Higueras thrust system to the west, which emplaces Paleozoic and Mesozoic volcanic and sedimentary rocks over Mesozoic and Cenozoic sedimentary sequences (Ahumada et al., 2006; Ahumada and Costa, 2009; Costa et al., 2015). To the east, the Las Peñas thrust system overrides Neogene sediments of the folded bedrock over Quaternary conglomerates (Harrington, 1971; Costa et al., 2000, 2014, 2019; Ahumada et al., 2006; Ahumada and Costa, 2009). This structure, over 30 km long, concentrates the most recent deformation and provides one of the best opportunities for neotectonic analysis throughout the entire Andes. The Neogene mountain building related to this thrust activity decreases toward both range tips. The geomorphic signature of the Las Peñas thrust at the northern tip vanishes beneath the piedmont alluvium through a complex geometry related to lateral ramps. In this study, we have conducted topographic and paleoseismological studies in natural exposures at the southern range end, to address the characteristics of the Quaternary thrust front where it transitions from emergent to blind.

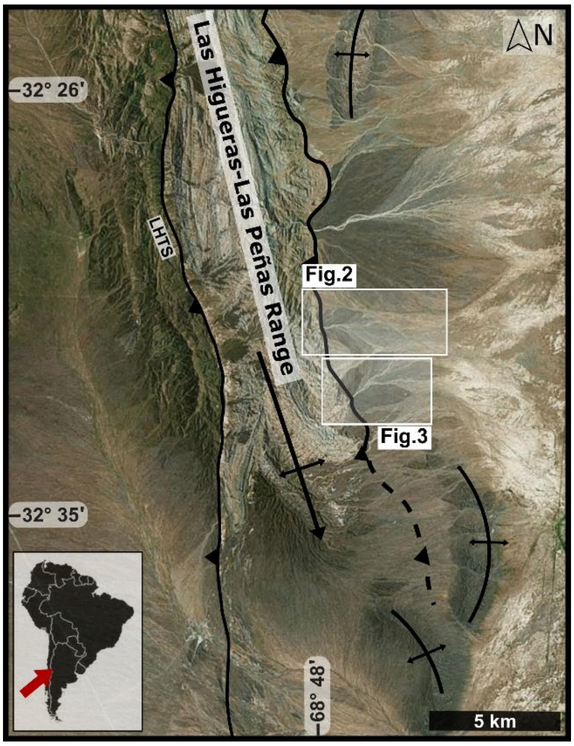

Figure 1: Southern Precordillera region (Las Peñas-Las Higueras range), between 32° 25' and 32° 40'S. The main neotectonic structures are shown in black. The white squares mark the study areas, corresponding to La Escondida and Baños Colorados creeks (Fig. 2, Fig. 3, correspondingly), where the main neotectonic structures, namely the Las Higueras Thrust System (LHTS) and Las Peñas Thrust System (LPTS) are shown.

Assessing shortening rates at the Las Peñas range is essential data to understand the processes of mountain building in this sector of the Southern Precordillera, as well as the related seismic hazard. Previous studies focused on this topic obtained variable shortening rates along its trace, tentatively assigned to geometric-kinematic complexities of the structure (Schmidt et al., 2011; Costa et al., 2019). Therefore, this work seeks to assess shortening rates and characterize thrust activity. Shortening rates have been estimated by retrodeforming geometric markers such as alluvial surfaces and key stratigraphic layers of an exposed natural trench, indicating shortening rates between 0.08mm/a and 1.38mm/a.

METHODS AND RESULTS

We reconstructed the original alluvial paleosurfaces through remains of deformed terraces to calculate shortening from line lengths, based on topographic profiles generated with Copernicus 30m digital elevation models (Figs. 2, 3, and 4; https://scihub.copernicus.eu/). Retrodeformation of these deformation markers allowed the estimation of shortening rates through ages obtained by previous works (Schmidt et. al., 2011; Fig. 2 and 3). Shortening rates were also estimated through trishear modeling of key layers preserved in a natural outcrop below a thrust scarp (Fig. 6).

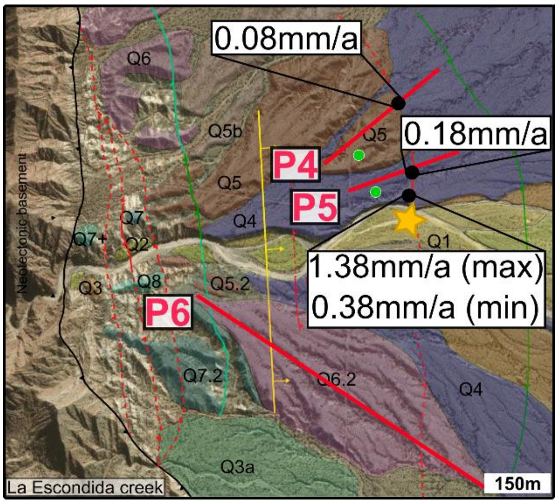

Figure 2: Shortening rates calculated by this study in the La Escondida creek. The location of the exposed natural trench is marked with a yellow star at a. Red lines indicate the location where the topographic profiles were made. Green dots indicate the location of samples dated by Schmidt et al. (2011).

The field evidence and the topographic profiles carried out then suggest the presence of folds related to the splays that propagate in the foothills.

At the La Escondida creek, the current topographic surface (P4 in Fig. 2) corresponding to units Q4 and Q5 were used, as footwall and hanging wall correspondingly, to calculate the shortening, and, from the ages obtained by previous works (Schmidt et al., 2011), a shortening rate of 0.08 mm/a was derived (Fig. 2). This value is envisaged as the very minimum because the calculation is made from diachronous terraces and with the maximum dating age of 12.6Ka. Another recent surface, Q4, was used for the calculation of the shortening (P5 in Fig. 4), obtaining a minimum rate of 0.18mm/a. This estimation is considered a minimum rate because the far field scarp profile was used for line restoration. Key layers interpreted to correlate in both thrust walls have been used as geometric markers to also constrain deformation through forwarding modeling using the trishear algorithm (Fig. 6; http://www.geo.cornell.edu/geology/faculty/RWA/programs/faultfoldforward.html). The shortening rates calculated through this approach range from 0.38mm/a to 1.38mm/a (see Table 1).

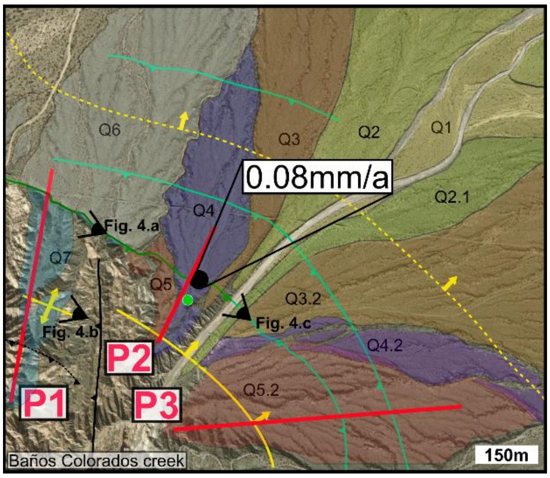

Figure 3: Profile location (red lines) for shortening rate estimation in the Baños Colorados creek. Green dots indicate the location where Schmidt et al. (2011) did the datations. Increasing numbering indicates older alluvium (Q). Yellow traces point out to observed (solid) and interpreted (dashed) monocline scarps.

At the Baños Colorados creek, the successive stages of thrust propagation have resulted in the folding of the hanging wall, as shown by the remains of older terraces and the attitude of the Neogene-Quaternary unconformity.

The clearest manifestation of this is seen to the north of the creek where east-tilted terraces (57ºE) corresponding to the fold forelimb crop out (Q7+; Fig. 5a and b), underscoring a dynamic relationship between sedimentation and thrust propagation (Fig. 5c).

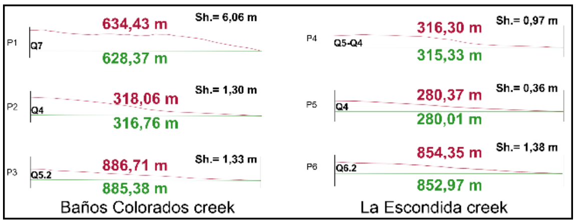

Figure 4: Topographic profiles in the Baños Colorados and La Escondida creeks (see location in Figs. 2 y 3) displaying the final length (in red) and initial length (in green). Sh: total shortening. See details in the text.

The gentle folding of terrace Q4 (see P2 Fig. 2) may account for the very minimum shortening rate (0.08 mm/a), considering the maximum age obtained by Schmidt et al. (2011; Fig. 3) for this level. This is because eventual modification of the thrust scarp by external processes is unknown. But most importantly, this broad approach only estimates the Quaternary shortening accrued in the hanging wall, whereas the slip along the thrust plane is unknown.

2

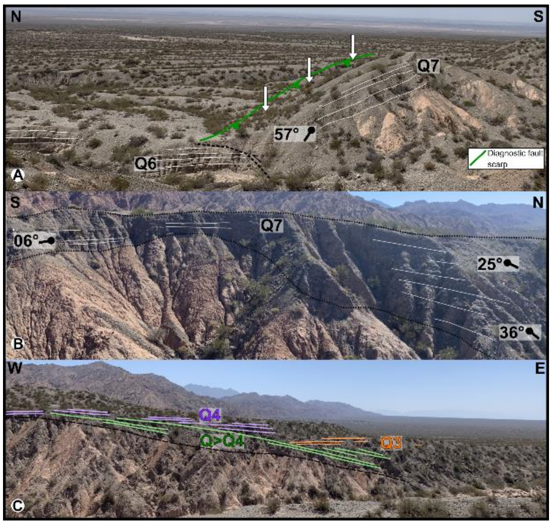

Figure 5: Baños Colorados creek. (a) and (b) folded Q7 strata related to a frontal monocline scarp. The frontal limb exhibits inclinations of ~57ºE (a) decreasing to 20º E closer to the fold axis. (c) North looking view showing the attitudes of different alluvial surfaces. See location in Fig. 1, suggesting dynamic interactions between thrust activity and sedimentation.

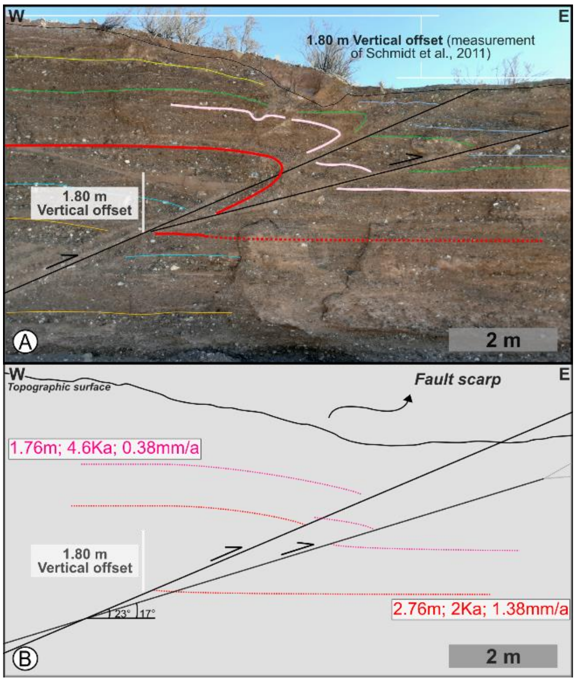

Figure 6: Preliminary interpretation of a rectified outcrop and modeling of the identified key layers. See location in Fig. 2. (a) The red and pink lines respond to correlatable layers between the hanging wall and the footwall. The height of the fault scarp seen at the surface is used to constrain the correlation of selected layers. (b) Trishear model of the key stratigraphic layers identified in (a). In white boxes are shown the shortenings calculated from the modeled key layers. Ages from Schmidt et al. (2011).

DISCUSSIONS AND CONCLUSIONS

At the La Escondida creek, the estimated maximum shortening rate would be the one calculated by Schmidt et al. (2011) (2mm/a), whereas we consider the rate proposed in this work as the very minimum (0.08mm/a). At the Baños Colorados creek, the shortening rate calculated by Schmidt et al. (2011) was 1.2mm/a and the rate we obtained in this work was 0.08mm/a. As in the La Escondida creek, these are considered to be the maximum and minimum rate ranges.

Trishear modeling / Geometric markers	Ramp angle	Trishear angle	P/S	Slip	Shortening (mm)	Age (a)	Shortening rate (mm/a)	
Red marker	23°	60°	5	370	2760	2000	1.38	LE
Pink marker (splay 1)	25°	85°	5	210	1760	4600	0.38	LE
Pink marker (splay 2)	17°	25°	5	160				LE
Unbalanced / Geometric markers	Shortening(mm)				Age (a)		Shorteningrate (mm/a)	
Red marker	31040				2000		1.73	LE
Pink marker	1878				4600		0.41	LE
Q5-Q4 (P4)	970				12600		0.08	LE
Q4 (P5)	360				2000		0.18	LE
Q4 (P2)	1300				16000		0.08	BC

Table 1: Parameters used and results obtained for the calculation of shortening rates from the use of the current topography of the alluvial surfaces and, for the La Escondida creek, the trishear modeling of two different stratigraphic levels exposed in the natural trench. The maximum and the minimum within the trench are given by choosing the most deformed layer (red line) with the maximum value of the age calculated by Schmidt et al. (2011) of 4.6Ka (taking into account the error). And the least deformed layer (pink line) with the minimum age, taking into account the error, of 2Ka.

The shortening rates of 0.27 ± 0.11 mm/a obtained by Costa et al. (2019) further north at the Las Peñas creek, fall within the rate ranges here assessed. However, aiming for a proper fault source assessment, further data are mandatory to understand if spatial-temporal variations in the thrust kinematics are significant.

Wherewith, we relate the cause of these differences to the plunging of the folding axis to the south together with the decrease in the shortening rate. Likewise, it is necessary to involve other terrace ages correlatable between both creeks and higher resolution topographic profiles to strengthen these preliminary data.

Acknowledgments: Financial support was provided by CONICET STRATEGY II formed by the UBA and UNSL team, among others. INQUA/TERPRO provided essential financial assistance to participate in the meeting.

REFERENCES

Ahumada, E. A, Costa, C. H. 2009. Antithetic linkage between oblique Quaternary thrusts at the Andean front, Argentine Precordillera. Journal of South American Earth Science 28: 207–216.

Ahumada E. A., Costa C. H., Gardini C. E., Diederix H. 2006. La estructura del extremo sur de la Sierra de Las Peñas-Las Higueras, Precordillera de Mendoza. Revista de la Asociación Geológica Argentina, Serie D, Publicación Especial, 6 ,11-17.

Cortés, J., Casa, A., Pasini, M., Yamin, M., Terrizzano, C. 2006. Fajas oblicuas de deformación geotectónica en Precordillera y Cordillera Frontal (31°30'–33°30'LS): Controles paleotectónicos. Revista de la Asociación Geológica Argentina 61: 639–646.

Costa, C., Ahumada, E., Gardini, C., Vázquez, F., Diederix, H. 2014. Quaternary shortening at the orogenic front of

3

the Central Andes of Argentina (32°15'–32°40'S): A field survey of the Las Peñas thrust. En S. Sepúlveda, L. Giambiagi, S. Moreiras, L. Pinto, M. Tunik, G. Hoke, M. Farías (Eds.), Geodynamic Processes in the Andes of Central Chile and Argentina, Geological Society of London 245–266.

Costa, C., Ahumada, E., Vázquez, F., Kröhling, D. 2015. Holocene shortening rates of an Andean front thrust, Southern Precordillera, Argentina. Tectonophysics 664: 191–201.

Costa, C., Diederix, H., Gardini, C., Cortés, J. 2000. The Andean orogenic front at Sierra de Las Peñas-Las Higueras, Mendoza, Argentina. Journal of South American Earth Sciences 13: 287-292.

Costa, C. H., Gardini, C., Diederix, H., Cisneros, H., Ahumada, E. A. 2006. The active Andean orogenic front at the Southernmost Pampean flat-slab. En: Backbone of the Americas, Boulder, Abstract with Programs, 15–1.

Costa, C. H., Schoenbohm, L. M., Brooks, B. A., Gardini, C. E., Richard, A. D. 2019. Assessing Quaternary shortening rates at an Andean frontal thrust (32° 30'S), Argentina. Tectonics 38 (8): 3034-3051.

Giambiagi, L., Mescua, J., Bechis, F., Martínez, A., Folguera, A. 2011. Pre-Andean deformation of the Precordillera southern sector, Southern Central Andes. Geosphere 7: 1–21.

Harrington, H. 1971. Descripción geológica de la Hoja 22c, 'Ramblón', provincias de Mendoza y San Juan. Dirección Nacional de Geología y Minería. Boletín 114.

Ramos, V., Cristallini, E. y Pérez, D. 2002. The Pampean flat-slab of the Central Andes. Journal of South American Earth Sciences 15: 59–78.

Ramos, V. y Kay, S. 1991. Triassic rifting and associated basalts in the Cuyo basin, central Argentina. Andean magmatism and its Tectonic Setting. Harmon, R. y Rapela C. (Eds.). Geological Society of America, Publicación Especial, 265: 79-91, Boulder.

Schmidt, S., Hetzel, R., Kuhlmann, J., Mingorance, F., Ramos, V. 2011. A note of caution on the use of boulders for exposure dating of depositional surfaces. Earth and Planetary Science Letters 302: 60–70.

Schmidt, S., Hetzel, R., Mingorance, F., Ramos, V. 2011. Coseismic displacements and Holocene slip rates for two active thrust faults at the mountain front of the Andean Precordillera (~33°S). Tectonics 30.

4

INQUA Focus Group Terrestrial Processes Perturbed by Tectonics (TPPT)

paleoseismicity.org

Biases caused by sampling strategy when extracting throw along complex normal faults imaged in 3D seismic reflection data: implications for understanding slip rates over several million-year timescales

Andrews, Billy (1), *Mildon, Zoë K. (1), Jackson, Christopher (2)*

(1) School of Geography, Earth and Environmental Sciences, Uni. of Plymouth, Plymouth, PL4 8AA, UK. Billy.andrews@plymouth.ac.uk.
(2) Basins Research Group (BRG), Department of Earth Science & Engineering, Imperial College, Prince Consort Road, London, SW7 2BP England

Abstract: *Throw and slip-rate data for normal faults should ideally be extracted orthogonal to fault strike. This is easy when using 3D seismic reflection data fully imaging buried, now-inactive systems, but difficult for active systems imaged by sub-optimally orientated 2D seismic surveys. Here we investigate how measurement obliquity impacts present-day fault properties, and our understanding of throw and slip-rate variability through time, for two faults imaged by the Chandon3D seismic survey, offshore Australia. We use 'arbitrary lines' to collect data from transects oriented at varying obliquities to a straight fault (±50°), before comparing two common measurement strategies for sampling throw along a fault-bend. We show an obliquity of 20° can cause >25% errors in slip-rate and that measurement obliquity induces errors that can change the derived slip-history of fault-bends. Because recurrence interval might relate to slip-rate, measurement orientation needs to be considered when using 2D seismic data to assess seismic hazard.*

Key words*: Slip-rate, objective bias, seismic reflection.*

Introduction

Seismic reflection datasets may be used to further our understanding of the long term (i.e., 100 kyr to Ma) slip- (or throw-) rate variability of active normal faults (e.g., Nicol et al., 2005; Gambino et al., 2022). Slip rate variations can be constrained by the across-fault offset of stratigraphic markers of known age, thus accurately determining present throw is critical, given this is a key input into calculations of throw accumulation, throw rate, and related seismic hazard. To accurately capture fault properties (e.g., throw, dip, slip), data should be collected orthogonal to normal fault strike, i.e., parallel to slip vector. However, in many active settings only 2D seismic surveys are available, which may not be optimally orientated to sample seismically active faults. For example, Nicol et al. (2005) use a series of 2D seismic lines to investigate the slip-history of the Cape Egmont Fault, offshore New Zealand (Fig 1a). Due to the non-planar nature of the fault network, the angle between the optimum measurement orientation and available sample line (referred to as measurement obliquity) ranged from 0.2˚ to 70.8˚ for the Cape Egmont fault (average = 18.7˚), and 0.1˚ to 64.2˚ (average = 18.5) for minor faults (Fig 1a, inset ii & iii). Additionally, both clockwise (+'ve) and anti-clockwise (-'ve) measurement obliquity were observed, with certain minor faults and fault-bends being particularly oblique.

Throw extracted from seismic data may be measured by comparing the vertical difference in horizon cut-offs (termed 'discontinuous throw (Td)'), or where continuous deformation (e.g., folding) is present, the cut-offs for regional horizons projected onto the fault surface (termed 'continuous throw (Tt)'). Throw backstripping, which sequentially subtracts the throw across the shallowest horizon from deeper horizons at the same along strike position, can be used to investigate how throw, and subsequently throw/slip rates, evolved through time (e.g., Peterson et al., 1992). Assuming the fault maintained a constant dip throughout its history, backstripped throw can be converted to slip, with slip-rate then calculated by dividing slip accumulated during a time interval by the duration represented by that interval (e.g., Lathrop et al., 2021).

To assess errors in our understanding of throw, slip, and slip-history caused by measurement obliquity we use a 3D seismic survey. Unlike 2D surveys, the sample orientation relative to the fault may be varied using 'arbitrary lines' (aka arblines). This, coupled with the presence of 'planar' normal faults in the dataset, enabled us to assess the error in throw extracted from sequentially oblique sample lines ranging by ±50˚ (Fig. 1c). Additionally, arblines enabled us to compare throw and slip rates extracted around a fault bend using: (i) multiple orientated arblines; and (ii) a single 'tip-to-tip' arbline (Fig 1d).

Data and geological setting

In this work we use a high-resolution 3D seismic survey (Chandon 3D) from the Exmouth Plateau, offshore NW Australia (**Fig 1b**). Following the methodology of Magee and Jackson (2021), check-shot data were used to depth convert the seismic data from TWT to metres. The Exmouth plateau underwent crustal extension between the Late Triassic-to-Jurassic and Cretaceous (e.g., Bilal and McClay et al., 2022), with additional extension caused by the intrusion of the Exmouth Dyke Swarm (Magee and Jackson, 2021). ~N-S striking, segmented faults formed to accommodate this extension. The syn-rift comprises a marine succession containing several laterally continuous, age-constrained horizons that permit throw back-stripping.

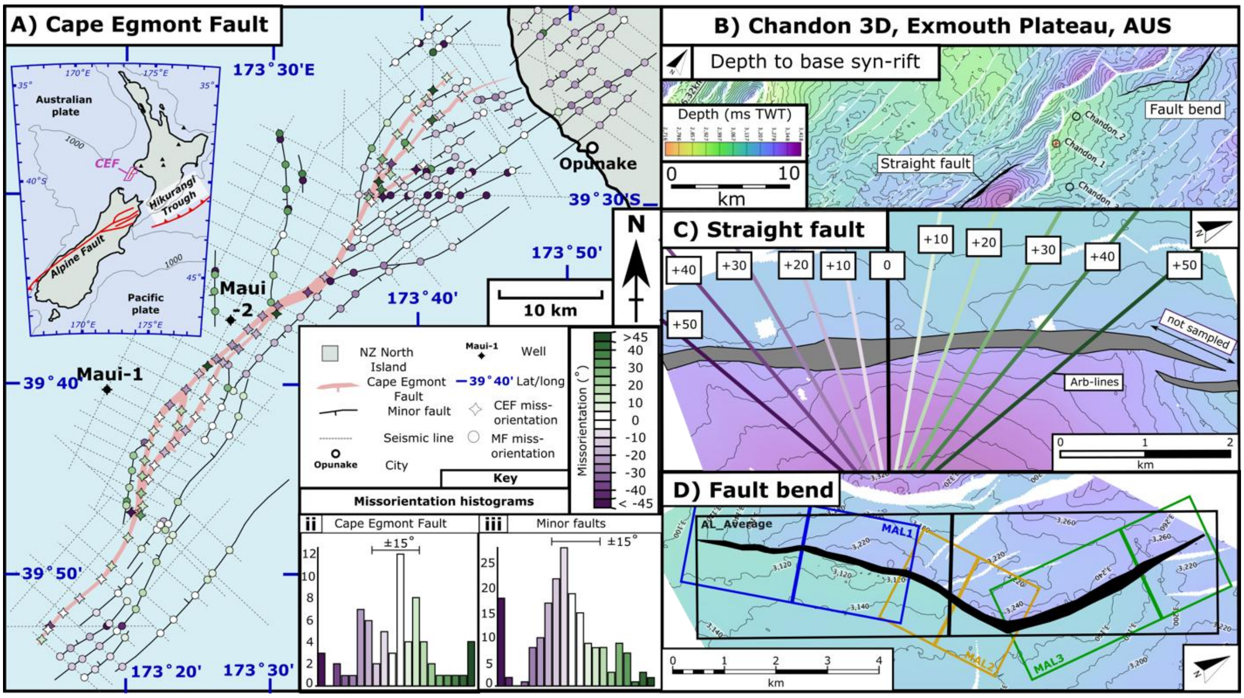

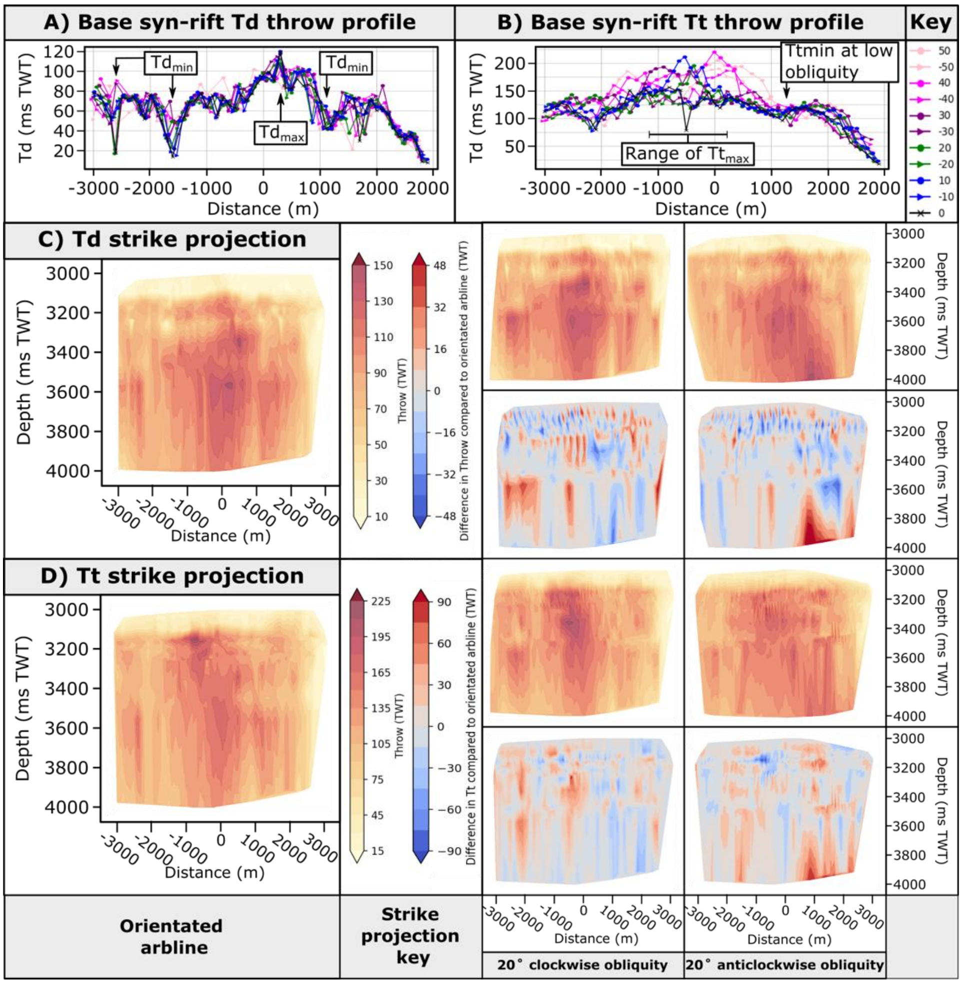

***Figure 1 (above):** Oblique fault sampling. A) Range of measurement obliquity along the Cape Egmont Fault (fault map adapted from Nicol et al., 2005). B) Depth to base syn-rift highlighting studied faults. C) The 'straight' fault used to assess the effect of sequential obliquity of sample strategy. D) The fault bend used to compare sampling fault properties along a 'tip-to-tip' profile (AL_Average) compared to multiple arblines (AL1, AL2 & AL3). Note: the rectangles represent the range of data collected with the bold line showing an example arbitrary line.*

***Figure 2 (left):** Throw variations caused by measurement obliquity across a straight fault. Throw profiles for Td (A) and Tt B). C) Strike projection for Td and difference between Td extracted from oblique arblines compared to an orientated arbline. D) Strike projection for Tt and difference between Tt extracted from oblique arblines compared to an orientated arbline.*

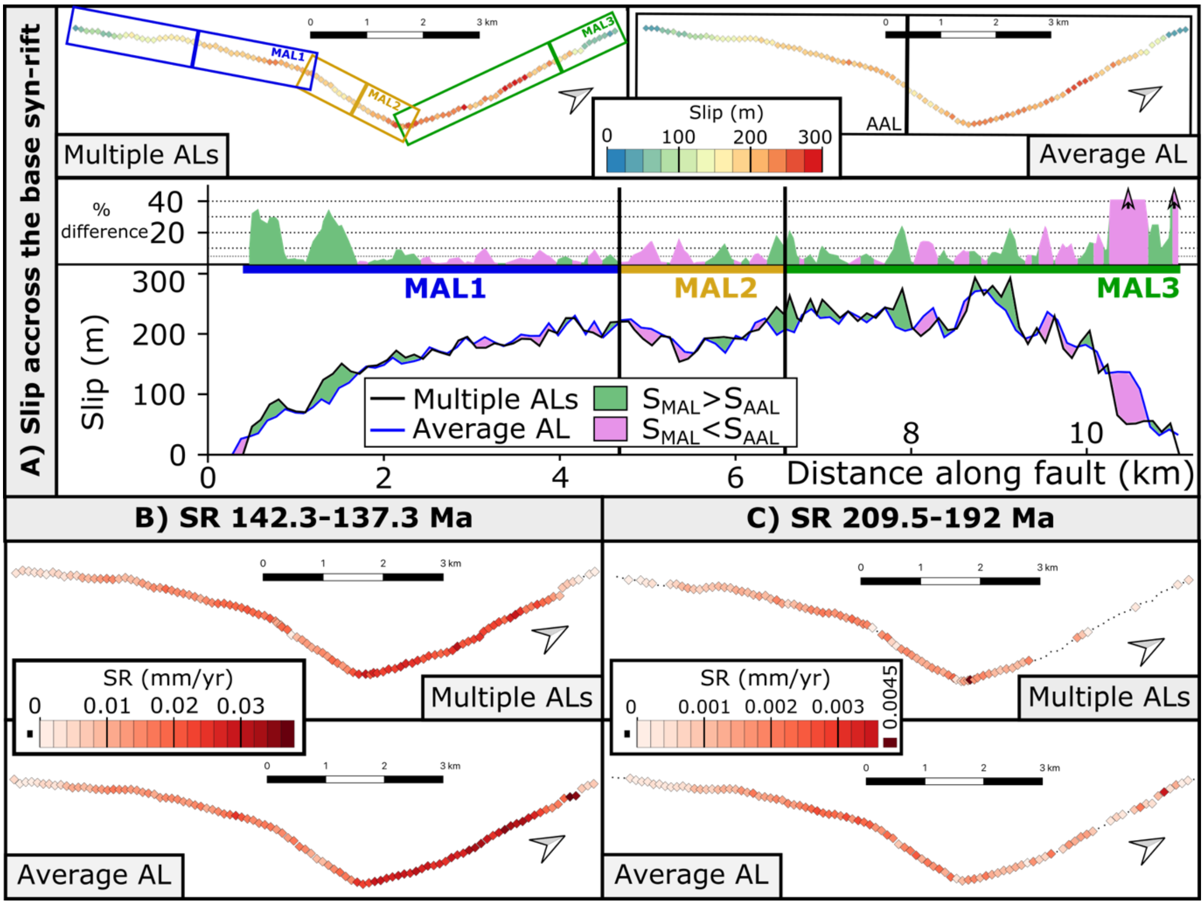

Figure 3: *Fault bend sampling. A) Map view of the present-day slip across the base syn-rift horizon. B) SR calculated between 137.3 and 142.3 Ma, C) slip rate calculated between 192 and 209.5 Ma.*

Fault data extracted from the straight fault

The straight fault is a 5.7 km long, easterly dipping, antithetic splay to a major fault system (**Fig 1c**). Discontinuous throw (Td) across the base syn-rift horizon displays an asymmetric along-strike throw profile, with Td_{max} (120 m) located at x = 0.3 km (distance along the fault), decreasing towards the fault tips. Additionally, there are several minor throw minima located as indicated on Fig 2a. Oblique sampling may over- or under-estimate throw at a given point along the fault (**Fig 2**), with the effect particularly evident for continuous throw (Tt). Additionally, Tt_{max} is located at different locations for different measurement obliquity (**Fig 2b**). Despite this, the general shape of the throw profile for both Tt and Td are similar, with greatest differences observed close to fault tips and at throw minima, with the latter not always captured at high measurement obliquity (**Fig 2a, b**).

Throw plotted on strike-projections, whereby the data is projected onto the fault plane and extrapolated between known points (**Fig 2c, d**), show spatial variations in the location and magnitude for differently orientated sample lines. For example, Tt is overestimated in the bottom right of the fault plane when obliquity is anti-clockwise, but not when clockwise (**Fig 2d**). Greater differences in throw are observed for Tt compared to Td. Differences depend on the value of throw and whether the arbline is oblique in a clockwise or anti-clockwise direction.

AL	Max SR (mm/yr)	X (m)	Max difference*		Median difference*	
			Mm/yr	%	Mm/yr	%
+40˚	0.049 (-6%)	4715	+0.039 -0.026	+935% -50%	+0.010 -0.010	+116% -39%
+20˚	0.055 (+6%)	2633	+0.035 - 0.0269	+609% -100%	+0.012 -0.003	+119% -28%
0˚	**0.052**	**2200**				

Table 1: *SR calculated over the period 137.3 to 209.5 Ma. X = distance along the fault where SR_{max} is measured. *note: the maximum difference and % difference may not be located at the same position on the fault.*

We calculate the time-averaged syn-rift slip-rate for +20˚ and +40˚ measurement obliquity. Differences in Tt extracted from oblique arblines, coupled with greater heave values due to the sampling of an apparent dip, directly impacts the calculated slip and therefore slip rate of different sample lines (**Table 1**). The median difference in slip-rate may be high and is >25%, even with an obliquity of only +20˚. Greatest differences are located at the fault tips, or at throw minima/maxima, where oblique arblines sample different points of the footwall and hangingwall cut offs compared to an optimally-orientated line. Additionally, the location of maximum slip-rate changes depending on the measurement obliquity, in some cases by >2km.

Fault data extracted from along a fault bend

The fault with a pronounced bend is 10.54 km long and comprises three segments with contrasting strikes (037˚, 062˚ and 005˚ respectively), defining two main changes or bends in the fault map-view trace (**Fig 1d**). Slip across the base syn-rift horizon displays a maximum slip (S_{max}) of 295 m to the north of the fault bend (x = ~8.7 km) (**Fig 3a)**. We observe a bi-modal distribution in throw, with a secondary S_{max} of 226 m at x = 4.1 km and 159 m at x = 5.5 km. Where data extracted using an average and multiple arblines are compared there is good agreement on the general shape of the slip profile (**Fig 3a**). However, the average arbline over- or under-estimates slip at different points along the fault. For example, large differences are observed near fault tips, with the average arbline underestimating slip for the southern fault tip (median % difference = 14%) and over-estimating it for the northern tip (median % difference = 25%). This is caused by the location of the FW and HW cut-offs differing between the average arbline and multiple arblines, along with the subtle (<10˚) changes in fault strike. Away from fault tips, the median % difference is lower and increases northwards (AL1 = 3%, AL2 = 4% and AL3 = 6.5%). Switches between areas of –'ve and +'ve difference are related to subtle (<10˚) changes in fault-strike.

Slip-rate across the fault with a pronounced bend has been calculated for two time periods; during rift initiation (209.5 to 192 Ma; **Fig 3b**), and rift climax (142.3 to 137.3 Ma; **Fig 3c**). The rift initiation slip-rate extracted using multiple arblines shows that the northern section of the fault bend was inactive at this time, with slip-rate being highest in sections MAL2 and MAL3. When an average arbline is used, parts of the northern section appear active, albeit with low slip-rate values, and the overall slip-rate is overestimated. During the rift climax, SR_{max} is located halfway along MAL3, with a secondary maximum at the north of MAL1. Whereas the locations of high and low SR broadly match between multiple arblines and the average arbline, the magnitude of SR differs. This is most notable to the north of the fault, where slip-rate extracted using an average arbline is >1.5 times that extracted using multiple arblines.

Implications for SR derived from 2D seismic surveys

Faults are generally non-planar and many fault traces show along-strike fault bends (**Fig 1**). This study highlights the potential error introduced by sampling a fault using non-optimal 2D seismic sample lines. Where 3D seismic datasets are available, measurement obliquity should not exceed 15˚ in order to get reliable results. However, non-optimally orientated 2D seismic surveys are often all that is available in active settings. For example, 50% of sample points along the Cape Egmont fault exceeded the recommended 15˚ maximum measurement obliquity suggested here (**Fig 1a)**. Therefore, our work suggests that half of the slip-rates presented in Nicol et al (2005) may be over- or under-estimated by >20% due to measurement error. To demonstrate this, the maximum throw reported for the Cape Egmont Fault by Nicol et al (2005) between the 3.2 and 3.7 Myr horizons is 1364 m. This would give a throw rate of 0.0028 mm/yr; however, the 2D survey at this location has a measurement obliquity of 21˚. Given a 20% difference in throw, the throw rate could range from 0.0022 to 0.0033 mm/yr. It is therefore important that users are aware that spatio-temporal variations in slip-rate may be caused by both geological controls (e.g. fault bends, clustering) and variations in measurement obliquity.

Conclusions

This study illustrates that measurement obliquity affects the measured throw, and therefore slip-rate, extracted across non-planar normal faults. When mapping faults using 3D seismic data, measurement obliquity should not exceed 15˚ from the local strike of the fault. Where only 2D seismic lines are available, the relative orientation of fault strike to the seismic profiles should be considered when assessing the seismic hazard potential of faults observed in the dataset. Although further work is required to better constrain the relationship between measurement error and obliquity, a conservative error of 20% should cover most slip values where obliquity exceeds 15˚, with the caveat that errors may be larger near fault tips and throw minima. Given that slip-rate is a key input when assessing the recurrence interval of active faults, it is reasonable to conclude that sample orientation needs to be considered when constructing seismic hazard maps using seismic reflection data.

Acknowledgements: Funding was provided by UKRI as part of the Future Leaders Fellowship "Quake4D" (MR/T041994/1). We acknowledge DUGInsight for provision of the seismic interpretation software.

REFERENCES

Bilal, A., McClay, K., 2022. Tectonic and stratigraphic evolution of the central Exmouth Plateau, NW Shelf of Australia. *Mar Pet Geol* 136, 105447.

Gambino, S., Barreca, G., Gross, F., Monaco, C., Gutscher, M., Alsop, G.I., 2022. Assessing the rate of crustal extension by 2D sequential restoration analysis: A case study from the active portion of the Malta Escarpment. *Basin Res.* 34 (1), 321-341.

Lathrop, B.A., Jackson, C.A.L., Bell, R.E., Rotevatn, A., 2021. Normal fault kinematics and the role of lateral tip retreat: An example from offshore NW Australia. *Tectonics* 40 (5), e2020TC006631.

Magee, C., Jackson, C.A.L., 2021. Can we relate the surface expression of dike-induced normal faults to subsurface dike geometry? *Geology* 49 (4), 366-371.

Magee, C., Duffy, O.B., Purnell, K., Bell, R.E., Jackson, C.A.L. and Reeve, M.T., 2016. Fault-controlled fluid flow inferred from hydrothermal vents imaged in 3D seismic reflection data, offshore NW Australia. *Basin Res.*, *28*(3), pp.299-318.

Nicol, A., Walsh, J., Berryman, K., Nodder, S., 2005. Growth of a normal fault by the accumulation of slip over millions of years. *J. Struct. Geol.* 27 (2), 327-342.

Petersen, K., Clausen, O.R. and Korstgård, J.A., 1992. Evolution of a salt-related listric growth fault near the D-1 well, block 5605, Danish North Sea: displacement history and salt kinematics. *J. Struct. Geol.*, *14*(5), pp.565-577.

INQUA Focus Group Terrestrial Processes Perturbed by Tectonics (TPPT)

paleoseismicity.org

Spatial and temporal variations in slip rate across extensional fault networks

*Andrews, Billy (1), **Mildon, Zoë K. (1)**, Jackson, Christopher (2), Roberts, Gerald (3), Faure Walker, Joanna (4), Iezzi, Francesco (5)*

(1) School of Geography, Earth and Environmental Sciences, University of Plymouth, Plymouth, PL4 8AA, UK. Zoe.mildon@plymouth.ac.uk
(2) Basins Research Group (BRG), Department of Earth Science & Engineering, Imperial College, Prince Consort Road, London, SW7 2BP, UK.
(3) Department of earth and planetary sciences, Birkbeck, University of London, Malet Street, Bloomsbury, London, WC1E 7HX, UK.
(4) Inst for Risk & Disaster Reduction, University College London, Gower Street, London, WC1E 6BT, UK.
(5) Dipartimento di Scienze della Terra, dell'Ambiente e delle Risorse, Università degli Studi di Napoli Federico II, Napoli, Italy

Abstract: *Slip rate is a key input for seismic hazard assessment; however, slip rate varies in space and time along active and inactive faults have been observed. Temporal variations in slip rate have been used to imply the clustering and anti-clustering of earthquakes. However, most work to date has focused on single data-points and lacks the combined spatial and temporal assessment of individual faults and fault networks. Here we present slip rates derived from an inactive fault network within the Chandon3D seismic reflection survey, offshore NW Australia. We show spatial and temporal slip rate variations across million-year time scales, likely caused by fault interaction. Slip rate profiles differed through time, with the location of maximum slip rate moving by kilometres between time periods. This has large implications for the seismic hazard assessment of active faults and raises the question whether a single slip rate measurement is sufficient to assess the seismic hazard posed by a fault.*

Key words*: Slip rate, heterogeneity, time periods of observation, fault network.*

Introduction

In recent years the need for fault parameters, including slip rate, to be incorporated into Seismic Hazard Assessments has become clear (e.g., Pace 2018). Slip rate is the in-plane displacement present across two marker horizons, divided by the time period between the horizons. For many active faults, this is derived using paleo-seismic trenching and covers the last 10s of kyrs of fault activity. Slightly longer time periods may be captured using ^{36}Cl dating of limestone fault scarps, enabling the Holocene slip history to be inverted (e.g. Benedetti et al., 2013). Million-year time scales can be investigated using geological throw derived from balanced cross sections and/or seismic reflection datasets, or through numerical modelling. Each method captures a snapshot of the slip-history, and where multiple horizons, or time intervals, are present a fuller picture of the slip-history may be obtained (Fig. 1).

In Italy and Greece, ^{36}Cl sampling shows that slip rates vary through time at the sampled location(s), implying the clustering and anti-clustering of earthquakes, and that activity switches between across-strike faults (e.g. Cowie et al., 2017, Iezzi et al., 2021; Mildon et al., subm.). On a millennial time scale, slip rate variability has been recognised in active extensional areas such as the Mediterranean (e.g., Nixon et al., 2016). Slip rates derived from geological throw show significant along-strike variability, with slip rate often increasing away from fault tips towards a central maximum. Recent work has also demonstrated that slip rate on active faults may be elevated within fault bends (e.g., Iezzi et al., 2018).

There are several published examples of increases and decreases in slip rate during the lifetime of faults within a fault network (Fig. 1; Cowie, 1998; Mayer et al., 2002). Mayer et al (2002) demonstrated across strike changes in slip rate for several faults from the Timor Sea, NW Australia (Fig. 1a). Slip rate was observed to increase on one fault, whilst decreasing on another. For example, over the time periods of 6 to 4 Ma and 4 to 2.8 Ma, slip rate on the yellow fault decreases as the orange fault increases. However, changes in slip rate may vary through time, as indicated by the orange fault in Fig. 1a.

Temporal and spatial variations in slip rate have also been observed in numerical models (Fig. 1b). To demonstrate this, we show the slip-history at two points (A and B; Fig. 1b) within a fault system derived using a thin-plate elastic brittle model by Cowie (1998). On average, point B displays a higher slip rate (50.5 mm/yr) than A (38.2 mm/yr) over the model run (Fig. 1b-i). However, where changes in the slope of the cumulative displacement curves are considered (i.e., higher resolution sampling) a more complex slip-history is observed (Fig. 1b-ii). For most of the model point A slipped quicker than B; however, this is not always the case with periods of time where B was quicker than A. This is attributed to a combination of elevated displacement rates on optimally orientated fault strands (point B) and episodic slip behaviour caused by elastic-brittle failure and healing processes (Cowie, 1998). Whether this switching behaviour is observed is dependent on the time period that slip rate is calculated over (Fig. 1b-iii, iv). When the sampling time period is too long (e.g., 200kyr; Fig. 1b-iii), subtle switches in slip rate may be missed, or the length of time the switch occurred over may be overestimated. This could lead to an over- or under-estimate of the seismic hazard posed by the fault during that time interval.

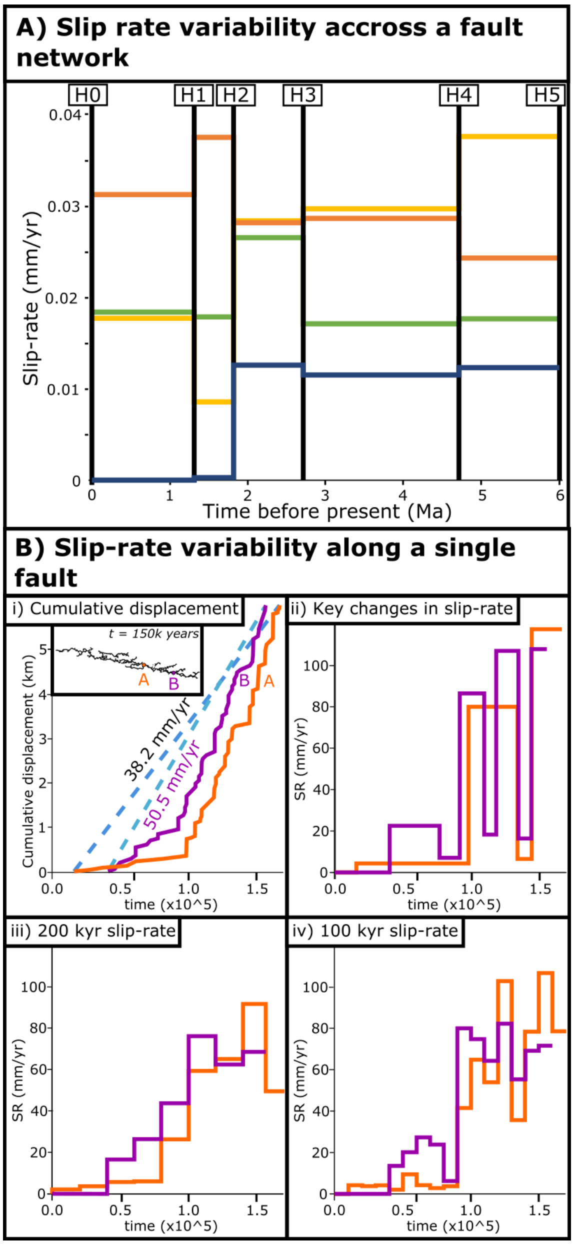

Figure 1: Temporal and spatial variations in slip rate. A) Maximum slip rate through time for a sub-section of the fault network presented in Mayer et al., 2002. Individual faults are represented by different colours. H0-5 are different stratigraphic horizons, representing different intervals in time. B) Cumulative displacement and slip rate measured across different time windows for two sample points in a numerical model of fault growth by Cowie 1998. Points are indicated on the inset within the 'cumulative displacement' subpanel (i).

To enable the investigation of the spatial and temporal variability of slip rate on normal faults over millennial time scales we study syn-sedimentary faults present in the high resolution Chandon3D seismic survey, offshore NW Australia. Rifting between the Late Triassic-to-Jurassic and base Cretaceous caused a network of ~N-S striking normal faults to develop that display complex slip-histories (Bilal and McClay et al., 2022). By measuring displacement across several age-constrained horizons every ~100 m along fault strike, it is possible to deduce how slip rate varied both spatially and temporally for the same fault/fault network (Fig. 2a).

Slip rate variability across a single fault

The single fault is a 16 km long, westerly dipping, structure that is part of a fault system running through the centre of the study area (Fig. 2a). Fault strike ranges from 000˚ to 040˚ (average 015˚), with maximum displacement across the base syn-rift horizon located close to the centre of the fault (D_{max} = 552 m, x = 9.9 km) (Fig. 2b). D_{max} is not located at the same position on the fault for each mapped horizon. For example, D_{max} along the end-rift horizon (211 m) is located 1.6 km to the south of the D_{max} across the base syn-rift (Fig. 2b). This variability affects the slip rate distributions. Slip rate has been calculated for four time periods from fault initiation to the end of active rifting (Fig. 2c-f). For the first 17.5 Ma of the fault's life (209.5 to 192 Ma; Fig. 2c), slip is observed across nearly the whole fault. Slip rates were high, with maximum slip rate (0.0139 mm/yr) located close to the centre of the fault and elevated slip rates observed within the central fault bend. Between 192 and 170 Ma, the fault slowed by a factor of 2 (maximum slip rate = 0.0063 mm/yr). Whilst maximum slip rate is located to the north of the fault, there is only a single datapoint with elevated slip rate, and areas of higher slip rate are also located in a similar position to the 209.5 to 192 Ma time period. It is therefore likely that this represents an outlier caused by low throw at this sample point across the 170Ma horizon. Between 170 and 142.3 Ma, the fault slowed by a factor of 2 again (maximum slip rate = 0.0031 mm/yr), with slip rate decreasing in the south of the fault and the magnitude of elevated slip rate within the central fault bend decreasing relative to earlier time periods. During the final stage of active rifting (142.3 to 137.3 Ma), the fault sped up with a maximum slip rate of 0.0494 mm/yr. However, unlike previous time periods, the location of elevated slip rate migrates 2.4 km northwards from the centre and some datapoints to the south do not display any slip rate suggesting that section of the fault is no longer active. Overall, the magnitude and location of slip rate along the single fault varies through time.

Slip rate variability across a fault network

Fault properties were extracted from a set of kinematically linked faults to the North of the study area (Fig. 2a; 3) using orientated sample lines and 9 age constrained horizons. Most of the throw across the network is taken up on Faults 1-3, with Fault 6 increasing in displacement as you move towards the south. Other faults in the network have <75 m displacement across the measured sample lines, with the majority being <45 m. Across each sample line the cumulative slip rate across all faults is higher between 140 and 137.3 Ma compared to 209.5 and 200 Ma, with the greatest increase observed on SL2 (0.053 mm/yr increase) (Fig. 3b, inset). Between these times periods, each sample line displays intervals of acceleration and deceleration (Fig. 3b). For example, SL1 displays an initial decrease in slip rate from 0.01 to 0.005 mm/yr, followed by steady increases in slip rate between 192 and 170 Ma. Between 170 and 142.3 Ma, the fault

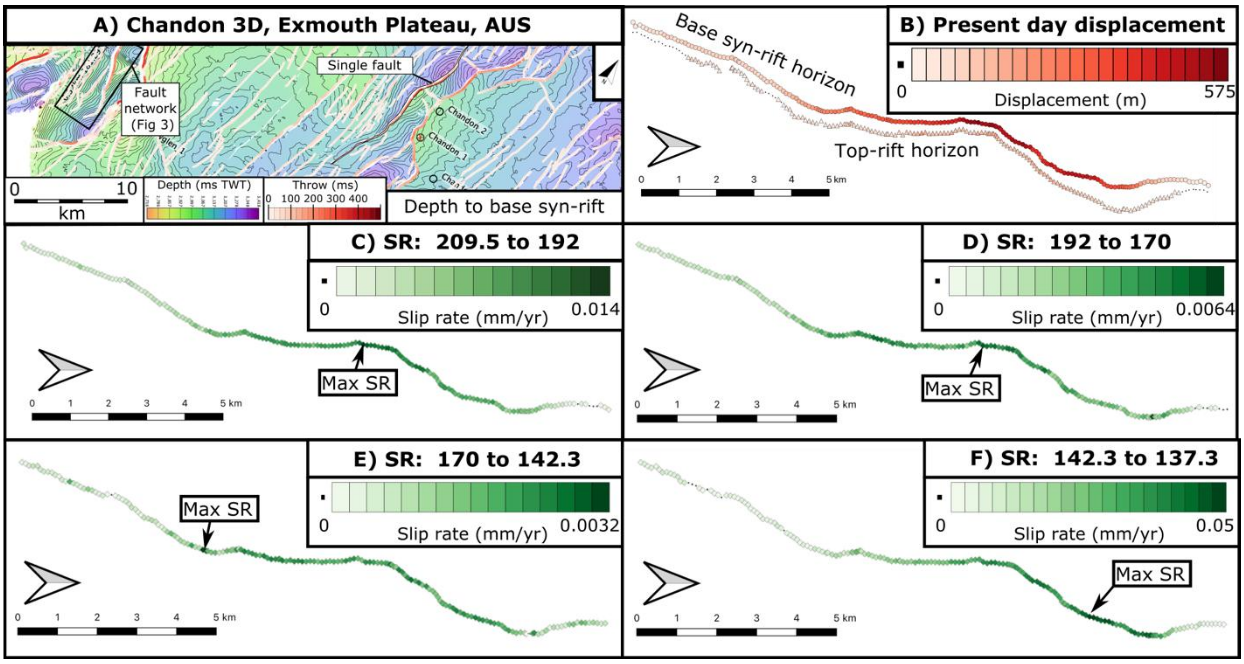

Figure 2 (above): *Slip rate variations along a single fault. A) Depth to base syn-rift showing the distribution of throw across the study area. B) Throw across each syn-rift horizon for the single fault identified in (A). C-F) Slip rate at each measurement point along the single fault, with the location of maximum slip rate (SR) indicated. Note: the differences in colour scales between panels. Note the variability in slip rate within and between time periods, as well as the location of maximum slip rate.*

Figure 3 (below): *Slip rate variations across a fault network. A) Fault polygons for the base syn-rift horizon showing the location of sample lines and studied faults. The colour of each fault is consistent across the entire figure. B) Slip rate changes through time for faults along sample lines (SL) 1-4. The inset on each panel indicates whether the slip rate speeds up or slows down. C) Slip rate profiles across three time periods.*

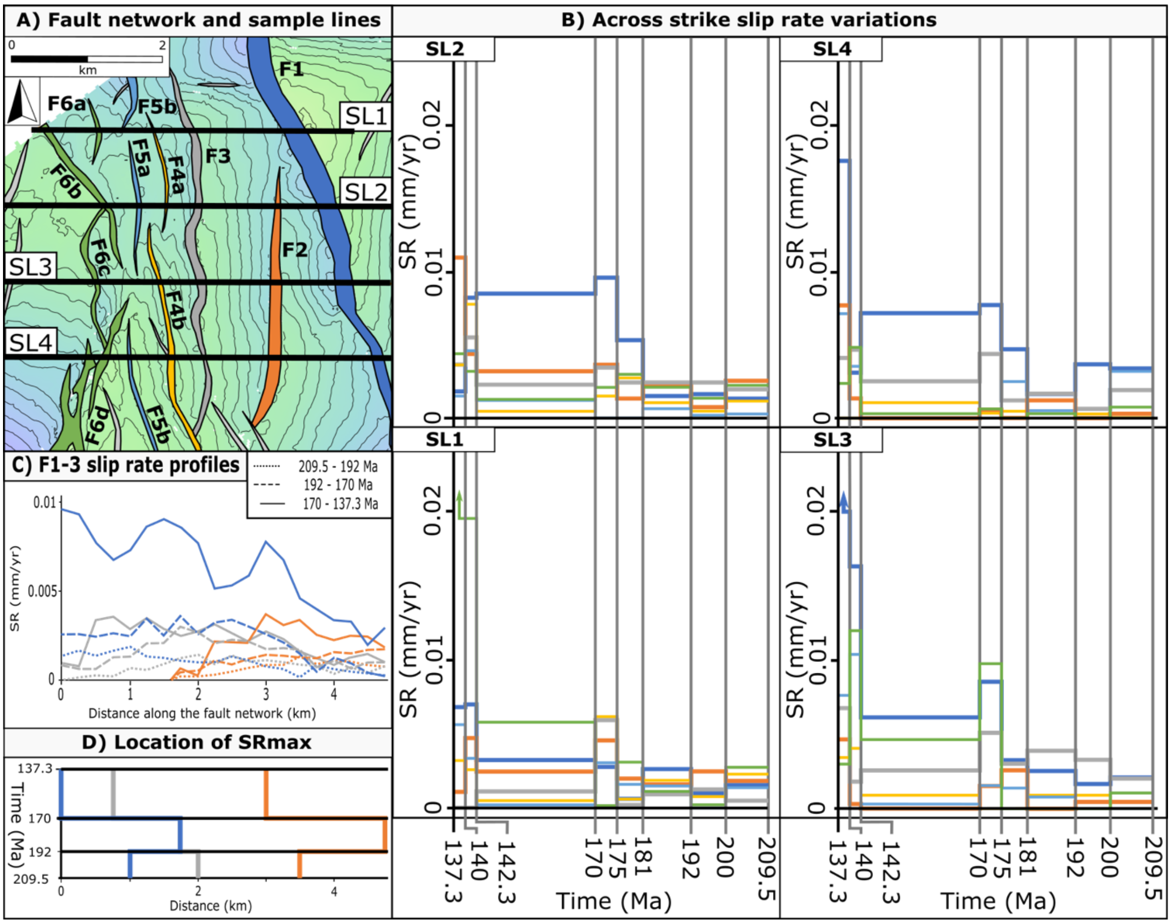

Network slowed, before accelerating again up to the end of active rifting. A deceleration of the fault network between 170 and 142.3 Ma is observed across all sample lines; however, not all changes in cumulative slip rate are consistent with the deceleration between 200 and 192 Ma not being present on SL2 where the fault network accelerates by 0.001 mm/yr.

Individual faults within the fault network may accelerate or decelerate through time (Fig. 3b). For example, Fault 1 accounts for 14% of the cumulative slip rate across SL3 for the 209.5 to 200 Ma time period, compared to 51% for the 170 to 142.3 Ma time period. For the same time periods, Fault 3 contributes 27% and 19% of the cumulative slip rate, highlighting inconsistencies in the way slip is partitioned across the network over time. Where single faults are compared across a sample line, the proportion of cumulative slip taken up by that fault varies. For example, Fault 1 takes up 35%, 38%, 14% and 16% of the slip between 209.5 and 200 Ma for SL1-4 respectively. Across the 170 to 142.3 Ma time period, the corresponding values are 64%, 43%, 51% and 25%. Therefore, it should be noted that the absolute slip rate, as well as proportion of the cumulative slip rate taken up by an individual fault, varies both through geological time and along strike.

To further explore along-strike variability, slip rate was calculated for Faults 1-3 at 250 m intervals along the fault network (Fig. 3c). The location of maximum slip rate (SR_{max}) are located at different locations of a fault at different time periods (Fig. 3d). For example, SR_{max} for Fault 2 is initially located at 3 km along the fault network, before moving ~1.7 km to the south during the 192 to 170 Ma time period followed by a 1.25 km shift to the south during the final 32.7 Ma of fault slip. Similar observations may be observed for slip rate minima, suggesting the position of slip rate minima and maxima may be short lived over geological timescales. Where the across-rift and along fault profiles are compared, a large proportion of the slip rate acceleration occurs following 140 Ma, with the slip rate between 170 to 142.3 Ma similar to the previous time periods. This demonstrates the importance of the time period where slip rate is calculated over.

Conclusions

Our data demonstrates that slip rate measurement along single faults, and fault networks, display high spatial and temporal variability. Where multiple faults are considered, we show that the location and magnitude of slip rate varies across the network through geological time, with changes in slip behaviour observed over <10 Ma time periods. Due to sampling constraints (e.g., funding, viable geological conditions, time) the number of slip rate measurements present along active faults is often limited, sometimes to a single datapoint. Additionally, the measurement of 'recent' slip rate may differ greatly from the slip rate at the same location in the past, and therefore may not be a reliable indicator of future fault slip rate. Further work using high resolution, age constrained, seismic reflection datasets will provide greater constraint on the optimum number and location of slip rate measurements required to classify the slip rate profile of faults over Myr time scales, with similar patterns likely to be also relevant to the Holocene slip history derived from ^{36}Cl and paleosesmic trenching. The complex slip rate evolutions observed in this study suggests that individual slip rate measurements may not be sufficient to classify the seismic hazard posed by an active fault, and that this hazard may change in the future due to changes in fault interaction.

Acknowledgements: Funding was provided by UKRI as part of the Future Leaders Fellowship "Quake4D" (MR/T041994/1) awarded to Zoë Mildon. We acknowledge DUGInsight for provision of the seismic interpretation software.

REFERENCES

Benedetti, L., Manighetti, I., Gaudemer, Y., Finkel, R., Malavieille, J., Pou, K., Arnold, M., Aumaître, G., Bourlès, D. and Keddadouche, K., 2013. Earthquake synchrony and clustering on Fucino faults (Central Italy) as revealed from in situ 36Cl exposure dating. *Journal of Geophysical Research: Solid Earth*, *118*(9), pp.4948-4974.

Bilal, A., McClay, K., 2022. Tectonic and stratigraphic evolution of the central Exmouth Plateau, NW Shelf of Australia. *Marine and Petroleum Geology* 136, 105447.

Cowie, P.A., Phillips, R.J., Roberts, G.P., McCaffrey, K., Zijerveld, L.J.J., Gregory, L.C., Faure Walker, J., Wedmore, L.N.J., Dunai, T.J., Binnie, S.A. and Freeman, S.P.H.T., 2017. Orogen-scale uplift in the central Italian Apennines drives episodic behaviour of earthquake faults. *Scientific Reports*, *7*(1), pp.1-10.

Cowie, P.A., 1998. A healing–reloading feedback control on the growth rate of seismogenic faults. *Journal of Structural Geology*, *20*(8), pp.1075-1087.

Iezzi, F., Roberts, G., Faure Walker, J., Papanikolaou, I., Ganas, A., Deligiannakis, G., Beck, J., Wolfers, S. and Gheorghiu, D., 2021. Temporal and spatial earthquake clustering revealed through comparison of millennial strain-rates from 36Cl cosmogenic exposure dating and decadal GPS strain-rate. *Scientific reports*, *11*(1), pp.1-12.

Iezzi, F., Mildon, Z., Faure Walker, J., Roberts, G.P., Goodall, H., Wilkinson, M. and Robertson, J., 2018. Coseismic throw variation across along-strike bends on active normal faults: Implications for displacement versus length scaling of earthquake ruptures. *Journal of Geophysical Research: Solid Earth*, *123*(11), pp.9817-9841.

Meyer, V., Nicol, A., Childs, C., Walsh, J.J. and Watterson, J., 2002. Progressive localisation of strain during the evolution of a normal fault population. *Journal of Structural Geology*, *24*(8), pp.1215-1231.

Mildon, Z.K., Roberts, G.P., Faure Walker, J.P., Beck, J., Papanikolaou, I., Michetti, A., Toda, S., Iezzi, F., Campbell, L, McCaffrey, K.J.W., Shanks, R., Sgambato, C., Robertson, J., Meschis, M., Vittori, E., (subm. to Nat. Comms.), Surface faulting earthquake clustering controlled by fault/shear-zone interactions. Preprint available on EarthArXiv (https://eartharxiv.org/repository/view/597/).

Nixon, C.W., McNeill, L.C., Bull, J.M., Bell, R.E., Gawthorpe, R.L., Henstock, T.J., Christodoulou, D., Ford, M., Taylor, B., Sakellariou, D. and Ferentinos, G., 2016. Rapid spatiotemporal variations in rift structure during development of the Corinth Rift, central Greece. *Tectonics*, *35*(5), pp.1225-1248.

Pace, B., Visini, F., Scotti, O. and Peruzza, L., 2018. Preface: Linking faults to seismic hazard assessment in Europe. *Natural Hazards and Earth System Sciences*, *18*(5), pp.1349-1350.

Vertical slip-rate on the Shibetsu fault zone in the most eastern part of Hokkaido, Japan

Takashi, Azuma (1)

(1) Geological Survey of Japan/AIST, Site Central 7, Higashi 1-1-1, Ibaraki Prefectura 305-8567 Japan . Email: t-azuma@aist.go.jp

Abstract: *The Shibetsu Fault Zone is a NE-SW trending reverse fault along the south-eastern margin of the Shiretoko Peninsula. This area is one of the most active volcanic zone and there are several calderas, which erupted catastrophic eruptions during the middle to the late Pleistocene period and early Holocene. Flexural scarps are recognized on the fluvial fans, which were produced in the last glacial period or rather older age. Vertical slip-rate of this fault zone are estimated as ca. 0.3 m/ky based on amount of vertical displacement by using DEM data and age of fans inferred from tephrochronology in this area.*

Key words: *Shibetsu fault zone, slip-rate, 14C dating, tephrochronology, Hokkaido*

INTRODUTION

Purpose

Fault parameters on the Shibetsu Fault Zone were not obtained although the local government of Hokkaido Prefecture had conducted active fault surveys, including drilling, trenching and seismic profiling, between 2002 and 2004. Therefore, the probability of occurrence of large earthquakes from this fault zone was unknown and it is a problem for establish of the National Seismic Hazard Map and the probabilistic seismic hazard assessment in Japan. We had opportunities to survey this fault zone in 2018, 2020 and 2021. This paper is a report of our surveys.

Geological Setting

Shibetsu Fault Zone is located on the south-eastern margin of the Shiretoko Peninsula in the most eastern part of Hokkaido (Figure 1). Shiretoko Peninsula is one of volcanic zones, that are located upthrown side of the Kuril subduction zone. Volcanic zones are lined with NE-SW trend, obliquely against the subduction zone. Several large calderas, such as Kussharo, Mashu and Akan, are distributed in the south-eastern part of the Shiretoko Peninsula. These calderas has a history of large eruptions during the middle/late Pleistocene and Holocene. In the northern part of this peninsula, steep scarps surround coast and marine terraces are distributed. In the southern part, fans and fluvial terraces are distributed along the topographic boundary between mountains and plains. And some of surfaces are composed of pyroclastic-flow deposits from calderas.

Active Fault Traces

Research Group for Active Fault in Japan (1991) published an active fault map in this area, which showed both side of the Shiretoko Peninsula were bounded by active reverse faults. On the south-eastern side, they mapped 4 fault traces, Maruyama, Kotanuka, Kaiyo and Arakawa-Paushibetsu, from northeast to southwest, respectively. All of these faults are reverse faults and up-thrown side is northwest. They described these faults displace higher fluvial terraces of the middle Pleistocene and lower fan terraces of the Last Glacial period in the late Pleistocene. However slip-rate of these faults were not discussed because reliable age data was not obtained at that time.

Tephrochronology in the eastern Hokkaido

From calderas in the southern part of the Shiretoko Peninsula, lots of volcanic materials erupted and felled on the fans and fluvial terraces in the affected area. Older pyroclastic frow deposits from the Kussharo Caldera in the late Pleistocene period were overlayed by fan gravels. Age of "Kussharo I" is ca. 40 ka and "Kussharo IV" is ca. 110 ka. Fan gravels were overlayed by pyroclastic deposits and pumice fall units erupted from the Mashu Caldera during the late Pleistocene and Holocene. Furthermore, some of the wide-spread ash, such as Aso-4 (ca. 90 ka) and Shikotsu (ca. 40 ka), were recognized in the these volcanic and fluvial sediments in this region. These tephra layers are key-layers for estimation of the ages of landforms.

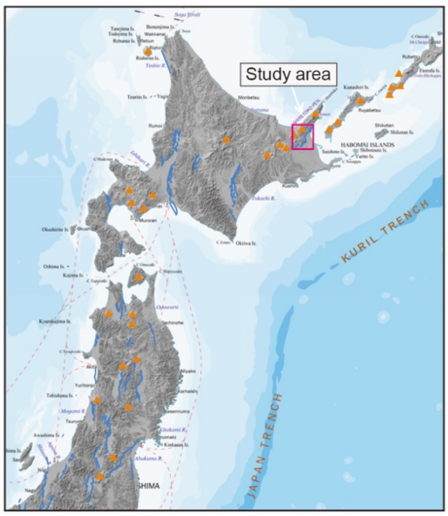

Figure 1: Location map of the study area in the eastern part of Hokkaido, Japan. Triangles shows location of Quaternary volcanos. Blue lines are fault trace of the major fault zone by HERP. Base map is after GSI Map.

SURVEYS

We conducted 1) Airboene LiDAR measuring, 2) paleoseismological trenching surveys, and 3) drilling surveys on the Shibetsu Fault Zone. Locations of survey sites are shown in figure 2.

Airborne LiDAR Survey

In order to recognize detailed tectonic landforms along the Kotanuka fault, we conducted an airborne LiDAR survey in 2018. Those data shows existence of several small scarps on a tectonic bulge (figure 3) and topographic features of small landslides and fault scarps. And other topographic data based on a previous LiDAR data shows fault scarps trending NS direction on the lower fluvial terraces in the plain. Up-thrown side is west and length is ca. 2 km. We named this active fault as the Higashi-Kotanuka fault. Additionally, we conducted UAV LiDAR survey on the Kaiyo fault for considering a trenching site although we didn't excavate a trench there.

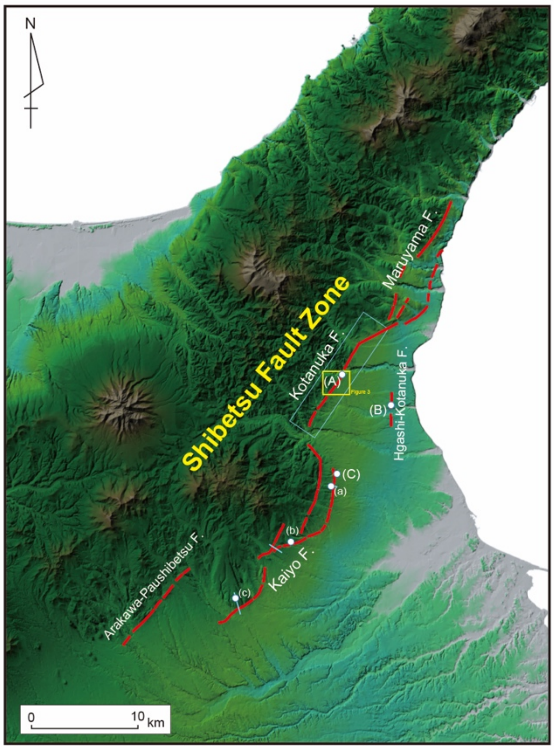

Figure 2: Active fault traces of the Shibetsu Fault Zone and locations of our survey sites. Red lines are active fault traces after HERP (2005). Names of active faults are after the Research Group for Active Faults of Japan (1991). Open box with light-blue line shows the area of the Airborne LiDAR Survey. Open box with yellow line shows location of figure 3. Circles with letters of (A)-(C) show locations of paleoseismological trenching sites. Circles with letters of (a)-(c) show locations of drilling survey sites. Base map is produced in the online mapping system of GSI Map (https:// maps.gsi.go.jp/)

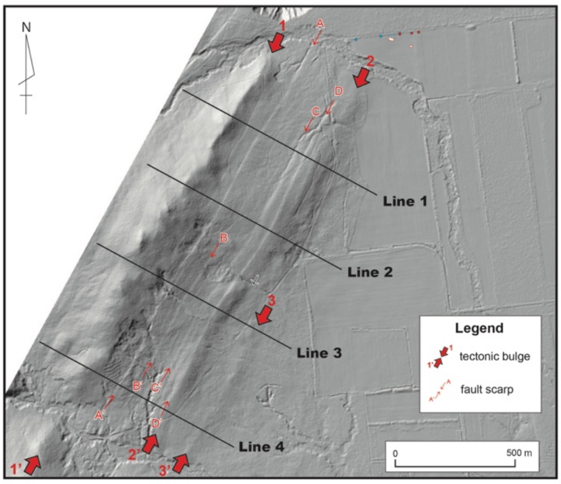

Figure 3: Detailed shade map along the Kotanuka fault. Shade map is produced by using 2 m DEM, a part of results of our air-borne LiDAR survey. Thick arrows with numbers 1-1'to 3-3' are showing locations of topographic anticlinal axis along the Kotanuka fault. Thin arrows with letters A-A' to D-D' are showing ends of small scarps facing NW, which may be produced by faulting related to bedding-slip caused by growth of fold of geological layers in the hanging wall of the Kotanuka fault.

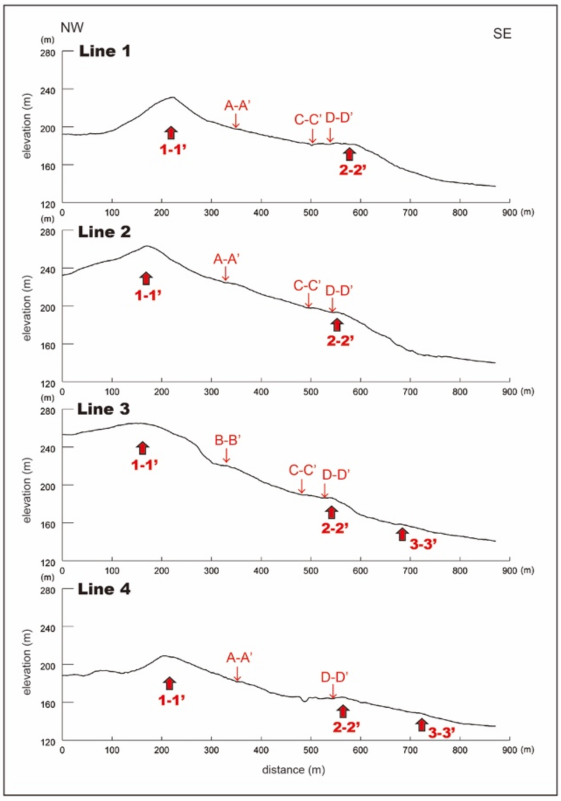

Figure 4: Topographic profiles of line 1-4 across Kotanuka fault. Profiles are produced by using 2 m DEM, a part of results of our air-borne LiDAR survey. Thick arrows with numbers 1-1' to 3-3' are showing locations of topographic anticlinal axis, whereas thin arrows with letters A-A' to D-D' are showing ends of small scarps facing NW. Locations of profile lines are shown in figure 3.

Paleoseismological Trenching Survey

We excavated 2 trenches on the Kotanuka fault (trench A) and the Higashi-Kotanuka fault (trench B) in 2018 and 1 trench on the Kaiyo fault (trench C) in 2021. Location of each trench site is shown in figure 2. We found a faulted structure in the trench on the Higashi-Kotanuka fault (trench B), but could not in other trenches. A fault in the trench B cut a pumice layer of Ma-l (ca. 13-14 ka) and was covered with another pumice layer of Ma-ghi (ca. 5-7 ka). Dip angle of this fault is almost vertical and it displaced a pumice layer of Ma-l about 0.5 m. Based on the lined drilling survey on this site shows amount of vertical offset of top of the gravel layer was 2.6 m. It indicates faulting events have occurred repeatedly since the late Pleistocene period. At the trench A site on the Kotanuka fault, fault structure was not observed on the trench walls. Drilling survey at this site reveals that the bottom of a layer of terrace gravels was vertically deformed. Trench C was excavated along the Kaiyo fault but it was not on the fault trace unfortunately.

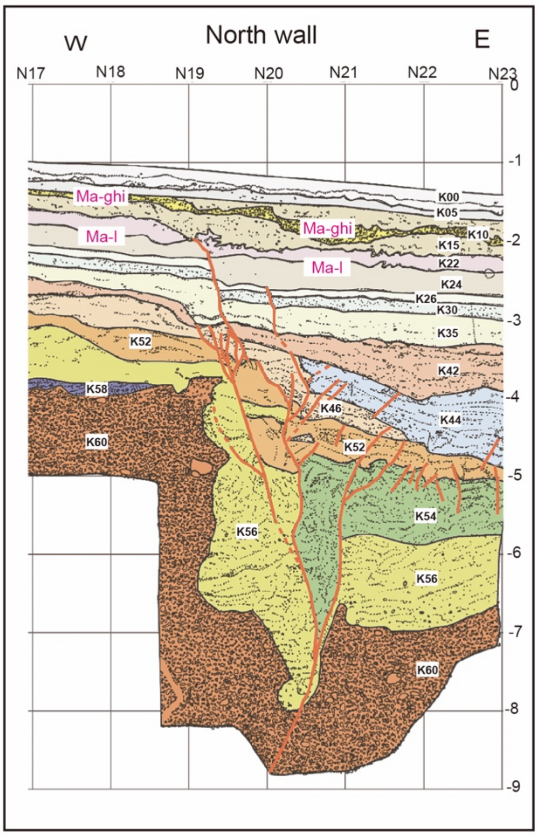

Figure 5: Sketch of the north wall of trench B excavated on the Higashi-Kotanuka fault. Dip of the fault plane is almost vertical. Pumice layer of Ma-l (ca. 13-14 ka) was vertically displaced with ca. 50 cm (west-side was uplifted), whereas Ma-ghi (ca. 5-7 ka) covered faulted structure. Accumulation of displacement was recognized at this site although those age could not be inferred because of absence of dating materials in the lower part of this trench wall.

Drilling Survey

In order to estimate ages of deformed fans and terraces, we conducted drilling surveys to observe tephra layers and to obtain ^{14}C dating samples. 3 sites, including Kawakita (a), Musa (b), Mataochi (c), were selected. Location of each drilling site is shown in figure 2. At Kawakita site (KK-05: 6 m), 2 m of aeolian loams were deposited before Ma-l eruption. This aeolian loam is not include Kussharo I (ca. 40 ka), indicating this terrace was formed after 40 ka. At Musa site (MS-01: 5 m), significant tephra layer was not observed in the drilling core, but there was the Atosanupuri Ash (ca. 30 ka) in the middle of aeolian loam layer on the outcrop (MS-02), indicating the age of this fan was 30-40 ka. At Mataochi site (MO-01: 10 m), the thickness of both of tephra and aeolian loam layers were ca. 5 m, indicating the age of this higher terrace was in the middle Pleistocene (ca. 150-200 ka).

Discussion

Distribution of Tectonic Landforms

Topographic analysis using the LiDAR DEM data lead to find a new fault trace of the Higashi-Kotanuka fault in the plain. From the result of trenching survey, this is not a reverse fault but the fault plane is almost vertical. It might be a strike-slip fault although we could not any evidence of strike-slip component of this fault in the trench. Along the Kotanuka fault, we found several traces of fault scarps on the tectonic bulge. Most of these scarps face to NW, which may be produced by faulting related to bedding-slip caused by growth of fold of geological layers in the hanging wall of the Kotanuka fault.

Faulting History

We obtained data of faulting history at only one site of our paleoseismological trenching surveys. Trench B on the Higashi-Kotanuka fault shows the last faulting event occurred between eruptions of Ma-ghi and Ma-l. Based on results of the ^{14}C dating, it occurred between 7,939 – 13,793 cal. yBP. Ages of older events could not be estimated although accumulated displacement was observed based on drilling survey at this site. Along the main trace of the Shibetsu Fault Zone, including Maruyama, Kotanuka, Kaiyo, Arakawa-Paushibetsu faults, we could not obtained any information about faulting history. That is still serious problem for the seismic hazard assessment of the Shibetsu Fault Zone and area in the eastern Hokkaido.

Vertical Slip-rate

We calculated vertical slip-rate on 3 sites, Kawakita, Musa, and Mataochi, along the Kaiyo fault. At Kawakita site, vertical displacement of fluvial terrace is measured as ca. 10 m (X-X' in figure 6). The age of formation of this terrace is estimated after 40 ka based on tephrochronological analysis, so that vertical slip-rate at this site is calculated as > 0.25 m/ky. At Musa site, vertical displacement of fun surface is measured as ca. 10 m (Y-Y' in figure 6). The age of formation of this fun is estimated 30-40 ka, so that vertical slip-rate at this site is calculated as 0.30-0.25 m/ky. At Mataochi site, vertical displacement of higher terrace is measured as ca. 52 m (Z-Z' in figure 6). The age of formation of this terrace is estimated 150-200 ka, so that vertical slip-rate at this site is calculated as 0.35-0.26 m/ky.

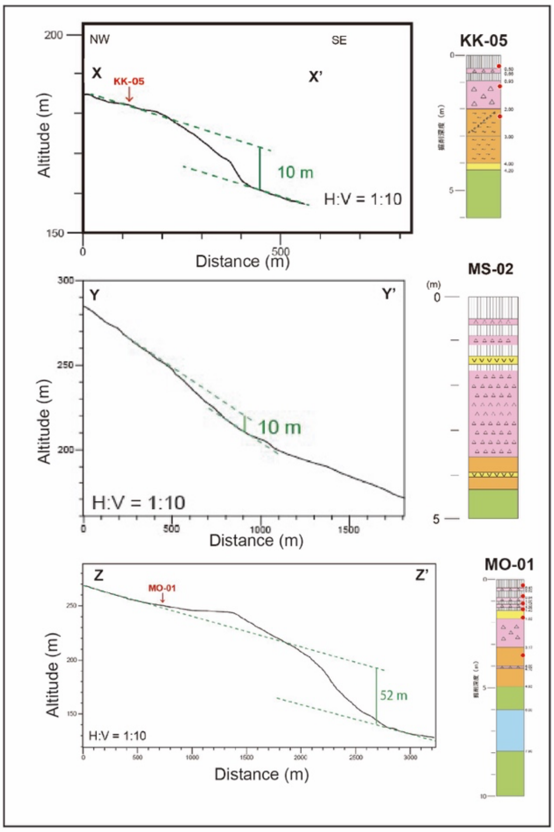

Figure 5: Topographic cross-sections and amount of vertical displacements across tectonic landforms along the Kaiyo fault. Vertical exaggeration is 1:10.

CONCLUSION

We surveyed the Shibetsu Fault Zone for 3 years and obtained new information and fault parameters as follow;

(1) A new fault trace are recognized in the plain of Shibetsu area, which trends NS direction and has almost vertical fault plane. And several small fault scarps were recognized along the Kotanuka fault based on the detailed topographic data obtained by the airborne LiDAR survey.

(2) Age of the last faulting event of the Higashi-Kotanuka fault occurred between 7,939 – 13,793 cal. yBP. However any fault history information on the main trace of this fault zone was not obtained by our surveys.

(3) Vertical slip-rate on the Kaiyo fault is calculated as ca. 0.3 m/ky based on amount of vertical deformation of fluvial terraces and fans and age of those landforms based on tephrochronology in this area.

Slip-rate will allow a estimation of the probabilistic seismic hazard assessment of this fault zone although it is not a time-dependent model. There are other problems, such as a relationship between the occurrence of earthquakes on active faults and mega earthquakes in the subduction zone and/or huge volcanic eruptions.

Acknowledgements: Fund of our surveys are from MEXT as projects of "Survey on active faults on-land and off-shore in 2018" and "Survey for the progress of active fault evaluation in 2020 & 2021". We thank for kind supports of researchers in Hokkaido prefecture and officers in a local government of Shibetsu town.

REFERENCES

Azuma, T., Hirouchi, D., & Okumura, K., 2019. Recognition of parallel scarps along the Kotanuka fault of the Shibetsu fault zone, eastern Hokkaido, revealed by an airborne LiDAR survey. Annual Report on Active Fault and Paleoearthquake Researches (19), 61-69. (in Japanese with abstract in English)

Earthquake Research Committee of Headquarters of Earthquake Research Promotions in Japan, 2005. Long-term evaluation for the Shibetsu Fault Zone. http://www.jishin.go.jp/main/chousa/katsudansou_pdf/01_shibetsu.pdf (in Japanese)

Hokkaido Prefecture, 2003. Report on the active fault surveys for Tokachi, Furano and Shibetsu Fault Zones in 2002. (in Japanese)

Hokkaido Prefecture, 2004. Report on the active fault surveys for Tokachi, Furano and Shibetsu Fault Zones in 2003. (in Japanese)

Hokkaido Prefecture, 2005. Report on the active fault surveys for Shibetsu and Furano Fault Zones in 2004. (in Japanese)

The Research Group for Active Faults of Japan, 1991. Active faults map of Japan -sheet maps and inventories-. University of Tokyo Press, Japan, 473p. (in Japanese with abstract in English)

Qualitative and quantitative assessment of a lake sensitivity to paleoseismic events in the NW Alps

Banjan, Mathilde (1,3), Christian Crouzet (1), Erwan Messager (2), Pierre Sabatier (2), Hervé Jomard (3), Ludmila Provost (3), Aurore Laurendeau (3)

(1) Institut des Sciences de la Terre, Université de Savoie, 73376 Le Bourget du Lac, France
(2) EDYTEM, Université de Savoie/ CNRS, 73376 Le Bourget du Lac, France
(3) Institut de Radioprotection et de Sureté Nucléaire, BERSSIN, 92260 Fontenay aux Roses, France

***Abstract:** Several mass movement deposits in western alpine lakes were identified as homogenites deposits related to seiche. New multiproxy data from Lake Aiguebelette sediments highlight the presence of 33 homogenites. Age-depth modelling based on short-lived radionuclides, varve counting, paleomagnetic data and radiocarbon ages, constrain the sediment time of deposition. Historical homogenites archived in Lake Aiguebelette cores are of similar age to events in the seismic catalogs. Lake Aiguebelette seems sensitive to strong and distant seismic events.*

The Pseudo-Spectral Acceleration (PSA) is a parameter of choice to better understand Lake Aiguebelette's sensitivity to earthquakes. For low frequencies input, highest PSA values are obtained (through Ground Motion Prediction Equations (GMPE)) for seismic events with high Mw and distant to the lake location. For a given GMPE and lake location, the frequency seems to be a determining parameter in the assessment of a lake sensitivity to seismic events.

***Key words**: paleoseismicity, lacustrine, homogemite, GMPE, frequency, models*

INTRODUCTION

Lake sediments are valuable archives for reconstructing seismic chronicles. In the perialpine area, several mass movement deposits have been archived and some of them were potentially triggered by earthquakes (Chapron et al., 1999; Strasser et al., 2006; Wilhelm et al., 2016; Kremer et al., 2017). At the junction between the Jura Mountains and the western Alpine domain, several active faults have been recognized (e.g. the Col du Chat and Vuache faults *(Figure 1)*, (Baize et al., 2011; de la Taille et al., 2015; Jomard et al., 2017)). Major historical and instrumental events could be related to the activity of the faults, such as the 1822 CE Bugey earthquake which probably occurred along the Culoz fault with an estimated Mw=5.5±3 or the 1996 Epgny earthquake (Mw=4.9), triggered along the Vuache fault (Manchuel et al., 2018).

Several studies show that the number of earthquake-triggered mass movement deposits varies between lakes of a same region. The variability between lakes' sequences suggests a different sensitivity to seismically-induced instabilities (Moernaut et al., 2014; Van Daele et al., 2015; Wilhelm et al., 2016). The main factors controlling a lake's variation in sensitivity are the sedimentation rates and slope recharge capabilities (Wilhelm et al., 2016). To this day, a wider lake compilation is required to better understand the relationship between lake sensitivity and earthquake shaking.

The aim of this work is to (1) improve the lacustrine paleoseismic catalog and (2) better understand a perialpine lake sensitivity to earthquake shaking (with the use of Pseudo-Spectral Accelerations), in a moderately active seismotectonic region.

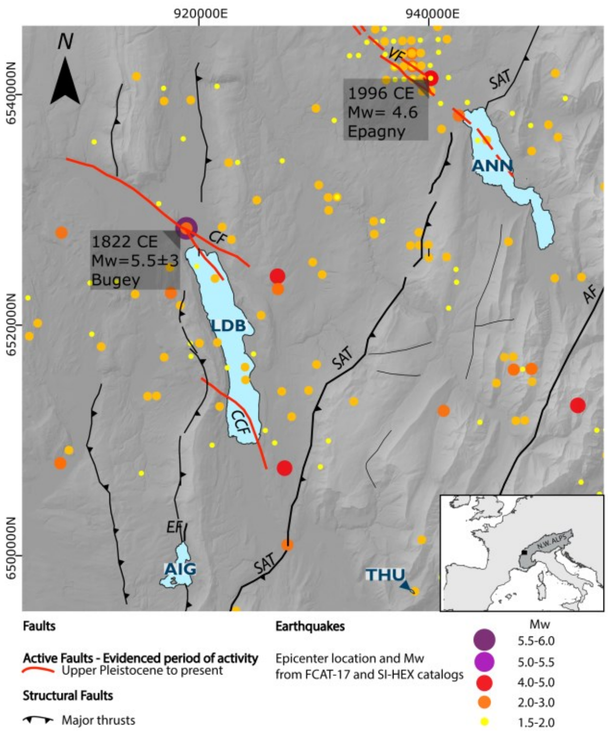

Figure 1: Seismicity map of the NW Alps at the border with the French Jura Mountains. Epicenter locations and magnitudes are based on the FCAT-17 and SI-HEX databases (Cara et al., 2015; Manchuel et al., 2018). The main active faults from the Upper Pleistocene are presented in red (CF: Culoz Fault; CCF: Col Du Chat Fault; VF: Vuache Fault). Lakes Aiguebelette (AIG), Annecy (ANN), Bourget (LDB) and La Thuile (THU) are presented in blue in the digital terrain model (IGN RGE ALTI 1 m). Projection: Lambert-93 (EPSG 2154).

STUDY SITE: LAKE AIGUEBELETTE AND ITS WATERSHED

Lake Aiguebelette is a postglacial perialpine lake located at 373 meters above sea level, in the inner Jura Mountains. The main tributary (Leysse de Novalaise) enters the northern part of the lake. The catchment area (~70km^2) is contrasted by the steep slopes of "Chaîne de l'Epine" covered by forests on the eastern flank of the lake, contrasting with flatter grasslands on the western side. The main lithologies and sediment sources in the watershed are Jurassic and Cretaceous limestones, Neogene sandy molasses and Quaternary Würmian tills *(Figure 2)*. The lake's morphology consists of three subasins. Depths reach up to 45m in the northern basin, 71m in the southeastern basin and 25m in the southwestern basin. Small islets separate the shallow and deep southern basins *(Figure 2; Figure 3)*. (m.s^{-2})

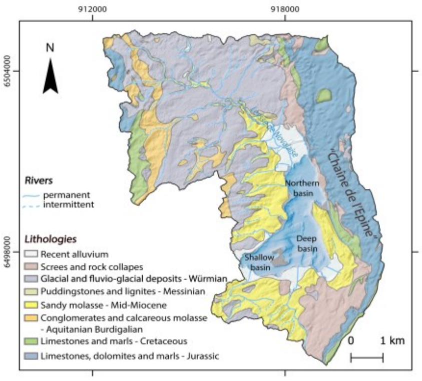

Figure 2: Lake Aiguebelette and its watershed. Colors are related to the geological layers modified from the BRGM 1/50000 regional map. Projection: Lambert-93 (EPSG 2154).

METHODS

This work is based on sediment analyses of 4 cores retrieved in the deepest basin of Lake Aiguebelette (*Figure 3*). Coring locations were selected far from the tributaries to minimize the impact of flood deposits in the sediment sequences.

Visual criteria allow the characterisation event layers, contrasting with background sediment in the sequences and complemented with grain-size and Scanning Electron Microscopy (SEM) analyses. Precise depositional ages are obtained through varves counting and age-depth modelling. The age-depth model is constrained by short-lived radionuclides analyses (^{210}Pb and ^{137}Cs activity profiles), paleomagnetic data (Characteristic Remanent Magnetisation declination-inclination chronological markers) and radiocarbon ages (vegetal macroremains). ^{14}C dates are calibrated with IntCal20 (Reimer et al., 2020).

Magnetic data (isothermal remanent magnetization (IRM)) are used to constrain core-to-core correlations at the scale of Lake Aiguebelette deep basin.

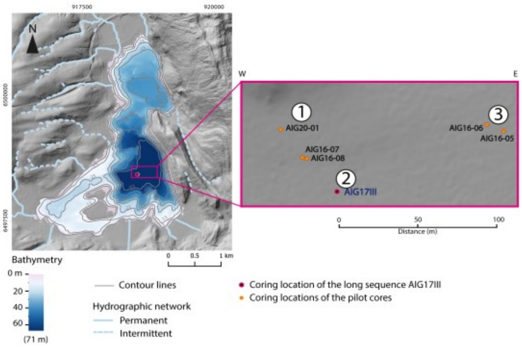

Figure 3: Bathymetric map of Lake Aiguebelette with a rectangle zoom on all cores locationretrieved in the deepest basin (AIG20-01, AIG16-07, AIIG16-08, AIG17III, AIG16-06, AIG06-05).White disks with black borders with digits ①, ② and ③ are associated with cores of interest for this study with characteristics as follows: ① core AIG20-01, radioelement dating; ② core AIG17III, long sequence covering the entire Holocene period; ③ cores AIG16-06 and AIG16-05, bearing the most recent event layers.

Pseudo Spectral Accelerations (PSA) are calculated for all the seismic events available in the French seismic catalog (FCAT-17) (Manchuel et al., 2018), based on Ground Motion Prediction Equations (GMPE) from Bindi et al. (2014) and Akkar et al. (2014). Parameters such as the event magnitude and distance to site (AIG17III coring location's coordinates) are based on the FCAT-17 dataset. Several input parameters are chosen arbitrarily:

- The average seismic shear-wave velocity from the surface to a depth of 30 meters (VS30) is fixed at 800 m/s;
- The focal mechanism for all events is set as strike slip;
- The frequency is chosen as a variable to evaluate its impact on the PSA values.

RESULTS AND INTERPRETATIONS

The analysed sequences are composed of clay-silty sediment. The first ten meters of the 16m-long AIG17III sequence and all pilot cores (AIG20-01, AIG16-05, AIG16-06) from the deep basin are mostly laminated. Varved sedimentation is confirmed by ^{210}Pb,^{137}Cs activity profiles, laminae-counting and SEM analyses where a triplet of laminae is visible (with one Ti-rich lamina, a second Si-rich and a third in Ca-rich), interpreted as yearly deposits providing a precise chronology (Kelts and Hsu 1978; de Vicente et al., 2006; Giguet-Covex et al., 2009).

A total of 33 event layers are interbedded in the continuous sedimentation and are visually identified as homogenite facies in the AIG17III sequence. Previous studies suggest high AMS foliation values are linked to water mass oscillation and subsequent seismically-induced homogenite deposition (Campos et al., 2013). Therefore, high foliation (Anisotropy of Magnetic Susceptibility) values (average of 4% in several event layers identified as homogenites and of 1% in the background sediment) confirm the visual observations and interpretations.

In the first top meter of the pilot cores AIG 16-05 and AIG16-06, seven event layers are identified but not visible in the long AIG17III sequence (probably due to coring issues in the top section of the latter).
Age-depth relationships calculated for the AIG17III sequence reveal the top 10 to 11 m are covering the Holocene (*Figure 4*). Vegetal macroremains were not found at lower depth, for this reason the base of the sequence is not age-constrained.

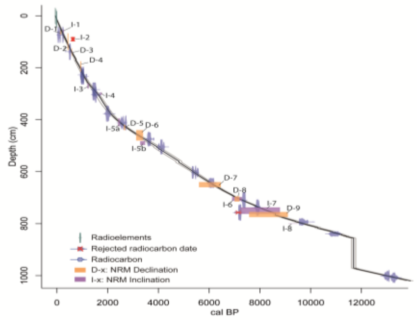

Figure 4: Age-depth model for the long deep basin sequence

The correlation between event layers in the long sequence and pilot cores are based on IRM data peak to peak correlations *(Figure 5)*.
They allow the attribution of a depositional age-range to each event layer, at the scale of the deep basin. Varve counting and radioelement data correlation between pilot cores AIG20-01 and AIG16-05 give a depositional age interval between 1921 and 1927 CE for the top four, successive event layers. A chronicle of event layers at the scale of the Lake Aiguebelette deep basin is now available and compatible with the time range covered by the seismic catalogs.

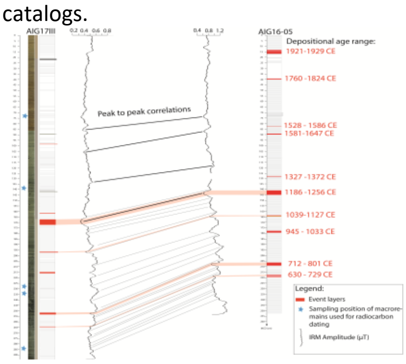

Figure 5: Core-to-core correlation between AIG17III and AIG16-05 sequences, based on IRM data. Depositional age ranges are in red next to each event layer of the sediment sequence AIG16-05.

DISCUSSION

Our results push the discussion towards the attribution of known historical and instrumental seismic events to each event layer (homogenite) archived in the sequence AIG16-05 *(Figure 5)*. It seems promising, knowing that the depositional time range of one of the event layers (1760-1824 CE) is compatible with the occurrence (1822 CE) of the major regional Bugey earthquake (Chapron et al., 1999; Manchuel et al., 2018). In the FCAT-17 catalog, several earthquakes occurred in the same time range as the deposition of AIG16-05's event layers. To narrow down the correlations between event layers and known seismic events, the conceptual diagram "distance of earthquakes to the lake versus epicentral MSK intensity" (*Figure 6*) was used, based on the FCAT-17 catalog and Wilhelm et al. (2016).

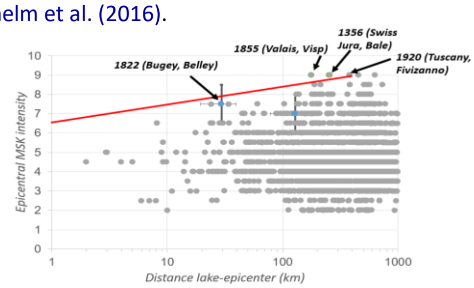

Figure 6: Conceptual diagram "distance of earthquakes to the lake versus epicentral MSK intensity". Grey dots indicate all events from the FCAT-17 catalogs at a distance ≤1000 km from Lake Aiguebelette deep basin. The continuous red line was placed to delimit the potentially recorded from nonrecorded earthquakes (Wilhelm et al., 2016).

None of the seismic events at a distance ≤10 km from the lake or with an epicentral MSK intensity ≤VI is compatible with the event layers (time of deposition) archived in the deep basin sequences. Therefore, the sensitivity threshold was pushed towards events with higher epicentral MSK intensities and greater epicentral distances to the lake. Based on the concept of this diagram, if the uncertainties on the epicentral MSK intensities were considered, (1) the sensitivity threshold (red line on the diagram) could be placed differently or (2) several other seismic events could be potential triggers of the archived event layers in AIG16-05 sequence (e.g. the 1822 CE Bugey earthquake in the diagram, which seems to be a reasonable candidate (*Figure 6*)). In this case, the epicentral intensity might not be the best parameter to estimate Lake Aiguebelette sensitivity to earthquakes, even if, it seems to be more sensitive to strong and distant seismic events (based on the diagram (*Figure 6*)).

Low-frequency seismic waves at Lake Aiguebelette would be characteristic of a distant and strong earthquake whereas high-frequency waves would be characteristic of small and local seismic events (Anderson et al., 1994). To test the sensitivity of Lake Aiguebelette, PSA values were calculated for all seismic events of the catalog FCAT-17, at high and low frequencies (*Figure 7*). For the same seismic event, PSA values are higher for a low frequency input and lower for a high frequency.

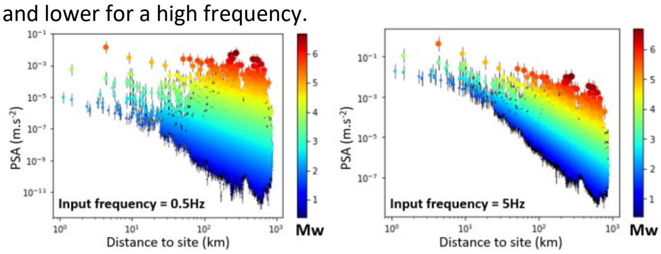

Figure 7: Diagrams: distance of earthquakes to the lake versus calculated PSA values. On the left: with a low frequency (0.5Hz) input, on the right: with a higher frequency (5Hz) input. Dots indicate all events from the FCAT-17 catalog. The colorbar corresponds to magnitude values for each event.

Lake Aiguebelette seems to have more sensitivity to strong and distant seismic events. For a given GMPE and lake location, the frequency (its impact on PSA values) seems to be a determining parameter in the assessment of a lake sensitivity to seismic events.

CONCLUSION

A multi-proxy sediment cores analysis at the scale of Lake Aiguebelette deep basin allowed the identification and robust dating of 33 homogenites (interpreted as seismically-induced: high AMS foliation values). Core-to-core correlations based on IRM data was key to build an event layer chronicle. The depositional age of event layers is compatible with seismic events from the seismic catalog FCAT-17, on the historical period. PSA values calculation for given frequencies seems to be a parameter of choice in the assessment of Lake Aiguebelette sensitivity to seismic events. It seems to be more sensitive to strong and distant events.

The next step is to include the sedimentation rates in the sensitivity assessment of Lake Aiguebelette to earthquake shaking. Analyses are in progress and will include PSA values multiplied by sedimentation rates. To further discuss the sensitivity of Lake Aiguebelette, additional GMPEs are going to be used as well as European seismic catalogs (including all the seismic events from neighbouring countries).

Acknowledgements: This work was conducted as part of a PhD project funded by a joint grant from the Université Savoie Mont Blanc and Institut de Radioprotection et de Sûreté Nucléaire.

REFERENCES

Akkar, S., Sandıkkaya, M. A., and Ay, B. Ö., 2014. Compatible ground-motion prediction equations for damping scaling factors and vertical-to-horizontal spectral amplitude ratios for the broader Europe region. *Bulletin of Earthquake Engineering*, 12(1), 517-547.

Anderson, J. G., Brune, J. N., Louie, J. N., Zeng, Y., Savage, M., Yu, G., Chen, Q. And dePolo, D., 1994. Seismicity in the western Great Basin apparently triggered by the Landers, California, earthquake, 28 June 1992. *Bulletin of the Seismological Society of America*, 84(3), 863-891.

Baize, S., Cushing, E.M., Lemeille, F. and Jomard, H., 2013. Updated seismotectonic zoning scheme of Metropolitan France, with reference to geologic and seismotectonic data. *Bulletin de la Société Géologique de France* 184(3), 225–259.

Bindi, D., Massa, M., Luzi, L., Ameri, G., Pacor, F., Puglia, R. and Augliera, P., 2014. Pan-European ground-motion prediction equations for the average horizontal component of PGA, PGV, and 5%-damped PSA at spectral periods up to 3.0 s using the RESORCE dataset. *Bulletin of Earthquake Engineering*, 12(1), 391-430.

Cara, M., Cansi, Y., Schlupp, A., Arroucau, P., Béthoux, N., Beucler, E., Bruno, S., Calvet, M., Chevrot, S., Deboissy, A., Delouis, B., Denieul, M., Deschamps, A., Doubre, C., Fréchet, J., Godey, S., Golle, O., Grunberg, M., Guilbert, J., Haugmard, M.,Jenatton, L., Lambotte, S., Leobal, D., Maron, C., Mendel, V., Merrer, S., Macquet, M., Mignan, A., Mocquet, A., Nicolas, M., Perrot, J., Potin, B., Sanchez, O., Santoire, J.-P., Sèbe, O., Sylvander, M., Thouvenot, F., Woerd, J.V.D. and Woerd, K.V.D., 2015. SI-Hex: a new catalogue of instrumental seismicity for metropolitan France. *Bulletin de la Société Géologique de France*, 186(1), 3–19.

Chapron, E., Beck, C., Pourchet, M. and Deconinck, J.-F., 1999. 1822 earthquake-triggered homogenite in Lake Le Bourget (NW Alps). *Terra Nova*, 11(2-3), 86–92.

Campos, C., Beck, C., Crouzet, C., Demory, F., Van Welden, A. and Eris, K., 2013. Deciphering hemipelagites from homogenites through anisotropy of magnetic susceptibility. Paleoseismic implications (Sea of Marmara and Gulf of Corinth). *Sedimentary Geology*, 292, 1-14.

de La Taille, C., Jouanne, F., Crouzet, C., Beck, C., Jomard, H., De Rycker, K., and Van Daele, M., 2015. Impact of active faulting on the post LGM infill of Le Bourget Lake (western Alps, France). *Tectonophysics*, 664, 31-49.

De Vicente, I., Cattaneo, K., Cruz-Pizarro, L., Brauer, A., & Guilizzoni, P., 2006. Sedimentary phosphate fractions related to calcite precipitation in an eutrophic hardwater lake (Lake Alserio, northern Italy). *Journal of Paleolimnology*, 35(1), 55-64.

Giguet-Covex, C., Arnaud, F., Poulenard, J., Enters, D., Reyss, J. L., Millet, L., Jérome Lazzaroto and Vidal, O., 2010. Sedimentological and geochemical records of past trophic state and hypolimnetic anoxia in large, hard-water Lake Bourget, French Alps. *Journal of Paleolimnology*, 43(1), 171-190.

Jomard, H., Cushing, E.M., Palumbo, L., Baize, S., David, C. and Chartier, T., 2017. Transposing an active fault database into a seismic hazard fault model for nuclear facilities – Part 1: Building a database of potentially active faults (BDFA) for metropolitan France. *Natural Hazards and Earth System Sciences*, 17(9), 1573–1584.

Kelts, K., & Hsü, K. J., 1978. Freshwater carbonate sedimentation. In Lakes. *Springer, New York, NY*, 295-323.

Kremer, K., Wirth, S.B., Reusch, A., Fäh, D., Bellwald, B., Anselmetti, F.S., Girardclos, S. and Strasser, M., 2017. Lake-sediment based paleoseismology: Limitations and perspectives from the Swiss Alps. *Quaternary Science Reviews*, 168, 1–18.

Manchuel, K., Traversa, P., Baumont, D., Cara, M., Nayman, E. and Durouchoux, C., 2018. The French seismic CATalogue (FCAT-17). *Bull Earthquake Eng*, 16, 2227–2251.

Moernaut, J., M. Van Daele, K. Heirman, K. Fontijn, M. Strasser, M. Pino, R. Urrutia, and M. De Batist, 2014. Lacustrine turbidites as a tool for quantitative earthquake reconstruction: New evidence for a variable rupture mode in south central Chile. *J. Geophys. Res. Solid Earth*, 119, 1607–1633.

Strasser, M., Anselmetti, F. S., Fäh, D., Giardini, D., and Schnellmann, M., 2006. Magnitudes and source areas of large prehistoric northern Alpine earthquakes revealed by slope failures in lakes. *Geology*, 34(12), 1005-1008.

Van Daele, M., et al., 2015. A comparison of the sedimentary records of the 1960 and 2010 great Chilean earthquakes in 17 lakes: Implications for quantitative lacustrine palaeoseismology. *Sedimentology*, 62(5), 1466–1496.

Wilhelm, B., Nomade, J., Crouzet, C., Litty, C., Sabatier, P., Belle, S., Rolland, Y., Revel, M., Courboulex, F., Arnaud, F. and Anselmetti, F.S., 2016. Quantified sensitivity of small lake sediments to record historic earthquakes: Implications for paleoseismology: Lake sensitivity to record earthquakes. *Journal Geophysical Research Earth Surface*, 121(1), 2–16.

Analysis of geomorphological index for the characterization of the neotectonic activity of the Tena Fault in the Amazon foothills

Belén Benites (1), Oswaldo Guzmán (2) Corina Campos (2)

(1) Universidad Regional Amazónica Ikiam, Ingeniería en Geociencias. Tena, Ecuador. Email: cinthia.benites@est.ikiam.edu.ec
(2) Grupo de investigación Ciencias de la Tierra y Clima. Universidad Regional Amazónica Ikiam. Tena, Ecuador. Email: oswaldo.guzman@ikiam.edu.ec; corina.campos@ikiam.edu.ec

Abstract: *The aim of this work is to apply geomorphological index (mountain front sinuosity, basin shape index, Hack index and drainage basin asymmetry factor) to analyze the tectonic activity of the Amazonian foothills in Ecuador. The analysis was performed on a 21.51 km segment of the Tena fault. First of all, the trace of the fault was mapped from morphotectonic evidence. Subsequently, the geomorphological index were calculated in a GIS environment. The quantitative results obtained show that: i) in the NNE part there is greater deformation, is observable in the fault trace, with NNE-SSO orientation of type reverse-transcurent, ii) the area investigated exposed to high to moderate tectonic activity demonstrated by the correlation between geomorphological index, iii) Finally, the results validated the usefulness of this technique to highlight tectonic activity in the Amazonian foothills of Ecuador, where tropical weathering processes and high vegetation cover complicate conventional qualitative analysis.*

Keywords: Geomorphologic index, active tectonic, Amazon piedmont, seismic hazard, Ecuador

Introduction

Ecuador is one of the South American regions affected by intense seismic activity, mainly caused by the subduction of the oceanic Nazca plate under the South American plate a rate of 58 ± 2 mm/year and in an E-W direction (Trenkamp et al., 2002). The morphological layout of Ecuador comprises three large regions: Coast, Andean zone or Sierra, Sub-andean zone or Oriente (Marocco & Winter, 1997).

The Ecuadorian Sub-andean zone is characterized by intense seismic and volcanic activity, and by striking erosion processes (Baby et al., 2004) and the tectonic inversion of old normal faults linked to a rift system of Triassic and/or Lower Jurassic age. These faults, currently inverse and strongly dipping, are oriented mainly N-S or NNE-SSW (Baby et al., 1999; Baby et al., 2004). Sub-andean has 3 morphotectonic units are developed, constituted by the Napo uplift, Pastaza Depression and the Cutucú Cordillera (Baby, et al., 2004). Napo uplift zone are formed by flower structures NNE-SSW with a positive trend that are still seismically active (Jaillard et al., 2000).

SARA project was as object increase the knowledge about the faults of South America. Then the project analyzed the Sub-andean zone to characterize the Neotectonics structures (Costa et al., 2020), through their geometry, kinematics and activity rate as main parameters. Although the project progress with respect to the pre-existing database (Eguéz et al, 2003) local analysis and complementary data such as fault slip rate are necessary to understand seismic capacity of the faults (Costa et al., 2020).

The representation of dangerous failures is very heterogeneous, and differs by geographical coverage, availability or reliability of the data (Costa et al., 2020). However, the mapping of faults is underrepresented in current regional neotectonic knowledge because they convey differences when compared to specific areas where much more detailed neotectonic mapping has been carried out.

The active Tena Fault (*Fig. 1a*) is a reverse fault that separates the Sub-andean from the Amazon foothills. The Tena fault is orientated N-S has a length of 35 km their last movement is postulated in the Quaternary (<1.6 Ma) and it has a slip rate of <1 mm/year (Eguez et al., 2003). Tena fault deforms Cenozoic marine sedimentary rocks and Jurassic granite rocks that are superimposed by Tertiary alluvial fans along the Sub-andean zone (Baby et al, 2004).

The database of the SARA project, describes the Tena Fault as a reverse transcurrent fault belonging to the Quaternary with an age <1.8 Ma and a length of 29.1 km, the rest of the information is unknown. Movements have been recorded of magnitude Mw 6.4 in Tena fault (Beauval et al., 2010). Additionally, the proximity of seismogenic nodes in Tena fault are capable of generating teluric movements (Chunga et al., 2010), it could affect nearby populations and infrastructure.

The Sub-andean reverse faults are related to the anticlines of the foothills. Its identification on the surface is complex due to the high vegetation in the tropical zone and the conditions of tropical. These faults can be identified through the interpretation of geomorphological evidence such as displaced fluvial system, triangular facets, displaced mountain crests. It which can be observed in satellite images and digital elevation models (DEM). A recently technique applied by several tectonic studies (Jaberi et al., 2018; Mahmood & Gloaguen, 2012; Molano & Torres, 2018; Singh & Bezbaruah, 2021; Toural & Moreiras, 2017) is the use of geomorphological index to be able to map and study active faults. It´s useful to identify areas that experience rapid tectonic deformation and detect anomalies produced by tectonic activities such as uplifts or subsidence of the area (Hamdouni et al., 2008). For this propuse, it is intended to evaluate the tectonic activity of the active Tena fault through the quantification of the geomorphological index.

Discussion

The geomorphological index calculated in this work suggest that the Tena fault is tectonically active.

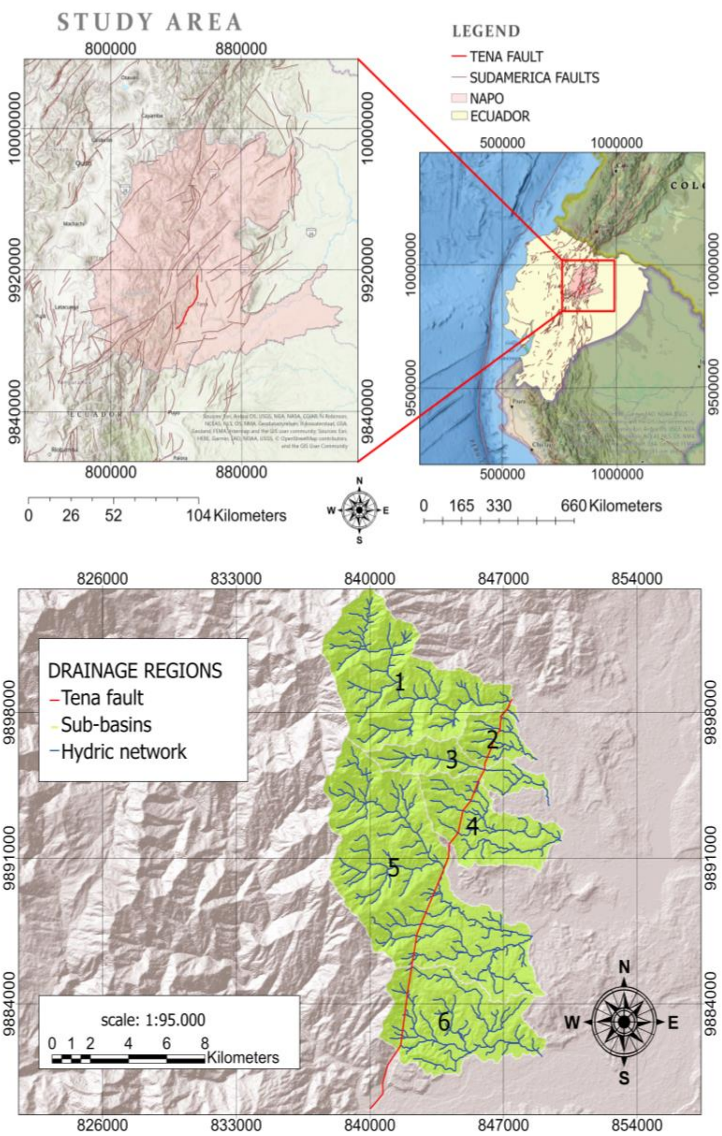

Figure 1. (a) Location of the study area and geometry of the Tena fault traced by the SARA project. (b) Cartography of the Tena fault through geomorphological evidence and delimitation of hydric network and sub-basins that will be analyzed with geomorphological index.

Fault mapping

The satellite images, the DEM and the drainage network present geomorphological evidence of displaced fluvial systems of the Tena, Pano and Jatunyacu rivers with signs of horizontal displacement. The schematic evolution of the deviations rivers is a consequence of the growth of the folds (Be`s de Berc, 2002). In addition to the triangular facet of sub-basin 4.

The fault is traced between the limits of the Tena rivers to the NNE and Jatunyacu to the SSW. Consequently, the main segment of the fault trace has a NNE-SSW trend (*Fig. 1b*), common between the faults that make up the orogenic front in the Sub-andean (Baby et al., 2004).

It´s inferred that the Tena fault is of a reverse-transcurrent nature. Therefore, it had an important vertical movement due to the presence of triangular facets that are sign of tectonic settings such as normal and thrust fault scarps (Bahrami, 2012; Bull, 2007). Furthermore, of a significant horizontal movement inferred for displacement of the rivers, which are reflections of structural control and slip faults (Bierman, 2014).

Division of sub-basins

The trace of the Tena fault is taken as a pattern to delimit the drainage network and the sub-basins. The hydric network obtained from the DEM is classified according to the Strahler method (Tarboton, 1991) and 8 levels of branches are obtained. For pertinent purposes, the rivers that emerge from the ramifications with level 4 are taken into account because they are the areas closest to the Tena fault. With the above information, 6 sub-basins are obtained without taking into account the main basin of the Jatunyacu river. This has a large area where the results can be affected by the presence of other faults to the west.

Analysis of geomorphological index

The AF index detects the tectonic transverse tilt and lateral migration of rivers (Pérez-Peña et al., 2010). The 2,4,5,6 sub-basins with the AF index present strongly asymmetric values that are a reflection of active tectonics. It is inferred that the drainage networks of the 2, 4, 5 sub-basins have a direction of migration towards the NNE (*Fig. 2*), therefore their tilting direction has this trend. In contrast, sub-basin 6 has an opposite direction of migration of the hydric network. It is interpreted that this behavior is caused by the presence of high mountainous relief geomorphs on the left side of the sub-basin 6 (MAG-SIGTierras, 2014).

The Smf index measuring the relationship between the erosion that cuts the beginning of the valleys and the tectonic forces that create the mountain front (Keller & Pinter, 2002). The areas belonging to sub-basin 5 and the second segment of sub-basin 6 have high Smf values. The sub-basin 5 linked to the lithology composed mainly of sandstones with little resistance to erosion (Bierman, 2014). While sub-basin 6 has differences in the Smf index in its two segments. It has been inferred that it is due to the type of geoforms present in each segment. The first segment, it is about a geoform high hilly relief. While the second segment, a geoform spreading glacis whose nature is erosive (Garcia et al., 2011; MAG-SIGTierras, 2014).

The other sub-basins exhibit a moderately active tectonic, it´s estimated that there is uplifting of the crustal blocks and that the erosion did not develop to a great extent because the sub-basins 1,2,3,4 are formed by fine materials (limonites, clays) it has resistance to erosion due to high cohesion (Bierman, 2014).

The Re index, most of the sub-basins have a value of highly elongated, indicating zones of more intense tectonic activity oriented in an E-W direction, sub-basin 2 is less elongated due to the fact that the migration of its watersheds and sediment capture cover a smaller area than the rest of the sub-basins, giving more circularity to the shape of sub-basin 2. The regional system is attributed an evolution of drainage of west to east, where drainage immaturity in mountain belts as in the case of the drainage network of interest characterizes growing tectonic structures (Be`s de Berc et al., 2005).

The Hack index identifying steep sections that may reflect signs of active tectonics throughout the drainage network (Hack, 1973). The sub-basins 1,3,4,5 has the higher values of Hack index analyzed. It is ruled out that there are index anomalies in the western area of these sub-basins, since it is inferred from its lithology that the uplifts are caused by the resistance of granite-type rocks (Bierman, 2014). Or the presence of immobile debris deposited in the channel by landslides or debris flows (Bierman, 2014). In the part east, the sub-basin 3 has the development of a parallel type drainage network with strong regional slopes. Although sub-basins 1, 4, 5 have signs of uplift in areas with lithology with less resistant rocks, attributing it to active tectonics (Piacentini et al., 2020; Wei et al, 2015). Rivers respond before slopes, so Hack index detect susceptible small disturbances in river gradients (Burbank & Anderson, 2009).

The Tena fault presents evidence of deformation and active tectonics along 21, 51 km of length is demonstrated through the correlation between the

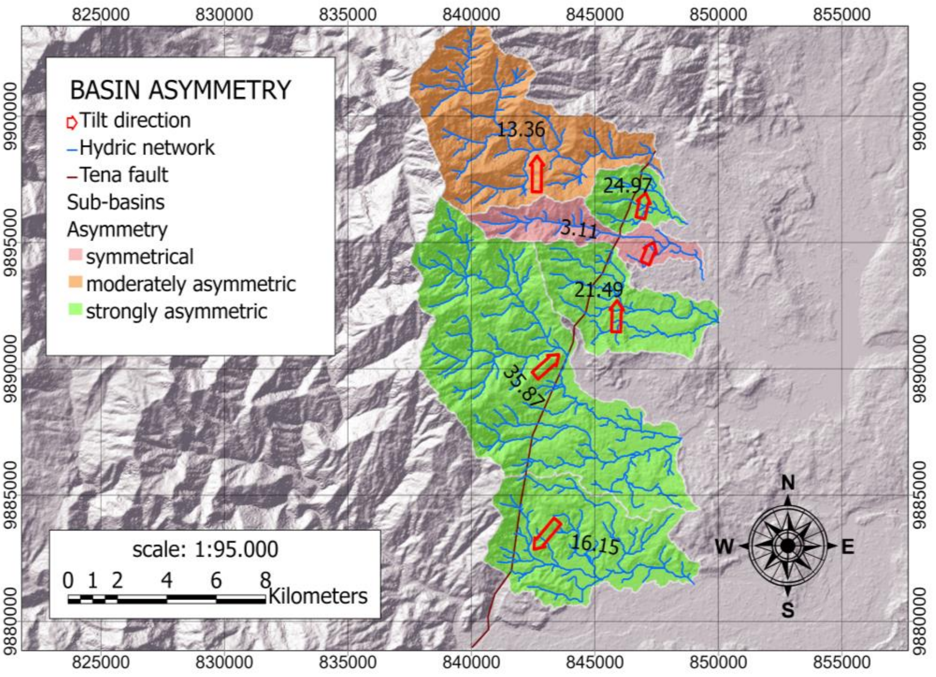

Figure 2. Basin asymmetry index and tilting direction of each sub-basin. It is inferred that the sub-basins have a trend towards the NNE. In addition, 4 of 6 sub-basins present a highly active tectonic basin asymmetry.

values obtained by the Hack index (SL), sinuosity of the mountain front (Smf), shape of the basin (Re) and asymmetry of the basin (AF) that corroborate that the greatest tectonic activity is located in the NNE zone of the fault.

Acknowledgements

My gratitude to the proyect ICGP-669 Ollin and CNRS for the scholarships awarded granted to attend the congress Pata-days 2022 and the project CTC-006-2020 of Ikiam for letting me be part of it.

References

Baby, P., Rivadeneira, M., Christophoul, F., & Barragan, R., 1999. Style and timing of deformation in the Oriente Basin of Ecuador. In *Fourth International Symposium on Andean Geodynamics, University of Goettingen, Germany, Extended Abstracts Volume* (pp. 68-72).

Baby, P., Rivadeneira, M., & Barragán, R., 2004. *La cuenca Oriente: geología y petróleo* (Vol. 144). Institut français d'études andines.

Bahrami, S., 2012. Morphotectonic evolution of triangular facets and wine-glass valleys in the Noakoh anticline, Zagros, Iran: Implications for active tectonics. *Geomorphology*, *159*, 37-49.

Bes de Berc, S., Baby, P., Soula, J. C., Souris, M., & Rosero, J., 2002. Uplift and active deformation of the Pastaza Alluvial Fan (Subandean zone of Ecuador). In *Proceedings International Symposium on Andean Geodynamics, Toulouse* (pp. 85-88).

Bes de Berc, S., Soula, J. C., Baby, P., Souris, M., Christophoul, F., & Rosero, J., 2005. Geomorphic evidence of active deformation and uplift in a modern continental wedge-top–foredeep transition: example of the eastern Ecuadorian Andes. *Tectonophysics*, *399*(1-4), 351-380.

Beauval, C., Yepes, H., Bakun, W. H., Egred, J., Alvarado, A., & Singaucho, J. C., 2010. Locations and magnitudes of historical earthquakes in the Sierra of Ecuador (1587–1996). *Geophysical Journal International*, *181*(3), 1613-1633.

Bierman, P. R., 2014. *Key concepts in geomorphology/Paul R. bierman y David R. Montgomery* (No. 551.41 B54.).

Bhat, F. A., Bhat, I. M., Sana, H., Iqbal, M., & Mir, A. R., 2013. Identification of geomorphic signatures of active tectonics in the West Lidder Watershed, Kashmir Himalayas: Using Remote Sensing and GIS. *International Journal of Geomatics and Geosciences*, *4*(1), 164.

Burbank, D. W., & Anderson, R. S., 2009. *Tectonic geomorphology*. John Wiley & Sons.

Bull, W.B., 2007. Tectonic Geomorphology of Mountains: A New Approach to Paleoseismology. Blackwell, Malden, USA. 20 pp.

Costa, C., Alvarado, A., Audemard, F., Audin, L., Benavente, C., Bezerra, F. H., & Garro, H., 2020. Hazardous faults of South America; compilation and overview. *Journal of South American Earth Sciences*, *104*, 102837.

Chunga, K., Michetti, A. M., Gorshkov, A. I., Panza, G. F., Soloviev, A., & Martillo, C., 2010. Aplicación del método de zonación morfo-estructural para identificar nudos sismogénicos en la región costera y cadenas montañosas de los Andes septentrionales del Ecuador.

Eguéz, A., Alvarado, A., Yepes, H., Machette, M., Costa, C., & Dart, R., 2003. Database and map of Quaternary faults and folds of Ecuador and its offshore regions. *US Geological Survey Open-File Report*.

García-Tortosa, F. J., Alfaro, P., de Galdeano, C. S., & Galindo-Zaldívar, J., 2011. Glacis geometry as a geomorphic marker of recent tectonics: The Guadix–Baza basin (South Spain). *Geomorphology*, *125*(4), 517-529.

Greenidge-Moro, S., Rodríguez-Infante, A., & Díaz-Barrios, I., 2020. Geomorfología tectónica del sureste del municipio de Mayarí, provincia de Holguín. *Minería y Geología*, *36*(2), 155-171.

Hack, J. T., 1973. Stream-profile analysis and stream-gradient index. *Journal of Research of the us Geological Survey*, *1*(4), 421-429.

Hamdouni, R., Irigaray, C., Fernández, T., Chacón, J., & Keller, E. A., 2008. Assessment of relative active tectonics, southwest border of the Sierra Nevada (southern Spain). *Geomorphology*, *96*(1-2), 150-173.

Jaillard, E., Hérail, G., Monfret, T., Díaz-Martínez, E., Baby, P., Lavenu, A., & Campos, D., 2000. Tectonic evolution of the Andes of Ecuador, Peru, Bolivia and northern Chile.

Jaberi, M., Ghassemi, M. R., Shayan, S., Yamani, M., & Zamanzadeh, S. M., 2018. Interaction between active tectonics, erosion and diapirism, a case study from Habble-Rud in Southern Central Alborz (Northern Iran). *Geomorphology*, *300*, 77-94.

Keller, E. A and Pinter, N., 2002. Active Tectonics: Earthquakes, Uplift and Landscape. NJ, USA: Prentice Hall.

Mahmood, S. A., & Gloaguen, R., 2012. Appraisal of active tectonics in Hindu Kush: Insights from DEM derived geomorphic indices and drainage analysis. *Geoscience Frontiers*, *3*(4), 407-428.

Marocco, R., & Winter, T., 1997. Bosquejo de la evolución geodinámica del Ecuador. Los paisajes naturales del Ecuador. Volumen 1–Las condiciones generales del medio natural, 16-52.

Ministerio de Agricultura y Ganadería (MAG-SIGTierras), 2014. Catálogo descriptivo de objetos geomorfológicos del Ecuador. http://metadatos.sigtierras.gob.ec/pdf/Manual_Identificaci%C3%B3n_Geoformas_140627.pdf

Molano Cárdenas, S. M., & Torres Rodríguez, M. D., 2018. Indices geomorfológicos cómo herramienta para la caracterización de la actividad neotectónica del sistema de fallas de Soapaga entre los municipios de Corrales y Pesca.

Pérez-Peña, J. V., Azor, A., Azañón, J. M., & Keller, E. A., 2010. Active tectonics in the Sierra Nevada (Betic Cordillera, SE Spain): Insights from geomorphic indexes and drainage pattern analysis. *Geomorphology*, *119*(1-2), 74-87.

Piacentini, D., Troiani, F., Servizi, T., Nesci, O., Veneri, F., 2020. *SLiX: A GIS Toolbox to Support Along-Stream Knickzones Detection through the Computation and Mapping of the Stream Length-Gradient (SL) Index. ISPRS International Journal of Geo-Information, 9(2), 69–.* doi:10.3390/ijgi9020069

Singh, A., & Bezbaruah, D., 2021. Evaluation of Active Tectonics and Geomorphic Indices in Siwalik Basin Around Dikrong River, Eastern Himalaya. *Journal of Scientific Research*, *65*(3), 11-22.

Tarboton, D. G., Bras, R. L., & Rodriguez-Iturbe, I., 1991. On the extraction of channel networks from digital elevation data. Hydrological processes, 5(1), 81-100.

Trenkamp, R., Kellogg, J. N., Freymueller, J. T., & Mora, H. P., 2002. Wide plate margin deformation, southern Central America and northwestern South America, CASA GPS observations. *Journal of South American Earth Sciences*, *15*(2), 157-171.

Toural Dapoza, R., & Moreiras, S. M., 2017. Aplicación de índices geomorfológicos en el piedemonte neotectónicamente activo de Mendoza (32º S). *GeoActa*, *42*(2), 45-63.

Wei, Z., Bi, L., Xu, Y., & He, H., 2015. Evaluating knickpoint recession along an active fault for paleoseismological analysis: The Huoshan Piedmont, Eastern China. *Geomorphology*, *235*, 63-76.

Characteristics of secondary (distributed) ruptures of normal and reverse surface faulting earthquakes: implications for fault displacement hazard analysis

Paolo Boncio (1), Francesco Visini (2), Stéphane Baize (3), Fiia Nurminen (4), Bruno Pace (1), Oona Scotti (3)

(1) Department of Engineering and Geology, Università "G. D'Annunzio" Chieti-Pescara, Chieti, Italy
(2) INGV – Istituto Nazionale di Geofisica e Vulcanologia, Italy
(3) IRSN—Institut de Radioprotection et de Sûreté Nucléaire, Fontenay-aux-Roses, France
(4) Università "G. D'Annunzio" Chieti-Pescara, Italy. Now at RINA Consulting S.P.A., Milan, Italy.

Abstract:
We analyse the characteristics of coseismic distributed ruptures (DRs), i.e. secondary ruptures that occur off the trace of the principal fault, from the scrutiny of numerous historical reverse and normal surface ruptures contained in a new release of the 'SUrface Ruptures due to Earthquake (SURE)' database (SURE 2.0, Nurminen et al., under review). The database contains slip measurements and mapped traces of 50 historical surface ruptures of global, dip-slip and strike-slip earthquakes occurred between 1872 and 2019. The novelty of the SURE 2.0 database compared to the previous version is a ranking scheme which categorizes the ruptures based on geological information. In this work we analyse the distance-frequency and displacement distributions of 34 reverse and normal events using the ranking information. The implications are new, improved predictive regressions for the probability of occurrence and expected displacement for distributed ruptures during dip-slip earthquakes that can be used in probabilistic analysis of fault displacement hazard.

Key words: *Fault displacement hazard analysis, distributed surface faulting, dip-slip earthquakes.*

INTRODUCTION

During surface faulting earthquakes, displacement on secondary faults or factures may occur off the trace of the principal fault (PF), in the vicinity or up to many kilometres away from the PF trace. This is called distributed faulting or distributed rupturing, also known as secondary faulting/rupturing. Though distributed ruptures (DRs) are discontinuous in nature and characterized by lesser amount of displacement compared to the PF, their occurrence may threaten structures the safety and functionality of which are sensible to low levels of permanent ground displacement, such as critical infrastructure. Often DRs occur in unpredictable locations, without previous geologic evidence, making the assessment of fault displacement hazard from DRs challenging.

In Probabilistic Fault Displacement Hazard Analysis (PFDHA), the distinction between principal and distributed faulting was first introduced by Youngs et al. (2003). This distinction is important because different equations are used in assessing the probability of occurrence and displacement of principal or distributed ruptures. In general, distributed faulting includes several different types of ground ruptures, from surface faulting along secondary splays and shears connected or unconnected to the PF, to ruptures triggered on remote pre-existing faults distant several kilometres from the PF. In Youngs et al. (2003) and in more recent updates of PFDHA models (Petersen et al., 2011; Takao et al., 2013; Ferrario and Livio, 2021) regressions for distributed faulting do not account of these different typologies, and all the DRs are considered equally. A first attempt of distinguishing regressions for different types of DRs was by Nurminen et al. (2020) for reverse faulting earthquakes. They propose regressions for DRs that are not related to pre-existing fault or fold structures, called 'simple' DRs (i.e., non-predictable DRs that may take place anywhere along the strike of the PF). Compared to other probability models, the Nurminen et al.'s regressions are characterized by significantly higher probability of having DRs is the vicinity of the PF (near-fault) and significantly stronger attenuation with distance (Valentini et al., 2021). A major limit of the Nurminen et al.'s model is that this is not a complete model for DRs, as it does not account for DRs deriving from reactivation of pre-existing structures of from structurally complex settings.

In this work we explore the characteristics of DRs from the analysis of numerous historical reverse and normal surface ruptures contained in a new release of the 'SUrface Ruptures due to Earthquake (SURE)' database (SURE 2.0, Nurminen et al., under review), within which the ruptures are categorized based on geological information (ranking of ruptures). The aim is to obtain predictive regressions for the probability of occurrence and expected displacement for distributed rupturing during dip-slip earthquakes that account for the different expected typologies of DRs.

DATA

We used empirical data compiled in a new release of the SURE database (Baize et al., 2019), named SURE 2.0 (Nurminen et al., under review).

The SURE 2.0 database contains surface rupture data (rupture traces and slip observations) from 50 crustal earthquakes (depth ≤ 25 km) occurred worldwide, 16 of which with strike-slip, 18 normal, and 16 reverse kinematics, with Mw ranging from 4.9 to 7.9.

In particular, we analysed surface ruptures from normal (Mw 5.6 – 7.5) and reverse (Mw 4.9 – 7.9) earthquakes.

Rupture ranking

A significant novelty of the SURE 2.0 database is the surface rupture categorization (ranking) based on geological and structural information. The ranking scheme was first introduced for reverse faults by Nurminen et al. (2020), and a similar approach has been applied to normal and strike-slip earthquakes.

SURE 2.0 distinguishes 6 different rupture types, (Fig. 1):

Rank 1 is the principal fault rupture (PF), corresponding to the surface expression of the movement along the fault plane responsible for the release of the seismic energy during an earthquake, as previously defined by Youngs et al. (2003). PF has the most continuous surface expression, and generally the highest displacement. PF often occurs on fault traces that have the potential to be known and mapped prior to the earthquake, i.e., faults with long-term geologic and geomorphic evidence of activity.

All the surface rupturing off the PF is considered distributed rupturing and has ranking > 1.

Rank 2 is for simple distributed ruptures, which include discontinuous surface breaks around the PF that occurred as a direct response to the movement along the earthquake fault. Rank 2 DRs occur rather randomly around the PF trace, and the measured displacements are remarkably lower than the PF nearby. The occurrence of rank 2 DRs is largely guided by subsurface material and complexities of the PF. Rank 2 DRs are frequent around PF complexities, such as bends or stepovers. This is the most common DR type in earthquakes of all kinematics.

Rank 1.5 is for 'primary' DRs, indicating movement along pre-existing faults that have the potential to be recognized and mapped before an earthquake, as there can be geologic and geomorphic evidence of long-term activity on them. Rank 1.5 is applied only to cases when geological data (e.g., geologic maps and cross-sections) suggest these structures are pre-existing and directly connected to the PF at depth, such as synthetic and antithetic splays. As the rupturing occurs along a pre-existing fault, rank 1.5 DRs are usually more continuous and have larger displacement than rank 2 DRs. Faults reactivated as rank 1.5 DRs may or may not be able to provoke an earthquake by themselves. They may provoke rank 2 DRs of their own. Rank 1.5 DRs are identified in earthquakes of all kinematics.

Rank 3 is triggered distributed rupturing along pre-existing faults that are not likely to be connected to the PF, generally at far distance from the PF. Typically, rank 3 DRs are highly discontinuous along and around the pre-existing fault trace. Triggered DRs are hosted by active faults, but the level of their own activity may vary. Rank 3 rupturing can be triggered along faults that can act as PF during a different earthquake. Rank 3 DRs can be present in any fault kinematics.

Rank 21 (Bending-moment, B-M) and rank 22 (flexural-slip, F-S) are DRs occurring during reverse faulting earthquakes, when large-scale folding may lead bending-moment or flexural-slip rupturing. B-M DRs are normal faults that are formed close to the hinge zone of large-scale anticlines. F-S DRs are due to slip along bedding planes on steeply-dipping limbs of a bedrock fold.

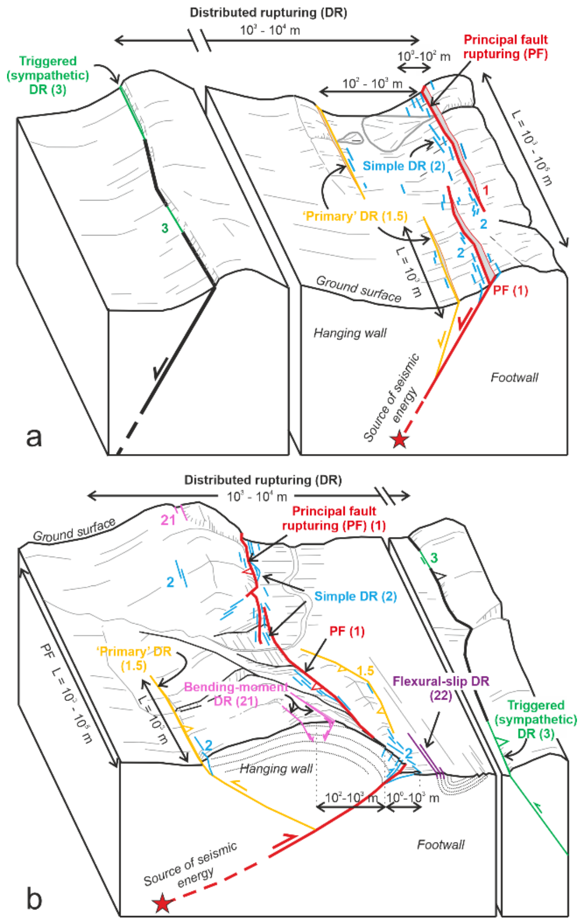

Figure 1: Diagrams schematizing the rupture ranking for normal (a) and reverse (b) surface rupturing earthquakes according to the SURE 2.0 database (Nurminen et al., under review).

RESULTS

Overall, there are 13,078 slip data points for dip-slip earthquakes within the SURE 2.0 database. Over 1200 slip observations are from reverse events, 71% of which are for PF. The DRs of reverse events are nearly equally divided between simple (rank 2, 16%) and complex DRs (rank 1.5, 3, 21 and 22, 13%). For normal faults, there are ca. 11,800 data points, more than 80% of which is from the 2016 central Italy earthquake sequence, which dominates the database. The data points are nearly equally divided between PF (53%) and DRs (47%: 28% rank 1.5; 16% rank 2; 3% rank 3). By removing the 2016 central Italy data, the percentages of PF and DRs data points do not change drastically (66% and 34%, respectively). The cumulative length of all the surface rupture segments is ~1672 km, ~732 km for normal and ~940 km for reverse events. For normal events, 55% of the cumulative rupture length is for PF and 45% for DRs. The percentages do not change if the 2016 central Italy events are not considered. For reverse events, 72% of the cumulative rupture length is for PF and 28% for DRs.

Distance - frequency distribution of DRs by ranking

Figure 2 shows a histogram obtained by measuring the distances of DR rupture traces from the PF. We used a method that we call «slicing» (Nurminen et al., 2020), consisting of re-sampling the DR traces every 10 m, measuring the DR-PF distance (r), and counting the number of DRs within each 10 m-wide slice parallel to the PF. DRs can occur very far from the PF (up to ~20 km for normal events), but most of them concentrate near the PF (hundreds of meters from PF). Therefore, it seems possible to distinguish between near-fault and far-fault distributed faulting.

Displacement on DRs by ranking

Figure 3 shows the vertical displacement (throw) on DRs plotted against the distance from PF, the magnitude of the event, and the mean vertical displacement on the PF. We analysed the vertical component of displacement, because in the database this is the measure most often available for dip-slip earthquakes. Therefore, throw values form a wider and more complete population of slip data.

To analyse the possible relations between displacement on DRs and displacement on PF, we plotted the DR throw against a mean PF throw that depends on the position of the DR point considered. The mean PF throw is calculated as the average of the PF slip profile contained in a circle centred on a point located on the PF trace, the closest to the DR point considered. The circle radius is the semi-distance between the DR point and PF. Therefore, the mean PF throw depends on the position of the DR point along- and across-strike the PF. DR points close to PF are compared with more local values of the displacement on the PF compared to more distant points. The displacement for distributed faulting is analysed considering separately simple (rank 2) and complex (ranks 1.5, 3, 21 and 22) DRs.

DISCUSSION

First-order observations from distance-frequency distribution of DRs are:

i) there is a clear asymmetric distribution of DRs, with ruptures mostly located in the hanging wall (HW) of the PF, for both normal and reverse earthquakes;

ii) in the near-fault, the hazard from distributed faulting is higher, mostly from simple DRs (rank 2);

iii) the occurrence of DRs attenuates with distance. The attenuation is faster in the FW. If simple and complex DRs are considered separately, one can observe that the attenuation is mostly driven by simple DRs. The attenuation of complex DRs is less evident. Probably because complex distributed faulting occurs only if there is a pre-existing structure prone to be reactivated, while simple DRs are more related to the faulting process operating on the PF;

iv) DRs for normal and reverse events have a similar distribution, but the far-fault seems to be shorter for reverse events (~20 km for normal and 7-8 km for reverse). Is this due to the difference in the mechanics of the process, or to completeness issues, or to a combination of both?

v) higher magnitude events have a larger number of DRs, and distributed faulting attenuates at longer distances, as expected.

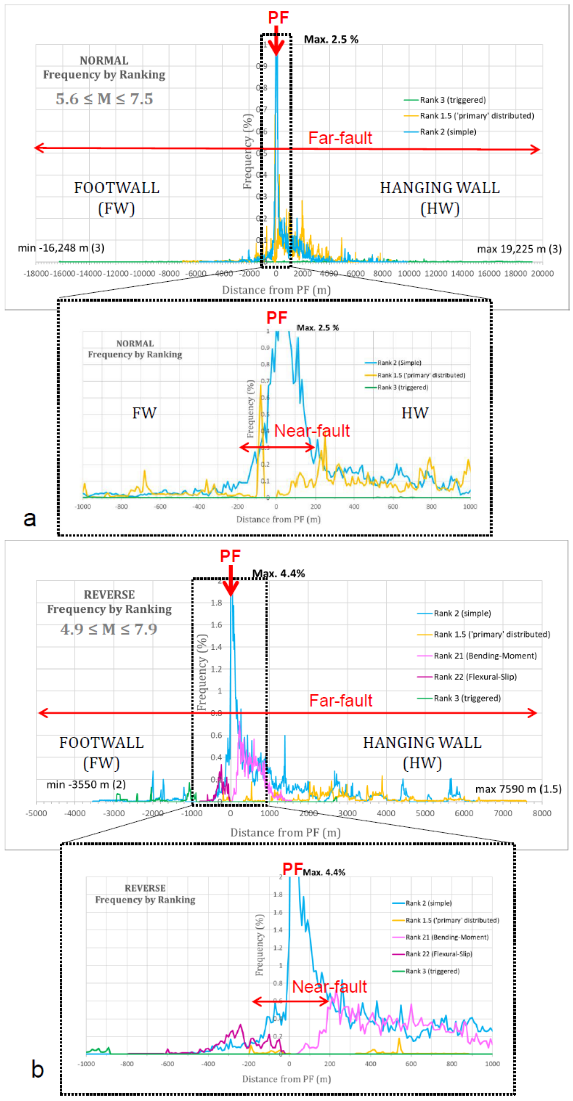

Figure 2: Frequency histograms of DR – PF distances for normal (a) and reverse (b) earthquake surface ruptures.

First-order observations from the analysis of displacement on DRs are:

i) there is a positive relation of the throw on DRs with magnitude, as expected, for all the ranking types;

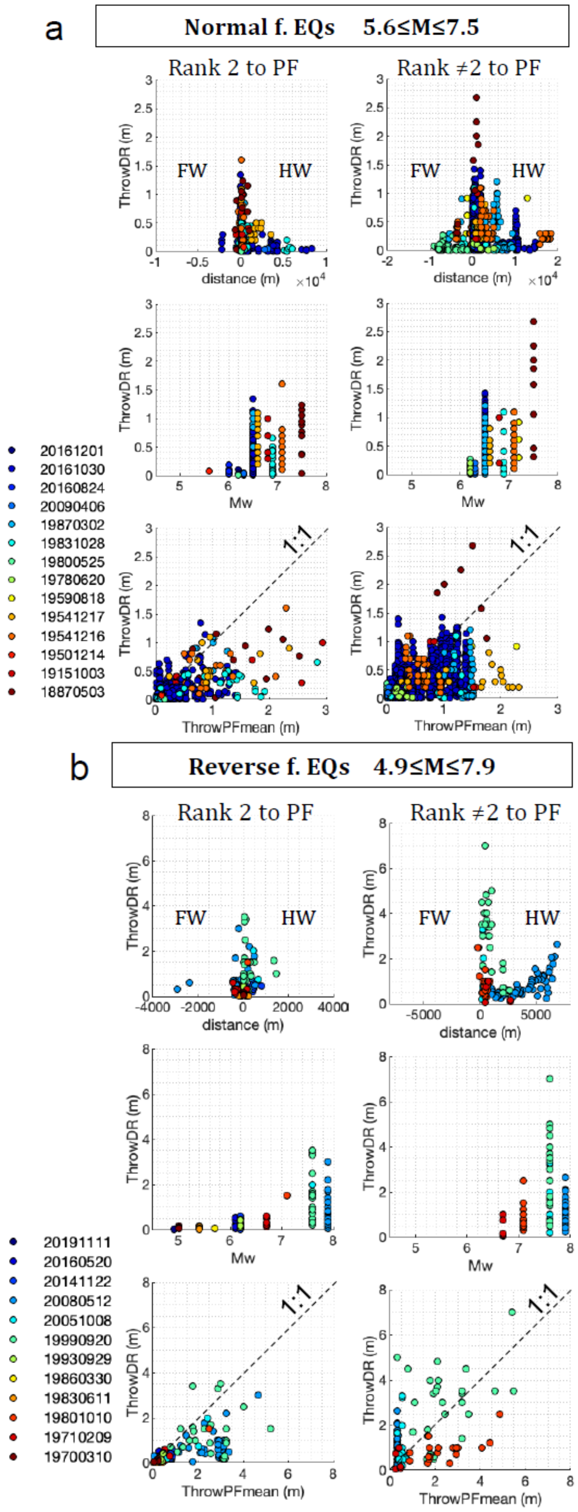

Figure 3: Vertical displacement (throw) on DRs by ranking plotted against distance from PF (top), Mw (middle) and mean throw on PF (bottom) for normal (a) and reverse (b) earthquakes. See text for definition of mean throw on PF.

ii) throw on DRs attenuates with distance. The attenuation is more evident for rank 2 DRs, particularly for normal faults;

iii) the relations between DR throw and PF throw are different for simple and complex DRs. Simple DRs throws are mostly below the 1:1 line (throw DR < throw PF), and there is a positive relation with PF throw. This suggest that displacement on DRs depends and is systematically smaller than displacement on PF (correlated secondary process). Instead, several complex DRs points lye above the 1:1 line (throw complex DR > throw PF), particularly for reverse events, and the relation between displacement on DR and displacement on PF is not obvious. Strain partitioning could be a possible controlling factor.

Acknowledgements:

This wark was possible thanks to the agreement between University of Chieti – Pescara (Resp.: P. Boncio) and IRSN (Resp.: S. Baize), with which the Ph.D. project of F. Nurminen was funded.

REFERENCES

Baize, S., Nurminen, F., Sarmiento, A., Dawson, T., Takao, M., Scotti, O., Azuma, T., Boncio, P., Champenois, J., Cinti, F. R. et al., 2019. A worldwide and unified database of surface ruptures (SURE) for fault displacement hazard analyses. *Seismological Research Letters* 91, 499–520. doi:10.1785/0220190144 2019

Ferrario, M. F. & Livio, F. 2021. Conditional probability of distributed surface rupturing during normal-faulting earthquakes. *Solid Earth* 12, 1197–1209, doi: 10.5194/se-12-1197-2021.

Nurminen, F., Baize, S., Boncio, P., Blumetti, A. M., Cinti, F. R., Civico, R. & Guerrieri, L. 2022. SURE 2.0 – New release of the worldwide database of surface ruptures for fault displacement hazard analyses. *Scientific Data*, under review.

Nurminen, F., Boncio, P., Visini, F., Pace, B., Valentini, A., Baize, S. & Scotti, O. 2021. Probability of occurrence and displacement regression of distributed surface rupturing for reverse earthquakes. *Frontiers in Earth Sciences* 8, doi: 10.3389/feart.2020.581605.

Petersen, M. D., Dawson, T. E., Chen, R., Cao, T., Wills, C. J., Schwartz, D. P. & Frankel, A. D. 2011. Fault displacement Hazard for strike-slip faults. *Bulletin of the Seismological Society of America* 101- 2, 805–825, doi: 10.1785/0120100035.

Takao, M., Tsuchiyama, J., Annaka, T. & Kurita, T. 2013. Application of probabilistic fault displacement hazard analysis in Japan. *J. Jpn. Assoc. Earthq. Eng.* 13, 17–36, doi: 10.5610/jaee.13.17.

Valentini, A., Fukushima, Y., Contri, P., Ono, M., Sakai, T., Thompson, S. C., Viallet, E., Annaka, T., Chen, R., Moss, R. E. S. et al., 2021. Probabilistic Fault Displacement Hazard Assessment (PFDHA) for Nuclear Installations According to IAEA Safety Standards. *Bulletin of the Seismological Society of America* XX, 1–12, doi: 10.1785/0120210083

Youngs, R. R., Arabasz, W. J., Anderson, R. E., Ramelli, A. R., Ake, J. P., Slemmons, D. B., McCalpin, J. P., Doser, D. I., Fridrich, C. J., Swan, F. H., et al. 2003. A methodology for probabilistic fault displacement hazard analysis (PFDHA). *Earthquake Spectra* 19-1, 191–219, doi: 10.1193/1.1542891.

Identification and measurement of the co-seismic fault offset along the North Anatolian Fault in the Central Basin through the co-seismic sedimentary episodes

Corina Campos (1), Christian Beck (2), Oswaldo Guzmán (1)

(1) Grupo de Ciencias de La Tierra y Clima. Universidad Regional Amazónica Ikiam, Ecuador
(2) Laboratoire ISTerre, UMR CNRS 5275, Université de Savoie/Grenoble-Alpes University, 73376 Le Bourget du Lac, France

Abstract: *In the deep part of the Sea of Marmara, Turkey, the sedimentation developing upon the North Anatolian Fault is strongly influenced by the associated seismic activity, gravity reworking and tsunamis. Specific layers named homogenites-turbidites representing individual sedimentary events, have been characterized along two giant piston cores retrieved from the Central (or Orta) basin. They are the results of re-depositional processes, which may result into specific complex layers, due to reflections on steep slopes and/or to oscillations of the whole water mass (reflected tsunami, seiche effect). In the present work, Pre-Holocene non-marine sediments were analyzed, representing the last 12 to 17 kyr BP. For a 2 kyr long interval, 11 events could be precisely correlated on both sides of the Central Basin's southwestern scarp. For each of them, based on the specific depositional process, the thickness difference between the two sites was considered as a direct estimation of the vertical component of a coeval coseismic offset.*

Key words*: Sea of Marmara, earthquakes, homogenite-turbidite, co-seismic scarp, Late Pleistocene.*

INTRODUCTION

Several studies conducted during the last decades in lakes and restricted marine basins located in tectonically actives zones have demonstrated its potential to record paleoseisms (Hempton & Dewey, 1983; Siegenthaler et al., 1987; Van Loon et al., 1995; Syvitski & Schafer, 1996; Chapron et al., 1999; Shiki et al., 2000). For the subaqueous records, two major groups of effects can be detected and analyzed: i) in situ post-depositional disturbances (e.g.: Sims, 1975; Marco & Agnon, 1995; Rodriguez-Pascua et al., 2003), ii) gravity-driven reworking and re-settling of large masses of unconsolidated sediments (e.g.: Adams, 1990). Two major questions arise for both groups: a) how to ensure the earthquake-triggering, b) how to identify the responsible active structure(s). For in situ disturbances, the first problem is generally solved; in particular, it benefits from analogical and/or numerical modeling (e.g. Moretti et al., 1999; Wetzler et al., 2010). On the other hand, for re-depositional processes (which deposits are studied in this work), is presented a specific deposit constituted by two layers. A basal layer coarse grained and an upper fine grain homogeneous layer, this deposit is called "homogenite-turbidite". Recent observations made in subaquatic environments after catastrophic events, shortly after their occurrence (Thunell et al., 1999; McHugh et al., 2011; Lorenzoni et al., 2012); reinforced the earthquake-induced interpretation proposed for some of this type of deposits (Chapron et al., 1999; Beck et al., 2007).

For historical and older events, the seismic origin of a specific layer can be established: a) directly, using intrinsic characteristics as texture, origin of components, overall geometry, magnetic fabric, etc. (Beck et al., 2007; Beck 2009; Bertrand et al., 2008) indirectly, b) on the basis of correlations with reported seismic events (for historical seismicity) (e.g. Siegenthaler et al., 1987; Piper et al., 1992; Chapron et al., 1999; Goldfinger et al., 2007; Beck et al., 2012); c) when detecting the same paleo-event in a large area independantly from local setting (e.g. variable slope dip). (e.g., Goldfinger et al., 2007; Gracia et al., 2010, Moernaut, 2011; Pouderoux et al., 2012).

Direct relationships between an active structure and earthquake-induced sedimentary events are investigated for active faults reaching a sediment/water interface (sea- or lake-bottom), through high resolution imagery or/and coring. This favourable setting recently permitted detailed analyses of fault activity (offsets, slip rates) through adjacent sedimentation (Carrillo et al., 2006, 2008; Bull et al., 2006; Barnes & Pondard, 2010; Beck et al., 2012, Beck et al 2015). In this work we are dedicated to the study of the relation between an active fault and the earthquake-induced coseismic deposits in the deep part of the Sea of Marmara. This Sea (Northwestern Turkey) is a pull-apart basin developed along the North Anatolian Fault (NAF (Hancock & Barka, 1981). East-West elongated (200 km) it is composed of several aligned sub-basins (Tekirdağ, Orta, Kumburgaz and Çinarcic basin). In this work we will study two giant piston cores retrieved from the Central (or Orta) basin (figure 1).

DISCUSSION

The data used for the present study was two long cores as well as, high resolution (3.5 kHz) seismic profiles acquired with the VICTOR R.O.V. The two analyzed cores were retrieved during R/V MARION-DUFRESNES cruises using the CALYPSO giant-piston coring device, the MD01-2429 and MD01-2431 cores were retrieved at 1230 m, and 1170 m depths, with 37.30 m, and 26.40 m respective lengths. The following detailed analyzes were performed on both cores:

a) Grain-size analyses, with a laser diffraction microgranulometer MALVERN™ Mastersizer 2000 at the ISTerre laboratory; base-to-top paths on binary diagrams for turbidites/homogenites layers (*in* Beck, 2009; Eriş et al., 2012); and particle shape analysis for silt-clay fraction (SYSMEX FPIA-2100 device) were conducted.
b) Determination of sediments composition: microscopic observations, carbon and carbonates contents (LOI), XRF profiles in selected portions (AVAATECH instrument); bulk magnetic content (BARTINGTON contact sensor with 5 mm measurement interval).
c) XRay pictures (SCOPIX device, Migeon et al, 1998).
d) Anisotropy of Magnetic Susceptibility profiles (2 cm interval) on selected portions (Campos et al, 2013), completed with Anhysteretic Remanent Magnetization (ARM) and Isothermal Remanent Magnetization (IRM) (AGICO MFK1-FA Kappabridge, SQUID and 2G 760R systems).
e) The chronology is based on AMS ^{14}C calibrated ages: previously published measurements performed in Woods Hole Oceanographic Institution (NOSAMS facility) (in Beck et al, 2007), and a set of new measurements performed at CEA-Saclay (CNRS-INSU ARTEMIS facility).

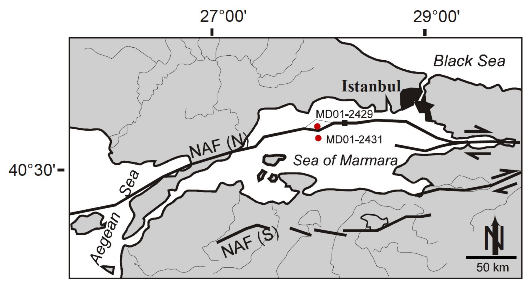

Figure 1: The Sea of Marmara and the North Anatolian Fault. Location of analyzed core. NAF geometry simplified from Armijo et al. (2002, 2005).

The MD01-2429 and MD01-2431 cores represents about 14 kyr, and 18 kyr BP of continuous deposition. They register a change of environmental conditions, which go from non-marine to marine conditions, occurred around 12 kyr BP (Perissoratis et al., 2000; Collier et al., 2000) and 13.2 kyr BP (Moretti et al., 2004), due to the connexion of the Marmara Basin with the Mediterranean Sea. The sedimentary deposits collected in both cores are predominantly hemipelagic silty-clayey muds, interbedded with millimetric to decimetric layers of sand, silty sands and normal graded sand (classical turbidites). Additionally, homogenites-turbidites (HmTu) deposits are found, especially, they are concentrated in the non-marine session. They are characterized by a basal coarse layer with overall normal graded bedding, (similar to classical turbidite lower term), followed by a strongly homogenous fine-grained (2 to 8 µm mean grain size) interval, lacking internal variation, and displaying an anomalously high magnetic foliation. As the content and particle shapes of the homogeneous upper component are identical to what is observed in the hemipelagic mud, the AMS contrast is attributed to a particular grain array (Campos et al., 2013) and, by mean, to a specific settling process. The sharp break between the two components is often preceded by a thin interval with flaser bedding-type layering indicating to-and-fro (oscillatory) current, and/or by a specific grain-size evolution. We interpreted this transitional interval as a consequence of oscillation of the whole water mass (seiche effect and/or reflected tsunami), thus an effect of earthquake and/or massive subaqueous landslide.

A characteristic of homogenites is a systematic settling in deepest areas, in marine basins, as well as, in large lacustrine basins (see references in Chapron et al., 1999). Due to, the homogenite occurrences needs the combination of gravity reworking (re-suspension) and tsunami effect (especially in case of reflected tsunamis vs. seiche effect in closed basins), this process may also withdraw a bottom relief created simultaneously with the sedimentary reworking, such as the front of a landslide or a co-seismic fault scarp. These direct relationships (time and location) between a submarine co-seismic scarp and synchronous specific layers have been proposed by Barnes & Pondard (2010) and Beck et al. (2012), and used 1) to decipher co-seismic rupturing from creep, 2) to estimate the vertical component of co-seismic offsets.

The selected section used to study the co-seismic rupturing and to estimate the vertical component of co-seismic offsets was the pre-Holocene part of the retrieved succession. This section shows well-defined homogenites+turbidites, being possible to establish a detailed correlation, event by event between both cores, both located on opposite sides of the fault; the core MD01-2431 collected in the footwall and the MD01-2429 collected in the “hanging wall”.

To carry out the correlation, a guide “reference” thin layer was taken into account. This layer has no seismic or landslide-triggered origin. It was recognized throughout the basin, indicating a general paleo-environmental event (chemical, mineralogical, and biological modification). Starting from this layer, a layer-by-layer correlation was established downcore. The proposed event-by-event correlation (Figure 2) was strengthened by: i) precise delimitation of the hemipelagic intervals, with same thicknesses, ii) similarities of subdivisions within HmTu composite layers. The correlation could be achieved for a 2 m succession in Core MD01-2431, which appears equivalent to a 6.2 m succession in Core MD01-2429, the whole for a 2 kyr duration. 11 homogenite+turbidites events (HmTu A, B, C, etc) were identified and correlated. For the thickest ones (HmTu A, C, E, H, K) the homogeneous component accounts for about 90 % of the thickness increase in the deeper site. Applying the model proposed by Beck et al. (2012) in the Lesser Antilles Arc, which described an active normal fault upon which the sea floor is maintained flat and horizontal, being each co-seismic offset quite exactly compensated by a coeval silty-sandy homogenite. We determined the vertical component of the fault displacements, based on the difference in thickness of the HmTu on both sides of the fault, being the thickness difference values between 40 cm to 160 cm. Although the investigated sediments are recent with a reduced depth-in-core, a possible compaction effect has to be discussed as: i) it concerns mainly clayey-silty material, ii) the thickness of the homogenite term is up to ten times higher on the hanging wall with respect to the footwall. Based on this differential compaction, a 10 % maximum estimate is thus proposed for a correction of the thickness difference, estimating that the vertical component of the fault displacement varied between 44 to 178 cm. Finally, taking into account this slip values and added local structural and seismological data, was performed an exercise to estimate paleomagnitudes, obtaining M_W magnitudes between 5.9 and 6.6 for the different events.

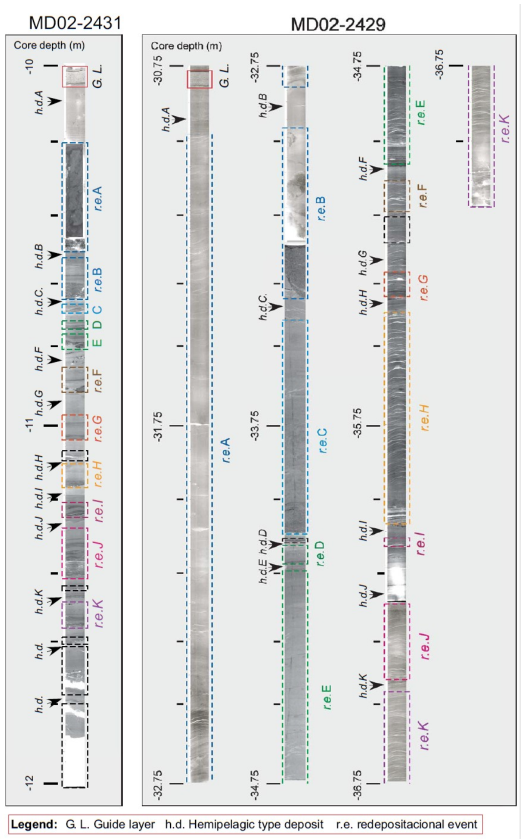

Figure 22: X-ray close up of two synchronous portions of Cores MD01-2429 and MD01-2431, displaying individually correlated re-depositional sedimentary events (homogenite+turbidite).

Acknowledgements: The presented investigations were possible thanks to CNRS-INSU funding through ISTerre Laboratory and the Universe Sciences Observatory of Grenoble. CNRS-INSU is acknowledged for the access to ARTEMIS national AMS radiocarbon measurement facilities. We thank Anne-Lise Develle (EDYTEM Laboratory) for XRF profiles performing and help for their interpretation.

REFERENCES

Adams, J., 1990. Paleoseismicity of the Cascadian subduction zone: evidence from turbidites off the Oregon–Washington margin. *Tectonics*, vol. 9, 4:569–583.

Armijo R., Meyer B., Navarro S., King G. C. P., Barka A. A., 2002. Asymmetric slip partitioning in the Sea of Marmara pull-apart: a clue to propagation processes of theNorth Anatolian Fault? *Terra Nova* 14:80-86.

Armijo, R., Pondard, N., Meyer, B., Uçarkus, G., Mercier de Lépinay, B., Malavieille, J., Dominguez, S., Gutscher, M.-A., Schmidt, S., Beck, C., Çagatay, N., Çakir, Z., Imren, C., Eriş, K., Natalin, B., Özalaybey, S., Tolun, L., Lefèvre, I., Seeber, L., Gasperini, L., Rangin, C., Emre, O., Sarikavak, K., 2005. Submarine fault scarps in the Sea of Marmara pull-apart (North Anatolian Fault): Implications for seismic hazard in Istanbul. *Geochemistry, Geophysics, Geosystems*, vol. 6, N° 6, Q06009, doi:10.1029/2004GC000896.

Barnes, P.M., and Pondard, N. (2010). Derivation of direct on-fault submarine paleoearthquake records from high-resolution seismic reflection profiles: Wairau Fault, New Zealand. *Geochemistry, Geophysics, Geosystems* 11, Q11013, doi:10.1029/2010GC003254.

Beck, C., 2009. Late Quaternary lacustrine paleo-seismic archives in north-western Alps: Examples of earthquake-origin assessment of sedimentary disturbances. *Earth-Science Reviews*, 96:327–344.

Beck, C, Mercier de Lépinay, B., Schneider, J.-L., Cremer, M., Çağatay, N., Wendenbaum, E., Boutareaud, S., Ménot, G., Schmidt, S., Weber, O., Eris, K., Armijo, R., Meyer, B., Pondard, N., Gutscher, M.-A., and the MARMACORE Cruise Party, J.-L. Turon, L. Labeyrie, E. Cortijo, Y. Gallet, H. Bouquerel, N. Gorur, A. Gervais, M.-H. Castera, L. Londeix, A. de Rességuier, A. Jaouen., 2007. Late Quaternary co-seismic sedimentation in the Sea of Marmara's deep basins. *in* "Sedimentary Records of Catastrophic Events" (F. Bourrouilh-Le Jan, C. Beck, D. Gorsline, Eds.) Spec. Iss *Sedimentary Geology*, 199:65–89.

Beck, C., Reyss, J.L., Leclerc, F., Moreno, E., Feuillet, N., Barrier, L., Beauducel, F., Boudon, G., Clément, V., Deplus, C., Gallou, N., Lebrun, J.F., Le Friant, A., Nercessian, A., Paterne, M., Saurel, J.M., Pichot, T., Vidal, C., 2012. Identification of deep subaqueous co-seismic scarps through specific coeval sedimentation in Lesser Antilles: implication for seismic hazard. In "Subaqueous Paleoseismology" (D. Pantosti Ed.), *Natural Hazards and Earth System Sciences*, doi:10.5194/nhess-12-1-2012.

Beck, C., Campos, C., Eriş, K. K., Çağatay, N., Mercier de Lepinay, B., and Jouanne, F., 2015. Estimation of successive coseismic vertical offsets using coeval sedimentary events – application to the southwestern limit of the Sea of Marmara's Central Basin (North Anatolian Fault), *Nat. Hazards Earth Syst. Sci.,* 15, 247–259.

Bertrand, S., F. Charlet, E. Chapron, N. Fageland and M. De Batist., 2008. Reconstruction of the Holocene seismotectonic activity of the Southern Andes from seismites recorded in Lago Icalma, Chile, 39°S, *Palaeogeography, Palaeoclimatology, Palaeoecology,* 259(2-3), 301-322.

Bull, J.M., Barnes, P.M., Lamarche, G., Sanderson, D.J., Cowie, P., Taylor, S.K., Dix, J.K.., 2006. High-resolution record of displacement accumulation on an active normal fault: implications for models of slip accumulation during repeated earthquakes. *Journal of Structural Geology*, 28:1146-1166.

Campos, C., 2014. Comparative study of co-seismic sedimentation in two tectonically active areas: the Sea of Marmara and the Gulf of Corinth. Methodological evelopments, implication for seismic hazards assessment. PhD Thesis Memoir, Grenoble University, 248 pp.

Campos, C., Beck, C. Crouzet, C., Demory, F., Van Welden, A., and Eris, K., 2013. Deciphering hemipelagites from homogenites through Magnetic Susceptibility Anisotropy. Paleoseismic implications (Sea of Marmara and Gulf of Corinth). *Sedimentary Geology*, 292:1-14.

Carrillo, E., Audemard, F., Beck, C., Cousin, M., Jouanne, F., Cano, V., Castilla, R., Melo, L., and Villemin, T., 2006. A Late Pleistocene natural seismograph along the Boconò Fault (Mérida Andes, Venezuela): the moraine-dammed Los Zerpa palæo-lake. *Bulletin of the French Geological Society*, 177(1):3-17.

Carrillo, E., Beck, C., Audemard, F.A., Moreno, E., Ollarves, R., 2008. Disentangling Late Quaternary climatic and seismo-tectonic controls on Lake Mucubají sedimentation (Mérida Andes, Venezuela) *in* M De Batist and E. Chapron Eds. "Lake systems: sedimentary archives of climate change and tectonic", *Palaeogeography, Palaeoclimatology, Palaeoecology*, 259:284–300.

Collier, R., M. R. Leeder, M. Trout, G. Ferentinos, E. Lyberis and G. Papatheodorou., 2000. High sediment yields and cool, wet winters: Test of last glacial paleoclimates in the northern Mediterranean*, Geology*, 28(11), 999-1002.

Chapron, E., Beck, C., Pourchet, M., and Deconinck, J.-F., 1999. 1822 earthquake-triggered homogenite in Lake Le Bourget (NW Alps). *Terra Nova*, 11:86-92.

Eriş, K., Çağatay, N. Beck, C., Mercier de Lepinay, B., Campos, C., 2012. Late-Pleistocene to Holocene sedimentary fills of the Çınarcık Basin of the Sea of Marmara. *Sedimentary Geology*, 281:151-165.

Gracia, E., Vizcaino, A., Escutia, C., Asioi, A., Rodes, A., Pallas, R., Garcia-Orellana, J. Lebreiro, S., Goldfinger, C. 2010. Holocene earthquake record offshore Portugal (SW Iberia): testing turbidite paleoseismology in a slow-convergence margin. *Quaternary Science Reviews* 29:1156-1172.

Goldfinger, C., Morey, A.E., Nelson, C.H., Gutierez-Pastor, J, Johnson, J.E., Karabanov, E., Eriksson, A. and shipboard scientific party, 2007. Rupture lengths and temporal history of significant earthquakes on the offshore and north coast segments of the Northern San Andreas Fault based on turbidite stratigraphy, *Earth and Planetary Science Letters,* 254:9-27.

Hancock, P.L., Barka, A.A., 1981. Opposed shear senses inferred from neotectonic mesofractures systems in the North Anatolian fault zone. *Journal of Structural Geology*, 3:383–392.

Hempton, M. R. and J. F. Dewey., 1983. Earthquake-induced deformational structures in young lacustrine sediments, East Anatolian Fault, southeast Turkey, *Tectonophysics*, 98(3-4), 7-14.

Lorenzoni, L., Benitez-Nelson, C. R., Thunell, R. C., Hollander, D., Varelan, R., Astor, Y.,Audemard, F. A., Muller-Karger, F. E., 2012. Potential role of event-driven sediment transport on sediment accumulation in the Cariaco Basin, Venezuela. *Marine Geology*. 307/310:105–110,

Marco, S., and Agnon, A., 1995. Prehistoric earthquake deformations near Masada, Dead Sea graben. *Geology*, 23:695–698.

McHugh, C., Seeber, L., Braudy, N., Cormier, M.-H., Davis, M.B., Diebold, J.B., Dieudonne, N., Douilly, R., Gulick, S.P.S., Hornbach, M.J., Johnson, H.E. III, Ryan Miskin, K., Sorlien, C., Steckler, M., Symithe, S.J., Templeton, J., 2011. Offshore sedimentary effects of the 12 January 2010 Haiti earthquake. *Geology*, vol. 39, 8:723-726; doi: 10.1130/G31815.1.

Migeon, S., Weber, O., Faugères, J.C., Saint Paul, J., 1998. A new X-ray imaging system for core analysis. *Geomarine Letters*, 18, 251-255.

Moernaut, J., 2011. Sublacustrine landslide processes and their paleoseismological significance: revealing the recurrence rate of giant earthquakes in South-Central Chile. PhD Thesis, University of Ghent, 274 pp.

Moretti, M., Alfaro, P., Caselles, O., Canas, J.A., 1999. Modelling seismites with a digital shaking table. *Tectonophysics*, 304:369:383.

Moretti, I., V. Lykousis, D. Sakellariou, J.-Y. Reynaud, B. Benziane and A. Prinzhoffer., 2004. Sedimentation and subsidence rate in the Gulf of Corinth: what we learn from the Marion Dufresne's long-piston coring, Comptes Rendus *Geoscience*, 336(4-5), 291-299.

Perissoratis, C., D. J. Piper and V. Lykousis., 2000. Alternating marine and lacustrine sedimentation during late Quaternary in the Gulf of Corinth rift basin, central Greece, *Marine Geology,* 167(3-4), 391-411.

Piper, D.J.W., Cochonat, P., Ollier, G., Le Drezen, E., Morrison, M, Baltzer, A., 1992. Evolution progressive d'un glissement rotationnel en un courant de turbidité : cas du séisme de 1929 des Grands Bancs (Terre Neuve). *Comptes-Rendus de l'Académie des Sciences*, Paris, 314:1057-1064.

Pouderoux, H., Lamarche, G., Proust, J.-N., 2012. Building a 18,000 Year-Long Paleo-Earthquake Record from detailed Deep-Sea Turbidite Characterization in Poverty Bay, New Zealand. *Natural Hazards Earth System Science* 12:2077-2101

Rodriguez Pascua, M.A., De Vicente, G., Calvo, J.P. and Perez-Lopez, R., 2003. Similarities between recent seismic activity and paleoseismites during the late miocene in the external Betic Chain (Spain): relationship by the b value and the fractal dimension. *Journal of Structural Geology*, 25: 749.

Siegenthaler, C., Finger, W., Kelts, K., Wang, S., 1987. Earthquake and seiche deposits in Lake Lucerne, Switzerland. *Eclogae geologicae Helvetiae*, 80:241-260.

Sims, J., 1975. Determining earthquake recurrence intervals from deformational structures in young lacustrine sediments. *Tectonophysics,* 29: 141-152.

Shiki, T., M. B. Cita and D. S. Gorsline., 2000. Sedimentary features of seismites, seismo-turbidites and tsunamiites - an introduction, *Sediment. Geol*. 135, 7-9.

Syvitski, J. P. M and C. T. Schafer., 1996. Evidence for an earthquake-triggered basin collapse in Saguenay Fjord, Canada, *Sedimentary Geology,* 104(1-4), 127-153.

Thunell, R., Tappa, E., Valera, R., Llano, M., Astor, Y., Muller-Karger, F. and Bohrer, R.,1999. Increased marine sediment suspension and fluxes following an earthquake. *Nature*, 398: 233-236.

Van Loon, A. J., K. Brodzikowski and T. Zielinski., 1995. Shock-induced resuspension deposits from a Pleistocene proglacial lake (Kleszczow Graben, central Poland), *Journal of Sedimentary Research*, 65(2), 417-422.

Wetzler, N., Marco, S., and Heifetz, E., 2010. Quantitative analysis of shear-induced turbulence in lake sediments. *Geology*, vol. 38, 4:303-306.

INQUA Focus Group Terrestrial Processes Perturbed by Tectonics (TPPT)

paleoseismicity.org

Analysis of paleoseismological trenching data in central Apennines (Italy): from data uncertainties to earthquake recurrence estimates and rupture scenarios

Cinti, Francesca R. (1), Daniela Pantostil (1), Anna Maria Lombardi (1), Riccardo Civico (1)

(1) Istituto Nazionale di Geofisica e Vulcanologia, Rome, Italy. francesca.cinti@ingv.it

Abstract: *Based on the paleoseismological trenching data available for the Central Apennines (Italy), we evaluated the uncertainties affecting the recognition and dating of the paleo-surface faulting events for each individual trench and built a dataset (Cinti et al., 2021). The analyzed compilation contains 191 paleoearthquakes occurred since 28kyr, recognized on 67 trenches excavated on 16 faults. Through a quantitative multistep method integrating paleoseismic data from multiple trenches, we built the surface faulting earthquake history for each individual fault (fault rupture scenario). The whole set of age ranges was analyzed to picture the regional earthquake recurrence within different intervals of time. Based on fault scenarios, we also preliminary explore the probability distribution of recurrence of ruptures along individual faults defined from different models.*

Key words*: Paleoseismology, Statistical modeling, Surface rupture scenarios, Regional earthquake recurrence, Central Apennines.*

INTRODUCTION

Paleoseismology is powerful to provide long histories of recurrent earthquakes back to pre-historical times (McCalpin, 2009), this is critical for the understanding of fault behavior over multiple earthquake cycles to be of use for seismic hazard assessment. Individual paleoearthquakes recognition is based on the detailed study of sediments and tectonic structures that can be produced by coseismic faulting in the near fault or by seismic shaking in the near and far field. The reconstruction of the paleoseismic histories includes uncertainties mainly depending on the evidence used to recognize the paleoearthquake, on discontinuous stratigraphy, and particularly on the definition of the event age.

Based on the paleoseismological trenching data available for the Central Apennines (Italy) (Figure 1) and through a deep analysis of the records, we evaluated the uncertainties affecting the recognition and dating of the paleo-surface faulting events for each individual trench and built a dataset (Cinti et al., 2021). The availability of more sites along an individual fault (Figure 2), increased the possibility to compile a complete and robust history of surface faulting earthquakes on the individual fault. On a larger scale, the earthquake histories on individual faults allowed testing the contemporaneity of ruptures on nearby faults, but also defining the regional characteristics of earthquake recurrence and rupture scenarios. Hence, the whole set of age ranges was analyzed to picture the regional earthquake recurrence within different intervals of time. Moreover, based on fault scenarios, we also preliminary explore the probability distribution of recurrence of ruptures along individual faults, *i.e.*, the faults' behavior, defined from different models.

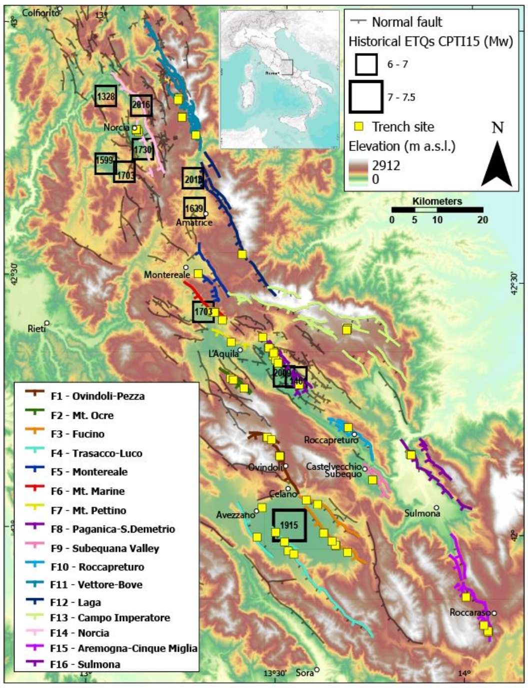

Figure 1. Paleoseismic Trenching sites (yellow squares) available for the Quaternary faults of the Central Apennines, Italy (F1 to F16, fault map modified after Vezzani and Ghisetti, 1998; Galli et al., 2008; Pierantoni et al., 2013; Civico et al., 2015, 2016; ITHACA Working Group, 2019), and used to compile the dataset of paleoearthquakes. Open black squares are historical earthquakes that hit the study area (Rovida et al., 2020).

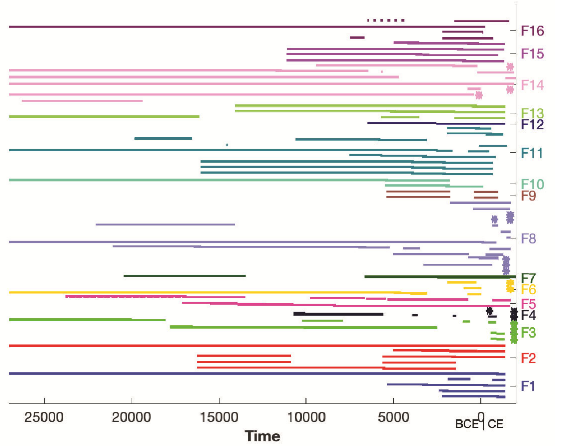

Figure 2. Chronogram of the paleoearthquakes recognized in each trench from the dataset compiled for the 16 faults (F1 to F16). The length of the bars show the uncertainty on the definition of the paleoearthquake age. We assume an equal probability of occurrence within each age interval. Same colors identify the records of events on the same fault.

DATA AND METHOD

With the aim of understanding the robustness of the trenching data and providing answers to the vivid debate open at a European scale on the definition of paleoseismological data uncertainties and their inclusion in modeling, we analyzed the activity of the main active faults within the Central Apennines for which existing trench paleoseismic data define the rupture patterns in time.

In the first step, we investigated 10 faults (Cinti et al., 2021) and successively added other 6 faults (this work; Figure 1), reaching the completeness of records available for the area at year 2021. For each of the trenches we reconstructed and revised an individual surface faulting history (Figure 2) by analyzing the impact on the results of the expert judgment expressed by the authors in their published scientific papers. Moreover, to work of a clean and reproducible set of data, for most of the cases where multiple trenches on the same fault/fault section were integrated in a single paper, we re-process the data to extract those related to each individual trench to avoid potential biases related to correlation directly provided by the Author/s.

We evaluated the uncertainties affecting the recognition and dating of the paleo-surface faulting events in individual trench and selected a final dataset built on original trench data from published papers, integrated with standardized constraints. The compilation contains 191 paleoearthquakes occurred since 28kyr, recognized on 67 trenches excavated on 16 faults (Figures 1 and 2). The first result of this analysis shows that the last 7 kyr-time span paleoearthquake data are quite homogeneous and are characterized by the smallest uncertainties (upper plot of Figure 5); therefore, we considered this interval as the most adequate to be statistically processed and used for building fault rupture scenarios and recognizing recurrence patterns.

In the second step, we build the surface faulting earthquake histories for each individual fault (fault rupture scenarios) through the development of a quantitative multistep method integrating paleoseismic data from multiple trenches (Figure 3 and 4).

In the third step, we defined methods to integrate and analyze paleoearthquake timelines of individual faults to define the average regional Inter Event Times (IETs) (Figure 4). This provides insights on the time spacing for M6+ surface faulting events in the study region, independently from which fault ruptured.

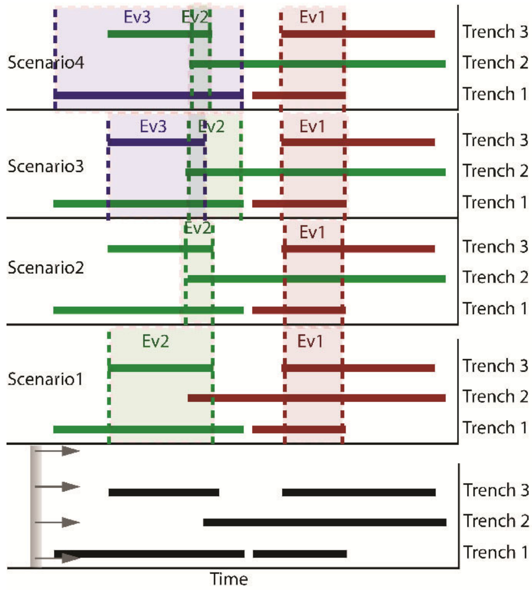

Figure 3. Example of individual fault rupture scenarios defined by the Sweep Line algorithm. Given the age of the paleo-earthquakes from three trenches along the same fault (lower black bars in the lower box), this algorithm identifies all possible intersections between ages of these paleoseismic events and provides different scenarios (upper box). Colors mark paleoseismic events from different trenches that overlap in time for each scenario (Ev1, Ev2, etc.).

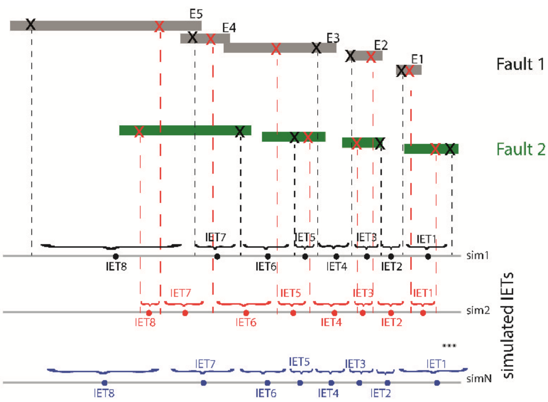

Figure 4. Visual representation of the simulations of earthquakes occurrence times, for each fault and each scenario.

RESULTS

Major outcomes derived from the analysis of the paleoearthquake dataset of this portion of the Central Apennines, are the reconstructed paleoearthquake timelines of individual faults and for the studied region within different intervals of time. A general lesson learned is that a deep analysis of the available trenching records is an indispensable requirement for understanding the robustness of data and properly use them to build rupture scenarios.

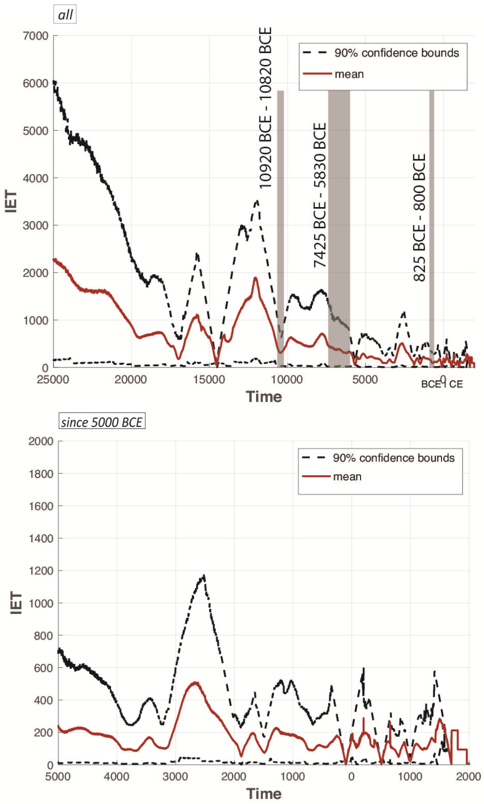

Figure 5. Temporal plot of mean (solid red line) and 90% confidence bounds (dotted black lines) of regional interevent times (IETs) calculated for the 16 faults dataset. The 27 kyrs plot (above) shows increases of the uncertainties from 5000 BCE back in time (change point, thick grey bar). Change points of the IET indicate the variation of data uncertainty (see also Table 1). For this reason the analysis is framed in the past 7kyr-time window (plot below).

Time window	average IET
before 10900 BCE	945 (605) yr
10900 BCE - 6600 BCE	495 (105) yr
6600 BCE - 800 BCE	190 (90) yr
800 BCE - 2000 CE	120 (50) yr

Table 1. Change points divide the whole period of observation in intervals (upper plot in Figure 5): within each of these it is possible to calculate the Average IET and (its error).

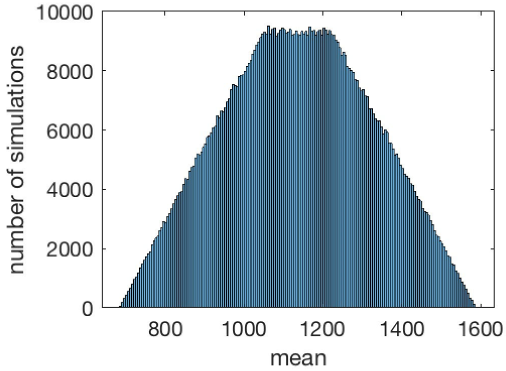

Figure 6. Preliminary analysis of mean rupture recurrence on one fault scenario of the Aremogna-Cinque Miglia Fault - F15 (most recent event: 800 BCE-1349 CE) from simulations. The mean recurrence is ~1200 yr.

Other main outcomes are:

-increasing the number of data in the analysis (this work has included #6 extra faults in addition to Cinti et al., 2021) brings to a greater "stability" of the regional IET back to 800 BCE (Figure 5).

-the resulting regional IETs are strongly affected by the smaller number of detected paleoearthquakes back in time having also larger the age uncertainties (Figures 2 and 5).

- the built scenarios define a regional average inter event time (IET) of 120±50 yr in the past 2800 yr (historical times) (see Table 1). The paleoseismologically estimated IETs fit with the IET derived from the historical catalogues for the same area (11 events in 700 years: 70 yr) (Figure 1).

- preliminary analysis of rupture recurrence on individual fault through IETs simulations confirm that the average recurrence for surface faulting on individual fault is of the order of several hundreds of years (Figure 6). Most of the 16 faults have recurrence between 850 yr and 2500 yr.

- an ongoing development of the study is the definition of recurrence models and estimate of the 30yr-probability of occurrence for each individual fault (Lombardi et al., in prep). Preliminary results show the different impact of the MRE age on the models.

REFERENCES

Cinti, F.R., Pantosti, D., Lombardi,A.M., Civico, R., 2021. Modeling of earthquake chronology from paleoseismic data: Insights for regional earthquake recurrence and earthquake storms in the Central Apennines. *Tectonophysics*, 816, 10.1016/j.tecto.2021.229016

Lombardi, A.M. et al. 2023 (in prep).

McCalpin, J. P. (ed.), 2009. Paleoseismology, 2nd edn. Academic Press. International Geophysics Series, Vol. 95, 613 pp.

First paleoseismology analysis in Ecuadorian Amazon piedmont: implication for seismic risk analysis.

Cornejo, Carolina (1), Oswaldo Guzmán (1), Corina Campos (1), Jefferson Cargua (2)

(1) Grupo de investigación de Ciencias de la Tierra y Clima. Universidad Regional Amazónica Ikiam. Tena, Ecuador. Email: estefany.cornejo@est.ikiam.edu.ec

(2) Universidad Nacional Mayor San Marcos. Lima, Perú.

Abstract: *Paleoseismology in the Ecuadorian Sub-Andean zone has been little used despite being a tectonically active region. In this work we study a trench south of the Porotoyacu fault that exhibits deformations in sedimentary deposits. The objective of this research is to estimate the magnitudes and events through paleoseismology and characterization of seismites. The analysis of the two mains ruptures planes allows to identify at least two seismic event in one of the rupture plane, while one seismic event is recognized in the other, these events registered magnitudes between 6.22 <Mw< 6.75. On the other hand, the seismites identified like load cast, ball and pillow, loops bedding and sand dykes would have originated with earthquakes with Mw>5. Finally, it is estimated that the ruptures evidenced in the trench of the study area are a southward extension of the Porotoyacu Fault.*

Key words*: Paleoseismology, Seismites, Sub-Andean Ecuadorian*

Introduction

Seismic activity in Ecuador is controlled by the subduction of the Nazca plate with the South American plate (Figure. 1) and by shallow and deep faults focused within the continental plate. Ecuador has about 92 Quaternary surface faults, some of which have only been identified by geographic accident (Eguez et al., 2003; Costa et al., 2020). In the sub-Andean zone, seismic events caused by surface faults usually have magnitudes lower than 4.5, however, there were events with atypical magnitudes, for example, in 1987 in Baeza with Mw =7.1, in 1995 in Macas with Mw =7.0, both events related to a fault system called Cutucú-Napo (Figure. 1) (Baby et al., 2004).

The seismic activity of surface faults can be characterized through paleoseismology, this technique identifies effects of past seismic events that have left observable traces and are preserved in sediments as a sedimentary record (McCalpin and Nelson, 2009). Paleoseismology studies can be complemented with the analysis and interpretation of structures generated by the liquefaction of sediments (a phenomenon caused by external forces where the soil acquires a heavy liquid consistency) (Rodríguez-Pascua et al., 2000), these structures develop in non-cohesive sediments and are mainly triggered by earthquakes and are called "seismites" (Alfaro et al., 2002). The paleoseismology analysis allows the identification of deformations in the rocks, which are correlated with the interpreted magnitudes of historical and modern seismic events, allowing the magnitudes of a fault to be obtained (Rodríguez-Pascua et al., 2000).

In Ecuador, paleoseismology has been implemented in faults located only in the Sierra region, such as the Quito Fault and the Pallatanga Fault (Hibsch et al., 1996; Alvarado, 2012; Baize et al., 2020), little or no work has been done in the Amazon piedmont using this technique. However, there are active faults identified in this region that can cause high magnitude earthquakes. One of them is the Porotoyacu Fault of superficial scale which is catalogued by Costa et al. (2020), with an approximate length of 15 km and reverse kinematics, which have been just interpreted only geographically and at a regional scale. In this work a trench has been identified south of the Porotoyacu Fault which exhibits deformations in sedimentary deposits. The present work aims to estimate the paleomagnitudes of the earthquakes generated by this structure through the implementation of paleoseismology and characterization of seismites, in addition to reinterpreting the length and kinematics in order to improve the interpretation at regional scale.

Seismic context of the study area

The sub-Andean zone is formed by the Cutucú mountain range in the south, in the central part by the Pastaza depression and the Napo uplift in the north (Baby et al., 2004). This region includes Jurassic-Cretaceous formations that are deformed by the Cutucú-Napo fault system. This system is divided into the Cutucú and Napo seismogenic zone (Bes de Berc, 2003; Beauval et al., 2018). The sub-Andean deformation is compressional and transpressional and is controlled by basement thrusts (Baby et al., 2004). Most of the structures of the reverse fault system correspond to inverted normal faults that control Triassic-Jurassic sedimentation and are of shallow scale (Baby et al., 2004). The fault system that covers the sub-Andean zone is active from the northern part of the Napo region to Pastaza (Bes de Berc, 2003; Eguez et al., 2003).

Seismicity in the study area is moderate to high and superficial, concentrated mainly within the Napo seismogenic source, located north of the Ecuador (Beauval et al., 2018). In this area at least 24 seismic events have been recorded between 1927-2022 with magnitudes ranging from 2.5 to 6.3 (IGEPN, 2022).

Discussion

In the study area, the ruptures of two segments of a fault and deformation structures interpreted as seismites will be analyzed. The seismic faults evidenced in the outcrop were formed when the sediments were still soft, therefore, these events are associated with the time of rock formation.

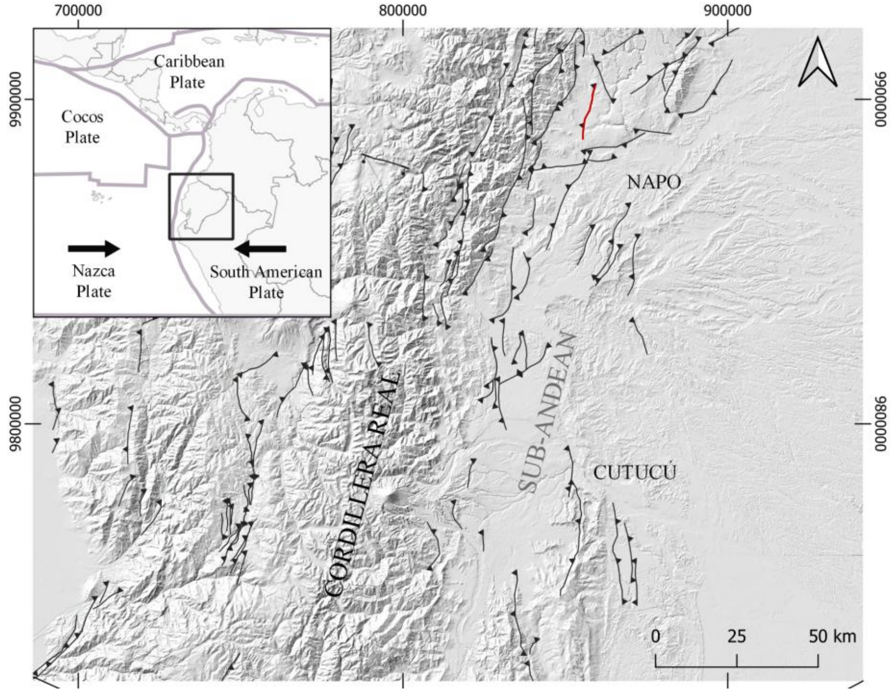

Figure 1. In the upper left box, the location of the investigated area and its geodynamic context are shown, showing the stresses and boundaries related to the Nazca plate (oceanic plate) and the South American plate (continental plate). Location of the Cutucú-Napo fault system, the black lines are active faults (Quaternary), the red line represents the Porotoyacu Fault with its inverse kinematics (Modified from Costa et al., 2020).

For this reason, the events determined through the vertical displacement obtained in each of the trench ruptures are not necessarily the same event that gave rise to the seismites. However, we analysis both in this work.

Paleoseismic events and stratigraphic rupture

From the information revealed in the trench, the events and corresponding magnitudes were estimated. According to the evidence of the rupture of segment 1 (R1) two events occurred, this was deduced because there is a vertical displacement of 0.17m from unit 5 to unit 6 and there is an approximate vertical displacement of 0.31 m that goes from unit 1 to unit 5. This indicates that the displacement evidenced from unit 1 to unit 5 is cumulative, therefore, there would be a vertical displacement of 0.14 m corresponding to the first event and the displacement of 0.17 m corresponding to the second event. On the other hand, for the rupture of segment 2 (R2) it is deduced that there was only one event because from unit 1 to unit 11 there is a similar vertical displacement of 0.61 m.

For these ruptures, two scenarios of fault kinematics are proposed, because according to the study of (Baby et al., 2004) the surface structures located in the Cutucú-Napo fault system are normal faults that were inverted changing their regime to reverse faults. However, in the field observations, ruptures with normal kinematics were identified; therefore, it is possible that these structures are faults with normal kinematics or normal faults that are in the process of inversion. For this reason, the magnitudes are calculated with the equation proposed by Wells and Coppersmith (1994) for both normal faults (N) and undefined faults (All).

For the rupture of segment 1 (R1) (Figure. 2b) with a scenario that the fault that caused it is of normal type, we obtain a magnitude of 6.22 for the first event and a magnitude of 6.27 for the second event. For the rupture of segment 2 (R2) (Figure 2b) with this same scenario we have a magnitude of 6.64 for the single event. For the second scenario with reverse type faulting, for the rupture of segment 1 (R1) we have a magnitude of 6.22 for the first event and a magnitude of 6.29 for the second event. For the rupture of segment 2 (R2), a magnitude greater than 6.75 is obtained for the first and only event.

Seismites and their potential for estimating paleoseismic magnitudes.

The study area is located in the Napo seismogenic source, an area that has been exposed to high seismic activity (Beauval et al., 2018). According to Marco and Agnon (1995), seismic events with magnitudes greater than 5 have the necessary characteristics to initiate processes related to liquefaction and, therefore, generate seismites. For the study area, it has been considered that sedimentary deposits consisting of fine-grained claystone and sandstones allow seismic events of magnitude 5 and higher to give rise to ductile deformations.

Pillows structure interpretation

Classified within the pillows structures are load cast and ball-and-pillow seismites (Rodríguez-Pascua et al., 2000): Structures were identified that have the appearance of concave upward bodies at the base of unit 7 and the top of unit 6, which are constituted by fine-grained sediments and present internal lamination. The morphology of the structure suggests that it is a load-cast. These structures have diameters ranging from 15 cm wide to 10 cm high (Figure. 3a).

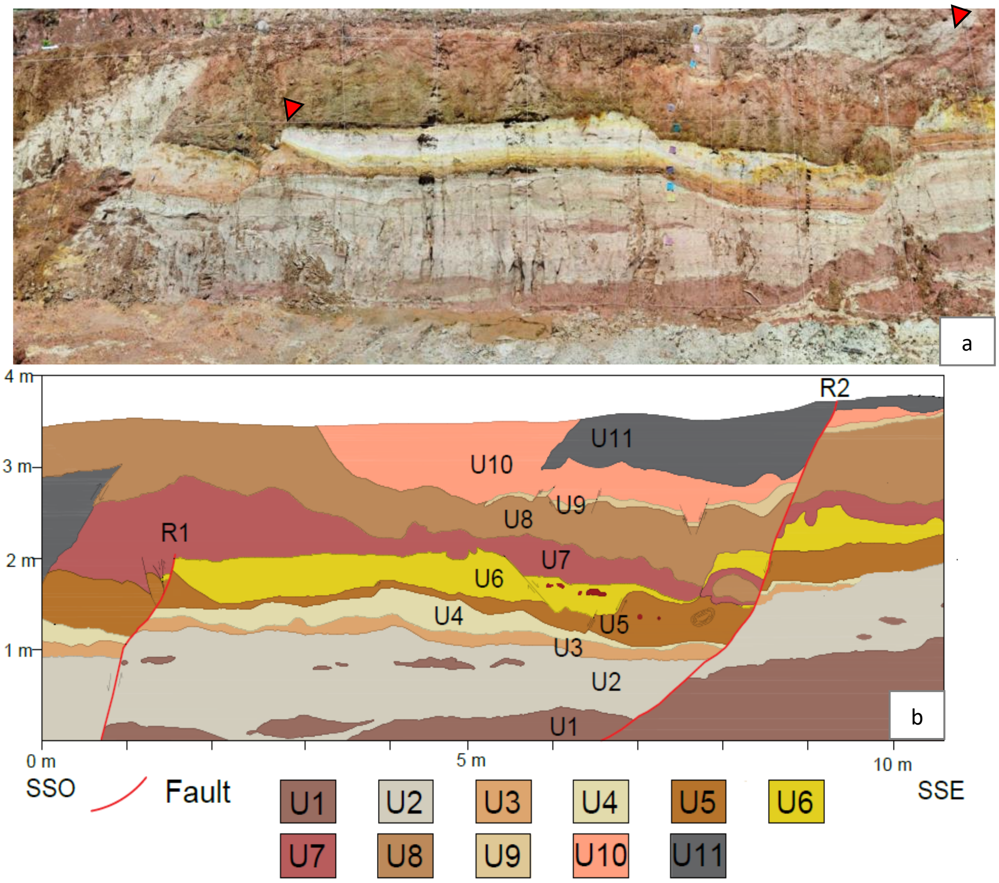

Figure 2. (a) Photomosaic of the trench, where the presence of fault rupture planes and deformation structures were identified. (b) Illustration of rupture plane segments, micro-ruptures and stratigraphic units (U) from the trench results.

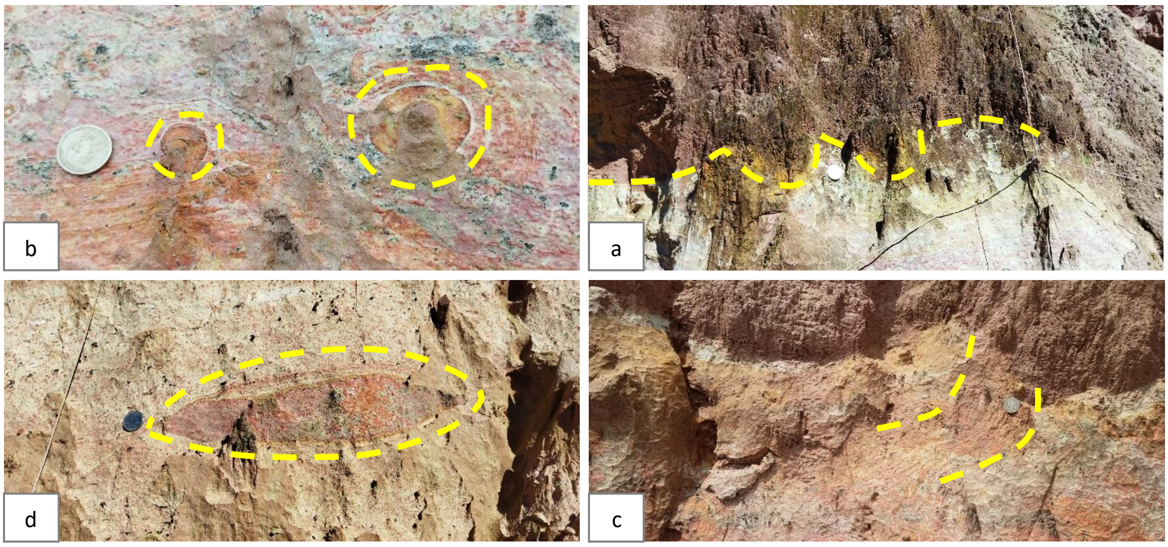

Figure 3. (a) Ball and pillow observed in the middle part of unit 5. (b) Load cast seismite observed between the top of unit 6 and the base of unit 7. (c) Loop bedding seismite observed in the middle part of unit 2. (d) Sand dikes seismite observed between the top of unit 6 and the base of unit 7.

Structures with a concentric ball morphology were identified that are distributed in the middle part of unit 5 and in the middle part of unit 6, which have claystone as lithology. These structures present laminations that are curved or deformed. This lamination is located next to the outer edge of the hemispheres, adjusting to the shape of the edge of the structure. The balls and pillow are isolated and enclosed in the sediment of each of the units. The diameters of these structures can range from 3 cm to 20 cm wide and 3 cm to 12 cm high (Figure. 3b). Morphology suggests that they are ball and pillow structures.

The presence of active faults in the area and the correlation of the presence of these structures in other places that have been related to seismic events, allows postulating that both structures are related to seismic action. Thus, according to Obermeier (1996) and Rodríguez-Pascua et al. (2000), these structures may originate with seismic events of magnitudes 5.5 to 8.

Sand dikes interpretation

Sand dike-shaped seismites were identified that have the appearance of an isolated column. This deformation structure intrudes U7 which consists of fine-grained sandstone. Fractures in this seismite typically cut stratigraphic units of different lithologies ranging in diameter from 12 cm wide to 30 cm long and project downward with deformed lamination (Figure. 3c). Sand dike structures usually originate from seismic events with magnitudes of 5 to 8 (Audemard and de Santis, 1991).

Loop bedding interpretation

Seismites with loop bedding morphology were identified and have the appearance of long thin loops or links in a chain. These structures are present in the lower and middle parts of unit 2, which consists of claystone. The diameter of the loops ranges from 80 to 150 cm in width of lateral extent (Figure. 3d). The loops beddings present in this area are interpreted as the result of stretching of non-lithified sediments that were the consequence of the occurrence of seismic events, related to the movement of extensional or normal faults (Martín-Chivelet et al., 2011; Rodŕiguez-Pascua et al., 2000). According to reports made in other studies, this structures are associated with magnitudes less than 4 (Martín-Chivelet et al., 2011).

Implications on the Porotoyacu fault

The SSE and SSW orientations and the kinematics of both ruptures, analyzed in the field, indicate normal faulting, although reverse faults predominate in the sub-Andean zone. Therefore, it is presumed that these structures could be normal faults or normal faults that are being inverted. The estimated magnitudes (6.22<Mw<6.75) for both types of displacement and the interpreted magnitudes (Mw>5) of the seismicity indicate that the seismic events that originated in the ruptures were able to generate liquefaction processes. For this reason, it is likely that the Porotoyacu fault has developed under active tectonics, thus affecting the Tena Formation (Cretaceous). It is even evident that this structure continues to be tectonically active, because the stratigraphic units of the trench show displacements. By analyzing the characteristics, it is estimated that the ruptures they are part of the Porotoyacu Fault, which is located 1.62 km NE of the study area.

Acknowledgements: Thanks to the project ICGP-669-Ollin Network for the financial support to participate in PATA-days 2022. I also appreciate the Comité INQUA/TERPRO for the grant otorgaded and the Universidad Regional Amazónica Ikiam for supporting me to be here. We are also very grateful to Anderson Guamán for his great help in carrying out this work and to Dennys Chalco for his support in the field trips.

REFERENCES

Alfaro, P., Delgado, J., Estévez, A., Molina, J., Moretti, M., Soria, J., 2002. Liquefaction and fluidization structures in Messinian storm deposits (Bajo Segura Basin, Betic Cordillera, southern Spain). Int J Earth Sci (Geol Rundsch) 91, 505–513. https://doi.org/10.1007/s00531-001-0241-z

Alvarado, A., 2012. Néotectonique et cinématique de la déformation continentale en Equateur (PhD Thesis). Université de Grenoble.

Audemard, F., de Santis, F., 1991. Survey of liquefaction structures induced by recent moderate earthquakes. Bulletin of the International Association of Engineering Geology 5–16. https://doi.org/10.1007/BF02602705

Baby, P., Rivadeneira, M., Barragán, R., 2004. La cuenca Oriente: geología y petróleo. Institut français d'études andines.

Baize, S., Audin, L., Alvarado, A., Jomard, H., Bablon, M., Champenois, J., Espin, P., Samaniego, P., Quidelleur, X., Le Pennec, J.-L., 2020. Active Tectonics and Earthquake Geology Along the Pallatanga Fault, Central Andes of Ecuador. Front. Earth Sci. 8, 193. https://doi.org/10.3389/feart.2020.00193

Beauval, C., Marinière, J., Yepes, H., Audin, L., Nocquet, J. -M., Alvarado, A., Baize, S., Aguilar, J., Singaucho, J. -C., Jomard, H., 2018. A New Seismic Hazard Model for Ecuador. Bulletin of the Seismological Society of America 108, 1443–1464. https://doi.org/10.1785/0120170259

Bes de Berc, S., 2003. Tectonique de chevauchement, surrection et incision fluviatile:(exemple de la zone subandine équatorienne, Haut bassin amazonien) (PhD Thesis). Universite Touluse III.

Costa, C., Alvarado, A., Audemard, F., Audin, L., Benavente, C., Bezerra, F.H., Cembrano, J., González, G., López, M., Minaya, E., Santibañez, I., Garcia, J., Arcila, M., Pagani, M., Pérez, I., Delgado, F., Paolini, M., Garro, H., 2020. Hazardous faults of South America; compilation and overview. Journal of South American Earth Sciences 104, 102837. https://doi.org/10.1016/j.jsames.2020.102837

Eguez, A., Alvarado, A., Yepes, H., Machette, M.N., Costa, C., Dart, R.L., Bradley, L., 2003. Database and map of Quaternary faults and folds of Ecuador and its offshore regions. US Geological Survey Open-File Report 03-289 3, 289.

Hibsch, C., Alvarado, A.P., Yepes, H.A., Sébrier, M., Pérez, H.V., 1996. Falla activa de Quito y fuentes sismogenéticas regionales: un estudio del riesgo sísmico de Quito (Ecuador) con el análisis de los sedimentos cuaternarios 25, 359–388.

IGEPN, 2022. Instituto Geofísico - EPN [WWW Document]. Catálogo 2012-Actualidad. URL http://www.igepn.edu.ec/

Marco, S., Agnon, A., 1995. Prehistoric earthquake deformations near Masada, Dead Sea graben. Geol 23, 695. https://doi.org/10.1130/0091-7613(1995)023<0695:PEDNMD>2.3.CO;2

Martín-Chivelet, J., Palma, R.M., López-Gómez, J., Kietzmann, D.A., 2011. Earthquake-induced soft-sediment deformation structures in Upper Jurassic open-marine microbialites (Neuquén Basin, Argentina). Sedimentary Geology 235, 210–221. https://doi.org/10.1016/j.sedgeo.2010.09.017

McCalpin, J.P., Nelson, A.R., 2009. Introduction to Paleoseismology, in: Paleoseismology. Elsevier, Burlintong.

Obermeier, S.F., 1996. Use of liquefaction-induced features for paleoseismic analysis—An overview of how seismic liquefaction features can be distinguished from other features and how their regional distribution and properties of source sediment can be used to infer the location and strength of Holocene paleo-earthquakes. Engineering Geology 44, 1–76. https://doi.org/10.1016/S0013-7952(96)00040-3

Rodríguez-Pascua, M.A., Calvo, J.P., De Vicente, G., Gómez-Gras, D., 2000. Soft-sediment deformation structures interpreted as seismites in lacustrine sediments of the Prebetic Zone, SE Spain, and their potential use as indicators of earthquake magnitudes during the Late Miocene. Sedimentary Geology 135, 117–135. https://doi.org/10.1016/S0037-0738(00)00067-1

Wells, D.L., Coppersmith, 1994. New Empirical Relationships among Magnitude, Rupture Length, Rupture Width, Rupture Area, and Surface Displacement. Bulletin of the Seismological Society of America 84, 974–1002.

Impact of far-field glacially induced stresses on fault stability in the eastern Paris basin

Adrien Damon (1,2), Stéphane Mazzotti (2), Philippe Vernant (2), Rémi Vachon (3), Juliette Grosset (2), Frédéric Ego (1), David Baumont (4)

(1) ANDRA, 7, rue Jean-Monnet, 92298 Châtenay-Malabry cedex, France. Email: adrien.damon@umontpellier.fr
(2) Géosciences Montpellier, CNRS, Université de Montpellier, 34000 Montpellier, France
(3) Department of Earth Sciences (MPT), Geocentrum, Villavägen 16, 752 36 Uppsala
(4) Seister S.A.S., Immeuble Le Quartz, 58 chemin de la justice, 92290 Châtenay-Malabry, France

Abstract: *Earthquakes occur in stable continental regions (SCR) with Mw>5 and up to Mw≈7, and research on the origins of SCR seismicity is ongoing. Glacial Isostatic Adjustment (GIA) is commonly considered as a factor of SCR stress perturbation that can trigger seismicity in past glaciated areas, and studies suggest that fault failure may occur around those past glaciated areas. In this study, we model western Europe GIA in order to estimate their far-field impact on fault stability in the eastern Paris basin. We show that the considered GIA can induce stress perturbations great enough to potentially reactivate faults, but we show that known fault structures in the eastern Paris basin are more likely to be clamped when integrating these stress perturbations to ambient crustal stresses.*

Key words*: Seismotectonics, glacial isostasy, fault reactivation, stable continental region, Paris basin*

INTRODUCTION

Seismicity is observed in Stable Continental Regions (SCR), which can be defined as areas where the continental crust is largely unaffected by plate boundary processes and exhibits no major deformation since several tens of Myrs (Johnston et al., 1994). Earthquakes of Mw>5 up to Mw≈7 are reported in these regions (Schulte and Mooney, 2005). Research on the origins and characteristics of this seismic activity is ongoing and suggests that SCR seismicity may be triggered by transient stress perturbations, even with no evidence of strain accumulation nor previous seismicity (Calais et al., 2016; Long, 1988). Glacial Isostatic Adjustment (GIA) is frequently considered as a factor of SCR deformation and stress perturbation, and known fault activity is related with ice loading and unloading (Steffen et al., 2021). Most of the studies on the GIA impact on fault stability are applied to areas covered by past glaciations, but some works also suggest that fault activity could be triggered in the surroundings of glaciated areas (Brandes et al., 2015; Steffen and Steffen, 2021), suggesting that far-field GIA may possibly induce sufficient stress perturbations to trigger fault reactivation.

The Paris basin consists in the sedimentary covering of an Hercynian basement, with the first deposits dated from the Permian (250 Ma), and the last one from the Pliocene (5.3-2.6 Ma). It features subvertical (around 80° dip) basement faults inherited from the Hercynian orogeny and graben faults affecting the whole sedimentary pile that formed during the Cenozoic western Europe rifting (40-25 Ma). It has experienced three noticeable deformation events evidenced by fault activity. They are associated with the Pyrenean orogeny (55-25 Ma), Cenozoic western Europe rifting and Alpine orogeny (40-15 Ma). No recent (i.e. quaternary) significant deformation is observed, thus the Paris basin can be defined as a SCR. Last known fault reactivation is proposed to be linked with the Alpine deformation phase around 15-20 Ma, based on the dating of calcite cementation of fractures in the basin. Even though no significant quaternary seismic event is known in the Paris basin, where only very few earthquakes of Mw<4 are recorded (with most of them being triggered by anthropic activity; BCSF RENASS, 2022), GNSS-derived strain rates indicate that there is ongoing small deformation in and around the Paris basin (EPOS, 2022; Masson et al., 2019). Such deformation is related to far-field GIA induced by Fennoscandian and Celtic ice sheets (Nocquet et al., 2005), and we suggest that the Alpine and Massif Central glaciers could also induce deformation in the Paris basin.

In this study, we model LGM & present-day far-field GIA stress perturbations, and we apply them to a critically stressed crust in order to discuss potential fault reactivation in the eastern Paris basin.

METHODS

We compute stress perturbations associated with Alpine, Massif Central, Fennoscandian & Celtic GIA for the LGM and present-day. In order to compute the Earth's response to ice loading and unloading, we consider an Earth model integrating lithosphere elasticity and mantle viscosity. We use ice reconstructions (fig. 1) to compute the loads on Earth's surface.

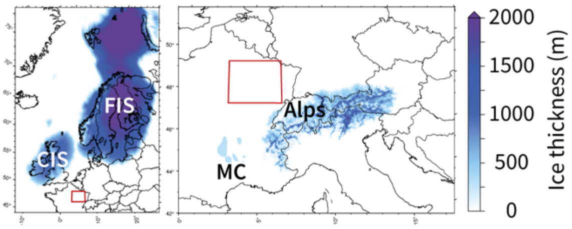

Figure 1: considered ice loads, as LGM ice thickness. Red rectangle is the study area. FIS and CIS: Fennoscandian and Celtic Ice Sheets.

We integrate lithosphere elasticity using equivalent elastic thickness (T_e) maps that are based on rheological models of the European lithosphere. These maps allow us to include lateral lithosphere rigidity heterogeneity, while the lithosphere rigidity is commonly considered to be uniform in GIA models. Finally, we integrate mantle viscosity in our models using standard values (Lambeck et al., 2017; Steffen and Kaufmann, 2005) in the 10^{20} Pa.s range for the upper mantle and 1.3×10^{22} Pa.s for the lower mantle.

We consider the maximum GIA stress perturbation at the top of the elastic lithosphere. We test multiple lithosphere rigidity scenarios using three T_e maps (fig. 2) to account for variability on the computed GIA effects. According to their Te values, the "mean" and "max" models may be the most reasonable.

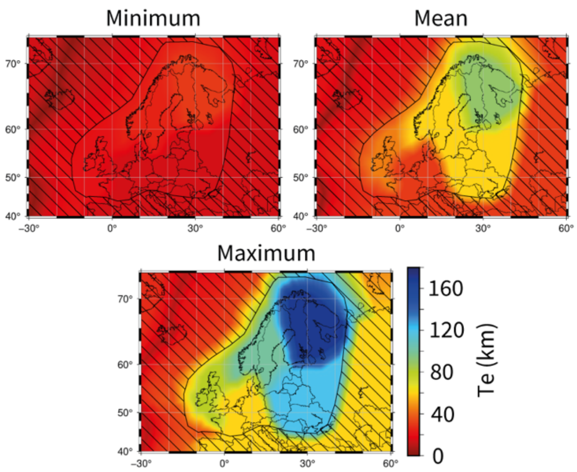

Figure 2: T_e maps used in computations. Hatched domain values have no impact on results in the study area.

In order to investigate fault stability, we compute Coulomb Failure Stress (CFS) perturbations and full values in ambient stress fields for fault geometries of 0-360°N azimuths and 60-90° dips. Ambient stress fields are oriented 150°N based on regional measurements and their amplitude is modeled based on the observation that SCR crust is generally critically stressed for failure on preferentially oriented fault planes of friction = 0.6 (Brudy et al., 1997; Townend and Zoback, 2000; Zoback and Healy, 1992). We test both the stress regime (based on observed regimes around the study area (Mazzotti et al., 2021)) and stress tensor shape ratio (fig. 3).

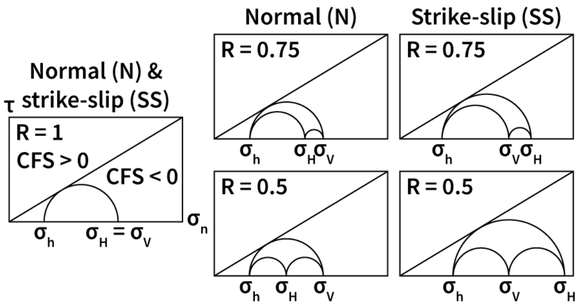

Figure 3: schematic representation of the tested critical stress fields as Mohr circles.

RESULTS

LGM and present-day stress perturbations are shown in figures 4 & 5, respectively. At the LGM, the GIA effects associated with the considered ice loads interplay in the study area and result in NNE-SSW compression or NW-SE tension, depending on the T_e model. Tensile stress perturbations are between 2-7 MPa, and compressional stress perturbations are between 2-3 MPa. At present-day, only tension is computed in the study area, mainly associated with the far-field effect of the Fennoscandian GIA, and stress perturbations are between 1-3 MPa. For both LGM and present-day, CFS perturbations in the middle of the study area are representative of those computed over the whole study area and are mostly positive, which results in a fault unclamping tendency. The amplitude of the positive CFS perturbations is between 1-8 MPa for the LGM and 0.8-2 MPa for present-day.

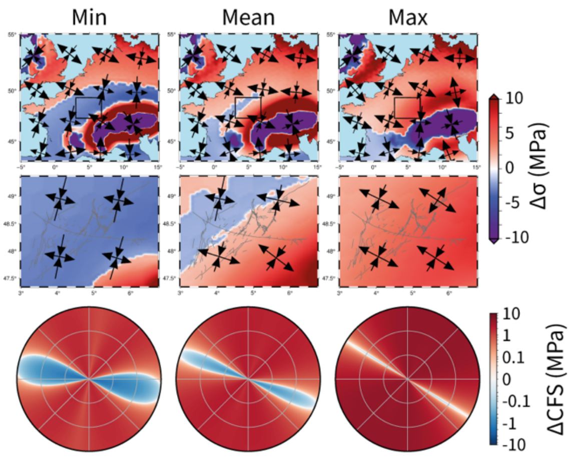

Figure 4: LGM stress perturbations fields in western Europe (upper row), detail in the study area (middle row), CFS perturbations in the middle of the study area (lower row, vertical = N-S fault, horizontal = E-W fault, circle center = 90° dip, circle border = 60° dip). Positive values: tension/unclamping, negative values: compression/clamping.

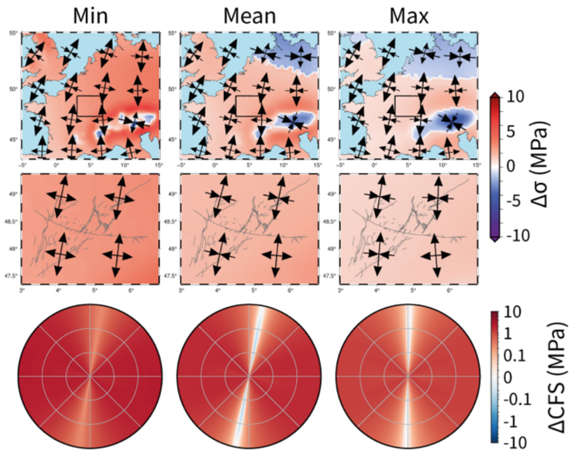

Figure 5: present-day stress perturbations fields in western Europe (upper row), detail in the study area (middle row), CFS perturbations in the middle of the study area (lower row, vertical = N-S fault, horizontal = E-W fault, circle center = 90° dip, circle border = 60° dip). Positive values: tension/unclamping, negative values: compression/clamping.

Yet, these CFS perturbations only show the isolated GIA effects in the study area, so we combine them with our ambient crustal stresses models to estimate full fault stability (fig. 6 & 7). We show full CFS at 1 km deep as representative of the maximum GIA effect: at this depth, the GIA stresses are the greatest (top of elastic plate) and ambient stresses are at most 10 times greater than the highest GIA stress perturbations. Overall, because the GIA stress perturbations are small compared to the ambient stresses, faults showing a potential for reactivation (positive CFS) are those with a geometry close to the Andersonian model: 60° dipping normal faults oriented 150°N and vertical strike-slip faults oriented 120°N and 180°N. However, the GIA stress perturbations at the LGM expand the range of potentially reactivated normal faults to azimuths of 130-220°N and dips of 60-80°, particularly for the maximum lithosphere rigidity model (fig. 6). LGM positive CFS values are up to 1-2 MPa.

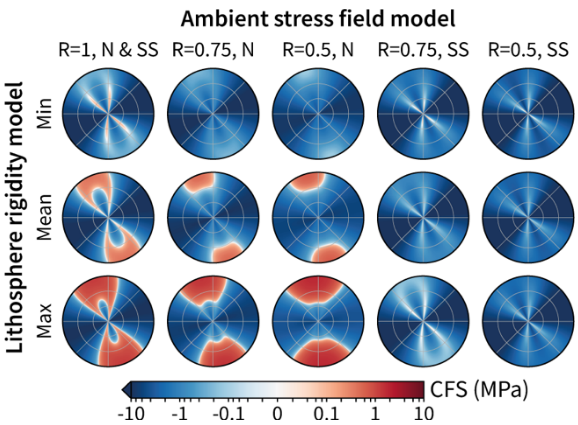

Figure 6: LGM CFS at 1 km deep depending on lithosphere rigidity and ambient stress field model. For each plot: vertical = N-S fault, horizontal = E-W fault, circle center = 90° dip, circle border = 60° dip.

At present-day, more subvertical faults show a potential for strike-slip reactivation compared to the LGM, and those oriented ±10° to Andersonian fault geometries show positive CFS values up to 0.8 MPa (fig. 7). Otherwise, the range of potentially reactivated normal faults and the amplitude of positive CFS are reduced compared to the LGM, but normal faults within ±20-30° to the Andersonian fault geometries remain associated with CFS values of 0.1-1 MPa (fig. 7).

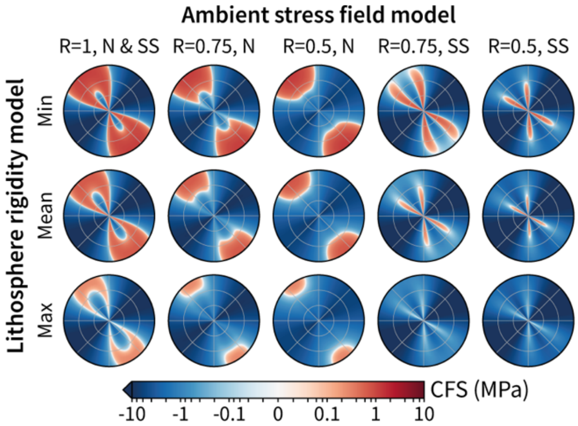

Figure 7: present-day CFS at 1 km deep depending on lithosphere rigidity and ambient stress field model. For each plot: vertical = N-S fault, horizontal = E-W fault, circle center = 90° dip, circle border = 60° dip.

At greater depths (5-15 km) for which seismic hazard assessment is commonly made, geometry ranges showing positive CFS are reduced, and mostly only 150±5°N, 60-63° dip or 120/180°N, 85-90° dip geometries that are close to Andersonian geometries may potentially be reactivated, with positive CFS reaching 1 MPa at most.

According to the synthesis of our CFS computations at LGM and present-day and for depths of 1 to 15 km, most known faults are not well oriented, and only a few may at most possibly be destabilized for scenarios in which subvertical geometries show positive CFS (fig. 8).

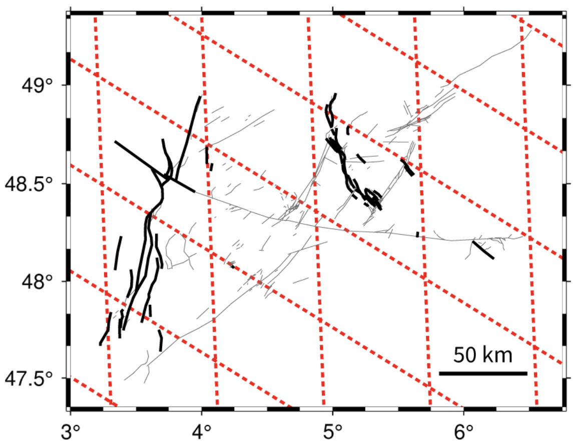

Figure 8: synthesis LGM and present-day, 1-15 km deep: dotted lines = mean preferential orientation at 80° dip (same as known faults), black lines = known faults that may show positive CFS, grey lines = other known faults.

DISCUSSION

The GIA stress perturbations we compute are as high as stress perturbations that are estimated in regions where fault reactivation has been observed (Calais et al., 2010; Stein et al., 1992). The GIA stress perturbations we compute could then potentially trigger fault reactivation in the eastern Paris basin. Yet, when considering ambient crustal stresses, most known faults become clamped or not well oriented for potential failure, and only a few of them may potentially be reactivated in few scenarios promoting subvertical faults reactivation.

Fracture sealing in the eastern Paris basin is dated around 15-20 Ma (ANDRA, 2021, pers. com.), which suggests that no fault activity has occurred in the basin since this time. Furthermore, research of geomorphological markers for quaternary fault activity only results in the observation of old fault scarps due to differential erosion (ANDRA, 2008, pers. com.). Otherwise, eventual markers are occulted by anthropic activity (ANDRA, 2008, pers. com.). Other work by Petit et al. (2019) suggests that Paris basin faults may be stabilized by an increased cohesion in the sediments.

The T_e and ambient stress models are difficult to constrain. Rheological computations from which we estimate T_e show a great variability that cannot be ignored, and we can only infer that the “mean” and “max” models may be the most reasonable according to their T_e values. Ambient stress regime and ratio can as well only be inferred from available in-situ borehole measurements and focal mechanisms around the study area that only provide ranges of variability for these parameters.

Despite our results showing that GIA may hardly reactivate the studied faults, there still is a need to investigate the impact of other environmental forcings. Work by Vernant et al. (2013) and Malcles (2021) show that erosion may also induce measurable deformation, and we will next take this forcing into account in order to estimate its impact on fault stability in our study area.

REFERENCES

BCSF RENASS, 2022. franceseisme.fr [WWW Document]. URL https://renass.unistra.fr/fr/zones/ (accessed 7.7.22).
Brandes, C., Steffen, H., Steffen, R., Wu, P., 2015. Intraplate seismicity in northern Central Europe is induced by the last glaciation. Geology 43. https://doi.org/10.1130/G36710.1
Brudy, M., Zoback, M.D., Fuchs, K., Rummel, F., Baumgärtner, J., 1997. Estimation of the complete stress tensor to 8 km depth in the KTB scientific drill holes: Implications for crustal strength. Journal of Geophysical Research: Solid Earth 102, 18453–18475. https://doi.org/10.1029/96JB02942
Calais, E., Camelbeeck, T., Stein, S., Liu, M., Craig, T., 2016. A New Paradigm for Large Earthquakes in Stable Continental Plate Interiors. Geophysical Research Letters 43. https://doi.org/10.1002/2016GL070815
Calais, E., Freed, A., Arsdale, R., Stein, S., 2010. Triggering of New Madrid Seismicity by late-Pleistocene erosion. Nature 466, 608–11. https://doi.org/10.1038/nature09258
EPOS, 2022. EPOS GNSS [WWW Document]. URL https://gnss-epos.eu/ (accessed 1.31.22).
Johnston, A.C., 1989. The Seismicity of ‘Stable Continental Interiors,’ in: Earthquakes at North-Atlantic Passive Margins: Neotectonics and Postglacial Rebound. Springer Netherlands, Dordrecht, pp. 299–327. https://doi.org/10.1007/978-94-009-2311-9_18
Lambeck, K., Purcell, A., Zhao, S., 2017. The North American Late Wisconsin ice sheet and mantle viscosity from glacial rebound analyses. Quaternary Science Reviews 158, 172–210. https://doi.org/10.1016/j.quascirev.2016.11.033
Long, L., 1988. A Model for Major Intraplate Continental Earthquakes. Seismological Research Letters 59, 273–278. https://doi.org/10.1785/gssrl.59.4.273
Malcles, O., 2021. Analyse des mouvements verticaux récents associés aux reliefs cévenols; Implications en terme de dynamique des déformations en domaine intraplaque.
Masson, C., Mazzotti, S., Vernant, P., Doerflinger, E., 2019. Extracting small deformation beyond individual station precision from dense Global Navigation Satellite System (GNSS) networks in France and western Europe. Solid Earth 10, 1905–1920. https://doi.org/10.5194/se-10-1905-2019
Mazzotti, S., Aubagnac, C., Bollinger, L., Coca Oscanoa, K., Delouis, B., Do Paco, D., Doubre, C., Godano, M., Jomard, H., Larroque, C., Laurendeau, A., Masson, F., Sylvander, M., Trilla, A., 2021. FMHex20: An earthquake focal mechanism database for seismotectonic analyses in metropolitan France and bordering regions. Bulletin de la Société Géologique de France 192, 10. https://doi.org/10.1051/bsgf/2020049
Nocquet, J.-M., Calais, E., Parsons, B., 2005. Geodetic constraints on glacial isostatic adjustment in Europe. Geophysical Research Letters 32. https://doi.org/10.1029/2004GL022174
Petit, C., De Barros, L., Duclaux, G., Mazabraud, Y., 2019. Why Are There No Earthquakes in the IntracratonicParis Basin? Insights from Flexural Models.
Schulte, S.M., Mooney, W.D., 2005. An updated global earthquake catalogue for stable continental regions: reassessing the correlation with ancient rifts. Geophysical Journal International 161, 707.
Steffen, H., Kaufmann, G., 2005. Glacial isostatic adjustment of Scandinavia and northwestern Europe and the radial viscosity structure of the Earth’s mantle. Geophysical Journal International 163, 801–812. https://doi.org/10.1111/j.1365-246X.2005.02740.x
Steffen, H., Olesen, O., Sutinen, R. (Eds.), 2021. Glacially-Triggered Faulting. Cambridge University Press, Cambridge. https://doi.org/10.1017/9781108779906
Steffen, R., Steffen, H., 2021. Reactivation of Non-Optimally Orientated Faults Due to Glacially Induced Stresses. Tectonics 40, e2021TC006853. https://doi.org/10.1029/2021TC006853
Stein, R.S., King, G.C.P., Lin, J., 1992. Change in Failure Stress on the Southern San Andreas Fault System Caused by the 1992 Magnitude = 7.4 Landers Earthquake. Science 258, 1328–1332. https://doi.org/10.1126/science.258.5086.1328
Townend, J., Zoback, M.D., 2000. How faulting keeps the crust strong. Geology 28, 399–402. https://doi.org/10.1130/0091-7613(2000)28<399:HFKTCS>2.0.CO;2
Vernant, P., Hivert, Chery, J., Steer, Cattin, R., Rigo, A., 2013. Erosion-induced isostatic rebound triggers extension in low convergent mountain ranges. Geology 41, 467–470. https://doi.org/10.1130/G33942.1
Zoback, M.D., Healy, J.H., 1992. In situ stress measurements to 3.5 km depth in the Cajon Pass Scientific Research Borehole: Implications for the mechanics of crustal faulting. Journal of Geophysical Research 97, 5039.

Studying seismic supercycles through coral microatolls: the study case of Ishigaki island, Japan.

S. Debaecker[1,2], K. Satake[1], N. Feuillet[2], K. Sowa[3], T. Sato[1], M. Yamada[4], A. Watanabe[1], M. Nakamura[5], A. Saiki[1], C.-C. Shen[6], T.-L. Yu[7], J.-M. Saurel[2], G. Occhipinti[2]

[1]Earthquake Research Institute, The University of Tokyo, Japan,

[2]Institut de Physique du Globe de Paris, Université de Paris, France,

[3]Japan Agency for Marine-Earth Science and Technology, Kanagawa, Japan,

[4]Shinshu University, Matsumoto, Japan,

[5]Ryukyus University, Okinawa, Japan,

[6]National Taiwan University, High-Precision Mass Spectrometry and Environment Change Laboratory (HISPEC), Taipei, Taiwan ROC,

[7]National Taiwan University, Research Center for Future Earth, Taipei, Taiwan ROC

Abstract: *The Ryukyu islands belong to the curved Ryukyu subduction zone, between Japan main island and Taiwan. Along the megathrust, no significant earthquake has been documented in at least the past 250 years. Debate is therefore ongoing on whether the megathrust is aseismic and steadily creeping, or if this subduction zone has already hosted large earthquakes and has been loading strain ever since. In this work, we aim to improve our understanding of subduction zone behavior. We propose to review and extend the earthquake catalog through the analysis of coral microatolls. In Ishigaki island, we documented plenty of fossil coral microatolls in Nagura site. Coral microatolls are paleo-geodetic markers of the relative past sea-level. They can record vertical motions with precision of centimeters. Through different fieldtrips between 2018 and 2021, we sliced and analyzed up to five corals with age ranking between 2 to 4.5 ka. Their intern stratigraphy revealed different events of the past relative sea-level. Some of them are sudden and pluridecimetric, and can be linked to earthquakes. We discuss the origin of the different events, and we use elastic modelling to test the influence of megathrust processes in the signal we documented. Our results tend to draw patterns of seismic supercycles, with periods of frequent subduction earthquakes of magnitude of class 7 to 9, and periods of quiescence. Using correlation with traces of past tsunamis in the region, we suggest that some of these past earthquakes could have ruptured to the surface and generated tsunamis.*

Key words*: Seismic supercycle, subduction, fossil microatolls, seismic potential, paleoseismology, coupling.*

INTRODUCTION

Located between Japan and Taiwan, the Ryukyus archipelago is an island arc that runs along the Ryukyus Trench, where the Philippine Sea plate plunges below the Eurasian plate with a convergence rate of 8 cm/year (Figure 1; Ando et al., 2009). The subduction zone is characterized in its structure by its curvature, which makes it possible to differentiate the southern Ryukyus, where subduction is oblique, from the central Ryukyus, where subduction is perpendicular to the plate boundary. Except for two earthquakes in 1911 and 1771 whose origin is uncertain, no major subduction earthquake has been observed in this region for at least 250 years (Utsu, 1989).

The seismic coupling of the Ryukyus is the subject of scientific debate, because while the subduction zone has much in common with subduction zones that have hosted Mw 9 earthquakes, recent GPS and seismic data describe an aseismic accommodation of the convergence (Nakamura and Sunagawa, 2015). The Ryukyus is a remarkable study area since it contains features that allow discussion of long and short-term vertical deformation of the overriding plate, namely marine terraces and coral microatolls respectively (Weil-Accardo et al., 2020; Debaecker et al., 2022; Debaecker, 2021).

In this study, we propose a multi-temporal approach to a subduction zone, and to improve our understanding of the Ryukyu area, through fossil coral microatolls.

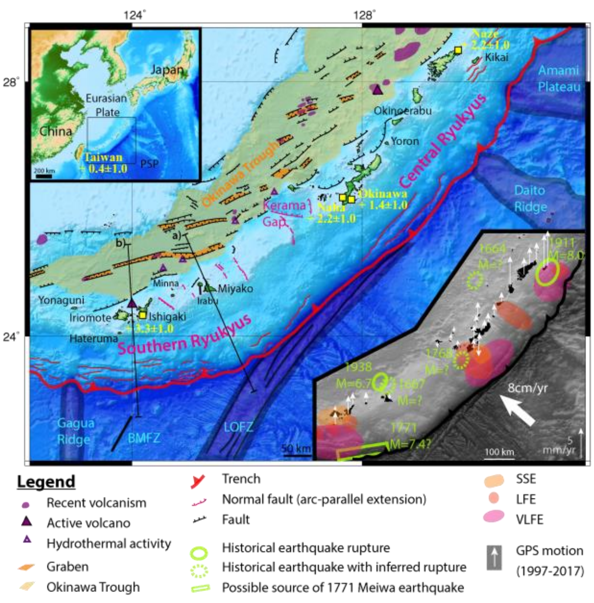

Figure 1. Geodynamic setting of the Ryukyu archipelago. Inset map: Location of the Ryukyus. PSP= Philippine Sea Plate. Main figure: Tectonic setting in the Ryukyus. Orange area: Okinawa Trough, with

volcanic activity in violet and grabens in darker orange. Normal faults are indicated in pink color. Accretionary wedge front and splay faults are indicated in red color. Dark blue areas: bathymetric asperities in the subducting plate. LOFZ= Luzon-Okinawa Fracture Zone. BMFZ=Bonin-Mariannes Fracture Zone. Faults are modified after Sibuet et al. (1998), Hsu et al. (2013), Minami and Ohara (2018) and Goto et al. (2018). Information on hydrothermal activity is from Minami and Ohara (2018). Yellow squares: tide gauge stations from Permanent Service for Mean Sea-Level with mean value of the sea-level rise estimated over the past 40 years. Inset: Distribution of historical large-magnitude earthquakes. White arrows: vertical GPS motion between 1997 and 2017 from Geospatial Information Authority of Japan. LFE and VLFE are from Nakamura (2017). SSE are from Nishimura (2014). Hypothetic location of the 1771 Meiwa earthquake source is from Nakamura (2009). Historical earthquakes are from Nakata and Kawana (1995). From Debaecker et al. (2022).

DATA AND METHOD

On a millennial scale, we have studied the vertical deformations of the islands using coral microatolls. During their growth, these corals record each year and with a centimetric precision the relative variations of the sea-level (Meltzner et al., 2015). Once they are big enough to reach the sea-level, their upper part dies and their evolution is conditioned by the relative sea-level changes. If the sea-level rises they grow upward, covering the previous dead part. If the sea-level decreases, they will continue their growth laterally, underwater. These variations are themselves the result of the combination between tectonic motions and climatic sea-level variations. The identification of the vertical deformation signal related to subduction thus often allows to characterize past overriding plate motions related to subduction earthquakes, interseismic periods preceding them or aseismic slip motions along the megathrust (Debaecker et al., 2022).

Through different fieldtrips between 2018 and 2021, we sampled and analyzed a total of 7 fossil corals in the Southern Ryukyus in Ishigaki island, which allowed us to reconstruct the relative sea-level variations up to 5 ka. From X-ray and scan imagery, we analyzed growth band distribution. HLS are reported on a curve, and mean trend between several HLS events are calculated by Zachariesen et al. (2000) and Meltzner et al. (2010) method. We used Uranium/Thorium dating for the most complex slices to better constrain the age assigned to the different annual growth bands identified in the internal stratigraphy.

RESULTS

In Nagura site in Ishigaki island, we observed plateaus of microatoll colonies that have similar elevations and whose death seems to be marked by a sudden drop in relative sea-level (Figure 2). Using Uranium/Thorium dating, we were able to date most of these plateaus to 5 ka. We sampled 10 fossil microatolls from the plateaus located in the bay and in the mangrove. These microatolls recorded the relative variations of sea level ~860 and ~4900 years B.P..

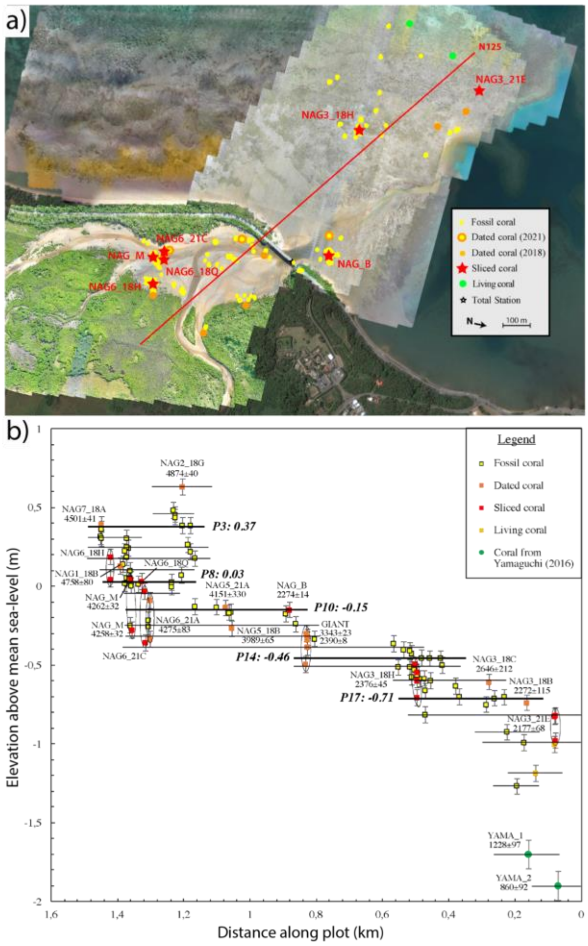

Figure 2. Nagura site survey. a) Mapping of total station and RTK-GPS survey in Nagura. We used Google Earth screenshot and drone imagery of the bay area. Red line is the plotting direction. b) Plot of the absolute elevation of the surveyed corals. Elevation is corrected with tide measurements with an absolute uncertainty of ±7 cm, and level 0 is the mean sea-level. Age of the fossil corals was dated using U/Th method. Green points are from Yamaguchi (2016).

The study of the internal stratigraphy of these corals reveals the occurrence of several sudden and significant drops in relative sea-level (Figure 3). In Nagura, the corals we sliced revealed massive drops of the RSL of up to ~30 cm. Those events are consistent with our topographic survey of the site. At that scale, those events are not climatic-related, and may correspond to earthquakes, which has never been documented in the area before.

The relative sea-level signal between these events indicates both periods of submergence and relative emergence. The trend in the signal between sudden events is approximated by a relative subsidence of about 2 mm/year. Combining the relative sea-level signals recorded from the fossil colony plateaus at the sites or from the sampled coral slices allowed us to reconstruct the relative sea-level variations in the Southern Ryukyus over 5 ka. This reconstruction highlighted a slow uplift of the sites of around 0.6 mm/year over 5 ka, as well as 12 main events of sudden drop of the relative sea-level with a minimum amplitude of 15 cm.

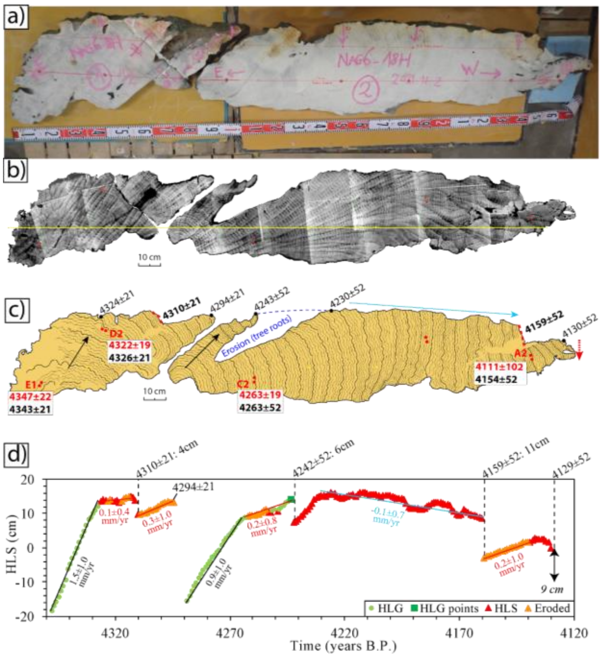

Figure 3. Study of the NAG6_18H slice. a) Picture of the raw slice. b) CT-scan imagery of NAG_6_18H. Yellow line is the horizontal direction. Red dots are micro-cores samples for U/Th datation. c) Interpreted slab of NAG_6_18H. Black lines are annual growth bands. Thicker black lines are growth bands every five years. Black, red and blue arrows represent the initial growth of the coral, relative submergence and emergence periods, respectively. Black dots mark the beginning or end of a RSL relative or decrease period. d) HLS variations of NAG_6_18H. Blue and red lines stand for relative emergence and submergence periods, respectively, with rate calculated from Zachariasen et al. (2000) using all points from the first HLS. Date uncertainties reflect growth band counting and U/Th uncertainties. Other dates show beginning or end of a RSL decrease or increase period. Rates in black are the inferred natural growth rate of the two colonies.

DISCUSSION

A discussion on the impact of the components of the relative sea-level signal related to climatic and glacio-isostatic adjustment phenomena, as well as those related to the local tectonics of the islands allowed us to suggest for the identified trends and sudden movements an origin at the subduction interface. This hypothesis has been supported by models of dislocation in an elastic half-space. Our models showed that the subsidence motions between two earthquakes would imply a loading on the whole seismogenic zone. The identified earthquakes would be due to sudden motions either on the whole seismogenic zone, either on its deep part only, confirming moreover the depth of the seismogenic zone at 60 km in front of Ishigaki Island. Their magnitude would vary between Mw 7.7 and Mw 9.1.

At least two of these earthquakes can also be associated with tsunamis identified in the geology of the islands and reported in the literature. The correlation of these earthquakes with the motions of the subduction interface leads us to estimate a seismic cycle of the Southern Ryukyus Islands over the last millennia, which would actually be composed of several seismic supercycles. These supercycles include seismic periods of a few hundred years defined by earthquakes with a recurrence time ranging from a few decades to a few centuries, followed by periods of seismic quiescence of a few hundred years also.

Extensive study of fossil microatolls is crucial to improve the characterization of past supercycles and investigate the ongoing one. Such results call for more assessment of the past megathrust earthquakes in the Ryukyus, to define at best size and origin of major past events and affine the characteristics of a possible actual seismic supercycle of this subduction zone.

REFERENCES

Ando, M., Nakamura, M., Matsumoto, T., Furukawa, M., Tadokoro, K., & Furumoto, M. (2009). Is the Ryukyu subduction zone in Japan coupled or decoupled? The necessity of seafloor crustal deformation.

Debaecker, S. (2021). *Seismic supercycles in the Ryukyus subduction zone: insights from marine terraces and coral microatolls* (Doctoral dissertation, Université Paris Cité).

Debaecker, S., Feuillet, N., Satake, K., Sowa, K., Yamada, M., Watanabe, A., et al. (2022). Recent relative sea-level changes recorded by coral microatolls in Southern Ryukyus islands, Japan: Implication for the seismic cycle of the megathrust. Geochemistry, Geophysics, Geosystems, 24, e2022GC010587. https://doi.org/10.1029/2022GC010587

Goto, H., Arai, K., & Sato, T. (2018). Topographic anaglyphs from detailed digital elevation models covering inland and seafloor for the tectonic geomorphology Studies in and around Yoron Island, Ryukyu Arc, Japan. Geosciences, 8(10), 363..

Hsu, S. K., Yeh, Y. C., Sibuet, J. C., Doo, W. B., & Tsai, C. H. (2013). A mega-splay fault system and tsunami hazard in the southern Ryukyu subduction zone. Earth and Planetary Science Letters, 362, 99-107.

Meltzner, A. J., & Woodroffe, C. D. (2015). Coral microatolls. *Handbook of Sea-Level Research*, 125.

Minami, H., & Ohara, Y. (2018). Detailed volcanic morphology of Daisan-Miyako Knoll in the southern Ryukyu Arc. Marine Geology, 404, 97-110.

Nakamura, M. (2009). Fault model of the 1771 Yaeyama earthquake along the Ryukyu Trench estimated from the devastating tsunami. Geophysical Research Letters, 36(19).

Nakamura, M., and Sunagawa, N. (2015). Activation of very low frequency earthquakes by slow slip events in the Ryukyu Trench. Geophysical Research Letters, 42(4), 1076-1082.

Nakamura, M. (2017). Distribution of low-frequency earthquakes accompanying the very low frequency earthquakes along the Ryukyu Trench. Earth, Planets and Space, 69(1), 49.

Nakata, T., & Kawana, T. (1995). Historical and prehistorical large tsunamis in the southern Ryukyus, Japan. In Y. Tsuchiya, & N. Shuto (Eds.), Tsunami: Progress in prediction, disaster prevention and warning (Vol. 4, pp. 211–221). Dordrecht: Springer.

Nishimura, T. (2014). Short-term slow slip events along the Ryukyu Trench, southwestern Japan, observed by continuous GNSS. Progress in Earth and Planetary Science, 1(1), 1-22.

Sibuet, J. C., Deffontaines, B., Hsu, S. K., Thareau, N., Le Formal, J. P., & Liu, C. S. (1998). Okinawa trough backarc basin: Early tectonic and magmatic evolution. Journal of Geophysical Research: Solid Earth, 103(B12), 30245-30267.

Utsu, T. (1989), Table of destructive earthquakes in the world, http://iisee.kenken.go.jp/utsu/.

Weil-Accardo, J., Feuillet, N., Satake, K., Goto, T., Goto, K., Harada, T., ... & Shen, C. C. (2020). Relative sea-level changes over the past centuries in the central Ryukyu Arc inferred from coral microatolls. *Journal of Geophysical Research: Solid Earth*, *125*(2), e2019JB018466.

Yamaguchi, T. (2016). A review of coral studies of the Ryukyu Island arc to reconstruct its long-term landscape history. *Coral Reef Science*, 55-63p.

Zachariasen, J., Sieh, K., Taylor, F. W., & Hantoro, W. S. (2000). Modern vertical deformation above the Sumatran subduction zone: Paleogeodetic insights from coral microatolls. *Bulletin of the Seismological Society of America*, *90*(4), 897-913.

INQUA Focus Group Terrestrial Processes Perturbed by Tectonics (TPPT)

paleoseismicity.org

Impact of variable fault geometries and slip rates on earthquake catalogues from physics-based simulators for the Cape Egmont Fault, New Zealand

Efstratios Delogkos (1), Andrew Howell (2, 3), Hannu Seebeck (2), Bruce E Shaw (4), Andrew Nicol (3), John J Walsh (1)

(1) Fault Analysis Group, UCD School of Earth Sciences, University College Dublin, Dublin, Ireland. Email: stratos.delogkos@ucd.ie, john.walsh@ucd.ie

(2) Te Pū Ao – GNS Science, Lower Hutt, New Zealand. Email: a.howell@gns.cri.nz, h.seebeck@gns.cri.nz

(3) School of Earth and Environment, University of Canterbury, Christchurch, New Zealand. Email: andy.nicol@canterbury.ac.nz

(4) Lamont Doherty Earth Observatory, Columbia University, Palisades, New York, U.S.A. Email: shaw@ldeo.columbia.edu

Abstract: *Physics-based earthquake simulators have been developed to overcome the relatively short duration and incompleteness of historical earthquake and paleoseismic records. Earthquake simulators produce millions of synthetic earthquakes over thousands to millions of years using predefined fault geometries, locations and slip rates. Due to the sparsity of geological and/or geodetic data combined with limited computing-power capabilities, it is common to simplify input parameters for earthquake simulators. This study uses an exceptionally well-defined 3D geometry of an active normal fault in offshore New Zealand, the Cape Egmont Fault, to demonstrate the impact of using non-uniform slip rates and realistic fault geometries on the resulting synthetic earthquakes. Adopting variable slip rates reduces unexpectedly high nucleation rates of seismicity along the fault edges and unrealistic distributions of events with increasing depth. Introduction of complex 3D fault geometries, including fault segmentation and bends, produces less characteristic earthquake populations.*

Key words: *physics-based earthquake simulators, fault geometry, slip rate, Cape Egmont fault.*

1. Introduction

The relatively short duration and incompleteness of historical earthquake and paleoseismic records, respectively, has led to the development and utilization of the physics-based earthquake simulators (e.g., Robinson and Benites, 1995; Richards-Dinger and Dieterich, 2012; Console et al., 2017). Earthquake simulators produce millions of synthetic earthquakes over thousands to millions of years using predefined fault geometries, locations and slip rates.

Due to the sparsity of geological and/or geodetic data combined with limited computing-power capabilities, it is common to simplify input parameters (e.g., planar faults with uniform slip rates) for earthquake simulators. However, faults are rarely single planar surfaces and often present a complex 3D structure comprising multiple sub-parallel fault segments (e.g., Delogkos et al., 2020; Deng et al., 2020; Roche et al., 2021). Uniform slip rates on fault surfaces are also a simplification because cumulative slip, and associated slip rates, generally reach a maximum towards the fault centre with a gradual decrease towards the fault tip lines (e.g., Walsh and Watterson, 1988; Roberts and Michetti, 2004; Nicol et al., 2005, 2020).

In this study, we use an exceptionally well-defined 3D geometry of an active normal fault in offshore New Zealand, the Cape Egmont Fault (Nicol et al., 2005; Seebeck et al., 2020; 2021), to examine the effect of realistic fault geometries and non-uniform slip rates on the synthetic earthquakes produced by RSQSim, a physics-based earthquake simulator (Richards-Dinger and Dieterich, 2012).

2. Data and methodology

2.1 The Cape Egmont Fault

The Cape Egmont Fault (CEF) is located in the offshore Southern Taranaki Basin southwest of the Taranaki Peninsula, North Island, New Zealand, within the continental crust of the Australian Plate. This active normal fault commenced its most recent phase of activity at ca. 3.7 Ma (Nicol et al. 2005; Seebeck et al. 2020).

2.2 The earthquake simulator RSQSim

In this study we use RSQSim, a multicycle physics-based earthquake simulator developed by Dieterich and Richards-Dinger (2010). RSQSim is a boundary element model based on approximations of the rate-and-state friction equations. Faults are loaded using the backslip method, where slip rates are specified on each fault surface and based on their static stress interactions, stressing rates applied to reproduce the specified slip rates for the fault system (Savage, 1983).

2.3 Model fault geometries and slip rates

The 3D structure of the Cape Egmont Fault (CEF) is resolved using industry standard 2D and 3D seismic-reflection data covering a region 80 km long and up to 35 km-wide (Seebeck et al., 2020, 2021). In total, four main fault surfaces, two synthetic and two antithetic faults were interpreted (Fig. 1a – the 'Realistic fault geometry').

In order to examine at what level fault geometry impacts the earthquake catalogues, three additional scenarios of fault geometries were considered: (1) a 'simplified fault surface' where the main fault trace was extrapolated with a dip of 60° (Fig. 1b), (2) a 'simple planar fault surface' with a dip of 60° (Fig. 1c), and (3) a 'simple listric fault surface' with 70° dip at shallow depths that gradually decreases (Fig. 1d). Each fault surface was populated with either constant or variable slip rates.

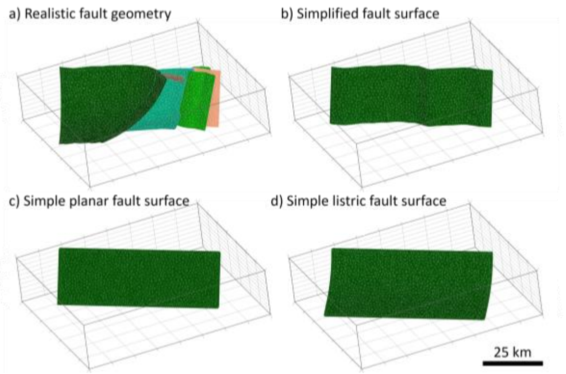

Figure 1: Different approximations of the CEF structure used to examine the impact of fault geometry on the synthetic earthquake catalogues derived from the RSQSim simulator.

3. Results and discussion

The application of the physics-based earthquake simulator (RSQSim) for variable fault geometries and slip rates of the CEF resulted in synthetic catalogues spanning 500 kyr and containing thousands of events. These catalogues are long enough for statistical analysis and comparisons between different fault geometry and slip rate scenarios (Fig. 2).

Constant slip rates produce stressing rate singularities at the fault boundaries resulting in higher frequencies of earthquakes. These catalogues also present unrealistic depth distributions of the hypocenters with most of the events nucleating at the depth of ca. 20 km (Fig. 2a). In contrast, variable slip rates appear to resolve the singular stressing rates at the fault surface edges. Variable slip rates present a more realistic depth distribution of seismicity that matches the distribution of natural seismicity (e.g., Sherburn and White, 2005; Fig. 2b). Furthermore, the combination of realistic 3D fault geometries with variable slip rates produces less characteristic earthquake populations with a more Gutenberg-Richter distribution of events (Figs 2c and 2d).

The seismic moment appears to be larger for the 'simple listric fault surface'. This increase in moment arises because all fault geometries (Fig. 1) extending down to 20 km depth and, therefore, the 'simple listric fault surface' has the largest continuous surface area that can produce larger earthquakes. The seismic moment is also relatively smaller for the faults with variable slip rates, suggesting that the decrease in slip rate towards the edges of a fault surface restricts the rupture area and, therefore, the magnitude of the corresponding earthquake.

This study demonstrates that the use of realistic fault geometries and non-uniform slip rates has a significant impact on the resulted earthquake catalogues, with more realistic earthquake depth distributions, multi-fault ruptures, and Gutenberg-Richter earthquake populations.

In many natural fault systems, it can however be challenging to specify these fault properties in three-dimensions. In the absence of such information, imposing slip-rate distributions decreasing towards fault tip lines and stochastic variations in fault-surface roughness could produce more realistic synthetic earthquakes than planar faults with uniform slip rates.

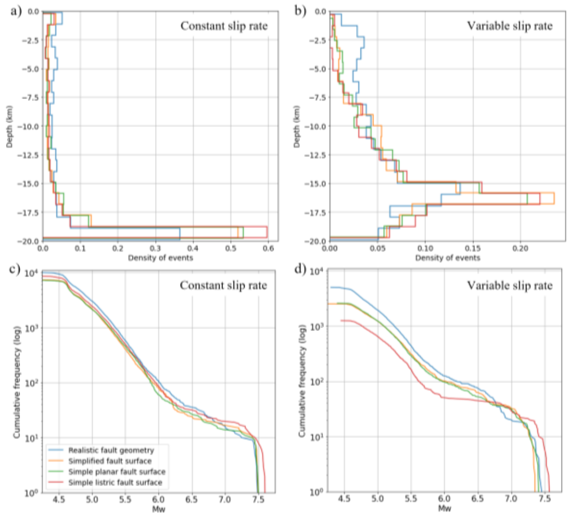

Figure 2: Depth distributions (a and b) and frequency-magnitude distributions (c and d) for synthetic catalogues produced by RSQSim using different fault geometries (Fig. 1) with constant and variable slip rates.

Acknowledgements: This project has received funding from the Irish Research Council under grant number GOIPD/2020/530. It was also partly supported by a grant from the New Zealand Resilience to Natures Challenges programme "Earthquakes and Tsunami" theme. Academic Licenses of the software Petroleum Experts MOVE provided to the University College Dublin are kindly acknowledged.

REFERENCES

Console, R., Nardi, A., Carluccio, R., Murru, M., Falcone, G. and Parsons, T., 2017. A physics-based earthquake simulator and its application to seismic hazard assessment in Calabria (Southern Italy) region. Acta Geophysica, 65(1), pp.243-257.

Delogkos, E., Manzocchi, T., Childs, C., Camanni, G. and Roche, V., 2020. The 3D structure of a normal fault from multiple outcrop observations. Journal of Structural Geology, 136, p.104009.

Deng, H., McClay, K. and Bilal, A., 2020. 3D structure and evolution of an extensional fault network of the eastern Dampier Sub-basin, Northwest Shelf of Australia. Journal of Structural Geology, 132, p.103972.

Dieterich, J.H. and Richards-Dinger, K.B., 2010. Earthquake recurrence in simulated fault systems. In Seismogenesis and Earthquake Forecasting: The Frank Evison Volume II (pp. 233-250). Springer, Basel.

Field, E.H., Arrowsmith, R.J., Biasi, G.P., Bird, P., Dawson, T.E., Felzer, K.R., Jackson, D.D., Johnson, K.M., Jordan, T.H., Madden, C. and Michael, A.J., 2014. Uniform California earthquake rupture forecast, version 3 (UCERF3)—The time-independent model. Bulletin of the Seismological Society of America, 104(3), pp.1122-1180.

Herrero-Barbero, P., Álvarez-Gómez, J.A., Williams, C., Villamor, P., Insua-Arévalo, J.M., Alonso-Henar, J. and Martínez-Díaz, J.J., 2021. Physics-Based Earthquake Simulations in Slow-Moving Faults: A Case Study From the Eastern Betic Shear Zone (SE Iberian Peninsula). Journal of Geophysical Research: Solid Earth, 126(5), p.e2020JB021133.

Nicol, A., Walsh, J., Berryman, K. and Nodder, S., 2005. Growth of a normal fault by the accumulation of slip over millions of years. Journal of Structural Geology, 27(2), pp.327-342.

Nicol, A., Walsh, J.J., Childs, C., Manzocchi, T., 2020. The growth of faults. Chapter 6 in "Understanding Faults: Detecting, Dating, and Modelling". Editors D. Tanner and C. Brandes. Published by Elsevier. Pages 221-256.

Reyners, M., 1989. New Zealand seismicity 1964–87: an interpretation. New Zealand journal of geology and geophysics, 32(3), pp.307-315.

Richards-Dinger, K. and Dieterich, J.H., 2012. RSQSim earthquake simulator. Seismological Research Letters, 83(6), pp.983-990.

Roberts, G.P. and Michetti, A.M., 2004. Spatial and temporal variations in growth rates along active normal fault systems: an example from The Lazio–Abruzzo Apennines, central Italy. Journal of Structural Geology, 26(2), pp.339-376.

Robinson, R., Calhaem, I.M. and Thomson, A.A., 1976. The Opunake, New Zealand, earthquake of 5 November 1974. New Zealand journal of geology and geophysics, 19(3), pp.335-345.

Robinson, R. and Benites, R., 1995. Synthetic seismicity models of multiple interacting faults. Journal of Geophysical Research: Solid Earth, 100(B9), pp.18229-18238.

Robinson, R., Van Dissen, R. and Litchfield, N., 2011. Using synthetic seismicity to evaluate seismic hazard in the Wellington region, New Zealand. Geophysical Journal International, 187(1), pp.510-528.

Roche, V., Camanni, G., Childs, C., Manzocchi, T., Walsh, J., Conneally, J., Saqab, M.M. and Delogkos, E., 2021. Variability in the three-dimensional geometry of segmented normal fault surfaces. Earth-Science Reviews, 216, p.103523.

Savage, J.C., 1983. A dislocation model of strain accumulation and release at a subduction zone. Journal of Geophysical Research: Solid Earth, 88(B6), pp.4984-4996.

Seebeck, H., Thrasher, G.P. and Viskovic, G.P., 2020. Inversion history of the northern Tasman Ridge, Taranaki Basin, New Zealand: implications for petroleum migration and accumulation. New Zealand Journal of Geology and Geophysics, 63(3), pp.299-323.

Seebeck H, Thrasher GP, Viskovic GPD, Macklin C, Bull S, Wang X, Nicol A, Holden C, Kaneko Y, Mouslopoulou V, Begg JG. 2021. Geologic, earthquake and tsunami modelling of the active Cape Egmont Fault Zone. Lower Hutt (NZ): GNS Science. 370 p. (GNS Science report; 2021/06). doi:10.21420/100K-VW73.

Sherburn, S. and White, R.S., 2005. Crustal seismicity in Taranaki, New Zealand using accurate hypocentres from a dense network. Geophysical journal international, 162(2), pp.494-506.

Walsh, J.J. and Watterson, J., 1988. Analysis of the relationship between displacements and dimensions of faults. Journal of Structural geology, 10(3), pp.239-247.

INQUA Focus Group Terrestrial Processes Perturbed by Tectonics (TPPT)

paleoseismicity.org

Assessing historical earthquake sequences with Coulomb stress models

*Diercks, Manuel-L. (1) *, Zoë K. Mildon (1), Sarah J. Boulton (1), Ekbal Hussain (2)*

(1) School of Geography, Earth and Environmental Sciences, University of Plymouth, Plymouth, PL4 8AA, United Kingdom.
(2) British Geological Survey, Nicker Hill, Keyworth, Nottingham NG12 5GG, United Kingdom
*corresponding author: manuel-lukas.diercks@plymouth.ac.uk

Abstract: *When modelling Coulomb stress transfer (CST) from earthquakes, it is crucial to identify the source faults of earthquakes to produce a robust CST model. Models incorporating historical earthquakes rely on historic, paleoseismologic or archeoseismologic evidence, and thus there may be uncertainties about the source fault(s). We introduce an approach to assess historic earthquake sequences and respective source faults from Coulomb stress models. Using historical and instrumental records, we create a range of plausible scenarios for historical earthquakes. We model coseismic and interseismic Coulomb stress transfers for each plausible scenario. We filter and evaluate all models based on physical criteria to (1) gain knowledge on historic earthquakes and their source faults and (2) assess the stress state and related seismic hazard of the investigated fault network. The results can provide further constraints on the source faults of several historic earthquakes, and therefore can be used to refine historic earthquake studies from a new viewpoint.*

Key words*: Fault-based Seismic Hazard Assessment, Earthquake source faults*

THE SOURCE FAULT PROBLEM

Fault-based deterministic Seismic Hazard Assessment (SHA) is an increasingly popular addition to SHA. Several studies have modelled Coulomb stress transfer (CST) for earthquake sequences spanning centuries to millennia by combining coseismic, interseismic and in some cases postseismic CST (e.g., Freed et al., 2005, Verdecchia & Carena, 2015, Mildon et al., 2017). These models reveal insights into the stress state of fault networks, but strongly depend on a reliable correlation of recorded earthquakes and source faults. For recent earthquakes source faults can be reliably determined, e.g. by seismological constraints or surface deformation. However, for pre-instrumental earthquakes these techniques are unavailable, and instead we must rely on historic, archeoseismologic or paleoseismologic data, which is often only available for well-studied faults or events. For poorly studied faults or events, it may be difficult to identify the causative fault.

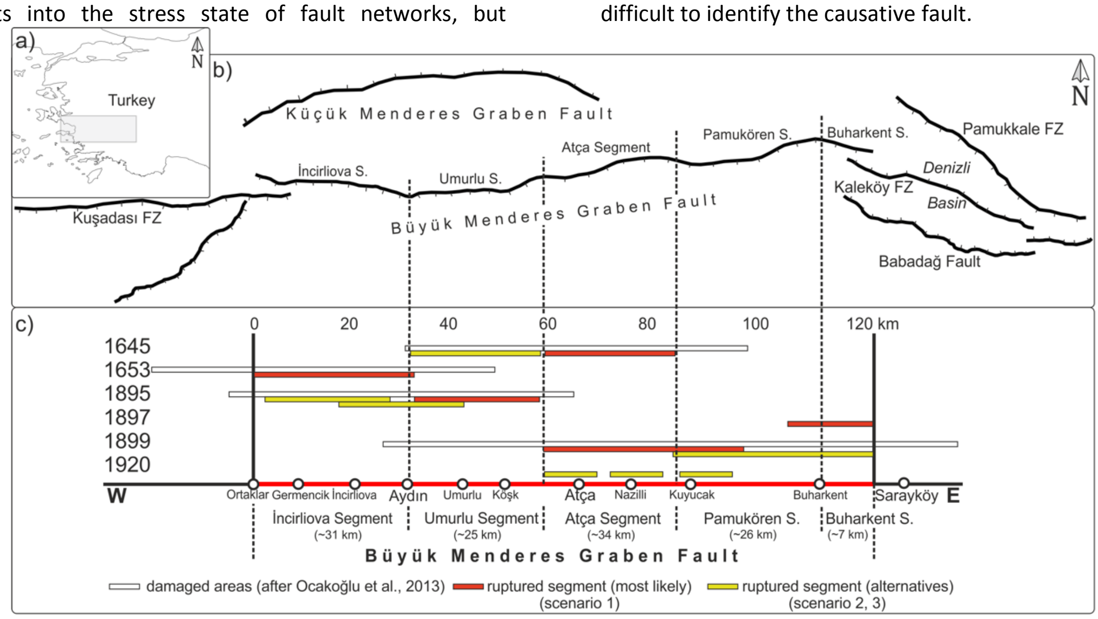

Figure 1: a) Location of the studied fault network in SW Turkey. b) Map of the fault network showing the studied faults (after Emre et al., 2018 and field mapping) and segments of the BMGF. c) Damaged areas along the BMG and adjacent basins from Ocakoğlu et al. (2013) and plausible ruptured segments for earthquakes at the BMGF based on historical data, expected rupture length (Well & Coppersmith, 1994) and fault segmentation.

To address this problem, we present a novel approach to try and correlate historical earthquakes and their causative faults using Coulomb stress modelling. Our approach follows the hypothesis that individual earthquakes interact due to CST, and that cumulative CST can be used to analyse whole earthquake sequences (e.g.

Mildon et al., 2017, Verdecchia & Carena, 2015). We use an earthquake sequence in the Büyük Menderes Graben in SW Turkey (Fig. 1a), consisting of 16 moderate to large earthquakes (> M_W 5.5) between 1645 and 1965 as our case study. It provides a well-studied set of faults and sufficient earthquake record, although the source faults of several events remain uncertain. We are confident that no large earthquakes are missing from the records in this period and region, which is important for the modelling. The modelled fault network (Fig. 1b) comprises the ~120 km long Büyük Menderes Graben Fault (BMGF), with five mapped segments. We further model four active fault zones in the Denizli basin, east of the BMGF, the Söke and Kuşadası Fault Zones in the west and the Küçük Menderes Graben Fault in the north.

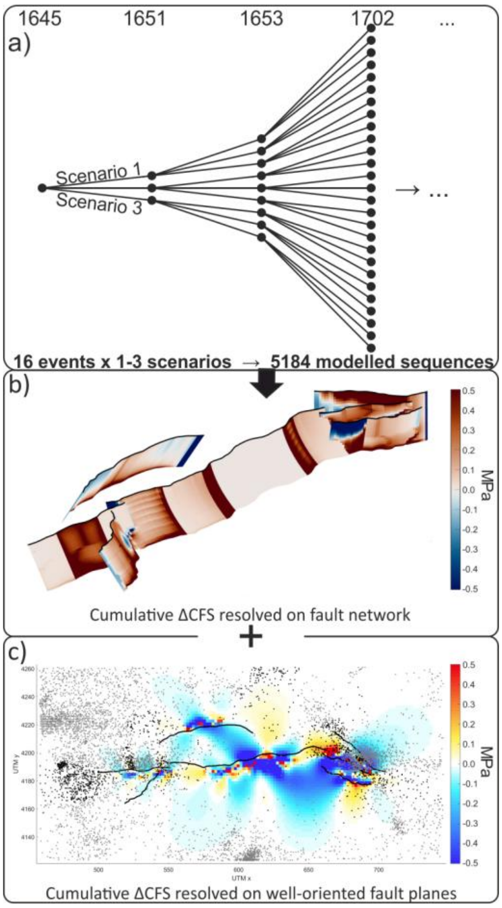

Figure 2: Schematic overview of the modelling workflow. a) Combination of all scenarios of each earthquake through the entire sequence, resulting in 5184 modelled sequences. b) Cumulative CST for one modelled sequence. c) Cumulative stress on specified faults from one modelled sequence compared to background seismicity (black dots).

METHODS

In the first step, data on the active fault network and earthquakes (both instrumental and pre-instrumental) are compiled. The fault data comprise mapped fault traces, geometry, kinematics and activity (seismicity, geomorphic expression). Earthquake data are compiled from earthquake catalogues and literature, comprising recorded and historical events, their epicentre locations, magnitudes, and damaged areas. For each historical earthquake, several plausible scenarios are decided. Scenarios feature varying source faults or segments and rupture parameters, such as magnitude, rupture area and slip. Even the occurrence versus non-occurrence of an earthquake can be represented by different scenarios. Figure 1c depicts the rupture scenarios of earthquakes on the BMGF, based on historical studies (Ocakoğlu et al., 2013 and citations therein), geological segmentation of the fault (Emre et al., 2018) and expected rupture length inferred from magnitude-length relationships (Wells & Coppersmith, 1994). A double-earthquake scenario proposed by Ocakoğlu et al. (2013) is currently not considered in our models. Subsequently, we calculate all possible combinations of all scenarios (Fig. 2a).

The modelling process begins with building the 3D fault network using '3D-Faults' v2.5 (improved version of the code published by Mildon et al. (2016), available at www.github.com/MDiercks/3D-Faults). The modelled faults consist of a total of >8000 rectangular elements with a size of ~1 km² of varying dip angles and dip direction, which creates a strike-variable fault surface with either listric or planar geometry to depth. Fault zones with multiple segments (e.g. BMGF) are simplified into a single continuous fault, then earthquakes can be modelled on individual segments by specifying the position of the segment along the fault zone (Fig. 2). A concentric slip distribution is assigned to the source fault/segment with the highest slip in the centre of the rupture. If no data on rupture length is available, empirical relationships (Wells & Coppersmith, 1994) are used to determine the approximate rupture dimensions from the magnitude. Rupture length can also be estimated based on the actual length of mapped fault segments. The CST is calculated for each event using Coulomb 3.4 (Toda et al., 2011). Annual interseismic stress loading is calculated using the 'backslip' method (Deng & Sykes, 1997), where 'virtual negative displacements' are modelled based on fault slip rates. Coseismic CST is modelled for each historical earthquake scenario, and the cumulative Coulomb stress change for each possible combination of coseismic CST and interseismic loading is accumulated throughout the entire earthquake sequence. While this is a well-established technique for modelling earthquake sequences, the novelty in our approach is to combine all possible scenarios of each earthquake to attempt to better constrain historical earthquakes. In total 5184 earthquake sequences are modelled, consisting of 16 individual earthquakes where each has one to three possible scenarios (Fig. 2a). For each modelled earthquake sequence, the following data are extracted: the percentage of ruptured elements exceeding (1) 0.2; and (2) 0.5 MPa stress prior to rupture, and (3) mean stress on the ruptured segment/fault prior to rupture. These will be used as metrics to evaluate the modelled sequences.

In addition, we calculate CST for receiver fault planes with specified geometry at a specified depth. This approach is adapted from the commonly applied technique of resolving stress onto 'optimally oriented faults' (e.g. King et al., 1994). In our case the geometry of the receiver faults must be specified because the stress is accumulated from multiple earthquakes, therefore the optimal orientation of receiver faults will vary for each event. However, as Steacy et al. (2005) pointed out, most earthquakes (i.e., aftershocks) triggered by static stress transfers occur on planes similarly oriented as the source fault. Therefore, we use a geometry similar to the BMGF with dip direction 180°, dip angle 60°, rake -90° and we calculate the CST at 8 km depth (which is the approximate depth of the majority of hypocentres in the region). The fault network and slip distribution are again built with '3D-Faults' and stress transfers are calculated with Coulomb 3.4. CST resolved on specified faults is accumulated (summed up) for each modelled earthquake sequence. Assuming the presence of these receiver fault planes anywhere in the vicinity of the large fault zones, stress is mapped on a grid over the extent of the studied region. The resulting stress patterns are compared to locations of recorded seismicity from the ISC catalogue (ISC, 2022) and the percentage of seismicity in stress-triggering zones (areas of positive CST) is used as a fourth metric for model evaluation.

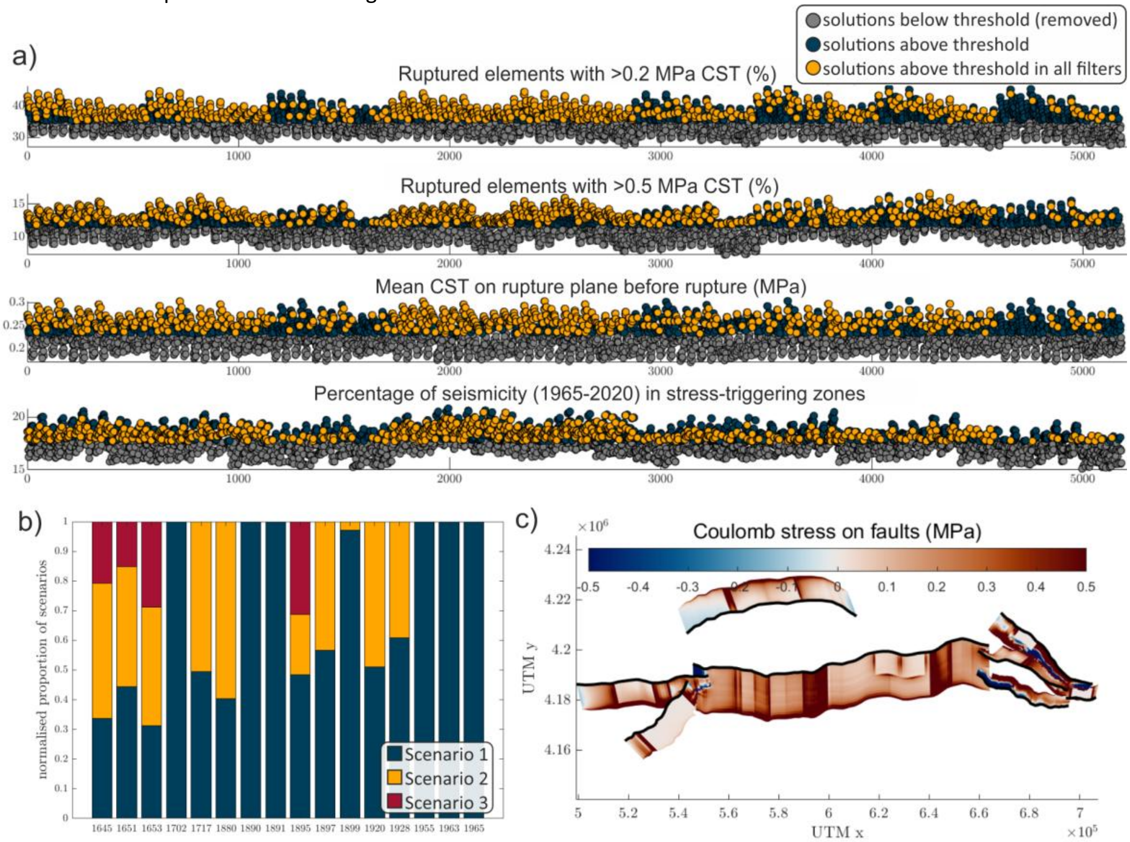

Figure 3: Evaluation of Coulomb stress models. a) Filtering all 5184 models by four different criteria; 1137 solutions remaining (yellow circles) where the solutions exceed all thresholds. b) Proportions of scenarios for each event in the remaining solutions. c) Average stress on the fault network from all remaining solutions.

RESULTS AND INTERPRETATION

Background of interpretation

We assume that fault segments featuring high Coulomb stress are more likely to rupture an earthquake than segments with low or negative stress. Accordingly, modelled earthquake sequences with high average stress on faults prior to rupture are hypothesised to be more plausible. Similarly, model solutions that result in a stress pattern where most recorded seismicity occurs within stress-triggering zones are hypothesised to be most plausible.

Historical earthquake studies commonly investigate single earthquakes without consideration of other events and related stress changes. By evaluating entire rupture sequences, modelled sequences that are physically more unlikely will result in lower average values (e.g., mean stress on rupture plane) and the related model solutions are removed from the results. Accordingly, rupture scenarios that might appear plausible based on historical studies might be implausible when the entire sequence is modelled.

Filtering

Our approach of combining earthquake scenarios results in 5184 models of the same earthquake sequence, the key of this approach is the evaluation of the models. Using the four above-mentioned metrics (Fig. 3a), all solutions are filtered to determine which of the modelled sequences meet or exceed the threshold metric values. As an initial filter on the modelled sequences, the median value of all solutions is used as a threshold and all solutions below it are removed. The four filters are applied independently, leaving only those solutions that exceed the median value in all four filters (yellow circles in Fig. 3a).

This initial filtering reduces the number of modelled sequence solutions to 1137. The remaining models are then used to infer interpretations on the most probable earthquake scenarios and the current stress state of the fault network. The latter is important to assess the current seismic hazard in the region. We hypothesise that the remaining models after filtering will contain the sequences that are physically more likely to occur than most other modelled sequences.

Determining plausible scenarios (and source faults)

We suggest that this technique can be used to determine which historic earthquake scenarios are most plausible, reasoning that these will more often occur in the remaining (filtered) solutions. Solutions featuring certain combinations of scenarios are generally removed by the filters. Figure 3b shows the proportions of scenarios for each earthquake on the BMGF after filtering the modelled sequence solutions. Note that for events in 1702, 1890, 1891, 1955, 1963 and 1965, only one scenario was modelled. For each of the first three events (1645, 1651 and 1653), the first and second scenario appear more plausible than the third. For the 1717 and 1880 earthquakes, both input scenarios occur approximately equally in the filtered results, hence we cannot determine which scenario is most likely. The clearest result can be seen for the 1899 earthquake. More than 95 % of the filtered solutions feature the first input scenario, rupturing the Atça and Pamukören segments of the BMGF, hence we interpret that these fault segments are the most plausible rupture scenario for this earthquake.

Current stress state and seismic hazard

From the current study, we cannot determine which of the 1137 filtered modelled sequences is the most plausible. However, we hypothesise that we can use the range of models to infer the most likely current state of stress on the fault network. To do this, we calculate the mean stress from all filtered modelled sequences for each element on the fault network after the last modelled earthquake (Fig 3c). The faults or fault segments with the highest resultant stress will be the faults that are most consistently positively stressed across the range of filtered modelled sequences. Therefore, we suggest that these faults/segments are the most likely regions that are positively stressed at the present day, and therefore have the highest potential seismic hazard. This is most accurate for the BMGF in the centre of the studied region because earthquakes from outside the study area might affect the stress state of the fault at the margins.

CONCLUSIONS

We present a novel approach to investigate historic earthquake sequences, which can be used to add additional constraints to determining the location of historical earthquakes and to identify faults in a region that are most likely to be positively stressed. The presented technique overcomes problems which arise from investigating events independently or from a lack of historical data. While we are not able to exactly determine historic earthquake source faults, the technique contributes towards determining the most likely scenarios if historic data is incomplete or contradictory. Our approach itself relies on input from historical sources, hence we are not aiming to replace but to improve historical studies. Furthermore, we produce a hypothesis of which faults are most likely to be positively stressed, and thus pose higher seismic hazard based on a long-term earthquake record of Coulomb stress transfers. To improve this study, we plan to test this approach on a well constrained historical earthquake sequence, and we plan to explore other filtering possibilities to refine physically plausible scenarios

Acknowledgements: We would like to thank Alessandro Verdecchia for support on Coulomb stress modelling issues. M. Diercks is funded by a University of Plymouth PhD studentship.

REFERENCES

Deng, J. and Sykes, L. R., 1997. Evolution of the stress field in southern California and triggering of moderate-size earthquakes: A 200-year perspective. *Journal of Geophysical Research: Solid Earth* 102.B5, pp. 9859–9886.

Emre, Ö., Duman, T.Y., Özalp, S., Şaroğlu, F., Olgun, Ş., Elmacı, H. and Çan, T., 2018. Active fault database of Turkey. Bulletin of Earthquake Engineering, 16(8), pp.3229-3275.

Freed, A.M., 2005. Earthquake triggering by static, dynamic, and postseismic stress transfer. *Annual Review of Earth and Planetary Sciences*, 33(1), pp.335-367.

King, G. C., Stein, R. S., and Lin, J., 1994. Static stress changes and the triggering of earthquakes. *Bulletin - Seismological Society of America* 84.3, pp. 935–953.

Mildon, Z. K., Toda, S., Faure Walker, J. P., & Roberts, G. P., 2016. Evaluating models of Coulomb stress transfer: Is variable fault geometry important? *Geophysical Research Letters* 43.24, pp. 12, 407–12, 414. doi: 10.1002/2016GL071128.

Mildon, Z.K., Roberts, G.P., Faure Walker, J.P. and Iezzi, F., 2017. Coulomb stress transfer and fault interaction over millennia on non-planar active normal faults: the M w 6.5–5.0 seismic sequence of 2016–2017, central Italy. *Geophysical Journal International*, 210(2), pp.1206-1218.

Ocakoğlu, F., Açıkalın, S., Güneş, G., Özkes, S., Dirik, K. and Özsayın, E., 2013. Was the 1899 Menderes Valley Earthquake a double earthquake? Historical and paleosismological constraints. Journal of Asian Earth Sciences, 67, pp.187-198.

Steacy, S., Nalbant, S. S., McCloskey, J., Nostro, C., Scotti, O., & Baumont, D., 2005. Onto what planes should Coulomb stress perturbations be resolved? *Journal of Geophysical Research: Solid Earth* 110.5, pp. 1–14. doi: 10.1029/2004JB003356.

Stucchi, M., Rovida, A., Gomez Capera, A.A., Alexandre, P., Camelbeeck, T., Demircioglu, M.B., Gasperini, P., Kouskouna, V., Musson, R.M.W., Radulian, M. and Sesetyan, K., 2013. The SHARE European earthquake catalogue (SHEEC) 1000–1899. *Journal of Seismology*, 17(2), pp.523-544.

Toda, S., Stein, R.S., Sevilgen, V. and Lin, J., 2011. Coulomb 3.3 Graphic-rich deformation and stress-change software for earthquake, tectonic, and volcano research and teaching—user guide. *US Geological Survey open-file report*, 1060(2011), p.63.

Verdecchia, A. and Carena, S., 2015. One hundred and fifty years of Coulomb stress history along the California-Nevada border, USA. *Tectonics*, 34(2), pp.213-231.

Wells, D.L. and Coppersmith, K.J., 1994. New empirical relationships among magnitude, rupture length, rupture width, rupture area, and surface displacement. Bulletin of the seismological Society of America, 84(4), pp.974-1002

INQUA Focus Group Terrestrial Processes Perturbed by Tectonics (TPPT)

paleoseismicity.org

A paleoseismic attempt using archeoseismology in a region of low intraplate seismicity within the Chalk of the Paris Basin, Normandy, France. Is the Fécamp-Lillebonne fault active ?

Anne DUPERRET (1), Sara VANDYCKE (2), Elisabeth ROBERT-BARZMAN (3), Tassadit KACI (1)

(1) Normandie Univ, UMR 6294 LOMC CNRS-Université Le Havre Normandie, France. anne.duperret@univ-lehavre.fr
(2) Université de Mons, Génie Minier, Faculté Polytechnique de Mons, Belgique. sara.vandycke@umons.ac.be
(3) Normandie Univ, UMR 6266 IDEES-Le Havre CNRS-Université Le Havre Normandie, France. elisabeth.robert-barzman@univ-lehavre.fr

Abstract: *The northwestern part of the Paris Basin in France presents mostly a very low level of seismic hazard with very weak and sparse historical and instrumental seismicity. Swarm extends to about 40 km on each part of the Fécamp-Lillebonne fault (FFL), suspected to be active during the Quaternary in the french BDFA database. The FFL is a N150° normal strike-slip fault extending over 30 km inland from the Channel coast to the Seine river. We thus study correlations between the historic seismic activity location and the direct disturbances recorded on historic buildings. Some walls and stairs show active deformation, with a sinistral strike-slip faulting N150-155°E and conjugate faulting N135°E-N45°E at Grands-Ifs castle, Tancarville castle, Bailleul castle, Mentheville Manor. Fractures reported on historical buildings represent some indices of a very recent activity of the FFL, probably linked to the 1848 and 1849 earthquakes. FFL appears now as a senestral strike-slip fault.*

Key words*: Paris basin chalk, historic buildings, Tectonics, Paleoseismicity, Fault, Karst*

INTRODUCTION

The northwestern part of the Paris Basin in France presents mostly a low level of seismic hazard with very weak and sparse historical and instrumental seismicity, slightly increasing toward the Belgium border. Even if the regional seismicity is low, a swarm of shallow earthquakes is recorded in the Chalk of Normandy in the Caux region both offshore and onshore. Swarm extends to about 50 km around the Fécamp-Lillebonne fault (FFL), suspected to be active during Quaternary in the BDFA database (2016) (Fig. 1).

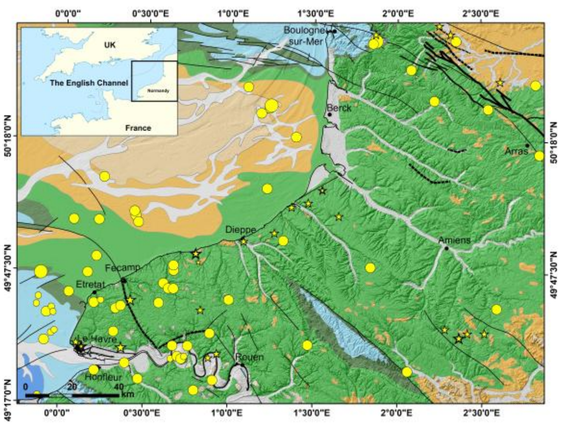

Figure 1: Geological map of NW France with superposed hillshade DEM, including the English Channel, Normandy, Hauts-de-France and a part of Belgium (BRGM, 1/ 1 000 000). Green : Cretaceous, Blue : Jurassic, Orange: Eocene. Large black dashed lines are faults considered as potentially active during Quaternary (BDFA) (Jomard et al, 2017). Yellow circles are the instrumental seismicity, reported from SI-Hex, BCSF-RéNaSS, LDG, with Mw varying from 1.6 to 3.4. Yellow stars are historical seismicity epicentres from SisFrance, MSK intensity varying from III to VI-VII.

THE FECAMP-LILLEBONNE FAULT (FFL)

The FFL is a N150° normal strike-slip fault extending over 25 km inland from Fécamp (the Channel coast) to Lillebonne (the Seine river) in the Upper Cretaceous Chalk of the Paris Basin, in Normandy. To the north, the FFL prolongates offshore in the Channel, where it shows an NW-SE trend changing westward to EW in the Channel. To the south, at Lillebonne, FFL is connected to the east with an orthogonal fault system N60° called the Villequier-Pavilly normal fault (VPF). FFL and VPF delineates a NE elevated block. Some indices of vertical offsets were reported along the VPF, with 25m on Pliocene deposits and 4m on Holocene deposits. FFL and VPF fault segments are marked by local anticline deformation parallel oriented to the fault segments (Ragot, 1988, Hauchard et al, 2008). Also offshore, to the north, the E-W lineament of FFL is marked by a clear anticlinal structure developing north of the fault segment (Paquet et al, 2017). The southern part of the FFL evidences also inland, north of Bolbec, a N150°E anticlinal. Between Triquerville and Villequier, an E-W axis anticline is developed north of the entire fault segment (VPF) (Meire et al, 2019).

As observed along the cliffs of the Channel near Fécamp, stratigraphic offsets within the Upper Cretaceous Chalk evidences syn and post Cretaceous, with a westward normal component. This is reinforced by the occurrence of various alterites types on each part of the fault compartment. Finally, as noted by Mégnien (1971), the FFL represents the northern branch of the Seine fault in Normandy. The FFL is a normal fault which evidences a westward offset of about 100-150m (Dollfus, 1929) at Fécamp and only 40-50m near Lillebonne (Meire et al, 2019), with a NE block made of Cenomanian to Coniacian chalk in front of a SW block made only of Coniacian chalk

(Mortimore and Pomerol, 1987; Juignet and Breton, 1992).

Along this southern segment, fractures appear as a serie of stacked faults (N150° and N60°), bounding tilted blocks on a strip of 300m wide through the FFL. This conducts to cumulated vertical offsets varying from 150m at Bolbec to 40m at Lillebonne from each side of the fault. The fault segment near Bolbec is deeply affected by a karstic developement and local karstic collapses, such as the Beau Soleil hole (called "bétoire") at Bolbec (Ragot, 1988). The other implication is the underground water circulation guided by the fault system through the karst, mainly localised along the anticline structure (Meire et al, 2019). Recent geophysical surveys evidenced a positive gravimetric anomaly associated to an anticline deformation of the chalk along the northeastern flank of the fault, conducting to a thickening of the surficial alterites (Meire et al, 2019). There is no instrumental seismic activity recorded near this fault segment.

RESULTS

Historical seismicity

Some historical earthquakes are reported in the region near the coast and near the FFL fault. A first swarm is localised near Veules-les-Roses, the 1st december 1769, the 26th february 1770 and the 15th sept 1835, with intensity MSK-64 VI, V and IV respectively. The others are located between Fécamp and Bolbec, the 10th July 1847 with intensity MSK VI and near the Seine river, the 30th september 1848, with intensity MSK VI (Lambert et al, 1996, www.sisfrance.net) (Fig. 2).

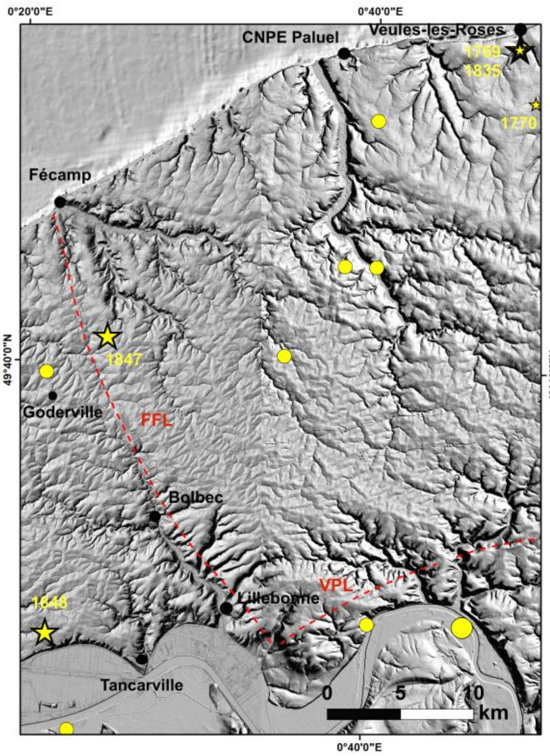

Figure 2 : Hillshade DEM of the Caux region in Normandy. (RGE-Alti and BDAlti 25, from IGN). Dashed red line is the track of the Fécamp-Lillebonne Fault (FFL) and the Villequier-Pavilly fault segment (VPF) (BRGM, 50 000, Quesnel et al, 2008). Yellow stars with year of occurrence of historical earthquakes and yellow circles for epicenters of instrumental earthquakes.

Geomorphology

The new RGE Alti topographic dataset with 1m resolution, provided by IGN allow to better describe precise landform geomorphology on the hillshade DEM (Fig. 2). FFL fault is not continuously recognized in the chalky landscape. Only the northern and the southern segments of the FFL may be recognized. To the north, it is assumed to follow a N150° dry valley called Grainval valley near Fécamp and to the south, FFL is assumed to guide the Commerce and Bolbec rivers before they connect to the Seine valley. Along about 15 km long, the FFL does not evidence morphological scarp in the chalk landscape. The same is observed for the VPF system.

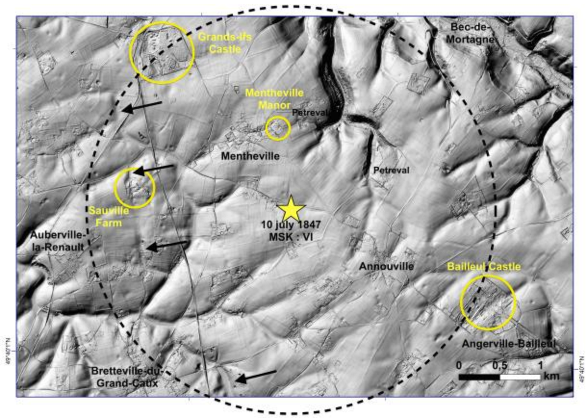

Figure 3 : Detailed hillshade DEM (RGE-Alti) 1m resolution, around the 10th july 1847 earthquake. Location of historic buildings detailed in the text. Circle represents an area of influence of 2.5 km centered on the earthquake epicenter location. Dots indicate location of the linear N170E track on the ground, extending on a minimal distance of 2 km long.

Archeoseismology

We thus study correlations between the historical seismic epicenters and the direct disturbance recorded on traditional buildings of the norman historic patrimony, such as castles, manors and traditional farms. We have selected various edifices to prospect near the 10th july 1847 historic earthquake, with a macroseismic intensity MSK of VI. (Fig. 3).

The Bailleul Castle was built in 1560 (16th century) and modified later in 1870-1890. This castle is located 2 km SE of the 1847 earthquake and 4km east of a supposed track of the FFL. At Bailleul castle, a (dextral) strike-slip fault N150° was reported on the bounding wall of the vegetable garden of the castle. Such type of wall was built in traditional norman briks with silex alternances and was a witness of the primar period of the castle. It could be the track of a surficial rupture linked to the 1847 earthquake. Unfortunately, this wall has been destroyed after this picture taken in 2015.

Figure 4 : Picture of the vegetable garden bounding wall, affected by the N150E axis strike-slip fault, that appears as dextral but with low confidence due to the free borders of the wall) at the Bailleul Castle, Angerville-Bailleul.

The Grand-Ifs Castle was built with briks and Chalk as facing stones at the end of the 16th century and modified during the 19th-20th centuries. The castle is located 2 km NW of the 1848 earthquake. Its main frontage is dated around 1500, with two symetric towers. The SW tower is affected by a continuous fault crossing the tower on all its height and the pediment of the highest window of the tower, with a clear horizontal 5-10 cm displacement of the stones (Fig. 5). This shows a N155E senestral strike-slip fault and a very good candidate for the surficial expression of the 1847 earthquake, linked to the FFL activity. A few thousand meters to the SW, less than 85 years (seen by a witness), a karstic feature collapsed in the adjoining forest and let a large hole. It is a proof of the occurrence of a karstic system near this castle, probably associated with the FFL in this area.

Figure 5 : Picture of the SW tower of the Grands-Ifs Castle, affected by the N155E senestral strike-slip fault, Tourville-les-Ifs.

The Sauville Farm is a traditional fenced hove farm house called “clos-masure” of the Caux region. It is a farm surrounded by a man-made windbreak consisting of an earth bank with tall trees on the top. This one is located at 1.5 km east of the 1847 earthquake and on the linear N170E surficial track that appears on the high-resolution DEM (Fig. 3). The bounding linear depression is locally infilled with water to form a pond during winter. Such depression-type is also observed in the field located immediatly to the north of the Sauville farm. They could correspond to the roof of a linear karst, that locally collapse (Fig. 6). In the Sauville farm, an old bread oven is located near the pond and its walls show two fractures trending N170E. One of these fracture has favored the collapse of the entire wall of the oven in the SW side of the building. The enigmatic dotted N170E track observable on the DEM is therefore a good candidate to be the surficial track of the FFL on which an underground karstic system has developed. Moreover, immediatly south of the Sauville farm, a “marnière” entrance is reported. “Marnières” (underground marl pit) of the Caux region are anthropic cavities used to exploit the underground chalk to improve the chemical quality of the fields.

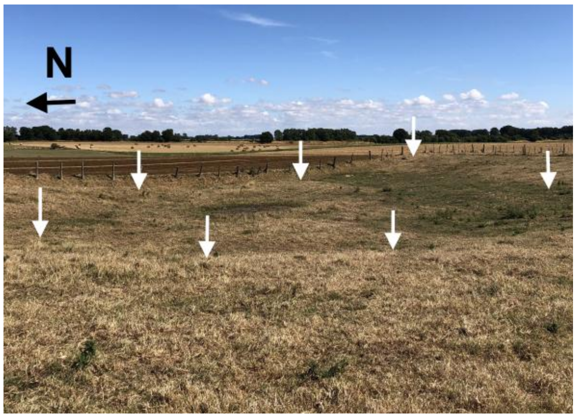

Figure 6 : Depression guided by a lineament in a field, North of the Sauville farm, Auberville-la-Renault. This corresponds probably to a “bétoire” at the top of a karstic system.

The Mentheville Manor was built during the 17th century using the Pétreval Stone extracted from the neighboring career. This is a Glauconite-Quartz greenish Chalkstone with bioclasts dated from lower Cenomanian, called glauconitic chalk and equivalent to the West Melbury Marly Chalk Formation in the UK (Lasseur et al, 2009 ; Ballesteros et al, 2021). Petreval stone appears also to be equivalent to the Fécamp Stone, widely used in the traditional building around Fécamp. The Mentheville farm shows also a square dovecote in the garden (Fig. 6) and a barn in the field corner, all built with the same Petreval stone. The dovecote and the barn are affected by the same N135E fault, with a possible conjugate fracture system N45E observed only in the barn’s corner. Such conjugate fracture system has conducted to the collapse of the eastern corner of the barn, now repaired. This evokes also a recent tectonic impact of the FFL activity, at less than 1 km to the north of the 1847 earthquake.

Figure 7 : Picture of the square dovecote of the Mentheville Manor (17th century). Mentheville. The background shows the entrance of the barn, also affected by the N135E fault.

The Tancarville Castle, built during the XIIe century and remodeled between 1709 and 1730. This castle is built on a promontory of the chalk cliff near the Seine valley and the southern segment of the FFL, at 7 km Est of the historic earthquake reported the 12 dec 1848, with MSK intensity of 6 and at equal distance to the west of the FFL track at Lillebonne. On the Tancarville castle, some faults were observed on the castle walls and windows corners. A senestral strike-slip shift of 5-10cm was observed between the stones of an outside staircase, along a N135°E axis, that could be related to the 1848 earthquake.

CONCLUSION

Even if the Paris Basin Chalk in Normandy, NW France, is considered as a region of low seismicity, favoring the implantation of two nuclear power stations on the Seine-Maritime littoral (Paluel in 1977 and Penly in 1982), the new high resolution tools of topographic mapping (LiDAR) performed by IGN evidences surficial and suspect disturbances in the ground. A multi-parameter analysis including high-resolution topographic mapping (DEM), seismology relocation, field geology, and historical buildings examinations allow to propose to integrate the Fécamp-Lillebonne Fault (FFL) in the BDFA database of IRSN as a Quaternary active fault. The modalities of the activity through time needs to be decipher to better understand faults behaviour within the Chalk. One of the characteristics of this fault is to be linked to an intense karstic activity and associated features, such as local collapses at the top of the karst, himself guided by the fault. In the Caux region, the large amount of N150-170°E lineaments need thus to be prospected in details to better evidence relationships between the tectonic FFL system, karstic developement and underground water circulation and seismic activity. Nevertheless, the recent tectonic activity reported on historical buildings, appears to focus on the FFL system using senestral strike-slip motion on N150-155°E nodal plane and locally along conjugated N135°E-N45°E planes, in accordance with the present-day NW-SE to NNW-SSE compressional stress field in NW France (Beucler et al, 2021). The FFL appears thus as a present-day senestral strike-slip fault, in opposition with the dextral motion evoked previously (Hauchard and Laignel, 2008).

Acknowledgements: This project begins in 2015 and benefits of a financial support to initiate an international collaboration, from the FR 3730 CNRS SCALE sustained by the Normandy Region, through the BATHIST project : Le Bâti historique de Normandie comme marqueur d'une activité tectonique sur le dernier millénaire en Seine-Maritime.

REFERENCES

Ballesteros D., Painchault A., Nehme C., Todisco D., Varano M., Mouralis D., 2021, Normandy chalkstone (France): Geology and historical uses from quarries to monuments, Episodes 2021, 44(1): 31-42.

Beucler É. et al, 2021. Characteristics and possible origins of the seismicity in northwestern France. Comptes Rendus Géoscience 353, n°S1, 53–77.

Dollfus G.F., 1929, La faille de Bolbec-Lillebonne (Seine-inférieure). Bull. Soc. Geol. France. P. 232-250.

Hauchard E. and Laignel B., 2008, Evolution morphotectonique de la marge nord-occidentale du Bassin de Paris. Z.F. Geomorph. N.F., 463-488. 2008

Jomard, H., Cushing, E.M., Palumbo, L., Baize, S., David, C., Chartier, T., 2017. Transposing an active fault database into a seismic hazard fault model for nuclear facilities – Part 1: Building a database of potentially active faults (BDFA) for metropolitan France. Nat. Hazards Earth Syst. Sci. 17, 1573–1584.

Juignet P. and Breton G., 1992, Mid-cretaceous sequence stratigraphy and sedimentary cyclcicity in the western Paris basin, Paleogeography, Paleoclimatology, Paleoecology, 91, 3-4, 1992, 197-218.

Lasseur E., Guillocheau F., Robin C., Hanot F., Vaslet D., Coueffe R., Neraudeau D., 2009, A relative water-depth model for the Normandy Chalk (Cenomanian-Middle Coniacian, Paris Basin, France) based on facies patterns of metre-scale cycles, Sedimentary Geology, 213, 1-2, 1-26.

Megnien C., 1971, Synthèse géologique du Bassin de Paris, Mémoire du BRGM, n°102.

Meire B., Portal A., Jacob T., Paquet F., Bitri A., Mathieu F., David P. Y. (2019) – Fonctionnement de l'hydro-système, interactions et cheminements des eaux naturelles et de la n-nitrosomorpholine dans le secteur de la Faille de Fécamp-Lillebonne–Volet géologique et géophysique. Rapport BRGM/RP- 67087-FR, 175 p.

Mortimore R. and Pomerol B., 1997, Upper cretaceous tectonic phases and end Cretaceous inversion in the Chalk of the Anglo-Paris Basin. Proceedings of the Geologist's Association, 108, 231-255

Paquet F., Allanic C., Lasseur E., Caline B., Thinon I., 2017, Reactivations and interactions of cadomian and variscan inherited structures within the intracratonic Anglo-Paris Basin revealed by offshore studies: The Fécamp-Lillebonne and Nord-Baie-de-Seine faults. IAS meeting, Toulouse, 2017.

Quesnel F., Coueffe R., Duriez M., Lasseur E., Carte géologique harmonisée du département de la Seine-Maritime. Rapport BRGM/RP-56185-FR.

Ragot J., 1988, La sedimentation crétacée aux abords de l'accident Fécamp-Lillebonne-Villequier (Seine-Maritime). Biostratigraphie et contrôle structural. Mémoire de Diplôme d'Etudes Doctorales, Université de Rouen. 141p.

INQUA Focus Group Terrestrial Processes Perturbed by Tectonics (TPPT)

paleoseismicity.org

Capable or not? The intriguing case of the Pescopagano fault in the area of the 1980, Mw 6.9 Irpinia earthquake, southern Italy

Ferranti, Luigi (1), Francesco Iezzi (1), Alberto Bacchiani (1), Salvatore Buoninfante (1), Felice Menna (1), Monica Sposato (1), Vincenzo Di Fiore (2), Daniele Bellini (3), Alessandro Citterio (3), Roberto Calabrò (3), Claudio Pasqua (4)

(1) DiSTAR - Dipartimento di Scienze della Terra, dell'Ambiente e delle Risorse Università di Napoli "Federico II"; lferrant@unina.it; francesco.iezzi@unina.it; a.bacchiani@studenti.unina.it; s.buoninfante@studenti.unina.it; feli.menna@studenti.unina.it; mo.sposato@studenti.unina.it;
(2) CNR-ISPC - Istituto di Scienze del Patrimonio Culturale; vincenzo.difiore@cnr.it;
(3) Edison SpA; Daniele.Bellini@edison.it; Alessandro.Citterio@edison.it; Roberto.Calabro@edison.it;
(4) FrosioNext; claudio.pasqua@frosionext.com

Abstract: *We studied the Pescopagano fault (PF), part of the extensional system that ruptured during the 1980, Mw 6.9 Irpinia earthquake. The PF lies above the blind antithetic fault NE of the mainshock fault, and it is considered capable of producing surface ruptures. We tested this hypothesis through structural analysis, high-resolution seismic profiles and paleoseismological trenching. The seismic profiles did not show appreciable offsets down to 20 m depth in the fault hanging-wall. Paleoseismological trenches document that ~6.8 ka BP colluvial deposits and LGM to Early Holocene slope and alluvial gravels seal the fault scarp, and underlying marsh clays in the hanging-wall are not offset. Our findings document that the PF has not released surface-rupturing earthquakes at least for the last 6.9 ka, and presumably since the ~LGM. Structural data suggest that the fault maybe an Early Quaternary structure rooted at 3-4 km depth, not reaching the 10 km seismogenic depth.*

***Key words**: Pescopagano fault, Paleoseismological trenches, Irpinia 1980 earthquake fault system, Southern Italy.*

INTRODUCTION

The identification of capable faults often relies on the presence of hanging-wall scarps that are assumed to have slipped after the LGM (~15±3 ka). However, this approach can have severe pitfalls in the absence of independent evidence of recent activity (trench paleoseismology, cosmogenic dating of fault planes), particularly in areas of recent change of tectonic regime and with a complex structural setting, such as the Southern Apennines of Italy.

We report here the preliminary results of a study carried on the Pescopagano fault (PF) for a major infrastructure planning. The PF is part of the Antithetic fault of the NE-dipping Irpinia normal fault, which ruptured during the 1980, Mw 6.9 Campania-Basilicata earthquake (**Fig. 1;** Bernard & Zollo, 1989).

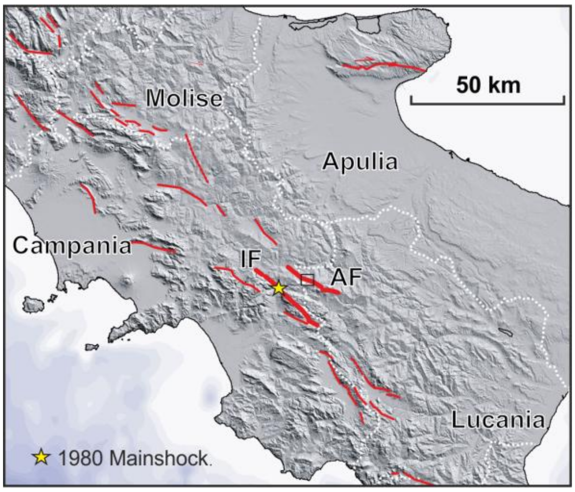

Figure 1: Late Pleistocene-Holocene faults in the Southern Apennnines. In bold, the Irpinia main fault (IR) and its anthithetic fault (AF). The Pescopagano fault lies in the central part of the AF (box). The star shows the 1980 earthquake epicenter.

The SW-dipping antithetic fault is a blind (1.5-1.8 km; Amoruso et al., 2005) structure that failed 40 sec. after and ~10 km NE of the mainshock rupture (**Fig. 1**) (Pantosti & Valensise, 1990). According to some workers, the 1980 antithetic fault including the PF caused a surface rupture (Blumetti et al., 2002; Bello et al., 2021). The PF is present in the ITHACA Catalogue of the Active and Capable Faults (http://sgi2.isprambiente.it/ithacaweb/viewer/) and is assigned a pre-historic (3-9 ka) last activity and an association with the 1980 event. The latter scenario has major implications for the local seismic hazard and territorial management, but robust kinematic and age analysis and paleoseismological constraints on the PF are lacking. We have therefore performed a detailed geological and paleoseismological survey of the Pescopagano fault, in order to establish its recent activity and its capability of causing surface ruptures.

BACKGROUND CONTEXT

The ~5 km long PF is part of the ~22 km long, NW-SE striking, SW-dipping Conza della Campania fault, which is viewed as the central segment of the 60 km long Irpinia Antithetic fault (DISS WG, 2018; Bello et al., 2021). The PF lies at the SE termination of the Conza fault and has an oblique (WNW-ESE) strike relative to the main fault.

The PF cuts across Upper Cretaceous-Oligocene rocks of the Flysch Rosso formation, part of the Lagonegro basin succession, which forms one of the main litho-tectonic units of the Southern Apennines fold and thrust belt (Patacca and Scandone, 2007). About 2 km north of the PF, the Lagonegro rocks are thrust above Middle Pliocene clay and silt of the Ofanto basin along the E-W striking Pescopagano and Ofanto thrust faults (**Fig. 2**).

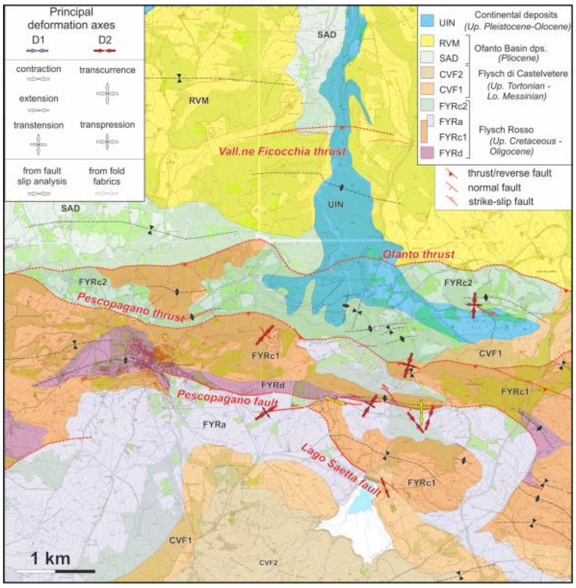

Figure 2: Geological-structural map of the Pescopagano area.

STRUCTURAL ANALYSIS OF THE PESCOPAGANO FAULT

Mapping has showed that the PF is divided in three strands. We studied in detail the central (Croce dello Staccato, CS) and eastern (Madonna di M. Mauro, MM) strands (**Fig. 3**), of broadly similar length (~1 km).

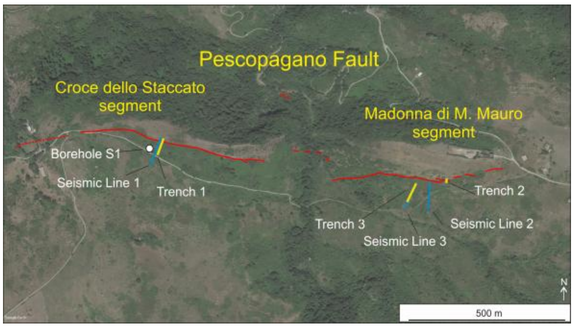

Figure 3: Central and eastern segments of the PF and ubication of geophysical and paleoseismological surveys.

Based on the offset of a marker level of the Flysch Rosso and on the presence of a damage zone at depth within borehole S1 (**Fig. 3**), a ~100 m max throw and a 60°-70° dip are estimated for the fault.

The fault scarp is rather degraded and only at one location along the MM strand a limited (0.5 m high x 5 m wide) fault plane exposure is present. Altered tectogrooves with a ~90° pitch were observed on the 55° southward dipping fault plane, providing a N-S extension axis (**Fig. 2**). The finding of a fresh ~8 cm high ribbon at its base, however, induced further investigations to prove or dismiss involvement of the fault during the 1980 or preceding earthquakes.

NEAR SURFACE GEOPHYSICAL AND PALEOSEISMOLOGICAL ANALYSIS

We performed high-resolution seismic reflection investigations and dug paleoseismological trenches on both the CS and the MM strands of the PF (**Fig. 3**).

Seismic tomographic sections provided images down to ~20 m depth, and revealed three seismic units in the Vp model. The seismic lines highlighted the presence of a sharp lateral change in Vp at an average depth of 5-10 m. However, it was unresolved whether they reflect faults or erosive contacts.

Three paleoseismological trenches co-linear with the seismic profiles were opened in the proximities of the fault scarps (**Fig. 3**). Specifically, Trench 1 crossed the fault scarp along the CS fault strand, Trench 2 is located in the immediate hanging-wall of the exposed fault plane along the MM strand, Trench 3 was designed to explore the nature of the abrupt lateral change in Vp shown by Seismic Line 3, together with exploring the possible presence of distributed faulting.

The combination of the stratigraphic record of the three trenches (**Fig. 4**) allowed us to reconstruct the geological setting of the hanging-wall deposits (**Fig. 5**), which helped us in understanding the time range of activity of the PF.

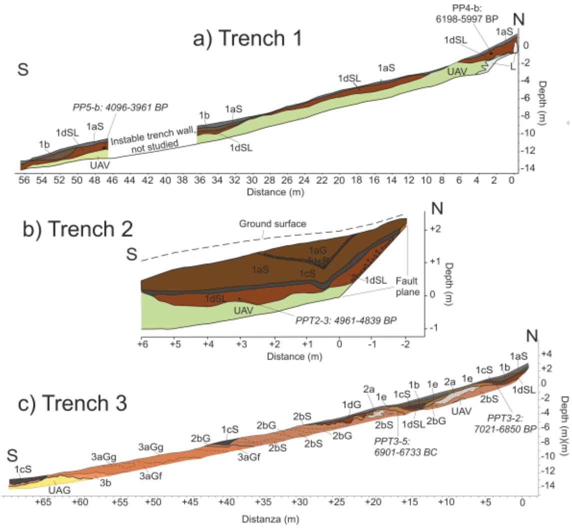

Figure 4: Logs of trenches T1, T2, T3.

The three trenches showed that multiple sedimentary units seal the fault (**Figs. 4, 5**).The uppermost unit (Unit 1) is composed by recent soil and colluvial deposits, often channelized, and has ^{14}C ages back to ~6.8 ka BP (**Fig. 5**). Unit 2 includes laterally variable thickness of alluvial sands and gravels, which forms tight channels in the upper part, and passes downward to alluvial and slope gravel wedges (Unit 3). Units 2 and 3 rest with sharp erosive contacts on at least two generations of marshy clays (AV and AG) developed at the expense of the Flysch Rosso pelites and argillites in the hanging-wall of the PF. Although radiometric age constraints are so far available only for Unit 1, we suggest that units 2 and 3 span the transition from the last glacial to the de-glacial conditions. Units AV and AG reflects interglacial or interstadial conditions.

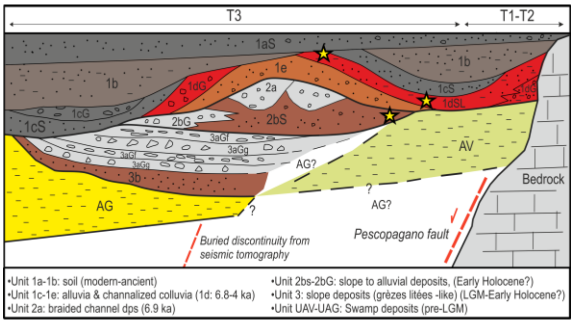

Figure 5: Stratigraphic scheme reconstructed from paleeoseismological trenches. Numbers with letters refer to specific sub-units. Bold solid lines indicates the contacts between the main depositional units. Stars are dated samples. Arrows with letters T1, T2, T3 show the spatial extent of stratigraphy revealed by each trench.

DISCUSSION: THE ORIGIN AND CAPABILITY OF THE PESCOPAGANO FAULT

Based on trench observations, trench units ages assessment, and morpho-structural data, we conclude that the PF did not cause surface ruptures since 6.8 ka BP and probably since the Latest Pleistocene. Structural data indicate that the PF lies in the back-limb of a steep N-verging Pliocene fold-thrust train, which about 2 km north of the PF, carries the Lagonegro rocks above Middle-Late Pliocene clay and silt of the Ofanto basin along the E-W striking Ofanto thrust fault (**Fig. 2**). Because the extension axis on the PF is sub-parallel to the Pliocene shortening axis determined from structural analysis (**Fig. 2**), we suggest that the PF could represent a back-limb collapse structure developed during or after thrusting, implying that the PF may have an early Quaternary age at most. Structural reconstructions let us to infer that the PF merges with the Ofanto thrust ramp at ~3-4 km depth, which that corresponds to the detachment level of the thrust sheet composed by the Lagonegro basinal rocks (Nicolai and Gambini, 2007). Thus, the PF could not reach the 10-12 km nucleation depth of large earthquakes in the area.

REFERENCES

Amoruso, A., Crescentini, L., and Scarpa, R. (2005). Faulting geometry for the complex 1980 campania-lucania earthquake from levelling data. Geophys. J. Int 162, 156–168. doi:10.1111/j.1365-246X.2005.02652.x

Bello, S., De Nardis, R., Scarpa, R., Brozzetti, F., Cirillo, D., Ferrarini, F., ... & Lavecchia, G. (2021). Fault pattern and seismotectonic style of the Campania–Lucania 1980 earthquake (Mw 6.9, southern Italy): New multidisciplinary constraints. Frontiers in Earth Science, 8, 608063.

Bernard, P., amd Zollo, A. (1989). The Irpinia (Italy) 1980 earthquake: detailed analysis of a complex normal faulting. Journal of Geophysical Research: Solid Earth, 94(B2), 1631-1647.

Blumetti, A. M., Esposito, E., Ferreli, L., Michetti, A. M., Porfido, S., Serva, L., & Vittori, E. (2002). New data and reinterpretation of the november 23, 1980, M 6.9 Irpinia-Lucania Earthquake (Southern Apennines) coseismic surface effects, Studi Geologici Camerti.

DISS Working Group (2021). Database of Individual Seismogenic Sources (DISS), Version 3.3.0: A compilation of potential sources for earthquakes larger than M 5.5 in Italy and surrounding areas. Istituto Nazionale di Geofisica e Vulcanologia (INGV). https://doi.org/10.13127/diss3.3.0

Nicolai, C., & Gambini, R. (2007). Structural architecture of the Adria platform-and-basin system. Bollettino della Società Geologica Italiana, 7, 21-37.

Pantosti, D., and Valensise, G. (1990). Faulting mechanism and complexity of the november 23, 1980, campania-lucania earthquake, inferred from surface observation. J. Geophys. Res 95, 15319. doi:10.1029/jb095ib10p15319

Patacca, E., & Scandone, P. (2007). Geology of the southern Apennines. Bollettino della Società Geologica Italiana, 7, 75-119.

Historical earthquakes in Lower Silesian Block (Poland) - an archeoseismological approach

Gaidzik, Krzysztof (1), Miklós Kázmér (2)

(1) University of Silesia in Katowice, Będzińska 60, 41-200, Sosnowiec, Poland. Email: krzysztof.gaidzik@us.edu.pl
(2) Eötvös University, 1117 Budapest, Pázmány Péter sétány 1/c, Hungary.

Abstract: *We present here the results of a comprehensive archeoseismological study of 55 churches located in the Lower Silesian Block adjacent to the SMF. We report several structures with unusual buttresses, tilted inward/outward walls, dropped keystones, displaced masonry, shifted blocks and/or columns, etc. Based on the history of deformations and repairs, our results suggest that some sites experienced more than one moderate to destructive earthquake. For ten of the studied sites, the assigned archeo-intensity exceeds VIII. Further studies are needed to date the recorded seismic events and establish their potential sources.*

Key words*: archaeoseismology, historical earthquake, Lower Silesia, deformation, buttress.*

INTRODUCTION

Archeoseismology, due to the common lack of written testimonies and incompleteness of seismic catalogs, might play a crucial role in filling the gaps in historical earthquake records and, therefore, in improving the seismic hazard assessments. This is particularly true for regions opulent in archeological sites and/or medieval structures (especially churches). This task is even more relevant and challenging in intraplate regions characterized by the low deformation rate and associated low to moderate seismicity with an usually long recurrence period.

STUDY AREA

Lower Silesian Block in the NE Bohemian Massif has abundant medieval to modern buildings presenting a rich history of damage/repair/renovation suitable for archeoseismological studies (Gaidzik and Kázmér, 2021). The unit is cut by the 200-km long Sudetic Marginal Fault (SMF), i.e., one of the most prominent tectonic zones in central Europe that exhibits the pronounced morphotectonic escarpment of the Sudetic Mountains front.

Its Quaternary activity, mainly late Pleistocene, with a prehistoric earthquake of minimum moment magnitude M 6.3 and the inferred slip rate of about 0.03 mm/year (late Pleistocene slip rate of ~1.1 mm/yr) have been corroborated by paleoseismological trenching (Štěpančíková et al., 2010, 2022) and damaged speleothems (Szczygieł et al., 2021). Moreover, several historical earthquakes since the XV century have been reported (e.g., Guterch and Kozák, 2015; Sana et al., 2021).

METHODS

We applied the archeoseismological analysis to 55 churches located in the Lower Silesian Block adjacent to the SMF, as these are the best to recognize past damaging seismic events (e.g., Kázmér, 2015). During fieldwork, any deviation from the architectural traditions and norms was recorded, either related to deformation, e.g., bent (folded), bulging, torn, or collapsed walls, dropped, shifted, rotated, extruded blocks, dropped keystones, fracture across blocks, walls, an entire building, etc. or associated with restoration, e.g., repair, support, reconstruction, reuse of spoiled masonry, unnecessary, exaggerated buttresses, etc. (Kázmér, 2018). Survey and documentation were carried out by photography together with structure-from-motion 3D modeling, drawings, and by handheld instruments (GPS, compass, vertical and horizontal distances were measured by laser range finder Nikon Forestry Pro II, and wall tilting, if possible, by a digital compass-clinometer FieldMove Clino. Construction and repair history is based on observations and published archaeological results. A succession of recognized events is correlated to historical data, if available. Earthquake intensity was assessed based on the Earthquake Archaeological Effect (EAE13) scale (Rodríguez-Pascua et al., 2013).

Table 1. Main historical earthquakes in the studied area (based on Guterch and Kozák, 2015).

Date	Local magnitude	Intensity	Date	Local magnitude	Intensity
1443.06.05	6.0	8-9	1751.06.31	>4.3	6-7
1496.06.23	3.5	5	1778.05.10	>3.5	5-6
1562.02.10	5.2	7	1829.06.02/03	3.5	5
1594.09.15	3.5	5	1877.11.25	3.5	5
1615.02.13	3.5	5	1895.06.11	>4.4	6-7

Figure 1. Examples of observed deformation/restoration suggesting seismic origin. A – Leaning Tower in Ząbkowice Śląskie presenting >2 m deviation from the vertical; B & C – Castle in Ząbkowice Śląskie with folded wall (fold with subvertical axis); D-H – Church of the Assumption of the Blessed Virgin Mary in Kłodzko; D – general view on the exaggerated buttresses supporting two uneven towers and NW wall; E – tilted inward NW wall; F – dropped keystone above the portal on the NW wall; G – dropped and shifted keystone above window in SW wall; H – deformed arch below N tower.

RESULTS AND DISCUSSION

Conducted fieldwork revealed numerous churches in the Lower Silesia region in Poland and partly in the Czech Republic that show different types of anomalies in their construction/reconstruction (Fig. 1). The most common features include:

- unusual or oversized buttresses (almost all of the studied buildings)
- tilted inward/outward walls (e.g., Kłodzko, Karszów, Prusy, Ząbkowice Śląskie, Złotoryja, Dziwiszów, Ścinawa Mała, Lwówek Śląski)
- dropped keystones (e.g., Kłodzko, Złotoryja, Dziwiszów, Świerzawa, Pogwizdów, Lwówek Śląski, Środa Śląska)
- displaced masonry (e.g., Kłodzko, Prusy, Złotoryja, Lwówek Śląski, Środa Śląska)
- shifted blocks and/or columns (e.g., Kłodzko, Złotoryja)
- deformed arches (e.g., Kłodzko, Lwówek Śląski, Złotoryja, Środa Śląska)
- folded wall (e.g., Ząbkowice Śląskie, Lwówek Śląski)

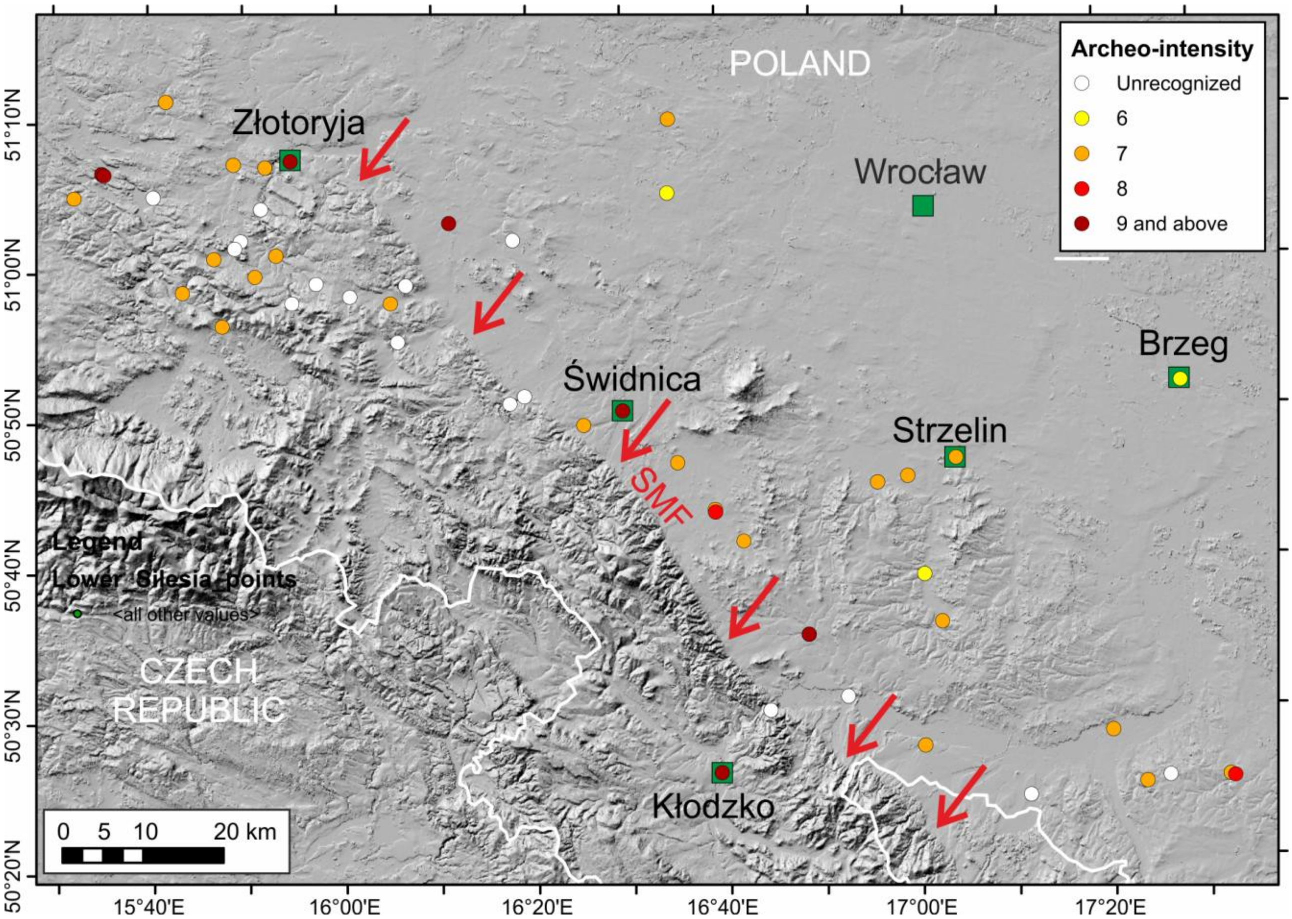

Figure 2. Maximum archeo-intensities for studied churches in the Lower Silesia region based on our field observations and measurements. Red arrows present the SMF – Sudetic Marginal Fault.

Based on the history of deformations and repairs, our results suggest that some sites experienced more than one moderate to destructive earthquake. For ten of the studied sites (i.e., St. George Church in Dzierżoniów, Church of the Visitation of the Blessed Virgin Mary in Ścinawa Mała, Church of the Assumption of the Blessed Virgin Mary and Church of Saint Francis of Assisi in Lwówek Śląski, St. Martin Church in Jawor, Cathedral of St. Stanislaus and St. Vaclav in Świdnica, St. Anna Church and Leaning Tower in Ząbkowice Śląskie, Church of the Nativity of the Virgin Mary in Złotoryja, Church of the Assumption of the Blessed Virgin Mary in Kłodzko), the assigned archeo-intensity exceeds VIII based on the Earthquake Archaeological Effect (EAE13) scale (Rodríguez-Pascua et al., 2013) (Fig. 2). However, for many sites, the exact archeo-intensity was not possible to assess and/or requires further detailed studies.

Preliminary results of dating using historical records, known earthquakes (Guterch and Kozák, 2015), and history of construction/destruction/restoration of each specific church suggest that at least some of the recorded deformations, e.g., Leaning Tower in Ząbkowice Śląskie and Church of the Assumption of the Blessed Virgin Mary in Kłodzko, could be related to known historical events. On the other hand, deformations observed in the Church of the Assumption of the Blessed Virgin Mary and Church of Saint Francis of Assisi in Lwówek Śląski, St. Martin Church in Jawor for example, suggest additional events, not included in the seismic catalogs. However, further studies to date these more precisely and establish their potential sources.

Acknowledgements: The research activities co-financed by the funds granted under the Research Excellence Initiative of the University of Silesia in Katowice.

REFERENCES

Gaidzik, K., & Kázmér, M., 2021. Potential archeoseismological evidence of historical earthquakes in Lower Silesia, Poland. In: *37th General Assembly (GA) of the European Seismological Commission* (ESC 2021), 19-24 September 2021.

Guterch, B., & Kozák, J., 2015. *Studies of Historical Earthquakes in Southern Poland. Studies of Historical Earthquakes in Southern Poland*. Series: GeoPlanet: Earth and Planetary Sciences. Springer International Publishing Switzerland, Springer Cham Heidelberg New York Dordrecht London. 179 p.

Kázmér, M., 2015. Damage to ancient buildings from earthquakes. In: *Encyclopedia of Earthquake Engineering* (Beer, M., Patelli, E., Kouigioumtzoglou, I., Au, I. S.-K. eds.), Springer, Berlin, 500-506.

Kázmér, M., 2018. Towards a protocol of archaeoseismological survey. In: *Sixth International Colloquium on Historical earthquakes & paleoseismology studies*. Han-sur-Lesse (Belgium), 24-25 October 2018. Abstract Book, p. 28.

Rodriguez-Pascua, M.A., Silva, P.G., Pérez-López, R., Giner-Robles, J.L., Martín-González, F., Perucha, M.A., 2013. Preliminary intensity correlation between macroseismic scales (ESI07 and EMS98) and Earthquake archaeological effects (EAEs). In: *Seismic Hazard, Critical Facilities and Slow Active Faults* (Grützner. C. and Reicherter C. eds.). Proceedings of the 4th International INQUA Meeting on Paleoseismology, Active Tectonics and Archeoseismology, 133-137.

Sana, H., Štěpančíková, P., Szameitat, A., Stemberk, J., 2021. Macroseismic intensity re-evaluation of the 11 June 1895 Mid-Silesia, Poland, Earthquakes. – Seismological Research Letters 92(2A), 1159-1167.

Štěpančíková, P., Hók, J., Nývlt, D., Dohnal, J., Sýkorová, I., & Stemberk, J., 2010. Active tectonics research using trenching technique on the south-eastern section of the Sudetic Marginal Fault (NE Bohemian Massif, central Europe). *Tectonophysics*, 485 (1-4), 269-282.

Štěpančíková, P., Rockwell, T. K., Stemberk, J., Rhodes, E. J., Hartvich, F., Luttrell, K., Myers, M., Táborík, P., Rood, D:H., Wechsler, N., Nyvlt, D., Ortuno, M., & Hók, J., 2022. Acceleration of Late Pleistocene activity of a Central European fault driven by ice loading. *Earth and Planetary Science Letters*, 591, 117596.

Szczygieł, J., Sobczyk, A., Hercman, H., Mendecki, M. J., & Gąsiorowski, M., 2021. Damaged speleothems and collapsed karst chambers indicate paleoseismicity of the NE Bohemian Massif (Niedźwiedzia Cave, Poland). *Tectonics*, 40(3), e2020TC006459.

INQUA Focus Group Terrestrial Processes Perturbed by Tectonics (TPPT)

paleoseismicity.org

Seismogenic faults, seismo-lineaments, and related thermal waters in the Colca basin, S Peru – preliminary results

Gaidzik, Krzysztof (1), Andrzej Tyc (1), Jerzy Żaba (1), Justyna Ciesielczuk (1), Andrzej Paulo (2), Malwina Więsek (1), Carlos Benavente (3), Laurence Audin (4)

(1) University of Silesia in Katowice, Będzińska 60, 41-200, Sosnowiec, Poland. Email: krzysztof.gaidzik@us.edu.pl
(2) AGH University of Science and Technology, Mickiewicza 30, 30-059 Kraków, Poland.
(3) Instituto Geológico Minero y Metalúrgico (INGEMMET), Av. Canadá 1470, San Borja 15034, Lima, Peru.
(4) IRD, ISTerre, Université Grenoble Alpes, 1381 rue de la Piscine, 38610 Gieres, France.

Abstract: *We propose a multidisciplinary approach combining morphotectonic analysis of crustal faults, field survey, focal mechanism review, and seismo-lineaments computation, together with hydrogeochemical and isotopic analysis of springs and geysers. Morphotectonic analysis and field observations concur with the principally W- to NW-striking seismo-lineaments and highlight the surface expressions of seismogenic faults in the Colca basin together with focal mechanisms of crustal earthquakes. The active fault network in the Colca basin is a crucial agent in the complex hydrogeological thermal system. The reactivation of identified structures can be related to the following sources of stress: 1) strain partitioning in the oblique subduction zone, 2) crustal seismicity induced by megathrust earthquakes, 3) extension in the most upper part of the uplifting area above the subducting slab, and 4) volcanic activity.*

Key words*: seismogenic fault, seismo-lineament, thermal water, Colca, crustal earthquake.*

INTRODUCTION

Crustal faults in the overriding plate above the subducting slab are usually less studied when compared to the subduction zone itself and omitted and/or underestimated in seismic hazard assessments. However, even smaller seismic events with epicenters originating along crustal faults due to the shallow focal depth and closeness to the human settlements can be equally hazardous, producing analogous if not more fatalities and economic losses than some of the megathrust earthquakes (e.g., Baize et al., 2015). Even though pronounced in satellite imagery, these geologic structures in the Colca River basin are still not properly studied. To fully understand the complex system of crustal faults in the Colca basin, we propose a multidisciplinary approach combining morphotectonic analysis of crustal faults, field survey, focal mechanism review, seismo-lineaments computation, together with hydrogeochemical and isotopic analysis of springs and geysers.

STUDY AREA

The study area, i.e. Colca drainage basin, located in the Central Andes in southern Peru, extends from south latitude 15–17◦, west longitude 71–73◦. It is characterized by a high seismic activity related to both (1) repeated large and great megathrust earthquakes related to the subduction of the Nazca Plate beneath the South American Plate (e.g., Chlieh et al., 2011), and (2) shallow events along seismogenic crustal faults on the overriding plate (e.g., Benavente et al., 2017). Of the latter, predominate NW-striking strike-slip faults (especially sinistral) and W-striking normal faults (Benavente et al., 2017; Gaidzik et al., 2020). The seismic record of crustal events from the last several years includes numerous earthquakes of magnitude usually not exceeding 6.0, yet still destructive for infrastructure and catastrophic for local communities (e.g., Antayhua et al., 2002; Benavente et al., 2017; Gaidzik and Więsek, 2021). However, pronounced in the morphology of the area, these crustal structures are still poorly studied.

METHODS

We implemented a multidisciplinary approach combining different tools and methods to determine evolution, seismogenic potential, impact on morphology, and geohazard of active crustal faults in the Colca basin. The most important of these include field survey, morphotectonic analysis, focal mechanism review of recent events, seismo-lineaments computation, hydrogeochemical and isotopic analysis of springs and geysers associated with crustal faults, palaeoseismological trenching, absolute dating of potentially coseismic rockslides, and disrupted/deformed sediments seen in trenches and natural outcrops, calculation of Coulomb stress-transfer between studied faults, and archaeoseismological studies of churches and pre-Hispanic archaeological sites. Here, we report the preliminary results of this ongoing project.

RESULTS AND DISCUSSION

Morphotectonic analysis of digital elevation models and satellite images together with field observations concur with the principally W- to NW-striking seismo-lineaments and highlight the surface expressions of seismogenic faults in the Colca basin together with focal mechanisms of crustal earthquakes (Fig. 1) (see also Gaidzik and

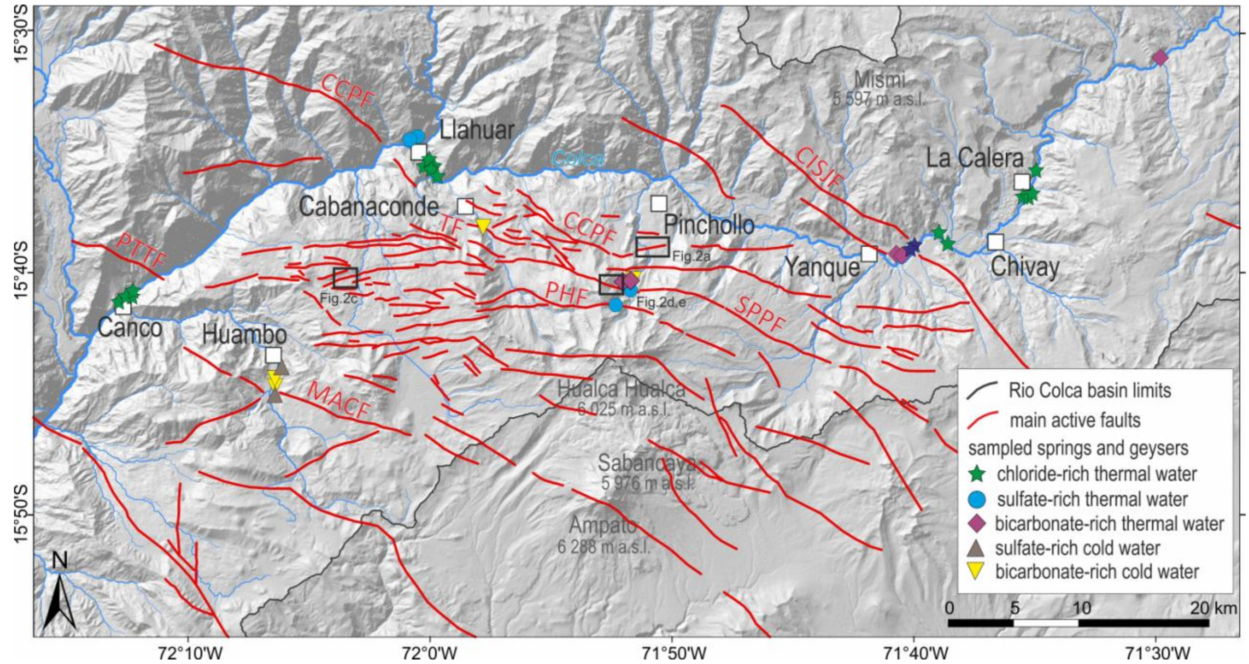

Figure 1. Major active crustal faults in the central Colca River basin (according to Benavente et al., 2017) and studied associated thermal springs and geysers (according to Tyc et al., 2022). CCPF - Chachas-Cabanaconde-Patapampa Fault, SPPF - Solarpampa-Puye Puye-Pillo Fault, PHF - Pungo-Hornillo Fault, CISJF - Río Cotahuasi-Ichupampa-San Juan de Tarucani Fault, TF - Trigal Fault, PTTF - Pallca-Tunupacha-Toro Fault, MACF - Mucurca-Ampato-Casablanca Fault.

Więsek, 2021). Features like river offsets, fault scarps, sag ponds, beheaded streams, pressure ridges, etc. observed in remote sensing imagery and recorded in the field indicate the geomorphological expressions of studied crustal faults (Fig. 2). Clearly marked in the field, fault scarps reach usually between 15 and 20 m height, but locally, especially in the case of Trigal and Solarpampa faults, might reach c. 100 m. In the latter cases, numerous rockslides were observed and sampled for cosmogenic exposure dating (Fig. 2c).

The scaling relationships, applied to seismo-lineaments and fault traces mapped in the field and based on literature data (see Benavente et al., 2017; Gaidzik and Więsek, 2021), suggest a seismic potential for earthquakes of maximum moment magnitudes up to 6.8–6.9 for segments of the recorded crustal structures. These calculated values exceed the magnitudes in the catalog of shallow events in this region for the time period 1976-2021 recorded by the Global Centroid-Moment-Tensor (CMT) Catalog (www.globalcmt.org). Although we cannot exclude the possibility that these sections might experience aseismic deformations, like creeping or slow slip events, large earthquakes are equally probable.

The active fault network in the Colca basin is a crucial agent in the complex hydrogeological thermal system (Tyc et al., 2022). Thermal springs and geysers (especially those in the areas of Llahuar and Cabanaconde, Yanque, and those located on the northern slopes of Hualca Hualca volcano) show a clear spatial correlation with active and seismogenic crustal W- to NW-tracing normal and strike-slip faults recorded in the field (e.g., Żaba et al., 2012; Ciesielczuk et al., 2013; Gaidzik et al., 2020), mapped on a neotectonic map (Benavente et al., 2017) and/or derived from focal mechanisms as seismo-lineaments (Gaidzik and Więsek, 2021) (Fig. 1, 2d). These might act as a barrier to infiltrating meteoric waters, pathways to hydrothermal solutions, and gases assisting in meteoric water heating, and passages for heated waters ascending into the surface.

The reactivation of identified structures can be related to the following sources of stress: 1) strain partitioning in the oblique subduction zone, 2) crustal seismicity induced by megathrust earthquakes, 3) extension in the most upper part of the uplifting area above the subducting slab, and 4) volcanic activity; however, further studies are needed.

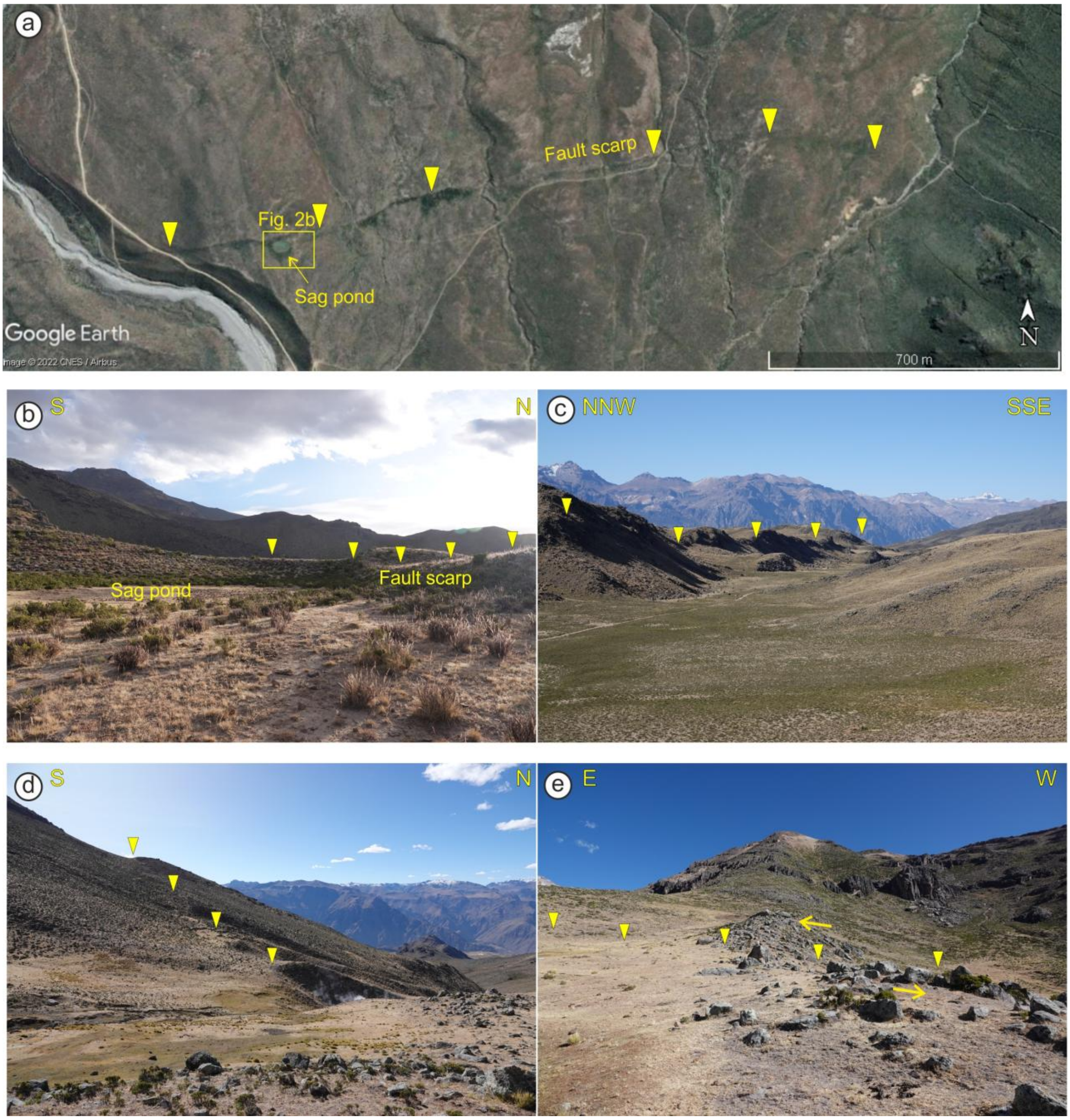

Figure 2. Examples of morphological expressions of crustal faults in the Colca basin (for location of photographs see Fig. 1); a – Fault scarps and sag pond in the WSW-trending seismo-lineament north of Pinchollo geyser, b – field photo of sag pond and faults scarp in the western part of the seismo-lineament presented in Fig. 2a, c – 60-80 m high scarps delimiting the western section of the Solarpampa Fault between Huambo and Cabanaconde, d – WNW-trending fault on the northern slopes of the Hualca Hualca volcano associated with active thermal spring, e – the same WNW-trending fault offsetting small ridge on the slope of the Hualca Hualca volcano (accumulated offset – 10.5 ± 0.5 m). Yellow triangles – a trace of the mapped active faults; yellow arrows – direction and sense of relative displacements along a fault.

Acknowledgments: This research was funded by National Science Centre (Poland), grant No 020/39/B/ST10/00042. We are grateful to the local communities of the Colca drainage basin for kindly giving us access to work and for help in the field.

REFERENCES

Antayhua, Y., Tavera, H., Bernal, I., Palza, H., & Aguilar, V., 2002. Localizacion hipocentral y caracteristicas de la fuente de los sismos de Maca (1991), Sepina (1992) y Cabanaconde (1998), Región del Volcan Sabancaya (Arequipa). *Bol. Soc. Geol. Peru* 93, 63–72.

Baize, S., McCalpin, J., Scotti, O., Costa, C., Cinti, F. R., Michetti, A. M., ... & Dawson, T., 2015. Earthquake geology of shallow crustal faults and Seismic Hazard Assessment: Challenges ahead. In *6th INQUA International Workshop on Active Tectonics Paleoseismology and Archaeoseismology*, 19-24.

Benavente, C., Delgado, G., García, B., Aguirre, E., & Audin, L., 2017. Neotectónica, evolución del relieve y peligro sísmico en la Región Arequipa, INGEMMET. Boletín, Serie C, Nº64. Geodinamica e Ingeniería Geológica, p. 370.

Chlieh, M., Perfettini, H., Tavera, H., Avouac, J.-P., Remy, D., Nocquet, J.-M., Rolandone, F., Bondoux, F., Gabalda, G., & Bonvalot, S., 2011. Interseismic coupling and seismic potential along the Central Andes subduction zone. *Journal of Geophysical Research* 116, B12405.

Ciesielczuk, J., Żaba, J., Bzowska, G., Gaidzik, K., & Głogowska, M., 2013. Sulphate efflorescences at the geyser near Pinchollo, southern Peru. *Journal of South American Earth Sciences* 42, 186–193.

Gaidzik, K., & Więsek, M., 2021. Seismo-lineaments and potentially seismogenic faults in the overriding plate of the Nazca-South American subduction zone (S Peru*). Journal of South American Earth Sciences* 109, 103303.

Gaidzik, K., Żaba, J., & Ciesielczuk, J., 2020. Tectonic control on slow-moving Andean landslides in the Colca Valley, Peru. *Journal of Mountain Science* 17(8), 1807-1825.

Tyc, A., Gaidzik, K., Ciesielczuk, J., Masías, P., Paulo, A., Postawa, A., & Żaba, J., 2022. Thermal springs and active fault network of the central Colca River basin, Western Cordillera, Peru. *Journal of Volcanology and Geothermal Research* 424, 107513.

Żaba, J., Małolepszy, Z., Gaidzik, K., Ciesielczuk, J., & Paulo, A., 2012. Fault network in Rio Colca Valley between Maca and Pinchollo, Central Andes, Southern Peru. *Annales Societatis Geologorum Poloniae* 82, 279-290.

Collisional (Indenter) Tectonics of the Santa Ana Mountains and the Southern Los Angeles Basin, Orange County, California

Eldon Gath (1)

(1) Earth Consultants International, Santa Ana, California, USA. gath@earthconsultants.com.

***Abstract**: The Santa Ana Mountains (SAM), a plutonic-cored Mesozoic intrusive body dominating Southern California's Orange County landscape, are being thrust into the sediment-filled Los Angeles Basin at ~6 mm/yr by the right-lateral Elsinore fault. This SAM indenter has resulted in ~18 km of northwest-vergent penetration into the Cretaceous to Pleistocene sedimentary section. This in turn has and is generating multiple secondary tectonic geomorphic structures including strike-slip faults, anticlines, imbricate thrust sheets, and disseminated secondary faulting and fracturing of the surrounding rocks. Simultaneously, the south-vergent Puente Hills are uplifting along a blind Puente Hills thrust fault. As these two structures converge, the uplift rate of the Puente Hills is increased, the right-lateral Whittier fault accommodates westward escape tectonics of the basin sediments at 2-3 mm/yr, and 1-2 mm/yr left-lateral shearing is developed within a deformable shale unit along the western SAM margin due to weak coupling of the sedimentary rocks and the plutonic indenter. Microseismicity is concentrated within the deforming sedimentary section above and in front of the indenting pluton, reactivating pre-existing secondary faults and posing a regional ground deformation (and seismic shaking) hazard to the 3+ million people of Orange County, California.*

***Key words**: Tectonic geomorphology, Seismic hazards, Indenter tectonics*

INTRODUCTION

Rising 1700 m, the Santa Ana Mountains (SAM) form the northwesternmost tip of the Baja California peninsula (Fig. 1), a piece of the Pacific plate that is moving north at about 50 mm/yr relative to the North American plate. On land, this plate boundary is defined by the 20-30 mm/yr right-lateral San Andreas fault (SAF) and multiple secondary faults to the west of the SAF; notably the San Jacinto (12-18 mm/yr) and Elsinore (5-6 mm/yr) faults. These faults also accommodate some of the plate motion as the Baja indenter fractures in its oblique collision against North America (Fig. 1 & 2).

Figure 1: High-elevation (~2500 km) DEM image of the Baja California, Mexico peninsula as an indenter colliding at ~50 mm/yr with Southern California; Los Angeles (LA), San Andreas fault (SAF) and Santa Ana Mountains (SAM). Inset red box approximates the area of Fig. 2. Note the northern head of the indenter is obliquely splintering against the California Transverse Ranges, while also creating them.

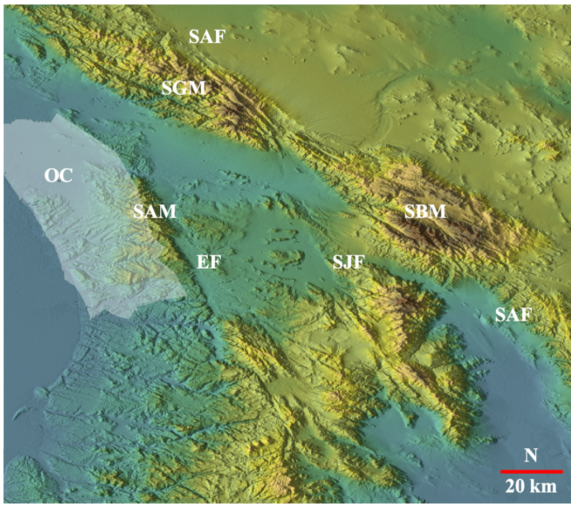

Figure 2: Expanded and oblique portion of Fig. 1 showing the location of Orange County (OC – shaded area in left-central portion of figure) and key regional structural features. Elsinore fault (EF), San Andreas fault (SAF), San Bernardino Mountains (SBM), San Gabriel Mountains (SGM), San Jacinto fault (SJF), and Santa Ana Mountains (SAM).

Orange County (OC) lies immediately south of Los Angeles (LA) in Southern California and is home to over 3 million residents (Fig. 2). The dominant geomorphic feature of OC is the Santa Ana Mountains (SAM), which form the OC's eastern boundary, while the coastline of the Pacific Ocean, including a series of elevated marine terraces, forms its western margin (Grant et al. 1999). The OC's northern boundary is approximately defined by the Whittier fault as it cuts northwesterly across the foothills of the Puente Hills for 40 km (Fig. 3), right-laterally deforming all of the fault-crossing drainages at a rate of 2-3 mm/yr (Gath, et al., 1992). Tectonic geomorphic mapping of the deflected drainages reveals that the smallest recognized deflection is 4 m (Gath, 1997); this may reflect displacement during the most recent event, and implies a significant M7 event.

The Santa Ana Mountains rise to a height of 1734 m at Santiago Peak, and tower over the majority of central and northern OC, which is a 15- to 60-m-elevation delta created by the Santa Ana River (Fig. 3). Southern OC is more geologically complex, as evidenced by the actively uplifting San Joaquin Hills, the anticlinally folded and northward-vergent Loma Ridge, and the relatively shallow Irvine Basin filled by <300 ka Trabuco Creek sediments (Grant et al., 1999).

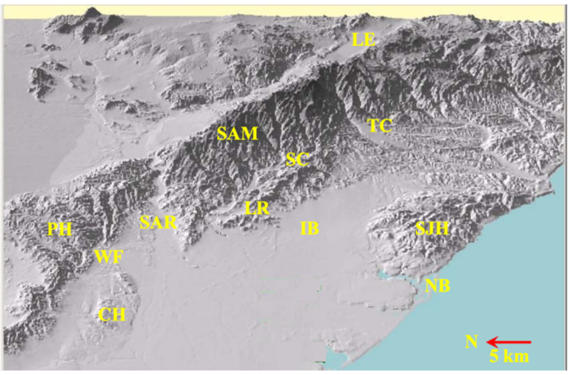

Figure 3: Index map to Orange County; Coyote Hills CH), Irvine Basin (IB), Lake Elsinore (LE), Loma Ridge (LR), Newport Beach (NB), Puente Hills (PH), San Joaquin Hills (SJH), Santa Ana Mountains (SAM), Santa Ana River (SAR), Santiago Canyon (SC), Trabuco Canyon (TC), and Whittier fault (WF).

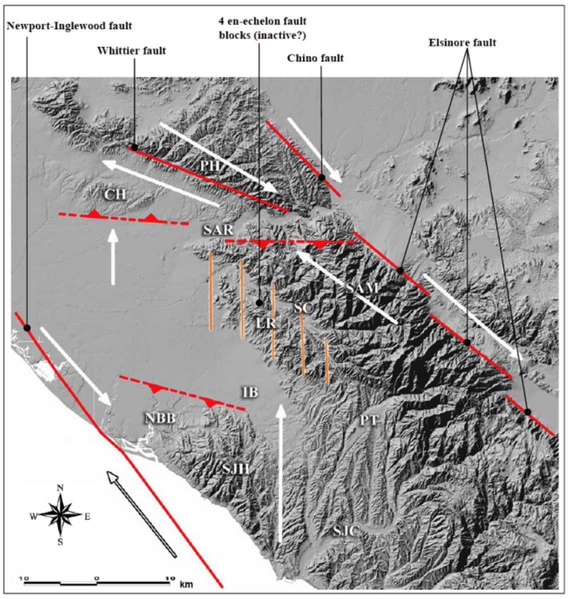

Figure 4: Structural geologic features of Orange County.

The Santa Ana block is being thrust northward at about 6 mm/yr by the right-lateral Elsinore fault along its eastern flank (Fig. 4). The Puente Hills are uplifting at 0.7±0.1 mm/yr, verging southward at 1.4±0.2 mm/yr on the blind, north-dipping Puente Hills thrust (Grant et al., 2006), and are being expressed geomorphically by the Coyote Hills (Fig. 4). Loma Ridge, a north-vergent ridgeline west of the SAM, is segmented by a series of N-S faults that are old Miocene extensional normal faults that have been reactivated by the indenter's penetration of the basin. This reactivation is expressed geomorphically by en échelon 3200-m-long right-lateral northward deflections of Santiago Creek. Santiago Creek itself is pinned between the Santa Ana Mountains and Loma Ridge, forcing a >20 km northwestward diversion around the northern tip of Loma Ridge, and then southward to the Pacific Ocean via Newport Back Bay (Fig. 4). About 4-6 ka, Santiago Creek was captured by the Santa Ana River, reducing its tectonically stretched journey by more than 20 km (see SCD on Fig. 6).

AN INDENTER MODEL FOR ORANGE COUNTY

In 1982, Tapponnier (et al., 1982) published the illustration of a hydraulic piston physically pushing into a clay cake model to simulate the tectonic development of Indochina, with India as the piston (indenter). Fig. 5 flips their model horizontally and labels the geomorphic features of Orange County that mimic the Indochina results, applying the Santa Ana Mountains as the indenter. The similarity is striking (Fig. 6).

Figure 5: Hydraulic piston experiment (mirror-image of Tapponnier et al., 1982) through a layered medium which perfectly replicates the conditions in the southern LA Basin of Orange County. Anaheim Hills (AH), Peralta Hills (PH), others as per prior figures.

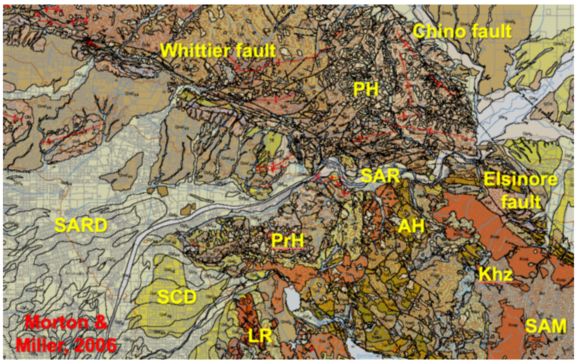

Figure 6: Geologic map of the Orange County indenter collision zone (from Morton and Miller, 2006) between the south-vergent Puente Hills (PH) to the north and the north-vergent Santa Ana Mtns (SAM) to the south. The Anaheim Hills (AH) are a northerly tilted Late Cretaceous through Miocene sedimentary sequence thrust onto the nose of the SAM indenter. The Santa Ana River (SAR) is antecedent between the two converging blocks, displaced 4-5 km from its easterly channel on the east side, and forming a delta (SARD) on the west side of the collision. Loma Ridge (LR), Cretaceous Holtz Shale (Khz), Peralta Hills (PrH), Santiago Creek delta (SCD).

The geologic map of this collision zone (Fig. 6) closely reflects the hydraulic piston model of Fig. 5. The point of collision in the Santa Ana River canyon exhibits hundreds of faults as the crust is being shattered by the impact and thrust over the northern nose of the SAM. The Whittier fault serves as the right-lateral accommodation zone whereby the OC Basin sediments are extruded westward by the oblique collision with the Puente Hills. The collision and uplift have periodically caused the Santa Ana River to pond against the eastern flank of the Puente Hills (Fig. 6).

STRUCTURAL GEOLOGY, TECTONIC GEOMORPHOLOGY AND SEISMICITY

The Elsinore fault is estimated to have initiated about 3.2 Ma (Hull and Nicholson, 1992). Using its ~6 mm/yr slip rate, the Santa Ana Mtns would have been about 20 km south of their current location at the initiation of the fault (Fig. 7). Today, the NE tip of the SAM block is in collisional contact with the SE corner of the Puente Hills block, with a >6-km-thick sequence of Cretaceous through Pliocene sediments thrust over the nose of the SAM forming the Anaheim Hills, thrust aside as the Loma Ridge, or buckled in front as the Peralta Hills (Fig. 6).

The western side of the SAM block provides the structural and geomorphic evidence that the SAM are an indenter into the basin as per Fig. 5, and not just two colliding terranes. As shown on Fig. 7, the Cretaceous Holtz Shale unit has been exploited as a weak link, and has been dragged 18 km northward by the SAM, forming a lateral shear zone that accommodates the indenter movement through the stratigraphic section. and imbricate thrusts that accommodate the basin's compression. 18 km of penetration over 3.2 Ma yields a 6 mm/yr rate, identical to the Elsinore fault's slip rate. Fig. 7 shows a similar 18-km penetration of the Eocene Sespe Formation (McCulloh & Beyer, 2004) and the Miocene Monterey Formation.

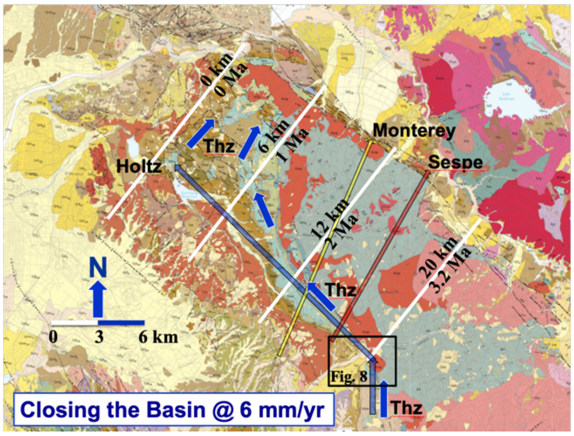

Figure 7: Time slices for the 6 mm/yr northwestward movement of the SAM into the southern LA Basin. The northern tip of the SAM terrane is now colliding with the SE corner of the Puente Hills [need to add labels] at the Santa Ana River. Insertion of the indenter is driven by the Elsinore fault on the eastern side, but facilitated by the weak Holtz Shale on the western side, as illustrated by the dark blue arrows and light blue units on the geologic map. On the northern nose of the indenter, the Cretaceous through Pliocene sedimentary units are stacked as imbricate thrust sheets exploiting the weak Holtz shale, repeated at least three times. Additional stratigraphic correlations across the indenter are the Sespe Formation (brown arrow and unit) and the Monterey Formation (yellow arrow and unit), both of which also show ~18 km of indenter penetration.

That the SAM are acting as a hydraulic piston through the southern basin is further supported by the geomorphology of the two principal rivers that have cut across the Holtz shear zone on the west side of the SAM. If the hypothesis is correct, both of these canyons should show left-lateral deflections where they cross the Holtz Shale, and both do. Silverado Creek is left-deflected ~300 m and exposes intensely sheared and fractured Holtz Shale within the canyon wall at the deflection.

A geomorphic analysis of Trabuco Creek shows a suite of three fluvial terraces progressively offset left-laterally up to 900 m from their feeder channel at the range front (Fig. 8). Age control is provided by a pedogenic profile on the lower terrace that is estimated at about 60 ka. The ages of the two older terraces are estimated based on their vertical separation from the 60-ka terrace assuming a constant uplift rate. It is possible that the ~60-ka terrace is actually 120 ka, which would reduce the uplift rate by 50%, but it would not eliminate the presence of a previously unrecognized late Quaternary to potentially Holocene fault zone across the western margin of the SAM.

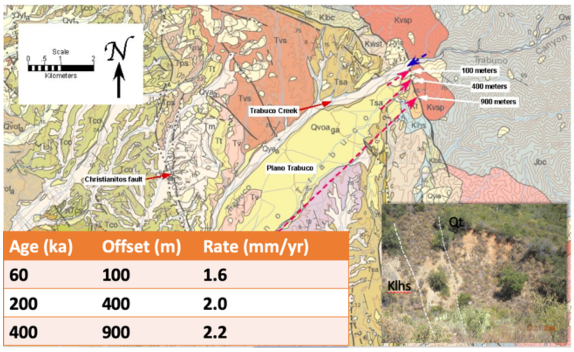

Age (ka)	Offset (m)	Rate (mm/yr)
60	100	1.6
200	400	2.0
400	900	2.2

Figure 8: Geologic map of the Trabuco Creek area illustrating the left-lateral displacement of the creek and its elevated terraces. The inset photo shows the area of the map on the south side of the creek where the lowest terrace is in fault contact against the Holtz Shale (Klhs) shear zone. An estimated 60-ka soil development age of the lowest terrace, and estimated ages of the higher terraces based on topographic position, yields a left-lateral average slip rate of 1.9±0.3 mm/yr.

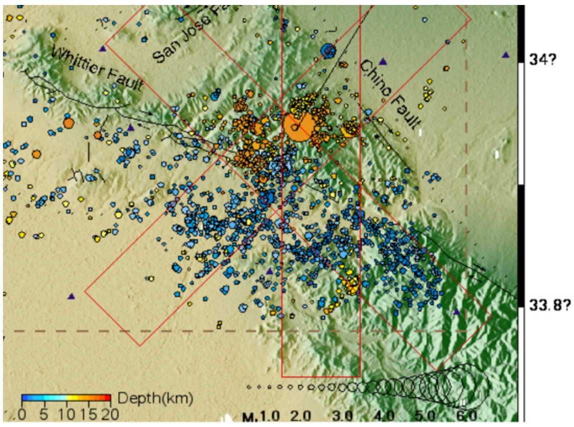

Figure 9: Seismicity map of the southern LA Basin where the SAM and the Puente Hills (PH) are colliding. The large orange circle in the middle of the PH is a M5.4 event in 2008.

The geologic map of the collision zone ((Fig. 6), shows that the rock is intensely faulted and fractured. If still active, the collision zone should show significant microseismicity, and it does. Fig. 9 presents a depth and magnitude summary of 80 years of seismicity within the collision zone, including a M5.4 in 2008 along what is likely a left-lateral transpressive structure related to the northern end of the Chino fault (Fig. 9). Almost all of the seismicity in the collisional zone is within the upper 5 km, corresponding to the overthrust and deformed sedimentary section in front of the SAM indenter (Figs 9 & 10).

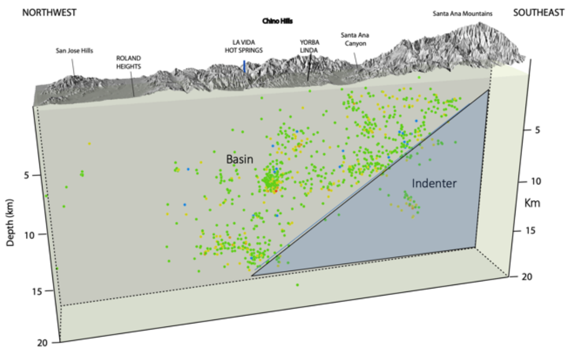

Figure 10: Depth profile of the seismicity in the NW-SE red rectangle of Fig. 9, with the proposed SAM indenter shown in light blue. Note that the shallowest seismicity occurs on the shallowest hanging wall of the indenter. As the indenter pushes farther into the Basin, the seismicity deepens.

As this seismicity is within only a few kilometers of the ground surface in the area south of the Santa Ana River (Fig. 10), it is of concern that surface deformation may pose a hazard to the built environment of this part of OC, especially in response to a large magnitude event on the Elsinore fault driving the indenter farther into the Basin. Fig. 6 already shows hundreds of faults and folds in the rocks south of, and immediately north of the Santa Ana River, the shallow parts of Fig. 10 where the seismicity is the shallowest. Are there exposures of relatively recent (late Holocene) surface deformation? There are, as shown in (Fig. 11).

Figure 11: Photo mosaic of probable Holocene fault deformation within the SAM collision zone of Fig. 6. Clockwise from upper left: A. Colluvium offset against bedrock, with at least two 1-meter events interpretable; B. bedrock fault flowering to the current ground surface; C. bedrock fault entraining colluvium and channel cobbles; D. construction exposure of the Peralta Hills fault thrusting bedrock over late Quaternary terrace deposits of Santiago Creek to the left.

CONCLUSIONS

The SAM are acting as an indenter into the southern Los Angeles Basin. Starting 20 km to the south about 3.2 Ma, the indenter is moving north at ~6 mm/yr by the Elsinore fault on its eastern side. Because of weak coupling on the western side, a 1-2 mm/yr, left-lateral shear zone has developed within the Holtz Shale. The SAM indenter has penetrated Cretaceous, Eocene, and Miocene sedimentary units by 18 km (which confirms the 6 mm/yr rate), while thrusting the entire Cretaceous through Pliocene section onto the nose of the indenter (Anaheim Hills) via a series of imbricate thrust faults developed within the Holtz. The indenter has generated folding of the sedimentary units on the west side (Loma Ridge) and in front of the indenter (Peralta Hills), and the folding in turn has deformed and offset Santiago Creek, pushing it 20 km northward, until finally captured into the Santa Ana River about 4-7 ka.

<u>The implications of this tectonic model are:</u>

- An active left-lateral shear zone along the western side of the Santa Ana Mountains
- An active set of imbricate thrusts at the nose of the Santa Ana Mountains
- Active folding and lateral shearing within the Loma Ridge foothills
- Active folding and thrusting within the eastern Puente Hills
- Left-lateral faulting in the northern part of the Chino Hills
- Disseminated seismicity of uncertain magnitude
- Literally hundreds of surface-deforming faults, folds, and bedding plane shears with uncertain spatial locations, displacement magnitudes or recurrence
- Thousands of homes and millions of residents are potentially affected.

Acknowledgements: The research and ideas of this paper have originated over several decades, including an MS and two PhD attempts. Partial support for this work originated via USGS grants No. 1434-95-G-2525 (1994) with Tom Rockwell of San Diego State, No. 1434-95-G-2525 (1994), No. 01HQGR0117 (2001), and No. 03HQGR0062 (2003), the latter two with Lisa Grant of Univ. Calif. Irvine. The ideas have benefited by decades of discussion with Robert Yeats, Tania González, Tom Rockwell, Lisa Grant, Chris Madugo, and everyone else who has been with me to see the geology of this fascinating area.

REFERENCES

Gath, E.M., T. González, and T.K. Rockwell, 1992, Evaluation of the late Quaternary rate of slip, Whittier fault, southern California; USGS Final Technical Report, NEHRP Contract No. 14-08-0001-G1696, 24 p., numerous plates.

Gath, E.M., 1997, Tectonic geomorphology of the eastern Los Angeles Basin; USGS Final Technical Report, NEHRP Contract No. 1434-95-G-2526, 13 p., 1 plate, 6 figures, 6 tables.

Grant, L.B., K.J. Mueller, E.M. Gath, H. Cheng, R.L. Edwards, R. Munro, and G.L. Kennedy, 1999, Late Quaternary uplift and earthquake potential of the San Joaquin Hills, southern Los Angeles basin, California; Geology, v.27, p. 1031-1034.

Grant, L.B., E.M. Gath, L.A. Owen, E.E. Runnerstrom, 2006, Active deformation and earthquake potential of the southern Los Angeles Basin, Orange County, California, <u>in</u> Bonsangue, J. and R. Lemmer (eds), *Geology of the Orange County Region, Southern California;* South Coast Geol. Soc., Field Trip Guidebook No. 33, p. 101-134.

Hull, A.G. and C. Nicholson, (1992). Seismotectonics of the northern Elsinore fault zone, southern California, Bulletin of the Seismological Society of America, 82, (2), 800-818.

McCulloh, T.H. and L.A. Beyer, 2004, Mid-Tertiary Isopach and Lithofacies Maps for the Los Angeles Region, California: Templates for Palinspastic Reconstruction to 17.4 Ma; USGS Professional Paper 1690, 32 p.

Morton, D.M., and F.K. Miller, 2006, Geologic map of the San Bernardino and Santa Ana 30' x 60' quadrangles, California; USGS Open-File Report OF-2006-1217, 1:100,000 scale.

Tapponnier P, G.L. Peltzer, A.Y. Le Dain, R. Armijo, and P. Cobbold, 1982, Propagating extrusion tectonics in Asia: New insights from simple experiments with plasticine, Geology, v 10, n 12, p. 611-616.

Upliftment History along Eastern Himalayan Syntaxis Zone in Neogene and Quaternary Time: Formation of Manabhum Anticline.

Chandreyee Goswami Chakrabarti (1,2), Erhan Guluyuz(1), Belligraham Narzary(3) , Manoj Jaiswal(3), Fatih Karaoglan(4)

(1) Ustav Struktury a Mechaniky Hornin, Czech Republic
(2) University of Calcutta, India
(3) Indian Institute of Science Education and Research Kolkata, India
(4) Institute of Geology of the Czech Academy of Sciences, Czech Republic

Abstract: *Eastern Himalayan Syntaxis (EHS) is bounded by India-Eurasia and India-Burmese collision systems in the north and the southeast, respectively. The main active structure responsible for the upward movement of the metasedimentary as well as granitic rocks in the easternmost part of the EHS is the NW-SE trending Mishmi Thrust (MT). The spectacular anticlinal, Manabhum Hill, has also formed during Quaternary as a ramp anticline over a splay of Mishmi Thrust in the foreland region. Our work aims to understand Neogene to the recent uplift/exhumation rate of basement rocks along the Mishmi thrust which is hitherto unknown from this part of the Himalayas. We used low-temperature thermo-chronology (LTT) and OSL dating techniques for the Neogene to early Quaternary and late Quaternary time intervals, respectively. The Neogene uplift rate varies between 0.91 to 2.3mm/yr whereas the early Quaternary uplift rate is ~3mm/yr.*

Key words: Collisional Tectonics, EHS, Uplift Rate, Thermochronology.

Introduction:

Understanding collisional tectonics involves both the spatial and vertical movement of crust over time. The Eastern Himalayan Syntaxis (EHS) represents a classical example of the junction of two collisional plate boundaries although data regarding both the spatial and vertical movements are scanty than its western counterpart (Zeitleret al. 2001). This area deserves more attention from earth scientists as it represents one of the most tectonically active areas in South East Asia. The EHS can be defined as the juncture between the E-W-trending Himalayas and the NNE-SSW-trending Indo Burma Mobile Belt (IBMB) or Naga Schuppen belt(Yin, 2006) (Fig.1).

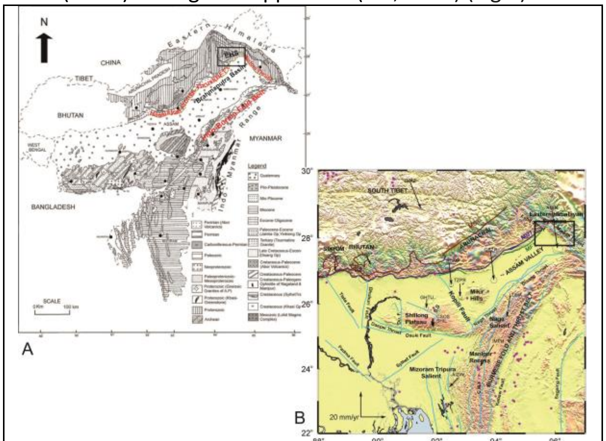

Fig. 1 A. Regional Geological Map of Eastern Himalayas and the Study area (After GSI report, 1998). B. Fault lines, major earthquake sites >5 with pink circles and velocity directions after Jade et al. 2017. The black rectangles represent the proposed areas of study

Part of the Indian plate, east of the Meghalaya plateau, is characterized by the vast Brahmaputra valley, which is constricted by two major fold-thrust belts along its northern and eastern boundary. This area has witnessed several major historical and recent earthquakes including three earthquakes greater than M_W7 and more than ten earthquakes greater than M_W 6 during the last hundred years. Epicentres of these earthquakes occur both on Himalayan thrusts and transverse faults like Kopili and Mishmi (Dasgupta et al., 2021 and references therein).

It is inferred from the GPS data that the Brahmaputra valley is separated from the rest of the Indian plate along the Kopili fault and rotates clockwise, distressing the Indian plate (Kayal et al., 2010, Vernant et al., 2014). Shillong Plateau and Brahmaputra valley blocks move southward with ~7mm/year (Jade et al., 2017). The EHS acts as a rigid block and with respect to Eurasia, it is moving ~24mm/yr northeasterly (Gupta et al., 2015). The strain rate reaches its maximum in the Eastern Himalayan sector within the EHS(Fig. 1).

The EHS is expressed as a large antiform with a core of high-grade metamorphic rocks and consists of three broad zones; a. Namche Barwa antiform, b., Siang antiform and c. Mishmi Hills. The Mishmi Hill is the easternmost part of the Arunachal Himalaya with a controversial status about its formation. According to some researchers, the Mishmi Block is a continuation of the western Arunachal Himalaya (Gansser, 1964; Thakur and Jain, 1974; Misra, 2013) while others interpret it to be a part of the Mogok Metamorphic Belt (MMB) which is a part of Indo Burma Mobile Belt (IBMB) (Gururajan and Choudhuri, 2003; Sharma et al., 2011) which extends for over 1500 km along the western margin of the Shan-Thai block, from the Andaman Sea to north of the EHS (Searle et al., 2007). Happroff et al. 2018 suggest a westward younging deformation consistent with the development of an accretionary fold-thrust belt across the northern Indo-Burma Ranges, as observed along the Himalayan arc. They have shown that the dominant structures across a ~100-km wide deformation zone are southwest-directed thrusts that have accommodated > 10's km of crustal shortening during the Cenozoic.

Along with the GPS data calculating the strain rate, large earthquakes can also be evidenced by steep fault scarps cutting across fluvial deposits and uplifting the terraces along both the Himalayan and Mishmi hills mountain fronts. A minimum of 200km long surface rupture on both the Mishmi Thrust (MT) and Himalayan Frontal Thrust (HFT) has been estimated (Coudurier-Curveur et al., 2019). The northeastern part of EHS is dominated by southwest to west directed thrust faults that accommodated >280 km (~86%) of horizontal shortening since the Cenozoic India-Asia collision.

Faults in the EHS are required to accommodate ~30% of the ~28 mm/yr convergence rate between the Shillong Plateau and Indo Burmese Arc (IBA) (Jade et al. 2017 and references therein). GPS measurements of the Mishmi block reveal slow motion (2.26 mm/yr with an azimuth of 45.88°N) relative to the Eastern Tibetan Block (6 - 11 mm/yr), China (14 - 20 mm/yr) and Burmese Arc (19 mm/yr). Although the present spatial data regarding the movement of Indian plate in this area is available though scanty the information about the vertical movement is really negligible.

Apatite fission track (AFT), zircon (U-Th)/He (ZHe) and 40Ar/39Ar multi-thermochronometric ages across the Dibang valley in the Mishmi hills towards the core of the EHS suggests late Oligocene exhumation (Salvi et al. 2019).

The present study area comprises the southwest part of the Mishmi hills along with its Quaternary-Holocene foreland within the Upper Assam Basin within the Lohit and Dihing basin (Fig. 1). Our work focuses on upliftment history along the Mishmi thrust during Neogene and Quaternary time and how it is responsible for the formation of present-day landform. The landform in the study area includes the impressive antiformal Manabhum Hill that rises out of a generally flat, broad alluvial plain. The geomorphological, geological studies through field work and satellite image analysis along with both OSL dates and U-Th low-temperature thermochronology have been used to understand the Neogene-Quaternary tectonics in this area.

Discussion

Our study area can be divided into two parts; a. the foreland area within the upper Assam basin in Dihing and Lohit valley and b. the deformed metamorphic terrain within the Mishmi hills in its south-eastern extremity.

Two prominent structural trends dominate the immediate surroundings of the study area: the NE-SW trend of the Naga-Patkoi range and the NW-SE trend of the Mishmi hills (Fig. 2). Manabhum hill occurs within the generally undeformed Quaternary alluvial fill of the Dihing valley in the foothills of the Mishmi Hills. we have focused on its formation and evolution in the present study.

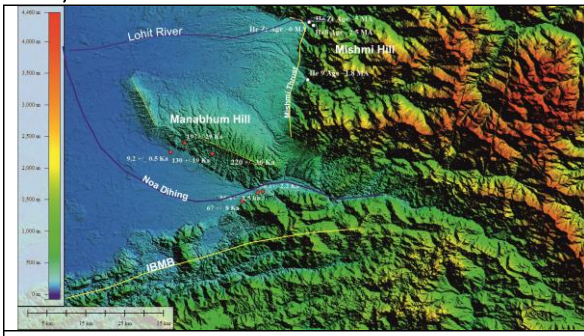

Fig. 2. Area of study on the Cartosat DEM with sample locations and dates.

Manabhum Hill and its surroundings can be divided into three major geomorphic units: i) Manabhum Hill, and ii) river terraces along the Noa Dihing and its tributary river banks. d Manabhum Hill is separated from the Mishmi hills by an NW-SE trending river valley. The thrust contacts between the Mishmi crystallines and Quaternary sediments can be seen along this valley. The main river in this area is Noa Dihing, which originates from the southeast within Naga- Schuppen belt. It first flows north, then takes a westerly bend and cuts the southern end of Manabhum Hill. Then again it takes a sharp NNW'sterly bend and flows along the foothill and western flank of the Manabhum Hill. A well-developed terrace system is present along the Noa Dihing River both its E-W and NW-SE tracts. We have studied this area in detail from satellite images and DEM analysis with extensive fieldwork and generated a detailed geological geomorphological map. We have interpreted that this anticline is a manifestation of a ramp anticline over the splay of Mishmi thrust (Goswami Chakrabarti et al. 2022)(Fig. 3a).

We have sampled for dating the Quaternary sediments from Manabhum Hill and the terraces in its foothill along the Noa Dihing River for OSL dating and crystallines from Mishmi Hills along Lohit River valley. The sediments towards the core of the Manabhum anticline are more compact and deformed into a close-folded structure. We have taken systematic samples from the terraces as well as from the core of the antiform to date by the OSL method(Fig. 3b).

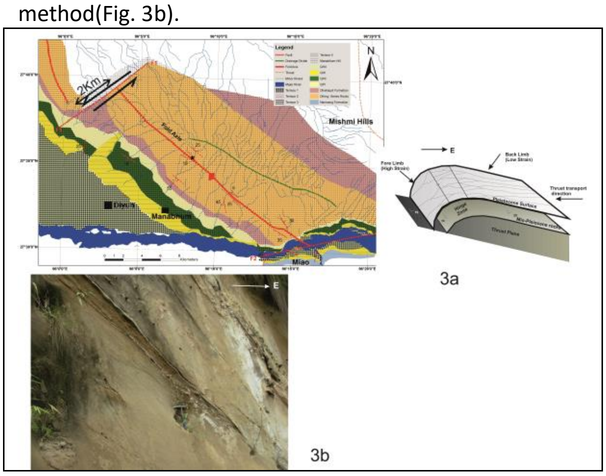

Fig. 3a Geological and geomorphological map along with interpretative modelo f formation of Manabhum anticline after Goswami et al. 2022. 3b. The oldest sediment at the core of the anticline.

The oldest date from the core of the antiform is dated ~0.22Ma from the feldspars by the IRSL method. This sample is from the Dihing formation of Late Pleistocene time. The elevation difference of these rocks from the present-day flood plane is ~175m. So the uplift rate during the Quaternary time in this area is ~3.2mm/year which is quite significant. The geomorphology of the area also supports this high uplift in terms of the formation of high terraces along the rivers.

The Quaternary sediments show direct thrust contacts with the metasedimentary rocks along its northeastern boundary. We sampled the metasedimentary rocks from low-grade slate and mica schists to high-grade garnetiferous mica schists along the Lohit River valley in the hanging wall side of the Mishmi thrust(Fig. 4).

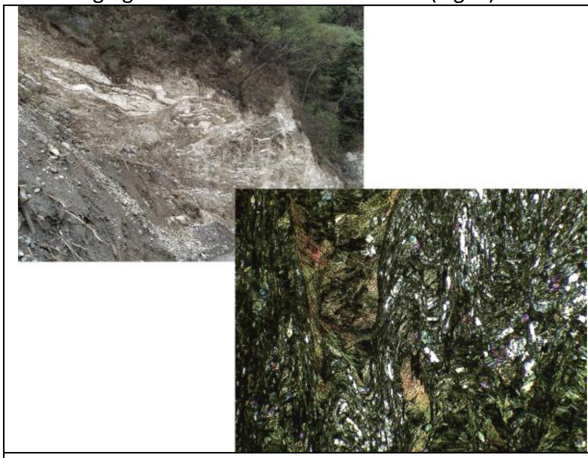

Fig. 4 Folded amphibolite gneiss from the Mishmi Hills. Field ocuurrance and its microphotograph shows folding with small zircón grains.

We have separated the zircon and apatite grains from these rocks and dated them in U-Th/He low-temperature thermochronology method. The full-vector LTT ages from a single point of the hanging wall of the thrust are represented by 4.83_0.68 Ma (Zircon Helium { ~200_C), 1.85_0.27 Ma (Apatite Fission Track- ~110_C) and 1.34_0.5 Ma (Apatite Helium- ~70_C) ages. Based on a 33_C/km geothermal gradient, the average uplift rate of the hanging block varies between 0.91 to 2.33mm/year for about the last 5 Ma. So the uplift rate in this area has increased during the Quaternary time making this area highly vulnerable to big earthquakes in recent times.

Acknowledgements:

The present study is part of the Women Scientists Project (WOS-A) granted to CGC by the Department of Science and Technology, Government of India (Grant No. SR/WOSA/EA-13/2018) and institutional project of Institute of Rock Structure and Mechanics, Czech Academy of Sciences, Prague. CGC thanks the Head of the Department of Geology, University of Calcutta and Director of IRSM, Prague for providing infrastructural support. Belligraham thanks the HOD, Department of Earth Science, IISER, Kolkata for infrastructural support.

References:

Coudurier Curveur, A., Okal, E., Tapponnier, P., Kali, E., van der Woerd, J., Choudhury, S., Baruah, S., Etchebes, M., & Karakaş, Ç., 2019. Source process of the Mw= 8.7, 1950 Assam earthquake, Eastern Himalayas, inferred from field observations and relocated aftershocks. In EGU General Assembly Conference Abstracts (p. 8843).

Dasgupta, S., Mukhopadhyay, B., Mukhopadhyay, M., & Pande, P., 2021. Geo-and seismo-tectonics of Eastern Himalaya: Exploring earthquake source zones from foredeep to Tibetan hinterland. Physics and Chemistry of the Earth, Parts A/B/C, 103013.

Gansser, A., 1964. Geology of the Himalayas. New York. Wiley Interscience, 289p.

Goswami Chakrabarti C., Narzary B., Weber J. C., Jana P., Bhattacharjee S., Jaiswal M., 2022: Preliminary Study of the Manabhum Anticline: A Possible Key to Better Understanding the Quaternary Tectonics of the Eastern Himalayan Syntaxial Zone. In Bhattacharya H. N., Bhattacharya S., Das B. C., Islam A. (eds.): Neotectonic Movements and Channel Evolution in the Indian Subcontinent. A Book of collection, Springer Nature

Gupta, T.D., Riguzzi, F., Dasgupta, S., Mukhopadhyay, B., Roy, S., & Sharma, S., 2015. Kinematics and strain rates of the Eastern Himalayan Syntaxis from new GPS campaigns in Northeast India. Tectonophysics, 655, 15-26.

Gururajan, N.S., Choudhuri, B.K., 2003. Geology and tectonic history of the Lohit Valley, Eastern Arunachal Pradesh, India. J. Asian Earth Sci. 21, 731–741. https://doi.org/10.1016/S1367-9120(02)00040-8.

Jade, S., Shrungeshwara, T. S., Kumar, K., Choudhury, P., Dumka, R. K., & Bhu, H., 2017. India plate angular velocity and contemporary deformation rates from continuous GPS measurements from 1996 to 2015. Scientific reports, 7(1), 1-16.

Misra, D.K., 2013. Tectono-stratigraphic framework of the Eastern Syntaxis, Arunachal Pradesh, India. Himalyan Geol. 34, 49–56.

Salvi, D., Mathew, G., Kohn, B., Pande, K., Borgohain, B., 2019. Thermochronological insights into the thermotectonic evolution of Mishmi hills across the Dibang Valley, NE Himalayan Syntaxis. *Journal of Asian Earth Sciences 190 (2020) 104158* https://doi.org/10.1016/j.jseaes.2019.104158

Searle, M.P., Noble, S.R., Cottle, 1J.M., Waters, D.J., Mitchell, A.H.G., Hlaing, T., Horstwood, M.S.A., 2007. Tectonic evolution of the Mogok metamorphic belt, Burma (Myanmar) constrained by U-Th-Pb dating of metamorphic and magmatic rocks. Tectonics 26, TC3014. https://doi.org/10.1029/2006TC002083.

Sharma, K.P., Bhattacharya, S., Nandy, S., Konwar, P., Mazumdar, N., 2011. Thrust Bound Lithounits of Western and Eastern Sectors of Arunachal Himalaya, India: An Integrated Approach of Correlation. Memoir of the Geological Society of India 77, 33–41.

Thakur, V.C., & Jain, A.K., 1974. Tectonics of the region of Eastern Himalayan syntaxis. Current Science, 43(24), 783-785.

Yin, A., 2006. Cenozoic tectonic evolution of the Himalayan orogen as constrained by along-strike variation of structural geometry, exhumation history, and foreland sedimentation. Earth-Science Reviews, 76(1-2), 1-131.

Zeitler, P.K., Meltzer, A.S., Koons, P., Craw, D., Hallent, B., Chamberlain, C.P., Kidd, W.S.F., Park, S.K., Seeber, L., Bishop, M., Shroder, J., 2001. Erosion, Himalayan geodynamics and the geomorphology of metamorphism. GSA Today 4–9.

INQUA Focus Group Terrestrial Processes Perturbed by Tectonics (TPPT)

paleoseismicity.org

Remote sensing of active tectonics in the Eastern and Southern Alps

Grützner, Christoph (1), Manuel Diercks (2), Mattis Grenier (3), Klaus Reicherter (4), Kamil Ustaszewski (1)

(1) Institute for Geosciences, Friedrich-Schiller University Jena, Jena, Germany, christoph.gruetzner@uni-jena.de
(2) School of Geography, Earth and Environmental Sciences, University of Plymouth, UK
(3) Earth Science Department, ENS Lyon, France
(4) Neotectonics and Natural Hazards Group, RWTH Aachen University, Aachen, Germany

Abstract: *About 3 mm/yr of northward motion of Adria are taken up mainly by thrusting along the South Alpine Front and by strike-slip faulting in W Slovenia. Historical and instrumental seismicity as well as geodetic data show that some deformation is also accommodated further north, but little is known about which faults are active. Here we present results from a remote sensing study that aimed at identifying areas with tectonic activity based on landscape features. We used high-resolution LiDAR digital elevation models and calculated the most used geomorphic indices that might indicate active tectonics. Drainage system analysis was also done using several common indices and we validated our findings with field work. We show that several factors complicate the application of large-scale tectonic geomorphology in the Alps: changing lithologies, variations in bedding, karst, and glacial overprint. We discuss ways to overcome some of these problems and we highlight potential pitfalls.*

Key words: *Alps, tectonic geomorphology, active faulting, geomorphic indices*

INTRODUCTION

The Eastern and Southern Alps are deforming due to the collision of the European and Adriatic plates (Fig. 1). GPS data show about 3 mm/yr of northward motion of Adria with respect to Europe at the longitude of 13.5°E (e.g., D'Agostino et al., 2008; Metois et al., 2015). This shortening is mainly taken up by thrusting along the South Alpine Front and by strike-slip faulting in W Slovenia (e.g., Burrato et al., 2008; Moulin et al., 2016; Grützner et al., 2021). Historical and instrumental seismicity as well as geodetic data show that some deformation is also accommodated further north (e.g., Grünthal et al., 2013; Stucchi et al., 2013; Petersen et al., 2021). Still, little is known about which faults are active in the interior of the Alps. The main reason for that are the low deformation rates in the range interior, which indicate that large earthquakes – if they happen – must have large recurrence intervals. Another problem is the general landscape reset during and after the glacials. Large parts of the study area were either covered by glaciers or subject to intense erosion and sedimentation during and after the glaciation.

The aim of this study was to identify those regions where active faulting affects the landscape, and where more detailed (paleoseismology) studies could be conducted. We focussed on the Eastern and Southern Alps, and we divided the study area in two regions, that roughly encompass NE Italy and NW Slovenia, respectively.

Tectonic geomorphology techniques are now widely used to investigate regional variations in tectonic activity by analysing (high-resolution) digital elevation models (DEMs) and the drainage patterns (e.g., Silva et al., 2003; Mahmoud & Gloaguen, 2011; El Hamdoumi et al., 2018; and many others). The number of such studies is rapidly increasing since essentially only a DEM and free software tools (e.g., Schwanghart & Scherler, 2014) are needed for the analysis, and according to the literature for almost all tectonic settings there are suitable methods available.

Here we used a large set of tectonic geomorphology tools to investigate the relative tectonic activity of the Eastern and Southern Alps. We report on our results, and we show the limits of these techniques despite the availability of DEMs with metre-scale resolution.

METHODS

We used high-resolution digital elevation models from aerial laser scanning campaigns downsampled to 5 m resolution to balance resolution and computing time/file handling. From these DEMs we calculated the most used geomorphic indices that might indicate active tectonics: the surface roughness (SR), the terrain ruggedness index (TRI), and the surface index (SI), which is a combination of surface roughness and hypsometric integral. Drainage system analysis was done using the normalised steepness index k_{sn}, stream knickpoints (higher than 30 m), hypsometric curves, hypsometric integrals, the basin asymmetry factor (AF), and the χ-value. The χ-value can help identifying uplifting areas when stark contrasts in the value appear on the different sides of drainage divides.

We compare our results with published geological maps, fault databases, and seismicity data. Extensive field work was done to verify the results, for example checking knickpoints in streams and lineaments in the landscape that showed up in the ruggedness maps.

RESULTS

NE Italy study area

In the NE Italy study area, higher k_{sn} values concentrate in the dolomites north of the Valbelluna and in the Italy-Slovenia border area (Fig. 2a). Commonly, higher k_{sn} values are attributed to tectonic uplift. The terrain ruggedness is also relatively increased in these regions (Fig. 2d), which might be interpreted as a signal of ongoing, localised uplift.

The χ-maps (Fig. 2c) show large contrasts across drainage divides near the South Alpine Front and in the East of the study area. This indicates differential uplift of the associated drainage basins, which in the case of the South Alpine Front is no surprise since it is known that seismic activity concentrates here (e.g., Burrato et al., 2008).

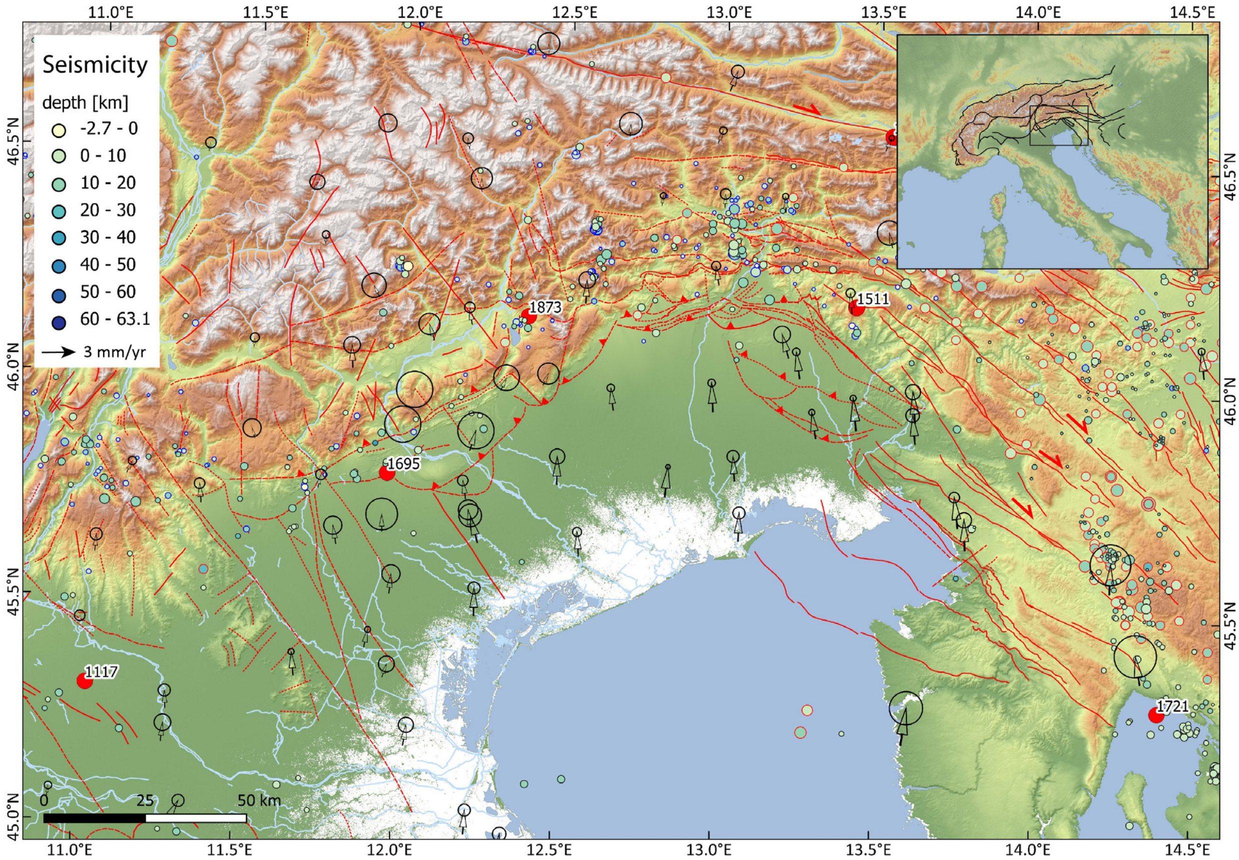

Figure 1: Overview of the study area. GPS data: Metois et al. (2015). Red circles: historical earthquakes >M6 from 1000-1900, dots with red outlines: SHEEC catalogue 1900-2006 (Stucchi et al., 2013; Grünthal et al., 2013). Dots with black outlines: AlpArray Research Seismicity-Catalogue 2016-2019 (Bagagli et al., 2022). Dots with blue outlines: relocated earthquakes detected by the SWATH D experiment between September 2017 and December 2018 (Jozi Najafabadi et al., 2021). Circles size scales between M_W0-7. Main faults in Italy are from the ITHACA database (Guerrieri et al., 2015), faults in Slovenia are from Atanackov et al. (2021).

Knickpoints in the study area are ubiquitous and do not exhibit a first order pattern in distribution or height (Fig. 2b). A more detailed inspection of knickpoints showed that they cluster along certain mountain fronts, but in this study, we were rather interested in the large-scale picture. We checked dozens of promising knickpoints in several field campaigns, but we found no clear evidence for Late Quaternary faulting in the range interior for any of them. Instead, many knickpoints result from steeply-dipping or even vertical layers. Others were found to result from lithologically controlled erodibility contrasts.

NW Slovenia study area

In the NW Slovenia study area, we were interested to see if the known active faults show up in the analyses, and if other active faults could be found that were not previously identified as such.

Surface roughness (Fig. 3) and surface index (Fig. 4) are sensitive to large-scale topographic features like the limestone plateaus and the mountainous region in the northwest. Most fault traces are hardly visible on both maps, except for the Sava fault. A notable signal in SR and SI can be observed at the Raša fault, especially on the Komen Plateau. The other faults are hardly or not at all detectable by means of these indices, or at least their signal cannot be differentiated from other lineaments in the maps that are not related to active faults, but to the general NW-SE trend of most geological units.

The large strike-slip faults hardly have sufficiently large morphological imprint for being detectable on large-scale maps of morphometric indices. The Idrija Fault can only be traced along parts of its length on SI, TRI and slope maps, due to the pronounced fault-parallel valley. The Predjama and Ravne Faults are not detectable by any of the indices. The Raša Fault leaves a noticeable signal in SR and TRI, especially in the SE, where it crosses the Komen Plateau. These faults are supposed to be the largest and by far the most active faults in the region.

While the morphometric signal of these faults is rather small, the Sava Fault with its large thrust component can clearly be identified. The Udine-Buttrio-Thrust on the Friuli Plain is detectable by SR and TRI.

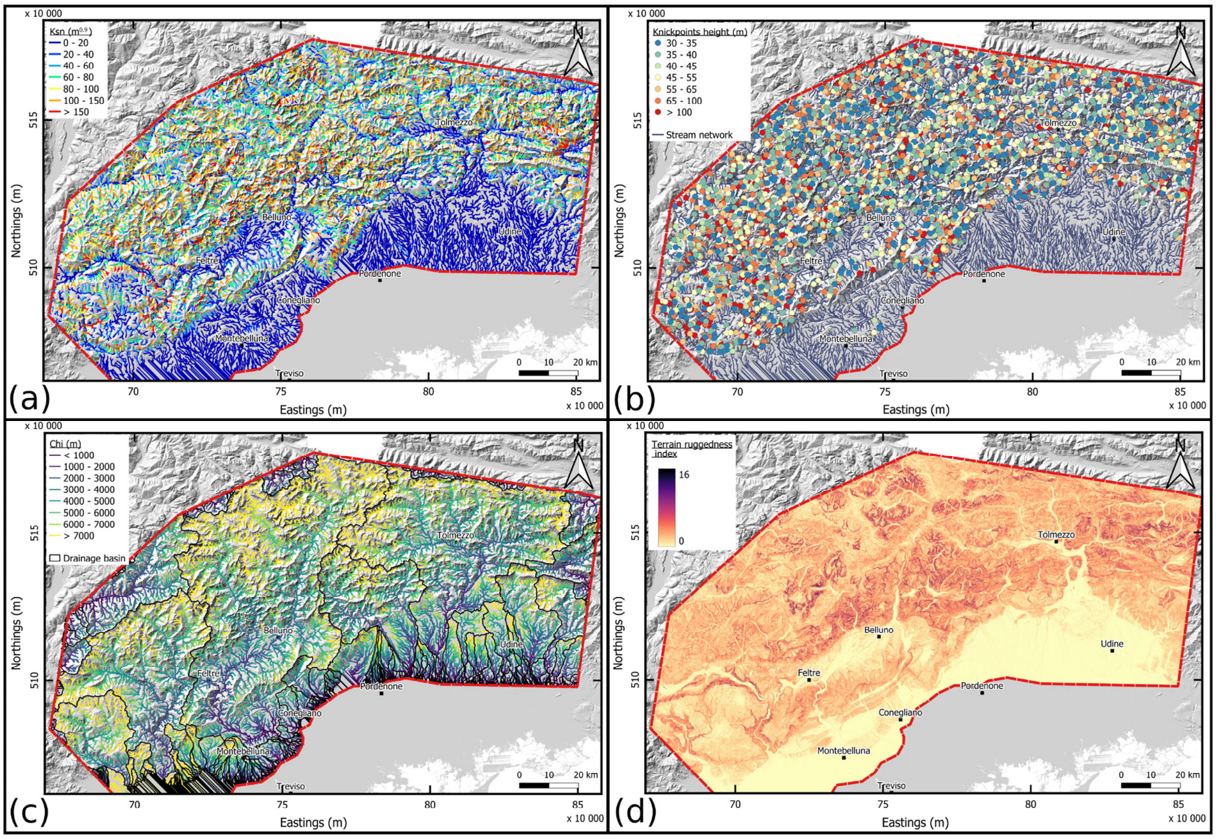

Figure 2: Geomorphic indices along the South Alpine Front, plotted onto the hillshaded 5 m DEM. (a) Map of k_{sn} values along the stream network using 0.5 km² to define stream headwaters. (b) Knickpoint position and height represented on the stream network; only knickpoints with a minimal height of 30 m are considered. (c) Map of χ-values and drainage basin limits derived from the stream network. (d) Map of the Terrain Ruggedness Index.

The basin Asymmetry Factor (AF) helps to identify catchments that are affected by tectonic tilt. Values close to 0.5 indicate symmetric (= tectonically inactive) catchments; values close to 0 and 1 point to tilt. For rivers draining towards the south or south-east (towards the Mediterranean Sea), the asymmetry factor (AF) ranges from 0.09 to 0.26 while it is 0.63 and 0.64 for the Ljubljanica and the Sava catchments, respectively (Fig. 5). If Torre and Soča and Sava and Ljubljanica are treated as single catchments, the AF gets closer to symmetry. The Reka also drains into the Mediterranean Sea, however the stream drops into a cave ~15 km south-east of Postojna, so only the portion of the network which is exposed to the surface was analysed.

DISCUSSION

Our study shows that several factors complicate the application of large-scale tectonic geomorphology in the Alps to an extent that makes it very difficult to achieve meaningful results. This is caused by several factors.

(i) In the Alps, lithologies often change over short distances. This is caused by the steep topography, which exposes hundreds and even thousands of meters of stratigraphy with varying competence. Nappe stacking during the Alpine orogeny led to a complicated outcrop pattern and the juxtaposition of different lithological units.

(ii) Strong variations in bedding dips with occasionally vertical strata lead to false positive signals.

(iii) Karst features dominate the drainage in large areas of Slovenia and inhibit the use of standard techniques that are based on landscape sculpturing by rivers.

(iv) Glacial features have overprinted the traces of known faults. Essentially, the Alpine landscape is very young due to glacial and fluvial erosion and the deposition of huge sediment volumes after the last glaciation.

We call for caution when interpreting the results of tectonic geomorphology studies without detailed ground truthing. Although some of our results could be verified in the field and fit published data, in most cases they would have been misleading when not put in the geological context.

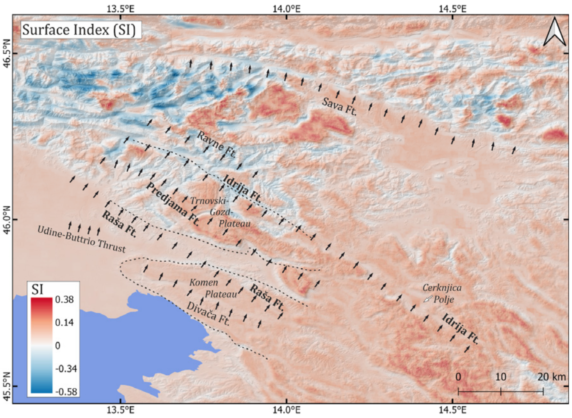

Figure 3: Surface Index (SI), draped over the hillshaded 1-arcsecond ALOS 2 DEM. Arrows indicate the mapped locations of faults (after Atanackov et al., 2021 and Burrato et al., 2008).

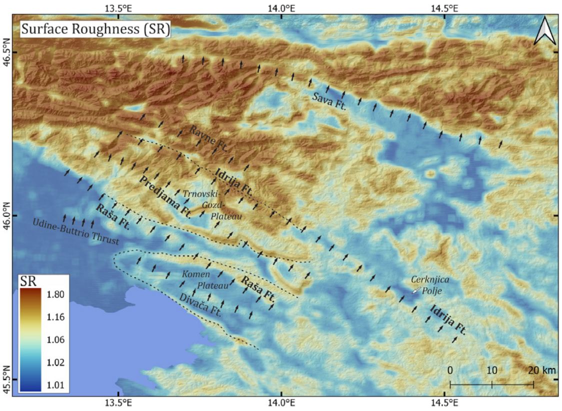

Figure 4: Terrain Ruggedness Index (TRI), draped over the hillshaded 1-arcsecond ALOS 2 DEM. Arrows indicate the mapped locations of faults (after Atanackov et al., 2021 and Burrato et al., 2008).

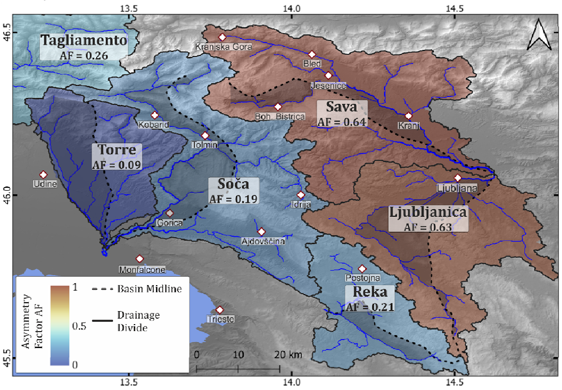

Figure 5: Drainage basins colour coded by basin asymmetry factor (AF). Dashed lines show the midlines of the catchments and grey shaded areas highlight the difference between the basin midlines and the location of the trunk stream. Small catchments on the Komen Plateau and the Friuli plain are neglected.

REFERENCES

Atanackov, J., Jamšek Rupnik, P., Jež, J., Celarc, B., Novak, M., Milanič, B., Markelj, A., Bavec, M., & Kastelic, V., 2021. Database of active faults in Slovenia: compiling a new active fault database at the junction between the Alps, the Dinarides and the Pannonian Basin tectonic domains. *Front. Earth Sci.*, 9, 151.

Bagagli, M., Molinari, I., Diehl, T., Kissling, E., Giardini, D. & the AlpArray Working Group, 2022. The AlpArray Research Seismicity-Catalogue. *Geophys. J. Int* 231, 2, 921–943.

Burrato, P., Poli, M. E., Vannoli, P., Zanferrari, A., Basili, R., & Galadini, F., 2008. Sources of Mw 5+ earthquakes in northeastern Italy and western Slovenia: an updated view based on geological and seismological evidence. *Tectonophysics*, 453(1-4), 157-176.

D'Agostino, N., Avallone, A., Cheloni, D., D'Anastasio, E., Mantenuto, S., & Selvaggi, G., 2008 Active tectonics of the Adriatic region from GPS and earthquake slip vectors. *J. Geophys. Res.-Sol. Ea*., 113, B12413.

El Hamdouni, R., Iriagaray, C., Fernández, T., Chacón, J. & Keller, E. A., 2008. Assessment of relative active tectonics, southwest border of the Sierra Nevada (southern Spain). *Geomorphology*, 96, 150-173

Grünthal, G., Wahlström, R., & Stromeyer, D., 2013 The SHARE European Earthquake Catalogue (SHEEC) for the time period 1900–2006 and its comparison to the European-Mediterranean Earthquake Catalogue (EMEC). *J Seismol.*, 17, 1339–1344.

Grützner, C., Aschenbrenner, S., Jamšek Rupnik, P., Reicherter, K., Saifelislam, N., Vičič, B., Vrabec, M., Welte, J., & Ustaszewski, K., 2021. Holocene surface-rupturing earthquakes on the Dinaric Fault System, western Slovenia. *Solid Earth*, 12, 2211–2234.

Guerrieri, L., Blumetti, A. M., Comerci, V., Manna, P. D., Michetti, A. M., Vittori, E., & Serva, L., 2015. Surface Faulting Hazard in Italy: towards a first assessment based on the ITHACA database. In: *Engineering Geology for Society and Territory*-Volume 5 (pp. 1021-1025). Springer, Cham.

Jozi Najafabadi, A., Haberland, C., Ryberg, T., Verwater, V. F., Le Breton, E., Handy, M. R., & Weber, M., 2021. Relocation of earthquakes in the southern and eastern Alps (Austria, Italy) recorded by the dense, temporary SWATH-D network using a Markov chain Monte Carlo inversion. *Solid Earth*, 12(5), 1087-1109.

Mahmood, S. A. and Gloaguen, R., 2011. Appraisal of active tectonics in Hindu Kush: Insights from DEM derived geomorphic indices and drainage analysis. *Geosci. Front.*, 3, 407–428.

Metois, M., D'Agostino, N., Avallone, A., Chamot-Rooke, N., Rabaute, A., Duni, L., Kuka, N., Koci, R., & Georgiev, I., 2015. Insights on continental collisional processes from GPS data: Dynamics of the peri-Adriatic belts. *J. Geophys. Res.-Sol. Ea.*, 120, 8701–8719.

Moulin, A., Benedetti, L., Rizza, M., Jamšek Rupnik, P., Gosar, A., Bourles, D., Keddadouche, K., Aumaître, G., Arnold, M., Guillou, V., & Ritz, J. F., 2016. The Dinaric fault system: Large-scale structure, rates of slip, and Plio-Pleistocene evolution of the transpressive northeastern boundary of the Adria microplate. *Tectonics*, 35, 2258–2292.

Petersen, G. M., Cesca, S., Heimann, S., Niemz, P., Dahm, T., Kühn, D., Kummerow, J., Plenefisch, T., and the AlpArray and AlpArray-Swath-D working groups, 2021. Regional centroid moment tensor inversion of small to moderate earthquakes in the Alps using the dense AlpArray seismic network: challenges and seismotectonic insights. *Solid Earth*, 12, 1233–1257.

Schwanghart, W., & Scherler, D., 2014. TopoToolbox 2–MATLAB-based software for topographic analysis and modelling in Earth surface sciences. *Earth Surface Dynamics*, 2(1), 1-7.

Silva, P.G.,Goy, J.L., Zazo, C. & Bardají, T., 2003. Fault-generated mountain fronts in southeast Spain: geomorphologic assessment of tectonic and seismic activity. *Geomorphology*, 50, 203-225.

Stucchi, M., Rovida, A., Capera, A. G., et al., 2013. The SHARE European earthquake catalogue (SHEEC) 1000–1899. *J. Seismol.*, 17, 523–544.

Combining ESR and ^{10}Be ages in fluvial terraces of the Santo Domingo River on the South Andean flank of Venezuela: Methodology and tectonic implications.

Guzmán, Oswaldo (1), Díaz, Marisel (2), Vassallo, Riccardo (3), Audemard, Franck (4), González, Aleida (2), Mugnier, Jean-Louis, (5) C. Campos (1)

(1) Grupo de Ciencias de la Tierra y Clima. Universidad Regional Amazónica Ikiam, Ecuador. Email: oswaldojoseguzman@gmail.com

(2) Instituto Venezolano de Investigaciones Científicas – IVIC, Centro de Física-Laboratorio de Materia Condensada, 1020-A, Altos de Pipe, Venezuela

(3) ISTerre – Université de Savoie Mont-Blanc, 73370, Bourget du Lac, France *Université de Savoie Mont Blanc, CNRS-UMR5204, Campus scientifique, Bâtiment « Pôle Montagne », 73376, Le Bourget du Lac, France*

(4) Departamento de Ciencias de la Tierra e Fundacion Venezolana de Investigaciones Sismológicas, Caracas, Venezuela

(5) CNRS - ISTerre, Université de Savoie Mont-Blanc, CNRS, F-73376 Le Bourget du Lac, France. *Centre national de la recherche scientifique - CNRS (France)*

Abstract: *In this study we discuss the first ESR dating of river terraces located in the middle and lower reaches of the Santo Domingo River (Southeastern flank of the Mérida Andes, Western Venezuela). ESR ages were compared and combined with previously performed ^{10}Be ages and integrated with sedimentologic and geomorphic observations allowed the restoration of the temporal evolution of incision rate, which was analyzed in terms of tectonic, climatic and geomorphic processes. Our results show that in materials deposited under stable conditions involving long-term sediment transport processes, the ESR and 10 Be ages tend to be similar. While in rapidly deposited materials, the ESR ages tend to be overestimated, highlighting the importance of selecting the appropriate material for each type of dating. On the other hand, the ages that converge allow us to estimate that the long-term incision rate in the area has been constantly around 1 mm/a over the last 70 ka. Taking into account the geological and geomorphologic setting, this value can be converted into the Late Pleistocene uplift rate of the Southeastern flank of the Mérida Andes.*

Key words*: Electron Spin Resonance, Quaternary Dating, ^{10}Be ages, Mérida Andes, Fluvial Terraces*

Introduction

Electronic Spin Resonance (ESR), is a spectroscopic technique that allows detecting species with a non-null magnetic moment present in a sample. It is frequently used in solid physics and crystallography. Its application to geochronology was first suggested by Zeller et al. (1967), and its application was first carried out by Ikeya (1975, 1977, among others) in the dating of cave stalagmites in Japan. The temporal range for the application of ESR dating extends from several thousand to several million years (Grün, 1989; Bahain, 1993; Ikeya and Miki, 1985; Rink, 1997), and it has been successfully applied to various types of materials (e.g. volcanic sediments, stalagmites, bones, quartz) in geological, geomorphological and/or archaeological studies (e.g., Laurent et al., 1994; Li et al., 1993; Tanaka et al., 1997). These two aspects make the technique versatile, as it can be applied to a wide spectrum of materials and in a time range where other dating techniques (e.g. Radiocarbon -14C-, Terrestrial Cosmogenic Isotopes - 10Be and 26Al, Thermoluminescence –TL- and Optical Stimulated Luminescence –OSL-) may sometimes reach their temporal limits of applicability.

In this work, we intend to date three samples of Quaternary sediments of alluvial terraces located in the Central and Southeastern flank of the Mérida Andes in Venezuela (Figs. 1 and 2), The dating was performed using ESR technique applied to optically bleached quartz grains. The results are compared with Terrestrial Cosmogenic Isotope ages (^{10}Be ages, in the text) previously published for the same deposit at the same location. This independent age controls will allow the validating of the experimental and analytical procedure employed.

Geological and Geomorphological context

The Mérida Andes (MA) mountain system is situated in the Western part of Venezuela. This range is around 400 km long with an SW-NE direction from the Colombian-Venezuelan border in the Southwest to Barquisimeto city in the Northeast (Fig. 1a). The mountain building of MA is related to a complex geodynamic interaction between the Caribbean, South America and Nazca plates and other minor continental blocks (Taboada et al., 2000; Audemard and Audemard, 2002; Bermudez, 2009; Monod et al., 2010). This interaction of plates leads to the oblique convergence between the Maracaibo Triangular Block and South America Plate. It is responsible for the present MA build-up (Colletta et al., 1997; Audemard and Audemard, 2002).

The Santo Domingo River is located in the central part of the MA, and drains the Southeastern flank of the chain (Fig. 1b and c). Its catchment has a surface of 1250 km2 upstream to Barinas city. In the upper reaches, the river flows over igneous and metamorphic Paleozoic rocks (granite, gneiss and pegmatite) (Fig. 1c) (Hackley et al., 2005). In the middle and lower reaches, the river is orthogonal to the structural trend of the chain. It flows over crystalline-metamorphic Palaeozoic, calcareous Cretaceous, siliciclastic, Neogene rocks and alluvial Quaternary sediments (Fig.1c) (Hackley et al., 2005).

This work is geographically focused on the middle and lower reaches of Santo Domingo River (Fig. 1b and c, Fig. 2). Guzmán (2013) and Guzmán et al. (2013), based on

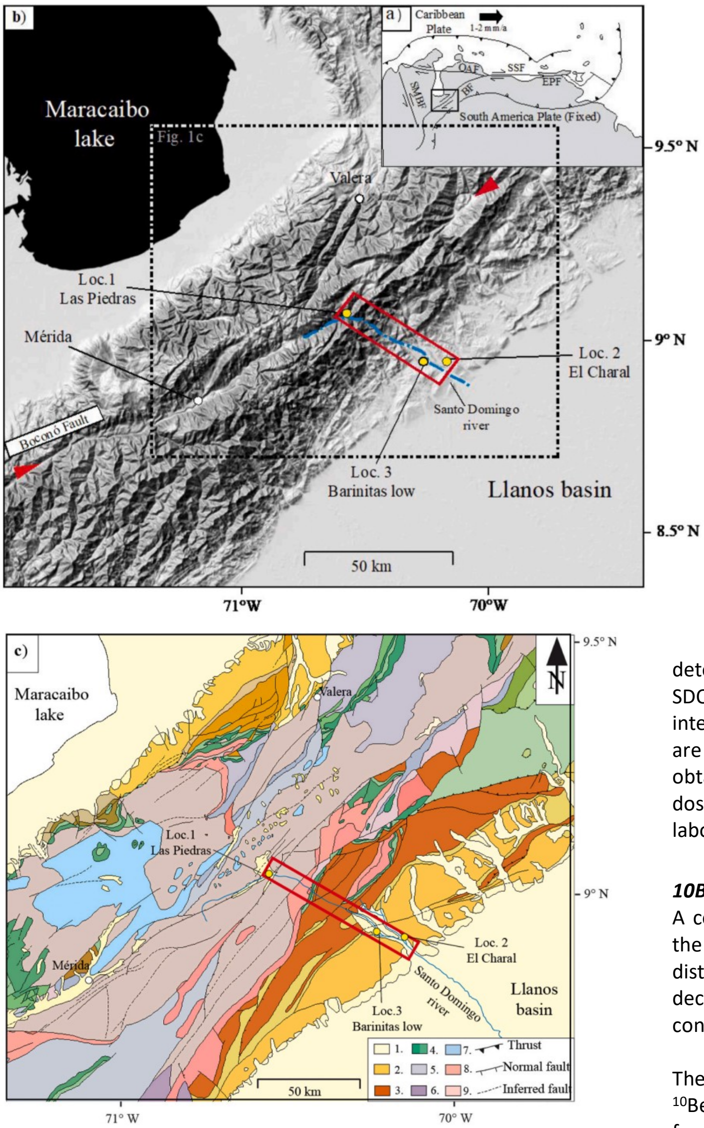

Figure. 1. Geodynamic and morphological settings of the study area. a) Main present-day active tectonics of Northern South America (from Audemard and Audemard, 2002). (SMBF) Santa Marta Bucaramanga Fault; (OAF) Oca-Ancon ´ Fault; (SSF) San Sebastian ´ Fault; (EPF) EL Pilar Fault; (BF) Boconó Fault. b) Shaded relief map of the MA based on SRTM. Location of the study area is shown by a red square. Main active trace of the Boconó Fault is located between the two red arrows. Sampled locations are indicated with a yellow circle. c) Geological map of the study area from Hackley et al. (2005). 1. Pleistocene to Holocene alluvial sediments; 2. Oligocene, Miocene and Pliocene conglomerates and sandstones; 3. Paleocene to Eocene shales and sandstones; 4. Jurassic to Cretaceous (Undifferentiated) limestones and sandstones; 5. Carboniferous to Permian phyllites and limestones; 6. Ordovician to Silurian shales and silstones; 7. Upper Paleozoic to Mesozoic intrusives rocks; 8. Upper to Lower Paleozoic intrusives rocks, phyllites, schist and gneiss; 9. Proterozoic gneiss, schist and granites.

geomorphological, sedimentological and geochronological data (exposure ages estimated from Terrestrial Cosmogenic Isotope ^{10}Be concentration propose a chronostratigraphic framework of 12 alluvial terraces formed in the last 130 ka for this part of the river. In this study, we will date sediments from the alluvial fill of three of these terraces using the ESR dating technique.

Age Determination by ESR

In the three samples analyzed, the intensity of the aluminum centers shows an increase as the radiation to which the aliquot was exposed is higher (Figs. 3 and 4). In fact, the experimental data of the samples fit theoretical dose response curves. Here it can be observed that the parameters with the greatest uncertainty are associated with the sample PLL-RPE-1. In this case, the saturation intensity (IS) is 7.1 arbitrary unit (a.u.), while the highest intensity value measured is approximately 4.5 a.u. (for 800 Gy, see Fig. 3). This causes a high error (~36%) in the determination of the TD for this sample. In the case of the SDO-RPE-02 and SDO-RPE-03 samples, the maximum intensities measured and the saturation intensity values are closer (Figs. 3 and 4), and a better adjusted TD is obtained. Finally, with the TD values estimated from the dose-response curves and the da values calculated in the laboratory; sample ages were determined.

10Be age comparison

A cosmogenic depth profile (200 cm deep) was made in the alluvial deposit of Qt12 terrace (Guzmán, 2013). The distribution of ^{10}Be concentration shows an exponential decrease with depth (Fig. 3a). A maximum ^{10}Be inherited concentration was estimated.

The good fit reached between the observed and modeled ^{10}Be data allowed us to estimate a minimum exposure age for the terrace surface of 128 ± 6 ka with a high degree of confidence. In this work, an ESR age of 230 ± 93 ka has been obtained for the sediment sampled at a depth of 84 cm from the terrace surface (Fig. 3). The difference in the estimated ages could be explained considering the fundamentals bases of each dating technique. The ages estimated by ESR represent the moment since when the sample has not had exposure to sunlight (Grün, 1989; Rink, 1997); while those of 10Be represent the moment since when the samples have been exposed to the cosmic space (Gosse and Phillips, 2001; Dunai, 2010). However estimated ages could be explained considering the fundamentals bases of each dating technique. The ages estimated by ESR represent the moment since when the sample has not had exposure to sunlight (Grün, 1989; Rink, 1997); while those of 10Be represent the moment since when the samples have been exposed to the cosmic space (Gosse and Phillips, 2001; Dunai, 2010). However, the sedimentological characteristics of the sampled deposit (chaotic deposition) suggest that at least the final

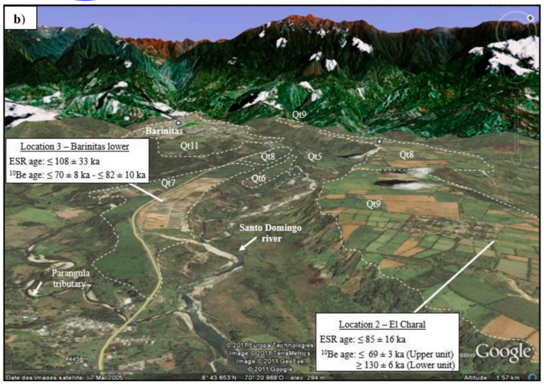

Figure. 2. Panoramic view of terraces at the Southeastern flank of the MA (lower reaches of the Santo Domingo River). The ESR ages calculated in the present study are assigned to the terraces. The ^{10}Be ages estimated by Guzmán (2013) and Guzmán et al. (2013) are also shown. The studied sites are shown by a white line.

200 cm were deposited very quickly or almost instantaneously, meaning that the sedimentation of the material dated by ESR and that of ^{10}Be occurred almost simultaneously. This rules out an explanation, along this vein, for the difference in the estimated ages.

Nonetheless, the same process of very fast chaotic deposition could be the root cause for the age difference. While this process has no impact on the ^{10}Be age, it does impact in the ESR age. Once it left its source area, the sedimentary material probably lacked the necessary sunlight exposure time to achieve optical bleaching and therefore a high % of dose not accumulated in situ is found in the Al centers of the sample. It was not possible to correct this component, because no artificial optical bleaching experiments were performed in this work. This likely caused an overestimation in the ESR age of the Qt12 terrace. Additionally, as previously mentioned, the dose-response curve adjustment parameters, for the PLL-RPE-1 sample, show a high error that propagates above the estimated TD. This sample would require the irradiation of more aliquots with higher radiation doses, which would allow for a better adjustment of the dose-response curve parameters and, therefore, a more reliable estimated TD.

Another cosmogenic depth profile (200 cm deep) was made in the alluvial deposit of Qt9 terrace (Guzmán, 2013). In this case, Guzmán (2013) modeled the distribution of ^{10}Be along the pit-soil as a simple exponential decrease with depth.

However, this distribution seems to suggest the overlapping of two main depositional sequences (Fig. 4). This is consistent with the stratigraphy observed in the pit, which shows at least 150 cm of conglomeratic material (lower sedimentary unit), 10 cm of coarse to medium grain sand (intermediate sedimentary unit) and 40 cm of silt-clay material (upper sedimentary unit). Although estimating the 10Be age is outside the scope of this study, we have modeled the distribution of ^{10}Be for two units.

Taking into consideration a probably denudation process (according to the rugosity of the terrace surface – Guzmán, 2013) and the ^{10}Be inherited concentration (0.30 ± 0.03 × 105 at/g – Guzmán, 2013), the models performed allow estimating a maximum exposure age of 69 ± 3 ka and a minimum exposure age of 130 ± 6 for the upper and lower sedimentary units of the Qt9 terrace, respectively. In this work, an ESR age of 85 ± 16 ka has been obtained for the intermediate sedimentary unit (sample located at a depth of 45 cm from the terrace surface) (Fig. 4). This age is stratigraphic and geochronologically consistent with the ^{10}Be ages obtained for the upper and lower units. In this case, the sedimentological characteristics of the Qt9 deposit show stable long-term energy conditions.

In this work, an ESR age of 85 ± 16 ka has been obtained for the intermediate sedimentary unit (sample located at a depth of 45 cm from the terrace surface) (Fig. 4). This age is stratigraphic and geochronologically consistent with the ^{10}Be ages obtained for the upper and lower units. In this case, the sedimentological characteristics of the Qt9 deposit show stable long-term energy conditions. The deposit also consists of a high percentage of materials that come from the upper part of the MA (about 20 km), a route that could have provided the time necessary to achieve a maximum optical bleaching of the Al centers. Therefore, the age estimated is close to the real one.

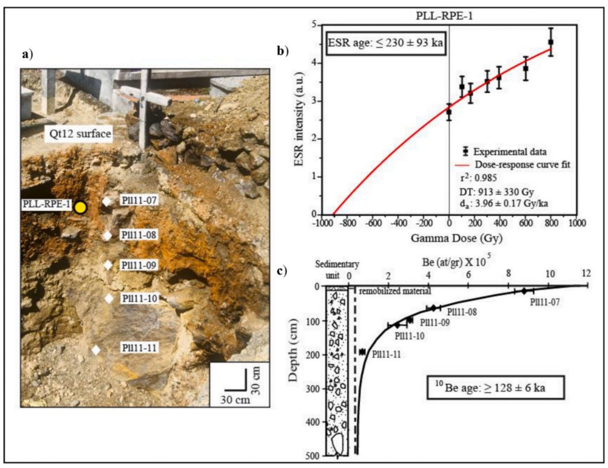

Figure 3. Pit-Soil and results obtained in location 1 - Las Piedras (Fig. 1b and c, 2a). a) Detail of the alluvial deposit of Qt12 terrace. The alluvial material consists of a deposit without sedimentary structure, very poorly sorted, and composed of very angular to rounded boulders, cobbles and pebbles, which are floating within a coarse sand matrix. The site where the PLL-RPE-1 sample was taken is marked with a yellow circle. b) Experimental results and dose-response curve obtained for the PLL-RPE-1 sample. Errors in measured ESR intensity are shown with a vertical bar. The total dose (TD) and the annual dose (da) are shown in the figure. c) Depth profile of the ^{10}Be (adapted from Guzmán, 2013). Samples are shown with white diamonds. The depth production best fit using a chi-squared inversion is in solid line. The dashed black line shows the inherited ^{10}Be concentration.

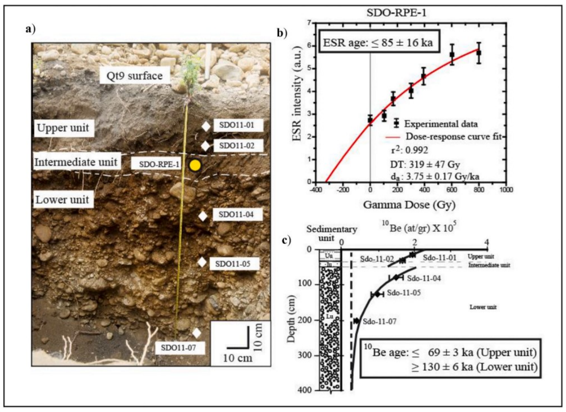

Figure 4. Pit-soil and results obtained in location 2 - El Charal (Fig. 1b and c, 2). a) Detail of the alluvial deposit of Qt9 terrace. Three main sedimentary units are observed. The site where the SDO-RPE-1 sample was taken is marked with a yellow circle. b) Experimental results and dose-response curve obtained for the SDO-RPE-1 sample. Errors in measured ESR intensity are shown with a vertical bar. The total dose (TD) and the annual dose (da) are shown in the figure. c) Depth profile of the ^{10}Be. Samples are shown with white diamonds. Distribution of ^{10}Be at depth suggests the overlapping of two main depositional sequences. This is consistent with the stratigraphy observed in the pit. Depth production best fit using chi-squared inversion is in solid line. The dashed black line shows the inherited ^{10}Be concentration for the lower sedimentary unit.

At Qt7 terraces, Guzmán et al. (2013) obtained a similar ^{10}Be concentration for five samples taken in boulders partially embedded into the alluvial deposit. Thus, a maximum exposure age between 70 ± 8 ka and 82 ± 10 ka was estimated. While the maximum age for ESR estimated in this study is 108 ± 33 ka. In this case, the Qt12 terrace scenario seems to be repeated; that is, the age for ESR is older than the 10Be age. In fact, once again, the sedimentological characteristics of the upper Qt7 terrace deposit (plurimetric boulders embedded in a silt-sandy matrix), show evidences of chaotic sedimentation processes of one or more events, probably of short duration. Once it left its source area, the sedimentary material probably lacked the necessary sunlight exposure time to achieve optical bleaching and therefore a high % of dose not accumulated in situ is found in the Al centers of this sample. Since it is not possible to correct this component in this work, the estimated age is probably overestimated.

Methodology and Tectonic Implications

Despite the differences obtained between the ages estimated by ^{10}Be and ESR, the results obtain in the present study results are consistent with the geochronological and sedimentological context for the material sampled. In fact, the samples taken in the two deposits, which show a chaotic and rapid deposition, give rise to overestimated ESR ages, because the material did not have time to undergo optical bleaching. On the other hand, in the deposit that show long-term stable energy conditions, the ESR age is consistent with the ^{10}Be ages estimated. This result suggests that those sediments that have undergone a long sedimentation and transport process are best suited for application of the ESR dating and obtaining reliable numerical ages.

On the other hand, the ages that converge allow us to estimate that the long-term incision rate in the area has been constantly around 1 mm/a over the last 70 ka. Taking into account the geological and geomorphologic setting, this value can be converted into the Late Pleistocene uplift rate of the Southeastern flank of the Mérida Andes.

Acknowledgements: O.G. thanks the Universidad Regional Amazónica Ikiam for the support provided for this research. Special thanks to Mr. Paolo Traversa (Manager of the PEGAMMA Unit) and his staff for the irradiation of the samples.

REFERENCES

Audemard, F.E., Audemard, F.A., 2002. Structure of the Mérida Andes, Venezuela: relations with the South America-Caribbean geodynamic interaction. Tectonophysics 345, 299–327.

Bahain, J., 1993. Datation par resonance de spin ´electronique (ESR) de carbonates et d´´email dentaire quaternaires. Potentiels et probl`emes. Th`ese du Mus´eum National d'Histoire Naturelle, Paris, p. 114.

Bermúdez, M., 2009. Cenozoic Exhumation Patterns across the Venezuelan Andes: Insights from Fission-Track Thermochronology. Ph.D. Thesis. Universit´e Joseph Fourier, France, p. 305.

Colletta, B., Roure, F., De Toni, B., Loureiro, D., Passalacqua, H., Gou, Y., 1997. Tectonic inheritance, cristal architecture, and contrasting structural styles in the Venezuelan Andes. Tectonics 16 (5), 777–794.

Gosse, J., Phillips, F., 2001. Terrestrial in situ cosmogenic nuclides: theory and application. Quat. Sci. Rev. 20, 1475–1560.

Grün, R., 1989. Electron spin resonance (ESR) dating. Quat. Int. 1, 65–109.

Guzman, O., 2013. Timing and Dynamics of River Terraces Formation in Moderate Uplifted Ranges: the Example of Venezuela and Albania. Ph.D. Thesis. Université de Grenoble, France, p. 269.

Guzmán, O., Vassallo, R., Audemard, F., Mugnier, J.-L., Oropeza, J., Yepez, S., Carcaillet, J., Alvarado, M., Carrillo, E., 2013. 10Be dating of river terraces of Santo Domingo River, on Southeastern flank of the M´erida Andes, Venezuela: tectonic and climatic Implications. J. S. Am. Earth Sci. 48, 85–96.

Hackley, P.C., Urbani, F., Karlsen, A.W., Garrity, C.P., 2005. Geologic Shaded Relief Map of Venezuela. U.S. Geological Survey Open File Report 2005-1038.

Ikeya, M., 1975. Dating a stalactite by electron paramagnetic resonance. Nature 255, 48–50.

Ikeya, M., 1977. Electron spin resonance dating and fission track detection of Petralona stalagmite. Anthropos 4, 152–166.

Ikeya, M., Miki, T., 1985. ESR Dating and Dosimetry. IONICS, Tokyo, p. 538.

Laurent, M., Falgu`eres, C., Bahain, J.J., Yokoyama, Y., 1994. Geochronologie du syst`eme de terrasses fluviatiles quaternaires du bassin de la Somme par datation RPE sur quartz, des equilibre des familles de l'uranium et magnetostratigraphie. C.R. de l'Academie des Sciences de Paris 318, 521–526 serie II.

Li, D., Gao, H., Ding, Z., Zhao, X., Yang, B., 1993. On the estimation of depositional ages of loess by ESR. Appl. Radiat. Isot. 44, 203–206.

Tanaka, K., Hataya, R., Spooner, N.A., Questiaux, D.G., Saito, Y., Hashimoto, T., 1997. Dating of marine terrace sediments by ESR, TL and OSL methods and their applicabilities. Quat. Sci. Rev. 16 (3–5), 257–264.

Zeller, E., Levy, P., Mattern, P., 1967. Geological dating by electron spin resonance. In: Proceedings of the Symposium on Rad. Dating and Low-Level Counting. IAEA, Vienne.

Paleoseismic characteristics along the southern part of the Ulsan Fault Zone, SE Korea

Ohsang Gwon (1), Kiwoong Park (1), Sambit Prasanajit Naik (2), Young-Seog Kim (1, 2)

(1) Major of Earth and Environmental Sciences, Pukyong National University,45, Yongso-ro, Nam-gu, Busan 45813 Korea. Email : osgwon@pukyong.ac.kr

(2) Active Fault and Earthquake Mitigation Research Institute, Pukyong National University,45, Yongso-ro, Nam-gu, Busan 45813 Korea.

Abstract: *Historical and paleoseismological data suggest that the Ulsan Fault Zone is a highly prone area to large earthquakes in Korea. It is known that the NNW-trending Ulsan Fault is a reverse slip dominant fault. In this study, we evaluated the paleoseismic characteristics for the southern part of the Ulsan Fault. In trench site, sediment stratigraphy was divided into five layers. From the trench section, two east dipping faults were identified and the net slip associated with the last faulting event was calculated as 1.41 m based on the vertical separation and slickenline. The moment magnitude(M_w 6.6) was estimated based on the maximum displacement. Last faulting event occurred between 2.1±0.1 - 88±6 ka from OSL dating for the sedimentary layers. These parameters indicate that high seismic potential with a long recurrence interval of the Ulsan Fault.*

Key words: *SE Korea, southern Ulsan Fault, trench survey, seismic displacement, moment magnitude*

INTRODUCTION

As the most intense damages are caused by large earthquakes of magnitude 6 or above, it is important to trace active faults and understand their characteristics for preventing earthquake disasters. Although instrumentally recorded earthquakes rarely exceed M_w>5.0 in Korea, records of historical earthquakes indicate frequent seismic activities at the southeastern part of the Korean peninsula(Choi et al., 2014). Yangsan-Ulsan Fault system has already been intensively investigated for last faulting events, recurrence intervals, slip rates, displacements, estimated earthquake magnitudes etc.(Okada et al., 1994; Ryoo et al., 1996; Kyung et al., 1999a; Chang. 2001; Kim and Jin, 2006; Jin et al., 2013; Cheon et al., 2020; Kim et al., 2020; Gwon et al., 2021). However, the southern part of the Ulsan Fault Zone remains poorly studied, even though several the Quaternary faults are reported to be potentially capable of generating large, damaging earthquakes(Lee and Yang, 2006). The southern part of the Ulsan Fault Zone is important because of its relatively close proximity to the Ulsan city, industrial complex and a nuclear power plant. In this study, the results of structural, geomorphological and active tectonical studies for the southern part of the Ulsan Fault Zone are documented.

TECTONIC SETTINGS

The Korean peninsula is located at the margin of the Eurasian Plate(Fig. 1). During the Cenozoic, boundary conditions between plates have changed several times due to recombination of the Eurasian Plate with surrounding plates. Major tectonic events that caused the Cenozoic tectonic deformation of East Asia are summarized as follows: 1) Collision between India and Eurasian Plates was initiated at approximately 55-50 Ma(Paleogene). 2) At ~43 Ma, direction of movement of the Pacific Plate changed from NNW to WNW. 3) At ~25 Ma, the Japanese archipelago separated from the East Asian continent, leading to expansion of the East Sea. 4) At ~15 Ma, the southwestern part of the Japanese archipelago collided with the Izu-bonin arc of the Philippine sea, and rotated rapidly clockwise(Son et al., 2007). These tectonic events led expansion of back-arc basin, stress inversion, and large-scale compressional deformation throughout East Asia(Cox and Engerbretson, 1985; Pollitz, 1986; Sato and Amano, 1991; Hall, 2002; Yin, 2010; Son et al., 2015). As a result of synthesis of current stress field, subduction zones of the Pacific Plate on the east side of Japanese islands exhibit reverse dominant stress condition, and the most of compression axes are arranged in systematic WNW-ESE direction, parallel to the overall movement direction of the plate (Heidhach et al., 2010). It indicates that the Pacific Plate subducts under the Eurasian Plate and continuously generates compressive stresses in WNW-ESE direction.

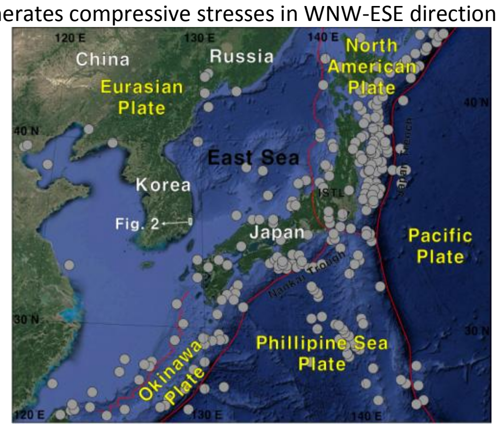

Figure 1: Tectonic map around the Korean Peninsula(modified from Schellart and Rawlinson, 2010). Note that gray circles represent epicenters of magnitude 6.5 or higher over past 100 years(modified from USGS, 2021).

Lineament analysis

From DEM(Digital Elevation Model) acquired by LiDAR(Light Detection And Ranging), several clear linear features were identified around the study area(Fig. 2). Among them, the NNW-SSE direction is extremely clear and distinct. Also, some knick points and deflected streams are identified from the DEM, and aerial photographs(Fig. 2 and 3).

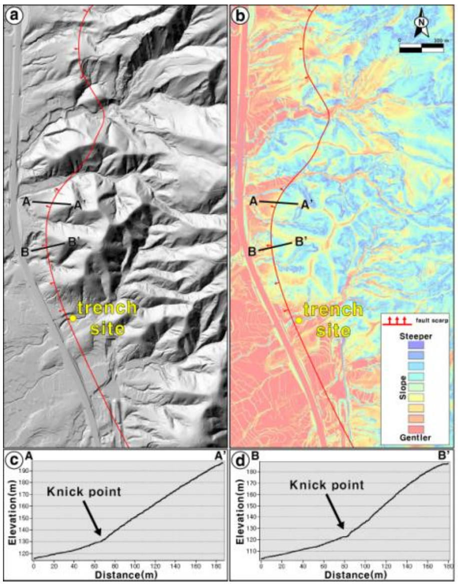

Figure 2: (a) Hillshade image showing a lineament. (b) DEM derived slope image showing lineament. (c) Topographic profile of A-A'. (d) Topographic profile of B-B'.

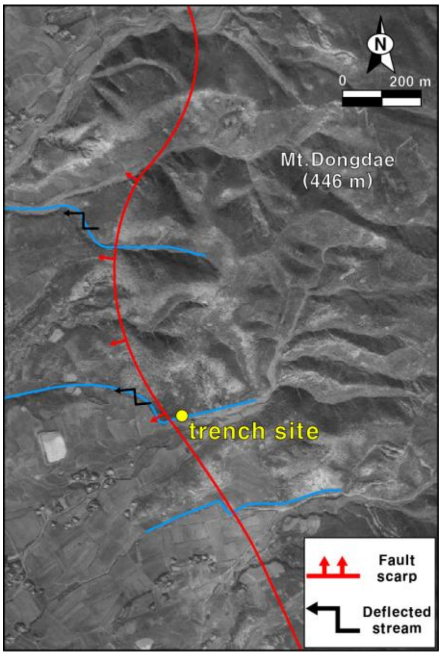

Figure 3: Aerial photograph(taken in 1954) showing lineament. Note that small streams(blue lines) are deflected across inferred fault scarp.

Geophysical survey

In this study, we conducted ERT(Fig. 4) perpendicular to fault trace. A significant variation in lateral resistivity at 40 to 60 m was detected on the surface, whereby low resistivity zone corresponds to fault zone in subsurface. This fault zone is clearly represented as an east-dipping low resistivity region.

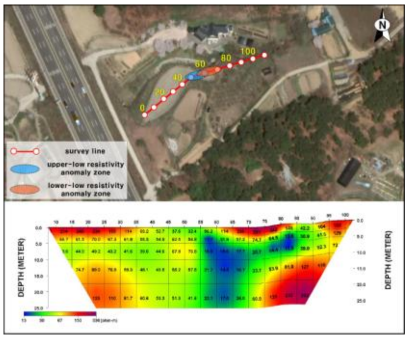

Figure 4: Location of resistivity survey line and result of 2D resistivity survey.

Trench survey

Two east dipping faults(F1, F2) were observed on the trench section, displacingthe bedrocks and sediment layers(Fig. 4). The hangingwall, bounded by F1, was composed of sandstones, whereas the footwall was composed of unconsolidated sediment layers presumed to be of the Tertiary and Quaternary. The sediment layers in the footwall are subdivided into unit A to unit D-2 based on the size of particles, type of content of gravels, sorting and colour. The boulders of unit A are sub-rounded to angular and mixed with dark brown sand-silt matrix. Unit B is composed of sub-rounded to angular cobbles-pebbles with yellowish sandy matrix. There are some sand patches within the pebble unit, which are indicative of fluvial origin. The boundary between unit B and unit C were deformed due to drag folding as they are close to the fault zone. Unit C is composed of uniformly rounded pebbles-cobbles with brownish sand-silt matrix. Unit D's composition is similar with unit C; however it can be subdivided into two layers(unit D-1, unit D-2) because of variations in matrix colour. Unit D-1 is composed of rounded granule or pebble with blue sand or silt matrix, and silt content is higher than unit C. Unit D-2 has almost similar composition as unit D-1; however, it has a brownish colour. The attitude of sand layer in unit D-2 was measured to be N10°W/50°SW, which shows that unit D-2, located at the footwall, was deformed into high angle due to drag-folding during the faulting. The attitude of bedding in the hanging wall is N24°E/60°SE. The fact that this layer has a higher angle compared to other areas indicates that the sedimentary rocks located in the hanging wall were tilted by faulting. Measured slickenlines from the F2 plane exhibit right-lateral sense with reverse dominant movement with the pitch of 72°N.

Age dating

We collected 4 samples in unit A(2010CPD-05, 06, 07, 09) and 1 sample in unit B(2010CPD-04) to determine ages using luminescence method. We obtained ages of 1.8±0.1 ka for 2010CPE-05, 2.1±0.2 ka for 2010CPE-06, 2.1±0.1 ka for 2010CPE-07, 1.7±0.1 ka for 2010CPE-09, 88±6 ka for 2010CPE-04. It indicates that the last faulting event occurred between 2.1±0.1 - 88±6 ka.

History of faulting

Based on the correlation analysis between unconsolidated sediment layers and faults observed in trench wall, here we discuss the number of faulting events and history of their movements. Figure 6 represents schematic diagram of the evolution of the faults. Faults were developed within bedrock prior to the Quaternary period. The bedrock was weathered by erosion and unit B was deposited with unconformity covering bedrock(Figure 6). Subsequently, reactivated fault truncated unit B(Event 1). The topographic relief generated by faulting and unit B in the hangingwall were almost flattened by denudation during subsequent inter-seismic period, and unit A was deposited.

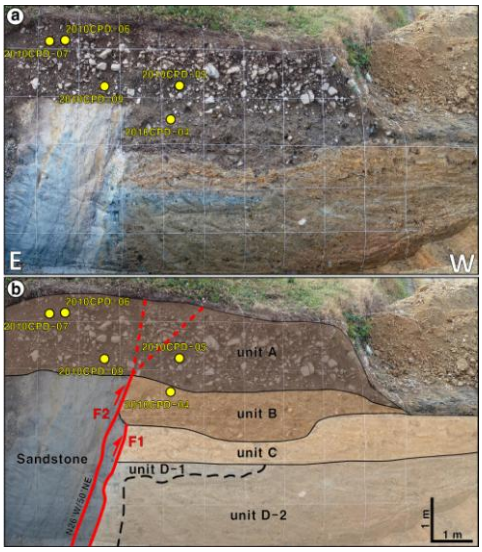

Figure 5: (a) Photomosaic of trench section on the southern wall. (b) Detailed sketch of trench section.

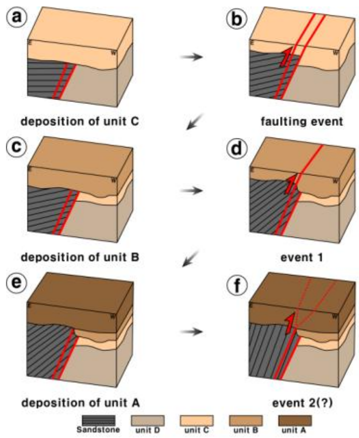

Figure 6: Schematic diagrams for reconstructions of faulting events at trench site. Based on cross-cutting relationships between faults and unit layers, at least two faulting events are recognized during the Quaternary.

True displacement

It is well known that displacement is closely related to the magnitude of earthquake(Wells and Coppersmith, 1994). Therefore, the easiest way to estimate the earthquake magnitude in paleoseismic study is to derive the displacement associated with one seismic event. The displacement can be derived relatively easily if key bed can be recognized in the hangingwall and footwall. However, in practice, most of hangingwall sediments are lost due to subsequent denudation in reverse faults. Furthermore, in general, trench wall is rarely exactly perpendicular to the strike of the fault. Therefore, it is not easy to derive true displacement from trench wall.

If apparent displacement associated with a single faulting event in trench wall is obtained, true displacement of the last faulting event can be calculated using information such as apparent displacement, trench wall angle, fault dip angle and pitch of the slickenline(Xu et al., 2009; Jin et al., 2013). The unconformity between unit A and sandstone in the hangingwall and the unconformity between unit B and unit C in the footwall were set as reference planes. Assuming the unit A was deposited by erosion and denudation during inter-seismic period, minimum displacement of the fault can be calculated. Since trench wall was not excavated exactly perpendicular to the fault, true displacement(S_t) was calculated using the apparent displacement(S_{vm}), trench wall angle(α), fault dip angle(β) and pitch of slickenline(γ). The apparent vertical displacement measured at trench wall was 1.1 m, the fault dip angle was 70˚, and calculated vertical displacement(S_v) was 1.03 m. The dip separation calculated using the vertical displacement and fault dip angle was 1.34 m(S_m; Eq. 1). Thus, the true displacement calculated using dip separation and pitch of slickenline was 1.41 m(Figure 7; Eq. 2).

$S_v = S_{vm}\sin\alpha,\ S_m = \dfrac{S_v}{\sin\beta}$ (Eq. 1) $\qquad S_t = \dfrac{S_m}{\sin\gamma}$ (Eq. 2)

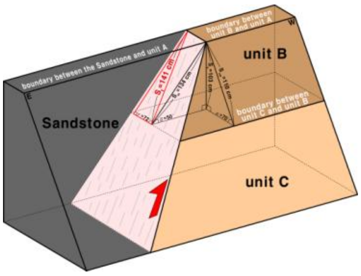

Figure 7: Schematic diagram showing the deduction of the true displacement(modified from Xe et al., 2009).

CONCLUSIONS

Topographic analysis, geophysical survey and paleoseismic survey were conducted to confirm faulting activities along the southern Ulsan Fault Zone. The results of this research are as follows.

1) By topographic analysis, evidences of fault activities such as fault scarps and deflected streams along lineament were identified. In geophysical survey, a low resistivity anomaly extending to the surface was recognized. Therefore, trench survey was conducted and the Quaternary fault activity was confirmed along the southern part of the Ulsan Fault Zone.

2) The true displacement caused by the last faulting event was calculated to be 1.41 m. Applying these data to empirical equation of the maximum displacement-moment magnitude, earthquake moment magnitude was estimated to be approximately 6.6. The last faulting event occurred between 2.1$\pm$0.1 - 88$\pm$6 ka. These parameters indicate that high seismic potential with a long recurrence interval along the Ulsan Fault Zone.

Acknowledgements: This research was supported by a grant(2022-MOIS62-001) of National Disaster Risk Analysis and Management Technology in Earthquake funded by Ministry of Interior and Safety(MOIS, Korea).

REFERENCES

Chang, T.W., 2001. Quaternary tectonic activity at the eastern block of the Ulsan fault. Journal of the Geological Society of Korea 37, 431-444.

Cheon, Y., Choi, J.-H., Kim, N., Lee, H., Choi, I., Bae, H., Rockwell, T.K., Lee, S.-R., Ryoo, C.-R., Choi, H., & Lee, T.-H., 2020. Late Quaternary transpressional earthquakes on a long-lived intraplate fault: A case study of the Southern Yangsan Fault, SE Korea. Quaternary International 553, 132-143.

Choi, S.-J., Jeon, J.-S., Choi, J.-H., Kim, B., Ryoo, C.-R., Hong, D.-G. & Chwae, U., 2014. Estimation of possible maximum earthquake magnitudes of Quaternary faults in the southern Korean Peninsula. Quaternary International 344, 53-63.

Cox, A., & Engerbretson, D., 1985. Change in motion of Pacific plate at 5 Myr BP. Nature 313, 472-474.

Gwon, O., Park, K., Naik, S.P., Shin, H.-C., & Kim, Y.-S., 2021. A study on the characteristics of fault activity in the southern part of the Ulsan fault using paleoseismic method. Journal of the Geological Society of Korea 57(2), 109-121.

Hall, R., 2002. Cenozoic geological and plate tectonic evolution of SE Asia and the SW Pacific: computer-based reconstructions, model and animations. Journal of Asian Earth Sciences 20, 353-431.

Heidbach, O., Tingay, M., Barth, A., Reinecker, J., Kurfeв, D., & Müller, B., 2010. Global crustal stress pattern based on the World Stress Map database release 2008. Tectonophysics 482, 3-15.

Jin, K., Kim, Y.-S., Kang, H.C., & Shin, H.C., 2013. Study on developing characteristics of the Quaternary Gusan Fault in Uljin, Gyeongbuk, Korea. Journal of the Geological Society of Korea 49, 197-207.

Kim, T., Shin, H.-C., & Kim, Y.-S., 2020. Characteristics of the topographical deformation in the central part of the Ulsan fault. Journal of the Geological Society of Korea 56, 193-209.

Kim, Y.-S., & Jin, K., 2006. Estimated earthquake magnitude from the Yugye Fault displacement on a trench section in Pohang, SE Korea. Journal of the Geological Society of Korea 42, 79-94.

Kyung, J.B., Lee, K., & Okada, A., 1999a. A paleoseismological study of the Yangsan fault - analysis of deformed topography and trench survey. Journal of the Korean Geophysical Society 2, 155-168.

Lee, K., & Yang, W.-S., 2006. Historical Seismicity of Korea, Bulletin of the Seismological Society of America 96, 846-855.

Okada, A., Watanabe, M., Sato, H., Jun, M.S., Jo, W.R., Kim, S.K., Jeon, J.S., Choi, H.C., & Oike, K., 1994. Active fault topography and trench survey in the central part of the Yangsan fault, Southeast Korea. Journal of Geography 103, 111-126.

Pollitz F.F., 1986. Pliocene change in Pacific-plate motion. Nature 320, 738-741.

Ryoo, C.-R., Yang, K., Lee, S.-W., & Kim, I.-S., 1996. Quaternary fault in the vicinity of the Ulsan fault. The Journal, College of Education, Pusan National University 33, 311-327.

Sato, H., & Amano, K., 1991. Relationship between tectonics, volcanism, sedimentation and basin development, Late Cenozoic, central part of Northern Honshu, Japan. Sedimentary Geology 74, 323-343.

Schellart, W.P., & Rawlinson, N., 2010. Convergent plate margin dynamics: New perspectives from structural geology, geophysics and geodynamic modelling. Tectonophysics 483, 4-19.

Son, M., Kim, J,-S., Chong, H.-Y., Lee, Y.H., & Kim, I.- S., 2007. Characteristics of the Cenozoic crustal deformation in SE Korea and their tectonic implications. Korean Journal of Petroleum Geology 13, 1-16.

Son, M., Song, C.W., Kim, M.-C., Cheon, Y., Cho, H., & Sohn, Y.K., 2015. Miocene tectonic evolution of the basins and fault systems, SE Korea: dextral, simple shear during the East Sea (Sea of Japan) opening. Journal of the Geological Society 172, 664-680.

USGS., 2021. https://earthquake.usgs.gov/earthquakes/search (May 24, 2021).

Wells, D.L., & Coppersmith, K.J., 1994. New empirical relationships among magnitude, rupture length, rupture width, rupture area, and surface displacement. Bulletin of Seismological Society of America 84, 974-1002.

Xu, S., Nieto-Samaniego, A.F., & Alaniz-Àlvarez, S.A., 2009. Quantification of true displacement using apparent displacement along an arbitrary line on a fault plane. Tectonophysics 467, 107-118

Yin, A., 2010. Cenozoic tectonic evolution of Asia: a preliminary synthesis. Tectonophysics 488, 293-325.

Paleoseismic study of the X̲EOLX̲ELEK̶–Elk Lake fault: A newly identified Holocene fault in the northern Cascadia forearc near Victoria, British Columbia, Canada

Harrichhausen, Nicolas (1), Theron Finley (2), Kristin D Morell (1), Christine Regalla (3), Scott E K Bennet (4), Lucinda J Leonard (2), Edwin Nissen (2), Eleanor McLeod (2), Emerson M Lynch (3), Guy Salomon (2), Israporn Sethanant (2)*

(1) Department of Earth Science, University of California, Santa Barbara, CA, USA.
(2) School of Earth and Ocean Sciences, University of Victoria, Victoria BC, Canada
(3) School of Earth and Sustainability, Northern Arizona University, Flagstaff AZ, USA
(4) U.S. Geological Survey, Geology, Minerals, Energy, and Geophysics Science Center, Portland OR, USA
* Now at: Univ. Grenoble Alpes, Univ. Savoie Mont Blanc, CNRS, IRD, Univ. Gustave Eiffel, ISTerre, 38000 Grenoble, France.
Email: n.harrichhausen@univ-grenoble-alpes.fr

Abstract: *High-resolution topographic data show a tectonic scarp formed in Quaternary sediments near the city of Victoria in the northern Cascadia forearc on Vancouver Island, British Columbia, Canada. A paleoseismic trench excavation across the structure, the X̲EOLX̲ELEK–Elk Lake fault, shows evidence for a Holocene (after 12.2 cal ka BP) surface-rupturing reverse-slip earthquake that produced a fault-propagation fold and resulted in the formation of a ~1.4 to 3.5 m-high scarp. Fault-propagation fold modelling indicates ~3.2 m of reverse slip on a 50°-dipping fault plane reproduces the observed deformation, and fault-scaling relations suggest a single earthquake rupture with this surface displacement could occur during a ~*M_w 6.1–7.6 *earthquake. Given the fault's location within the metropolitan area of Victoria, an earthquake near this magnitude would result in significant damage to local infrastructure and this fault is worth considering in future seismic hazard assessments.*

***Key words**: Paleoseismic trench, Holocene rupture, Fault-propagation fold, Vancouver Island, Cascadia.*

INTRODUCTION

Recent studies of Holocene surface-rupturing faults in the northern Cascadia forearc on Vancouver Island have highlighted the hazard they pose to this region. For instance, recognition of the Leech River fault as active and capable of producing ~M 7 earthquakes (Fig. 1a, Morell et al., 2018) has resulted in modifications of seismic hazard assessments for Victoria, the capital city of British Columbia, Canada, with a metropolitan population of ~400,000 people (e.g., Kukovica et al., 2019). These new assessments show that the greatest increase in hazard occurs closest to the fault trace, highlighting the importance of accurately mapping active structures.

Northeast of Victoria, a bathymetric and seismic reflection study in the Haro Strait indicates potentially Quaternary-active, northwest-striking faults that connect with the Devils Mountain fault in Washington State, USA (Fig. 1a, Greene & Barrie, 2022). The northwest continuation of these structures project onshore across the Saanich Peninsula, within the metropolitan area of Victoria. We identified scarps formed in Quaternary sediments and bedrock scarps that cut across Saanich Peninsula and underneath X̲EOLX̲ELEK̶ (pronounced: hul-lakl-lik; also known as Elk Lake), along strike from the offshore structures (Fig. 1b). To assess whether this structure, the X̲EOLX̲ELEK̶–Elk Lake fault (XELF), hosted recent surface-rupturing earthquakes, we excavated a paleoseismic trench across the Quaternary scarp in August, 2021 to examine the stratigraphy and deformation.

TOPOGRAPHIC ANALYSES

Analyses of a high-resolution lidar-derived digital elevation model from the British Columbia Open Lidar Portal (last accessed January 10, 2022 at: https://www2.gov.bc.ca/gov/content/data/geographic-data-services/lidarbc), shows an 11 km-long, 125°-striking, series of northeast-facing scarps across Saanich Peninsula (Fig. 1b). East of X̲EOLX̲ELEK̶ (Fig 1c), the scarp is formed in Quaternary glacial sediments deposited during and immediately after the last glacial maximum, which occurred ~14 calibrated kiloyears before present (cal ka BP) (James et al., 2009). These glacial deposits form a 40 m-high north–south oriented, streamlined, drumlinoid ridge, parallel with southward glacial flow direction during the last glacial maximum (Fig. 1b, James et al., 2009). The scarp offsets the surface of the drumlinoid, southwest-side up, by a vertical separation of ~1.4 to 3.5 m.

Exposures of bedrock faulting and the trace of the scarp across the drumlin are consistent with a ~50° south-dipping reverse fault forming the scarp (Fig. 1b). Assuming a planar fault produced the scarp across the drumlinoid, structural contour lines of the fault plane based on the surface elevation of the scarp indicate a fault oriented 127°/50° SW. Outcrops along the fault trace east of the drumlin show planar faults formed in bedrock that dip 45°–62° south and strike between 102° and 115°. West of X̲EOLX̲ELEK̶, we observed one bedrock fault with an orientation of 075°/36° SE, and slickenlines indicating reverse slip (Fig. 1b).

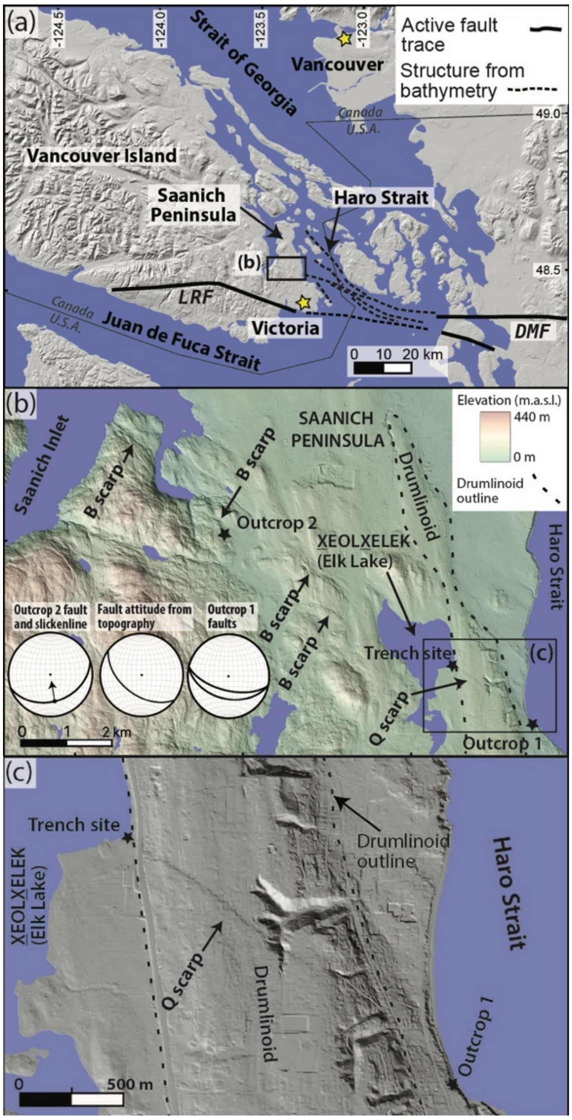

Figure 1: a) Map of southern Vancouver Island showing the Leech River fault (LRF), the Devils Mountain fault (DMF), and structures in Haro Strait. Fault traces adapted from Greene & Barrie, (2022). Basemap is from the United State Geological Survey (USGS) National Map service. b) Hillshade map coloured by elevation (meters above sea level: m.a.s.l.) of Saanich Peninsula with Quaternary (Q) and bedrock (B) scarps shown. Lower-hemisphere stereonet projections show bedrock fault plane orientations at Outcrops 1 and 2, slickenline orientation and slip sense of hanging wall at Outcrop 2, and the fault orientation derived from structural contour mapping of the Q scarp. c) Hillshade map showing the Q scarp offsetting the surface of a drumlinoid east of X̲EOLX̲ELEꝀ. Hillshade maps in (b) and (c) were derived from the BC Open Lidar digital elevation models.

PALEOSEISMIC TRENCH

On the eastern shore of X̲EOLX̲ELEꝀ (Fig. 1b), excavation of a 32 m-long paleoseismic trench and auger holes revealed deformed glacial sediments overlain by a colluvial wedge, undeformed beach sediments, and anthropogenic fill (Fig. 2). The glacial sediments, composed of diamict (Unit EB1) overlain by well-bedded silts and clay (Unit EB2), are deformed by a fault-cored monocline centered at the scarp. The monocline results in ~2.3 m of vertical separation of the top of Unit EB2 assuming no erosion of this unit. This assumption is based on a consistent ~2 m-thickness of Unit EB2 across the monocline, and the presence of a ~1 m-thick, paleosol horizon (EB2b) at the top of EB2 that is continuous across the fold. Both EB1 and EB2 are offset ~0.2 m by gently south-dipping (~090°/20°) reverse faults in the core of the monocline. South of the monocline, numerous fractures and normal faults crosscut these units and show minor offsets (<0.2 m).

A colluvial wedge (Unit EB3) we interpret as related to a single earthquake, overlies the toe of the scarp above down-thrown glacial sediments on the footwall of the fault-cored monocline (Fig. 2). This colluvial unit is a channel- or wedge-shaped body of poorly-sorted matrix-supported diamict and contains clasts of the underlying bedded clays and silts (Unit EB2). It thins both to the north, away from the scarp, and to the south, where it unconformably onlaps the fold scarp. The lack of internal deformation and paleosol horizons within this unit suggest this colluvial wedge began to form after a single earthquake event and has not been subsequently deformed by a second earthquake.

A thin (<0.3 m) layer of well-sorted medium-grained sand (Unit EB4) and two units (EB5 and EB6) of anthropogenic fill, containing glass fragments and bricks, overlie the older units. We interpret these units are the result of deposition of beach sands after the deposition of the colluvial wedge, and subsequent filling with anthropogenic material during park construction adjacent to X̲EOLX̲ELEꝀ.

DISCUSSION

Our observations suggest the topographic scarp observed on Saanich Peninsula was the result of a single Holocene earthquake. During the most recent glacial maximum at 14 cal ka BP, a continental ice sheet flowed southward across the peninsula (e.g., James et al., 2009) resulting in the formation of the drumlinoid ridge east of X̲EOLX̲ELEꝀ (Fig. 1b). If the scarp deformed the surface of the drumlin before deglaciation, it would have been eroded away by the overriding glacier. In addition, the paleosol at the top of the youngest deformed unit in our paleoseismic trench (Unit EB2) indicates this unit was exposed subaerially. A drop in relative sea level, due to isostatic rebound, likely exposed the trench site subaerially between 12.2 and 12.0 cal ka BP (James et al., 2009), suggesting soil formation and subsequent deformation after this date. Although there are no historical records of a surface-rupturing earthquake on Saanich Peninsula, debris flow deposits observed in drill cores from nearby Saanich Inlet (Fig. 1) suggest several ground shaking events not corresponding to documented megathrust earthquakes on the Cascadia subduction zone (Blais- Stevens et al., 2011). The youngest of these uncorrelated deposits accumulated between 410 and 435 years BP, suggesting a youngest possible earthquake age. Further constraint of event timing using ^{14}C-dating of detrital charcoal is ongoing.

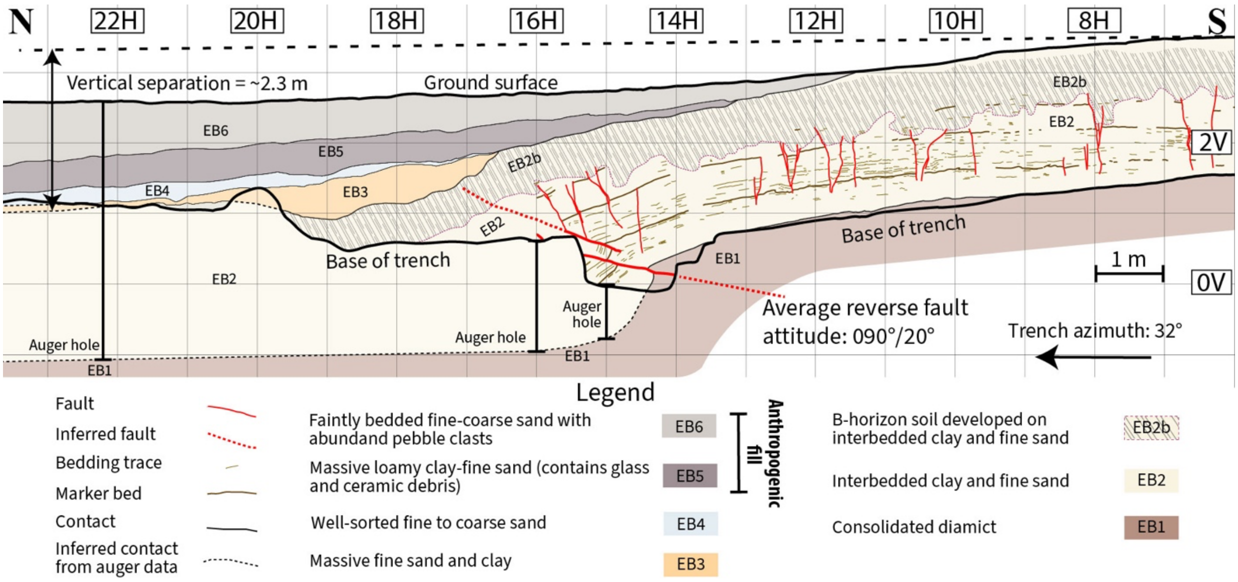

Figure 2: Interpretation of the east wall of paleoseismic trench across the XELF. Trench log from 6H to 24H, centered on the monocline and south-dipping reverse faults are shown. Contacts below trench floor were inferred using unit contacts in auger data.

The shallowly-dipping reverse faults in the paleoseismic trench (~090°/20°) do not match the moderately dipping (45° to 62°) reverse faults determined from Quaternary scarps and bedrock faults, making estimation of coseismic slip and earthquake magnitude difficult. The monocline and reverse fault geometry observed in the trench resembles folds formed above a propagating reverse fault tip (e.g., Livio et al., 2020). Therefore, we hypothesize the deformation in the trench is a result of a moderately dipping fault at depth that is consistent with fault orientations beyond the trench.

To test the hypothesis of a fault-propagation fold in the paleoseismic trench and place constraints on minimum fault slip, we used FaultFold (Allmendinger, 1998; Zehnder & Allmedinger, 2000) to forward model folding above a propagating 50°-dipping reverse fault to reproduce the observed deformation (e.g., Livio et al., 2020) (Fig. 3). Fold geometry in FaultFold is based on fault geometry, the fault propagation-to-slip ratio (P/S), and the trishear angle (TS) defining the triangular area in front of the propagating fault tip that is folded (Allmendinger, 1998). As initial conditions, we assumed horizontal, undeformed glacial sediments, a 50° south-dipping fault propagating towards the center of the monocline, and a TS of 60°. We also assumed the fault would propagate from bedrock to glacial sediments at a depth of 2.7 m below the base of Unit EB2, based on preliminary geophysical (electrical resistivity) survey results. We then varied the total slip and the P/S for the basal and glacial sediments until we best reproduced the deformation observed in the trench.

We found that a 50° south-dipping reverse fault accumulating 1.83 m of slip while propagating through bedrock with a high P/S of 10 (Fig. 3a), then slipping 1.37 m while propagating through glacial sediments with a lower P/S of 3.4 (Fig. 3b), closely reproduced the observed monocline. The P/S reduction is consistent with propagation through a less consolidated material and the P/S ratio of 3.4 is similar to P/S observed in silts and clay (Livio et al., 2020). We then initiated a minor 10°-dipping reverse fault near the tip of the main fault, and allowed it to slip 0.2 m with a P/S of 3.4 (Fig. 3c). This minor fault with a gentle dip allowed us to better match the observed fault and fold geometry in the paleoseismic trench (Fig. 3d). Although these parameters represent a non-unique solution, they show that ~3.2 m of total slip on a blind 50°-dipping reverse fault is consistent with the topographic analysis of the scarp and can produce a fault-propagation fold consistent with our paleoseismic trench observations.

Assuming ~3.2 m of coseismic slip at the surface during the surface-rupturing earthquake on the XELF, the paleo-earthquake magnitude can be roughly estimated. We neglect the slip on the minor reverse fault in the trench, because we infer that this structure nucleated near the surface (Fig. 3c), has a negligible surface area, and does not significantly contribute to moment release. Using the Wesnousky (2008) scaling relationships between average and maximum surface displacements and magnitude for reverse earthquakes, we estimate that the observed deformation was produced by a M 6.1–7.6 earthquake. However, the true uncertainty is likely greater still, as we lack constraints on surface slip along the length of the rupture trace. We also lack constraints on a potential strike-slip component of surface displacement, which would increase the net displacement and earthquake magnitude. Further analyses of the surface slip distribution, potential surface rupture length, and seismogenic depth extent could better constrain the paleo-earthquake magnitude for use in deterministic seismic hazard assessments.

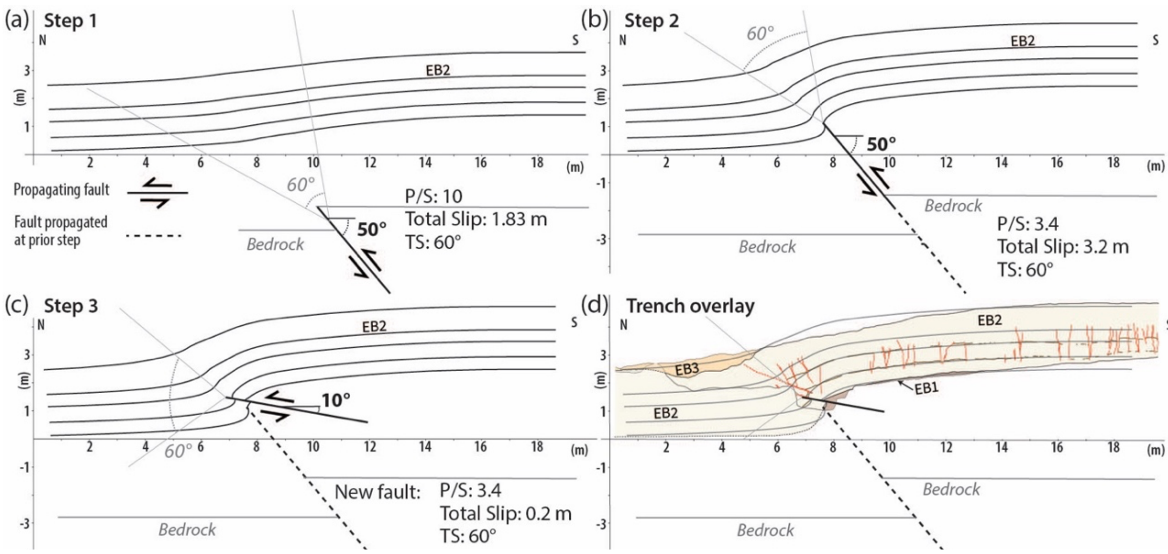

Figure 3: Forward fault-propagation fold model. a) 1.83 m of reverse fault slip and propagation through bedrock with P/S = 10. b) The fault tip has propagated to glacial sediments and P/S has dropped to 3.4. 1.37 m of fault slip (total slip of 3.2 m) is accumulated, and the fault tip has propagated close to the EB1-EB2 contact. c) A new fault dipping 10° southwest accommodates 0.2 m of slip. d) Overlay of Units EB1, EB2, and EB3 from the trench log (Fig. 2) on the final result of the model.

CONCLUSIONS

Topographic analyses and paleoseismic trenching indicate a Holocene earthquake on the newly identified X̱EOLX̱ELEK̶–Elk Lake fault across Saanich Peninsula on southern Vancouver Island, Canada. The trench revealed evidence that a single earthquake deformed glacial sediments via a fault-propagation fold above a blind reverse fault. Fault-fold propagation modelling indicates that ~3.2 m of reverse slip on a fault propagating through two different geologic units, each with different propagation-to-slip ratios, could reproduce the observed deformation. Average surface slip of 3.2 m along a reverse fault corresponds to a M 6.1–7.6 earthquake using established fault scaling relations. Although there is substantial uncertainty associated with this estimate, an earthquake close to this magnitude would cause significant damage to the Victoria region and is worth considering in future seismic hazard assessments.

Acknowledgements: This study was conducted on the traditional territory of the W̱SÁNEĆ people and the authors from the University of California, Santa Barbara, University of Victoria, and Northern Arizona University acknowledge their historical relationships with the land that continue to this day. This research was supported by an NSF EAR grant # 1756943 to Dr. Morell, an NSF EAR grant # 1756834 to Dr. Regalla, funding from the USGS National Cooperative Geologic Mapping Program to Dr. Bennett, an NSERC Discovery grant # 2017-04029 and Canada Research Chair to Dr. Nissen, and an NSERC Alexander Graham Bell Canada Graduate scholarship to Finley. We thank the Capital Regional District (especially A. Mitchell, J. Mollin and M. Solomon) for access to Elk Lake Regional Park, Walter Langer for the trench excavation and associated logistics, and Simon Smith for monitoring the excavation and sharing insights into the history of X̱EOLX̱ELEK̶. We also thank the USGS internal reviewers for their thoughtful comments on this document. Any use of trade, firm, or product names is for descriptive purposes only and does not imply endorsement by the U.S. Government

REFERENCES

Allmendinger, R. W. 1998. Inverse and forward numerical modelling of trishear fault-propagation folds. *Tectonics, 17 (4),* 640—656.

Blais-Stevens, A., Rogers, G. C., & Clague, J. J. 2011. A revised earthquake chronology for the last 4,000 years inferred from varve-bounded debris-flow deposits beneath an inlet near Victoria, British Columbia. *Bulletin of the Seismological Society of America, 101 (1),* 1–12.

Greene, H.G., & Barrie, J.V., 2022. Faulting within the San Juan-southern Gulf Islands Archipelagos, upper plate deformation of the Cascadia subduction complex. *Geological Society, London, Special Publications, 505(1),* pp.SP505-2019.

James, T. S., Gowan, E. J., Hutchinson, I., Clague, J. J., Barrie, J. V., & Conway, K. W. 2009. Sea-level change and paleogeographic reconstructions, southern Vancouver Island, British Columbia, Canada. *Quaternary Science Reviews, 28 (13),* 1200-1216

Kukovica, J., Ghofrani, H., Molnar, S., & Assatourians, K. 2019. Probabilistic Seismic Hazard Analysis of Victoria, British Columbia: Considering an Active Fault Zone in the Nearby Leech River Valley. *Bulletin of the Seismological Society of America, 109 (5),* 2050–2062

Livio, F., Ferrario, M., Frigerio, C., Zerboni, A., & Michetti, A. 2020. Variable fault tip propagation rates affected by near-surface lithology and implications for fault displacement hazard assessment. *Journal of Structural Geology, 130* ,103914

Morell, K. D., Regalla, C., Amos, C., Bennett, S., Leonard, L., Graham, A., Reedy, T., Levson, V., & Telka, A. 2018. Holocene surface rupture history of an active forearc fault redefines seismic hazard in southwestern British Columbia, Canada. *Geophysical Research Letters, 45 (210),* 11–605.729

Wesnousky, S. G. 2008. Displacement and geometrical characteristics of earthquake surface ruptures: Issues and implications for seismic-hazard analysis and the process of earthquake rupture. *Bulletin of the Seismological Society of America*, *98*(4), 1609-1632.

Zehnder, A. T., & Allmendinger, R. W. 2000. Velocity field for the trishear model. *Journal of Structural Geology, 22 (8),* 1009-1014**.**

Paleoseismological surveys for the identification of capable faults in urban areas: the case of the Mt. Marine Fault (Central Apennines, Italy).

Iezzi, Francesco (1), Marco Francescone (2), Alberto Pizzi (2), Anna Maria Blumetti (3), Paolo Boncio (2), Pio Di Manna (3), Bruno Pace (2), Tommaso Piacentini (2,4), Felicia Papasodaro (3), Francesco Morelli (2), Marco Caciagli (4), Massimo Chiappini (4), Francesca D'Ajello Caracciolo (4), Valerio Materni (4), Iacopo Nicolosi (4), Vincenzo Sapia (4), Stefano Urbini (4).

(1) Dipartimento di Scienze della Terra, dell'Ambiente e delle Risorse, University "Federico II" of Naples, Italy.
(2) Dipartimento di Ingegneria e Geologia, University "G. D'Annunzio" of Chieti-Pescara, Italy.
(3) Istituto Superiore per la Protezione e la Ricerca Ambientale, Rome, Italy.
(4) Istituto Nazionale di Geofisica e Vulcanologia, Rome, Italy.

Abstract: *In order to constrain the Fault Displacement Hazard (FDH) of the town of Pizzoli, located 10 km NW of L'Aquila (Central Apennines, Italy), we performed two paleoseismological trenches across multiple fault splays within the hanging wall of the main Mt. Marine active normal fault. Our trenches highlighted the presence of five faults arranged both synthetic and antithetic to the main fault. The fault splays are distributed within an across-strike distance of about 500 m. Each fault segment shows evidence of repeated surface-rupturing earthquakes occurring throughout the Late Pleistocene-Holocene, proving their capability of rupturing the surface during recent earthquakes. Our study shows that multiple parallel fault splays belonging to a principal segmented fault are active during the same time interval, although the slip rates of single faults may be different through time. Our work reiterates the importance of performing paleoseismological investigation for assessing FDH in urban areas.*

Key words*: Earthquake geology, paleoseismology, fault displacement hazard.*

INTRODUCTION

The Fault Displacement Hazard (FDH) is a localised seismic hazard due to the occurrence of coseismic surface ruptures during earthquakes. The FDH is strictly connected to the so-called capable faults, defined as faults able to release surface ruptures during earthquakes. The assessment of the FDH is very significant when capable faults are located within urban areas, with houses and facilities being exposed to permanent deformation due to the rupturing of the ground surface underneath. Hence, in order to mitigate the potential effects of the surface ruptures it is critical to identify the geometry and slip rates of such capable faults. However, the identification of capable faults in urban areas is not straightforward, because the anthropic activity often elides the geomorphological evidence of past earthquakes (e.g. fault scarps). The assessment of FDH becomes even more complex when capable faults are highly segmented, with multiple fault splays arranged both along- and across-strike. In such geological contexts, paleoseismological investigations become key for constraining both the geometry and the activity rates of the multiple fault splays.

We focus on the Mt. Marine fault (Central Apennines, Italy), an active normal fault that has already released surface-rupturing earthquakes in the past, with the most recent event occurred in 1703 AD (Blumetti, 1995; Moro et al., 2002; 2016; Galli et al., 2011; Figure 1). Paleoseismological investigations across some of the fault splays within the hanging wall of the main Mt. Marine fault identified multiple Late Quaternary surface-rupturing earthquakes. However, these studies have explored only some of the faults belonging to a more complex fault system (Figure 1b). In order to have an actual assessment of the FDH, it is important to observe whether all the fault splays are capable of producing surface ruptures and are active during the Late Quaternary with the same rates, or instead fault activity localises on some specific fault splays through time. To answer to this question, we have performed two paleoseismological surveys aimed at intercepting most of the fault splays belonging to the Mt. Marine fault. We show that there are at least five principal faults with evidence of repeated Holocene surface-rupturing earthquakes and different slip rates. We discuss the role of the identification and characterization of multiple capable faults in urban areas in taking action to mitigate the risk associated to the FDH.

METHODS

The paleoseismological trenches have been planned in order to explore (i) potential fault scarps modified by anthropogenic activity, identified through fieldwork, LiDAR and aerial photographs analysis, and (ii) discontinuities in the stratigraphic record highlighted by geophysical investigations (Electrical Resistivity Tomography (ERT), Ground Penetrating Radar (GPR)).

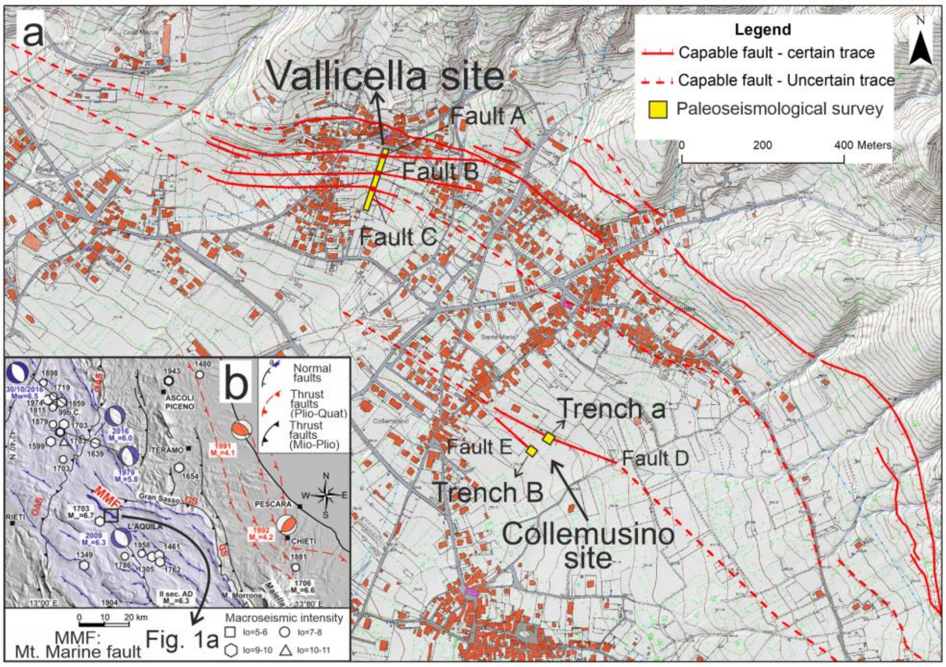

Figure 1. Location map of the study area. a) Location of the paleoseismological surveys across the multiple splays of the Mt. Marine fault. b) Location of the Mt. Marine fault within the Central Apennines Fault System. Historical earthquakes are from CPTI15 (Rovida et al., 2020).

The first paleoseismological survey (Vallicella site) is characterised by a continuous trench about 156 m long and 2.5 m deep. This trench aimed at verifying the nature of multiple topographic scarps and discontinuities in the stratigraphic record highlighted by the geophysical investigations. The second paleoseismological survey (Collemusino site) is composed by two adjacent smaller trenches of length about 20 m (Trench A) and 13 m (Trench B). These trenches aimed at exploring the nature of discontinuities in the stratigraphic record highlighted by the geophysical investigations.

The ages of the stratigraphic units were constrained by radiocarbon dating, performed at the Beta Analyitic Laboratory (Miami, FL, USA).

RESULTS AND DISCUSSION

The Vallicella site

The paleoseismological survey exposed three main faults, arranged both synthetic (Fault A and C, Figure 2a, 2b and 2d), and antithetic (Fault B, Figure 2c) to the principal Mt. Marine fault. The stratigraphic setting of the three faults is characterised by Upper Pleistocene alluvial fan deposits in the footwall of the faults, and Holocene colluvial deposits in their hanging wall. Stratigraphic units have been numbered as a whole for the entire trench, according to their combined stratigraphic position.

Fault A is characterised by a main SW-dipping fault plane (F1, Figure 2a,b), and minor faults located within its footwall (F2 – F3, Figure 2a,b). The stratigraphic record of the fault provides evidence of five surface-rupturing earthquakes. The Most-Recent Event (E1A-MRE) is suggested by the offset of the base of Unit 1 along the faults F2 and F3 (Figure 2a,b). The minimum measured offset is 12 cm, although Unit 1 has been severely reworked by anthropic activity through time. The age of the basal part of Unit 1 has been constrained in multiple localities along the trench wall, with ages being 321 BC-202 BC (sample Fb3c, Figure 2c) and 116 AD-239 AD (sample Fc6c, Figure 2d). This suggests that E1A-MRE could be representative of the 1703 AD earthquake, given that there are no other known earthquakes associated with the Mt. Marine fault in historical catalogues (Rovida et al., 2020). The penultimate event (E2-A) is shown along F1, and it is constrained by the faulting of the colluvial wedge CW1 (Figure 2a,b). No data are available to measure the coseismic offset of E2A. The *post-quem* term of the earthquake is provided by sample Fa10c (1888 BC-1792 BC) collected in Unit 3 (Figure 2b). F1 seems to be sealed by the base of Unit 1, suggesting that the earthquake occurred before its deposition. The previous event (E3A) caused the formation of CW1. The time range of occurrence of E3A is constrained by samples Fa6c (3769-3642 BC) and Fa10c (1888-1792 BC) (Figure 2b). The maximum vertical thickness of CW1 is about 60 cm. This therefore represent a minimum coseismic throw, with a maximum coseismic throw that could be as high as ~1.2 m, assuming that the coseismic offset is double the thickness of the colluvial wedge (e.g. McCalpin, 2009). Event E4A caused the faulting of CW2 (Figure 2a), with a vertical offset of about 70 cm. Event E5A caused the deposition of CW2 (Figure 2a,b). The thickness of CW2 is ~30 cm, therefore the coseismic throw could be up to ~60 cm, assuming again that the offset to be double the thickness of the colluvial wedge. Time constraints for E4A and E5A are provided by samples Fa8 (6076-5990 BC) and Fa6 (3769-3642 BC). Both E4A and E5A should have occurred within this time range.

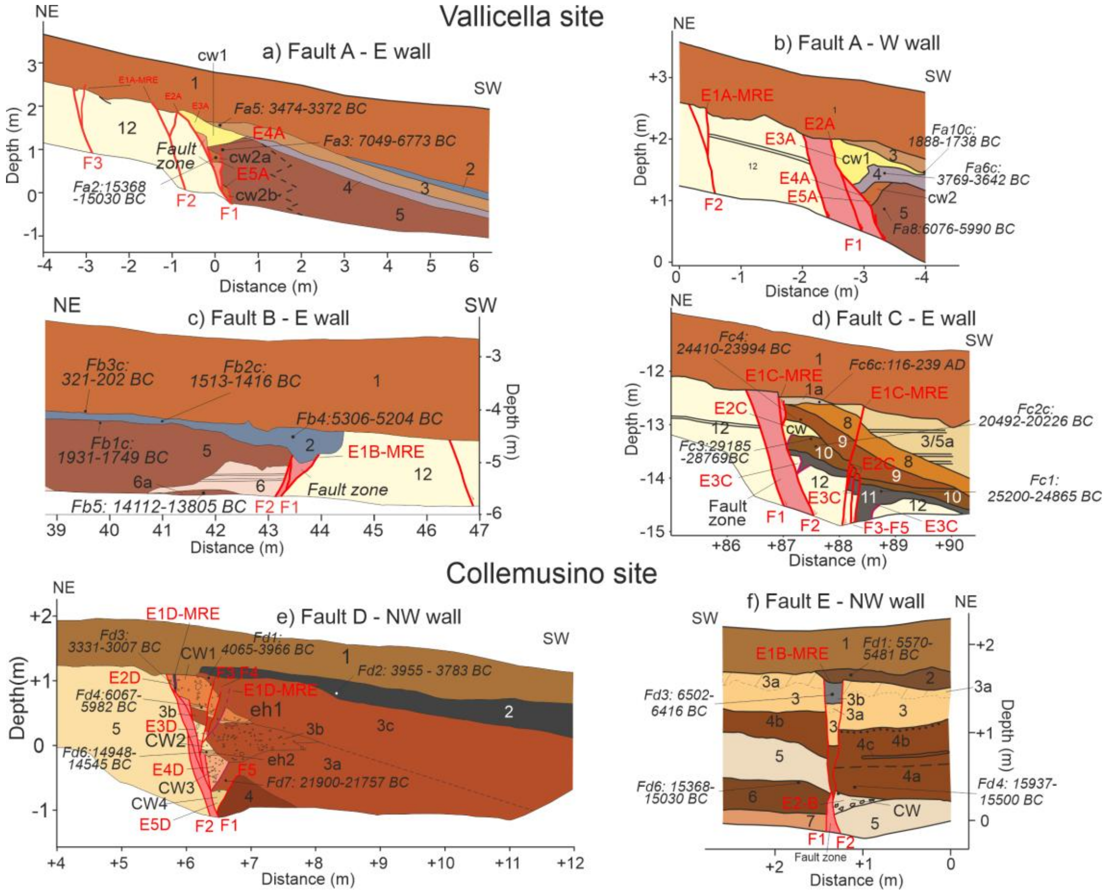

Figure 2. Stratigraphic logs of the faults shown by the paleoseismological trenches (location of the trenches in Fig.1).

Fault B is located 44 m SW of Fault A (Figure 1a). It is characterised by two NE-dipping fault planes showing evidence of one surface-rupturing earthquake (E1B-MRE; Figure 2c). The minimum measured vertical displacement is 12 cm, measured as the offset of the base of Unit 2 along F1. The time constraints for this earthquake are provided by samples Fb1c (1931-1749 BC) and Fb3c (321-202 BC).

Fault C is located 43 m SW of Fault B (Figure 1a). It is composed by a main SW-dipping fault splay (F1-F2 in Figure 2d) and a set of about vertical, slightly NE-dipping pseudo-reverse fault planes cutting across the colluvial deposits in the hanging wall of F2 (F3-F4-F5, Figure 2d). The stratigraphy shows evidence of three past earthquakes. The most recent one (E1C-MRE) cuts across the entire stratigraphy along both the main fault and the main hanging wall splay (F2 and F3, Figure 2d). The minimum cumulative offset is 24 cm. The offset of Unit 1a, dated 116-239 AD, allows us to suggest that E1C-MRE is representative of the 1703 AD earthquake. The penultimate event (E2C) caused the formation of the colluvial wedge CW and ruptured along most of the hanging wall fault splays (Figure 2d). The estimated cumulative minimum throw is 80 cm. E2C occurred prior to the deposition of Unit 9, dated 24410-23994 BC (sample Fc4). The oldest event (E3C) caused slip and opening of extensional fissures along both the main fault and the hanging wall splays (Figure 2d). The cumulative minimum throw, measured along the minor hanging wall splays, is 40 cm. The fissures are filled up by Unit 11, a colluvial unit that should have been deposited after the fractures have formed. Therefore, the age of Unit 11 (25200 - 24865 BC, sample Fc1) postdates E3C.

The Collemusino site

The two paleoseismological trenches of the Collemusino site highlighted the presence of a main SW-dipping fault (FD) in Trench A, synthetic to the principal Mt. Marine fault, and a NE-dipping secondary fault (FE) in Trench B, antithetic to the principal Mt. Marine fault (Figure 1b).

FD is characterised by a principal SW-dipping fault plane and a set of minor faults and open fissures in its hanging wall (Figure 2e), imposed in a stratigraphy of Upper Pleistocene alluvial fan deposits and Upper Pleistocene-Holocene colluvial deposits. FD recorded evidence of five past earthquakes. The most recent one (E1D-MRE) cut the entire stratigraphy along F1, being apparently sealed by Unit 1, and ruptured also along F3-F4 up to at least Unit 3c. The offset associated with the minor faults is about 10 cm, it is not possible to estimate the coseismic offset along the main fault. The infilling of a fissure within CW1 (sample Fd3, 3331-3007 BC) is interpreted to be the soil at the time of the E1D-MRE, therefore its age should predate the event. The penultimate event (E2D) caused the formation of the colluvial wedge CW1. The vertical offset estimated by the doubling the thickness of the wedge is ~90 cm. The time interval within which the earthquake occurred is 6067-5982 BC (Sample Fd4) and

4065-3966 BC (Sample Fd1). The event E3D is constrained by the formation of the colluvial wedge CW2. The vertical thickness of CW2 is 27 cm, therefore the coseismic throw could be as high as ~54 cm. The time interval within which the earthquake occurred is 14948-14545 BC (Sample Fd6) and 6067-5982 BC (Sample Fd4). The event E4D is constrained by an open fissure along the main fault splay infilled with material that recalls a colluvial wedge, for lithology and texture (Figure 2e). It is not possible to estimate the offset of the earthquake. The time interval within which the earthquake occurred is 21900-21757 BC (Sample Fd7) and 14948-14545 BC (Sample Fd6). The oldest event, E5D, is constrained by CW4, a unit localised in the hanging wall of both the main fault splay F2 and a secondary antithetic splay, F5 (Figure 2e). It is not possible to estimate the offset of the earthquake. This earthquake occurred prior to the deposition of Unit 3a, dated 21900-21757 BC (Sample Fd7).

FE is characterised by two sub-vertical NE-dipping faults. The stratigraphic setting is characterised by Upper Pleistocene alluvial fans and paleosols, and Holocene alluvial and colluvial deposits. FE shows evidence of two earthquakes. The most recent one (E1F-MRE) cuts the entire stratigraphy and it is sealed by Unit 2. The earthquake caused the collapse of the stratigraphy within F1 and F2, which has then been infilled by the paleosol of Unit 3a (marked as Unit 3b within the fissure, Figure 2f). The dating of Unit 3b (sample Fd3, 6502-6416 BC) therefore should predate E1F-MRE. The older earthquake, E2F, is constrained by the colluvial wedge CW, lying over the top of Unit 5 (Figure 2f). Moreover, the top of Unit 5 in the footwall seems to have retreated from its original position in proximity of the fault plane. The same nature of the sedimentary material forming both Unit 5 and CW suggests that the latter is made of the eroded material of Unit 5. The offset associated with E2F is 55 cm, calculated as the offset of the top of Unit 5 minus the offset associated with E1F-MRE. The age of Unit 6 immediately underneath Unit 5 dates the age of E2F to be post 15368-15030 BC (sample Fd6).

Overall, our study provides evidence of the occurrence of several surface-rupturing earthquakes on multiple fault splays arranged parallel to the strike of the main Mt. Marine fault. We show that multiple synthetic and antithetic fault splays have been active during the Late Pleistocene-Holocene, with most of the activity being localised on the synthetic faults. The studied faults seem to have different slip rates: FA experienced 5 earthquakes during the last 8 ka, FC shows evidence of two older earthquakes (>24 ka) and of a very recent one (1703 AD), FD experienced 5 earthquakes in the last 22 ka. Although the stratigraphic record of FC might be influenced by erosional processes that have possibly elided evidence of paleoearthquakes, our results suggest that most of the recent activity has been localised on FA. More work is needed to confirm this by comparing our results with existing paleoseismological studies on the Mt. Marine fault (e.g. Moro et al., 2002; 2016; Galli et al., 2011).

Moreover, our findings provide multiple insights on different aspects of seismic hazard. Firstly, we reiterate the crucial role that paleoseismological studies have in assessing the FDH in urban areas. That is because they have the ability to unveil active faults also where the anthropic activity may have elided their surficial evidence. Secondly, our study shows that multiple fault splays belonging to a principal fault are active during the Late Pleistocene-Holocene, suggesting that their simultaneous rupture during large earthquakes is a recurrent feature through time. Thirdly, the different slip rates we observe between the studied faults suggest that the earthquake activity may be localised on specific faults through time. This provides important insights also on probabilistic approaches for the FDH, because knowing where most of the activity is localised in recent time could help in weighing the probability of occurrence of fault displacement in future earthquakes, even if the studied faults appear to belong to the same fault ranking (e.g. Baize et al., 2019).

ACKOWLEDGEMENTS

This work was realized under the agreement between the University of Chieti-Pescara (Dep. INGEO) and the National Institute of Geophysics and Vulcanology (INGV): "Ridefinizione delle Zone di Attenzione delle Faglie Attive e Capaci emerse dagli studi di microzonazione sismica effettuati nel territorio dei Centri abitati di Barete e Pizzoli in provincia de L'Aquila, interessati dagli eventi sismici verificatisi a far data dal 24 agosto 2016", funded by the Commissioner structure for post-earthquake reconstruction of the Italian Government.

REFERENCES

Baize, S., Nurminen, F., Sarmiento, A., Dawson, T., Takao, M., Scotti, O., et al. (2020). A worldwide and unified database of surface ruptures (SURE) for fault displacement hazard analyses. Seismological Research Letters, 91(1), 499-520.

Blumetti A.M., 1995. Neotectonic Investigations and Evidence of Paleoseismicity in the Epicentral Area of the January-February 1703, Central Italy, Earthquakes. Perspectives in Paleoseismology, 7, 83-100.

Galli P., Giaccio B., Messina P., Peronace E., Zuppi G.M., 2011. Paleoseismology of the L'Aquila faults (Central Italy, 2009, Mw 6.3 earthquake): implications for active fault linkage. Geophysical Journal International, 187, 1119-1134.

McCalpin, J.P. (2009) Paleoseismology. 2nd Edition, Academic Press, Amsterdam-London, 615 p. (International Series, 95).

Moro M., Bosi V., Galadini F., Galli P., Giaccio B., Messina P., Sposato A., 2002. Analisi paleosismologiche lungo la faglia del M. Marine (Alta Valle dell'Aterno): risultati preliminari. Il Quaternario – Italian Journal of Quaternary Sciences, 15(2), 259-270.

Moro M., Falcucci E., Gori S., Saroli M., Galadini F., 2016. New paleoseismic data across the Mt. Marine Fault between the 2016 Amatrice and 2009 L'Aquila seismic sequances (Central Apennines). Annals of Geophysics, 59, Fast Track 5.

Rovida A, Locati M., Camassi R., Lolli B., Gasperini P. (2020). The Italian earthquake catalogue CPTI15. Bullettin of Earthquake Engineering 18(7), https://doi.org/10.1007/s10518-020-00818-y

INQUA Focus Group on Paleoseismology and Active Tectonics

paleoseismicity.org

Interactions between active tectonics and gravitational deformation along the Billecocha fault system (Northern Ecuador): insights from morphological and paleoseismological investigations

Jomard H. (1), Saqui D. (2), Baize S. (1), Alvarado A. (2), Bernard B. (2), Audin L. (3), Hidalgo S. (2), Pacheco D. (2), Ruiz M. (2) and Segovia M. (2)

(1) Institut de Radioprotection et Sûreté Nucléaire, 92262 Fontenay-aux-Roses, France
(2) Instituto Geofísico, Escuela Politécnica Nacional (IG-EPN), Ap. DI. 01-2759, Quito, Ecuador
(3) Institut des Sciences de la Terre, IRD: UR219, Université Joseph Fourier–Grenoble I–INSU–OSUG, Grenoble, France

Abstract: *The Billecocha plateau (4000 m a.s.l.) lies in the high elevation Ecuadorian Andes volcanic arc and overhangs by 2000 m above the interandean valley. The area is heavily affected by active faulting characterized by straight, sharp and discontinuous scarps within a 6km wide and 24km long corridor. The instrumental seismicity recorded around the BFS is low, however, a M≈7,2 earthquake heavily struck the region in 1868.*
With the aim to discuss the kinematic and coseismic nature of the encountered deformations as well as the seismogenic character of the BFS, we performed (1) morphological analysis to map and quantify evidence of active faulting and (2) paleoseismological investigations across the longer segment of the fault system.
In three trenches, we show that surface deformations are coseismic in origin during the Holocene, the last paleoseismic event being compatible in date with the 1868 earthquake. In addition, some of the enlightened paleoseismic events could have occurred in relationship with volcanic eruptions of the surrounding volcanoes.
However, while paleoseismological evidences suggests that regional tectonics could be involved, the geomorphological signature of the BFS at the mountain scale is compatible with the development of deep-seated gravitational deformations (DSGSD), suggesting an interaction between boundary (tectonic, volcanic) and body forces (gravity, post-glacial rebound).

Key words*: Ecuador, Active tectonics, Paleoseismology, deep seated gravitational slope deformations (DSGSD)*

INTRODUCTION

In the high mountains of Ecuador, a fault system affecting the Billecocha plateau (≈4000 m a.s.l.) and surroundings presents outstanding landforms related to active faulting (Fig. 1). A study published by Ego et al. (1996), the only one published to date concerning the Billecocha fault system (hereafter mentioned as BFS), concludes that the faults observed at the surface are not related to active tectonics but to lithospheric forces, and most likely due to the unloading of the Billecocha plateau after the last deglaciation. In contrast, a more recent study concludes that regional active faults (including the BFS) belongs to a wider dextral strike-slip fault system, in agreement with regional seismotectonic data (Alvarado et al., 2016).

Fig. 1: Picture of one of the principal fault segments of the Billecocha fault system (BFS).

We present a synthesis from new geomorphological analysis based on a high-resolution digital surface model (DSM) available at the country scale, and from paleoseismological data acquired during a field campaign in 2018. Our objectives being to refine the available fault mapping, estimate fault cumulative offset and slip history, and finally shed new light on the type of kinematics related to this fault system.

GENERAL SETTINGS

The Billecocha region (Fig.2) belongs to the northern part of the Western Cordillera. It encompasses the Billecocha plateau composed of cretaceous to Miocene sedimentary and volcanic formations., the Pleistocene Cotacachi (4937m a.s.l.) and Chachimbiro volcanoes (4076m a.s.l.) located repectively south and north of the plateau, and finally the slope running from the plateau toward the inter-andean Valley (IAV), corresponding to the eastern edge of the Western cordillera. This basement is ultimately covered by late Pleistocene/Holocene glacial and post glacial deposits, on which marshes and Andean páramo develop.
The eastern edge of the Western Cordillera is highly deformed along the Pujilí suture zone (Fig. 2) acting as a major tectonic boundary since the Cretaceous. Some segments of this large-scale structure have been characterized active and capable of producing earthquakes

(Alvarado et al., 2016). Among them, the BFS (Fig. 2) was described as a section of a larger system of dextral faults of unknown slip rates, probably less than 1mm/yr (Egüez et al., 2003). However, its morphological signature led Ego et al., (1996) to propose a normal kinematics and an origin due to local processes different from far-field tectonics.

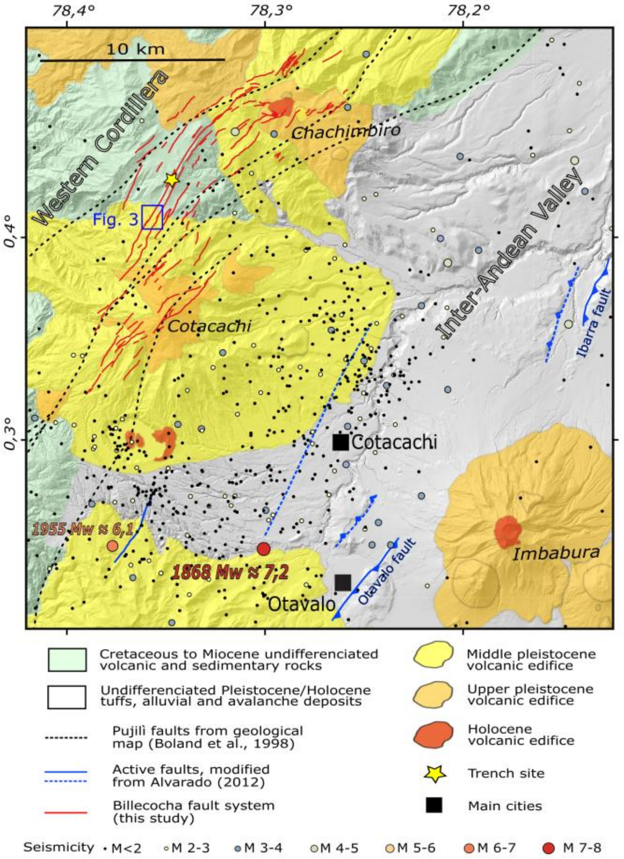

Fig. 2: Map of the Billecocha area, including the main geological units, the available seismicity catalogues and the Billecocha fault system (BFS) mapped during this study.

Instrumental seismicity rates and earthquake magnitudes are low in the region (Fig. 2). The few available focal mechanisms are compatible with right-lateral strike-slip motion and E-W shortening (Vaca et al., 2019). This stress regime is coherent with active faults mapped within the IAV, showing both reverse and right lateral strike slip evidences (e.g. Otavalo and Ibarra faults, Fig. 2).

However, two significant historical earthquakes have struck the area in 1868 (M≈7,2) and 1955 (M≈6,1). In particular, the 1868 Imbabura (or Ibarra) earthquake caused widespread damages and environmental effects. Beauval et al (2010) proposed an epicentral area compatible with its occurrence at or near Billecocha. This then makes the BFS a possible candidate for being the source of this earthquake.

RESULTS

Geomorphic signature of the BFS

Taking advantage of the 4 meters spatial resolution DSM available at the national scale, we mapped a series of 140 lineaments, occurring in a 24km long and 6km wide zone.

Faults are mainly linear, cutting sharply the crossed morphologies and deposits (Fig 1.). Faults are better expressed within the plateau and near the crests, more discontinuous in steep slopes, especially those toward the IAV where linear incision is higher. The BFS has a strong influence on the drainage system and related morphologies and deposits. This is especially the case along the Billecocha plateau where the slope gently dips toward the west and where fault scarps are, on the contrary, facing to the east. Such a configuration allows development of a series of ponds and river captures (Fig. 3).

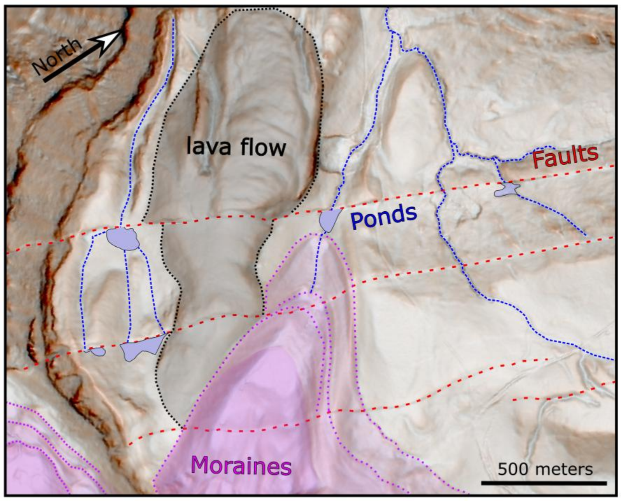

Fig. 3 : Focus on the main Billecocha fault strands (see location on Fig. 2), affecting frontal moraines and a Pleistocene lava flow. The main drainage system is presented as blue dotted lines and ponds developed along fault strands in blue. The basemap is a multidirectional hillshade derived from the 4m resolution DSM.

A careful analysis confirms that the geomorphic expression of active deformations along the BFS is predominantly dip-slip, with no significant cumulative horizontal movements, at least detectable with the 4m resolution DSM:

- Fluvial incision courses highlight evidence of either possible right or left lateral deflections, so that they couldn't be considered here as a relevant marker;
- A Pleistocene lava flow (Fig. 3), registering long-term deformations, show opposite apparent lateral deflections, compatible with dominant vertical deformations,
- The shape of ponds that developed along the BFS is often symmetrical around their outlet. There is no detectable and systematic lateral migration of the outlets;

• Crest lines does not provide evidence of any cumulative lateral deformations.

Hence, in order to discuss the origin of the vertical deformations, we performed ≈200 scarp-heights measurements from slope profile analysis along the different fault strands of BFS, attributing a positive displacement value for the east facing scarps and a negative to the west facing ones. We then performed an interpolation between those points in order to recover and discuss their spatial repartition with respect to the main relief (Fig. 4).

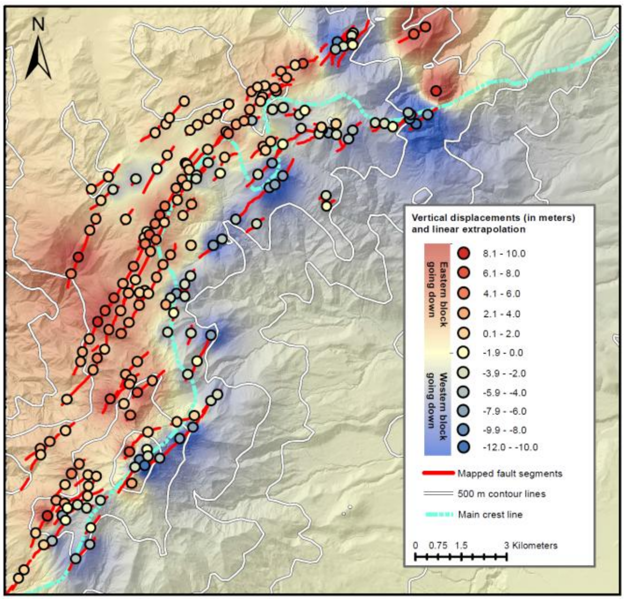

Fig. 4 : Vertical offset measurements performed along the BFS and comparison with respect to the crest-line (blue line). A blue color represents a west facing scarp while a red dot represents an east facing scarp, the density of the color depends on the quantity of deformation (light-smaller, dark-bigger).

Our main observation is that the crest separating the plateau from the slopes toward the IAV roughly coincides with a transition zone between east and west facing scarps, except for a clear outlier at the northern edge of the BFS, identified as a localized gravitational movement locally enhancing vertical deformations. Such a spatial repartition allows to highlight that the relief has a significant influence in controlling the direction of vertical motions observed along the BFS, meaning that at least part of these deformations could be gravitational in origin. The spatial extent of deformations would then imply considering a model compatible with the involvement of the entire slope during deep seated gravitational slope deformations (DSGSD).

Paleoseismological investigations

Three paleoseismological trenches were dug along the longer continuous fault segment (Fig. 5) in order to evidence the possible coseismic character of deformations at surface.

Trench 1 is the biggest, reaching 13m long and 3m deep, until the water table. Trench 2 and 3 are shorter (8.5 and 6m long respectively) and shallower (2 and 1m depth respectively). Trench 1 is the farthest from the pond outlet, where the scarp is higher and where the longest potential seismic record is expected. Trenches 2 and 3 are closer to the pond outlet, where the sedimentation is the most recent and where the most recent events may be captured.

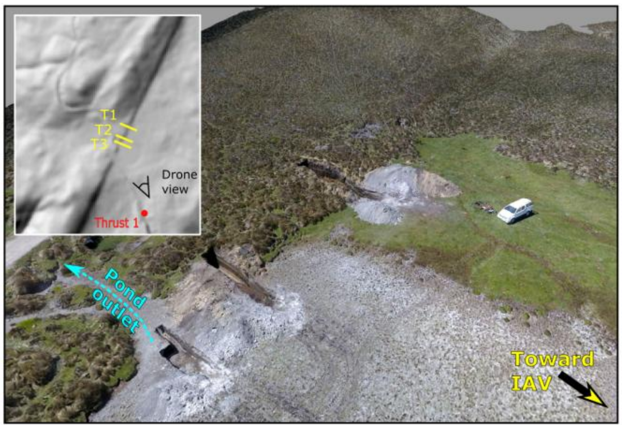

Fig. 5: Location of trenches T1, T2 and T3, and location of the road cut exposure (RF1). The trench site location (WGS84 coordinates: 0.4301°N; -78,3448°E) is reported on Fig. 2.

From our trench analysis (Fig.6), up to 7 and at least 6 distinct events occurred during the last ~6000 yrs. The last of them being compatible with the 1868 earthquake. Events are reported in table 1, as well as their possible relationships with known volcanic eruptions (following criteria proposed by Villamor et al., 2011). The reported offsets are those measured along the different fault strands, but they should be considered as minimum offsets because: (1) part of the deformation appear to be diffuse, (2) a lateral component of deformation is noticeable.

We stress that the peculiarity of the andisols (i.e. páramo) strongly limits their use as reliable markers of tectonic displacements because they continuously develop on ash-falls deposited along pre-existing topographies, hence possibly mimicking previous offsets. Geophysical investigations at the trench site however allowed to quantify a local cumulative vertical offset of 4.5 to 5 meters during a period ranging from 11202 yr. cal BP and 7722 yr. cal BP, hence providing a first order Holocene vertical separation rate of 0.4 - 0.65 mm/y along this fault segment.

Paleoseismic event	Datings (median calibrated ages) An underlined date indicates the best stratigraphic solution		Offset (i.e. without strike-slip component)	Relation to contemporary v eruption (red: possible ; green: prol
	Postdates (in yr. Cal. BP)	Predates (in yr. Cal. BP)		
E1	283 (and probably 183)	-	> 5-10 cm (trench 2)	No known eruption
E2* (possibly related to E1)	283	183 ?	~10 cm (trench 3)	No known eruption
E3	1579	1289	10 cm (trench 3)	No known eruption
E4	<u>1579</u>	1289	30cm (trench 2) >50cm (trench 1)	Chachimbiro (this stud
E5	2225	<u>1579</u>	5-10 cm (trench 2)	Chachimbiro (this stud
E6	6189	<u>5399</u>	~18 cm (trench 1)	Chachimbiro satellite dc (Bernard et al., 2011, 20

Table 1 : characteristics of paleoearthquakes derived from trench analysis. The possible relationships with known volcanic activity is also reported.

CONCLUSION

There is apparently not a single process obviously explaining our observations at the BFS:

- The main vertical signature of the BFS is compatible with gravitational processes occurring along an inherited tectonic structure. However, the source of such gravitational deformations may come from different processes acting at different timescales, from glacial unloading during the early Holocene, to volcanic and earthquake triggering.
- Evidences of coseismic deformations observed in trenches, where slight horizontal movements have been observed and where the 1868 earthquake is possibly recorded are compatible with the additional involvement of tectonic or volcano-tectonic processes.

Given the available data, we suggest that the BFS actually records the tectonic reactivation of the inherited Pujilí suture, enhanced by gravitational phenomenon. In this light, paleoearthquakes identified along the BFS may help evidencing the recurrence of major events in the region. However, it implies that the observed surface deformations shall not be used to derive fault slip rates for seismic hazard calculations.

Acknowledgements: Field word founded by Instituto Geofisico (EPN de Quito); LMISVAN from the "Institut pour la Recherche et le Développement"; ANR-REMAKE project from the "Agence Nationale pour la Recherche" , and proper funds from the IRSN.
Further details available in https://doi.org/10.1016/j.jsames.2021.103406

References

- Alvarado, A., Audin, L., Nocquet, J.M., Jaillard, E., Mothes, P., Jarrín, P., et al. (2016). Partitioning of oblique convergence in the Northern Andes subduction zone: Migration history and the present-day boundary of the North Andean Sliver in Ecuador. Tectonics.
- Beauval, C., Yepes, H., Bakun, W. H., Egred, J., Alvarado, A., & Singaucho, J. C. (2010). Locations and magnitudes of historical earthquakes in the Sierra of Ecuador (1587–1996). Geophysical Journal International, 181(3), 1613-1633.
- Ego, F., Sébrier, M., Carey-Gailhardis, E., & Beate, B. (1996). Do the Billecocha normal faults (Ecuador) reveal extension due to lithospheric body forces in the northern Andes? Tectonophysics, 265(3-4), 255-273.
- Egüez, A., Alvarado, A., Yepes, H., Machette, M. N., Costa, C., Dart, R. L., & Bradley, L. A. (2003). Database and map of Quaternary faults and folds of Ecuador and its offshore regions. US Geological Survey Open-File Report, 3, 289.
- Vaca, S., Vallée, M., Nocquet, J. M., & Alvarado, A. (2019). Active deformation in Ecuador enlightened by a new waveform-based catalog of earthquake focal mechanisms. Journal of South American Earth Sciences, 93, 449-461.
- Villamor, P., Berryman, K. R., Nairn, I. A., Wilson, K., Litchfield, N., & Ries, W. (2011). Associations between volcanic eruptions from Okataina volcanic center and surface rupture of nearby active faults, Taupo rift, New Zealand: Insights into the nature of volcano-tectonic interactions. GSA Bulletin, 123(7-8), 1383-1405.

Fig. 6: Trench logs of trenches 1, 2 and 3 (from top to bottom) Location of samples for mineralogical analysis of tephra (green), and results of C14 dating (mean calibrated ages)

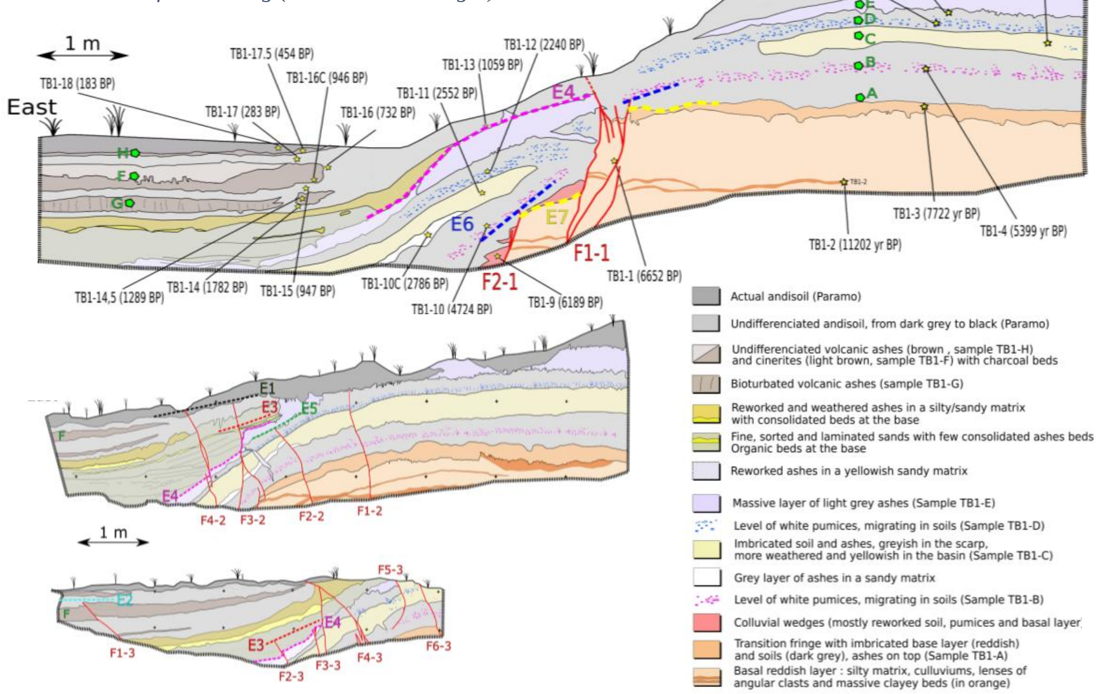

INQUA Focus Group Terrestrial Processes Perturbed by Tectonics (TPPT)

paleoseismicity.org

Seismotectonic activity in the Cotentin Peninsula and the Normano-Breton Gulf (NW France).

Tassadit KACI (1), Anne DUPERRET *(1)*, Yann MEAR *(2)*, David GRAINDORGE *(3)*, Bernard LE GALL *(3)*, Julie PERROT *(3)*, Stéphane BAIZE *(4)*

(1) Normandie Univ, UMR CNRS 6294 LOMC, Université Le Havre Normandie, France. tassadit.kaci@univ-lehavre.fr.
(2) EA 4253 LUSAC, CNAM-INTECHMER, Cherbourg-en-Cotentin, France.
(3) IUEM, UMR CNRS 6538, Géosciences Océan, Université de Bretagne Occidentale, Plouzané, France
(4) IRSN, BERSSIN, BP17, 92262 Fontenay-aux-Roses, France.

Abstract: *The Cotentin peninsula and the Normano-Breton Gulf are characterized by a low to moderate intraplate seismicity. To address the issue of the earthquake sources, we analyse a combination of offshore geomorphology, seismicity relocation and focal mechanism data. The detailed structural analysis from high-resolution bathymetry in the north of La Hague reveals a major fault system trending N150°E-N170°E inherited from the later stage of the Variscan orogeny. The Normano-Breton Gulf shows a similar fault system associated with N70°E-N90°E faults. The P-wave first motion polarities analysis of some major earthquakes located near Jersey (2014 and 2015) and Coutances (2020) associated with previously known focal mechanisms, show that these earthquakes could be related to the reactivation of major NW-SE Variscan structures, but also NE-SW structures linked to Cadomian shear zones.*

Key words*:* Cotentin, Structural inheritance, Submarine geomorphology, Seismicity, Active fault

INTRODUCTION

The Cotentin peninsula and the Normano-Breton Gulf is a unique region in Europe, where three orogens have succeeded between 2000 and 300 Ma. The region expresses a low to moderate seismotectonic activity (Beucler et al., 2022; Masson et al., 2019; Mazzotti et al., 2020) and is characterized by an intricate polyphased structural network (Fig. 1). The relationships between the regional inherited structures and the spatial repartition of earthquakes is a new challenge due to the scarcity of neotectonic evidence and the limitations of events registration (instrumental and historical). We cannot determine the relative contribution of the potential mechanisms conducting to the actual deformation. It can be considered probably related to mid-Atlantic ridge push and alpine compression, in addition to erosional and glacial processes and isostatic readjustment (Beucler et al., 2022; Mazzotti et al., 2020).
To understand whether the inherited regional structural network controls the current deformation, we analysed the recent seismicity. New focal mechanisms were calculated by a P-wave first motion polarity for some events located near Jersey (in 2014 and 2015) and Coutances (in 2020).

Structural Inheritance

The Cotentin and the Normano-Breton gulf are highly eroded and polyphased orogenic domains that recorded Cadomian and Variscan deformations. The south of the Cotentin peninsula (Fig. 1) is marked by a deep NE-SW fault system, corresponding to major Cadomian ductile shear zones (Bitri et al., 2001; Chantraine et al., 2001). From south to north, it is the Cancale-Granville Shear Zone (CGSZ), La Fresnaye-Coutances Shear Zone (LCSZ) and the Saint-Germain-sur-Ay Discontinuity (SGD). These shear zones are inherited from the Cadomian orogen (Le Gall et al., 2021) (Fig. 1). The LCSZ and SGD represent an important boundary that constraint the Paleozoic sedimentary basins to the north (Le Gall et al., 2021). The LCSZ appears to have controlled the repartition of the basins and has been rejuvenated during the permo-carboniferous distension (Pareyn, 1954) and the plio-pleistocene period (Pareyn, 1980). The LCSZ is identified in the BDFA database (French DataBase of Potentially Active Faults) as like a potentially active fault (Jomard et al., 2017).
The Proterozoic basement and the Paleozoic metasedimentary series have also preserved the Variscan deformation. A precise and complete structural picture of the Variscan pattern is deduced from the detailed structural analysis in the northwest Cotentin.

DATA AND RESULTS

A new high-resolution bathymetry map has been compiled by merging various datasets:
i) The Litto3D®, the land-sea altimetry database of the coastal fringe (2 km wide) with a planimetric resolution of 1 to 2m.
ii) The topographic data from the RGE Alti® (Référentiel Géographique à Grande Echelle) of IGN (Institut Géographique National) with a planimetric resolution of 1m, completed by Altimetric database BD Alti® (IGN) compiled from LiDAR acquisitions and airborne pictures, with a spatial resolution of 25m.

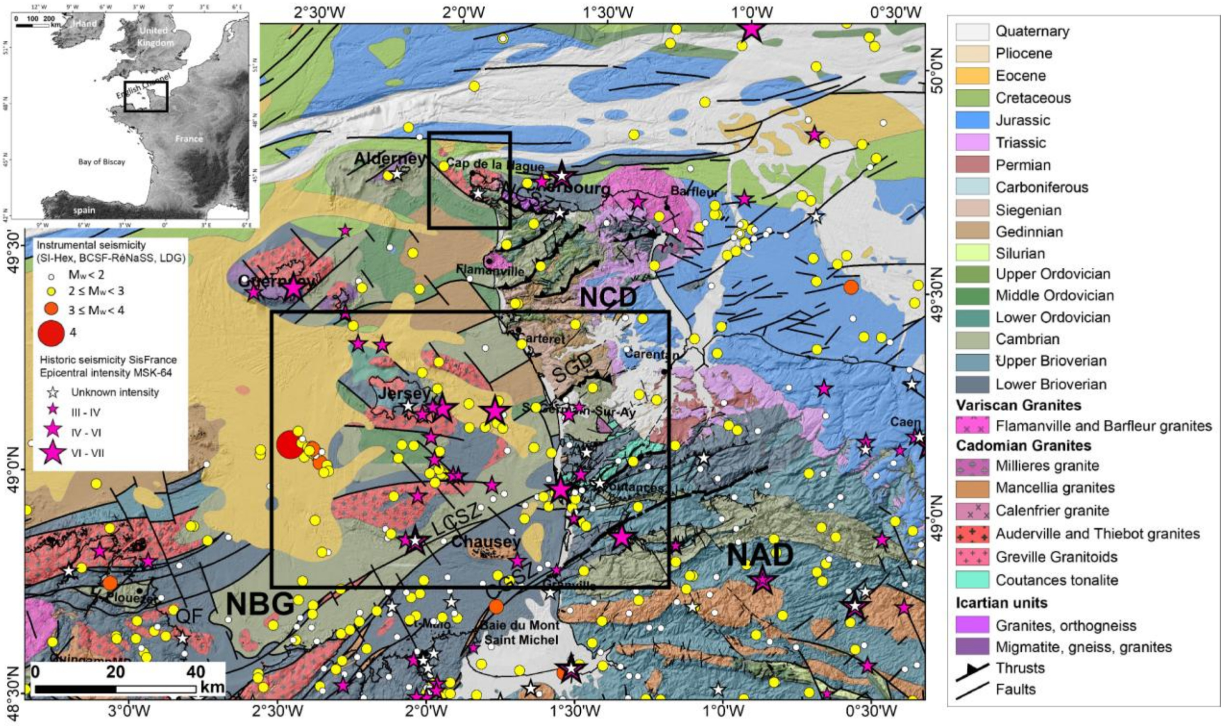

Figure 1: Instrumental seismicity from 1962 to 2020 (Cara et al., 2015) for 1962-2009 and unified catalog (LDG, BCSF-RéNaSS) for 2010-2021, coloured circles indicate earthquake magnitudes Mw. Historical seismicity between 1091 and 1962, SisFrance Catalog (www.sisfrance.net), Colour stars indicate epicentral intensity I0 MSK-64. Structural lineaments of the North Armorican Domain (NAD) and Normano-Breton Gulf (NBG) are modified from the BRGM geological maps (1/50 000 on land and 1/1000 000 off shore) and the Baie de Seine map (Benabdellouahed et al., 2014).

iii) The HOMONIM (*Historique, Observation, Modelisation des Niveaux Marins*) project for the main bathymetric dataset, acquired using multibeam echosounders collected between 2005 and 2017 (resolution up to 1m) or with single beam sounders (resolution up to 100m) (SHOM 2015).

iii) The multibeam echosounder around La Hague acquired with the R/V Haliotis (IFREMER) for shallow waters. The BATHAGUE cruises were performed in 2008 and 2010 west of La Hague cape (Bailly du Bois, 2008, 2010) and the COCOTEC cruise was conducted to the north of La Hague Cape (Duperret, 2019). They may reach a planar resolution of 1 m.

Structural Analysis

The produced continuous land-sea DEM (Fig. 2) provides the first comprehensive map covering Proterozoic and Paleo-Mesozoic units continuity offshore la Hague Cape. The contrast between the different units is very clear, as for the example the Meso-Cenozoic sedimentary cover. The resolution also allows us to identify a preserved network of ductile and brittle structures.

The inherited fault pattern is dominated by the N140°E-N170°E and N040°E-N070°E and N100°E-N120°E networks (Fig. 2).

Two major offshore dextral strike-slip faults are oriented N150° to N170° with a probable extensive component, west of Ecalgrain Bay and south of Moncaneval Bay, called the La Hague Offshore fault (LHOF) and the Moncaneval fault (MF), respectively (Fig. 2). These 5 to 12km long segmented two faults are affect the Icartian migmatite, Cadomian granites and Paleozoic units. The LHOF and MV show dextral strike-slope motion, as recognized with offsets of the fracture pattern on the bathymetry. The LHOF is sealed to the north by the Cretaceous sedimentary cover. We assume that these faults are initiated during the later stage of the Variscan orogeny (Dissler and Gresselin, 1988; Lagarde et al., 2003) and were later rejuvenated during the West European rifting and the Alpine compression (Baize, 1998). The relationship with the La Hague Jobourg fault (onshore), identified as a potentially active fault in the BDFA database, is still an open question. This NNW to NW-trending system of faults can be recognized at the regional scale, such as KF Kerforne type faults recognized along the SW Brittany coast (e.g. Raimbault et al., 2018).

Seismic Activity

To understand whether the regional structural network controls the current deformation, we have analysed the recent seismicity. First of all, we have compiled the historical seismicity catalogue (www.sisfrance.net) defined with the MSK-64 (Medvedev et al., 1964) intensity scale.

Before 1960, our research area experienced a few significant earthquakes with epicentral intensities reaching the VII MSK-64 (Fig. 1).

The first record of an earthquake in the Cotentin and the Normano-Breton Gulf dates back to 1091, in Granville city area. The highest epicentral intensity, VII MSK-64, was reached in the south Jersey islands, Normano-Breton gulf for the July 30th, 1926 event that is well documented in Amorèse et al (2020). Other notable earthquakes were recorded in Cherbourg area (North Cotentin): the July 30th 1889 event, and near Jersey Island with the February 17th 1926 events that reached an epicentral intensity of VI MSK-64.

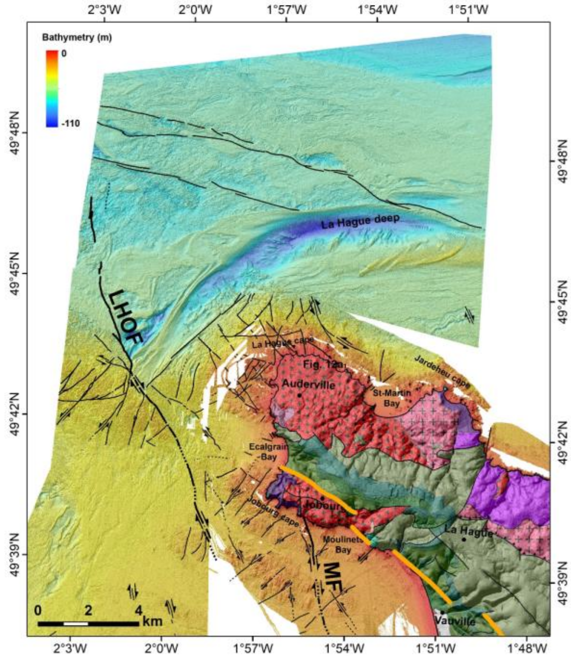

Figure 2: Detailed structural map of la Hague (North-west Cotentin peninsula) bases on our compiled DEM. Major lineaments are identified: LHOF: La Hague Offshore Fault; MF: Moncaneval Fault. Orange line corresponds to the La Hague-Jobourg fault segments (onshore), syn to post Pliocene potentially active fault (Jomard et al., 2017).

The Coutances April 1st 1853 event has an estimated epicentral intensity of VI-VII MSK-64 (Fig. 1).

The instrumental seismicity recorded after 1962 is produced by merging various datasets (Fig. 1). The SI-Hex project (Cara et al., 2015) is a homogenous catalog provided with moment magnitude for the 1962-2009 period. It was completed for the time period 2010 to 2021 by the BCSF-RéNaSS and the CEA catalogs. The two catalogs are only available with local magnitude ML which have been converted to M_W magnitudes using the relations defined for the SI-Hex catalog (Cara et al., 2015) updated in 2020. To ensure that we have a homogeneous and complete catalog, we allowed a comparison between the catalogs for the periods 2010-2011 and 2012-2021. Based on the completeness magnitude (M_c), number of stations, number of phases, RMS (Root Mean Square amplitude), we decided to choose the catalog CEA for the period 2010-2011 completed by the BCSF-RéNaSS catalog (2012-2021). The unified new instrumental catalog (1962–2021) reveals a significant seismic activity in the study area, more than 396 instrumental earthquakes have been recorded in the 59 last years. The highest moment magnitude Mw 4 (M_L 4.9) is reported for the July 11th 2014 event, located offshore SW Jersey islands (Fig. 1 and 3). In addition, more than 46% of the earthquakes in this region have an estimated moment magnitude (M_w) higher than the magnitude of the completeness M_c 2.

The seismicity is characterized by a diffuse spatial distribution in the NAD with a clustering in the south of Jersey island and east of Barfleur (NE Cotentin Peninsula). Fives new focal mechanisms have been determined in the NAD (Fig. 3) in addition to those determined in the west of France for more than thirty years (Lagarde et al., 2000; Mazabraud et al., 2005; Nicolas et al., 1990).

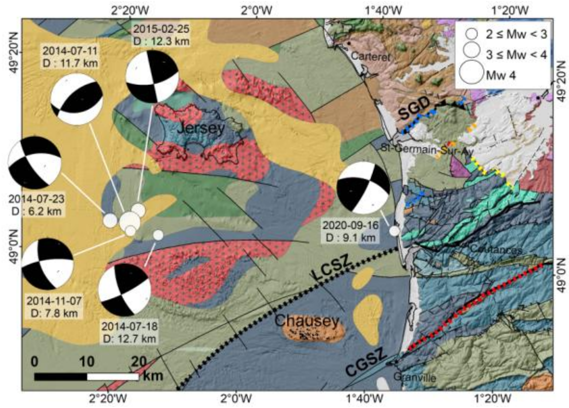

Figure 3: New Focal mechanisms of the recent earthquakes offshore Jersey (south Cotentin Peninsula). The white circles are the new epicentres locations expressed by a moment magnitude (M_w) of the unified catalog (See Figure 1). Major faults are reported from the geological map of France (Chantraine et al., 2003) *plotted in thin dark solid lines and the map of BDFA (Jomard et al., 2017). The age of last known movement is shown by a dotted lines colour (red: Quaternary; orange: Syn to post Pliocene; green: Syn to post late Miocene; blue: undetermined age; black: neotectonic map from Grellet et al., (1993).*

We used the method of analysis of P-wave first motion polarities recorded by the RESIF (Réseau Sismologique et Géodésique Français) and the BGS (British Geological Survey) seismic networks for the earthquakes that occurred between 2014-2015 in Jersey and 2020 near Coutances (Fig. 3). We used only the waveform of a closest seismological stations to the earthquake epicentres and the Seisan program and a most adapted velocity model NBCI already used by Amorèse (2000) adapted for our area.

The focal mechanisms are obtained from the P wave first motion polarities and calculated with FOCMEC and FPFIT software. The new relocation is different from those established by the RéNaSS for these events (Fig. 1 and 3). The focal mechanisms solutions show two possible solutions of strike-slip in two directions. The corresponding faults may be either N150°-170°E oriented like post Variscan regional structures or N70°-90°E oriented like Cadomian shear zones. They coincide with P and T axis orientations varying around NW-SE and NE-SW trending, respectively. They are consistent with the actual NW-SE to NNW-SSE compressional stress field (Fig. 3)

(Amorèse et al., 2000; Beucler et al., 2022; Delouis et al., 1993; Lagarde et al., 2003).

We consider also a potential activity along the variscan faults like LHOF and MF highlighted by the high-resolution bathymetric data in the North West Cotentin. In fact, along the LHOF, a major bathymetric relief (10m high) is preserved and may result from a tectonic offset maintained by bathymetric relief of the LHOF, in a very high energy tidal currents environment. Some solutions of the focal mechanisms determined to the south show consistent results, with the same orientation of some nodal planes than the previously described faults.

CONCLUSION

The distribution of seismicity in the Cotentin and the Normano-Breton Gulf is mainly diffuse with the presence of remarkable swarms of events in the northeast of the Cotentin (Barfleur) and south offshore the island of Jersey. The main earthquake recorded offshore Jersey (2014) reached a moment magnitude of Mw 4. The new analysis of the focal mechanism solutions highlights directions of the nodal planes related to the NW-SE and ENE-SSW fault system corresponding to the reactivated Variscan faults N150°E-N170°E and the Cadomian shear zone N060°-N070° (LCSZ and CGSZ). The focal mechanisms are consistent with the current state of stress with a compressional and tensional axis-oriented NW-SE and NE-SW, respectively. The onshore/offshore structural approach using high-resolution bathymetric data allows us to identify the existence of new unknown inherited Variscan structures (LHOF and MF) offshore La Hague cape (northwest of the Cotentin Peninsula) belonging to the NW-SE fault system that are potentially active. In these areas, where very poor geological data are available, we hope that the recent acquisition of high-resolution seismic reflection data (EMECHAT 2022, STOCKLINE 2020 and ECREHOU 1998) on some of the structures will provide more clarifications.

Acknowledgements

The present work has benefited from the financial support from the RIN Continuum Terre-Mer (CTM). The Doctoral thesis is funded by the Region Normandie (TD). The authors thank the PATADays for providing financial support (doctoral grant) to participate to this workshop.

REFERENCES

Amorèse, D., Walker, A., Lagarde, J.-L., Santoire, J.-P., Volant, P., Font, M., Lecornu, M., 2000. New seismotectonic data from an intraplate region: focal mechanisms in the Armorican Massif (northwestern France). Geophysical Journal International 143, 837–846. https://doi.org/10.1046/j.0956-540X.2000.01285.x

Baize, S., 1998. Tectonique, eustatisme et climat dans un système géomorphologique côtier. Le nord-ouest de la France au plio-pléistocène: exemple du Cotentin (Normandie) (Thèse). Caen.

Benabdellouahed, M., Dugué, O., Tessier, B., Thinon, I., Guennoc, P., Bourdillon, C., 2014. New geological map of the Bay of Seine and land-sea geological synthesis: Contribution of new seismic and biostratigraphic data 26.

Beucler, É. et al, 2022. Characteristics and possible origins of the seismicity in northwestern France. Comptes Rendus. Géoscience 353, 53–77. https://doi.org/10.5802/crgeos.86

Bitri, A., Brun, J.P., Truffert, C., Guennoc, P., 2001. Deep seismic imaging of the Cadomian thrust wedge of Northern Brittany. Tectonophysics 331, 65–80. https://doi.org/10.1016/S0040-1951(00)00236-5

Cara, M., Cansi, Y., Schlupp, A., Arroucau, P., Béthoux, N., Beucler, E., Bruno, S., Calvet, M., Chevrot, S., Deboissy, A., 2015. SI-Hex: a new catalogue of instrumental seismicity for metropolitan France. Bulletin de la Société Géologique de France 186, 3–19.

Chantraine, J., Autran, A., Cavelier, C., Alabouvette, B., Barféty, J.-C., Cecca, F., 2003. Carte géologique de la France à l'échelle du millionième.

Chantraine, J., Egal, E., Thiéblemont, D., Le Goff, E., Guerrot, C., Ballèvre, M., Guennoc, P., 2001. The Cadomian active margin (North Armorican Massif, France): a segment of the North Atlantic Panafrican belt. Tectonophysics 331, 1–18.

Delouis, B., Haessier, H., Cisternas, A., Rivera, L., 1993. Stress tensor determination in France and neighbouring regions. Tectonophysics 221, 25.

Dissler, E., Gresselin, F., 1988. The North cotentin shear-zone (Normandy-France): Variscan mobilization of the cadomian basement and its palaeozoic cover. Geological Journal 23, 191–204. https://doi.org/10.1002/gj.3350230301

Jomard, H., Cushing, E.M., Palumbo, L., Baize, S., David, C., Chartier, T., 2017. Transposing an active fault database into a seismic hazard fault model for nuclear facilities – Part 1: Building a database of potentially active faults (BDFA) for metropolitan France. Nat. Hazards Earth Syst. Sci. 17, 1573–1584. https://doi.org/10.5194/nhess-17-1573-2017

Lagarde, J., Baize, S., Amorese, D., Delcaillau, B., Font, M., Volant, P., 2000. Active tectonics, seismicity and geomorphology with special reference to Normandy (France) 15, 745–758.

Lagarde, J.L., Amorese, D., Font, M., Laville, E., Dugué, O., 2003. The structural evolution of the English Channel area: STRUCTURAL EVOLUTION OF THE ENGLISH CHANNEL AREA. J. Quaternary Sci. 18, 201–213. https://doi.org/10.1002/jqs.744

Le Gall, B., Authemayou, C., Graindorge, D., Duperret, A., Kaci, T., Ehrhold, A., Schmitt, T., 2021. Status of Basement Terranes in Orogens: Insights From the Cadomian Domain of the North Armorican Variscides, Western France. Tectonics 40. https://doi.org/10.1029/2020TC006578

Masson, C., Mazzotti, S., Vernant, P., Doerflinger, E., 2019. Extracting small deformation beyond individual station precision from dense Global Navigation Satellite System (GNSS) networks in France and western Europe. Solid Earth 10, 1905–1920. https://doi.org/10.5194/se-10-1905-2019

Mazabraud, Y., Béthoux, N., Deroussi, S., 2005. Characterisation of the seismological pattern in a slowly deforming intraplate region: Central and western France. Tectonophysics 409, 175–192. https://doi.org/10.1016/j.tecto.2005.08.021

Mazzotti, S., Jomard, H., Masson, F., 2020. Processes and deformation rates generating seismicity in metropolitan France and conterminous Western Europe. BSGF - Earth Sciences Bulletin 191, 19. https://doi.org/10.1051/bsgf/2020019

Nicolas, M., Santoire, J.P., Delpech, P.Y., 1990. Intraplate seismicity: new seismotectonic data in Western Europe. Tectonophysics 179, 27–53.

Pareyn, C., 1954. Le bassin houiller de Littry (Calvados). Bureau des Recherches géologiques, géophysiques et minières.

Raimbault, C., Duperret, A., Le Gall, B., Authemayou, C., 2018. Structural inheritance and coastal geomorphology in SW Brittany, France: An onshore/offshore integrated approach. Geomorphology 306, 141–154.

Vigneresse, J.-L., 1988. La fracturation post-hercynienne du Massif armoricain d'après les données géophysiques. Géologie de la France 4, 3–10.

New suggestion for the regulation of safe separation distance from active faults based on damage characteristics

Young-Seog Kim(1)(2), Yeji Hong(1), Kwangmin Jin(3)

(1) Active Fault & Earthquake Hazard Mitigation Institute, 45, Yongso-ro, Nam-gu, Busan, Republic of Korea.
(2) Pukyong National University, 45, Yongso-ro, Nam-gu, Busan, Republic of Korea. Email: ysk7909@pknu.ac.kr.
(3) Korea Institute of Geoscience and Mineral Resources, 124, Gwahak-ro, Yuseong-gu, Daejeon, Republic of Korea.

Abstract: *We suggest a new idea for the separation distance for safety based on previous studies of rupture characteristics. We classified the safe separation distance into three levels. First, zone 3 is defined as a wide notice zone to inform residents and property owners about the risk of earthquake hazards. Second, zone 2 is defined as a medium survey recommendation zone to recommend geological survey and seismic reinforcement when a development is planned within the area. Third, zone 1 is defined as a construction avoiding zone to strongly regulate the new construction of important facilities. In this study, we also considered fault types and related damage characteristics. For dip-slip faults, the safe separation distance for the hanging wall is suggested twice as wide as the footwall. For strike-slip faults, tip and linkage damage zones are considered and suggested to be establish 1.5 times wider than that of the main fault zone.*

Key words*: active fault, earthquake rupture hazard, surface rupture, safe separation distance.*

INTRODUCTION

The Korean Peninsula has historically been considered to be tectonically stable compared with other neighboring countries, because it is located at the Eurasian continental margin. However, more than 60 Quaternary faults have been reported in SE Korea (Kim et al, 2011; Jin et al., 2020). Recently, two moderate-sized earthquakes (2016 M_W=5.5 Gyeongju earthquake and 2017 M_W=5.4 Pohang earthquake) occurred in SE Korea, causing significant property damages. Thus, these have led to several intensive paleoseismological, structural, and seismological studies around this area.

The accumulated stresses along faults are released through large earthquakes, producing strong ground motion as well as surface ruptures, which result in permanent displacements (e.g. Bonilla et al., 1984). They also cause major losses of lives and extensive property damages. Because most large earthquakes are generated by the reactivation of pre-existing active faults, newly generated faults and joints are concentrated along or around active faults. Thus, earthquake prone areas could be avoided during site selection throughout identifying and deciphering active faults. In particular, it is necessary not only to establish the building regulation but also to determine the safe location for buildings against earthquake hazards based on reported active fault lines.

Actually, several countries, such as United States, New Zealand, and Italy, have already prepared related regulations (e.g. AP Act, 1999; Boncio et al., 2012; Boncio et al., 2018; Kerr et al., 2003; NTC08, 2008; Villamor et al., 2012). In Korea, because we just started to make a national active faults map, we now have to prepare proper guidelines for construction. This study focuses on the guidelines for the proper safe separation distances depending on damage patterns and fault types. Also, because this study is based on several overseas cases and damage factors, it is applicable to countries with relatively low earthquake activities such as Korea.

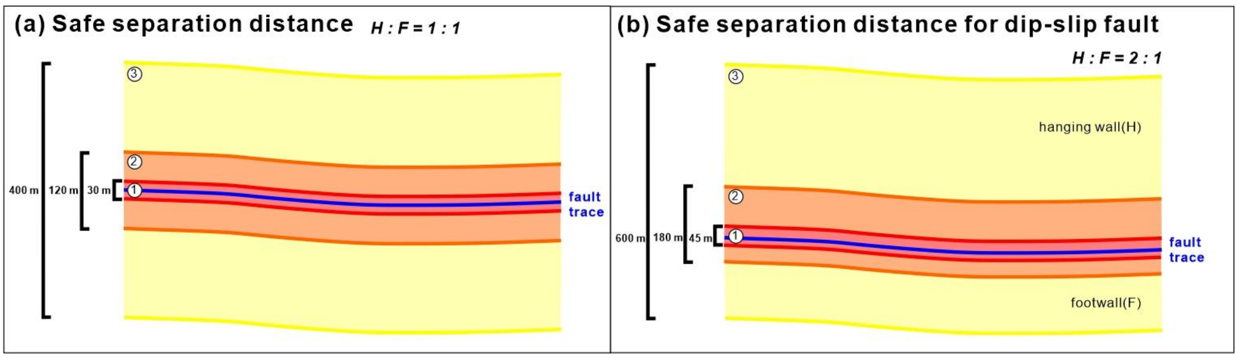

Figure 1: (a) General criteria of safe separation distacne from a fault trace. (b) Suggested safe separation distances for dis-slip faults. The safe separation distance ratio of hanging wall to foot-wall is 2:1.

SAFE SEPARATION DISTANCES FROM ACTIVE FAULTS

According to the regulations of the safe separation distance from several countries, such as United States, New Zealand, and Italy, it is estimated that the width of surface rupture zone on one side of a fault ranges from 60 to 200 m, assuming rupture zones are symmetrical along a fault trace. Also, most countries have consistently established the setback distance at least from 15 to 20 m, considering significant economic losses and uncertainties. Based on these previous studies and fault damage characteristics, we classified the safe separation distance into three levels. First, zone 3 is defined as 200 m each side (total 400 m) to inform residents and property owners about the earthquake hazards within the area. Second, zone 2 is defined as 60 m each side (total 120 m) to recommend geological investigation and anti-earthquake design if any development is planned within the area. Third, zone 1 is defined as 15 m each side (total 30 m) to restrict the development of new important facilities within the area, such as nuclear-related facilities, schools, and hospitals, etc. (Fig. 1a). Moreover, it is more useful if the safe separation distance is established in consideration of fault types and fault damage zones. For dip-slip faults, the safe separation distance on the hanging wall is considered twice as wide as that of the footwall as suggested by Italy. Therefore, we suggest the safe separation distance for the dip-slip faults as follows: 1) Zone 3 is totally defined as 600 m (400 m in hanging wall and 200 m in footwall, respectively), 2) Zone 2 is totally defined as 180 m (120 m in hanging wall and 60 m in footwall, respectively), and 3) Zone 1 as 45 m (30 m in hanging wall and 15 m in footwall, respectively) (Fig. 1b). For strike-slip faults, the separation distances of tip and linkage damage zones are wider than that of the wall damage zone along main fault trace (Fig. 2) (Kim et al., 2004). Especially, the linking damage zones caused by the interaction and linkage of two fault segments show relative complex and intensive fractures compared with other damage zones (Kim and Sanderson, 2004). Furthermore, the linkage damage patterns depend upon the stress conditions within the segment step zones, producing extensional and contractional steps. At the fault linkage, thus, transtention or transpression occurs depending on the slip-sense and stepping or bending. Tensile structures are formed when the direction of slip-sense is to the same as the direction of stepping, and compressional structures are formed when the direction of slip-sense is opposite to the direction of stepping (Kim et al., 2004; Fossen., 2016) (Fig. 2). In general, rocks are more susceptible to fracturing under tension than compression. Therefore, an environment in which tension is formed could be slightly riskier than environments under compression. Although there are not sufficient data to establish the safe separation distance for strike-slip faults, we propose the safe separation distance on the linkage damage zone and tip damage zones as 1.5 times wider than that along the main fault zone. Consequently, the safe separation distance for the strike-slip faults is as follows: 1) Zone 3 is 500 m in tip zone (200 m in contractional part and 300 m in dilational part, respectively), 400 m in wall zone, and at least 800 m in linkage zone; Zone 2 is 150 m in tip zone (60 m in contractional part and 90 m in dilational part, respectively), 120 m in wall zone, and at least 240 m in linkage zone; Zone 1 is 37.5 m in tip zone (15 m in contractional part and 22.5 m in dilational part, respectively), 30 m in wall zone, and at least 60 m in linkage zone. However, when two segments are overlapped in the linkage damage zones, the safe separation distance within the linkage zone is the width between two segments (Fig. 3).

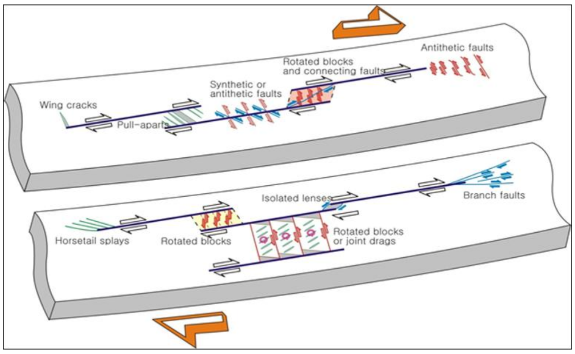

Figure 2: Schematic diagram showing fault damage zones around strike-slip faults (Kim et al., 2004).

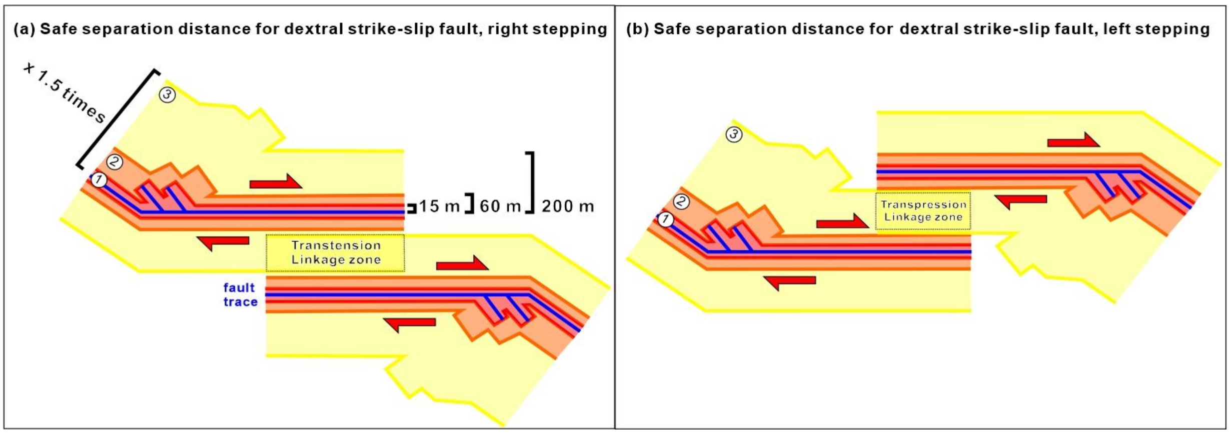

Figure 3: Suggested safe separation distances for strike-slip faults. (a) The case for the same sense of slip and stepping. Wide tensile structures are developed in the linkage zone. The safe separation distance on the tip damage zone and linkage zone is considered as 1.5 times wider than that along the main fault trace. (b) The case for different sense of slip and stepping. Relatively narrow compressional structures are developed in the linkage zone. The safe separation distance on the tip damage zone and linkage zone is considered as 1.5 times wider than that along the main fault trace.

CONCLUSIONS

Although this study suggests the safe separation distance based on previous studies and damage factors, the safe separation distance for important facilities should be established through a detailed investigation on the related faults in earthquake-prone areas. Finally, this can contribute significantly to site selection for important facilities to reduce earthquake hazard in earthquake-prone areas (Fig. 4).

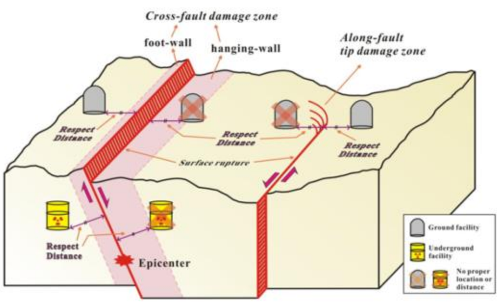

Figure 4: Schematic diagram for relatively safe locations around faults based on fault damage characteristics (Jin and Kim, 2018).

Acknowledgements: This research was supported by a grant (2022-MOIS62-001) of Natioanl Disaster Risk Analysis and Management Technology in Earthquake funded by Ministry of interior and Safety (MOIS, Korea). This work was also supported by a grant from the Korea Institute of Geosciences and Mineral Resources (GP2020-003; 22-3111-1).

REFERENCES

Act, Fault-Rupture Hazard Zones in California. Act, Alquist-Priolo Earthquake Fault Zoning, 1999, Fault-rupture hazard zones in California.

Bonilla, M. G., Mark, R. K., & Lienkaemper, J. J., 1984, Statistical relations among earthquake magnitude, surface rupture length, and surface fault displacement. *Bulletin of the Seismological Society of America*, *74*(6), 2379-2411.

Boncio, P., Galli, P., Naso, G., & Pizzi, A., 2012, Zoning surface rupture hazard along normal faults: Insight from the 2009 M w 6.3 L'Aquila, Central Italy, earthquake and other global earthquakes. Bulletin of the Seismological Society of America, 102(3), 918-935.

Boncio, P., Liberi, F., Caldarella, M., & Nurminen, F. C., 2018, Width of surface rupture zone for thrust earthquakes: implications for earthquake fault zoning. Natural Hazards and Earth System Sciences, 18(1), 241-256.

Fossen, H., 2016, Structural geology. Cambridge university press.

Jin K., & Kim Y.-S., 2018, Evaluation on Geological Structures to Secure Long-term Safety of Nuclear Facility Sites. Economic and environmental geology,51(2),149-166, (in Korean with English abstract).

Jin, K., Lee, J., Lee, K.-S., Kyung, J.B., & Kim, Y.-S., 2020, Earthquake damage and related factors associated with the 2016 ML=5.8 Gyeongju earthquake, southeast Korea. Geosciences Journal. V. 24, No. 6, 141–157.

Kerr, J., Nathan, S., Van Dissen, R., Webb, P., Brunsdon, D., & King, A., 2003, Planning for development of land on or close to active faults. Wellington: Ministry for the Environment.

Kim, Y.-S., Peacock, D.C.P. & Sanderson, D.J., 2004, The fault damage zones. Journal of Structural Geology, v.26, 503-517.

Kim Y.--S., Jin K., Choi W,-H. & Kee, W.-S., 2011, Understanding of active faults: A review for recent researches. Journal of the Geological Society of Korea. v.47, no. 6, p.723-752, (in Korean with English abstract).

NTC08., 2008, Norme Tecniche per le Costruzioni. Ministero delle Infrastrutture e dei Trasporti, Decreto Ministeriale del 14 Gennaio 2008, Supplemento Ordinario alla GU n. 29 del 4 Febbraio 2008.

Villamor, P., Litchfield, N., Barrell, D., Van Dissen, R., Hornblow, S., Quigley, M., & Grant, H., 2012, Map of the 2010 Greendale Fault surface rupture, Canterbury, New Zealand: application to land use planning. New Zealand Journal of Geology and Geophysics, 55(3), 223-23.

Quaternary mapping and paleoseismic trenching of the Bonham Ranch fault: an active structure along the Walker Lane/Basin and Range transition zone, Nevada USA

Koehler, Rich (1)

(1) Nevada Bureau of Mines and Geology, University of Nevada, Reno, 1664 N. Virginia St., MS 178, Reno, NV, 89557. rkoehler@unr.edu

Abstract: *The Bonham Ranch fault (BRF) extends for ~40 km in western Smoke Creek Desert, Nevada along the eastern margin of the northern Walker Lane, which accommodates 4-5 mm/yr of relative Pacific/North American plate dextral shear. In this area, a small amount of shear and extension is partitioned to faults in the western Basin and Range. Part of this deformation is accommodated by normal faulting along the BRF, however prior paleoseismic trenching has not been conducted and data on rupture parameters is limited. New mapping based on interpretation of lidar data and trenching observations along the BRF indicate the occurrence of at least two latest Pleistocene/Holocene events. The trenches show two primary fault strands that cut lacustrine clay interbedded with two distinct tephra layers. Two packages of post-faulting deposits bury the lacustrine deposits on the hanging wall. Dating analyses to place constrains on the timing of the earthquakes is in progress.*

Key words*: mapping, trenching, northern Walker Lane, slip partitioning.*

INTRODUCTION

The Bonham Ranch fault zone in the Smoke Creek Desert, Nevada is poorly characterized and accommodates oblique normal faulting within a zone of transition between Walker Lane shear and Basin and Range extension (Figure 1). At this latitude, approximately 4-5 mm/yr of the Pacific/North American relative plate boundary strain is accommodated east of the Sierra Nevada through a combination of normal oblique (dextral) slip on the Sierra Nevada frontal fault system, dextral slip along northwest trending faults in the northern Walker Lane, and oblique normal slip on north trending faults along the western margin of the Basin and Range province (Bormann, 2013; Hammond et al., 2011; Faulds et al., 2005, Wesnousky, 2005) (Figure 1). The U.S. National Seismic Hazards map, includes the Bonham Ranch fault zone as a source with a modeled slip rate of 0.26 mm/yr capable of Mmax 7.1 earthquakes that could generate damaging ground motions in the Reno region (Petersen et al., 2014).

Koehler (2019) described a series of north-striking oblique slip faults in the North Valleys located south of the Bonham Ranch fault (Figure 1) and suggested a model in which dextral shear is transferred from the Sierra Nevada range front across a right step to the eastern side of the Walker Lane defined by the left-stepping Pyramid, Warm Springs Valley, and Honey Lake faults. Geodetic studies of the North Valleys estimate that north-striking faults collectively accommodate 0.9-1.2 mm/yr of extension and <0.3 mm/yr of dextral slip (Bormann, 2013). Right oblique displacement has been suggested for north-striking faults that splay off the Walker Lane into the Basin and Range including the Bonham Ranch, San Emidio, and Dry Valley-Smoke Creek Ranch faults (Bell & Ramelli, 2009; Weick, 1990), however, lateral displacements are poorly documented. Thus, the style and rate of strain partitioning between the Walker Lane and Basin and Range remains allusive. One hypothesis is that slip is transferred through the Bonham Ranch fault to the relatively young Likely fault, an incipient northwest-striking fault within previously extended Basin and Range crust (Figure 1). This is consistent with the hypothesis that the Walker Lane is propagating to the north, an idea based on northward decreasing cumulative geologic displacement and geodetic strain accumulation, as well as less organized discontinuous faults to the north (Faulds et al., 2005, Wesnousky, 2005, Bormann, 2013).

The Bonham Ranch fault consists of predominantly intra-basin faults that extend from the southwestern side of Smoke Creek desert near the Terraced Hills to the west flank of the Buffalo Hills (Figure 1). Fault traces were originally mapped by Bonham (1969) and later refined by Weick (1990). Inspection of these maps indicates that many of the fault traces are coincident with lacustrine shorelines related to the recession of pluvial Lake Lahontan which desiccated ~15 ka (Adams and Wesnousky, 1999) and highstand shorelines associated with the Younger Dryas (Adams & Rhodes, 2019). Additionally, both Weick and Bonham showed faults along the range front. Weick (1990) also described a stream cut exposure at the base of a mapped fault scarp and inferred that the most recent earthquake occurred around 290 years ago, based on two radiocarbon samples within inferred graben fill. The exposure does not show faults and has been overgrown by vegetation, thus the relation of the deposits to tectonic activity is uncertain and cannot be verified. Reconnaissance observations related to this project indicate that the range front lacks tectonic geomorphic features indicative of progressive deformation (i.e. triangular facets, wineglass canyons) and that many of the previously mapped faults are indeed shorelines. The active trace of the Bonham Ranch fault is expressed as relatively continuous east-facing 1-5 m scarps that displace latest Pleistocene and Holocene lacustrine shoreline and basin deposits and alluvial fans along the western side of Smoke Creek Desert. Despite its clear expression, data on earthquake timing, recurrence, and slip rate have not been developed, resulting in large uncertainties in the fault's seismic potential.

Motivated by the inconsistencies in the previous mapping and general lack of paleoseismic rupture parameter data, I conducted Quaternary geologic mapping on recently acquired lidar data and excavated two paleoseismic trenches across the fault in northern Smoke Creek Desert. Here, I present observations from these studies that shed light on the style of deformation and the number of latest Pleistocene-Holocene earthquakes. The results contribute to ongoing efforts aimed at understanding the evolution and slip partitioning of the northern Walker Lane and have important implications for reducing uncertainties in regional seismic hazard models.

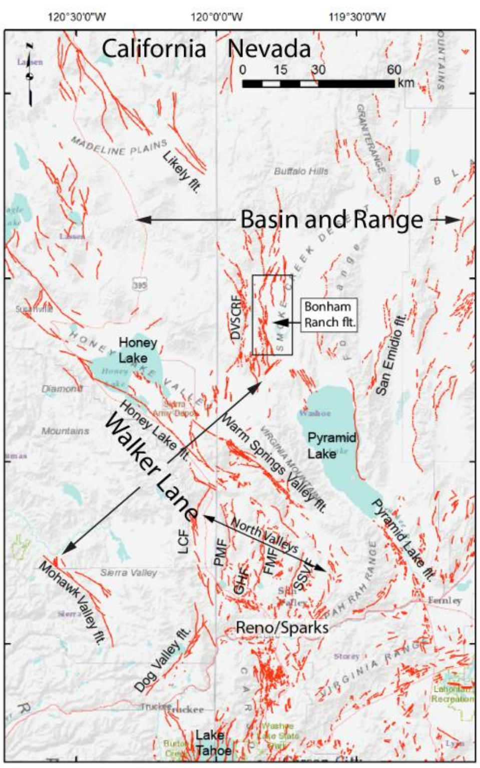

Figure 1: Regional fault map of the Walker Lane/Basin and Range transition zone. Faults from the USGS Quaternary fault and fold database. LCF, Last Chance fault; PMF, Petersen Mountain fault; GHF, Granite Hills fault; FMF, Fred's Mountain fault; SSVF, Spanish Springs Valley fault; DVSCRF, Dry Valley-Smoke Creek Ranch fault.

RESULTS AND DISCUSSION

Fault trace mapping was performed across an ~20-km-long section of western Smoke Creek Desert to independently evaluate previous mapping and to differentiate between fault scarps and lacustrine shoreline landforms (some previously reported as faults). The mapping was also conducted to identify viable sites for paleoseismic trenching. The mapping indicates that the fault is characterized by a relatively continuous singular trace that is well-expressed and clearly defined across latest Pleistocene-Holocene basin fill sediments predominantly east of the range front. The fault splays northward from the northwest-striking right-lateral Pyramid Lake fault and consists of several en echelon left bends or steps that vary in strike from 0°-030° (Figures 1 and 2). The fault is entirely within the basin and not expressed along the range front which lacks active faulting morphology typical of long-term Basin and Range normal faulting (i.e. triangular facets, wineglass canyons).

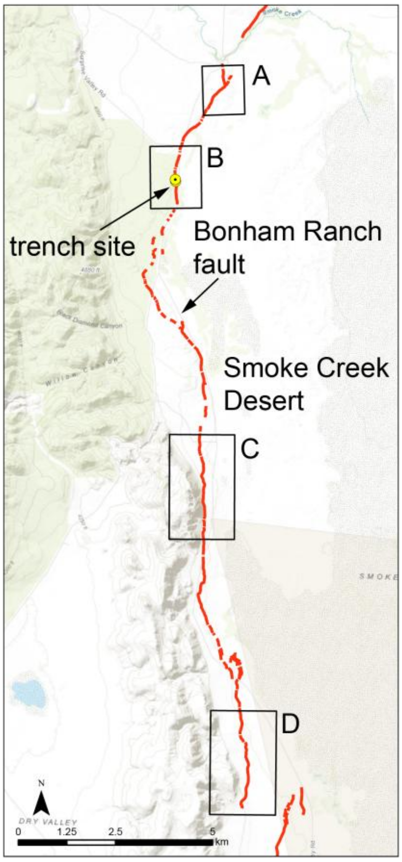

Figure 2: Traces of the Bonham Ranch fault mapped for this Project and location of paleoseismic trench. Areas of detailed lidar images in Figure 3 labeled A-D.

The range front was submerged by pluvial Lake Lahontan during its highstand (~15 ka) which reached an elevation of ~1340 m (Adams & Wesnousky, 1998; Adams et al, 2008). Thus, the lacustrine deposits provide an important stratigraphic framework to evaluate the history of faulting along the Bonham Ranch fault. The basin fill deposits along the western margin of Smoke Creek Desert reflect a progression from deep water lacustrine clay deposits to shallow water near shore sands and beach berms that were deposited during the recession of the lake. These deposits were buried in places by thin shoreline deposits related to two transgressions of the lake including the ~12 ka Younger Dryas highstand (elevation ~1212-1230 m) and a mid-Holocene highstand (elevation ~1190-1200 m) (Adams and Rhodes, 2019). The lacustrine deposits have been incised by Holocene alluvial fans within the basin and buried by boulder rich colluvial fans along the range front. Numerous sand dune complexes mantle all of the deposits within the basin.

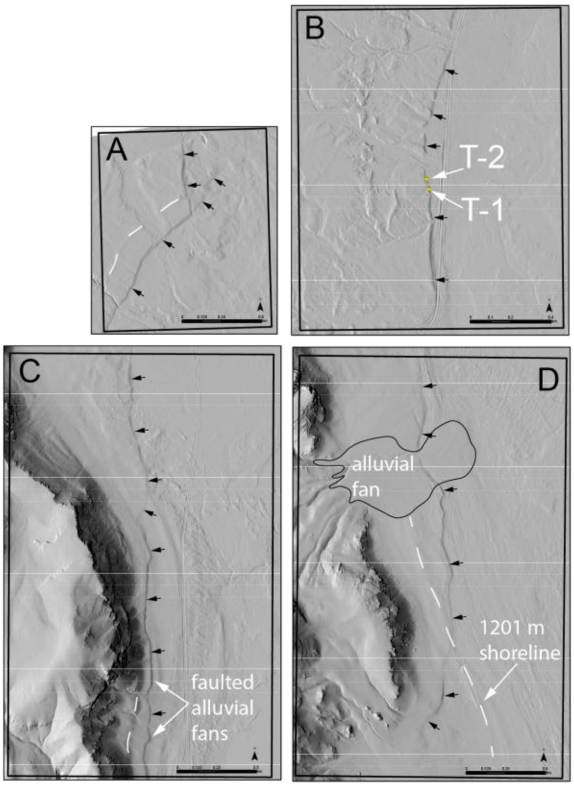

Figure 3: Lidar hillshade images of the Bonham Ranch fault for áreas A-D. Active fault trace extends along black arrow tips in each image. Prominent shorelines shown by dashed white lines. See figure 2 for locations.

Interpretation of lidar hillshades (Figure 3) and field reconnaissance conducted for this project as well as observations from DeMasi (2021) indicate that surficial fault scarps range in height from 1-5 m and are characterized by an oversteepened (sometimes near vertical) basal slope. Lacustrine tufa deposits are commonly exposed on the scarp face and active springs are common along the base of the scarps. The scarps displace Holocene alluvial fans (Figures 3C and 3D) and shorelines associated with the mid Holocene lacustrine highstand (Figure 3A and 3D). This combined with the beveled scarp morphology suggests the occurrence of at least two Holocene earthquakes associated with a normal sense of displacement. Although, lateral offsets were not observed it is acknowledged that lateral offset of up to a meter may not be recognizable due to the curvilinear pattern of geomorphic features where they cross the fault.

Two trenches (T-1 and T-2) were excavated across the fault in northwestern Smoke Creek Desert (site GPS coordinates 40.460011, -119.844049) (Figures 3B and 4). The purpose of the trenching was to better characterize the number and timing of paleoearthquakes. The trenches were excavated across an ~2-2.5-m-high east-facing scarp that cuts across a broad flat landform overlain by thin aeolian deposits. Similar stratigraphic and structural relations were revealed in both trenches, however trench T-2 was not deep enough to expose correlative units across the fault. A photograph of trench T-1 is shown in Figure 4 and a sketch of the exposure is shown in Figure 5. Trench T-1 exposed interbedded clay, fine sand, two distinct tephra deposits, and sandy clay (Units 1 and 2) displaced across two primary east-dipping faults. On the hanging wall, Unit 2 is overlain by Unit 3/4 a massive to weakly bedded mix of sandy silt to silty sand with trace gravel and pebbles and a 0.75 m wide block of Unit 2 that is clearly faulted across the easternmost fault. Unit 3/4 is overlain by well-bedded fine sand and gravel (Unit 5) at the eastern end of the trench and a massive triangular shaped deposit of silty sand and gravel at the fault zone.

Units 1 and 2 are interpreted to be related to deep water deposition when the site was inundated by Lake Lahontan. Based on comparison to field descriptions in the published literature the tephra beds within Unit 1 may correlate to the Wono and Trego Hot Springs tephras (Adams, 2010) which are widespread in the area and were deposited between ~23-27 ka (Benson et al., 1997). Evidence for the penultimate event includes the vertical displacement of 3.3 m of the top of Unit 2 and deposition of Unit 3/4, interpreted to be a post-earthquake deposit consisting of a mix of aeolian, fluvial, and scarp derived sediments. The fluvial deposits that comprise Unit 5 are interpreted to be related to streams flowing down alluvial fan channels that cut the scarp north of the site that meander across the hanging wall. Evidence for the most recent earthquake (MRE) includes the clear faulting of Unit 3/4 and burial of the fault by Unit 6 interpreted to be a colluvial wedge composed of aeolian and scarp derived colluvium. The stratigraphic and structural relations support the occurrence of two latest Pleistocene/Holocene earthquakes that postdate the deposition of the two tephras (~23-27 ka). This result is consistent with the geomorphic mapping observations although the surficial relations suggest that the two events may be younger (Holocene). Radiocarbon, optically stimulated luminescence, and tephachronologic analysis results are pending and may place tighter constraints on the timing of events.

CONCLUSION

Approximately ~4-5 mm/yr of Pacific/North American relative shear is distributed across the northern Walker Lane. Historical earthquakes (i.e. 1932 Cedar Mountain earthquake) indicate that a small amount of this deformation is partitioned onto faults in the western Basin and Range. Although right lateral offsets have not yet been identified along the Bonham Ranch fault the left stepping map view pattern of youthful ruptures suggests that the fault may accommodate a small component of right-lateral displacement. Field and lidar mapping observations indicate that the scarps are beveled indicating the occurrence of at least two latest Pleistocene/Holocene earthquakes. This result is corroborated by the trenching observations which indicate the occurrence of at least two earthquakes that post date the deposition of tephra deposits tentatively correlated to the Wono and Trego Hot Springs tephras (~23-27 ka). This ongoing work will contribute towards better characterizing seismic hazards in northwestern Nevada.

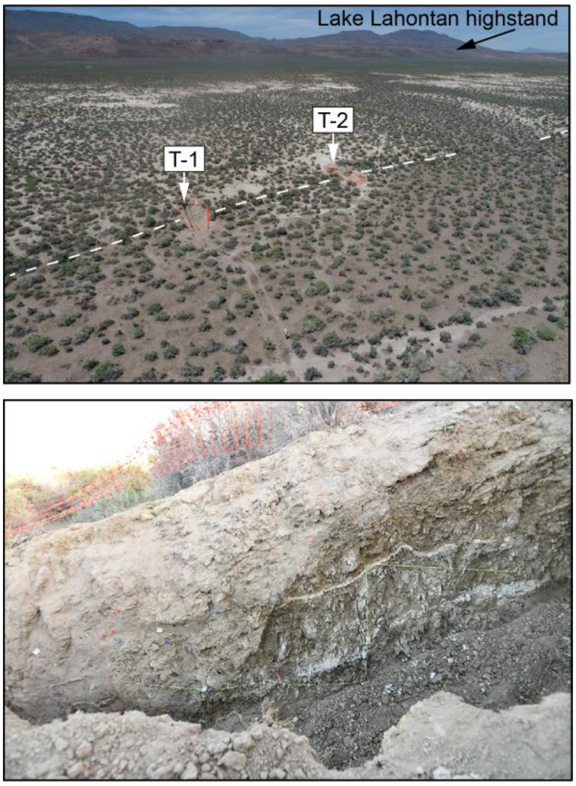

Figure 4: Drone photograph (top) showing highstand of pluvial lake Lahontan, trenches, and fault trace. Field photograph of the south wall of trench T-1 showing clearly defined fault and tephra layers in the footwall.

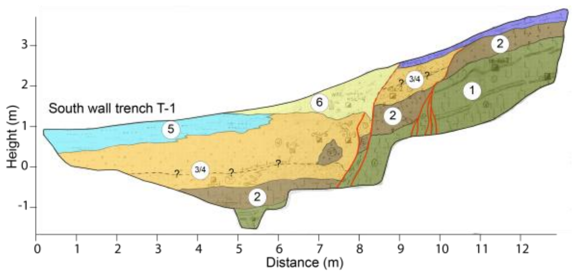

Figure 5: Stratigraphic log of the south wall of Bonham Ranch fault trench T-1. Unit 1, interbedded lacustrine clay, sand , and tephra; Unit 2, Sandy clay; Unit 3/4, penultimate colluvium; Unit 5, bedded fluvial deposits; Unit 6, most recent earthquake (MRE) colluvium. Units 3/4 and 6 are a mix of aeolian, storm wash, fluvial, and scarp derived colluvium.

Acknowledgements: The author wishes to thank the following individuals for field review of the trenches and discussions on the lacustrine stratigraphy: S. Wesnousky, S. Dee, G. Seitz, K. Adams and C. DeMasi. This work was funded by the USGS Earthquake Hazards Program award number G20AP00014. The views and conclusions presented are those of the author and should not be interpreted as representing the opinions or policies of the U.S. Geological Survey.

REFERENCES

Adams, K.D., & Rhodes, E.J., 2019. Late Pleistocene to present lake-level fluctuations at Pyramid and Winnemucca lakes, Nevada, USA. Quaternary Research 92, 146-164.

Adams, K.D., 2010. Lake levels and sedimentary environments during deposition of the Trego Hot Springs and Wono tephras in the Lake Lahontan basin, Nevada, USA. Quaternary Research 73, 118-129.

Adams, K.D., Goebel, T., Graf, K., Smith, G.M., Camp, A.J., Briggs, R.W., and Rhode, D. 2008. Late Pleistocene and early Holocene lake-level fluctuations in the Lahontan Basin, Nevada: Implications for the distribution of archaeological sites. Geoarchaeology 23(5), 608-643.

Adams, K.D., & Wesnousky, S.G., 1999. The Lake Lahontan Highstand: age, surficial characteristics, soil development, and regional shoreline correlation. Geomorphology, 30, 357-392.

Bell, J.W., & Ramelli, A.R., 2009. Active fault controls at high-temperature geothermal sites: Prospecting for new faults. GRC Transactions 33, 425-429.

Benson, L.V., Smoot, J.P., Kashgarian, M., Sarna-Wojcicki, A.M., and Burdett, J.W., 1997. Radiocarbon ages and environments of deposition of the Wono and Trego Hot Springs tephra layers in the Pyramid Lake subbasin, Nevada. Quaternary Research 47,251-260.

Bonham, H.F., 1969. Geology and mineral deposits of Washoe and Storey counties, Nevada, with a section on industrial rock and mineral deposits by K.G. Papke. Nevada Bureau of Mines and Geology Bulletin 70, 139 p.

Bormann, J., 2013. New insights into strain accumulation and reléase in the central and northern Walker Lane, Pacific-North American plate boundary, California and Nevada, USA. Ph.D. dissertation, University of Nevada, Reno.

DeMasi, C., 2021. Active faulting in the northern Walker Lane and post-earthquake reconnaissance in the central Walker Lane, Nevada and Eastern California. Ph.D. dissertation, University of Nevada, Reno.

Faulds, J.E., Henry, C.D., & Hinz, N.H., 2005. Kinematics of the northern Walker Lane: An incipient transform fault along the Pacific-North American plate boundary. Geology 33, 505-508.

Hammond, W.C., Blewitt, G., & Kreemer, C., 2011. Block modeling of crustal deformation of the northern Walker Lane and Basin and Range from GPS velocities. J. Geophys. Res. B Solid Earth Planets 116, 1-28.

Koehler, R.D., 2019. Active faulting in the North Valleys region of Reno, Nevada: A distributed zone within the northern Walker Lane. Geomorphology 326, 38-53.

Peterson, M.D., & 18 others, 2014. Documentation for the 2014 update of the United States National Seismic Hazard Maps. U.S. Geological Survey Open-File Report 2014-1091, 243 p.

Weick, 1990. Structural, tectonic, and Quaternary study of the eastern Madeline Plains, California and southwestern Smoke Creek Desert, Nevada. M.S. thesis, University of Nevada, Reno, 160 p., 5 plates.

Wesnousky, S.G., 2005. Active faulting in the Walker Lane. Tectonics 24, TC3009.

INQUA Focus Group Terrestrial Processes Perturbed by Tectonics (TPPT)

paleoseismicity.org

Recurrence time of large earthquakes at the western Alps-Mediteranean sea junction : from geological observations and modelling of the seismicity rate

Larroque Christophe (1,2), Scotti Oona (3), Trévisan Jenny (1), Courboulex Françoise (1)

(1) Université Côte d'Azur, CNRS, Observatoire de la Côte d'Azur, IRD,Géoazur, 06560 Valbonne, France

(2) Université de Reims Champagne-Ardenne, GEGENAA EA 3795, 51100 Reims, France

(3) BERSSIN, Institut de Radioprotection et de Sureté Nucléaire (IRSN), 92262 Fontenay-aux-Roses cedex, France

Abstract: *The junction between the Western Alps and the Ligurian basin in the Mediterranean Sea is one of the intraplate areas of Western Europe where strong earthquakes occur. The last of these earthquakes occurred in 1887 activating the Ligurian thrust, the major structure which has controlled most of the deformation in the area for about 5 Ma. The available data (GNSS, geological, seismological) allow us to hypothesize the recurrence time of M_w 6.8 earthquake, equivalent to the 1887 earthquake, and lead to a range of 6500-3000 years.*

Key words*: recurrence time, active fault, seismicity rate, Alps, Mediterranean sea.*

INTRODUCTION

The junction between the Western Alps and the Mediterranean Sea is one of the most seismic area in the westernmost Europe. This intraplate area suffered several damaging earthquakes in the last centuries and particularly the February 23, 1887 (M_w 6.8) which struck the towns along the Italian and French Riviera, killing at least 600 people, injuring several thousand and destroying many buildings.

While the recurrence time of strong earthquakes is one of the critical parameters to be determined, in intraplate and low deformation rate areas qualitative estimates of the order of several thousand to several hundred thousand years are sometimes proposed but usually without precise data to refine the range. In this paper we attempt to discuss the recurrence times of 1887-ligurian-type earthquakes : (i) by estimating slip-rates based on GNSS and geological data and (ii) by determining the earthquake rates from earthquakes catalog.

SEISMOTECTONIC SETTING

In the western Mediterranean, the junction between the western Alps and the Ligurian Basin corresponds to an area of moderate seismicity which belongs to the Western European intraplate domain (Larroque et al., 2011 ; 2021). The seismicity is mainly located in a zone of long-term cumulated deformation and seismotectonic analyses show mainly reverse faulting, along the so-called Ligurian thrust, extending for about 90 km-long at the foot of the continental margin from Nice to Savona (Fig. 1A,B). From the reappraisal of the 1887 Ligurian earthquake, taking into account macroseismicity, active tectonics and tsunami modelling, we propose that this emblematic earthquake resulted from the activation of the Ligurian thrust (Fig. 1C) Larroque et al., 2012 ; Ioualalen et al., 2014).

RECURRENCE PERIOD ESTIMATIONS FROM GNSS AND GEOLOGICAL DATA

Our approach is based on 2 hypotheses : *(i)* we consider that the convergence between the European mainland and the Corsica-Sardinia-block is accommodated by the Ligurian thrust (Fig. 1A,C). This hypothesis is supported on the long-term (~5 Myr), by the location of cumulated deformations, and on the short-term, by the distribution of the instrumental seismicity, both of which mainly along the Ligurian thrust (Fig. 1B,D). *(ii)* We consider also a characteristic slip for the targeted earthquake. Taking into account the scaling laws (Wells & Coppersmith, 1994; Leonard, 2010) we set a range of co-seismic slip between 1 m and 1.3 m for an earthquake of M_w 6.8 (Ioualalen et al., 2014).

Several geodetic and geological dataset are available to constrain the slip-rate on the Ligurian thrust through different time scales :

(1) The horizontal velocity estimated between permanent GPS stations in Corsica (AJAC) and on the mainland (NICE) is a shortening of 0.4 mm/yr maximum (Nocquet, 2012 ; Masson et al., 2019). Thus we consider a range of 0.2-0.4 mm/yr of present-day slip-rate on the Ligurian thrust to be realistic. The recurrence times (RT) for co-seismic slip of 100 and 130 cm on the 20° northward-dipping Ligurian thrust (Fig. 1C) for a shortening of 0.2 and 0.4 mm/yr are in the range of 5000-6500 yr and 2500-3250 yr, respectively (Table 1).

CoSS ----------------------- Vh		1 m	1.3 m
0.2 mm/yr	**RT~ (yr)**	**5000**	**6500**
0.4 mm/yr	**RT~ (yr)**	**2500**	**3250**

Table 1. CoSS : Co-seismic slip, Vh : horizontal velocity, RT : recurrence time for M_w 6.8 earthquake.

(2) Several geological markers of different ages attest to continuous uplift of the French-Italian coastline and of the northern Ligurian margin from Pliocene to present-day. Since the coastline and the margin are located on the hanging-wall of the fault (Fig. 1A,C), we use these cumulative offsets in order to estimate the slip-rate along the Ligurian thrust at different time intervals and then compute the corresponding RT :

- From underwater mapping, Collina-Girard (2002) identified a sequence of sub-aerial erosion notches dated around 10 kyr and located all along the submarine cliffs from Marseille to Monaco. These erosion notches are

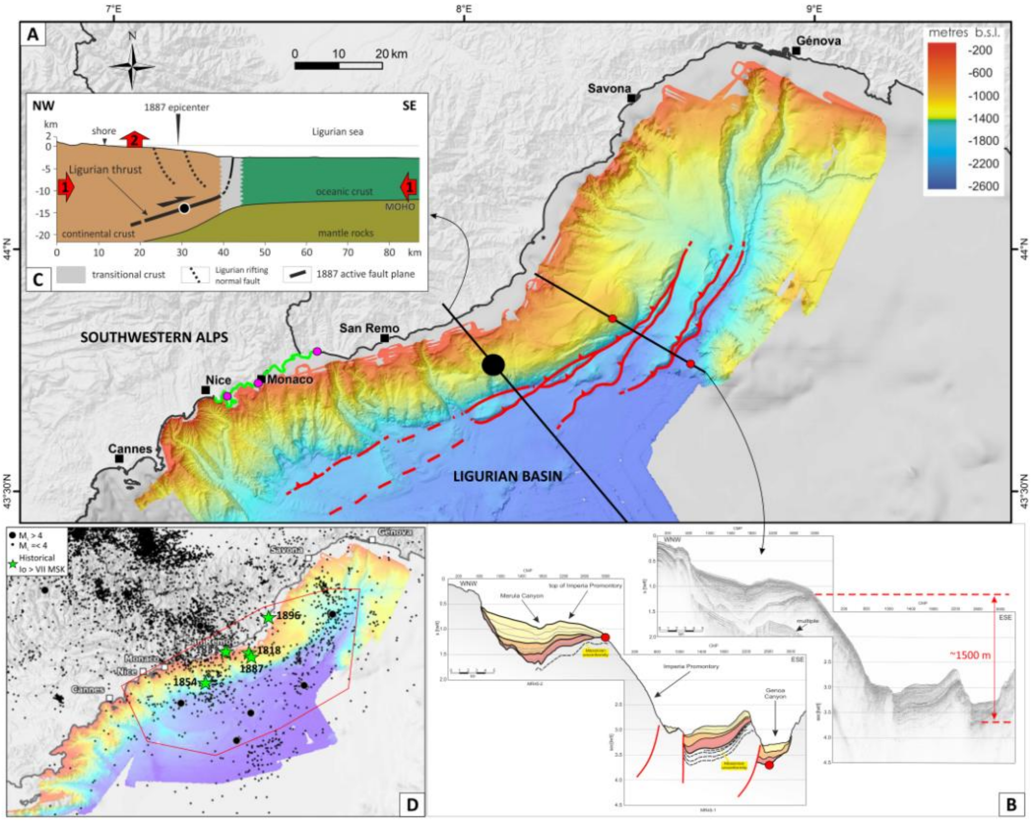

Figure 1. (A) Structural sketch of the western Alps-Ligurian basin junction : red lines are the Ligurian reverse faults system rooted at depth to the Ligurian thrust and extended from Nice to Savona, the black dot is the epicenter of the Ligurian 1887 earthquake. The green line corresponds to the coastal zone where well-marked Holocene erosion notches are raised about 2 m with respect to the area further west (Collina-Girard, 2002); the pink dots localise the uplifted Pleistocene marine terraces (Dubar et al., 2008); the red dots indicate the position of the Pliocene-Quaternary boundary showed on (B). (B) MCS profil MR-45 showing the offset of the Pliocene-Quaternary boundary surface on either side of the Ligurian faults system (red dots on A). (C) Seismotectonic sketch : the 1887 Ligurian earthquake (black dot) activated the northward low-dip Ligurian thrust (bold line). At shallow depth, the Ligurian faults system is located at the transitional oceanic/continental crust. 1: shortening between NICE and AJAC GPSc stations, 2: uplift of the hanging wall (modified from Larroque et al., 2012). (D) Instrumental and historical seismicity map from M_L 1.5 and Io VII MSK (CEA-LDG catalog, 1962-2018 and SisFrance), the red parallelogram corresponds to the background extraction from the SERA catalog (Danciu et al., 2021) in order to determine the Gutenberg-Richter distribution.

interpreted as submerged shorelines developed when sea level rise period. A major observation is that east of the Var River (~7°15'E) this sequence of notches is offset upwards by 2 m (Fig. 1A). We interpret this offset as a tectonic uplift of the hanging-wall related to the activation of the Ligurian thrust which ends ~7°15E. Taking into account the 20° northward-dip and the uplift of the hanging-wall related to a Mw 6.8 earthquake (0.34 m and 0.44 m for a co-seismic slip of 1 m and 1.3 m, respectively), for a cumulative uplift of 2 m over a period of 10 kyr, we obtain RTs in the range of 1666 yr and 2500 yr, respectively (Table 2).

- On the shore between Nice and San Remo (Fig 1A), several evidences of Pleistocene marine terraces developed during the high-stand sea level of the last interglacial period (MIS5.5, 130 kyr) are currently uplifted 20 m above the present-day sea level (Dubar et al., 2008). Because during the MIS5.5 period the sea level was ~5 m above the present-day one (Lambeck et al., 2004), the actual tectonic uplift of the hanging-wall would be 15 m since 130 kyr. Thus, the RTs for a cumulative uplift of 15 m for a period of 130 kyr are 2955 yr and 3824 yr for 1 m and 1.3 m of co-seismic slip, respectively (Table 2).

- On the northern Ligurian margin, Larroque et al. (2011) highlighted a 1500 m-uplift of the hanging wall based on the offset of the Pliocene-Quaternary boundary surface on either side of the Ligurian thrust (Fig. 1B). The RTs for a cumulative uplift of 1500 m over a period of 5.33 Myr are 1208 yr and 1563 yr for 1 m and 1.3 m of co-seismic slip, respectively (Table 2).

CoSS	1 m	1.3 m
uplift / event	~0.34 m	~0.44 m
RTs (yr) over 10 kyr	**1666**	**2500**
RTs (yr) over 130 kyr	**2955**	**3824**
RTs (yr) over 5.33 Myr	**1208**	**1563**

Table 2. CoSS : Co-seismic slip, RTs : recurrence times for M_w 6.8 earthquake on the Ligurian thrust for different periods of time and different types of data : offset of Holocene erosion notches (10 kyr, Collina-Girard, 2002), uplift of Pleistocene marine terraces (130 kyr, Dubar et al., 2008) and offset of the Pliocene-Quaternary boundary surface (Larroque et al., 2011).

EARTHQUAKE RATES DEDUCED FROM THE SERA CATALOG

We extracted seismicity from the SERA catalog (Danciu et al., 2021) for a background covering 30 km around the

Ligurian Thrust (Fig. 1D). Completeness periods were estimated based on an adaptation of the Albarello et al. (2002) approach for earthquakes occurred in the Western Alps region. Using the Weichert method (1980), the slope of the Gutenberg-Richter distribution was also estimated at the regional scale and found to be quite low, close to a value of 0.7 (b-value of 1 is also tested for comparison).

We infer that the Ligurian thrust can be considered seismogenic along its entire 90 km-long over a width of roughly 30 km with a slip-rate of 0.2 or 0.4 mm/yr.

Different earthquake recurrence models based on geological parameters have been proposed in the literature. The "Exponential" model formulation (Youngs & Coppersmith, 1985) considered here is as follows :

$$N\ (M_W \geq M) = Mfs*(1.5\text{-}b)\ (1 - \exp(-\beta\ (M_{max} - M))/\ b*MomentMax*\ \exp(-\beta\ (M_{max} - M)) \qquad \text{Eq. 1}$$

where the moment rate of the faults system, Mfs, is given by µ*A*s with µ the shear modulus, A the area of the faults system, s the slip-rate and b is the b-value, β=b*log(10), M_{max} is the maximum magnitude being tested, the MomentMax is the corresponding seismic moment given by the Hanks & Kanamori (1979) equation :

$$MomentMax = 10\text{^}(1.5*Mmax + 9.05) \qquad \text{Eq. 2}$$

Figure 2 shows the comparison between SERA earthquake catalog and theoretical recurrence models (Youngs & Coppersmith, 1985) for the Ligurian thrust, considering three M_{max} around the target magnitude, M_w 6.8, and the two slip-rate values considered (0.2 and 0.4 mm/yr).

Recurrence M_w≥6,8		M_{max}=6.9	M_{max}=7.0	M_{max}=7.4
b-value 0.7	SR 0.2	**5365**	**3485**	**3237**
	SR 0.4	NC	NC	**1618**
b-value 1	SR 0.2	NC	NC	4046

Table 3. RT estimates of M_w≥6,8 *coherent with activity rates deduced from the SERA catalog. SR : slip-rate, NC : Parameters not compatible with the SERA catalogue.*

Table 3 presents the range of recurrence values for M_w≥6.8 for different hypothesis of M_{max}, slip-rates and b-values that are compatible with the earthquake rates deduced from the catalogue. RTs estimations are comparable to the geological estimates and coherent with SERA earthquake catalogue rates only when considering b=0.7 and SR=0.2. For SR> 0.2 it is necessary to advocate the possibility M_{max} = 7.4 (equivalent to rupturing the entire faults system).

DISCUSSION AND CONCLUSION

In intraplate regions the process that triggers earthquakes has been recently questioned (e.g. Calais et al., 2016). Earthquakes in such regions could potentially occur as a result of transient stress/strength perturbations (deglaciation, erosion, fluid circulation…), releasing elastic energy from a pre-stressed crust rather than due to the localized accrual of tectonic stresses. Were this to be the case everywhere in intraplate regions, probabilistic seismic hazard assessments (PSHA) should also be questioned, since they are based on the assumption that earthquakes have a recurrent nature controlled by far-field tectonic forces. It is therefore paramount to document in which regions classical PSHA approaches can be still considered valid or may need to be revised.

The present-day setting of the western Alps-Mediterranean Sea junction is consistent with the long-term tectonic evolution attested by the uplift of the northern Ligurian margin relative to the basin since 5 Myr (Bigot-Cormier et al., 2011). Therefore, we consider that the Ligurian thrust is a major long-lived tectonic activated structure.

Our results show that whatever the data used and the time interval regarded, the RTs estimated for a M_w 6.8 on the Ligurian thrust are always lower than 6.5 kyr. The major result is that we obtain an upper bound for this intraplate context, which is supported by independent approaches but the values vary in a still quite wide range between 6.5 kyr and 1.2 kyr (Table 1 and 2).

The GNSS and geological data (Table 1 and 2) give fairly consistent RTs around 4000 years depending on the slip-rate and co-seismic slip assumptions. Analysis of the longest period (5.33 Myr) gives the shortest RTs (Table 2) but this result is highly questionable as it is based on a characteristic co-seismic slip which should not be a realistic condition given the likely changes in geodynamic conditions at this time scale. Nevertheless, this result could be an indication of a slowing down of the convergence rate between the Corsica-Sardinia block and the European mainland since 5 Myr.

RTs obtained by comparing theoretical RTs with the ones deduced from the SERA earthquakes catalog indicate a wider range of possible RT depending on the slip-rate hypothesis (Table 3). These results depend strongly on the earthquake catalog, in particular the computed b-value of 0.7 and also on the geometry chosen for the background seismicity used to compute it and supposed to represent the seismic activity surrounding the fault volume.

Finally, we consider that the transposition of the maximum convergence rate determined by GNSS (Masson et al., 2019) into a slip-rate on the Ligurian thrust is not realistic because diffuse seismicity occurs southward in the basin (Fig. 1D). The preferred value for the slip-rate on the Ligurian thrust is 0.2 mm/yr and leads to a range of RTs of 6500-5000 yr versus 3000 yr for GNSS data, geological data and Gutenberg-Richter-distribution approaches, respectively.

At the end, we must not forget that the 1887 Ligurian earthquake only broke part of the Ligurian thrust (about 35 km-long estimated, Larroque et al., 2012) and that the adjacent parts have not yet broken.

REFERENCES

Albarello, D., Camassi, R., & Rebez, A., 2002. Detection of space and time heterogeneity in the completeness of a seismic catalog by a statistical approach: an application to the Italian area. *Bull. Seism. Soc. Am.,* 91, 1694-1703.

Bigot-Cormier, F., Sage, F., Sosson, M., Déverchère, J., Ferrandini, M., Guennoc, P., Popoff, M., & Stéphan, J. F., 2004. Déformations pliocènes de la marge nord-Ligure (France): Les consequences d'un chevauchement crustal sud-alpin. *Bull. Soc. Géol. Fr.,* 175(2), 197-211.

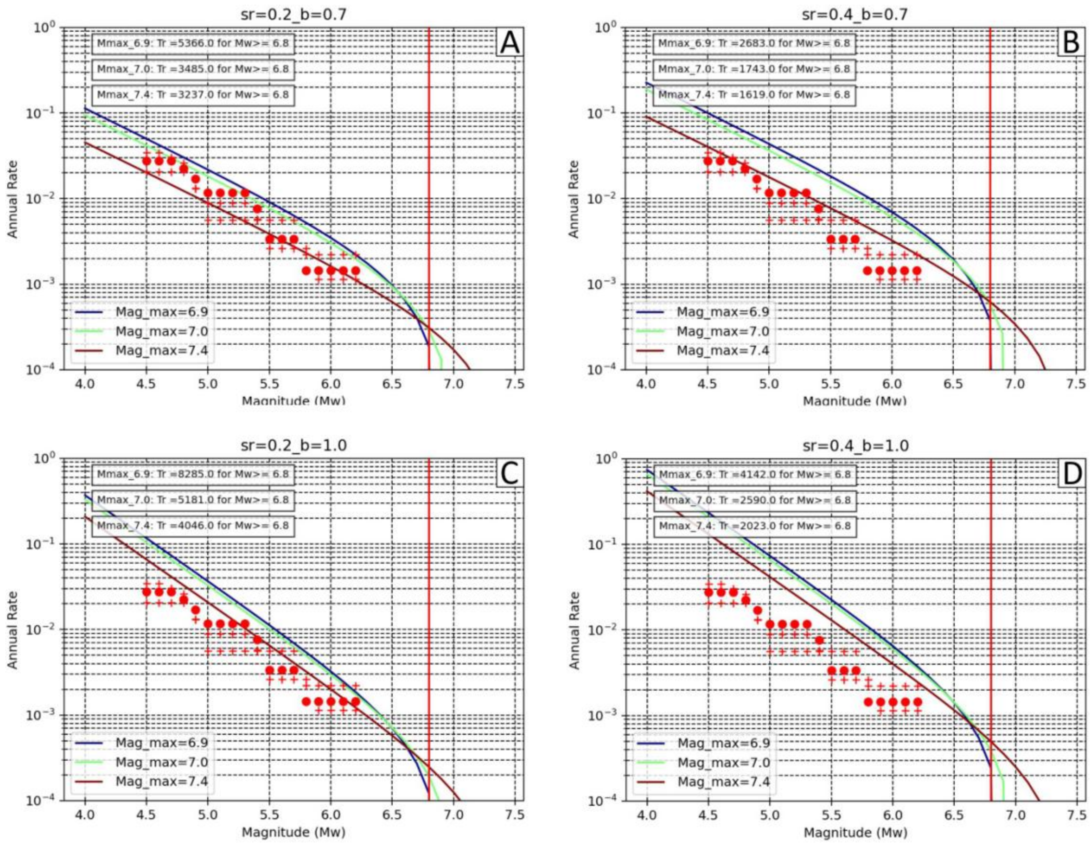

Figure 2. Theoretical earthquakes recurrence models for different Mmax (color curves) versus SERA catalog for the Ligure area (red dots). A, B : b-value=0.7 (suggested for the western alpine region based on the Weichert method) with a slip-rate of 0.2 and 0.4mm/yr respectively. C, D : b-value=1.0 (for comparison).The vertical red bar indicates the target magnitude M_w 6.8.

Calais, E., Camelbeeck, T., Stein, S., Liu, M., & Craig, T. J., 2016. A new paradigm for large earthquakes in stable continental plate interiors. *Geophys. Res. Lett.,* 43(20), 10621-10637.

Collina-Girard, J., 2002. Underwater mapping of Late Quaternary submerged shorelines in the Western Mediterranean Sea and the Caribbean Sea. *Quaternary International,* 92, 63-72.

Danciu, L., Nandan, S., Reyes, C., Basili, R., Weatherill, G., Beauval, C., Rovida, A., Vilanova, S., Sesetyan, K., Bard, P-Y., Cotton, F., Wiemer, S., & Giardini, D., 2021. The 2020 update of the European Seismic Hazard: Model overview. *EFEHR Technical Report* 001, v1.0.0.

Gutenberg, B., & Richter, C.F., 1944. Frequency of earthquakes in California. *Bull. Seism. Soc. Am.,* 34, 185-188.

Dubar, M., Innocent, C., & Sivan, O., 2008. Radiometric dating (U/Th) of the lower marine terrace (MIS5.5) west of Nice (French Riviera): morphological and neotectonic quantitative implications. *Comptes Rendus Geoscience,* 340, 723-731.

Ioualalen, M., Larroque, C., Scotti, O., & Daubord, C., 2014. The tsunami coastal distribution and hazard along the French–Italian Riviera. *Pure Appl. Geophys.,* 171, 1423-1443.

Hanks, T., & Kanamori, H., 1979. A moment magnitude scale. *Jour. Geophys. Res.,* 84, 2348-2350.

Lambeck, K., Antonioli, F., Purcell, A., & Silenzi, S., 2004. Sea-level change along the Italian coast for the past 10,000 yr. *Quaternary Science Reviews*, 23, 1567-1598.

Larroque, C., Mercier de Lépinay, B., & Migeon, S., 2011. Morphotectonic and fault–earthquake relationships along the northern Ligurian margin (western Mediterranean) based on high resolution multibeam bathymetry and multichannel seismic reflection profiles. *Mar. Geophys. Res.,* 32(1–2), 163-179.

Larroque, C., Scotti, O., & Ioualalen, M., 2012. Reappraisal of the 1887 Ligurian earthquake (western Mediterranean) from macroseismicity, active tectonics and tsunami modelling. *Geophys. J. Int.,* 190(1), 87-104.

Larroque, C., et al., 2021. Seismotectonics of southeastern France: from the Jura mountains to Corsica. *Comptes Rendus Géoscience,* 353, 105-151

Leonard, M., 2010. Earthquake fault scaling: self-consistent relating of rupture length, width, average displacement, and moment release. *Seismol. Soc. Am. Bull.,* 100, 5A, 1971-1988.

Masson, C., Mazzotti, S., & Vernant, P., 2019. Precision of continuous GPS velocities from statistical analysis of synthetic time series. *Solid Earth*, 10, 329-342.

Nocquet, J.M., 2012. Present-day kinematics of the Mediterranean: a comprehensive overview of GPS results. *Tectonophysics,* 579, 220–242.

Wells, D.L., & Coppersmith, K.J., 1994. New empirical relationships among magnitude, rupture length, rupture width, rupture area and surface displacement. *Bull. Seism. Soc. Am.,* 84, 974-1002.

Youngs, R.R., & Coppersmith, K.J., 1985. Implications of fault slip rates and earthquake recurrence models to probabilistic seismic hazard estimates. *Bull. Seism. Soc. Am.,* 75, 939-964.

Weichert, D.H., 1980. Estimation of the earthquake recurrence parameters for unequal observation periods for different magnitudes. *Bull. Seism. Soc. Am.,* 70, 1337-1346.

INQUA Focus Group Terrestrial Processes Perturbed by Tectonics (TPPT)

paleoseismicity.org

Seeking seismogenic sources for paleoearthquakes in the Alps: clues from a DSGSD in the Italian Southern Alps.

Franz Livio (1), Maria F. Ferrario (1), Andrea Zerboni (2), Rivka Amit (3), Guido S. Mariani (4), Elisa Martinelli (1)

1 – Dipartimento di Scienza ed Alta Tecnologia, Università degli Studi dell'Insubria, Como (CO), Italy. franz.livio@uninsubria.it
2 - Dipartimento di Scienze della Terra "A. Desio", Università degli Studi di Milano, Milano, Italy
3 - Geological Survey of Israel, Jerusalem, Israel.
4 - Dipartimento di Scienze Chimiche e Geologiche, Università degli Studi di Cagliari, Cagliari, Italy

Abstract: *Triggering mechanisms and causative processes of deep-seated gravitational slope deformations (DSGSD) in Alpine and high mountain areas include among others post-glacial de-buttressing, earthquake-induced ground shaking or co-seismic surface faulting. Distinguishing between climatic or tectonically driven factors is challenging since faults and fracture systems can play both an active and/or passive role in the process initiation. We applied an integrated approach, including morpho-structural analysis, geologic field survey, a paleoseismological approach flowed by radiocarbon dating and detailed sedimentological analysis, in analysing DSGSD located in the Cavargna Valley (N Italy), an area that was not occupied by extensive ice cover during the Upper Pleistocene and Holocene.*

We attempted to identify the triggering mechanism for the Cavargna Valley DSGSD by considering historical earthquake catalogue, a dataset of offshore lacustrine paleoseismological indicators and regional flood chronology.

We conclude that a seismic triggering is likely for the onset of the DSGSD during the initial Middle Holocene, based on the spatio-temporal clustering of offshore evidence, with a possible source located in an area lacking known historical seismicity or active faults, pointing to a possible knowledge gap in the seismotectonics of the Alps. Later evolution and successive pulses in the activity of the Cavargna Valley DSGSD (Late Holocene), seem to correlated with regional proxies of climatic changes, showing a possible association with periods of increased surface instability.

***Key words**: prehistoric landslides; seismic triggering; source location; offshore turbidites; Alpine lakes.*

Introduction

Triggering mechanisms and/or causative processes of deep-seated gravitational slope deformations (DSGSD) in Alpine and high mountain areas include, among others, post-glacial de-buttressing, earthquake-induced ground shaking or co-seismic surface faulting, however, they are generally hard to be identified. Still, the

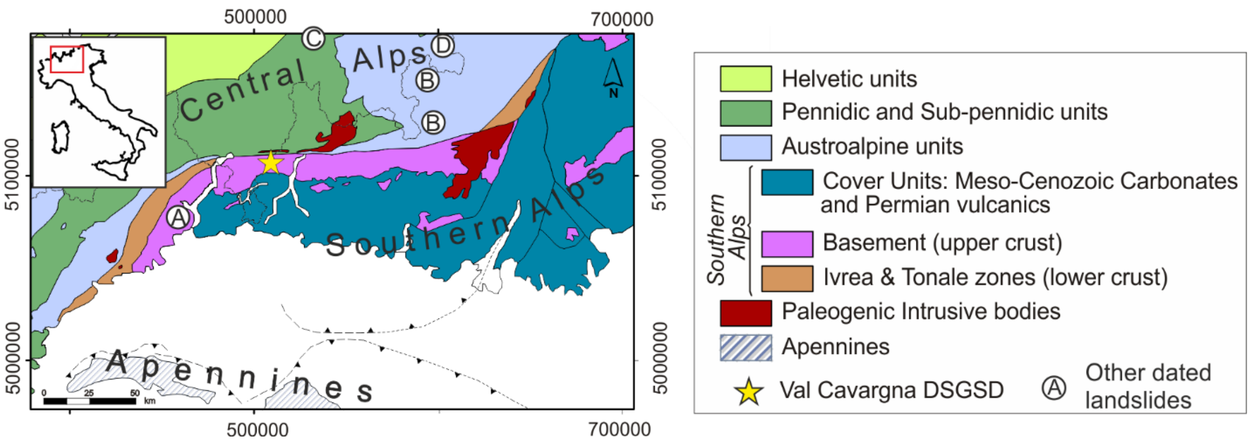

Figure 1: Regional geological sketch map of the Alps: the white circles indicate the locations of dated landslides nearby the study area (A, Tibaldi et al. (2004); B, Forcella et al. (2001); C, Poschinger et al. (2006); D, Agliardi et al. (2009).

information coming from such evidence are fundamental, especially in such a dynamic environment as the Alps.

We applied an integrated approach to a DSGSD in a mountain area of northern Italy that was never occupied by extensive ice tongues during the Upper Pleistocene and Holocene and thus slope unloading, due to the removal of glacial confinement, cannot be invoked. A key study site is located in the Cavargna Valley, N Italy (Figure 1) an area outside the extent of the Alpine ice cap during Last Glacial Maximum (LGM) and only partially was occupied by small cirque glaciers. As a result of our applied integrated approach, including morpho-structural analysis, geologic field survey, a paleoseismological approach applied to trenching, radiocarbon dating and detailed sedimentological analysis, we were able to identify two phases of slope deformation and discuss the different possible causative mechanisms of both.

Geological Setting

The study site is located in the European Southern Alps, close to the Tonale Line, a segment of the Periadriatic Lineament (Schmid et al., 1989) that accommodated a dextral strike-slip motion the indentation of the Southern Alps against the Central Alps during the Oligo-Miocene.

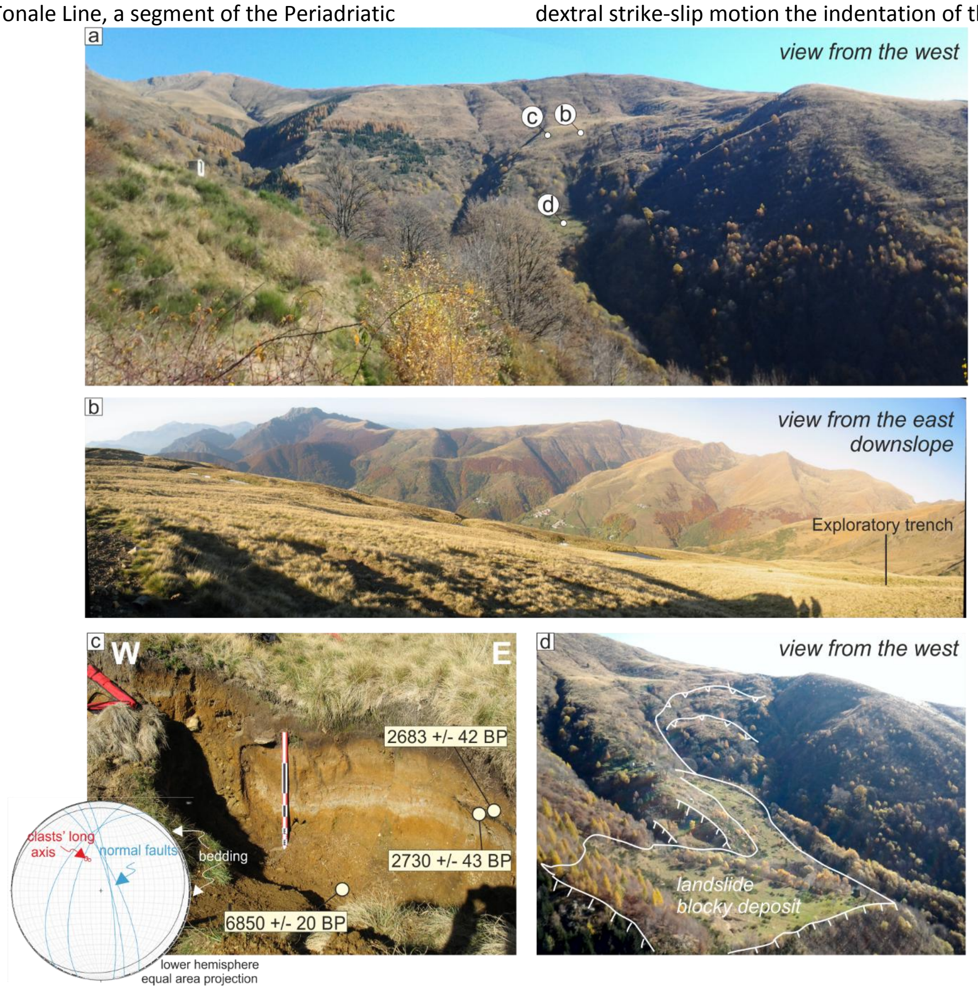

Figure 2: a) Panoramic view on the Cavargna Valley DSGSD: location of the photos in the other panels are indicated; b) View on one of the elongated depressions in the upper sector; c) View of the exploratory trench, the bar is 1 m, location of the trench is indicated in panel b; d) Terraced landslide blocky deposits located in the lower sector of the DSGSD.

The region is characterized by extensive mass wasting and landslide phenomena (see e.g., the Italian landslide inventory IFFI Project; https://www.isprambiente.gov.it/en/projects/soil-and-territory/iffi-project), including large DSGSDs (e.g., Pasquaré 2001; Ambrosi and Crosta 2006; Crosta et al. 2013; Agliardi et al. 2013), some of them provided chronological constraints on their onset and evolutive steps (Forcella et al., 2001; Tibaldi et al., 2004; Poschinger et al., 2006; Agliardi et al., 2009).

The study site is located at the head of Piazza valley, a small ca. NE-SW trending tributary of the main Cavargna Valley. The Piazza valley is almost entirely covered by a DSGSD feature, ca. 1250 m wide and 1300 m long, which deformed the valley slope. The Cavargna Valley DSGSD area and its surrounding were never dominate interested by extensive glaciations in the Upper Pleistocene. According to Bini et al. (2009), the main LGM ice cap reached an elevation of ca. 950 m asl; additionally, small cirque glaciers locally occupied the most elevated parts of the Alps, typically above 1700 m asl, as highlighted by glacial and periglacial erosional landforms.

The Val Cavargna DSGSD and evidence for a seismic triggering

We excavated an exploratory trench in the upper sector, across an elongated morphological depression (Figure 2). We exposed a multiple sequence of slope/colluvial deposits in which soils was developed in a depression bounded, at the sides, by two gravitationally driven normal faults; subsequent colluvial events show a fining upward trend.

Dating from three charcoal samples taken from the charcoal-rich lens result in 2730±43 and 2683±42 years uncal BP (2932–2756 years cal BP and 2865–2743 years cal BP, for the upper unit and 6850±20 years uncal BP (7733–7618 years cal BP) for the lower one (Figure 2c).

The sedimentary sequence deposited in the fault bounded depression (graben) is crosscut by two conjugated sets of normal faults.

The kinematic indicators are provided by the orientation of the clast's long axis orientation , along a fault zone followed by characteristic shear fabric and indicating an almost pure dip slip kinematic, with less than 10% of horizontal component. The bedding of the slope deposit is slightly dipping to the east, involved a gentle synclinal folding with the beds getting steeper close to the fault (drag folding). Brittle secondary structures cut through the infill of the trench. For a full description of the trench stratigraphy and the reconstruction of timing and phases of movements, refer to Livio et al. (2022).

Our conclusions show that the inception of the Cavargna Valley landslide is constrained in a quite long time window (i.e., 7.7 – 5.0 ka BP) contemporary to a period when nearby offshore lacustrine turbidites are reported (i.e., the 7.3 – 7.0 ka BP and 6.5 – 5.5 ka BP periods; Kremer et al., 2020). Livio et al. (2022) discussed possible earthquake vs climatic triggering for the inception of the Val Cavargna DSGSD and concluded that the temporal and spatial clustering of the indicators possibly suggest a seismic triggering, whereas a clear climatic forcing is lacking during that period (Wirth et al., 2013). The spatial distribution of the indicators, suggest that the likely location for the potential seismogenic source lies in the middle of the Ticino District (southern Switzerland) close to the Periadriatic Line, but so far a quantitative estimation of the possible source location and paleo-magnitude is lacking.

Inversion For Paleo-Earthquake and Magnitude Estimation

This grid-search approach calculates the moment magnitudes (Mw) over a grid of trial source locations (Bakun and Wentworth, 1997) using an empirical intensity attenuation relationship (Fäh, 2003; Fäh et al., 2011).

We adopted the attenuation regression, specifically developed by (Fäh et al., 2011) for deep Alpine earthquakes which is already adopted in other similar studies (Strasser et al., 2006, 2013; Kremer et al., 2017; Oswald et al., 2021).

For epicentral distances < 55 km:

$$I = -2.8941 + 1.7196\ Mw - 0.03\ D\ ;$$

for epicentral distances > 55 km:

$$I = -4.2041 + 1.7196\ Mw - 0.0064\ D;$$

where I is the local Intensity (EMS98); Mw is the earthquake Moment Magnitude and D is the epicentral distance (km).

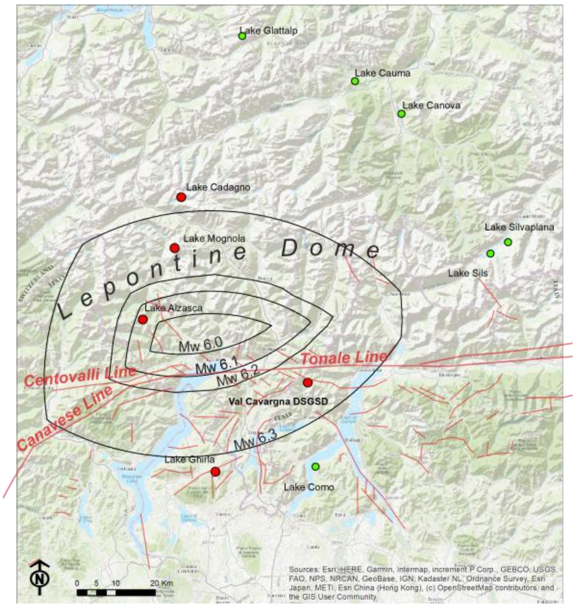

Figure 3: source inversion for the paleoearthquake location and Magnitude (Mw) given the locations of the Val Cavargna DSGSD and other spatially and temporally correlated evidence from offshore mass wasting movements (after Kremer et al., 2020); red dots indicate positive evidence; green dots indicate locations with negative evidence; potentially active faults (Hetényi et al., 2018) are drawn in the closeness of the study site (red lines).

Following the sensitivity analysis performed by Kremer et al. (2017), we solved the equations over an inverse grid search, by assuming an Intensity threshold value for mass wasting movement triggering of EMS98 VI 2⁄10. So far, we haven't considered locations with negative evidence (green dots in Figure 3); this would possibly reduce the possible source area of the seismogenic structure, especially excluding large part of the southernmost sectors.

After a comparison with the trace of the potentially active faults in central and Southern Alps (Hetényi et al., 2018) we can conclude that the potential source is located in the closeness of the Lepontine Dome. From this analysis, the most promising source is located at the junction between the Tonale and Centovalli Lines, where some evidence of Holocene active tectonics exists (e.g., Allanic and Gumiaux, 2013; Figure 3).

Alternatively, a deeper seismogenic source could be suggested , as recently pointed out by new crustal scale cross-sections across the area (Scaramuzzo et al., 2022).

REFERENCES

Agliardi, F., Crosta, G.B., Frattini, P., Malusà, M.G., 2013. Giant non-catastrophic landslides and the long-term exhumation of the European Alps. Earth and Planetary Science Letters 365, 263–274. https://doi.org/10.1016/j.epsl.2013.01.030

Agliardi, F., Crosta, G.B., Zanchi, A., Ravazzi, C., 2009. Onset and timing of deep-seated gravitational slope deformations in the eastern Alps, Italy. Geomorphology 103, 113–129. https://doi.org/10.1016/j.geomorph.2007.09.015

Allanic, C., Gumiaux, C., 2013. Are there any active faults within the Lepontine dome (central Alps)? Bulletin de La Société Géologique de France 184, 427–440. https://doi.org/10.2113/gssgfbull.184.4-5.427

Ambrosi, C., Crosta, G.B., 2006. Large sackung along major tectonic features in the Central Italian Alps. Engineering Geology 83, 183–200. https://doi.org/10.1016/j.enggeo.2005.06.031

Bakun, W. u, Wentworth, C.M., 1997. Estimating earthquake location and magnitude from seismic intensity data. Bulletin of the Seismological Society of America 87, 1502–1521.

Crosta, G.B., Frattini, P., Agliardi, F., 2013. Deep seated gravitational slope deformations in the European Alps. Tectonophysics 605, 13–33.

Fäh, D., 2003. Earthquake Catalogue Of Switzerland (ECOS) And The Related Macroseismic Database". Eclogae geol. Helv. Citeseer.

Fäh, D., Giardini, D., Kästli, P., Deichmann, N., Gisler, M., Schwarz-Zanetti, G., Alvarez-Rubio, S., Sellami, S., Edwards, B., Allmann, B., 2011. ECOS-09 earthquake catalogue of Switzerland release 2011 report and database. Public catalogue, 17. 4. 2011. Swiss Seismological Service ETH Zurich. RISK.

Forcella, F., Tibaldi, A., Onida, M., Galadini, F., 2001. Tecniche paleosismologiche per lo studio di deformazioni gravitative profonde di versante in ambiente alpino: esempi nella Valle del Foscagno e al Passo del Mortirolo (Alpi Centrali, Italia). Tettonica Recente e Instabilità Di Versante Nelle Alpi Centrali, Edited by: Pasquarè, G., Vol. Spec. CARIPLO, Milano 103–149.

Hetényi, G., Epard, J.-L., Colavitti, L., Hirzel, A.H., Kiss, D., Petri, B., Scarponi, M., Schmalholz, S.M., Subedi, S., 2018. Spatial relation of surface faults and crustal seismicity: a first comparison in the region of Switzerland. Acta Geodaetica et Geophysica 53, 439–461. https://doi.org/10.1007/s40328-018-0229-9

Kremer, K., Gassner-Stamm, G., Grolimund, R., Wirth, S.B., Strasser, M., Fäh, D., 2020. A database of potential paleoseismic evidence in Switzerland. Journal of Seismology 24, 247–262. https://doi.org/10.1007/s10950-020-09908-5

Kremer, K., Wirth, S.B., Reusch, A., Fäh, D., Bellwald, B., Anselmetti, F.S., Girardclos, S., Strasser, M., 2017. Lake-sediment based paleoseismology: Limitations and perspectives from the Swiss Alps. Quaternary Science Reviews 168, 1–18. https://doi.org/10.1016/j.quascirev.2017.04.026

Livio, F.A., Zerboni, A., Ferrario, M.F., Mariani, G.S., Martinelli, E., Amit, R., 2022. Triggering processes of deep-seated gravitational slope deformation (DSGSD) in an un-glaciated area of the Cavargna Valley (Central Southern Alps) during the Middle Holocene. Landslides 1–17.

Oswald, P., Strasser, M., Hammerl, C., Moernaut, J., 2021. Seismic control of large prehistoric rockslides in the Eastern Alps. Nature Communications 12, 1059. https://doi.org/10.1038/s41467-021-21327-9

Pasquaré, G. (Ed.), 2001. Tettonica recente e instabilità di versante nelle Alpi Centrali. Fondazione CARIPLO per la Ricerca Scientifica; CNR-Istituto per la Dinamica dei Processi Ambientali — Milano.

Poschinger, A.V., Wassmer, P., Maisch, M., 2006. The Flims rockslide: history of interpretation and new insiights. In: Evans, S.G., Mugnozza, G.S., Strom, A., Hermanns, R.L. (Eds.), Landslides from Massive Rock Slope Failure, NATO Science Series. Springer Netherlands, Dordrecht, 329–356. https://doi.org/10.1007/978-1-4020-4037-5_18

Scaramuzzo, E., Livio, F.A., Granado, P., Di Capua, A., Bitonte, R., 2022. Anatomy and kinematic evolution of an ancient passive margin involved into an orogenic wedge (Western Southern Alps, Varese area, Italy and Switzerland). Swiss Journal of Geosciences 115, 4. https://doi.org/10.1186/s00015-021-00404-7

Schmid, S.M., Aebli, H.R., Heller, F., Zingg, A., 1989. The role of the Periadriatic Line in the tectonic evolution of the Alps. Geological Society, London, Special Publications 45, 153–171. https://doi.org/10.1144/GSL.SP.1989.045.01.08

Strasser, M., Anselmetti, F.S., Fäh, D., Giardini, D., Schnellmann, M., 2006. Magnitudes and source areas of large prehistoric northern Alpine earthquakes revealed by slope failures in lakes. Geology 34, 1005–1008. https://doi.org/10.1130/G22784A.1

Strasser, M., Monecke, K., Schnellmann, M., Anselmetti, F.S., 2013. Lake sediments as natural seismographs: A compiled record of Late Quaternary earthquakes in Central Switzerland and its implication for Alpine deformation. Sedimentology 60, 319–341. https://doi.org/10.1111/sed.12003

Tibaldi, A., Rovida, A., Corazzato, C., 2004. A giant deep-seated slope deformation in the Italian Alps studied by paleoseismological and morphometric techniques. Geomorphology 58, 27–47. https://doi.org/10.1016/S0169-555X(03)00184-3

Wirth, S.B., Glur, L., Gilli, A., Anselmetti, F.S., 2013. Holocene flood frequency across the Central Alps – solar forcing and evidence for variations in North Atlantic atmospheric circulation. Quaternary Science Reviews 80, 112–128. https://doi.org/10.1016/j.quascirev.2013.09.002

INQUA Focus Group Terrestrial Processes Perturbed by Tectonics (TPPT)

paleoseismicity.org

Major California faults are smooth across multiple scales at seismogenic depth

Anthony Lomax (1), Pierre Henry (2)

(1) ALomax Scientific, 320 Chemin des Indes, 06360 Mouans-Sartoux, France. Email: anthony@alomax.net
(2) Aix Marseille Univ, CNRS, IRD, INRAE, Coll France, CEREGE, Aix-en-Provence, France. Email: henry@cerege.fr

Abstract: *Earthquake fault traces at the surface are typically complex on multiple scales. At seismogenic depth fault geometry is mainly constrained by earthquake locations. NLL-SSST-coherence earthquake location uses traveltime corrections to improve multi-scale precision (study extent to ~1km) and waveform similarity to improve fine-scale precision (e.g. sub-km). We apply NLL-SSST-coherence to large-earthquake sequences and background seismicity along strike-slip faults in California. Remarkably, the relocated seismicity at seismogenic depth often defines narrow, smooth, planar or arcuate, near-vertical surfaces from sub-km to 10's of km scales. This is the case along the San Andreas fault around Parkfield where previous precise relocations suggest twisting, kinked and offset fault surfaces. Our results suggest multi-scale smooth faulting is characteristic of mature, strike-slip fault zones, support use of smooth faults for earthquake rupture modeling, and underscore that surface traces of strike-slip fault zones may reflect complex, shallow deformation and not directly simpler, main slip surfaces at depth.*

Key words*: fault geometry, fault smoothness, seismicity, rupture physics, California.*

INTRODUCTION

The geometry, complexity and smoothness of earthquake faults are related to maturity of fault zones, rupture physics and earthquake hazard (Scholz, 2019). Surface traces of major, strike-slip faults are typically complex and segmented, and often associated with fault geometry at seismogenic depth and to the size, initiation, arrest and recurrence of large earthquake rupture (e.g. Bakun, 1980; Bakun et al., 1980; King & Nábělek, 1985; Manighetti et al., 2007; Wesnousky, 2006). Surface mapping and exhumed faults suggest faults are rough at all scales, from sub-mm to hundreds of km (Renard & Candela, 2017). However, on scales up to ~100 m the roughness of exposed fault surfaces is found to decrease with total slip (Sagy et al., 2007), and larger scale surface mapping implies a reduction in fault complexity with increasing geologic offset (Stirling et al., 1996).

For the ~60 km Parkfield segment of the strike-slip, San Andreas fault, California, high-precision and differential-timing relocations image a twisting surface (Kim et al., 2016; Perrin et al., 2019; C. Thurber et al., 2006) and, on the km scale, multiple, active fault patches offset by hundreds of meters perpendicular to the fault (Waldhauser et al., 2004). However, the geometry of mature faults and the main rupture zones of large earthquakes are often imaged (Cockerham & Eaton, 1984; Schaff et al., 2002; Graymer et al., 2007; Lomax, 2020a, 2020b) and modeled as smooth, near-planar surfaces.

So conflicting results underlie current understanding of the multi-scale geometry, complexity and smoothness of larger faults and large-earthquake rupture zones at seismogenic depth, and of the relation of this geometry to earthquake physics and to fault traces at the surface.

Seismicity shows the geometry and activity of faults, the stages of earthquake initiation, and the extent of large earthquake rupture, at seismogenic depth, including on and around surfaces of main, co-seismic slip and energy release. Useful and unbiased determination of the geometry, complexity and smoothness of faults from seismicity requires earthquake location with uniformly high precision over multiple scales.

NLL-SSST-coherence (Lomax & Savvaidis, 2022), an extended, arrival-time earthquake location procedure, uses travel-time corrections and waveform similarity to improve precision over many scales. Here we apply NLL-SSST-coherence to relocate recent large-earthquake sequences and background seismicity on major strike-slip faults in California. We find that the relocated seismicity at depth surrounding high-slip patches of large earthquakes and on long stretches of major fault zones generally defines narrow, planar or arcuate, multi-scale smooth, near-vertical surfaces. These results have implications for understanding of fault zone maturity, the physics of large earthquakes, for earthquake hazards and forecasting, and for the relation of surface traces and paleo-seismic results to faulting at depth.

MULTI-SCLAE HIGH-PRECISION EARTHQUAKE LOCATION

We obtain multi-scale, high-precision earthquake relocations using NLL-SSST-coherence (Lomax, 2020b; Lomax & Savvaidis, 2022), an extension of the NonLinLoc location algorithm (NLL; Lomax et al., 2000, 2014). NLL is highly robust to outlier data and performs efficient, global sampling to obtain a 3D, posterior probability density function (PDF) for hypocenter location. NLL-SSST-coherence extends NLL firstly with source-specific, station travel-time corrections over collapsing length scales (SSST; Richards-Dinger & Shearer, 2000), which reduce epistemic error and improve relative location accuracy and clustering of events over multi-scales (e.g. from study area size to ~1 km). Secondly, on the smallest scales (e.g. sub-km), NLL-SSST-coherence consolidates the SSST location PDF's of nearby, multiplet events, as measured by waveform similarity, greatly reducing aleatoric error.

SEISMICITY ALONG STRIKE-SLIP FAULTS IN CALIFORNIA

We first examine the 2004 Mw 6.0 Parkfield sequence and background seismicity along the central San Andreas fault, where Northern California Seismic System HypoDD relocations (NCSS-DD; Waldhauser, 2009) show a segmented and kinked fault geometry (Fig. 1ac, Video S1; Waldhauser et al., 2004), a common result for high-precision, differential-timing relocation. In contrast, NLL-SSST-coherence relocations (Fig 1bd, Video S2) show a smooth and near-planar fault surface across scales from sub-km to the ~50 km study extent. This near-planar surface follows the overall trend of surface faults on the largest scales, but not the smaller scale segmentation and complexity of these faults. The NLL-SSST-coherence relocations show no offsets or bends at seismogenic depth near the hypocenters of the 1966 M 5.5 and 2004 Mw 6.0 Parkfield earthquakes. These events ruptured nearly the same fault area but initiated at opposite ends of this area and propagated in opposing directions (Bakun et al., 2005); such differences in initiation point and rupture direction may be possible due to the planarity and smoothness of the fault at depth, i.e. fault complexity was not a controlling factor for initiation and other rupture characteristics (Bakun et al., 2005).

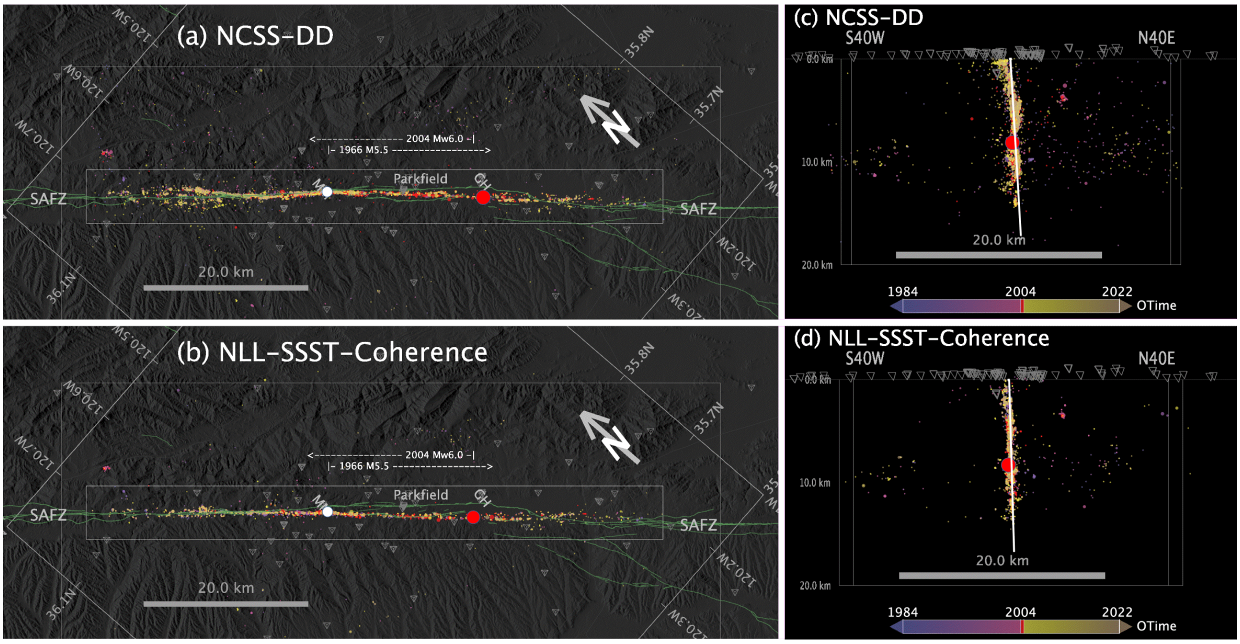

Figure 1: Seismicity along the central San Andreas fault zone around Parkfield. M ≥ 1.0, 1984 to 2022 hypocenters in map view for (a) NCSS-DD and (b) NLL-SSST-coherence relocations; inner gray box shows area used for SVD fit of plane to hypocenters. Section views from ~S40°E for (c) NCSS-DD and (d) NLL-SSST-coherence; near vertical, white line shows best fit SVD plane for each catalog. Hypocenter color shows origin time (red events within 6 months after the 2004 Mw 6.0 mainshock), symbol size is proportional to magnitude; larger white and red dots show 1966 M 5.5 and 2004 Mw 6.0 hypocenters, respectively. Inverted pyramids shows nearby seismic stations used for relocation. Green lines show faults from the USGS Quaternary fault and fold database for the United States, SAFZ – San Andreas Fault Zone, SWFZ – Southwest Fracture Zone, MM – Middle Mountain, GH – Gold Hill. Background topography from OpenTopgraphy.org.

We next examine the 1984 Mw 6.2 Morgan Hill sequence and background seismicity along the southern Calaveras fault zone. For this area, high-precision, NCSS-DD differential-timing relocations (Fig. 2a) again show a kinked and segmented character for the main lineation of seismicity. In contrast, NLL-SSST-coherence relocations (Fig. 2b) show a smoother, arcuate distribution of locations on intermediate and larger scales, especially along and around the 1984 Mw 6.2 aftershock zone (red events in figure). Neither set of relocations shows a clear relation of seismicity to the complex multitude of surface mapped faults, beyond similar, largest scale trends. And neither set shows a bend in the fault at seismogenic depth near the 1979 M 5.8 or 1984 Mw 6.2 hypocenters; such bends on surface fault traces have been proposed as related to the rupture initiation point for these and other earthquakes (Bakun, 1980; King & Nábělek, 1985). Both events ruptured to the southeast, which, given the sense of curvature of NLL-SSST-coherence seismicity and right-lateral rupture, is the direction where the fault forward of rupture falls in the dilatational quadrant of previous rupture, producing reduced normal stress across the fault and facilitating further slip. 1984 Mw 6.2 rupture terminates to the southeast where both sets of relocations show complexity and a possible small offset or kink. The 1979 M 5.8 main rupture likely terminated at a right step in fault segments, with later aftershocks along the segment to the SE (Reasenberg & Ellsworth, 1982).

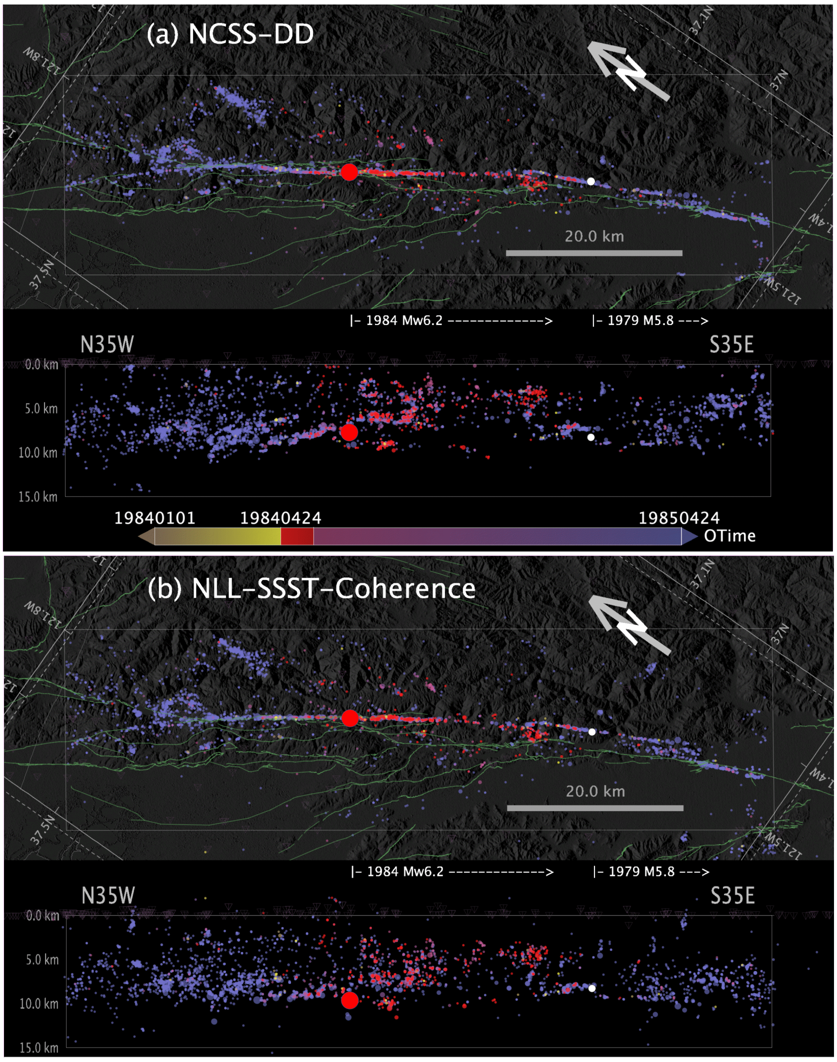

Figure 2: Seismicity along the southern Calaveras fault zone. Map and section views from S55°W of (a) NCSS-DD and (b) NLL-SSST-coherence relocations of events of M ≥ 1.5, 1984 to 2022. Hypocenter color shows origin time (red events within first month after the 1984 Mw 6.2 mainshock), symbol size is proportional to magnitude; larger white and red dots show 1979 M 5.8 and 1984 Mw 6.2 hypocenters, respectively. Map views are tilted to best align along the near-vertical plane of Mw 6.2 aftershocks: NCSS-DD view plunges 84° NE; NLL-SSST-coherence view plunges 81° NE. Arrows show approximate main rupture extent for the 1979 M 5.8 (Reasenberg & Ellsworth, 1982) and 1984 Mw 6.2 (Cockerham & Eaton, 1984) events. Inverted pyramids shows nearby seismic stations used for relocation. Green lines show faults from the USGS Quaternary fault and fold database for the United States. Background topography from OpenTopgraphy.org.

DISCUSSION

NLL-SSST-coherence greatly increases relative location accuracy on multiple scales within a standard, arrival-time location framework. With relocation of large-earthquake sequences and background seismicity along the San Andreas (Parkfield) and Calaveras strike-slip faults in California, we have shown that NLL-SSST-coherence relocated seismicity at seismogenic depth along major faults and surrounding large-earthquake ruptures often defines narrow, smooth, planar (Parkfield) or arcuate (Calaveras), near-vertical surfaces across multiple scales. NLL-SSST-coherence gives similar results for seismicity along other fault segments in California, including Cape Mendocino (Lomax et al., 2022) and Monte Cristo (Lomax, 2020b). In many of these cases, NCSS-DD and other high-precision, differential-timing relocations show twisting, kinked, segmented or offset fault surfaces.

There is no obvious reason why NLL-SSST-coherence would smooth seismicity as an artifact. Indeed, the multi-scale, NLL-SSST corrections should preserve any true roughness. In contrast, other high-precision location procedures could produce artifact kinks and offsets between nearby clusters of hypocenters if based on reference locations lacking multi-scale corrections for model and data error, with the precise, differential timing data improving precision only on the smallest scales.

Our NLL-SSST-coherence relocations suggest that multi-scale smooth faulting may be characteristic of mature, strike-slip fault zones, that planar and smooth alignments of background seismicity can delimit zones of earthquake hazard, and support use of planar or smoothly curved faults for earthquake rupture modeling. Furthermore, the smoothness and curvature of faults likely influences large earthquake initiation (possible anywhere within smooth fault segments), rupture (if the fault is curved, there may be a preferred direction for rupture), and arrest (favored at kinks, steps or other non-smooth fault complexities).

The NLL-SSST-coherence relocations mainly concentrate on a single, smooth surface at deeper than a few km depth below zones with a multitude of surface traces. This relation provides further evidence that surface traces and offsets of strike-slip fault zones reflect complex, shallow deformation, perhaps involving braided and upwards diverging splay faults (e.g. Christie-Blick & Biddle 1985; Graymer et al., 2007), and not directly simpler slip surfaces at depth (e.g. Schaff et al., 2002) where most co-seismic slip and energy release occurs.

REFERENCES

Bakun, W. H. (1980). Seismic activity on the southern Calaveras Fault in central California. Bull. Seism. Soc. Am., 70(4), 1181–1197. https://doi.org/10.1785/BSSA0700041181

Bakun, W. H., Stewart, R. M., Bufe, C. G., & Marks, S. M. (1980). Implication of Seismicity for Failure of a Section of the San Andreas Fault. Bull. Seismol. Soc. Am., 70. https://doi.org/10.1785/BSSA0700010185

Bakun, W. H., Aagaard, B., Dost, B., Ellsworth, W. L., Hardebeck, J. L., Harris, R. A., et al. (2005). Implications for prediction and hazard assessment from the 2004 Parkfield earthquake. Nature, 437(7061), 969–974. https://doi.org/10.1038/nature04067

Christie-Blick, N., & Biddle, K. T. (1985). Deformation and basin formation along strike-slip faults. In K. T. Biddle & N. Christie-Blick (Eds.), Strike-slip deformation, basin formation and sedimentation. Society of Economic Paleontologists and Mineralogists Special Publication, 37, 1–34. https://doi.org/10.2110/pec.85.37.0001

Cockerham, R. S., & Eaton, J. P. (1984). The April 24, 1984 Morgan Hill earthquake and its aftershocks: April 24 through September 30, 1984. In The Morgan Hill, California, Earthquake. San Francisco, California: Calif. Dept. of Conserv., Div. of Mines and Geol. https://doi.org/10.3133/b1639

Graymer, R. W., Langenheim, V. E., Simpson, R. W., Jachens, R. C., & Ponce, D. A. (2007). Relatively simple through-going fault planes at large-earthquake depth may be concealed by the surface complexity of strike-slip faults. Geological Society, London, Special Publications, 290(1), 189–201. https://doi.org/10.1144/SP290.5

Kim, W., Hong, T.-K., Lee, J., & Taira, T. (2016). Seismicity and fault geometry of the San Andreas fault around Parkfield, California and their implications. Tectonophysics, 677–678, 34–44. https://doi.org/10.1016/j.tecto.2016.03.038

King, G., & Nábělek, J. (1985). Role of Fault Bends in the Initiation and Termination of Earthquake Rupture. Science, 228(4702), 984–987. https://doi.org/10.1126/science.228.4702.984

Lomax, A. (2020a). Absolute Location of 2019 Ridgecrest Seismicity Reveals a Shallow Mw 7.1 Hypocenter, Migrating and Pulsing Mw 7.1 Foreshocks, and Duplex Mw 6.4 Ruptures. Bull. Seism. Soc. Am., 110(4), 1845–1858. https://doi.org/10.1785/0120200006

Lomax, A. (2020b). The 2020 Mw 6.5 Monte Cristo Range, Nevada earthquake: relocated seismicity shows rupture of a complete shear-crack system. https://doi.org/10.31223/X5X015

Lomax, A., & Savvaidis, A. (2022). High-Precision Earthquake Location Using Source-Specific Station Terms and Inter-Event Waveform Similarity. J. Gephys. Res.: Solid Earth, 127(1), e2021JB023190. https://doi.org/10.1029/2021JB023190

Lomax, A., Virieux, J., Volant, P., & Berge-Thierry, C. (2000). Probabilistic Earthquake Location in 3D and Layered Models. In C. H. Thurber & N. Rabinowitz (Eds.), Advances in Seismic Event Location (Vol. 18, pp. 101–134). Dordrecht: Springer Netherlands. https://doi.org/10.1007/978-94-015-9536-0_5

Lomax, A., Michelini, A., & Curtis, A. (2014). Earthquake Location, Direct, Global-Search Methods. In R. A. Meyers (Ed.), Encyclopedia of Complexity and Systems Science (pp. 1–33). New York, NY: Springer New York. https://doi.org/10.1007/978-3-642-27737-5_150-2

Lomax, A., McPherson, R. C., Patton, J. R., Hellweg, M., Dengler, L., et al. (2022) Application of High-precision, NLL-SSST-coherence Earthquake Location to Untangle the 3D Seismotectonics of the Mendocino Triple- junction, Northern California. Seismological Research Letters, 93(2B), 1240. https://doi.org/10.1785/0220220087

Manighetti, I., Campillo, M., Bouley, S., & Cotton, F. (2007). Earthquake scaling, fault segmentation, and structural maturity. Earth and Planetary Science Letters, 253(3–4), 429–438. https://doi.org/10.1016/j.epsl.2006.11.004

Perrin, C., Waldhauser, F., Choi, E., & Scholz, C. H. (2019). Persistent fine-scale fault structure and rupture development: A new twist in the Parkfield, California, story. Earth and Planetary Science Letters, 521, 128–138. https://doi.org/10.1016/j.epsl.2019.06.010

Reasenberg, P., & Ellsworth, W. L. (1982). Aftershocks of the Coyote Lake, California, earthquake of August 6, 1979: A detailed study. J. Gephys. Res.: Solid Earth, 87(B13), 10637–10655. https://doi.org/10.1029/JB087iB13p10637

Renard, F., & Candela, T. (2017). Scaling of Fault Roughness and Implications for Earthquake Mechanics. In Fault Zone Dynamic Processes (pp. 195–215). American Geophysical Union (AGU). https://doi.org/10.1002/9781119156895.ch10

Richards-Dinger, K. B., & Shearer, P. M. (2000). Earthquake locations in southern California obtained using source-specific station terms. J. Gephys. Res.: Solid Earth, 105(B5), 10939–10960. https://doi.org/10.1029/2000JB900014

Sagy, A., Brodsky, E. E., & Axen, G. J. (2007). Evolution of fault-surface roughness with slip. Geology, 35(3), 283–286. https://doi.org/10.1130/G23235A.1

Schaff, D. P., Bokelmann, G. H. R., Beroza, G. C., Waldhauser, F., & Ellsworth, W. L. (2002). High-resolution image of Calaveras Fault seismicity. J. Gephys. Res.: Solid Earth, 107(B9), ESE 5-1-ESE 5-16. https://doi.org/10.1029/2001JB000633

Scholz, C. H. (2019). The Mechanics of Earthquakes and Faulting (3rd ed.). Cambridge: Cambridge University Press. https://doi.org/10.1017/9781316681473

Stirling, M. W., Wesnousky, S. G., & Shimazaki, K. (1996). Fault trace complexity, cumulative slip, and the shape of the magnitude-frequency distribution for strike-slip faults: a global survey. Geophys. J. Int., 124(3), 833–868. https://doi.org/10.1111/j.1365-246X.1996.tb05641.x

Thurber, C., Zhang, H., Waldhauser, F., Hardebeck, J., Michael, A., & Eberhart-Phillips, D. (2006). Three-Dimensional Compressional Wavespeed Model, Earthquake Relocations, and Focal Mechanisms for the Parkfield, California, Region. Bull. Seism. Soc. Am., 96(4B), S38–S49. https://doi.org/10.1785/0120050825

Waldhauser, F., Ellsworth, W. L., Schaff, D. P., & Cole, A. (2004). Streaks, multiplets, and holes: High-resolution spatio-temporal behavior of Parkfield seismicity. Geophysical Research Letters, 31(18). https://doi.org/10.1029/2004GL020649

Wesnousky, S. G. (2006). Predicting the endpoints of earthquake ruptures. Nature, 444(7117), 358–360. https://doi.org/10.1038/nature05275

INQUA Focus Group Terrestrial Processes Perturbed by Tectonics (TPPT)

paleoseismicity.org

Structural architecture and kinematic properties of faults in the Dubrovnik area and its hinterland (Croatia, Bosnia and Herzegovina, Montenegro)

Maslač, Josipa (1), Bojan Matoš (2), Ivica Pavičić (2), Igor Vlahović (2)

(1) Croatian Geological Survey (HGI-CGS), Department of Geology, Sachsova 2, HR-10 000 Zagreb, Croatia. E-mail: jmaslac@hgi-cgs.hr
(2) University of Zagreb, Faculty of Mining, Geology and Petroleum Engineering, Department of Geology and Geological Engineering, Pierottijeva 6, HR-10 000 Zagreb, Croatia

Abstract: *Dalmatia is considered as one of the three tectonically most active regions in Croatia, characterized by moderate to strong seismicity with several instrumentally recorded earthquakes of M_w6. Identification of potential seismogenic sources and their detailed segmentation within epicentral areas is of great importance in seismic hazard and risk assessment procedure. Results of structural modelling with associated depths and faults geometrical relations as well as a seismological data indicate fault-related fold structure that accommodated vertical displacement more than 3500 m. Furthermore, faults geometrical peculiarities suggest complex tectonic history associated with presence of Triassic ductile deposits resulting with complex seismogenic source geometry alongside associated distribution of hypocenters. Based on the 3D modelling, empirical computations of identified fault segments maximal magnitudes are estimated in a range between M_w 6.29-7.53.*

Key words: *Dinarides, nappe tectonics, Dubrovnik, 2D/3D structural modelling, seismogenic source, estimated magnitudes*

INTRODUCTION

The area of southern Dalmatia has characterized by strong historically and instrumentally recorded seismicity with strong M_w>6 earthquakes, such as the Great Dubrovnik earthquake 1667, Herceg-Novi 1979, Ston-Slano 1996, Durrës 2018 (Herak et al. 1996; Markušić et al., 1998; Ivančić et al., 2018). This area is still an active deformation front confirmed by instrumental monitoring and several hundred earthquakes registered per year in the area of southern Dalmatia (Kastelic & Carafa, 2012). The epicenters are predominantly detected in the Adriatic Sea offshore, where the majority of seismogenic sources are located. Seismogenic sources are mostly NW-SE oriented reverse faults that accomodated tectonic uplift from late Eocene and Oligocene (Pamić et al., 1998). Focal depths of earthquakes range from 2 to 20 km due to crustal thickening in the collision zone of the undeformed part of the Adriatic microplate (Tomljenović et al., 2009 and references therein). The studied epicentral area (Fig. 1.) is located within the South Dalmatian zone of the External Dinarides, contact collision area of the Adria microplate with the Eurasian plate (Schmid et al., 2008; Balling et al., 2021). Convergence rates of the Adria microplate to the Eurasian plate is from 0.5 to 4.5 mm/year (Weber et al., 2010).

In this paper, an attempt was made to interpret the structural assembly based on five subparallel geological cross-sections in the area (Fig 2). Sections are perpendicular to the Dinarides, in order to obtain a clearer subsurface relations, 3D visualization and interpretation of the complex subsurface structure. The modelled fault surfaces with derived geometric parameters were used for the empirical calculation of the maximum magnitudes of possible earthquakes, whichmay address local seismic risk, for a specific area.

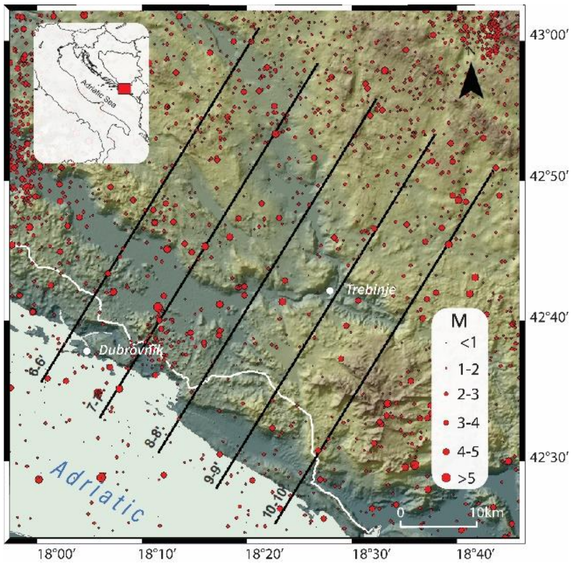

Fig. 1. The research area with historically and instrumentally recorded seismicity (time period) and lines of constructed profiles as initial data for creating a 3D structural model.

METHODS AND RESULTS

Initial dataset of five regional geological cross-sections (c. 55 km long, perpendicular to the Dinaridic structures) based on 1:100,000 Basic Geological Maps (Marković, 1966; Antonijević et al., 1969; Mojićević and Laušević, 1965; Vujisić 1967; Natević and Petrović, 1964–1965), were constructed and used for building a conceptual geological three-dimensional model of the study area (Fig 3). Input data were pre-processed using *Arc GIS Pro, Arc GIS 10.1* and *Adobe Illustrator* software, while conceptual three-dimensional model and assessment of modelled faults geometrical properties were assembled using *Petroleum Expert Move* software.

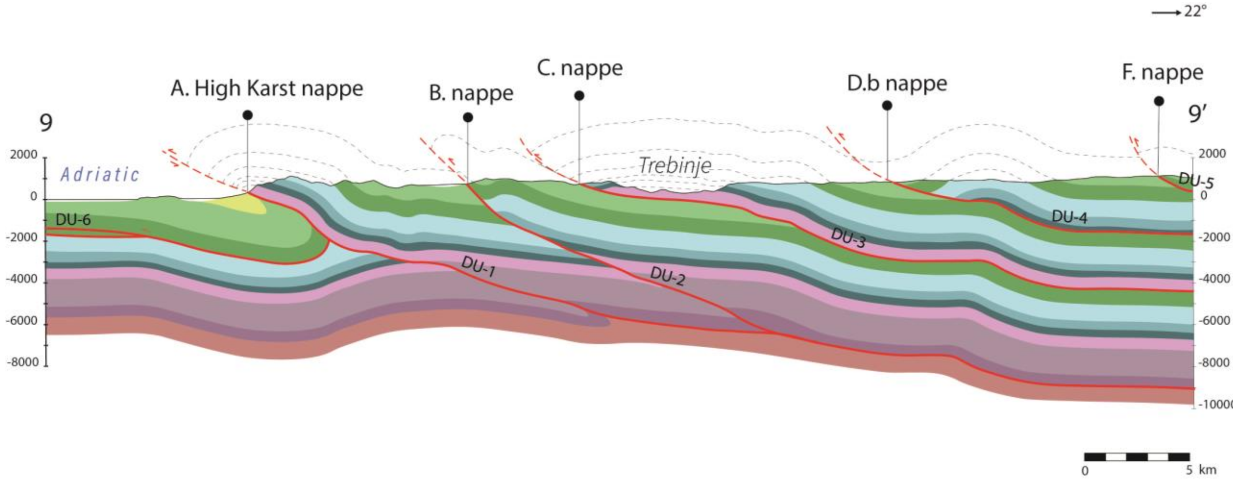

Fig. 2. Interpretation of one of the geological ccross-sections used in the construction of the conceptual 3D structural model

The geological structure of the High Karst tectonic unit generally consists three subunits: carbonate complex of Mesozoic age, Paleogene-Neogene carbonate-clastic deposits and Quaternary uncosolidated clastic deposits (Protrljan et al., 2015). Compresional structures, i.e., fault-bend and fault-propagation folds, are related to low angle faults (Fig 2,3 and 5). Reverse faults differ on average with slopes between 10° and 50°, that are adapted to the projection and resolution of the surface in the software, while strike-slip faults are completely ignored in modelling procedure due to the complexity of the structure. Thrusting related structures, i.e., High Kart tectonic unit have a complex geometry and indicate the formation of a series of asymmetric cogenetic folded structures formed as a consequence of tectonic activities during Eocene and Oligocene (Vlahović et al., 2005). The model is additionally supplemented with seismological data, i.e. a catalog of instrumentally recorded earthquakes provided by USGS. Results shows that the shallowest earthquakes (up to 5 km deep) are represented mostly in the southeastern part of the research area, between cross-section 6-6′ and 8-8′. In the same position, according to the data from the Basic geological maps 1:100.000, a horizontal displacement was observed. The same displacement is clearly expressed by the increased convexity of the High karst nappe during the quantitative analysis of the displacement along the modelled fault surfaces (Fig 4). The maximum measured throw in Jurassic deposits is in a range of 6 km, minimum throw in Middle Triassic deposits 1 km and average throw approximately 3,5 km. Throw values suggests the change of compression intensity during geological periods and detachment faulting in Triassic zone of ductile deposits.

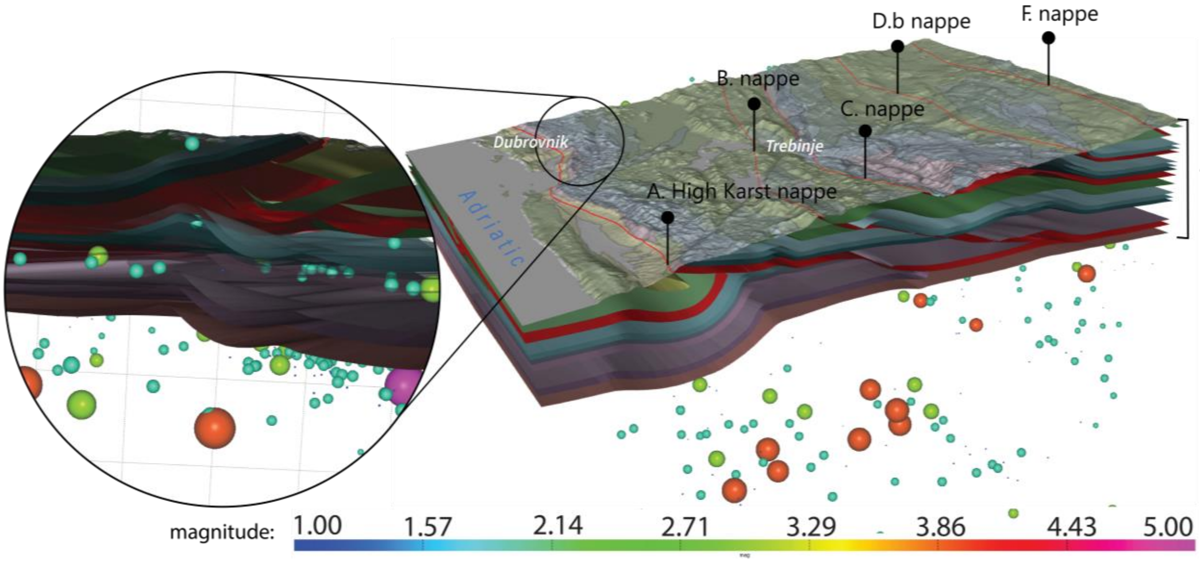

Fig. 3. The final version of the constructed 3D structural-geological model of the area. The models show thrust fault systems with interpreted stratigraphic units, surface geological relationships and the spatial relationship of earthquake hypocenters.

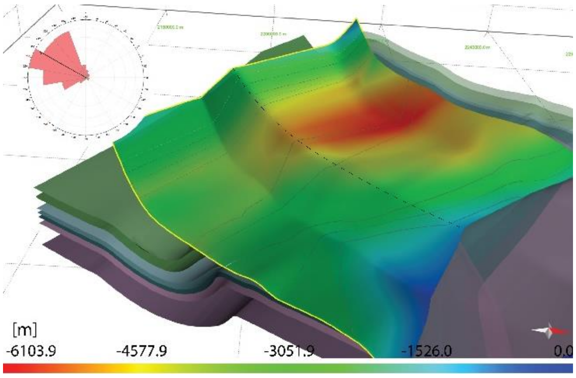

Fig. 4. Analysis of vertical displacements on the surface of the DU-1 fault oriented towards the NW

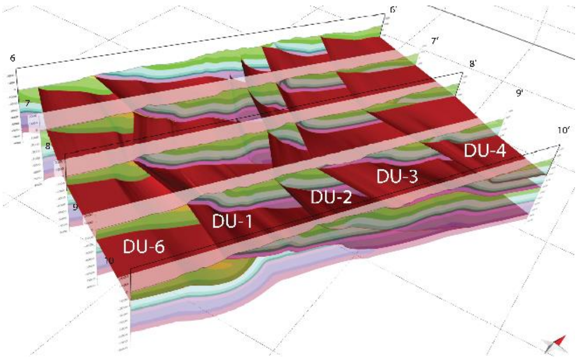

Fig. 5. The generated fault system of selected geometric parameters included in the assessment of seismogenic potential

fault	length (km)	dip (°)	type	active fault surface (km²)	estimated maximum magnitude
DU-1	38,6	11	REV	1690,7	7,53
DU-2	38,5	14	REV	956,7	7,28
DU-3	39,4	10	REV	966,4	7,29
DU-4	38,4	13	REV	486,9	6,99
DU-5	36,9	16	REV	96,2	6,29
DU-6	38,5	4	REV	515,5	7,02?

Table 1. Table of data used to estimate values of maximum magnitudes on generated fault surfaces

In this work, assessment of the seismogenic potential of the modelled fault surfaces in the constructed structural model is based on the fault parameters described in the work of Wells and Coppersmith (1994). For this purpose, the geometric parameters include the length of the fault along its strike and the width of the fault surface, i.e., total surface of the fault or the active surface of the faults. In addition to the geometric parameters of active faults, data on the type and character of displacement and the dip were also used in the calculation of empirical values of earthquake magnitudes. Empirical computation of maximal magnitudes of identified fault segments estimates potential between M_w 6.29-7.53.

DISCUSSION

Distribution of hypocenters and faults geometrical peculiarities suggest complex seismogenic source geometries, with general subvertical orientation in the near-surface, whereas in the deeper sections, hypocenters indicate listric-shaped geometry of seismogenic sources. Considering the values of the calculated magnitudes for the modeled distributions, it should be emphasized here that the values are large, suggesting a necessity of more detailed study of the identified seismogenic sources at the scale of individual seismogenic segment. This initial structural model will be further improved combining additional geological cross-sections with the proposed model, adding detailed seismological data collected by the Croatian-Seismological-Survey as well as including available seismic reflection profiles recorded in the nearby Adriatic offshore. It is expected that using such an approach will contribute to a detailed definition of local seismogenic sources, i.e., fault's segments in the wider Dubrovnik area, increasing overall knowledge on present seismogenic sources and potential geohazards in the area.

REFERENCES

Antonijević, R., Pavić, A., Karović, J. (1969): Basic Geological Map of Yugoslavia 1:100.000, Sheet Kotor K34-50. *Federal Geological Institute Beograd*, Belgrade.

Balling, P., Tomljenović, B., Schmid, S.M., Ustaszewski, K. (2021): Constrasting along-strike deformation styles in the central External Dinarides assessed by balanced cross-sections: Implications for the tectonic evolution of its Paleogene flexural foreland basin system. *Global and Planetary Change*, 205.

Herak, M., Herak, D., Markušić, S. (1996.): Revision of the earthquake catalogue and seismicity of Croatia, 1908–1992. *Terra Nova*, 8 (1): 86–94.

Ivančić, I., Herak, D., Herak, M., Allegretti, I., Fiket, T., Kuk, K., Markušić, S., Prevolnik, S., Sović, I., Dasović, I., Stipčević, J. (2018): Seismicity of Croatia in the period 2006–2015. *Geofizika*, 35 (2018), 1; 69–98.

Marković, B. (1971): Basic Geological Map of Yugoslavia 1:100.000, Sheet Dubrovnik K34–49, *Federal Geological Institute Beograd*, Belgrade.

Markušić, S., Herak, D., Ivančić, I., Sovi, I., Herak, M., Prelogović, E.,(1998.), Seismicity of Croatia in the period 1993–1996 and the Ston–Slano earthquake of 1996. *Geofizika*. 15 (1998) ; 83–101.

Mojićević, M. and Laušević, M. (1965.): Basic Geological Map of Yugoslavia 1:100.000, Sheet Nevesinje K34-32. *Federal Geological Institute Sarajevo*, Sarajevo.

Natević, Lj. and Petrović, V. (1965): Basic Geological Map of Yugoslavia 1:100.000, Sheet Trebinje K34-37. *Federal Geological Institute Beograd*, Belgrade.

Pamić, J., Gušić, I., Jelaska, V., 1998. Geodynamic evolution of the Central Dinarides. *Tectonophysics*, 297, 251–268.

Prtoljan, B., Vlahović, I., Velić, I. (2015): Basic Geological Map of Republic Croatia 1:50 000, Sheet Konavle, *Croatian Geological Survey*, Zagreb, ISBN: 978-953-6907-33-5.

Schmid, S.M, Bernoulli, S., Fügenschuh, B., Matenco, L., Schefer, S., Schuster, R., Tischler, M., Ustaszewski, K. (2008): The Alpine–Carpathian–Dinaridic orogenic system: correlation and evolution of tectonic units. *Swiss J. Geosci*., 101, 139–183.

Tomljenović, B., Herak, M., Herak, D., Kralj, K., Prelogović, E., Bostjančić, I. & Matoš, B., 2009. Active tectonics, seismicity and seismogenic sources of the Adriatic coastal and offshore region of Croatia. In: 28 Convegno Nazionale "Riassunti Estesi delle Comunicazioni", Eds: Slejko, D. & Rebez, A., Trieste. *Stella Arti Grafice*, 133–136.

Vlahović, I., Tišljar, J., Velić, I. i Matičec, D. (2005): Evolution of the Adriatic Carbonate Platform: Paleogeography, main events and depositional dynamics. *Palaeogeography, Palaeoclimatology, Palaeoecology*, 220, 333–360.

Vujisić, T. (1967): Basic Geological Map of Yugoslavia 1:100.000, Sheet Nikšić K34-38. *Federal Geological Institute Beograd*, Belgrade.

Wells, D.L. and Coppersmith, K.J., 1994. Empirical relationships among magnitude, rupture length, rupture width, rupture area, and surface displacement. *Bulletin of the Seismological Society of America* 84 (4), 974–1002.

ADVANTAGES OF RETRODEFORMING TRENCH LOGS

McCalpin, James

(1) GEO-HAZ Consulting, Inc., P.O. Box 837, Crestone, CO 81131 USA . Email: mccalpin@geohaz.com

Abstract: *The object of trenching fault scarps is to derive fundamental behavioral parameters for the fault, such as number of paleoearthquakes, displacement per event, and recurrence interval. For scarps created by only one or two paleoearthquake events, interpretation of the trench log is simple. But as the number of faulting events increases, the younger events begin to disrupt and obscure evidence of the earlier events on the trench wall. This paper discusses the importance of graphical retrodeformation of trench wall logs, as an objective, reviewable method for deriving the number of paleoearthquakes, displacement per event, and recurrence interval. The emphasis here is one normal faults, but retrodeformation can similarly apply to any faults with a significant vertical component.*

Key words*: trenching, trench logs, recurrence interval, dating.*

Introduction to the Problem

By the mid-1990s seismic hazard analysts were complaining that paleoseismic data submitted for PSHA logic trees was too imprecise, being mean values without a measure of variance. This criticism was valid, because most faults at the time were characterized from only one or two trench sites, and each trench captured only one or two paleoearthquakes. Two earthquakes could define only a single seismic cycle, so for recurrence interval, there was often only a single measurement with no way to assess the variance in recurrence interval through time. Hazard analysts said they would like a probability distribution of fault recurrence interval on each fault based on at least 10 seismic cycles….

The only way to capture the latest 11 paleoearthquakes on a dip-slip fault was to trench very high, multi-event fault scarps, some as much as 25 m high. This required very deep trenches ("megatrenches") that exposed strata on the downthrown block at least 12 m thick (approximately half the scarp height). The first such trench in North America was the Wasatch fault (Utah) megatrench of 1999 (McCalpin, 2002). The trench exposed 18 m of stratigraphic section on the downthrown block, exposing displacements from the latest seven surface-faulting events.

Although the trench was a success in exposing a long record of faulting, it also exposed a two new difficulties. First, the seven consecutive events produced a large number of fault strands of different ages. Second, colluvial-wedge deposits (and their paleosols) formed in earlier events had been progressively deformed by later events, to the degree it was hard to recognize them, or to measure their displacements during each displacement event. What was needed was an analytical tool that could reconstruct the trench wall at various points in time, up to the present. Such reconstruction was known as "retrodeformation" (see McCalpin, 2009, p. 250-263). The simplest type assumed brittle faulting and only translational & rotational movements along faults, as is typical in normal faulting (i.e., no plastic deformation).

Types of Rigid-Block Retrodeformations

Retrodeformations are classified by how much the trench log is generalized, and whether there is a drawing block representing every geologic event (Table 1).

Table 1. Retrodeformation terminology; simplified from McCalpin, 2009, p. 262.

Degree of Generalization of Trench Log	
Schematic	Geometry of deposits and structures is significantly simplified, but without sacrificing stratigraphic order or cross-cutting relationships. Contacts are made straight lines.
Simplified	All faults with displacement are made straight lines, so that displacements in each event can be reversed without creating gaps or overlaps in the deposits at the fault zone.
Realistic	The trench log to be retrodeformed is not modified in any way. However, if the faults are not perfectly planar, reversing their displacement will create gaps and overlaps in the fault zone. These will have to be fixed by reshaping fault-zone polygons, which consumes time & effort and but does not change the overall sequence of displacement events.
Degree of Temporal Completeness	
Complete	Every deformational, depositional, erosional, and weathering episode is represented by a separate cross-section (time stage).
Incomplete	Some reconstructed events in the chronology may be combined into a single time stage (e.g., deposition of a unit and subsequent development of a soil profile on it, or deposition of a series of conformable strata represented by a single stage). Or, the sequence of stages may stop before all the deformation is reversed.

In the following sections we show examples of rigid-block retrodeformations of Holocene normal fault trench logs in the western USA. Most retrodeformations would be classified as simplified & complete. However, it is also possible in journal publication to omit some steps, as long as the figure caption mentions this.

Wasatch Fault Zone, Utah (7 displacement events)

Fig. 1 shows the complexly faulted upper fault zone in the 1999 Wasatch megatrench, which has experienced seven meter-scale displacement events in the past ca. 20 ka.

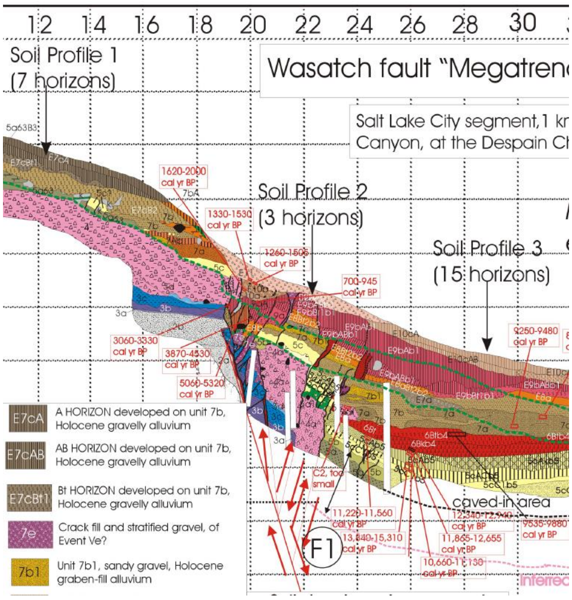

Fig. 1. Log of 6 m-deep exposure of main fault zone beneath upper scarp, Wasatch megatrench. Hanging wall adjacent to fault has fragmented into four fault-bounded blocks which topple toward the right. Seven displacement events are recognized. From McCalpin, 2002.

The retrodeformation sequence (Fig. 2) made all faults vertical, making it schematic/complete. Although seven displacement events are required to explain stratigraphic variations among the blocks, only four of those events are represented by colluvial wedges preserved today.

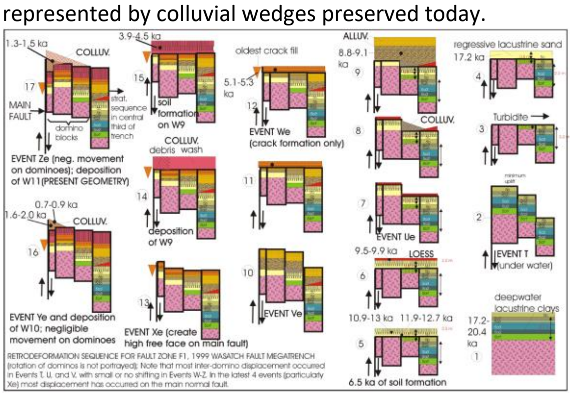

Fig. 2. Retrodeformation of fault-bounded blocks in the upper fault zone, Wasatch megatrench. Hanging wall fault-bounded blocks carry different stratigraphy, forming the basis of this analysis. Present geometry is Stage 17 (upper left); pre-faulting geometry is Stage 1 (lower right).

In the other three events, either no wedge was created by a subaqueous displacement (Stage 3), or all scarp-derived colluvium fell into a fissure (Stage 12), or a wedge formed but was eroded away (Stage 11) due to fluvial processes in the graben.

Stillwater Scarp, central Nevada (6 displacement events)

The Stillwater scarp is a ridge-crest sackung scarp which faces upslope and blocks the drainage outlet of the graben (McCalpin and Jones, 2021). Our 3.2 m-deep trench across the 0.6 m-high scarp in the drainage outlet exposed a normal fault. The fault footwall (FW) was composed of fault gouge, altered limestone, and fractured but fresh limestone (Fig. 3). The fault hanging wall (HW) was composed of 3.2 m of post-faulting deposits in six discrete packages that led us to adopt the following depositional model (after McCalpin, 2005). After each displacement event, an uphill-facing fault scarp was produced and blocked the graben drainage outlet. Most scarp-derived debris rapidly fell into large tension fissures at the scarp base, so colluvial wedges are absent or have small volume. Following the first significant runoff event, thin sag pond silts buried the fissure fill and/or colluvium.

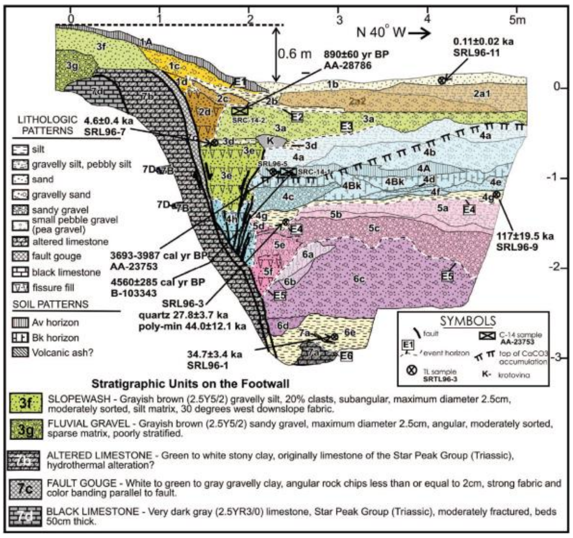

Fig. 3. Trench log of an antislope normal fault at the crest of the Stillwater Range, Nevada, USA (from McCalpin and Jones, 2021).

As the scarp was progressively buried by alluviation over thousands of years, HW deposits became coarser, indicating a more through-going outlet stream with greater bedload competence. Finally, the scarp was completely buried by HW aggradation, the stream channel flowed unimpeded from the HW over the FW, and channel-facies alluvium was deposited. This coarsening-upward package is often capped by a soil if sufficient time elapses between faulting events. In this last phase, channel scouring can occur on the FW, removing older fluvial deposits and paleosols. However, correlative deposits and paleosols were preserved on the down-dropped HW.

A simplified/complete retrodeformation indicated that six displacement events (two historic, four prehistoric) were required to explain the present trench-wall geometry (Fig. 4). The most surprising result was that, of the 35 ka represented by trench strata, 20-25 ka was consumed by a soil-forming hiatus (Stage 12, Soil 4A/B) during which no displacements occurred.

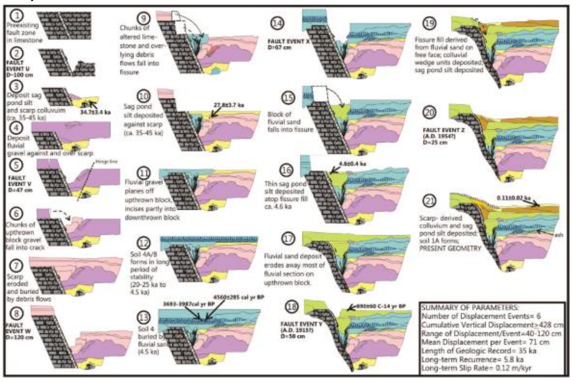

Fig. 4. Log of an antislope normal fault at the crest of the Stillwater Range, Nevada, USA. Sag pond deposits in yellow.

Zia Fault, Rio Grande Rift (>5 displacement events)

The Zia fault is a 37 km-long normal fault that bounds the western margin of the Albuquerque-Belen Basin. In the past 0.5-1.5 Ma vertical displacement on the Zia fault has created a 20 m-thick syntectonic depositional wedge that is presently exposed on the erosional badlands of the Ceja de Rio Jemez. Our trenches were located about 250 m south of the badlands rim, where a 100 m-wide graben has formed east of the main, 5 m-high fault scarp.

The middle trench (Fig. 5) across the steepest, highest part of the scarp reveals evidence for at least 5 faulting events with vertical displacements ranging from 0.6 to 2.6 m (average of 1.3 m). As with the Wasatch megatrench, the faults zone was 5 m wide and contained 12 faults. Faults 1 through 6b are in the FW and dip steeply east (normal faults), have significant displacement, and form five fault-bounded blocks which bring up old HW stratigraphic units (units 3 through 8). In contrast, the five F7 faults are in the HW, dip steeply west, and have minor displacement in younger HW strata (units 9 through 25). We tentatively correlate unit 12g on the HW with unit 12g on the FW fault sliver between faults F5 and F6b.

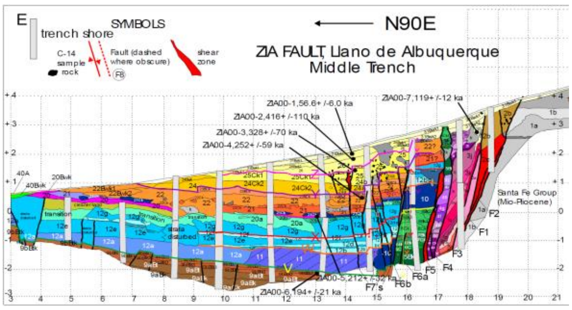

Fig. 5. Log of the 5 m-deep middle trench on the Zia fault, western margin of the Albuquerque Basin, New Mexico, USA. From McCalpin and Harrison, 2001.

Scarp deposition at this site is dominated by eolian sand and by alluvium composed of reworked sand. In the absence of clasts, scarp-derived colluvial wedges cannot be recognized except in the grossest sense. Our retrodeformation was based on the same technique used for the Wasatch megatrench; different tabular stratigraphic sequences on the different fault blocks of the HW bounded by faults F6b and F7's.

This tedious exercise identified five displacement events required to reproduce the present HW geometry. However, we became aware it was not really necessary to base the retrodeformation drawings on the detailed trench log, because we were only analysing differential displacements of the earthquake horizons. So we created a "wireframe" view of the trench log that contained only the earthquake horizons V through Z (Fig. 5).

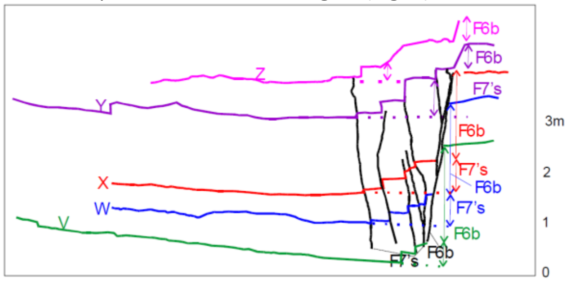

Fig. 5. Wireframe rendition of the Zia fault trench log showing only the paleoearthquake unconformities ("earthquake horizons").

From the wireframe we could remove displacement from the Most Recent Event (MRE) on each fault and then examine how much displacement was left (pre-dated MRE). By doing this with each event in turn, we established which events had been responsible for how much displacement on each fault (Fig. 6).

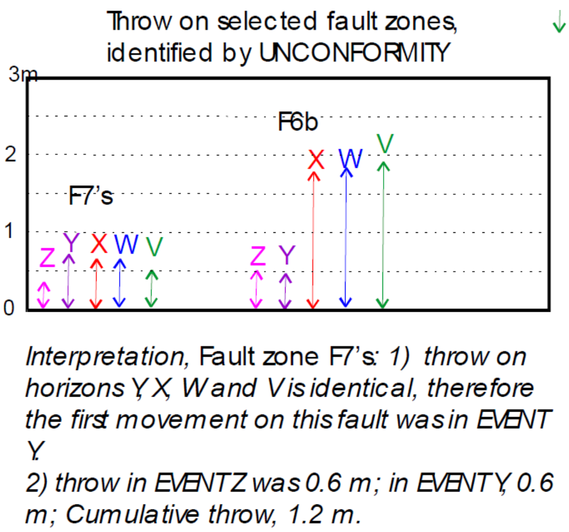

Fig. 6. Interpretation of throw on faults F7 and F6b in Events Z through V.

Discussion:

Retrodeformation can be considered a "quality control" technique for identifying the number of displacement events exposed in a trench and their vertical displacements. It is a more robust approach than simply identifying upward fault terminations, as done for strike-slip faults, because it links vertical displacement events to triggered post-displacement deposition. That is, deposition of colluvial wedges, opening and filling of fault zone fissures, and displacement-induced block rotation and subsequent infilling, which creates angular unconformities. If the scarp faces upslope, it temporarily blocks colluvial-alluvial transport, creating a closed depression that fills with ponded sediments (e.g., Fig. 4).

Past studies of measurement quality (ranking and scoring) of paleoseismic field measurements have been heavily concentrated on plate-boundary strike-slip faults in California (Table 2). But increasingly seismic hazard analysts worldwide are concerned with how paleoseismic data are measured in field studies, because the rigor with which that is done controls the uncertainty in the measurements. This trend is reflected in the increasing frequency of published papers on this topic.

Table 2. Papers that define or discuss quality of paleoseismic field measurements.

Year	Author and Region
1978	Sieh, central California
1991	McGill & Sieh, southern California
2000	Nelson et al., Phillipines
2007	Scharer et al., southern California
2011	Philibosian et al., southern California
2014	Scharer et al., southern California
2015	Rockwell et al., southern California
2021	Castillo et al., southern California
2022	McPhillips, California

Acknowledgements: The author is grateful for assistance from many trench loggers in the 1980s and 1990s who helped develop the techniques described herein: John Garr, Bob Robison, John Rice. Jr., Greg Warren, Darren Hinton, L.C. Allen Jones (Utah State University); Missy Eppes (Univ. of New Mexico); Margaret Berry (USGS); Susan Olig (Woodward-Clyde Consultants); Bill Lund, Mike Hylland, Greg McDonald (Utah Geol. Surv.); Patty Craw (Alaska Geol. Surv.); Yoshi Uemura (Bukkyo Univ.); and Bruce Eloff, Mike Neville, , Gerald Park, , and Mike Davis (consultants).

References

Castillo, B. A., S. F. McGill, K. M. Scharer, D. Yule, D. McPhillips, J. McNeil, S. Saha, N. D. Brown, and S. Moon (2021). Prehistoric earthquakes on the banning strand of the san andreas fault, north palm springs, California, Geosphere 17, no. 3, 685–710.

McCalpin, J.P. and Harrison, J.B.J., 2001, Paleoseismicity of Quaternary faults near Albuquerque, New Mexico: unpublished Final Technical Report submitted to U.S. Geological Survey by GEO-HAZ Consulting, Inc., Contract 99HQGR0056, Aug. 4, 2001, 58 p.

McCalpin, J.P., 2002, Post-Bonneville paleoearthquake chronology of the Salt Lake City segment, Wasatch Fault Zone, from the 1999 megatrench site: Utah Geological Survey, Miscellaneous Publication 02-7, 37 p. (http://ugspub.nr.utah.gov/publications/misc_pubs/MP-02-7WFZ-SLC.pdf)

McCalpin, J.P., 2005, Late Quaternary activity of the Pajarito fault, Rio Grande rift of northern New Mexico, USA; Tectonophysics, 408 (1-4), 213-236.

McCalpin, J.P., 2009, Paleoseismology, 2nd Edition: Elsevier Publishing, Amsterdam, 811 p.

McCalpin, J.P. and Jones, L.C.A., 2021, The Stillwater Scarp, central Nevada, USA; Coseismic gravitational failure on a 1,200-m-high range-front escarpment: Environ. & Engineering Geosci., XXVII (4), 377–393.

McGill, S. F., and Sieh, K. (1991). Surficial offsets on the central and eastern Garlock Fault associated with prehistoric earthquakes. J. Geophys. Res. 96, 21597–21621.

McPhillips, D., 2002, Revised Earthquake Recurrence Intervals in California, U.S.A.: New Paleoseismic Sites and Application of Event Likelihoods, Seismol. Res. Lett. XX, 1–15, doi: 10.1785/0220220127.

Scharer, K. M., Weldon, R. J., III., Fumal, T. E., and Biasi, G. P., 2007. Paleoearthquakes on the southern San Andreas fault, Wrightwood, California, 3000 to 1500 B.C.: A new method for evaluating paleoseismic evidence and earthquake horizons. Bull. Seis. Soc. Am. 97, 1054–1093.

Scharer, K.M., Salisbury, J.B., Arrowsmith, J.R. and Rockwell, T.K., 2014, Southern San Andreas fault evaluation field activity: Approaches to measuring small geomorphic offsets—Challenges and Recommendations for active fault studies. Seismol. Res. Lett. 85(1), 68-76.

Nelson, A. R., Personius, S. F., Rimando, R. E., Punongbayan, R. S., Tungol, N., Mirabueno, H., and Rasdas, A. (2000). Multiple large earthquakes in the past 1500 years on a fault in metropolitan Manila, the Philippines. Bull. Seis. Soc. Am. 90(1), 73–85.

Philibosian, B., T. Fumal, and R. Weldon (2011). San Andreas fault earthquake chronology and Lake Cahuilla history at Coachella, California, Bull. Seismol. Soc. Am. 101, no. 1, 13–38.

Rockwell, T. K., T. E. Dawson, J. Young Ben-Horin, and G. Seitz (2015). A 21-event, 4,000-year history of surface ruptures in the Anza seismic gap, San Jacinto Fault, and implications for long-term earthquake production on a major plate boundary fault, Pure Appl. Geophys. 172, no. 5, 1143–1165.

Sieh, K. E., 1978. Slip along the San Andreas fault associated with the great 1857 earthquake. Bull. Seismol. Soc. Amer. 68, 1421–1448.

INQUA Focus Group Terrestrial Processes Perturbed by Tectonics (TPPT)

paleoseismicity.org

Geological, geomorphological, geophysical and paleoseismic exploration along the Palomares Fault (southeast Iberian Peninsula)

Molins-Vigatà, Júlia (1)(2), Martín-Banda, Raquel (3), Ortuño, María (1), Insua-Arévalo, Juan Miguel (2), Pérez-Montoliu, Albert (1), Perea, Hector (2), Herrero-Barbero, Paula (2), Alcalde, Juan (4), Carbonell, Ramón (4), García-Mayordomo, Julián (3), Gómez-Novell, Octavi (1)(5), Masana, Eulàlia (1)

(1) RISKNAT Group, GEOMODELS, Departament de Dinàmica de la Terra i de l'Oceà, Facultat de Ciències de la Terra, Universitat de Barcelona, 08028 Barcelona, Spain
(2) Dpto. de Geodinámica, Facultad de Ciencias Geológicas, Universidad Complutense de Madrid. 28040 Madrid, Spain
(3) Instituto Geológico y Minero de España, CSIC, 28760 Madrid, Spain
(4) Geosciencies Barcelona, CSIC, 08028 Barcelona, Spain
(5) DiSPUTer, Università degli Studi "Gabriele d'Annunzio" Chieti-Pescara, 66013 Chieti, Italy

Abstract: *The Palomares Fault is one of the main structures of the Eastern Betics Shear Zone (SE Spain), bounding the Almenara and Alamgrera ranges trough the west. The fault produced, approximately, a 15 km left lateral displacement of the geological units found in Cabrera and Almagrera ranges; with this and other geological markers, different slip rates have been calculated along the fault plane and some evidences of Quaternary deformation have been found. However, few paleoseismological studies have been carried out on the fault, which makes it difficult to develop reliable seismic hazard models of the system. The main objectives of this study are to characterize the fault source parameters, redefine methodologies and introduce these new parameters into probabilistic seismic hazard calculation. The first steps to achieve these objectives, will require a multidisciplinary exploration of the zone, including detailed geomorphologic mapping, morphotectonic analysis, paleoseismological trenches and tomography profiles along the fault trace.*

Key words: *Eastern Betics Shear Zone, Palomares Fault, seismic hazard.*

INTRODUCTION

The Palomares Fault (PF) is one of the main structures of the Eastern Betics Shear Zone (EBSZ) (Fig. 1A), a crustal-scale structure that crosses the SE of Spain and one of the most active tectonic systems in the Iberian Peninsula. The EBSZ formed from SW to NE by the Carboneras (CF), Palomares (PF), Alhama de Murcia (AMF), Los Tollos (LTF), Carrascoy (CAF) and Bajo Segura (BSF) faults (Fig. 1A), absorbs part of the shortening between the Iberian and Nubian plates in the western Mediterranean under a transpressive regime (5-6 mm/year) (Palano et al., 2015). Paleoseismological studies have been successfully performed along the main faults of the EBSZ providing information on their geometry, kinematics and slip rates (Moreno, 2011, Martín-Banda, 2020, Gómez-Novell, 2021) crucial data for Seismic Hazard Analysis, especially in areas of low-to-moderate activity. Despite the clear geomorphological expression of the PF on surface, scarce paleoseismological studies (such as Silva et al., 1997; Roquero et al., 2019) have been carried out in the fault. This represents an important knowledge gap in the EBSZ, making difficult the development of reliable seismic hazard models. It has been notable this limitation in recent studies carried out in the zone which evaluated the seismic hazard, with the development of fault-hazard models based on magnitude-frequency distributions (Gómez-Novell et al., 2020), transfer of Coulomb stress (Álvarez-Gómez et al., 2018) or rate-and-state earthquake simulators (Herrero-Barbero et al., 2021). This study proposes the PF as an area to develop new approaches for characterizing earthquake sources, acquiring new paleoseismological data, and integrating the results into fault-based seismic hazard models.

THE PALOMARES FAULT

The PF borders the central-eastern part of the EBSZ and links the CF with the CAF (Fig. 1A). The fault is described as a strike-slip fault mainly with a left-lateral displacement (Bousquet, 1979; Roquero et al., 2019) and a length of 70 km onshore. Offshore, the fault probably connects with the SW/NE oriented CF (e.g. Bousquet, 1979). The PF (Fig. 1B) shows a marked N-S orientation and dip westward in its southern part, favouring the subsidence of the western block in this sector. However, to the north, this marked trend bends to the NE-SW following the northern flank of the Almenara range, and changes its dip to the east, that with a contractional regime favours the uplift of this mountain front (Booth-Rea et al., 2004). From the Puntarrón village to the NE, the mountain front is less marked, showing a lower relief (Hinojar range) and a more E-W orientation. Thus, the PF is traditionally divided into two or three segments, depending on whether the fault that controls the Hinojar range (Hinojar fault) is counted as a third segment (e.g. Silva et al., 1997) or not (e.g. ITGE, 1991). The deformation is distributed in several fault strands forming a fault zone of approximately 4 km wide. This configuration (unlike the other faults of the system where the deformation is more constricted) and the low

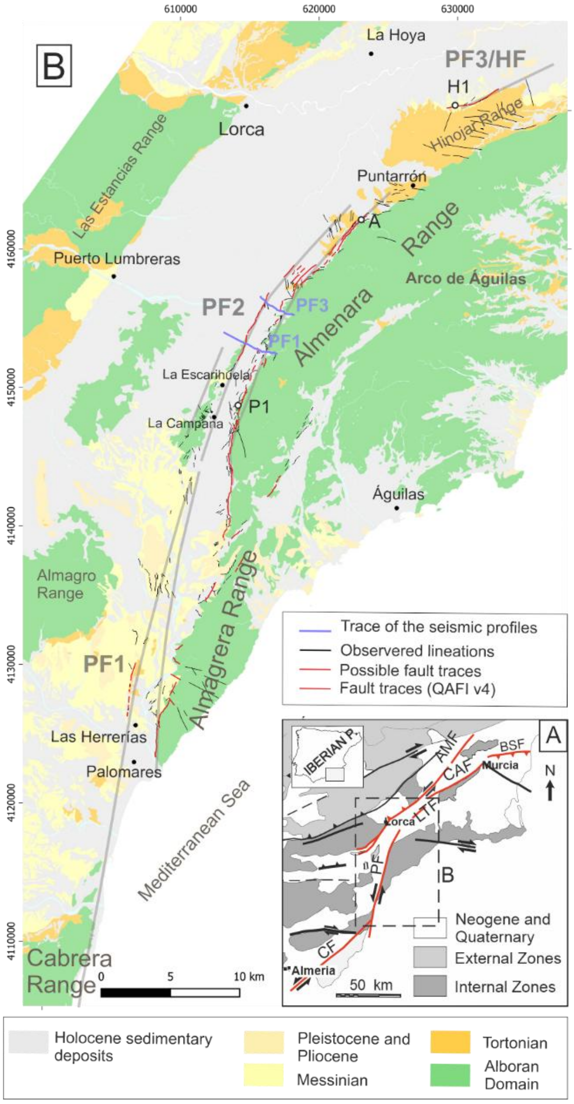

Figure 1: A- Geologic map of the EBSZ with the main active faults in red. B- Geological map of the study zone with the first structures detected from photointerpretation and analysis of DEMs, and the location of the different outcrops and seismic profiles. The PF segments are in grey (IGME, 2022)

vertical displacement registered, make difficult the geomorphological and structural interpretation of the fault, as well as the selection of paleoseismic trenches along PF trace.

The PF produced a lateral displacement of approximately 15 km of the upper Neogene series of the Cabrera range to the south of the Vera village during the late Neogene and Quaternary (e.g. Weijermars, 1987). This displacement implies a left-lateral slip rate of 0.15 mm/yr in the southern end of the PF (Roquero et al. 2019). Other authors suggest different slip rate values along the fault trace, mainly calculated by morphometric indices, and stratigraphic, geomorphic or structural markers. In the southern part of the Almagrera range, Booth-Rea et al. (2004) suggest a vertical-slip rate of 0.15-0.06 mm/yr and a lateral-slip rate of 0.46mm/yr calculated with different geologic markers. In the same zone, Stokes (2008) calculates an uplift of 0.01-0.02 mm/yr with Pliocene marine unit markers. These values, and the ones collected in the QAFI (IGME, 2022), are between one or two orders of magnitude smaller than values of the other faults of the EBSZ, where multiple paleoseismic studies have been done.

OBJECTIVES AND METHODOLOGY

The main objectives of this study are part of the N-SOURCES project and aim to: (1) characterize the seismic potential of the PF, determining its kinematics, slip rates, fault plane geometry (surface traces, dip, segments…), paleoearthquakes identification (last event, event recurrence) and its interaction with other faults of the EBSZ; (2) reassess the seismic hazard in the area with the new source parameters.

To acquire all these data, the following studies will be developed in the area. First, a detailed geomorphologic mapping, using geographic information systems (GIS) software. In this phase, a morphotectonic analysis of the most recent deformation, an analysis of the drainage network at different scales and the calculation of geomorphic indices will also be carried out. Detailed fieldwork will be done to complete the mapping, locate the outcrops of interest and select the best locations for the placement of the paeloseismological trenches.

The area will also be explored with geophysics to describe the fault in depth. In this phase, the geophysical data acquired during the seismic campaign of the Guadalentín Basin with the UNrIDDLE project will be processed to obtain velocity models at depth and two tomography profiles (PF1, PF3) along the fault (Fig. 1). During the campaign seven profiles were made, two in PF, four in AMF and one in CAF. The two profiles in PF are located in the PF2 segment, near La Escarihuela town. The space between vibration points were 5 m and between seismic stations 10 m, it is expected to reach between 1 and 2 km depth. The characteristics of the profiles in PF are sown in Table 1.

PF1

Length (m)	4088
Number of stations	422
Number of vibrations	786

PF3

Length (m)	2685
Number of stations	260
Number of vibrations	425

Table 1 – Information about the station location and vibration points in the profiles

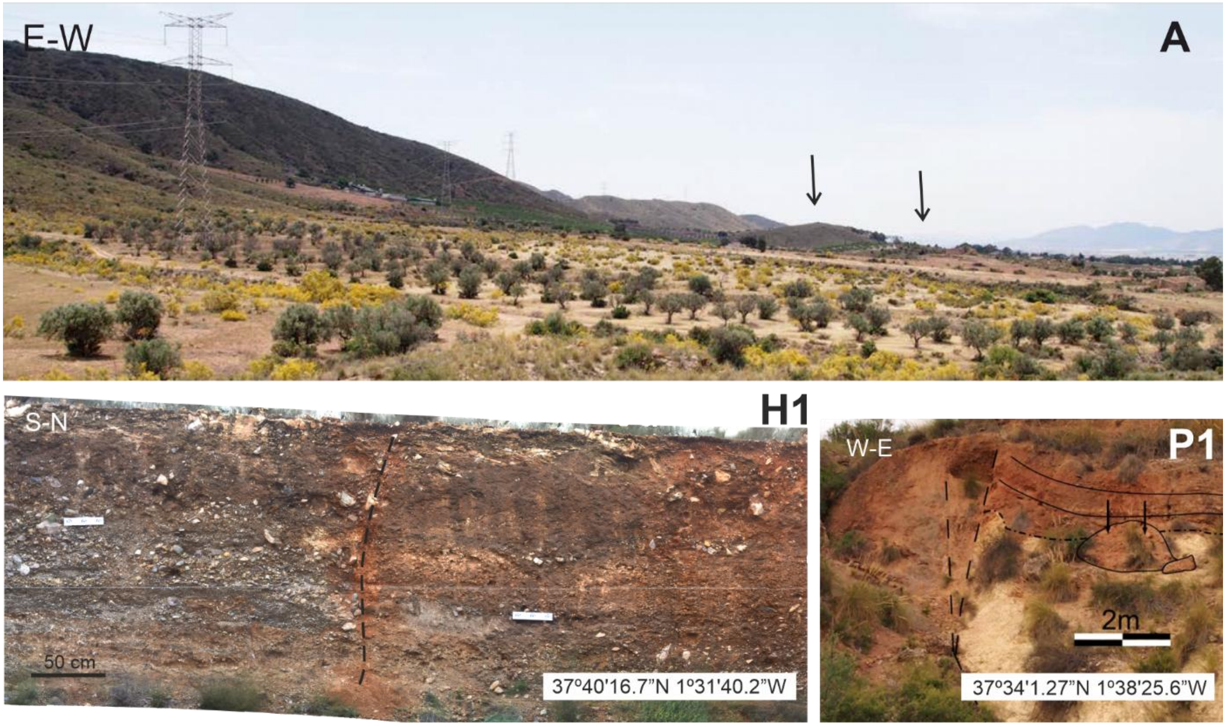

Figure 2- Studied outcrops in the zone and their coordinates. A- Panoramic of the PF zone, controlling the mountain front (Almenara range). The arrows show a secondary tectonic relief interrupting the colluvial deposit. P1- Purias. H1- Hinojar. The locations are shown in the figure 1.

EXPLORATION OF THE PALOMARES FAULT

Previous studies carried out in the PF discuss its Quaternary activity and analyse, for example, its segmentation and the geomorphological formations affected by the fault, such as fan surfaces or anomalies in the drainage network (e.g. Booth-Rea et al., 2004; Roquero et al., 2019). These studies also provide the location of interesting outcrops of the fault that show its geometry and constitute some examples of its activity. Beheaded streams, abandoned and dissected valleys and deflected channels have been observed through analysis of the drainage network, as well as structures of coseismic activity, such as implosive mineralized breccias and clastic dikes intruding Pleistocene sediments (Booth-Rea et al., 2004). Roquero et al. (2019) presented a detailed paleoseismological study from an artificial wall, with faulted paleosoils sequences, where two events were identified. This work analyses different faulted fan surfaces to try to constrict the age of identified events, providing a recurrence interval of 124 kyr.

In this study, we present some new outcrops with evidence of quaternary deformation related to the fault (Fig. 2).

Purias creek (P1)
In this outcrop, the Miocene marls and upper-middle Pleistocene gravels from alluvial fans are in direct contact by the fault plane. Both marls and gravels are gradually deformed next to the fault plane.

Hinojar (H1)
This outcrop is in the northern termination of the PF, in its third segment. It is an artificial wall perpendicular to the fault trace where the fault puts in contact creek deposits with red clays, gravels, and a well-developed calcrete. In the uppermost part, vertically oriented clasts are found, coinciding with the fault plane, evidencing deformation.

The zone has also been explored with historical orthophotos and with digital elevation models (DEMs). This preliminary analysis has provided information on possible fault traces located mostly in alluvial fans (Fig.1), in some cases beheaded. In some areas, several fault strands have been identified in relation to secondary reliefs blocking colluvial deposits, as shown in figure 2A. Another example of tectonic relief is Cabezo de Muro, located near la Escarihuela, where Roquero et al. (2019) identified sag pond deposits.

CONCLUSIONS

Producing improved fault-based seismic hazard models is challenging, especially in regions with low-to-moderate seismic activity. These systems can be complex: faults do not behave individually, show variable slip rates and complicated geometries, as well as the effect of surface processes, e.g., effective eroding their scarps. Acquiring new parameters and improving the characterization of the seismic sources are crucial to develop reliable seismic hazard models. In the specific case of the EBSZ, the knowledge gap in the PF is a clear example of the limitation that suppose for hazard model developers, the lack of information. Therefore, the PF is the perfect scenario to start a new study. A wide variety of studies have been conducted in the PF to date. The results of these studies, with the new outcrops presented in this work, show the potential of the PF to develop paleoseismological studies.

Acknowledgements: This work has been conducted under the frame of the NSOURCES project (PID2020-119772RB-100), funded by the Spanish Ministry of Economy, Industry and Competitiveness and the UNriDDLE project (2018-T1/AMB-11039, Comunidad de Madrid).

REFERENCES

Booth-Rea, G., Azanón, J.M., Azor, A. & García-Duenas, V., 2004. Influence of strike-slip fault segmentation on drainage evolution and topography. A case study: The Palomares Fault Zone (southeastern Betics, Spain). *Journal of Structural Geology*, 26:1615–1632.

Bousquet, J.-C., 1979. Quaternary strike-slip faults in southeastern spain. *Tectonophysics*, 52:277–286.

Eidelman, A. & Reches, Z., 1992. Fractured pebbles - a new stress indicator. *Geology*, 20:307–310.

Gómez-Novell, 2021. Paleoseismic transect across the Alhama de Murcia Fault and implications of a fault-based seismic hazard assessment for the Eastern Betics: PhD Thesis, Universitat de Barcelona, Barcelona, Spain, 399 p.

Gómez-Novell, O., García-Mayordomo, J., Ortuño, M., Masana, E. & Chartier, T., 2020. Fault System-Based Probabilistic Seismic Hazard Assessment of a Moderate Seismicity Region: The Eastern Betics Shear Zone (SE Spain). *Frontiers in Earth Science*, 8.

Herrero-Barbero, P., Álvarez-Gómez, J.A., Williams, C., Villamor, P., Insua-Arévalo, J.M., Alonso-Henar, J. & Martínez-Díaz, J.J., 2021. Physics-Based Earthquake Simulations in Slow-Moving Faults: A Case Study From the Eastern Betic Shear Zone (SE Iberian Peninsula). *Journal of Geophysical Research: Solid Earth*, 126:1–25.

IGME, 2022. Quaternary Faults Database of Iberia. from IGME web site, http://info.igme.es/qafi/.

ITGE, 1991. Mapa Neotectónico Sismotectonico y de Actividad de Fallas de la Region de Murcia. Instituto Tecnologico Geominero de España*,* 101 p.

Martín-Banda, R., 2020. Segmentación y evolución reciente del sistema de fallas de la Sierra de Carrascoy: implicaciones en su potencial sismogénico: PhD Thesis. Universidad Complutense de Madrid, Madrid, Spain, 220 p.

Moreno, X., 2011. Neotectonic and Paleoseismic Onshore-Offshore integrated study of the Carboneras Fault (Eastern Betics, SE Iberia): PhD Thesis. Universitat de Barcelona, Barcelona, Spain, 305 p.

Palano, M., González, P. J., Fernández, J., 2015. The Diffuse Plate boundary of Nubia and Iberia in the Western Mediterranean: Crustal deformation evidence for viscous coupling and fragmented lithosphere. Earth and Planetary Science Letters, 430: 439–447.

Roquero, E., Silva, P.G., Rodríguez-Pascua, M.A., Bardají, T., Elez, J., Carrasco-García, P. & Giner-Robles, J.L., 2019. Analysis of faulted fan surfaces and paleosols in the Palomares Fault Zone (Betic Cordillera, SE Spain): Paleoclimatic and paleoseismic implications. *Geomorphology*, 342:88–102.

Silva, P.G., Goy, J.L., Zazo, C., Lario, J. & Bardají, T., 1997. Paleoseismic indications along “aseismic” fault segments in the Guadalentin Depression (SE Spain). *Journal of Geodynamics*, 24:105–115.

Stokes, M., 2008. Plio-Pleistocene drainage development in an inverted sedimentary basin: Vera basin, Betic Cordillera, SE Spain. *Geomorphology*, 100:193–211.

Weijermars, R., 1987. The Palomares brittle-ductile Shear Zone of southern Spain. *Journal of Structural Geology*, 9.

INQUA Focus Group Terrestrial Processes Perturbed by Tectonics (TPPT)

paleoseismicity.org

A New Look at the Ground Rupture of the Motagua Fault in the 1976 Guatemalan Earthquake along the Caribbean-North American Plate Boundary

Niemi, Tina M. (1), Trenton McEnaney (1, 2), Jonathan Obrist-Farner (2), Omar Flores (3), and Carlos Perez Arias (4)

(1) Earth and Environmental Sciences, University of Missouri-Kansas City, Kansas City, MO 64110 USA. Email: Niemit@umkc.edu
(2) Dept. of Geoscience and Geological and Petroleum Engineering, Missouri University of Science and Technology, Rolla, MO 65409 USA
(3) Centro de Estudios Superiores de Energia y Minas, Universidad de San Carlos de Guatemala, Guatemala City, Guatemala
(4) Ingeotecnia S.A., Guatemala City, Guatemala

Abstract: *The 1976 magnitude 7.5 Guatemala earthquake ruptured the Motagua fault along the North American-Caribbean plate boundary in one of the most devastating earthquakes in the 20th Century that resulted in over 23,000 fatalities. For a major plate boundary, very little is known about the long-term rupture history of the Motagua fault and the probability of future earthquakes hazards it poses to the large and growing population in Guatemala City. In this study, we sought to relocate sites along the 1976 Motagua fault rupture by analyzing archival material from George Plafker of the U.S. Geological Survey who collected data on the effects of the earthquake within days of the event. The data included 1250 original 35 mm slides, numerous annotated 1:50,000 scale topographic maps, several hundred aerial photographs, a 1978 field trip guidebook, and various other original documents that are only available in paper format. These historical documents highlight the severity of the event, with primary and secondary strike-slip faulting, landslides, liquefaction, and structural damage. Maps, photographs, and reports from the 1976 Guatemalan earthquake were digitally scanned into a georeferenced database. In July 2021, we made a reconnaissance trip to relocate the 1976 Motagua fault earthquake rupture. Many of the offsets measured in the 1976 earthquake were in pastures and along dirt roads and are no longer visible. The offset of the concrete-lined canal at Gualán and the Zacapa asphalt highway are still extant. In some locations, the fault has a clear geomorphic expression of repeated late Quaternary slip with sag depressions and fault scarps crossing alluvial fans and terraces. However, in other locations, the 1976 fault rupture is difficult to locate and sites lack evidence of long-term Quaternary deformation. These data suggest a complex transform plate boundary history with strain likely partitioned onto subparallel faults.*

Key words: *Guatemala, Historical earthquake, ground rupture, Central America*

INTRODUCTION

The 1976 Guatemala earthquake ruptured the plate boundary separating the North American and Caribbean plates along part of the left-lateral, strike-slip Motagua and Polochic fault system (e.g., Plafker, 1976; Mann, 2007; Álvarez-Gómez et al., 2008; Authemayou et al., 2011). The magnitude M_W 7.5 earthquake occurred on 4 February 1976 at 3:03 A.M. local time and is responsible for an estimated 23,000 fatalities, 74,000 reported injuries, and more than 1 million people left homeless in a country with a population, at the time, of 5.5 million (*Plafker, 1976*). The total economic loss was estimated to be $1.1 billion USD (*Espinosa et al., 1976*).

Scientific studies of the effects of the 1976 earthquake started immediately after the earthquake when a team of geologists from the U.S. Geological Survey (USGS) joined local Guatemalan government officials and colleagues to begin mapping and making reconnaissance aerial flights along the rupture. The results of the geologic, seismologic, and engineering survey of the earthquake were summarized in the USGS Professional Paper 1002, *"The Guatemalan Earthquake of February 4, 1976, A Preliminary Report,"* edited by Alvaro Espinosa (1976) just months after the earthquake. Additional field surveys were conducted again in April 1976 and in October 1977 when repeat measurements of the offsets from fault rupture showed the presence of significant afterslip (Bucknam et al., *1978*).

Together these data show that the Motagua fault ruptured for a total identified length of at least 230 km in the Motagua Valley. The rupture may have extended farther but was obscured to the east by swamps and vegetation and to the west by earthquake-triggered landslides (Plafker, 1976; Harp et al., 1981). At that time, the 1976 Guatemalan earthquake rupture was the longest in the Northern Hemisphere since the 1906 San Francisco earthquake (Plafker, 1976). At the nearest point, the Motagua fault is just 25 km north of Guatemala City metro area, close enough to pose serious future risk and hazards for the city and its current population of 3.7 million. However, for a major plate boundary, very little is known about its long-term fault rupture history or the probability of future earthquakes and the hazards it poses to the large and growing population in Guatemala. The purpose of this study was to relocate sites where coseismic slip on the Motagua fault from the 1976 earthquake were measured and to build a digital georeferenced database of maps and photographs that could assist future paleoseismic study of the plate boundary.

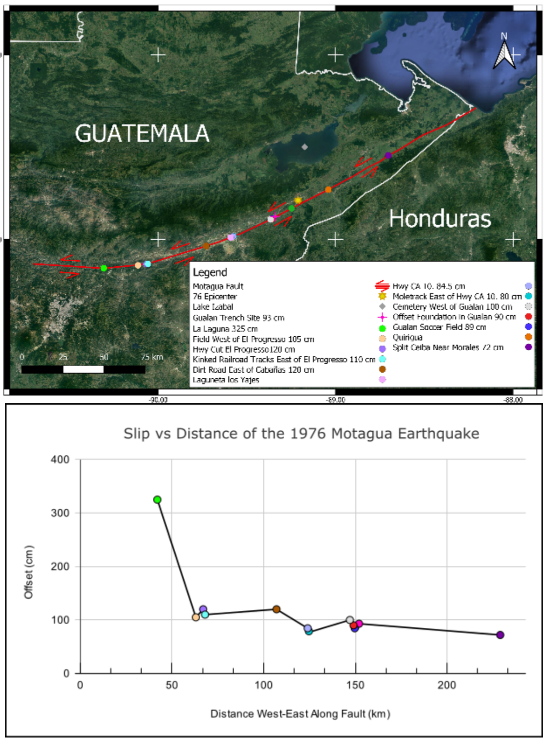

Figure 1: (A) Google Earth image showing the location of the Motagua fault that ruptured for a distance of at least 230 km in the 1976 M 7.5 Guatemala earthquake. The map shows the locations where left-lateral slip was measured across the earthquake rupture. (B) Graph showing coseismic slip along the length of the 1976 Guatemalan earthquake rupture of the Motagua fault. Key locations where offset features can still be seen in the field are shown.

METHODS

In order to identify sites along the 1976 Guatemala earthquake rupture where fault slip was documented, we requested and received the original field data from George Plafker of the U.S. Geological Survey who collected data on the effects of the earthquake starting two days after the event (February 6-16, 1976) and during a second research trip (April 14-May 4, 1976). The data include 1250 original 35 mm slides, numerous annotated 1:50,000 scale topographic maps, several hundred aerial photographs, a 1978 field trip guidebook, and various other original documents that are only available in paper format. The annotated topographic maps and black-and-white aerial photographs were digitized, georeferenced, and became the basemaps for the database. Photographs and 35 mm slides were scanned and located in Google Earth with the help of annotations on the photos and on the topographic maps. Metadata in the form of handwritten annotations, field books, and personal notes were added to the photos, slides, and maps when possible. Several georeferencing techniques were utilized to build this database, including the scaling, shifting, and orthorectification of data. After using these techniques to align the geographic data to a known coordinate system, the annotated maps and aerial photographs showing the ground rupture can be viewed, queried, and overlain on existing satellite imagery and geologic maps.

We conducted a field survey to locate the 1976 earthquake rupture during July 24-29, 2021. With the digital database loaded on an iPad and laptop and a paper copy of Plafker (1977) with color prints of the 35 mm slides that accompany that publication, we traveled along dirt roads to access sites where fault offsets were documented after the 1976 earthquake. This was very challenging as many of the 1976 coseismic slip sites were originally visited via a helicopter. We talked to the local residents and asked about the 1976 earthquake. Many Guatemalans remember exactly where the ground ruptured and particularly remember the landing of a helicopter which was often in the clearing of a soccer field! Most of the inhabitants were more interested in telling us about the most recent disaster from Hurricanes Eta and Iota in 2020. Heavy precipitation in these hurricanes caused massive flooding and landslides in the lower Motagua River Valley. We were able to visit some key locations where features offset from the 1976 earthquake are still visible and we documented them. Many other sites such as the ruptures across soccer and agricultural fields are no longer visible or have only subtle geomorphic expression.

Figure 2: Highway 10 near Zacapa is oriented nearly perpendicular to the Motagua Fault. The photograph on the left from 1976 and one on the right from 2021 both show repair to the original cracked and displaced drainage ditch.

THE 1976 EARTHQUAKE GROUND RUPTURE

The 1976 Guatemala earthquake rupture was documented from aerial reconnaissance and field observations to have developed a fairly continuous, well-defined fault trace located mostly south of the Motagua River (Plafker, 1976, 1977; Plafker et al., 1976). Most of the slip was concentrated on the clearly mapped fault with few splay traces (Fig. 1). Along the eastern section, the ground rupture was in general agreement with the previously mapped location of the Motagua fault (Schwartz et al., 1979; Schwartz, 1985).

Plafker et al. (1976) published 13 sites where sinistral displacement from the 1976 earthquake was measured. Additional fault offset data are presented in Plafker (1976; 1977) and Bucknam et al. (1978). The average left-lateral offset along the fault was about 110 cm (Fig. 1). The maximum slip was 325 cm measured on an offset line of trees near Laguna (Plafker, 1976; 1977).

Figure 3: Aerial photograph of the Gualán soccer field viewed northward showing the 1976 earthquake moletrack. A left-lateral offset of 89 cm was measured across the white sideline stripe (Pflaker, 1977).

Figure 4: Fault rupture through the soccer field in Gualán with photographs from 1976 shown above and from 2021 on the bottom. A slight slope marks the location of the rupture.

One of the most prominent offsets from the earthquake was Highway 10 near Zacapa (Fig. 2). This site is memorialized with a commemorative 1976 earthquake plaque. The asphalt highway and the concrete-lined drainage ditches that paralleled it had a sinistral offset of 60 cm measured four days after the earthquake (Plafker et al., 1976). Fractures were patched at least two times between February and April (Plafker, 1977) due to afterslip. Subsequent offset measurements up to a year and a half after the earthquake measured an additional afterslip of 24.5 cm for a total offset of 84.5 cm (Bucknam et al., 1978).

The earthquake ruptured directly through the city of Gualán causing structural damage to numerous buildings, bent the railroad tracks, and crossed the cemetery to the west of town. One of the most famous images of the earthquake is the fault rupture across the Gualán soccer field (Fig. 3). The moletrack formed by *en echelon* fractures oriented 15° to 20° counterclockwise to the strike of the fault with small pressure ridges developed in between the right-stepping fissures. The width of the zone of fracturing was 5m or less. Only a gentle slope is still slightly visible along the fault trace (Fig. 4).

About 2 km northeast of Gualán at Finca Los Limones, a concrete-lined irrigation canal was offset 93 cm (Fig. 5). The canal is oriented nearly perpendicular to the fault. At this location the Motagua fault follows a pronounced linear valley with a south-facing scarp and a sag pond indicating repeated slip of the fault. Farther to the northeast, the main Puerto Barrios to Guatemala City railroad line follows the linear valley that developed along the Motagua fault. The 1976 earthquake ruptured and bent the railroad track in several locations. Figure 6 shows then and now photographs of a location where the railroad track was bent and the ties offset by 107 cm.

Figure 5: Photographs viewed toward the south of a concrete-lined irrigation canal that was offset left laterally by 93 cm along the 1976 earthquake rupture east of Gualán at Finca Los Limones. The fault crosses the canal at nearly a right angle. The image on the left is from 1976 (Plafker, 1977) and one on the right from 2021.

Figure 6: Photograph looking north of the displacement of the Puerto Barrios to Gualemala City railroad tracks at marker 70 km located northeast of Gualán. On February 8, 1976, the left-lateral offset was measured as 107 cm (Plafker, 1977), but later measurements indicated that the tracks were offset only 70 cm. The photograph on the right is from 2021. Note that the metal tracks and some of the railroad ties have been removed but that the bridge is still standing.

SUMMARY

Many sites where the offset in the 1976 earthquake was documented are no longer visible because they were measured on crop rows in agricultural fields, painted lines on a soccer fields, or dirt roads or paths that have been plowed under or otherwise have disappeared. Natural processes of erosion and cultural modification of the landscape including changes in land use practices, redistribution of property boundaries, urbanization and numerous other factors have worked together to make it difficult to exactly relocate photos taken soon after the earthquake. As reported by Plafker (1976), Schwartz et al. (1979), and Schwartz (1976; 1985) and from our fieldwork it is clear that geomorphic features such as linear stream valleys, scarps, shutter ridges, and sag ponds along sections of the Motagua fault indicate repeated Quaternary slip. At other locations, the 1976 ground rupture cuts through flat topography and appears youthful.

Acknowledgements: This work was supported by grants from UMKC's Students Engaged in the Arts and Research (SEARCH) and Summer Undergraduate Research Opportunities (SUROP) to McEnaney.

REFERENCES

Álvarez-Gómez, J.A., Meijer, P.T., Martínez-Diaz, J.J., & Capote, R., 2008. Constraints from finite element modeling on the active tectonics of the northern Central America and the Middle America Trench. *Tectonics* 27. doi:10.1029/2007TC002162.

Authemayou, C., Brocard, G., Teyssier, C., Simon-Labric, T., Gutiérrez, A., Chiquín, E.N., & Morán, S., 2011. The Caribbean-North America-Cocos triple junction and the dynamics of the Polochic-Motagua fault systems: Pull-up and zipper models. *Tectonics* 30 (3). doi:10.1029/2010tc002814

Bucknam, R. C., Plafker, G., & Sharp, R.V., 1978. Fault movement (afterslip) following the Guatemala earthquake of February 4, 1976. *Geology* 6, 170-173.

Caccavale, M., Sacchi, M., Spiga, E., & Porfido, S., 2019. The 1976 Guatemala Earthquake: ESI scale and probabilistic/deterministic seismic hazard analysis approaches. *Geosciences* 9 (9), 403. doi:10.3390/geosciences9090403

Espinoza, A. F., Editor, 1976. *The Guatemalan Earthquake of February 4, 1976, A Preliminary Report,* U.S. Geological Survey Professional Paper 1002, 90 p.

Espinoza, A.F., Husid, R., & Quesada, A., 1976. Intensity distribution and source parameters from field observations, in A.F. Espinoza (ed.), *The Guatemalan Earthquake of February 4, 1976, A Preliminary Report,* U.S. Geological Survey Professional Paper 1002, p. 52-84.

Harp, E. L., Wilson, R.C., & Wieczorek, G.F., 1981. Landslides from the February 4, 1976 Guatemala Earthquake: U.S. Geological Survey Professional Paper 12-4-A, 35 p.

Mann, P. 2007, Overview of the tectonic history of northern Central America, *in* Mann P., ed. *Geologic and tectonic development of the Caribbean plate boundary in northern Central America*: Geological Society of America Special Paper 428, p. 1–19.

Plafker, G., 1976. Tectonic aspects of the Guatemala earthquake of 4 February 1976. *Science* 193 (4259), 1201-1208.

Plafker, G., 1977. *Color slides showing geologic effects and damage caused by the destructive Guatemala earthquake of February 4, 1976*. USGS Open-File Report 77-165.

Plafker, G., Bonilla, M. G., and Bonis, S.B., 1976. Geologic effects, in A.F. Espinoza (ed.), *The Guatemalan Earthquake of February 4, 1976, A Preliminary Report,* U.S. Geological Survey Professional Paper 1002, p. 38-51.

Schwartz, D.P., 1976, Geology of the Zacapa Quadrangle and vicinity. Ph.D. dissertation, State Univ. of New York, Binghamton, N.Y., 191 p.

Schwartz, D.P., 1985, The Caribbean-North American plate boundary in Central America: new data on Quaternary tectonics, in *Seismological Society of America Annual Meeting* (Austin, TX, 1985).

Schwartz, D.P., Cluff, L.S., & Donnelly, T.W., 1979. Quaternary faulting along the Caribbean-North American plate boundary in Central America. *Tectonophysics* 52 (1-4), 431-445.

New paleoseismic data for the characterization of the seismic potential in a complete transect of the Alhama de Murcia Fault (SE Spain)

Marc Ollé (1), Octavi Gómez-Novell (2, 1), Domitille Dufour (3), Júlia Molins-Vigatà (4, 1), Stéphane Baize (5), Raquel Martín-Banda (6), Juan Miguel Insua-Arévalo (4), María Ortuño (1), Raimon Pallàs (1), Giorgi Khazaradze (1), Eulàlia Masana (1)

(1) Departament de Dinàmica de la Terra i de l'Oceà, GRC RISKNAT, Facultat de Ciències de la Terra, Universitat de Barcelona (UB). 08028 Barcelona, Spain. Email: 99.olle.m@gmail.com
(2) DiSPUTer, Università degli Studi "Gabriele d'Annunzio" Chieti-Pescara, 66013 Chieti, Italy
(3) Department of Geosciences, Ecole Normale Supérieure, PSL Research University, 75230 Paris, France
(4) Departamento de Geodinámica, Estratigrafía y Paleontología, Universidad Complutense de Madrid (UCM), 28760 Madrid, Spain
(5) Institut de Radioprotection et de Sûreté Nucléaire (IRSN), 92260 Fontenay-aux-roses, France
(6) Instituto Geológico y Minero de España (IGME, CSIC), 28760 Madrid, Spain

Abstract: *The Alhama de Murcia Fault is one of the main seismogenic faults in the Eastern Betic Shear Zone. In the segment between Lorca and Totana, the fault is composed of five main branches, four of them having been studied previously with paleoseismology. This work focusses on the unexplored branch (N2a-AMF) to analyse its seismic potential and to refine the previously estimated paleoseismic parameters of the AMF in the area (El Saltador-La Hoya). We conducted a detailed geomorphological study and excavated a new paleoseismic trench that provided clear evidence of recurrent deformation (a minimum of three morphogenetic events) in the Upper Pleistocene. We measured a vertical offset of 87±4 cm and we calculated a minimum seismic recurrence of 14.4 kyr for the period between 82.4-39.2 kyr; and a minimum vertical slip rate between 0.010 and 0.011 mm/year for the last 82.4 kyr. In this work, we present the preliminary results of our ongoing research.*

Key words*: AMF; EBSZ; paleoseismology; geomorphology; seismic hazard*

INTRODUCTION

The Eastern Betics Shear Zone (EBSZ) absorbs much of the convergence between the Eurasian and Nubian plates (De Larouzière et al., 1998, Masana et al., 2004). The fastest seismogenic faults in the Iberian Peninsula are found in this region, including the Alhama de Murcia Fault (AMF), characterized by a slip rate of 1.55 +0.14/-0.18 mm/a (Gómez- Novell, 2021). Precisely establishing the seismic potential of this fault is important to determine the seismic hazard of SE Spain, not insignificant as evidenced by the 2011 Lorca earthquake (M=5.2). However, due to its slow to moderate slip rates, historical records are insufficient to characterize the frequency of large earthquakes, which is why geological studies are necessary to understand its functioning in the past.

The AMF extends about 80 km from Alcantarilla to the Góñar area with a NE-SW orientation and can be divided into four segments (Martínez-Díaz et al., 2012b). The two southern segments (including the Lorca-Totana segment) are the ones that show more evidence of recent activity. In El Saltador-La Hoya area of the Lorca-Totana (LT) segment, the fault divides into 5 subparallel branches. Gómez-Novell (2021) analysed the activity of the AMF in this sector and, by integrating paleoseismic data from 4 branches in a transect, estimated the total paleoseismic parameters of the AMF. However, one of these main faults, the N2a-AMF according to the nomenclature of Gómez-Novell (2021), was not taken into account due to the absence of suitable paleoseismic sites.

The main objective of this study is to characterize the paleoseismic activity of this branch. For this, it is intended to elaborate a detailed mapping of the geomorphology of El Saltador alluvial fan and to excavate and analyse a palaeoseismic trench perpendicular to the fault. From the analysis of the trench, it is expected to obtain the slip rate, slip per event and the mean recurrence of the aforementioned fault.

GEOLOGICAL SETTING

The AMF is located in the central part of the EBSZ, (SE of Spain), and bounds La Tercia range to the northwest and the Guadalentín Depression to the southeast. It is one of the main faults in the region. On a large scale it has a NE-SW orientation, but in the LT segment, its direction varies slightly until it is oriented towards N60E. This fact causes the regional stresses to be oriented almost perpendicular to the fault in such a way that they favour a vertical component of the displacement. As a result, different reverse faults have formed in this area that have given rise to a restraining bend in the form of a positive flower structure (Martínez-Díaz et al., 2012b).

La Tercia range is predominantly formed by Paleozoic metamorphic rocks, mainly slates and phyllites. These materials constitute the basement of the region and correspond to the Alpujárride and Maláguide complexes, part of the Internal Zones of the Betics. These rocks are highly deformed and metamorphosed and have been exhumed due to intense tectonic activity.

In addition, some Neogene materials from the Lorca Basin can also be found in this mountain range (Marín-Lechado et al., 2011), discordant over the Paleozoic rocks. The Guadalentín basin is infilled by Tortonian marls and conglomerates, and at the top (forming a progressive unconformity) by Pliocene sands and gravels deposited in proximal alluvial fans during the period of maximum growth of La Tercia range (Silva, 2014).

Several generations of Quaternary alluvial fans are found on top of these materials. They are made up of sands and gravels and, occasionally, silts (Silva, 2014). The recent activity of some branches of the AMF fault (push-up type structures) confine some of the alluvial fans. The most recent materials correspond to Holocene fluvial sediments in the beds of the current channels and in the Guadalentín Depression (Silva, 2014).

MAPPING

For the elaboration of the cartography, recent and ancient (flight 1956-1957) aerial orthophotographs were used; as well as digital terrain models (DTM) (0.5 m resolution) and some of the previous geological maps of the area (Masana et al., 2004; Martínez-Díaz et al., 2012; Ferrater et al., 2016; Gómez-Novell, 2021). The maps were supplemented with information collected through fieldwork.

A new geomorphological map focused on El Saltador area was done, paying special attention to the layout of the N2a-AMF and N2b-AMF branches in order to better understand their relationship. Structures associated with the fault activity were identified, such as shutter ridges, dislocated channels, and beheaded channels. From this information, the location of the 5 main branches of the AMF in the area was precisely traced (Fig. 1).

Within the Quaternary, 4 generations of alluvial fans, the filling of the Guadalentín Depression and recent fluvial sediments were distinguished (Fig. 1).

PALEOSEISMIC RESULTS

A trench (named "Torre") was excavated and analysed in El Saltador fan zone across the N2a-AMF branch (its location is shown in Figure 1). This site was selected due to the observation of the fault in the NE wall of the adjoining El Saltador ravine. The place, moreover, was suitable for carrying out a palaeoseismic analysis due to the sufficient presence of recent sediments. The excavated trench (2,5 m deep and 66 m long) has a NW-SE orientation, perpendicular to the fault trace.

The excavation exposed Quaternary deposits from the upper part of El Saltador fan sequence (gravels, sands and silts) coming from the erosion of La Tercia range. Most of the detected units have a limited lateral continuity, since they would have been generated during the obliteration processes derived from the dynamics of alluvial fans.

From top to bottom, we identified the following stratigraphic units in the trench walls (Fig. 2):

A) Current soil: fine-grained materials affected by current edaphic processes. Edaphization has altered the appearance of the materials, making it difficult to identify internal sedimentary structures.

B) Upper unit: This unit is characterized mainly by matrix-supported gravels, with the presence of some layers that are very rich in silt (and some are only formed by silts). Some of the units stand out for their canaliform appearance and their marked erosional base (such as unit Bd).

C) Intermediate unit: subangular and matrix-supported heterometric gravels, with some matrix-rich parts.

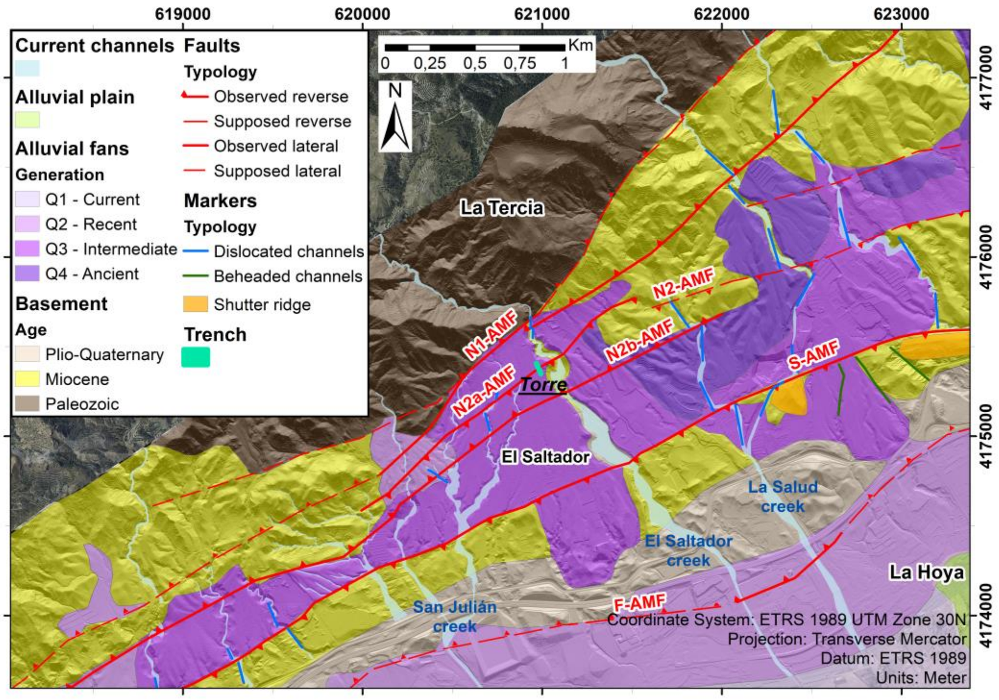

Figure 1: Detailed geomorphological map of the Lorca-Totana segment in La Hoya area, displaying some possible new branches not mapped previously.

D) Lower unit: Mostly clast-supported gravels. They are generally formed by angular pebbles. Some units can be found composed of well-selected gravels with practically zero matrix content. Two paleosoils have been identified within this unit (units D1 and D6).

On both walls it was possible to identify a zone of deformation with a variable amplitude between 1.2 and 1.5 metres, in which two contiguous synformal folds (and their respective antiformal) have been distinguished. Each of these folds accommodate a vertical deformation of approximately 30 cm, generating a total jump of between 50 and 70 cm. Although the deformation is concentrated in a relatively narrow band, the influence of the fault extends for several meters through metric-wavelength bending. Based on this, it was possible to estimate the total deformation from measurements in unit D1 in the SW wall, and a total (minimum) deformation value of 87±4 cm was obtained for this unit.

On the NE wall, two silt units were distinguished that provided valuable information to understand the Quaternary activity of the fault. The Bg unit was affected by both planes of deformation, while the Ba unit (located in a higher position in the profile) lacks deformation (Fig. 2).

Two OSL samples were taken from unit Bg (one sample at the base and another at the top) and one more sample was taken from unit Ba with the aim to limit the age of the last event that occurred in the fault (Fig. 2). These dates are currently in process.

DISCUSSION

Our mapping enabled us to affirm a structural relationship between the N2a-AMF and N2b-AMF faults, that might be connected at a shallow depth and that, together, produce a push-up structure. The N2a fault would be an antithetical fault with respect to the AMF, while the N2b would be a synthetic one. From their geomorphological expression, we interpreted that N2a is more active in the NE sector of the El Saltador fan, while N2b would only be active in the SW zone.

Two planes (F1, and F2 in Fig. 2) were defined in the trench following the synformal limbs as representative of the deformation produced by N2a-AMF fault at depth. At surface (in the trench), we do not strictly observe faults, but axial surfaces, corresponding to a fault propagation folding mechanism. However, for practical interpretation purposes, these axial surface planes were used as branches of the fault (marked in red on the profiles).
Based on the observations made, we interpret a minimum of three events that occurred on the N2a-AMF fault during the Quaternary:

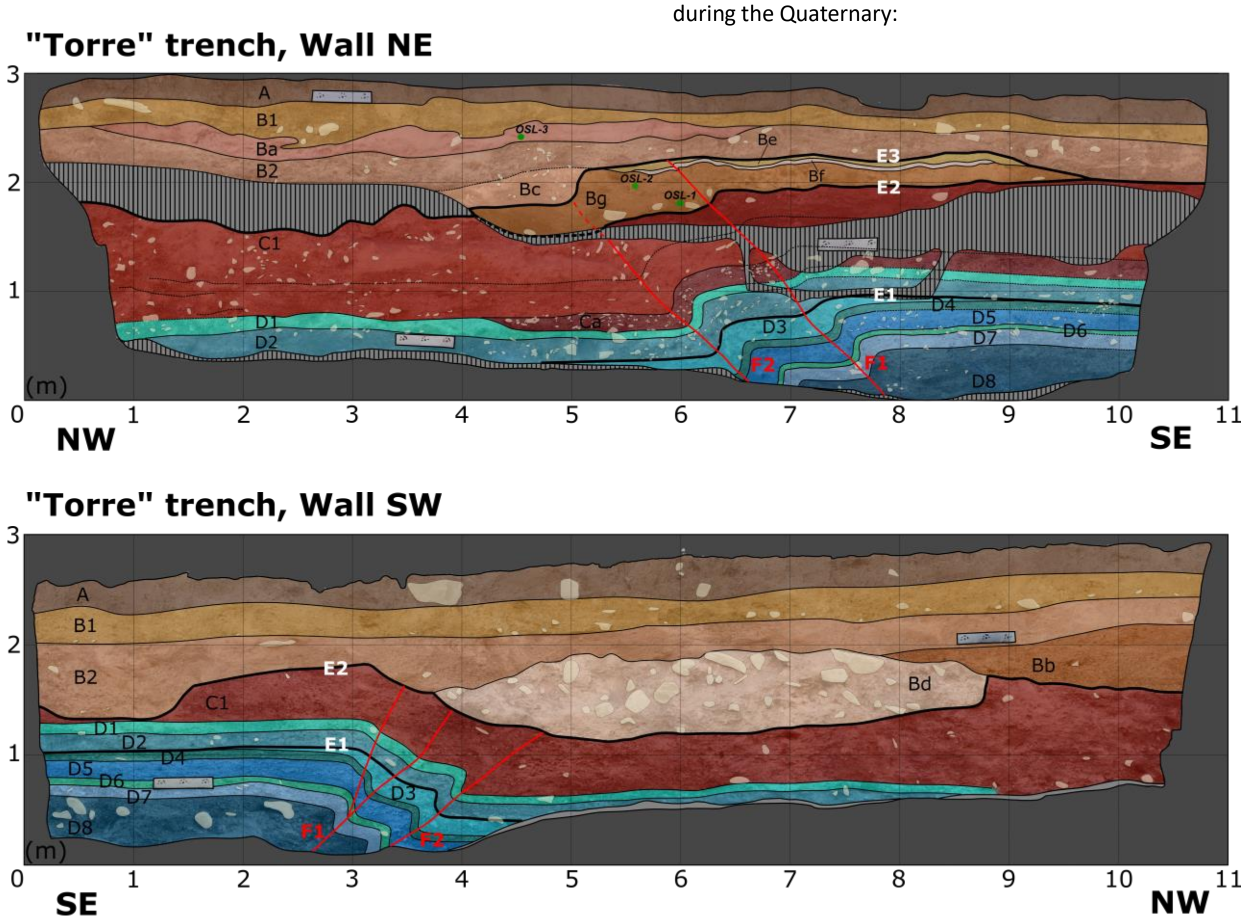

Figure 2: Stratigraphic and paleoseismical interpretation of both trench walls. NE wall on top, SW wall on the bottom.

E1: The first of these events would have involved only F1. It would have occurred when the D3 unit was on the surface, so it would only have affected the D8-D3 units. After the occurrence of E1, there would have been an erosion of unit D3 in the upper block, which would have eliminated the fault scarp generated on the surface as a result of the event.

E2: This event would have involved both F1 and F2 and would have affected the entire D8-C1 sequence. E2 would have given rise to two counterslope fault scarps on the surface of unit C1. These scarps could have acted as a sediment trap, allowing the stagnation of the Bg unit, made up of massive silts with some blocks at its base. Unit Bg, therefore, was interpreted as a co-seismic deposit. Similar units have been observed by Ferrater et al. (2016) and Gómez-Novell (2021) in their respective trenches in the S-AMF fault and interpreted them as produced by the erosion (and damming by the scarp) of the large amount of dust caused by the shaking at La Tercia during a large earthquake.

E3: The last of the detected events would have involved the F1 branch again. It would have affected the set of D8-Be units, up to what would be the topographical surface at that time. A vertical jump of 5±2 cm would have occurred, although later erosion would have eliminated the small fault scarp generated on the Be surface. It is possible that this earthquake also reactivated branch F2, affecting unit Bg.

The identified units and their stratigraphy can be correlated with the units of the Q3 alluvial generation described by Gómez-Novell (2021). This is also in accordance with the new mapping observations. Q3 alluvial fans correspond, according to Ferrrater (2016), to the Upper Pleistocene, with a minimum age of 101 kyr (Ferrater, 2016).

We used Gómez-Novell (2021) dates from "El Roser" trench to constrain the age of the materials of our trench. In "El Roser", Gómez-Novell dated a unit of the base of the Q3 generation with an age of 76.8±5.6 kyr. He also dated a unit at the base of the Q2 generation with an age of 39.6±0.4 kyr. As the materials in our trench should correspond to the upper part of the Q3 generation, we used those dates to establish an approximate range for them, obtaining a time frame between 82.4 and 39.2 kyr.

The results of the dating in progress will allow us to limit the estimated ages in the future.

Therefore, as we identified at least three events in that fault during the quaternary, it can be established that the minimum recurrence of the earthquakes in the N2a-AMF is about 14.4 kyr for the period between 82.4-39.2 kyr.

The recent activity of the fault has given rise to a total vertical deformation of 87±4 cm, in the D1 unit. Based on these data, the minimum vertical slip rate of the fault for the last 82.4 kyr would be between 0.010 and 0.011 mm/year.

CONCLUSIONS

Throughout this work we have analysed, by means of geomorphology and paleoseismology, a branch of the Alhama de Murcia Fault that had not been previously studied (the N2a-AMF branch). We have been able to demonstrate its neotectonic activity, with at least three different events along the Upper Pleistocene. In the new trench, we have measured a vertical offset of 87±4 cm, and we have collected data to calculate some of the seismic parameters of this branch: The N2a-AMF would have had a minimum seismic recurrence of 14.4 kyr for the period between 82.4-39.2 kyr; and a minimum vertical slip rate between 0.010 and 0.011 mm/year for the last 82.4 kyr.

Through our mapping, we also certified a structural relationship between the N2a-AMF and N2b-AMF faults. Moreover, from their geomorphological expression, we interpreted that N2a is more active in the NE sector of the El Saltador fan, while N2b would only be active in the SW zone.

Acknowledgements: This work is funded by the "Ministry of Science and Innovation" through the NSOURCE research project (PID2020-119772RB-100) and has been carried out within the framework of a Master+UB grant.

REFERENCES

De Larouzière, F.D., Bolze, J., Bordet, P., Hernandez, J., Montenat, C., and Ott d'Estevou, P., 1988, The Betic segment of the lithospheric Trans-Alboran shear zone during the Late Miocene. Tectonophysics, 152: 41–52, doi:10.1016/0040-1951(88)90028-5.

Ferrater, M., Ortuño, M., Masana, E., Pallàs, R., Perea, H., Baize, S., García-Meléndez, E., Martínez-Díaz, J.J., Echeverria, A., Rockwell, T.K., Sharp, W.D., Medialdea, A., Rhodes, E.J., 2016. Refining seismic parameters in low seismicity areas by 3D trenching: The Alhama de Murcia fault, SE Iberia. Tectonophysics, 680: 122–128. doi: 10.1016/j.tecto.2016.05.020

Gómez-Novell, O., 2021. Paleoseismic transect across the Alhama de Murcia Fault and implications of a fault-based seismic hazard assessment for the Eastern Betics. Tesis doctoral, Univ. Barcelona, 387 p.

Marín-Lechado, C., Roldán-García, F.J., Pineda-Velasco, A., Martínez-Zubieta, P., Rodero-Pérez, J., and Díaz-Pinto, G., 2011, Mapa Geológico Digital Continuo de España 1:50000, Zonas Internas de las Cordilleras Béticas (Zona-2100), GEODE. https://mapas.igme.es/gis/services/Cartografia_ Geologica/IGME_MAGNA_50/MapServer/WMSServer.

Martínez-Díaz, J.J., Masana, E., Ortuño, M., 2012. Active tectonics of the Alhama de Murcia fault, Betic Cordillera, Spain. Journal of Iberian Geology, 38: 269–286. doi: 10.5209/rev_JIGE.2012.v38.n1.39218

Masana, E., Martínez-Díaz, J.J., Hernández-Enrile, J.L., Santanach, P., 2004. The Alhama de Murcia fault (SE Spain), a seismogenic fault in a diffuse plate boundary: Seismotectonic implications for the Ibero-Magrebian region. Journal of Geophysical Research: Solid Earth, 109: 1-17. doi: 10.1029/2002jb002359

Silva, P.G., 2014. The Guadalentín Tectonic Depression, Betic Cordillera, Murcia. World Geomorphological Landscapes. Springer: 25–35. doi: 10.1007/978-94-017-8628-7_2

INQUA Focus Group Terrestrial Processes Perturbed by Tectonics (TPPT)

paleoseismicity.org

Outreach on Earthquake Geology as a tool to increase social seismic awareness

María Ortuño (1), Eulàlia Masana (1), Raimon Pallàs (1), Octavi Gómez (1), Marta Ferrater(2), Jaume Bordonau (1)

(1) RISKNAT Group, Institute Geomodels, Earth and Ocean's dynamics Dept. Facultat de Ciències de la Terra, Universitat de Barcelona, 08028 Barcelona, Spain
(2) Secondary School Manuel de Cabanyes, Av. Francesc Macià 110-114, Vilanova i la Geltrú, Barcelona, Spain.

Abstract: *Social identification of seismic risk in many regions is often challenging because the long-elapsed time span since the last destructive event, especially common in moderate and slow deformation areas. We propose to strengthen the use of outreach tools in Earthquake Geology to capture the attention of the population towards seismic risk, especially among children. We present an outreach short-film on Earthquake geology ("Earthquake land", available in YouTube), and provide three classroom activities to: 1) introduce the concepts of Plate tectonics and tectonic blocks with the help of large puzzles; 2) explore the seismic cycle by reproducing the cumulative changes imprinted in the landscape by repetitive fault movements (consecutive earthquakes) and; 3) reproduce the site-effects in sedimentary infills through the "amplification pie". The effectiveness of the activities is being tested in several schools in Catalonia. We aim to improve seismic education by incorporating the suggestions of young participants, who evolve from passive recipients to main actors in the prevention strategy.*

Key words: *Earthquakes, Social impact, Education*

INTRODUCTION

Starting an educational approach to increase seismic awareness in places with no earthquakes in the recent historical record is challenging. Seismic hazard awareness is highly reinforced when a damaging earthquake happens during a person's life or happened during the life-span of his/her ancestors, becoming part of the family memories. However, in regions of moderate and slow deformation, if a large time-lapse exists since the last destructive event, the social identification of seismic risk is not so straightforward. A first step towards rising seismic risk awareness in these areas should be convincing the population that earthquakes happen recurrently. Would you start taking a pill to face an illness if you don't identify any symptoms?

In SE Spain, a damaging earthquake struck the city of Lorca ten years ago (the Lorca earthquake, Mw = 5.2, 11/10/2011) causing nine causalities, hundreds of injured and forcing near 10,000 people to leave their homes as a consequence of structural damages in buildings. The event is considered the largest urban catastrophe in Spain since the Civil War (García, 2021) and the most destructive earthquake in Spain since the beginning of the XX century, followed by the Albolote earthquake in Granada, M 5, 17/04/1956 (IAG, 2021). The seismic perception of the Lorca inhabitants is contrastingly higher than the one in neighboring localities, and also higher than in other seismic regions of the Iberian Peninsula, as it is the case of Catalonia.

Within this approach, we aim to explore how the recent experience of an earthquake influences the seismic perception among children and youngsters and propose a series of outreach activities designed to increase the awareness of exposure to seismic risk in primary and secondary school at the time that they learn some basic concepts of earthquake geology.

We assume that, under the lack of a direct experience of an earthquake, the seismic awareness can be increased by becoming familiar with the impact that past earthquakes have produced in the landscape (seismic landscape) surrounding us, both natural and architectural.

Three main lines of activities are developed following the principles of active and long-lasting learning (e.g., Brown et al., 2001; Wirth, 2007); 1) classroom activities (for primary and secondary courses) around a documentary on earthquake geology "Earthquake land"; 2) an online survey to understand the previous perception and test the effectivity of the short-documentary in understanding some basic concepts of earthquake geology; 3) a web page compiling concepts, definitions and links on earthquake geology, with special focus, in this first stage, on the Iberian Peninsula.

Figure 1. A snapshot during the filming of the short-documentary, November 2018, in Tostana trenching site (Carboneras fault, SE Spain).

THE SHORT DOCUMENTARY

"Earthquake land" (*Tierra de temblores*) is a short documentary on earthquake geology produced by the RISNKNAT research group and *Paral·leles* production in the frame of the PREVENT project (supported by the Spanish government). It was designed and filmed during 2018/2019. In march 2020, the short-film become available in YouTube. The final version was published in this link: https://www.youtube.com/watch?v=4ZrmgHA6y1g

The short film is conceived as a tool to be used in schools, community colleges, city hall prevention actions, etc. The last aim of this film is to promote the interest for the record of the "seismic past". This can be achieved by identifying the imprints of past earthquakes (architectural/cultural heritage and the living memory) in the buildings but also in the natural landscape surrounding our towns. The short film tells the story of Aitana, an 8 years old girl and grown in Lorca city. She was only one year old when the city was struck by an earthquake (Mw = 5.2) in 2011. After a nightmare, Aitana starts making herself many questions about why the earthquakes happen and about the possibility to anticipate them. Then, her mother takes her to visit her aunt, who is an earthquake geologist. Through different games and the visit to a trenching site (Fig.1), Aitana explores the relationship of earthquakes and faults, and gets a new vision of the landscape of her region.

PROPOSED ACTIVITIES

Departing from the short film and with the support of shorter videos, we propose three different classroom activities. These are designed to get a first basic knowledge on earthquake geology but also to increase awareness on the seismic risk exposure. To pique pupil's interest and promote the active learning, we rely on "hands-on" activities and refer to elements that have to do with past earthquakes and are not in California, but are part of their urban and natural landscape and (from building damage to the formation of mountains).

Figure 2. The Plate tectonics puzzle activity

The puzzle

Puzzles can be a good representation of the tectonic blocks, from local scale (Iberian Peninsula or Eastern Betics) to whole Planet scale (lithospheric plates). For the younger students, we propose playing with the use of colored stickers representing earthquakes to define the plate boundaries (Fig. 2). The main mountain ranges are sculpted in modelling clay. In the case of the Eastern Betics, since main fault slips are lateral, we can just apply horizontal forces and observe the resulting relative movements (Fig. 3). Support video: https://youtu.be/XGSRfazcgbI

Figure 3. Tectonic blocks of the Eastern Betics and representation of main mountain ranges.

The amplification pie

The amplification pie allows directly observing the effect of the amplification of a wave when travelling through different materials. In this experiment, we build a sponge cake (representing the basement) and empty one part within it to get a valley or a lake. Then, we fill it with gelatin (sedimentary filling, Fig. 4). This configuration is an analog model (not properly scaled though) that allows to observe the different response to a mechanical wave (in this case, tapping the cake will be the representation of the seismic shaking). Support video: https://youtu.be/6ts6JtnRXiY

Figure 4. Close-up view of "the amplification pie" experiment.

The earthquake machine

The "earthquake machine" is used to experiment the seismic cycle. It is inspired in previous experiments (as Martínez Moreno et al., 2012; IRIS, 2021) but adapted to show how the morphogenic earthquakes do generate changes in the landscape. The block that slides over the sandpaper is dragged with the use of a rubber band (stretched and representing the inter-seismic strain accumulation). The novelty is that the recreated landscape is displaced during the seismic event (Fig. 5). We place the sliding block next to a fixed block and represent the offset of mountain relieves and creeks, the blockage of a river and the formation of sag ponds (by obturation ridges).

Figure 5. The earthquake machine

FURTHER PERSPECTIVES

Evaluating the effectiveness in increasing awareness

Hazard awareness activities are already being implemented at different localities in Spain (e.g., CUIDAR project, 2018) and recall the need to generate an inclusive and living discourse, by incorporating the proposals and suggestions of young participants (subjects of the experiences), which go from passive recipients to primary actors of the prevention strategy. One of the ways to detect how effective is the short-documentary in changing the seismic perception of the students is analyzing their responses to a test, which is completed before and after watching the film. The test queries about four aspects: their knowledge about the seismic exposures and the prediction of earthquakes, their knowledge of what to do during and after the earthquake and their perception of the seismic nature of the mountains around their town.

So far, we have counted with the collaboration of high school teachers in four schools in Catalonia. They have organized a screening of the short documentary and have compiled more than 1300 tests that we are analyzing. Our next objective is to extend this "sensitivity test" to different towns of Murcia, including Lorca, where the seismic educational degree is expected to be larger: the commemoration of the 10 years after the Lorca earthquake last year brought the subject to the forefront of news and for sure, the exposure to earthquakes is still part of the classroom discussions.

Other resources

Part of the approach developed by our group is inspired in other local and international projects, which we recommend and refer to teachers and educational professionals dealing with seismic risk. Some of these are:

- Oikos Software (2004). The risk management game, coordinated by Guadagno, F.M. (Università degli Studi del Sannio) and developed as a Leonardo da Vinci (EU) project. http://www.e-oikos.net/gmap/oikos.htm
- "Putting down roots in Earthquake Country, (USGS and SCEC), first version 1995; Lucy Jones (coordinator with Mark Benthien), updated versions in 2006 available in English and Spanish athttp://scecinfo.usc.edu/resources/catalog/roots.html)
- Edubox at EDURISK (2004-2015) http://www.edurisk.it/, Istituto Nazionale di Geofisica e Vulcanologia e del Dipartimento nazionale della Protezione Civile.
- U.S. Geological Survey, 2011, Putting down roots in earthquake country-Your handbook for earthquakes in the Central United States: U.S. Geological Survey Information product 119, 47 pg.
- ESLorca. EsLorca: una iniciativa para la educación y concienciación sobre el riesgo sísmico. Martínez Moreno et al., 2012). http://www.eslorca.com/.

Acknowledgements: This work was supported by the PREVENT project (CGL2015-66263-R). We thank Candela-Camacho family for the collaboration in the record of the film, specially to Aitana Fuentes Candela (main character). Zoraida Roselló and María Romero (*Paral·leles* Prod.) were in charge of the production, animations and collaborated in the short-film script.

References

García, Ana. (2021). Lorca, una década después del terremoto: "Fue la mayor catástrofe urbana en España desde la Guerra Civil". News RTVE 11.05.21 (https://www.rtve.es/noticias/20210511/terremoto-lorca-10-anos-despues/2089250.shtml)

Brown, L., Kelso, P, Rexroad, C. (2001). Introductory geology for elementary education majors utilizing a constructivist approach. Journal of Geoscience Education. V. 49, 5, 450-453.

CUIDAR project (2018). Cultures of Disaster Resilience among children and young people. Horizon 2020 project https://cordis.europa.eu/project/id/653753/es

IAG, Intituto Andaluz de Geofísica (2021). El Terremoto de Atarfe-Albolote de 19 de Abril de 1956. Información y Divulgación. Retrieved on april 2011 (http://iagpds.ugr.es/pages/informacion_divulgacion/terremoto_atarfe_albolote_1956)

IRIS, 2021. Earthquake machine 1, Defining an erathquake. Incorporated Research Institutions for Seismology-United States. Web page: https://www.iris.edu/hq/inclass/lesson/defining_an_earthquake (retireved in April 2021)

Martínez-Díaz, José J.; Bejar-Pizarro, Marta; Álvarez-Gómez, José A.; de Lis Mancilla, Flor; Stich, Daniel; Herrera, Gerardo; Morales, Jose (2012). "Tectonic and seismic implications of an intersegment rupture. The damaging May 11th 2011 Mw 5.2 Lorca, Spain, earthquake". Tectonophysics. 546–547: 28–37

Martínez-Díaz, J.J., Masana, E., and Ortuño, M., 2012, Active tectonics of the Alhama de Murcia fault, Betic Cordillera, Spain: Journal of Iberian Geology, v. 38, p. 253–270, doi:10.5209/rev_JIGE.2012.v38.n1.39218

Martínez Moreno, F., Salazar Ortuño, A., Martínez Díaz, J., López Martín, J. A., Terrer Miras, R. y Hernández Sapena, A. (2012). EsLorca: una iniciativa para la educación y concienciación sobre el riesgo sísmico. Boletín Geológico y Minero, 123 (4): 575-588 ISSN: 0366-0176

Wirth, K. R. (2007). Teaching for deeper understanding and lifelong learning. Elements, v. 3, 101-106.

INQUA Focus Group Terrestrial Processes Perturbed by Tectonics (TPPT)

paleoseismicity.org

Paleoseismological investigation in a remote region of Kalimantan, Indonesia

Pamumpuni, Astyka (1,2), Dee Ninis (3), Naomi Maria Neysa Prayacita (1)

(1) Institut Teknologi Bandung, Ganesa 10, Bandung, West Java, Indonesia 40132, email: pamumpuni@itb.ac.id.
(2) Centre for Earthquake Science and Technology ITB, Ganesa 10, Bandung, Indonesia
(3) Seismology Research Centre, 141 Palmer Street, Richmond, Victoria, Australia

Abstract: *We undertook a paleoseismological investigation of a fault in a remote region of Kalimantan, Indonesia, to determine whether the fault should be considered active (defined as having ruptured in the last 11 ka) for a nearby site-specific PSHA. Our study relied on the National Seamless Digital Elevation Model (DEMNAS) and LiDAR-derived elevation data to first identify the fault and associated fault strands. We delineated the structure with a total length of ~60 km; magnitude-area scaling relationships suggest that this fault is capable of hosting an earthquake of ~Mmax7.1. In the field, resistivity surveying at two sites identified potential planes which coincided with the approximate location of the fault strands as interpreted from the LiDAR data. Trenching at both sites – which, due to the remote nature, had to be undertaken manually – exposed un-faulted alluvial deposits. Samples of organic matter collected from these un-faulted sediments yielded ages of between 1669 cal AD and 3960 cal BC at one site and 1151-1206 cal AD from the second site, suggesting that the fault has not produced a ground-rupturing earthquake in at least the last ~834-732 years; these young sediment ages are not surprising in such a humid environment. Because of the obvious surface expression of the fault in digital elevation imagery, we suspect this structure may have ruptured within the last 11 ka, and may therefore be active, albeit with a relatively low slip rate. Based on previously identified active faults in Kalimantan whose morphological expression appears similar, we have inferred a slip rate for this fault of 0.3-0.5 mm/yr.*

Keywords: *paleoseismology, Kalimantan, Indonesia.*

INTRODUCTION

Kalimantan (also known as Borneo) is one of the islands in Indonesia that rarely experiences earthquakes in contrast to other regions in Indonesia. However, several earthquakes occurred in the northern part of Kalimantan Island based on the National Seismic Centre earthquake catalog (Pusgen, 2017) e.g. 1923 M6.8 located in the north of Mangkalihat Peninsula; 2015 M6.1 located in north Tarakan; and 1995 M6.1 located off the coast of North Kalimantan Province of Indonesia. Based on the current active fault map of Indonesia (Pusgen, 2017), only two active faults have been identified in the northern part of Kalimantan; these are inferred to be the source of the aforementioned earthquakes. In this paper we identify a fault from remote sensing data and then proceed with field observations, acquisition of shallow geophysical data, and also paleoseismology trenching, to determine prior ground-rupture earthquake activity on this structure.

DATA AND METHOD

In this investigation, we used remote sensing techniques to first identify faults. We employed the *National Seamless Digital Elevation Model (DEMNAS)* (*DEMNAS*, n.d.) as well as LiDAR-derived elevation data, alongside regional geological maps (Heryanto et al., 1995). DEMNAS data is open downloadable DEM data with 8m horizontal resolution. Data from LiDAR has a lateral resolution of 1m. From the DEMNAS and LiDAR data, fault traces were obtained which were then compared with regional geological maps. Field observations were made to confirm the fault trace locations found from remote sensing.

Based on remote sensing evaluation and field observations, geophysical data acquisition was carried out for one fault of interest, the 'Main Fault', at two locations - the first on a fault splay we hereby refer to as 'West Main Fault' and the second on another splay we call 'East Main Fault'. The results of the shallow geophysical data acquisition were then evaluated to determine the location of the subsurface fault plane and therefore the most suitable location for trenching. Paleoseismological trenching was carried out at sites that were accessible, and which had fault crossing deposits which were young enough to provide evidence for recent ground rupture, namely late Quaternary deposits.

RESULT AND DISCUSSION

Reconnaissance observations were conducted at seven locations, shown in Figure 1, with the objective of investigating the general geology (including geomorphology, type, and age of the lithology) for possible evidence of active fault occurrence and accessibility to each location.

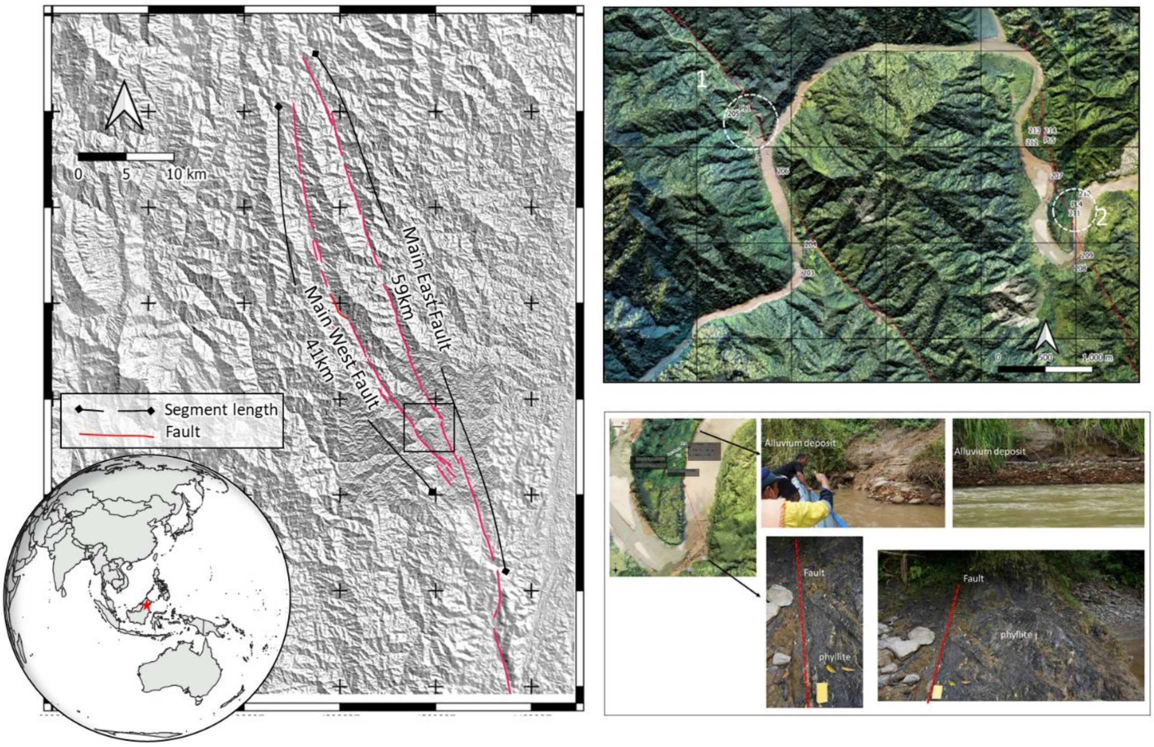

Figure 1. Study location and regional fault trace from remote sensing analysis (left). Area 1 and Area 2 from detail LiDAR and orthomozaic image (upper right). Field observation and drone photo (lower right).

Based on reconnaissance observations, the best location for further investigation of the West Main Fault was Area 1 (Figure 1); other areas of West Main Fault were not suitable for paleoseismology investigation due to the absence of young deposits and active morphological evidence, or because of altered morphology due to road construction.

Area 1 was observed further to locate geomorphological evidence of the West Main Fault and to determine a suitable location for geophysics surveying. Access to Area 1 is only by long boat via the main river.

East Main Fault was best observed in Area 2 (Figure 1). Area 2 has flat morphology, sandy alluvial deposit, less dense vegetation, access from a nearby village, and is across from observed fault evidence (Figure 1). Area 2 was therefore suitable for further paleoseismology investigation.

Geophysical survey has been conducted in Area 1 and Area 2 (Figure 1); two resistivity lines in Area 1, and three lines in Area 2. Resistivity survey line locations were chosen based on the interpretation of fault lines, topographic survey results, and reconnaissance surveys. All five resistivity survey lines were located on Quaternary sediment and crossed interpreted fault lines.

Area 1 resistivity survey results (Figure 2) show a low resistivity anomaly just in the cliff where the contact between bed rock and alluvial deposits was located. Low resistivity in Area 1 also correlated with fault line interpreted from LiDAR and aerial photomosaic. For further investigation, Area 1 was a possible site for fault trenching.

Resistivity results of Area 2 show a low resistivity anomaly in two of three lines. A low resistivity zone in Area 2 did not continue to the surface and appeared wider with depth. This may be due to a shallow water table in the area. The two low resistivity anomalies in Area 2 correlated with fault interpretation from LIDAR and aerial ortho-mosaic.

Trenching was conducted in Area 1 and Area 2, where the low resistivity anomaly corresponded to the LIDAR-interpreted fault location. Trenching in Area 1 was performed using manual digging and showed no evidence of ground rupture activity (Figure 2). Three samples from Area 1 taken from an alluvial sand deposit were sent for radiocarbon dating. Two samples show good confidence results, while one was inconsistent with the other two ages. The calibrated radiocarbon age of three samples in Area 1 are 281-170 cal BP, 225-136 cal BP, and 5909-5746 cal BP.

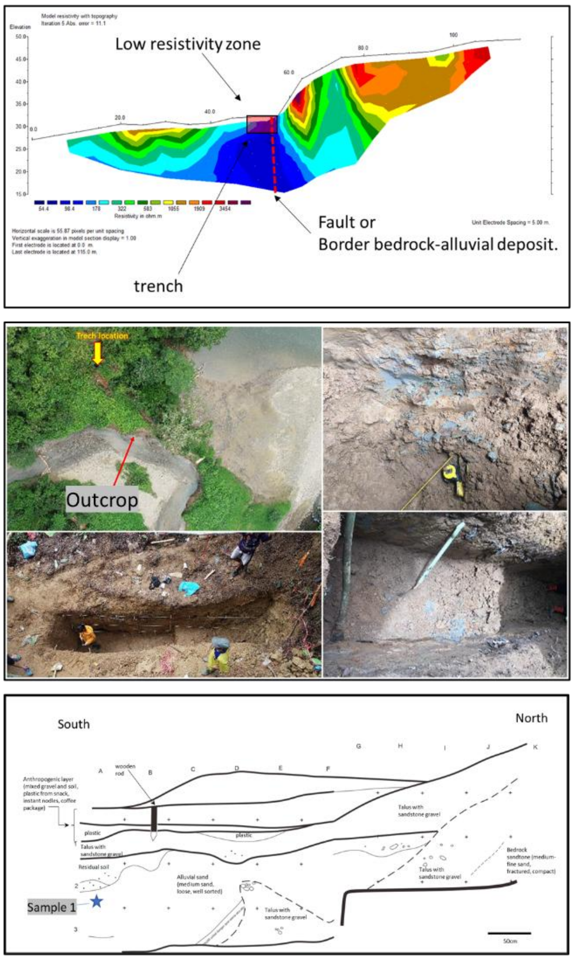

Figure 2. One of resistivity result in Area 1 (upper), manual trench in Area 1, and trench log and interpretation of Area 1 trench (bottom).

Trenching in Area 2 encountered a shallow water table and wall stability problems. The results shows no evidence of ground rupture activity. Two samples from the trench location and two from the nearby riverbank were collected and sent for radiocarbon dating. Calibrated radiocarbon dating ages were all consistent, ranging from 224-137 cal BP to 834-732 cal BP. All samples from the two trench location showed very young sediment, with the oldest at 834 cal BP. Since there is no evidence of fault activity found in trench, we can infer that the West Main Fault and the East Main Fault have not produced ground rupturing earthquakes at least in the last 834 years.

CONCLUSION

Morphology suggest that Main Fault may have been active during last 11,000 years. No evidence of fault activity during last 834 years suggest the slip rate may very low. Based on Tarakan Fault and Mangkalihat Fault which are in the same tectonic setting, the Main Fault likely has a slip rate, 0.3-0.5mm/year. Main East Fault at least has 59km length, while Main West Fault 41 km length. Using empirical relationship formula (Wells & Coppersmith, 1994), Main East Fault is capable of Mmax7.1, and Main West Fault could produce Mmax7.0.

Acknowledgements: The authors would like to thank Entura for permission to share the geological findings of this otherwise ‘commercial in confidence’ investigation.

REFERENCES

DEMNAS. (n.d.). Retrieved February 22, 2022, from https://tanahair.indonesia.go.id/demnas/#/

Heryanto, R., Supriatna, S., & Abidin, H. Z. (1995). *Geological Map of Malinau Sheet, Kalimantan*. Geological Research and Development Center - Bureau of Mineral Resources.

Pusgen. (2017). *Peta Sumber dan Bahaya Gempa Indonesia 2017*. Pusat Penelitian dan Pengembangan Perumahan dan Permukiman Balitbang Kementrian PUPR.

Wells, D. L., & Coppersmith, K. J. (1994). New empirical relationships among magnitude, rupture length, rupture width, rupture area, and surface displacement. *Bulletin - Seismological Society of America*, *4*, 974–1002.

Neotectonic of Papua, Indonesia

Pamumpuni, Astyka (1, 2), Benyamin Sapiie (1), Danny H. Natawidjaja (3), Irwan Meilano (1, 2)

(1) Faculty of Earth Science and Technology, Institut Teknologi Bandung, Ganesa 10, Bandung, West Java, Indonesia, pamumpuni@itb.ac.id
(2) Center for Earthquake Science and Technology ITB, Ganesa 10, West Java, Indonesia, 40132
(3) National Research and Innovation Agency, Sangkuring 19, Coblong, Bandung, West Java, Indonesia. 40135.

Abstract: *Interactions between the Australian, Pacific, Eurasian, and Philippine Plate generate complicated geology of Papua Islands. Those interactions still occur today and produce high seismic activity in the area. Several active faults result from the tectonic activity in Papua, e.g., Sorong Fault Zone, Manokwari Fault Zone, Yapen Fault Zone, Mamberamo Fault Zone, Lengguru Fold Thrust Belt, Papua Fold Thrust Belt, Tarera-Aiduna Fault, Gauttier Thurst, New Guinea Trench. Powerful earthquakes with more than 7 Mw have been recorded in the earthquake catalog even in the last 1-3 decades. Tsunami wave often follows earthquake, e.g., Biak 1996. The characteristic of segmentation and activity for each fault of Papua is still unclear. The source of these earthquakes is yet to be defined.*

This neotectonic study of Papua utilizes remote sensing data, bathymetry, seismic section, seismicity, surface geology, and GPS data. The methods used in this study are tectonic geomorphology, active fault mapping, GPS analysis, seismic interpretation, and focal mechanism analysis. The result suggests that the Pacific-Australia interaction has been partitioned into shortening and shear interactions. This study provides an active fault map, including fault segmentation in Papua. The active fault of Papua can be divided into structural domains, i.e., Bird's Head, Yapen Fault Zone, Mamberamo-Nawa Hill Fault Zone, Papua Fold Thrust Belt, and Bird's Neck.

Faults kinematic in Papua result from northwest moving Pacific Plate and Australia Plate interaction. GPS velocity data shows that Pacific Plate motion is mainly accommodated by the Mamberamo Fault Zone and Nawa Hill in the north, stepping to the left to Tarera-Aiduna Fault Zone in the south, connected through Wapoga Trough. New Guinea Trench and Manokwari Fault Zone also accommodate Pacific Plate motion in the northernmost part of Papua.

Key words*: Papua, neotectonic, bathymetry, geomorphology*

INTRODUCTION

The interaction between the Australian Plate, the Pacific Plate, the Eurasian Plate, and the Philippine Plate in the eastern part of Indonesia causes the geological conditions of Papua to be complex. Large earthquakes with a magnitude of more than 7 Mw have occurred in Papua and have been recorded in existing earthquake catalogs, even within the last 1-3 decades. Earthquakes with a magnitude of more than 7 Mw have occurred several times in northern Papua, from Sorong to the border with PNG in the east (Figure 1). A large earthquake with a magnitude of more than 7 Mw has also occurred in the Aru Trough, in the southwest part of Papua. Some earthquakes are also accompanied by tsunamis, such as the Biak earthquake in 1996.

Based on GPS (Global Posotioning System) data modeling, the relative movement of the Pacific Plate to the Australian Plate is 112.5 mm/yr (DeMets et al., 2010). GPS data, both from previous researchers (Puntodewo et al., 1994; Stevens et al., 2002) as well as recent data from the BIG (Geospatial Information Agency) show different velocity.

Sapiie et al. (1999) stated that the deformation that occurred in Papua was influenced by changes in the movement of the Caroline Plate and the Pacific Plate at 5 million years ago. This change in movement is accommodated by the main faults in Papua, especially the Sorong-Yapen and Mamberamo Fault Zones. Tarera-Aiduna Fault, Central Mountains, and Wapoga Trough according to Sapiie et al. (1999) accommodate the deformation caused by the interaction of the Pacific Plate and the Australian Plate.

The distribution of accommodation for each existing fault is defined in this study. This study also defines which faults are active based on subsurface geomorphology and geophysics data including geometry, fault type, and segmentation. The maximum earthquake that can be generated by each fault segment is also calculated in this study. The existence of an active fault map produced in this study can be used to determine the potential for earthquakes in Papua.

DATA AND METHOD

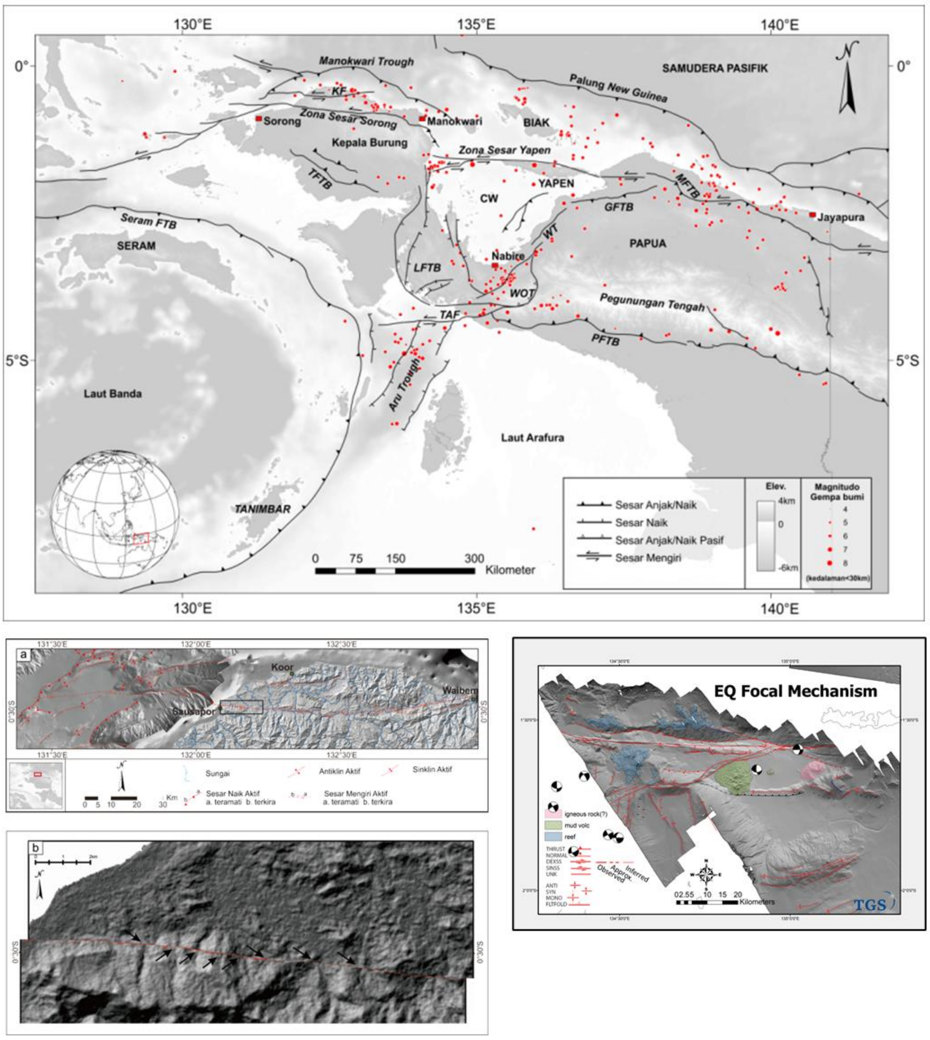

Figure 1. Updated tectonic regional from this study (upper). Interpretation of active fault based on DEM in Bird's Head (lower left). Interpretation of multibeam bathymetry data in Cenderawasih Bay.

The data used in this study are DSM Radarsat, SRTM30 (Farr et al., 2007) and SRTM90, multibeam bathymetry, topographic maps, seismic cross-section, epicentre, and earthquake focus mechanism, and GPS velocity data (BIG). Geomorphological mapping methods and interpretation of seismic data, earthquake mechanisms, and GPS data were carried out to compile the neotectonics map of Papua.

RESULTS

Based on geomorphological interpretation and interpretation of existing data, Papua can be divided into several tectonic zones or domains. There are at least six domains, namely: Bird's Head, Yapen, Mamberamo, Nawa Hill, Papua Folds Thrust Belt, Bird's Neck (Figure 1).

There are at least four sources of earthquakes in the Bird's Head which are part of the Pacific-Australian deformation zone, namely: Sorong Fault, Koor Fault, Manokwari Trough and Taminabuan Fold Zone. These active faults were identified based on the interpretation of available radar data and bathymetric data (Figure 2). The focal mechanism data and the relocation results of earthquakes with a magnitude of M>6 is generally located to the northeast of the Bird's Head.

The Seismicity at Bird's Head shows a history of earthquakes with a magnitude of more than M6. One of the recent earthquakes was the September 24, 2015, earthquake, which was located 31 km west of Sorong City. This earthquake had a magnitude of 6.3 Ms which left 62 people injured and more than 200 houses heavily damaged. On January 3, 2009, earthquakes (doublet) with magnitudes 7.6 and 7.4 Mw occurred in the west of Manokwari City with 4 people dead, 500 people injured, and 2000 buildings damaged.

The segmentation of the Yapen Fault Zone is based on available bathymetric and radar interpretations. Based on the data, there are several main faults and fault segments in the Yapen Fault Zone, namely the Ransiki-Num Fault, Randaway Fault, Jobi Fault and Wirundi Fault.

Geomorphological mapping of the seabed shows ridge, underwater flow, and the escarpment (Figure 1). Some of the identified escarpments are in a west-east direction as the direction of Yapen Island that forms a very firm line with a continuity of up to 40km. These escarpments provide evidence of the activity of the Sorong-Yapen Fault. The identified fold direction is generally northwest-southeast. Reflection seismic section shows the presence of young sediments filling the basin which is influenced by geological structures. Based on seismic data, it was also found that the Sorong-Yapen Fault has wide deformation zone, reaching ~20 km.

Earthquakes with a magnitude >7 M occurred in 1979 in the central part of Yapen Island, in 1985 to the west of Yapen Island, and in 1996, 1947 and 1941 to the east of Biak Beach (Okal, 1999; Henry and Das, 2002). Earthquakes were reported in 1957 and 1972 which occurred in the north and south of the eastern part of Yapen Island (Henry and Das, 2002). The 1979 earthquake on Yapen Island was reported to have caused a tsunami (Okal, 1999). Based on empirical calculations, faults in the Yapen Fault Zone can cause earthquakes with a magnitude of 7.8 Mw.

The Mamberamo Fault Zone is located from the eastern tip of Yapen Island all the way to Jayapura. From the eastern tip of Yapen Island (137°E) to the east to the Mamberamo River (138°E), this fault zone has a west-east direction of ±96 km (Figure 2). The area 2° 15'-2° 40'

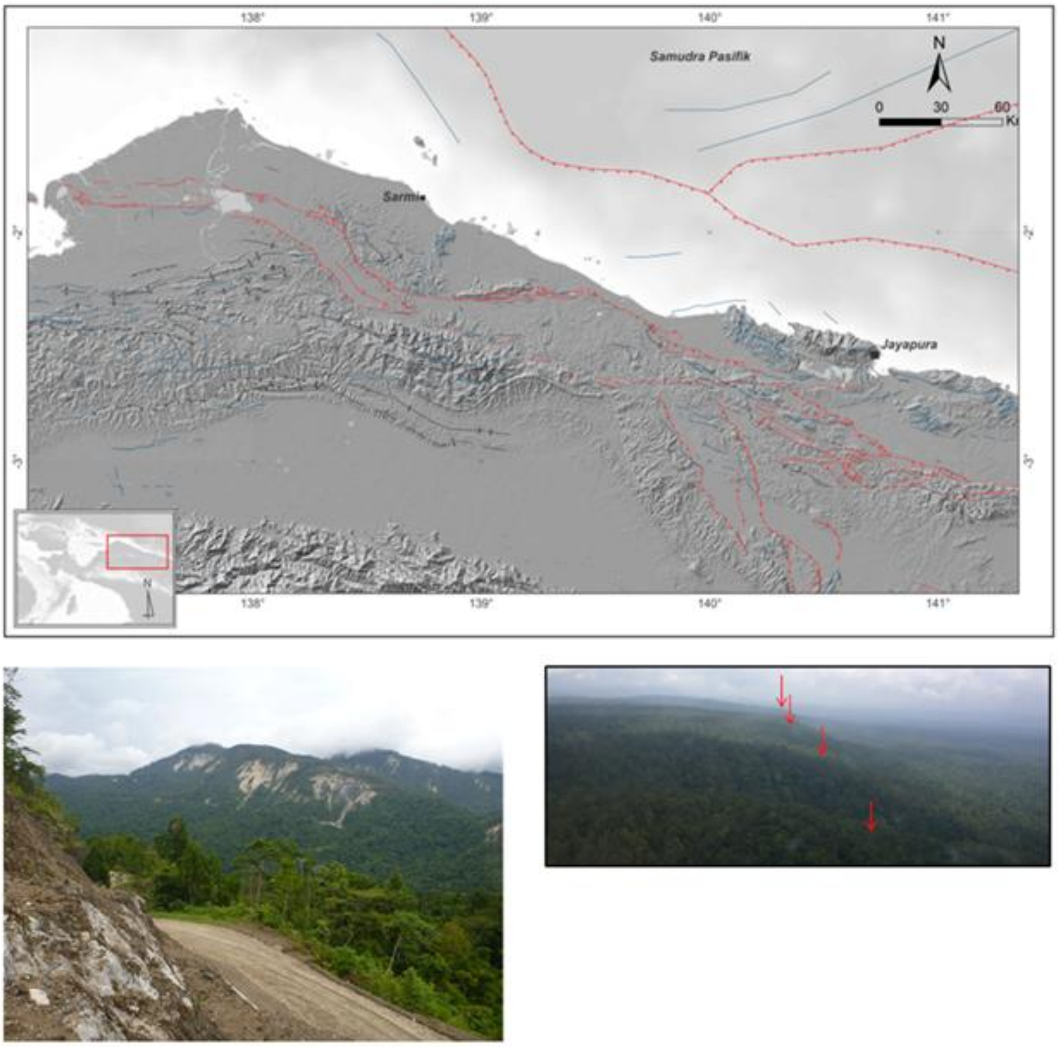

Figure 2. Geomorphological interpretation of Mamberamo Area (upper), morphological view from field observation of Yapen Fault in Yapen Island (lower left), Papua Fold Thrust Belt in Timika (lower right)

South -139° 10'-139° 40' East is dominated by the geomorphology of mud volcanoes. From the area around 139° 40' east longitude to 141° east longitude, the Mamberamo Fault Zone has a southeast direction with several short faults trending west-east. The Mamberamo Fault Zone is divided into five major fault domains. The division of this domain is based on the direction and continuity of the faults and or folds that exist in this fault zone.

There were at least 22 earthquakes with a magnitude of more than 6 M in the Mamberamo Fault Zone. These earthquakes are concentrated around the Wiroe Toarim Domain generally have a reverse fault mechanism. From the empirical calculation between the magnitude and length of the fault segment on the surface proposed by Wells and Coppersmith (1994), fault segments in the Mamberamo Fault Zone can produce earthquakes with a magnitude of 7.1 to 7.5 Mw.

The Nawa Hill area is to the south of Jayapura. The Nawa Hills area consists of Mesozoic rock hills and plains of silt deposited by a mud volcano eruption (Visser and Hermes, 1962). The faults rise in a northwest-southeast direction and slope to the southwest limiting the hills and silt plains. The earthquakes that occur are generally in the form of reverse mechanism with some earthquakes having a vertical nodal plane. The depth of the earthquake that occurred around the Nawa Hill Fault Zone had a depth of up to 100 km. Calculation of the magnitude that can be caused by faults in Bukit Nawa has a value of up to 7.6 Mw.

The Papua Folds and Thrust Belt extends east-west from the eastern part of the Bird’s Neck to Papua New Guinea. This thrust fault zone is in the southern part of the Central Mountains of Papua. This fault zone involves rocks that are old to young, from Palaeozoic to Recent. The thrust fault zone is dominated by folds with a zone width of tens of kilometres and reverse faults with a dip direction to the north.

Seismic section shows the presence of fault and folds involving youngest rock. Some of these thrust faults reach the surface and some are in the form of blind thrust faults. The blind thrust fault below the surface merges with thrust fault identified from surface. These thrust faults generally have shallow decollement and turn as a thick skin rising fault to the north.

The seismicity in the Papua Thrust Fault Zone is generally located right in front of the thrust fault, which is the boundary between the southern plain and the mountains to the north. The existing focus mechanism is generally in the form of reverse fault. Several strike-slip mechanisms were observed at the eastern part. In the western most area earthquake data show a strike-slip mechanism along with reverse fault mechanism. The existing seismicity is generally at a depth of 10-30 km.

Active faults in the Bird's Neck region consist of the Wandamen Fault Zone, the Tarera-Aiduna Fault, and the normal faults that create the Aru Trough. These faults can be seen clearly intersecting the existing folds (Lengguru FTB). Earthquakes with strike-slip mechanisms and normal faults often occur in the bird's neck area.

CONCLUSION

Mapping of active faults using a combination of subsurface data (seismic section and bathymetry), surface geological data, GPS, and focal mechanisms has succeeded in identifying active faults and active fault kinematics in Papua. The Bird's Head moves in the direction of the Pacific at almost the same speed as the horizontal velocity of Pacific Plate. Strain due to interaction between Pacific, Australia, and Eurasia accommodate as a complex neotectonic deformation across Papua Island.

Acknowledgements: Author thanks to Geological Agency of Indonesia and TGS for providing data in this study.

REFERENCES

DeMets, C., Gordon, R. G., dan Argus, D. F. (2010): Geologically current plate motions, Geophysical Journal International, 1, 1-80.

Farr, T. G., Rosen, P. A., Caro, E., Crippen, R., Duren, R., Hensley, S., Kobrick, M., Paller, M., Rodriguez, E., Roth, L., Seal, D., Shaffer, S., Shimada, J., Umland, J., Werner, M., Oskin, M., Burbank, D., dan Alsdorf, D. E. (2007): The shuttle radar topography mission, Reviews of geophysics, 2.

Henry, C., dan Das, S. (2002): The M w 8.2, 17 February 1996 Biak, Indonesia, earthquake: Rupture history, aftershocks, and fault plane properties, J. Geophys. Res., B11, ESE 11-1-ESE 11-16.

Okal, E. A. (1999): Historical seismicity and seismotectonic context of the great 1979 Yapen and 1996 Biak, Irian Jaya earthquake, Pure Applied Geophysic, 663-675.

Puntodewo, S. S. O., McCaffrey, R., Calais, E., Bock, Y., Rais, J., Subarya, C., Poewariardi, R., Stevens, C., Genrich, J., Fauzi, Zwick, P., dan Wdowinski, S. (1994): GPS measurements of crustal deformation within the Pacific-Australia plate boundary zone in Irian Jaya, Indonesia, Tectonophysics, 3-4, 141-153.

Sapiie, B., Natawidjaja, D. H., dan Cloos, M. (1999): Strike-slip Tectonic of New Guinea: Transform motion between the Caroline and Australian Plate, Proceedings of the Ikatan Ahli Geologi Indinesia, Jakarta.

Stevens, C. W., McCaffrey, R., Bock, Y., Genrich, J. F., Pubellier, M., dan Subarya, C. (2002): Evidence for block rotations and basal shear in the world's fastest slipping continental shear zone in NW New Guinea, 87-99 dalam Stein, S. dan Freymueller, J. T., Plate Boundary Zones, American Geophysical Union, Washington D.C.

Visser, W. A., dan Hermes, J. J. (1962): Geological results of the exploration for oil in Netherlands New Guinea: Carried out by the Nederlandsche Nieuw Guinee Petroleum Maatschappij, 1935-1960, Staatsdrukkerij-en Uitgeverijbedrijf, S'Gravenhage.

Wells, D. L., dan Coppersmith, K. J. (1994): New empirical relationships among magnitude, rupture length, rupture width, rupture area, and surface displacement, Bulletin - Seismological Society of America, 4, 974-1002.

INQUA Focus Group Terrestrial Processes Perturbed by Tectonics (TPPT)

paleoseismicity.org

Paleoseismic characteristics based on geomorphological and structural geological analysis for the central part of the Ulsan fault zone, SE Korea

Kiwoong Park (1), Ohsang Gwon (1), Sambit Prasanajit Naik (2), Young-Seog Kim (1,2)

(1) Major of Earth and Environmental Sciences, Pukyong National University, 45, Yongso-ro, Nam-gu, Busan 45813 Korea.
Email : pko8108@pukyong.ac.kr
(2) Active Fault and Earthquake Mitigation Research Institute, Pukyong National University, 45, Yongso-ro, Nam-gu, Busan 45813 Korea.

Abstract: *The Ulsan fault zone is NNW-SSE trending reverse fault with a length of approximately 50 km in the southeast Korean Peninsula. The study area is located in the central part of the Ulsan fault zone, where Cretaceous granitic bedrock are covered by the Quaternary deposits. The trench location was selected based on the results of the geomorphic analysis and field survey. In the trench section, the east dipping fault indicates predominantly reverse movement with a minor strike-slip component. The slickenline and vertical separation of the cumulative displacement indicate at least 18 m of net displacement. it is notable that the dip of the fault plane varies from the bottom to the top. It seems to reflect complex changes in physical properties, kinematic properties, and fault geometry along this fault. Based on the OSL ages of the topmost sedimentary unit, the timing of the most recent event is younger than 43±3ka.*

Key words: *active fault, Ulsan fault zone, trench, thrust system*

INTRODUCTION

The Korean Peninsula located far from the plate boundary has been regarded as a relatively stable region compared with the plate boundary in terms of earthquakes (Figure 1). However, recent earthquakes in Gyeongju (September 12, 2016, M_L 5.8) and Pohang (November 15, 2017, M_w 5.4) have triggered a change in the national perception of earthquakes (Kim et al., 2017; KMA, 2017). Consequently, research on active faults that will assist in understanding the mechanism of earthquakes and government-level research for earthquake disaster prevention are underway. Reported active faults in Korea are mainly distributed along Yangsan and Ulsan fault zones in the southeastern part of the Korean Peninsula (Kyung et al., 1997; Okada et al., 1998; Yang, 2006; Lee et al., 2015). The study area is located in the central part of the Ulsan fault zone, where Large-scale alluvial fans from the eastern mountainous areas are linearly arranged in the N-S direction and a large number of Quaternary faults displacing the alluvial fan have been reported. The broad aims of this study are to report new active faults and identify the characteristics of paleoseismological faulting to establish correlations with the existing reported faults in the central region of the Ulsan Fault Zone.

GEOMORPHOLOGICAL/GEOLOGICAL SETTINGS

The mountain area on the east side has an altitude of 400–750 m, and the northern mountain area is connected by Mt. Toham (745m) and Samtaebong (629m) to form a high-altitude mountain range, while the southern mountain area has a relatively low altitude (Hwang and Yoon, 2001; Kim et al., 2020). The alluvial fans formed by rivers flowing from the slope of the mountain on the east side to the west side form confluent alluvial fans, which connect with each other in the N-S direction and show a

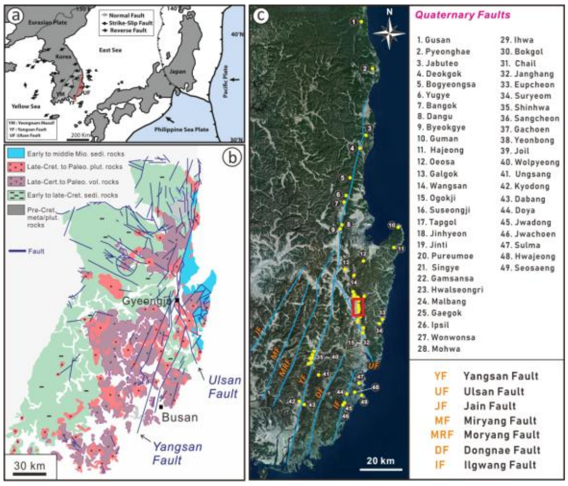

***Figure 1:** (a) Tectonic map of the region surrounding the Korean Peninsula (modified from Naik et al., 2020). (b) Geological map of Gyeongsang basin (modified from Lee, 2000), (c) Distribution map of the reported Quaternary faults in SE Korea(modified from Kim et al., 2016).*

continuous arrangement. The alluvial fans are subdivided into three groups based on their elevation from the riverbed, shape of topographic surface, degree of dissection, and sediment features (Hwang, 1998; Yoon and Hwang, 1999).

The basement of the study area is composed of Cretaceous and Tertiary granite and local intrusive dikes. These granites and intrusive dikes are covered by Quaternary deposits (Choi, 2003; Kim et al., 2020; Figure 2). Quaternary deposits are alluvial fan deposits that were supplied from the eastern mountain area and were distributed widely in the study area. Quaternary deposits are mainly composed of conglomerate layers, and sand layers distributed in the lens phase interact with these conglomerate layers. The conglomerate layers include pebbles to boulders and are mainly composed of granite and sedimentary rocks, such as sandstone and mudstone, and igneous rocks, such as diorite and andesite are distributed in minute quantities. The condition of Quaternary deposits differs depending on the location; generally, they are fresher at the lower surface than the higher surface of alluvial fans (Kim et al., 2020).

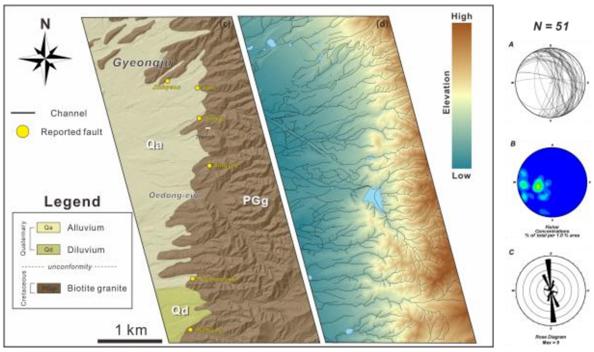

Figure 2: Geological map of the central region of the Ulsan fault zone (modified from Geological Survey of Korea, 1922). Right stereonet, pole contour and rose diagram show attitude of all faults developed in central region of the Ulsan fault zone.

METHODS

Paleoseismological studies aimed to estimate earthquake parameters (displacement, slip rate, recurrence interval, magnitude, etc.) by tracing surface ruptures caused by previous earthquakes and examining the history of the faults. The trench sites were selected by conducting a fault-related geomorphological analysis and mapped through a detailed geological survey. To identify the fault-related landforms, previous aerial photographs with slight changes in the artificial topography due to human activities were used. The aerial photographs with a scale of 1:20,000 were read stereoscopically to conduct the first landform classification. additionally, they were mapped with estimated fault lines extracted from DEM data to increase reliability. Geological survey was conducted along the referred fault line extracted by lineament analysis. Trench survey sites were selected by interpreting the results of these surface geological surveys.

TRENCH

The fault outcrop was located on the slope of the valley 800 m south of the previously reported Singye fault and was named Singye 2 fault (Figure 3). The bedrock granite thrusted over the Quaternary deposits had a cumulative displacement of more than 16 m. The thrust fault had a NNW-striking orientation and dipped at a very low angle of approximately 10° to the east. The fault gouges showed a variety of colors, including red, gray, yellow, and blue. All the fault gouges were cut by the gray fault gouge. This indicated the occurrence of multiple fault events. In the overhanging wall, granite was partially lost due to erosion and denudation by faults and was covered by sediments. additionally the northern and southern walls differed. We divided the Quaternary deposits into two layers, upper and lower sections. The sandy matrix of the upper layer was unconsolidated and differed from the granite of the eastern mountain. Approximately all the gravels distributed within the layers were fresh with the absence of weathering rind. moreover, gravels located near the fault zone were worn out. The bottom layer is a fine-grained sandy layer and differs in color from the upper layer. Soil wedge and liquefaction in the layers occur and these structures tend to develop in the Quaternary deposits in some regions of the study area (Kyung, 1997). Based on the OSL ages of the sedimentary unit in the footwall, the timing of the most recent event is younger than 55±3 ka.

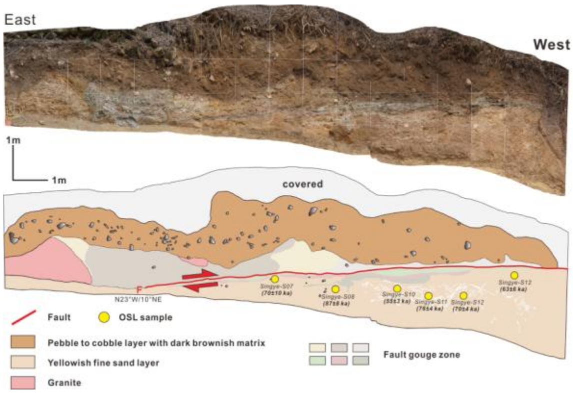

Figure 3: Trench photo and sketch of Singye2 fault. It is view of southern wall of the trench site and Detailed sketch.

The fault outcrop was located on the slope of the valley 200 m south of the previously reported Singye fault and was named Singye 3 fault (Figure 4). In the trench section, the east dipping fault indicates predominantly reverse movement with a minor strike-slip component. The unconsolidated sediments are subdivided into 10 unit layers based on grain type, size, color, roundness of gravel, and degree of sorting. Unit 1 is brown and yellow fine sand layer with occasional gravels. Unit 2 is Yellow fine to medium sand layer. Unit 3 is yellowish brown medium sand layer with occasional pebbles. Unit 4 is mud layer with some boulders. Unit 5 is blackish brown coarse sand layer which paleochannel is observed. Unit 6 is brown fine sand layer with occasional pebbles. Unit 7 is sand to mud layer with weathered boulders. Unit 8 is coarse sandy pebble layer. Unit 9 is conglomerate layer which sandy matrix is highly weathered. Unit 10 is hydrothermal altered gravel layer. The slickenline and vertical separation of the cumulative displacement indicate at least 18 m of net displacement. In particular, it is notable that the dip of the fault plane varies from 30° to 71° to 12° from the bottom to the top. It seems to reflect complex changes in physical properties, kinematic properties, and fault geometry along this fault. Based on the OSL ages of the topmost sedimentary unit, the timing of the most recent event is younger than 43±3 ka.

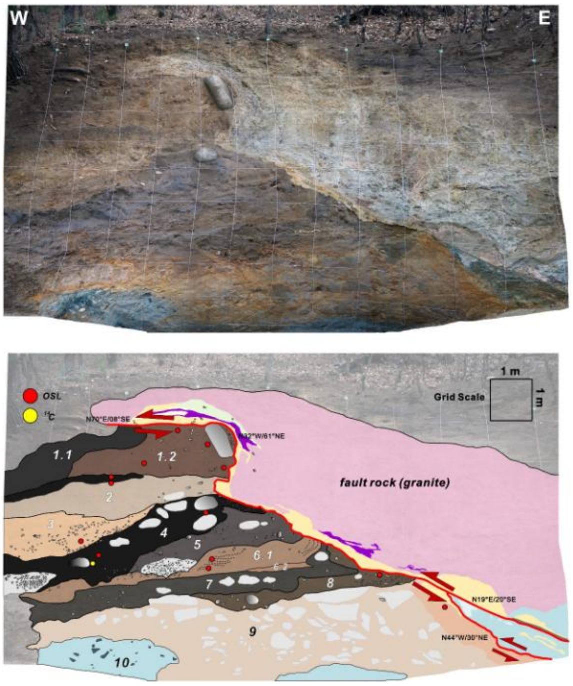

Figure 4: Trench photo and sketch of Singye3 fault. It is view of northern wall of the trench site and Detailed sketch.

Acknowledgements: This research was supported by a grant (2022-MOIS62-001) of National Disaster Risk Analysis and Management Technology in Earthquake funded by Ministry of Interior and Safety (MOIS, Korea).

REFERENCES

Choi, W.-H., 2003. Neotectonics of the Gyeongju-Ulsan Area in the Southeastern Part of Korean Peninsula. Paper of Docters degree, Seoul National University graduate school.

Geological survey of Korea., 1922. 1/50,000 geological map CHOYO sheet.

Hwang, S.-I., 1998. The geomorphic development of alluvial fans and tectonic movements at Ha-Dong, Kyungju-City. Journal of the geomorphological association of Korea, 5, 189-200. (in Korean with English abstract)

Hwang, S.-I., & Yoon, S.-O., 2001. The Distribution and Geomorphic Development of Alluvial Fans along the Bulguksa Fault System in Gyeongju and Ulsan city, Southeastern Korea. Journal of the Korean Geographical Society, 36, 217-232. (In Korean with English abstract)

Kim, M.-C., Jung, S.-H., Yoon, S.-W., Jeong, R.-Y., Song, C.-W. & Son, M., 2016. Neotectonic Crustal Deformation and Current Stress Field in the Korean Peninsula and Their Tectonic Implications: A Review. The Journal of the Petrological Society of Korea, v.25, 169-193. (in Korean with English abstract)

Kim, T.-H., Shin, H.-C., & Kim, Y.-S., 2020. Characteristics of the topographical deformation in the central part of the Ulsan fault. Journal of the Geological Society of Korea, 56(2), 193-209. (in Korean with English abstract)

Kim, Y.-S., Kim, T.-H., Kyung, J.-B., Cho, C.-S., Choi, J.-H. & Choi, C.-U., 2017. Preliminary study on rupture mechanism of the 9.12 Gyeongju Earthquake. Journal of the Geological Society of Korea, v.53, 407-422. (in Korean with English abstract)

KMA, Korea Meteorological Administration, http://www.kma.go.kr/.

Kyung, J.-B., 1997. Paleoseismological study on the mid-northern part of Ulsan Fault by trench method. J. Eng. Geol., 7, 81–90. (In Korean with English abstract)

Lee, J.M., Kong, Y.-J., Chang, T.W., Park, D. & Kim, T., 2000. Shallow subsurface structure of the Yaksoo area, Ulsan Korea by geophysical surveys. Journal of Korean Geophysical Society, 3, 57-66. (in Korean)

Naik, S.P., Gwon, O., Porfido, S., Park, K., Jin, K., Kim, Y.-S. & Kyung, J. B., 2020. Intensity reassessment of the 2017 Pohang earthquake Mw=5.4 (South Korea) Using ESI-07 Scale. Geosciences, 10(11), 471.

Yoon, S.-O. & Hwang, S.-I., 1999. The active fault topography of the northern part of the Bulguksa fault system in Kyungju city, southeastern Korea, Journal of the Korean Geographical Society, 34(3), 231-246. (in Korean with English abstract)

INQUA Focus Group Terrestrial Processes Perturbed by Tectonics (TPPT)

paleoseismicity.org

Mendocino Triple Junction, Humboldt County, California: Latest Quaternary Terraces and Tectonics

Patton, Jason R. (1,2), Hemphill-Haley, Mark (2), Streig, Ashley (3)

(1) California Geological Survey, Campton Rd., Eureka, CA 95501 USA. Email: Jason.Patton@conservation.ca.gov
(2) Cal Poly Humboldt Department of Geology, 1 Harpst St., Arcata CA 95521 USA. Email: Jason.Patton@humboldt.edu
(2) Cal Poly Humboldt Department of Geology, 1 Harpst St., Arcata CA 95521 USA. Email: mark@humboldt.edu
(3) Portland State University, 17 Cramer Hall, 1721 SW Broadway, Portland, OR 97201 USA. Email: streig@pdx.edu

Abstract: *The Mendocino triple junction, where overlapping and interfingering southern Cascadia and northern San Andreas plate boundaries exist, is complicated, where oblique convergence and dextral shear interact. We locate a topographic scarp that suggests a south-vergent reverse fault that offsets late Quaternary fluvial terraces. We map these terraces to establish a chronostratigraphic framework, linking numerical ages and associated incision rates from nearby to the terraces in our study area. We use a ground penetrating radar survey to explore subsurface evidence for faulting and to constrain fault dip. Using regionally derived incision rates as a proxy for terrace age, correlated terrace ages, and topographic swath profiles that provide scarp heights, we bracket a preferred slip rate for this fault that ranges from 1.8 and 3.0 mm/yr.*

Key words*: Terrace Mapping, Active Faulting, Paleoseismology.*

INTRODUCTION

While the largest source of annual seismicity is intraplate Gorda plate earthquakes, the two largest contributors to seismic hazards in California are the Cascadia subduction zone (CSZ) and the San Andreas fault (SAF) systems (**Figure 1**).

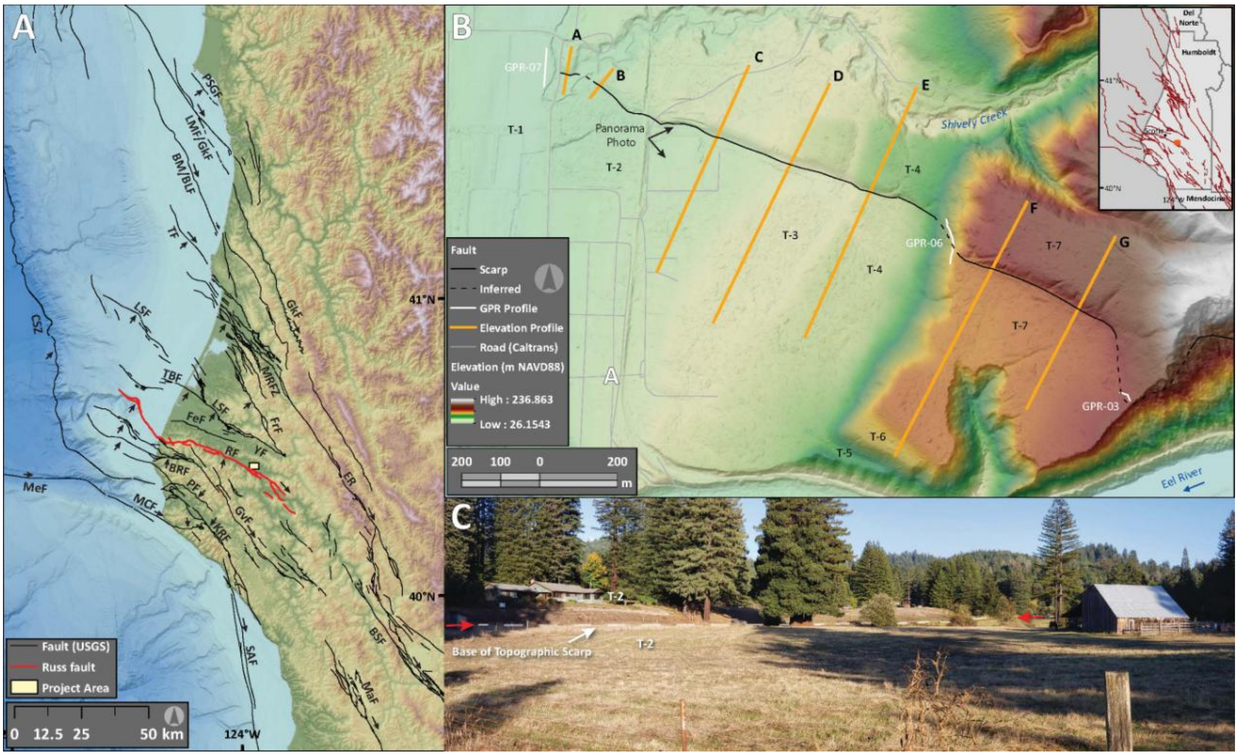

Figure 1: (A) Mendocino triple junction map. Fault data from USGS Quaternary Active Fault and Fold Database (2019). Faults: BRF, Bear River; BSF, Bartlett Springs; BM/BLF, Bald Mountain/Big Lagoon; CSZ, Cascadia subduction zone; ER, Eaton Roughs; FeF, Ferndale; FrF, Freshwater; GkF Garlock; GvF, Garberville; KRF, King Range; LM/GF, Lost Man/Garlock; LSF, Little Salmon; MCF, Mendocino Canyon; MaF Maacama; MeF Mendocino; MRFZ, Mad River; PF, Petrolia; PSGF, Point St. George, RF, Russ in red; TBF, Table Bluff; TF, Trinidad; YF, Yager. Arrows designate direction of fault motion. (B) USGS lidar topography as a base map (color represents elevation) with topographic profiles in orange. Terrace treads and GPR profile locations are labeled. (C) Panorama photo of topographic scarp, looking eastwards (view shown on map).

These sources overlap in the region of the Mendocino triple junction (MTJ) and may interact in ways we are only beginning to understand as evidenced by the 2016 M7.8 Kaikōura earthquake in New Zealand (Clark et al., 2017 Litchfield et al., 2018), which occurred along a similar subduction/transform boundary, and included co-seismic rupture of more than 20 faults.

The northward migration of the MTJ is evidenced by rapid uplift of the King Range (Merritts and Bull, 1989), deformation along the leading western edge of the Sierra Nevada, termination of the San Andreas fault system which may step eastward to the Eaton Roughs and Grogan fault zones (Beeson et al., 2017; Kelsey and Carver, 1988), north and northeastern vergence of the King Range Thrust and Russ faults (McLaughlin et al., 2000, 2012), east-west trending faults and folds in the Humboldt Bay region (e.g. Table Bluff, Eel River syncline; (Ogle, 1953), and overlap of strike-slip tectonics with Cascadia subduction thrust tectonics (Kelsey & Carver, 1988; Gulick and Meltzer, 2002; Williams et al., 2006; McKenzie et al., 2020).

Lidar data acquisitions (Dietrich, 2014; USGS, 2019) have revealed previously unknown active faults within the CSZ/SAF transition. We have identified a topographic escarpment that shows evidence for vertical displacement of Eel River fluvial terrace treads. This south facing scarp crosses multiple latest Quaternary fluvial terraces along the Eel River near Shively, California with increasing scarp heights on progressively older terraces (**Figure 1 B**).

We mapped geomorphic and geologic units in the Shively area to better understand the stratigraphy, to correlate local terraces that have numerical age constraints with those in Shively, to assess how faulting controls topography, and to locate potential future field investigations. We extended this terrace mapping 25 km upstream 35 km and downstream.

We use regionally derived incision rates and fluvial terrace correlations (Bickner, 1992; Stallman and Kelsey, 2006; Bold, 2022; Bold et al., 2022; Patton, 2022) as a proxy for terrace age, recognizing that these incision rates may be from the time of strath formation instead of terrace abandonment. We then use 10-m wide topographic swath profiles to measure scarp heights along with the GPR based fault dip approximations to estimate a late Pleistocene mean slip rate for the source fault.

We apply Stallman and Kelsey (2006), Bold (2022), and Bold et al. (2022) incision rates developed on nearby terraces to terrace heights in Shively to estimate the ages for these terraces in slightly different ways. For Stallman and Kelsey (2006) rate estimates we apply a single incision rate to the terrace relative elevations. For Bold (2022) rate estimates, we calculate incision rates using their chronostratigraphy (using a ~moving average incision rate). We also use preliminary terrace correlations and apply ages from Bold (2022) directly to terraces in Shively. Patton (2022) presents the terrace mapping and correlation with the Bold (2022) terraces that form a basis for these terrace ages. For Shively terraces T-3, 4, and 7, we correlate the youngest, the preferred, and the oldest probable Bold (2022) terrace. Using these correlations, we bracket the ages of the terraces in Shively.

To locate evidence for subsurface faulting, we conduct multiple Ground Penetrating Radar (GPR) surveys in collaboration with Dr. Ashley Streig's graduate student Ryan Levinson from Portland State University. These GPR profiles are located on terraces T-1, along a road spanning T-4 and T-7, and T-7 (**Figure 1 B**).

RESULTS

We present several topographic profiles across the scarps in **Figure 2 A**. Each point is plotted with 1 standard deviation uncertainty. We calculate the scarp height by projecting linear regression lines to meet at the scarp, shown as a vertical black line. This scarp height represents our estimate for the vertical separation across the scarp.

Results from GPR profile 3 (**Figure 1 B**) are presented in **Figure 2 B**. We thank Mitchell Craig, CSU Monterey Bay, who helped model these data. Preliminary data from profiles on T-2, T-7, and along a road that traverses T-4 and T-7 (**Figure 1 B**), suggest a fault that dips between 20° and 30° to the north. These results are preliminary and have not yet been corrected for GPS/GNSS positioning, nor have they been processed in an advanced manner.

Using Stallman and Kelsey (2006) rates, Shively terraces T-2, 3, 4, & 7 may be 9.5 ± 0.4, 20.1 ± 0.9, 27.1 ± 1.2, and 92.0 ± 4.1 ky old. We propose two ways to correlate Shively terraces with Bold (2022) terraces. Based on our preferred correlation we interpret Shively terrace T-7 to be 22.4 ± 2.4 ky old (**Table 1**). For our alternative correlation, we interpret Shively T-7 to be 46.3 ± 3.6 ky old.

We present our estimates for terrace ages (**Table 2**) using incision rates calculated using data from Bold (2022). Since the ages have large uncertainties, we do not propagate uncertainty. Using our preferred correlations, terraces T-3, 4, & 7 are estimated to be 4.3, 5.6, and 22.4 ky old. Stallman and Kelsey (2006) rates produce ages two- to four-times older than the ages produced using correlations with Bold (2022).

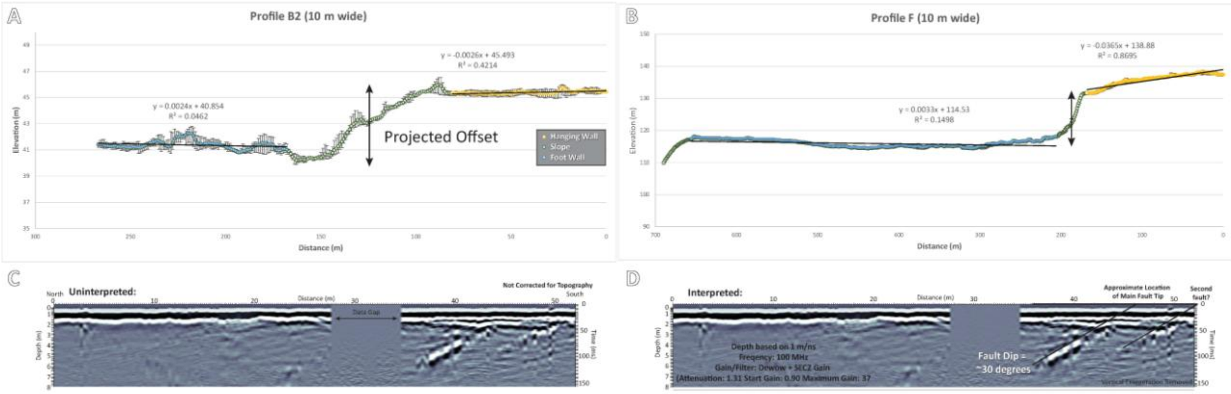

Figure 2: (A, B) Elevation profiles across representative topographic scarps on different terraces, locations shown on Figure 1. Elevation in meters NAVD88. Vertical separation distance is shown as double headed black arrows. (B) Ground penetrating radar profile across terrace tread T-7. Right panel shows the interpretation of main fault dipping to the north at about 30°. There may be a second fault outboard of the main fault.

Table 1. Vertical separation and fault slip rate calculations using two methods to establish terrace ages: (1) incision rate and (2) preliminary correlation with terraces along Van Duzen River with ^{10}Be minimum limiting exposure ages (Bold, this volume).

Shively Terrace	Age (ky)[1]	±	Age (ky)[2]	±	Age (ky)[3]	±	Profile	Scarp Height	Vertical Separation Rate (mm/yr)[1]	Vertical Separation Rate (mm/yr)[2]	Vertical Separation Rate (mm/yr)[3]	Slip Rate (mm/yr)[1]	Slip Rate (mm/yr)[2]	Slip Rate (mm/yr)[3]
T-2	9.5	0.4					A	3.6	0.4			0.8		
T-2	9.5	0.4					B2	4.0	0.4			0.9		
T-2	9.5	0.4					C	7.4	0.8			1.7		
T-3	20.1	0.9					D	5.7	0.3			0.6		
T-4	27.1	1.2					E	8.5	0.3			0.7		
T-7	92.0	4.1	22.4	2.4	38.3	1.9	F	16.9	0.2	0.8	0.4	0.4	1.7	1.0
T-7	92.0	4.1	22.4	2.4	38.3	1.9	G	19.8	0.2	0.9	0.5	0.5	1.9	1.1
								Mean	0.4	0.8	0.5	0.8	1.8	1.1
								Standard Dev.	0.2	0.1	0.1	0.4	0.2	0.1

1. Age based on incision rates calculated by Stallman and Kelsey (2004) for late Pleistocene fluvial terraces in the North Fork Elk River (35 km from Shively).
2. Age based on correlation option 1 using ages and mapped terraces from Bold (2022).
3. Age based on correlation option 2 using ages and mapped terraces from Bold (2022).

Table 2. Slip rates bracketed by range of possible correlations between Shively and Hydesville regions.

Shively Terrace[1]	Bold Terrace[2]	Relative Age[3]	Age (years)[4]	Terrace Height[5]	Incision Rate[6]	Scarp Height[7]	Separation Rate[8]	Dip[9] 20	30	40
								Slip Rate[10]		
T3	T3	oldest	5600	17.9	3.2	5.7	1.0	3.0	2.1	1.6
	T2	preferred	4300	17.9	4.2	5.7	1.3	3.9	2.7	2.1
	T1	youngest	2500	17.9	7.1	5.7	2.3	6.7	4.6	3.6
T4	T4	oldest	6900	24.1	3.5	8.5	1.2	3.6	2.5	1.9
	T3	preferred	5600	24.1	4.3	8.5	1.5	4.4	3.0	2.4
	T2	youngest	4300	24.1	5.6	8.5	2.0	5.8	4.0	3.1
T7	T17	oldest	38250	81.9	2.1	19.8	0.5	1.5	1.0	0.8
	T12	preferred	22400	81.9	3.7	19.8	0.9	2.6	1.8	1.4
	T9	youngest	20000	81.9	4.1	19.8	1.0	2.9	2.0	1.5

1. Terrace number, Shively region.
2. Terrace number, Hydesville region (Bold this volume).
3. The Hydesville terrace age relative to the Shively terrace.
4. Bold terrace age. Ages for Bold T-9, 12 & 17 from Bold (this volume). Other ages explained in the text.
5. Terrace relative elevation measured from topographic cross section.
6. Incision rate calculated from the age[4] and height[5].
7. Scarp height measured from 10 meter wide swath profile.
8. Separation rate (scarp height divided by terrace age) for the vertical displacement of terrace tread.
9. Range of fault dips assumed for slip rate calculation.
10. Slip rate using the separation rate and the dip angle. Preferred rates in cyan rows.

DISCUSSION

Based on scarp size, a fault dip of 27°, and incision rates from two nearby studies, we estimate the slip rate for this fault to be between 0.8 and 1.8 mm/year (**Table 1**). Based on scarp size, GPR-estimated fault dips ranging from 20° to 40°, and a range of preferred potential terrace ages, we bracket the slip rate for this fault to be between 1.4 and 4.4 mm/year (**Table 2**). The entire range of slip rates in **Table 2**, for preferred correlations and all three fault dips, is between 0.8 and 6.7 mm/year.

The mapped surface trace of the fault is 3 km long which, based on historic surface rupture length versus M data could represent a ca. M_W 5.6 earthquake (Wells and Coppersmith, 1994). However, we believe it unlikely that an earthquake of this magnitude will produce fault scarps in excess of 1 m in height. If the 4m high scarp on the lower terrace represents a single event scarp, the magnitude could be ~ M_W 6.7 (Wells and Coppersmith, 1994). If the scarp forming fault is part of the longer Russ fault as currently mapped, using Wells and Coppersmith (1994), the fault has a potential for a M_W 7 to M_W 7.2 earthquake. The USGS NSHM scenario earthquake for the RF uses a M_W 7.41 magnitude as a source (Petersen et al., 2014).

Presuming the ~4m scarp represents a single event (M_W 7.1 based on Wells and Coppersmith, 1994), and this is a characteristic offset, the ~20 m high scarp formed in the T-7 terrace may represent 5 earthquakes. If T-7 is 92 ky old, this translates to a return period of ~23,000 years (ignoring time since most recent event). If T-7 is 38.25 ky old, this translates to a return period of ~9,600 years. If T-7 is 22.4 ky old, this translates to a return period of 5,600 years. If T-7 is 20.0 ky old, this translates to a return period of 5,000 years.

Some scarp profiles suggest that the terrace treads may have been either modified since they were abandoned or that they have been deformed. The scarp height measurements include some amount of uncertainty that does not account for these post abandonment modifications of the ground surface.

CONCLUSION

We use terrace mapping and topographic interpretation to calculate slip rates for a potential thrust or reverse fault that displaces terrace treads in the region of Shively, California. The preferred slip rate for this fault is between 1.8 and 3.0 mm/year as estimated using numerical ages from Bold (2022) derived for a nearby drainage with terrace correlations presented here. This fault activity likely represents between 25ky and 91ky of prehistory.

Acknowledgements: We thank the community of Shively for welcoming us into their area so that we could conduct this study. We thank Humboldt Redwoods Company for providing land access for this study.

REFERENCES

Bold, S.E., 2022. New Mapping of the Goose Lake Fault and Fluvial Terraces at the Yager Creek–Van Duzen River Confluence, Northern California, M.S. Thesis, Cal Poly Humboldt, Department of Geology

Bold, S., et al., 2022. Incision and Deformation of the Yager Creek–Van Duzen River Fluvial Terraces from Quaternary Mapping and Geochronology in Patton, et al., 2022, The Triangle of Doom V 2.0: Archeology, Stratigraphy, Tectonics, Geomorphology, and Geophysics in the Region of the Mendocino Triple Junction, Friends of Pleistocene, Pacific Cell, Field Trip Guidebook

Bickner, 1992. Soil Chronosequence and Tectonic Uplift Rates of Fluvial Terraces near Garberville, California in 1992 Pacific Cell Friends of the Pleistocene field trip guidebook.

Bickner, F., 1993. A Soil Chronosequence of the Mitchell Ranch Fluvial Terraces on the South Fork Eel River - Age Estimates and Tectonic Implications, M.S. Thesis, Cal Poly Humboldt.

Carver, G. A., Burke, R. M., and Kelsey, H., 1986. Quaternary deformation in the region of the Mendocino triple junction: U.S. Geological Survey.

Clark, K. J., Nissen, E. K., Howarth, J. D., Hamling, I. J., Mountjoy, J. J., Ries, W. F., Jones, K., Holdstein, S., Cochran, U. A., Villamore, P., Hreinsdottir, S., Litchfield, N. J., Mueller, C., Berryman, K. R., and Strong, D. T., 2017. Highly variable coastal deformation in the 2016 MW7.8 Kaikōura earthquake reflects rupture complexity along a transpressional plate boundary: Earth and Planetary Science Letters, v. 474, p. 334-344.

Dietrich, W., 2014. Critical Zone Observatory: Eel River LiDAR Data Collection and Processing, National Center for Airborne Laser Mapping

Gulick, S. P. S., and Meltzer, A. S., 2002. Effect of the northward-migrating Mendocino triple junction on the Eel River forearc basin, California: Structural evolution: GSA Bulletin, v. 114, no. 12, p. 1505-1519.Williams, T. B., Kelsey, H. M., and Freymueller, J. T., 2006, GPS-derived strain in northwestern California: Termination of the San Andreas fault system and convergence of the Sierra Nevada–Great Valley block contribute to southern Cascadia forearc contraction: Tectonophysics, v. 413, p. 171-184.

Kelsey, H., and Carver, G. A., 1988. Late Neogene and Quaternary Tectonics Associated With Northward Growth of the San Andreas Transform Fault, Northern California: Journal of Geophysical Research, v. 93, no. B5, p. 4797-4819.

Stallman, J. D., and Kelsey, H. M., 2006. Transient geomorphic response to late Pleistocene baselevel change and climate forcing in the southern Cascadia thrust-and-fold belt, north coastal California in Hemphill-Haley, M., McPherson, R., Patton, J. R., Stallman, J., Leroy, T. H., Sutherland, D., and Williams, T. B., eds., 2006 Pacific Cell Friends of the Pleistocene Field Trip Guidebook, The Triangle of Doom: Signatures of Quaternary Crustal Deformation in the Mendocino Deformation Zone (MDZ) Arcata, CA.

Litchfield, N. J., Villamoor, P., Van Dissen, R. J., Nicol, A., Barnes, P. M., Barrell, D. J., Pettinga, J. R., Langridge, R. M., Little, T. A., Mountjoy, J. J., Ries, W. F., Rowland, J., Fenton, C., Stirling, M. W., Kearse, J., Berryman, K. R., Cochran, U. A., Clark, K. J., Hemphill-Haley, M., Hhajavi, N., Jones, K. E., Archbald, G., Upton, P., Asher, C., Benson, A., Howarth, J. D., Kane, T. J., Lamarche, G., Lawson, S., Lukovic, B., McColl, S. T., Madugo, C., Manousakis, J., Noble, D., Pedley, K., Sauer, K., Stahl, T., Strong, D. T., Townsend, D. B., Toy, V., Williams, J., Woelz, S., and Zinke, R., 2018. Surface Rupture of Multiple Crustal Faults in the 2016 Mw 7.8 Kaikoura, New Zealand, Earthquake: BSSA, v. 108, no. 3B, p. 1496-1520.

Merritts, D., and Bull, W. B., 1989, Interpreting Quaternary uplift rates at the Mendocino triple junction, northern California, from uplifted marine terraces: Geology, v. 17, p. 1020-1024.

McLaughlin, R. J., Ellen, S. D., Blake, M. C., Jayko, A. S., Irwin, W. P., Aalto, K. R., Carver, G. A., and S.H., C. J., 2000, Geology of the Cape Mendocino, Eureka, Garberville, and Southwestern Part of the Hayfork 30 x 60 Minute Quadrangles and Adjacent Offshore Area, Northern California: USGS, Miscellaneous Field Studies Map MF-2336.

McLaughlin, R. J., Sarna-Wojcicki, A. M., Wagner, D. L., Fleck, R. J., Langenheim, V. E., Jachens, R. C., Clahan, K., and Allen, J. R., 2012, Evolution of the Rodgers Creek-Maacama right-lateral fault system and associated basins east of the northward-migrating Mendocino Triple Junction, northern California: Geosphere, v. 8, p. 342-373.

McKenzie, K. A., Furlong, K. P., & Herman, M. W., 2020. Bidirectional loading of the subduction interface: Evidence from the kinematics of slow slip events. Geochemistry, Geophysics, Geosystems, 21, 2020GC008918. https://doi.org/10.1029/2020GC008918

Ogle, B. A., 1953. Geologic map of the Eel River Valley area, California, California Division of Mines and Geology, Bulletin 164, p. 128.

Patton, J. R., 2022. Tectonic Datums: Eel River Fluvial Terraces in Patton, et al., 2022, The Triangle of Doom V 2.0: Archeology, Stratigraphy, Tectonics, Geomorphology, and Geophysics in the Region of the Mendocino Triple Junction, Friends of Pleistocene, Pacific Cell, Field Trip Guidebook

Petersen, M. D., Moschetti, M. P., Powers, P. M., Mueller, C. S., Haller, K. M., Frankel, A. D., Zeng, Y., Rezaeian, S., Harmsen, S. C., Boyd, O. S., Field, N., Chen, R., Rukstales, K. S., Luco, N., Wheeler, R. L., Williams, R. A., and Olsen, A. H., 2014. Documentation for the 2014 update of the United States national seismic hazard maps: U.S. Geological Survey.

Wells, D. L., and Coppersmith, K. J., 1994. New empirical relationships among magnitude, rupture length, rupture width, rupture area, and surface displacement: Bulletin of the Seismological Society of America, v. v. 84, p. P. 974-1002.

Williams, T. B., Kelsey, H. M., and Freymueller, J. T., 2006. GPS-derived strain in northwestern California: Termination of the San Andreas fault system and convergence of the Sierra Nevada–Great Valley block contribute to southern Cascadia forearc contraction: Tectonophysics, v. 413, p. 171-184.

INQUA Focus Group Terrestrial Processes Perturbed by Tectonics (TPPT)

paleoseismicity.org

Paleoseismic characterization of the eastern Rhine Graben Boundary Fault (RGBF), Southern Germany

Sara Pena-Castellnou (1), Jochen Hürtgen (1), Stéphane Baize (2), Hervé Jomard (2), Edward M. Cushing (2), Thomas K. Rockwell (3), Gordon Seitz (4), Francesca R. Cinti (5), Wahid Abbas (6), Frank Preusser (7), Daniela Mueller (7), Joachim Ritter (8), Klaus Reicherter (1)

(1) Institute for Neotectonics and Natural Hazards, RWTH Aachen University, Aachen, Germany. Email: s.pena-castellnou@nug.rwth-aachen.de
(2) Institut de Radioprotection et de Sûreté Nucléaire, Fontenay-aux-Roses, Cedex, France
(3) Department of Geological Sciences, San Diego State University, San Diego, CA, U.S.A.
(4) California Department of Conservation, California Geological Survey, San Mateo, CA, U.S.A
(5) Istituto Nazionale di Geofsica e Vulcanologia, Roma, Italy
(6) Department of Earth Sciences, COMSATS University Islamabad, 22060, Abbottabad, Pakistan
(7) Institute of Earth and Environmental Sciences, University of Freiburg, Germany
(8) Karlsruhe Institute of Technology, Geophysical Institute, Germany

Abstract: *The eastern Rhine Graben Boundary Fault (RGBF) constitutes the eastern margin of the Upper Rhine Graben (URG), an intraplate graben located in the center of the European Cenozoic Rift System. The URG, with low to moderate seismicity and records of damaging historical earthquakes, is one of central Europe's most seismically active regions. Despite that, few studies have documented its paleoearthquake history and associated seismic hazard and focused only on the western margin. Therefore, following up with the first studies engaged by the cooperation between the IRSN (France) and the RWTH Aachen University (Germany), we aim to evaluate the paleoseismic activity of the eastern margin of the URG to assess its seismic potential. We present the first paleoseismological data from subsurface geophysics and paleoseismological trenching collected on the eastern RGBF fault that provides new evidence for late Pleistocene and Holocene activity at the sites of Oberweier and Tunsel.*

Key words*: Neotectonics, Upper Rhine Graben, Tectonic geomorphology, Paleoseismology, Intraplate tectonics.*

INTRODUCTION

The Upper Rhine Graben (URG), with low to moderate seismicity, is one of the most seismically active regions in the plate interiors of Europe (Fig. 1a) and hosts a set of major faults that have caused damaging earthquakes in historical times (e.g., the 1356 Basel earthquake). Given the low surface deformation rates (< 1 mm/yr) in Central Europe, instrumental and historical seismic catalogs are insufficient to depict the larger seismic cycles of most faults, which can be thousands of years long and, for instance, fail to document the occurrence of large and surface rupturing earthquakes. To adequately picture the seismic cycle of those faults and evaluate their seismic potential, we must expand the seismic catalog with the geological record, opening the earthquake observation window to tens of thousands of years (e.g., McCalpin, 2009). Several research efforts (Fig. 1b) have been made in this field, documenting the paleoearthquake history of some of the western structures bounding the URG (Colbeaux et al., 1981; Monninger, 1985; Cushing et al., 2000; Peters et al., 2005); and the Basel-Reinach fault (Meghraoui et al., 2001; Ferry et al., 2005), located in the southernmost east region.

In contrast, up to date, no paleoseismological study has been carried out along the eastern graben bounding faults; therefore, we aim to evaluate its paleoseismic activity and associated seismic hazard. We have investigated two target sites: Oberweier (south of Karlsruhe) and Tunsel (south of Freiburg) (Fig. 1b), using paleoseismic methods including tectonic geomorphology, geophysical surveys, paleoseismological trenching and dating. We present here the first paleoseismological data ever collected on the eastern RGBF fault, providing new evidence of active tectonics and contributing significantly to the completeness of its earthquake history.

SEISMOTECTONIC SETTING

The URG is an intraplate graben approximately 300 km long and 40 km wide, located in the center of the European Cenozoic Rift System (ECRIS) (Fig. 1a). The formation of the ECRIS was driven by Alpine deformation with the main extensional stage during the Oligocene. During the onset of the Miocene, a reorientation of the stress field reactivated the main graben-bounding faults, resulting in a second phase of rifting marked by sinistral transtension (Villemin & Bergerat, 1987; Schumacher, 2002; Reicherter et al., 2008), persisting until present-day under a horizontal stress orientation of approximately 140°N (Heidbach et al., 2018) (Fig. 1b). Present-day seismicity is low to moderate and distributed throughout the graben and graben shoulders with clear regional variations (Fig. 1b). The southern part of the URG exhibits most of the seismicity with a wide distribution of small earthquakes concentrated on the eastern margin (Barth et al., 2015). This area hosted the largest recorded instrumental (2004 M_w 4.6 Waldkirch earthquake) and historical (1356 M_w 6.7-7.1 Basel earthquake) events. In the northern part, seismicity is significantly lower, with widely distributed moderate earthquakes. The central part appears to have a quiescence in instrumental records with just a few scattered earthquakes. Nevertheless, it has hosted several significant historical events (Fig. 1b).

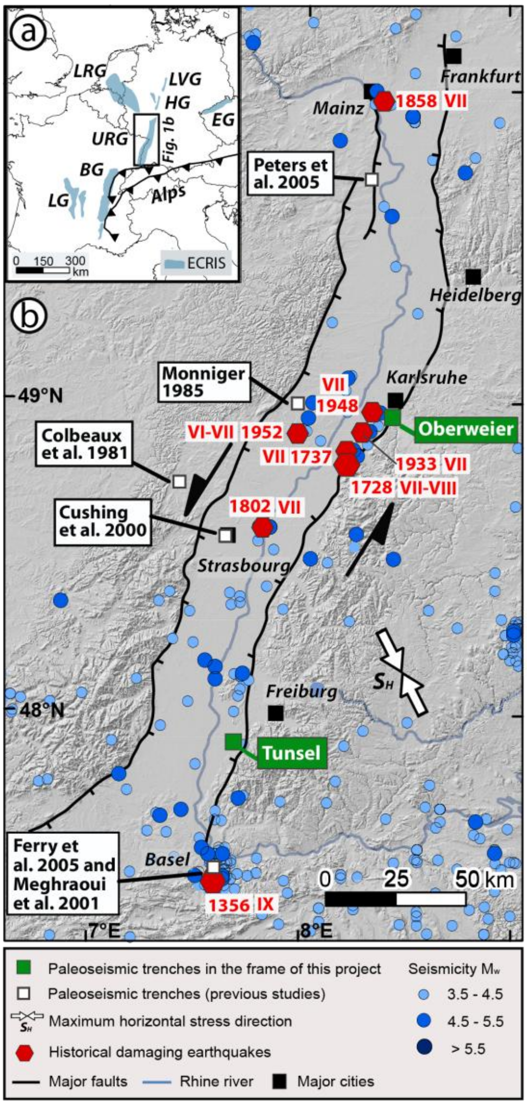

Figure 1. a) Location of the Upper Rhine Graben within the European Cenozoic Rift System (ECRIS) in the Alpine foreland. Abbrev.: BG: Bresse Graben, EG: Eger Graben, HG: Hessian Grabens, LG: Limagne Graben, LRG: Lower Rhine Graben, LVG: Leine Valley Graben, URG: Upper Rhine Graben. b) Seismotectonic overview of the Upper Rhine Graben and location of the study areas (green squares). White squares indicate the location of previous paleoseismological trenches. Historical and instrumental seismicity in the time-period 1000-2006 from the EMEC catalog (Grünthal and Wahlström, 2012).

METHODS

We combine several field techniques classically used in paleoseismic investigations (e.g., Burbank and Anderson, 2001; McCalpin, 2009), including remote sensing observations, shallow geophysical surveys (ground penetrating radar - GPR and electrical resistivity tomography - ERT), paleoseismological trenching and dating. We study the neotectonic imprint in the morphology of the eastern margin of the URG based on the 1 m resolution DEM of Baden-Württemberg derived from LiDAR data (LGL-BW, 2016) together with data from the regional geological map (LGRB-BW GK50). Following up on the previous surveying studies (Baize et al., 2017) which provided key geomorphological and geophysical data, we trenched in two target sites: Oberweier (south of Karlsruhe) and Tunsel (south of Freiburg) (Fig. 1b).

FIRST RESULTS

Oberweier

We focus on a section of the eastern RGBF fault (defined based on fault scarp morphology) that extends 40 km from the city of Bruchsal to Rastatt in a NE-SW direction. The fault delineates the mountain front that bounds the eastern URG margin with steep slopes (20%), where triangular facets and incised hanging valleys have developed (Fig. 2a), suggesting rapid incision and shoulder-uplift. We have identified beheaded channels approx. 200 m left-laterally offset from its presumable catchment of origin, indicating a considerable sinistral strike-slip component that is also evidenced by the migration of the position of the apex of several alluvial fans towards the Rhine River floodplain (Fig. 2b), suggesting as well transtensional kinematics. Secondary parallel lower ridges marked by topographic steps form NE-SW lineaments extending approximately one kilometer from the foot of the mountain front (Fig. 2). We have investigated those lineaments with shallow geophysical ERT and GPR profiles and found vertical and lateral anomalies in resistivity and lateral changes in different water content conditions suggesting a tectonic disturbance.

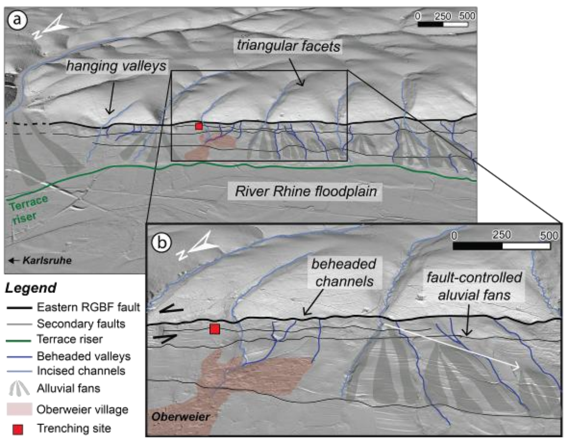

Figure 2. a) Morphology of the eastern Rhine Graben shoulder mountain front in the Oberweier area from a 3D view of the 1 m resolution LiDAR-based Baden-Württemberg DEM (LGL-BW, 2016). b) Zoom in to depict beheaded channels and the propagation of the apex of alluvial fans towards the southwest and into the River Rhine floodplain. The red square shows the location of the trenching site.

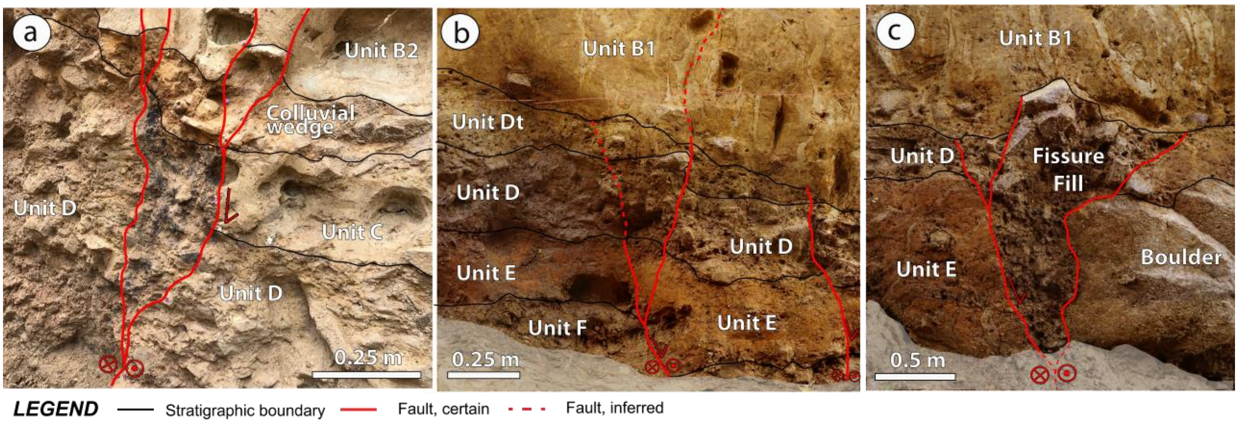

Figure 3. Evidence of surface rupturing paleoearthquakes in the scarp-perpendicular trenches dug in Oberweier. a) Main fault zone (F1) and offset colluvial wedge in OBW-T1S; b) Downward growth in displacement along fault F8 in OBW-T5S; c) Fissure fill with vertically aligned pebbles in OBW-T5S. Short description of stratigraphic units: B2: Ocher-white sandy loam rich in charcoal and manganese concretions (reworked B1 material); B1: Ocher-white sandy loam with periglacial features; C: Ocher-white very fine sand-silt with cobble to boulders gravel at its base; Dt: Orange-reddish silt-very fine sand with rounded floating pebbles; D: Matrix-supported heterometric gravels with a light brown silt-sandy matrix; E: Reddish clay-silt with floating pebbles and periglacial features. F: Matrix-supported heterometric gravels with a clay-silty red-brownish matrix; The colluvial wedge consists of material from unit C. The fissure fill is constituted with sediment from units D, E and F.

Based on the geophysical data, we excavated six trenches along and across the NNE-SSW topographical fault scarp of one of the secondary fault strands of the eastern RGBF in the north of Oberweier (Fig. 2). The entire sedimentary sequence exposed in the trenches (consisting of colluvium and periglacial deposits), except for the youngest layer (AD 1030-1160), is offset by a fault zone spreading within 6 m in multiple NNW-SSE en-echelon branches in a negative flower structure. The style and orientation of these branches are consistent with the left-lateral slip observed in the morphology. Scarp-derived colluvium wedges evidence dip-slip component. The displacement on free faces is on the order of 0.3-0.6 m per event vertically and amounts to c. 2 m left-laterally (cumulative). Cross-cutting relationships and dating based on the radiocarbon and OSL methods reveal a minimum of three paleoearthquakes with a minimum magnitude M_w of 6, the youngest of which occurred after the LGM. We have defined the paleoearthquakes based on 1) fault terminations, 2) colluvial wedge (Fig. 3a), 3) downward growth in displacement (Fig. 3b) and 4) fissure fills (Fig. 3c).

Tunsel

We study the southern section of the Rhine River Fault (RRF), located south of Freiburg eight kilometers from the Black Forest mountain front into the graben interior and striking in a NE-SW direction parallel to the eastern RGBF fault (Fig. 4). The RRF morphology has been studied by Nivière et al. (2008) and Baize et al. (2017). They have described vertical and horizontal offsets of various landforms suggesting late Pleistocene tectonic activity. The RRF offsets the distal part of the Neumagen-Möhlin alluvial fan (Fig. 4), where older higher fan terraces on the footwall are back-tilted, and several drainage features seem to be left-laterally displaced. We further investigated the subsurface geophysics of the RRF scarp near the village of Tunsel (Fig. 4). We have observed in the ERT profiles vertical and lateral anomalies in resistivity denoting potential tectonic features. We excavated three trenches perpendicular to this scarp. Trenches exposed a sequence of alluvial fan deposits composed of consolidated and non-consolidated gravel packages and a more than 5m thick ocher silt loess deposit. The exposed fault zone spreads within 7 m in several parallel faults dipping towards the WNW. We unveiled a minimum of two seismic events. The youngest offset deposit consists

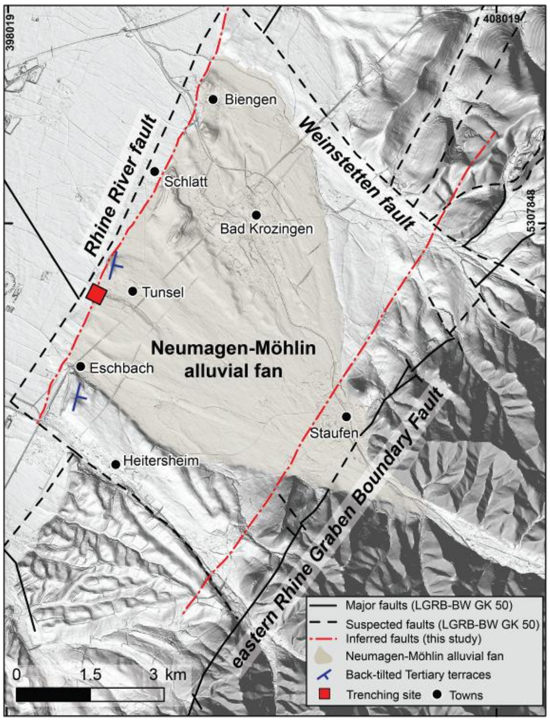

Figure 4. Morphology of the southern section of the RRF fault and the Neumagen-Möhlin fan area (south of Freiburg, Germany) from the regional 1 m LiDAR-based Baden-Württemberg DEM (LGL-BW). Black faults are from the regional geological map (LGRB-BW GK 50), red faults are from this study. A red square indicates the trench site near the village of Tunsel.

of ocher silt with charcoal and pieces of ceramics (reworked loess, what we define as unit U8) and dates from AD 1040 - 1180 (Fig. 5). We observe a cumulative 0.5 m of vertical separation and lateral mismatching of the sedimentary units and their thickness, indicating transtensional left-lateral kinematics (Fig. 5). Furthermore, we observe steep fractures bonding consolidated from non-consolidated gravels, which attenuate beneath the gravel unit, above a clay deposit acting as detachment layer. We interpret those fractures as generated due to lateral spreading during an older paleoearthquake pre-deposition of the non-consolidated gravel unit (what we define as unit U3).

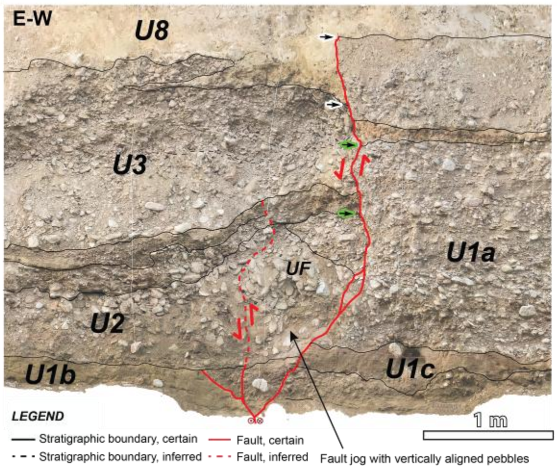

Figure 5. Geological interpretation of the eastern end of the northern wall of scarp-perpendicular trench TUN-T1, exposing the westernmost fault. The fault is cemented in-depth by a block of vertically aligned gravels confined by a second fault strand that we interpret as a fault jog. Different colored arrows indicate clear piercing points offset by the fault. Short description of stratigraphic units: U1: Matrix-supported, well-consolidated heterometric gravels with a silt-sandy matrix (1a) with a homogeneous layer of silty clay at the bottom (1b) and interbedded with coarse sand layers (1c); U2: Non-consolidated heterometric and poorly sorted gravels with silt-sandy matrix; U3: Non-consolidated heterometric gravels with carbonated silt-sandy matrix; U8: ocher silt with charcoal and pieces of ceramics; UF: Non-consolidated and heterogeneous gravels with vertically aligned pebbles.

CONCLUSIONS

In both study sites, trenches exposed surface rupturing paleoearthquakes providing the first evidence of Late Pleistocene and Holocene activity in the eastern RGBF fault zone. Our results show the bias between the paleoseismic record and seismogenic landforms (scarps, hanging valleys, triangular facets, offset alluvial fans, and beheaded channels) and present-day instrumental seismicity, as most of the activity is moderate to low. Further studies must be addressed to extend further the seismic catalog of the eastern RGBF and associated faults and characterize them for PSHA analysis.

Acknowledgements: This study is co-funded by the IRSN (France) and the RWTH Aachen University (Germany). We wish to thank everyone that take part and contributed to the trenching and geophysical field campaigns including the owner of the lands, excavators and visiting international scientists.

REFERENCES

Baize, et al., 2017. First steps in assessing paleoseismic activity along the eastern boundary of the Upper Rhine Graben. Extended Abstract, 8th INQUA PATA Days, New Zealand.

Barth, A., et al., 2015. Spatial variations of earthquake occurrence and coseismic deformation in the Upper Rhine Graben, Central Europe. Tectonophysics, 651-652, 172–185. doi:10.1016/j.tecto.2015.04.004

Burbank, D.W., & Anderson, R.S., 2001. Tectonic Geomorphology, Blackwell Science, Malden (USA). 274 pp.

Colbeaux, J.P., et al., 1981. Tectonique quaternaire dans le Nord de la France: l'apport du gisement paléolithique de Biache-Saint-Vaast. Bulleting de l'Association française pour l'étude du quaternaire 18, 183-192.

Cushing, M., et al., 2000. Paleoearthquakes investigations in the Upper Rhine Graben in the framework of the PALEOSIS project, in: PALEOSIS - HAN2000 - potential for large earthquakes in low seismic activity regions of Europe, 39–43.

Ferry, M., et al., 2005. Evidence for Holocene palaeoseismicity along the Basel-Reinach active normal fault (Switzerland): a seismic source for the 1356 earthquake in the Upper Rhine graben. Geophysical Journal International 160, 554–572. doi:10.1111/j.1365-246X.2005.02404.x

Grünthal, G. & Wahlström, R., 2012. The European-Mediterranean Earthquake Catalogue (EMEC) for the last millennium. J Seis 16, 535-570.

Heidbach, O., et al., 2018. The World Stress Map database release 2016: Crustal stress pattern across scales. Tectonophysics, 744, 484-498. doi: 10.1016/j.tecto.2018.07.007

LGL-BW DEM 2016. Landesamt für Geoinformation und Landentwicklung Baden-Württemberg: LiDAR Geobasisdaten (1x1m)

LGRB (Landesamt für Geologie, Rohstoffe und Bergbau), Regierungspräsidium Freiburg: Hydrogeologische Karte 1: 50 000 (GeoLa): WMS LGRB-BW HK50: http://services.lgrb/bw.de/index.phtml?SERVICE=WMS&REQUEST=GetCapabilities&VERSION=1.1.1&SERVICE_NAME=lgrb_geola_hyd <Last viewed 22 March 2022>

McCalpin, J.P., 2009. Paleoseismology: Amsterdam, Academic Press, Elsevier, 613 p.

Meghraoui, M., et al., 2001. Active normal faulting in the upper Rhine Graben and Paleoseismic Identification of the 1356 Basel earthquake. Science 293, 2070–2073. doi:10.1126/science.1010618

Monninger, R., 1985. Neotektonische Bewegungsmechanismen im mittleren Oberrheingraben. Karlsruhe University, Karlsruhe.

Nivière, B., et al., 2008. Active tectonics of the southeastern Upper Rhine Graben, Freiburg area (Germany). Quaternary Science Reviews, 27, 541-555.

Peters, G., et al., 2005. Interplay between tectonic, fluvial and erosional processes along the Western Border Fault of the northern Upper Rhine Graben, Germany. Tectonophysics 406, 39-66. doi:10.1016/j.tecto.2005.05.028

Reicherter, K., et al., 2008. Alpine tectonics II - Central Europe north of the Alps, in: McCann, T. (Ed.), Geology of Central Europe. Geological Society of London.

Schumacher, M.E. 2002. Upper Rhine Graben: the role of pre-existing structures during rift evolution. Tectonics 21, 6-1, 6-17. doi: 10.1029/ 2001TC90002

Villemin, T., & Bergerat, F. 1987. Tectonique cassante et paléocon-traintes tertiaires de la bordure nord-est du fossé rhénan. Oberrhein. Geol. Abh. 14, 63 – 87.

High-Resolution multichannel seismic reflection experiment with active tectonics objectives: Defining the deep geometry of the faults bounding the Guadalentin Depression (SE Iberia)

Perea, Hector (1), Paula Herrero-Barbero (1), Júlia Molins-Vigatà (1), Juan Alcalde (2), José Antonio Álvarez Gómez (1), María Barriolópez Llamosas (1), Ramon Carbonell (2), Yolanda de Pro Díaz (1), Domitille Dufour (4), Julián García Mayordomo (3), José Luis Granja Bruña (1), Juan Miguel Insúa Arévalo (1), David Martí (2), Raquel Martín Banda (3), Eulàlia Masana (4), Marc Ollé (4), Elena Pascual Sánchez (1), Juan J. Portela (5), Jhonatan S. Rivera Rivera (5), José Luis Sánchez Roldán (1), Alejandra Staller (5), Sarmad Rameez (4)

(1) Facultad de Ciencias Geológicas, Universidad Complutense de Madrid, 28040 Madrid, Spain. Corresponding author: hperea@icm.csic.es.
(2) Geociencias Barcelona (GEO3BCN), CSIC, 08028 Barcelona. Spain
(3) Instituto Geológico y Minero de España, CSIC, 28760 Tres Cantos, Spain
(4) RISKNAT, GEOMODELS, Facultat de Ciències de la Terra, Universitat de Barcelona, 08028 Barcelona, Spain
(5) ETSI Topografía, Geodesia y Cartografía, Universidad Politécnica de Madrid, 28031 Madrid, Spain

Abstract: *To produce seismic hazard assessments to the current state-of-the-art, it is essential to characterize the active faults in terms of geometry, interrelation and seismotectonic activity. The Guadalentin Depression is the main basin within the Eastern Betic Shear Zone (SE Iberia), which corresponds to a NE-SW tectonic corridor bounded by the Carrascoy, Alhama de Murcia and Palomares active faults. Although a number of active tectonics and paleoseismological studies have been carried out in these faults, almost nothing is known about their geometry at depth. To reveal their deep structure and geometry, we have conducted a high-resolution seismic reflection survey. The acquired data will allow to improve our understanding of the deep geometry of these faults (up to 2 km depth) and will help to reduce the uncertainties in seismic hazard assessment.*

Key words*: Active faults, Seismic reflection, Fault depth geometry, Eastern Betics Shear Zone, SE Iberia.*

INTRODUCTION

The seismic hazard of a region is strongly controlled by the presence of active faults and their degree of activity. To perform a modern evaluation of seismic hazard, it is essential to characterize these faults as precisely as possible, particularly in terms of their geometry, interrelationship and seismotectonic state.

The current crustal deformation in the southeast of the Iberian Peninsula is mainly driven by the NW-SE convergence (4-5 mm/yr) between Africa and Iberia (Palano et al., 2015). This convergence is partially accommodated over a large deformation zone with significant seismic activity (Buforn et al., 1995; Stich et al., 2006). Some of the main active faults in this area are related to a large fault system, with left lateral slip and sigmoidal geometry, called the Eastern Batic Shear Zone (EBSZ) (Sanz de Galdeano, 1990). This fault system extends over 450 km from Alicante to the south of Almería. Within the EBSZ there is the Guadalentín depression, a NE-SW trending basin controlled tectonically by the Carrascoy, Alhama de Murcia and Palomares faults, from north to south (Fig. 1) (Silva et al., 1993). Paleoseismology studies have already been carried out on some of these faults that have made possible to characterize the earthquakes that they could generate (e.g., Ferrater et al., 2017; Martín-Banda et al., 2021). On the contrary, knowledge of the geometry at depth is only known in the case of the NE termination of the Alhama de Murcia fault (Herrero-Barbero et al., 2020); for the rest of the faults in the system it is unknown. Establishing their geometry is a fundamental datum in order to reduce uncertainty in seismic hazard studies.

In order to improve the current knowledge about the geometry at-depth of the different faults that border the Guadalentín depression, a high-resolution reflection seismic survey was carried out within the framework of the UNRIDDLE project. This survey was carried out in May 2022 in the municipalities of Lorca, Alhama de Murcia and Murcia (Fig. 1 and Table 1).

ACQUISITION METHODOLOGY AND PARAMETERS

The acquisition of reflection seismic profiles allows us to obtain images of geological units and structures located at depth. In this study, we have focused on conducting a shallow exploration (1-2 km) and looking for a high spatial resolution, both vertical and horizontal.

An 8-ton Envirovibe-Minibuggy model 290 vibrator truck or vibroseis vehicle was used as the seismic energy source (Fig. 2a). These vehicles are equipped with a hydraulic system that allows for weak vibrations that generate a controlled seismic wave train, transmitting a continuous signal to the ground that contains a determined range of frequencies. To obtain a high-resolution record, the vibration points were separated by 5 m and in each of them three sweeps of 15 s duration were generated with a frequency content between 10 and 150 Hz progressively increasing and with a time of listening between sweeps of 5 s.

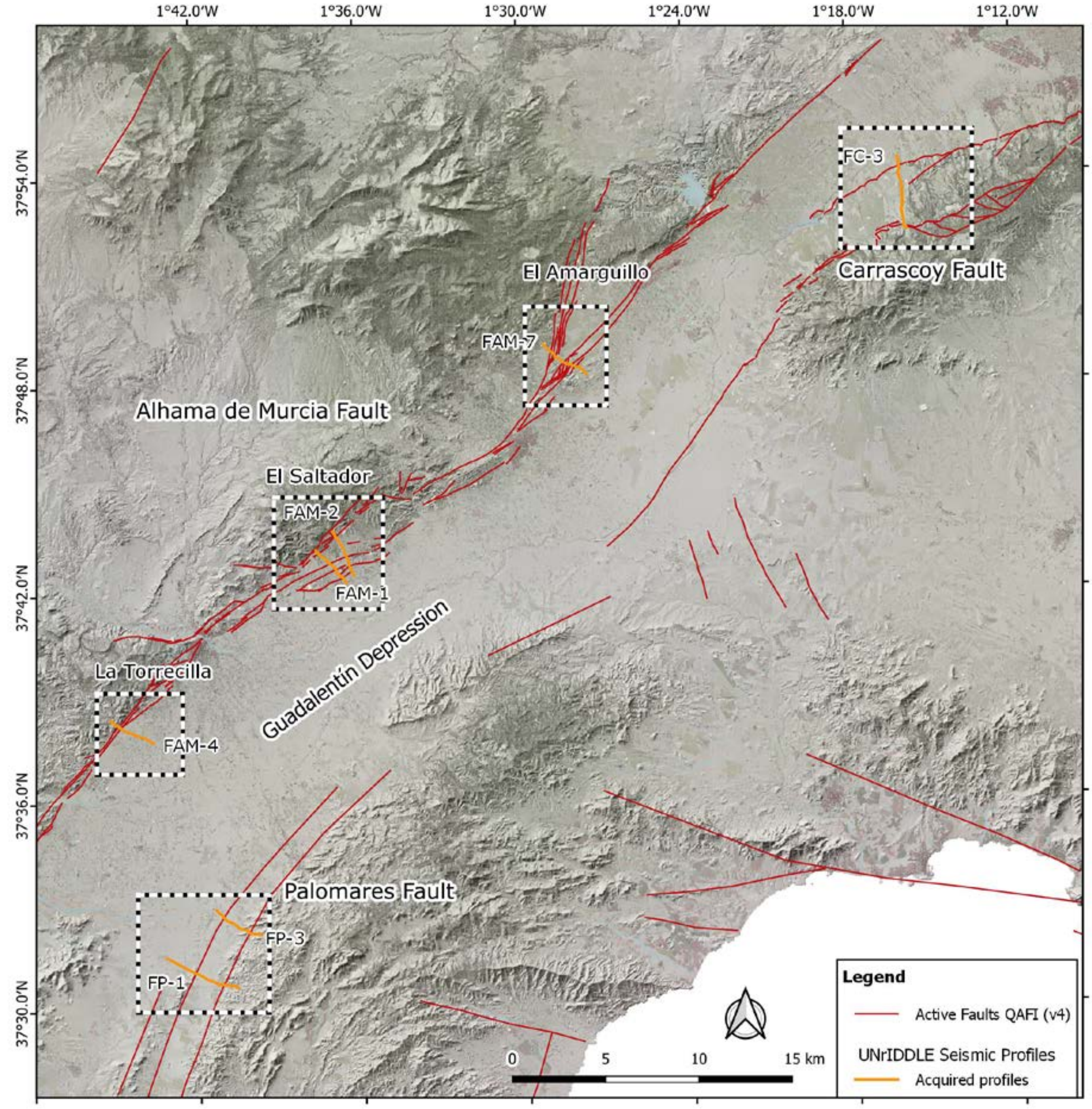

Figure. 1: Map of the Guadalentín Depression with the localization of the QAFI v4 active faults (IGME, 2022) and of the high-resolution seismic profiles acquired during the UNrIDDLE seismic survey (Table 1).

Wireless units made up of a recording box or UNITE and a geophone cable-connected to the UNITE were used to record the seismic signal (Fig. 2b). During the experiment, we distributed the recording units every 10 m along the profiles. This implied the deployment of between 100 and 450 registration units at the same time depending on the length of the profile (Table 1).

Both the trigger points and the registration sensors have been positioned redundantly by means of the GPS system integrated in the instrumentation (vibrator truck and UNITE) and by means of a differential GPS topographic total stations. This redundancy has allowed carrying out a quality control in the positioning obtaining a centimetric precision.

SURVEY RESULTS AND CONCLUSIONS

Throughout 20 days of seismic acquisition, 7 high-resolution seismic reflection profiles were acquired (Fig. 1 and Table 1). Two of these profiles are located across the Palomares fault (FP1 and FP3). Crossing the Alhama de Murcia fault, four profiles were acquired, one in the Torrecilla zone (FAM4), two in the El Saltador zone (FAM1 and FAM2) and another in the El Amarguillo zone (FAM5). Finally, a profile was acquired through the Carrascoy fault (FC3).

Figure 3 shows an example of the raw log of a full offset shot after the effect of the seismic source has been removed. The record shows a good signal to noise ratio where first arrivals can be recognized up to each side of the trigger point.

The acquired data will reveal the deep structure (up to 1 or 2 km), the geometry and the deformation history of the Upper Neogene, with emphasis on the Upper Quaternary, of the Carrascoy, Alhama de Murcia and Palomares faults.

Acknowledgements: We would like to thank the collaboration of the town councils of Lorca, Alhama de Murcia and Murcia, and especially to *Emergencias Lorca*, which allowed us to use their facilities as work base. We also want to thank EARMUR for permission to acquire a profile on their land and *Dinamo Instalaciones* for their assistance in the fieldwork. H. Perea was a postdoctoral researcher of the "Atracción de Talento" program at the Universidad Complutense de Madrid funded by the Community of Madrid (2018-T1/AMB-11039). P. Herrero and J. Molins were contracted by the UNrIDDLE project (2018-Q1/AMB-11039). J. Alcalde has received funding from grants IJC2018-036074-I funded by MCIN/AEI/10.13039/501100011033.

Table 1: Identification of the high-resolution seismic reflection profiles acquired across the different studied active faults, indicating their length and the total length (in red) in each fault system.

Fault zone	**Profile length (m)**
Palomares fault	
FP1	4088
FP3	2685
Total length	10444
Alhama de Murcia fault	
FAM1 (El Saltador)	2413
FAM2 (El Saltador)	2623
FAM4 (La Torrecilla)	2525
FAM7 (El Amarguillo)	2637
Total length	15393
Carrascoy fault	
FC3	3901
Total length	13681

a)

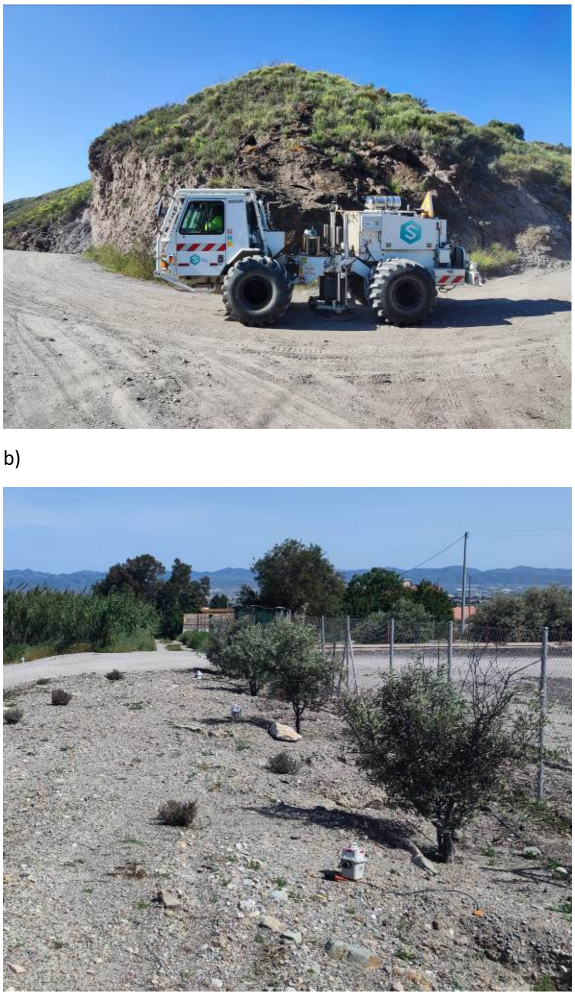

b)

Figure 2: Photographs of the vibrator truck Envirovibe-Minibuggy model 290 8 ton (a) and of the UNITE wireless recording units with the cable-connected geophone (orange top) nailed to the ground (b).

REFERENCES

Buforn, E., Sanz de Galdeano, C. & Udías, A., 1995. Seismotectonics of the Ibero-Maghrebian region. *Tectonophysics*, 248, 247–261.

Ferrater, M., Ortuño, M., Masana, E., Martínez-Díaz, J.J., Pallàs, R., Perea, H., Baize, S., García-Meléndez, E., Echeverria, A., Rockwell, T., Sharp, W.D. & Arrowsmith, R., 2017. Lateral slip rate of Alhama de Murcia fault (SE Iberian Peninsula) based on a morphotectonic analysis: Comparison with paleoseismological data. *Quaternary International*, 451, 87–100.

Herrero-Barbero, P., Álvarez-Gómez, J.A. & Martínez-Díaz, J.J., Klimowitz, J., 2020. Neogene basin inversion and recent slip rate distribution of the northern termination of the Alhama de Murcia Fault (Eastern Betic Shear Zone, SE Spain). *Tectonics*, 39(7), e2019TC005750.

IGME, 2022. QAFI: Quaternary Active Faults Database of Iberia. Accessed May 2022, from IGME web site: https://info.igme.es/QAFI.

Martín-Banda, R., Insua-Arévalo, J.M. & García-Mayordomo, J., 2021. Slip rate variation during the last ⍰ 210 ka on a slow fault in a transpressive regime: The Carrascoy Fault (Eastern Betic Shear Zone, SE Spain). *Frontiers in Earth Science*, 8, 1–21.

Palano, M., González, P.J. & Fernández, J., 2015. The Diffuse Plate boundary of Nubia and Iberia in the Western Mediterranean: Crustal deformation evidence for viscous coupling and fragmented lithosphere. *Earth and Planetary Science Letters*, 430, 439–447.

Sanz de Galdeano, C. (1990). Geologic evolution of the Betic Cordilleras in the Western Mediterranean, Miocene to the present. *Tectonophysics*, 172 (1–2), 107–119.

Silva, P.G., Goy, J.L., Somoza, L., Zazo, C. & Bardají, T., 1993. Landscape response to strike-slip faulting linked to collisional settings: Quaternary tectonics and basin formation in the Eastern Betics, southeast Spain. Tectonophysic, 224, 289–303.

Stich, D., Serpelloni, E., de Lis Mancilla, F. & Morales, J. (2006). Kinematics of the Iberia–Maghreb plate contact from seismic moment tensors and GPS observations. *Tectonophysics*, 426 (3–4), 295–317.

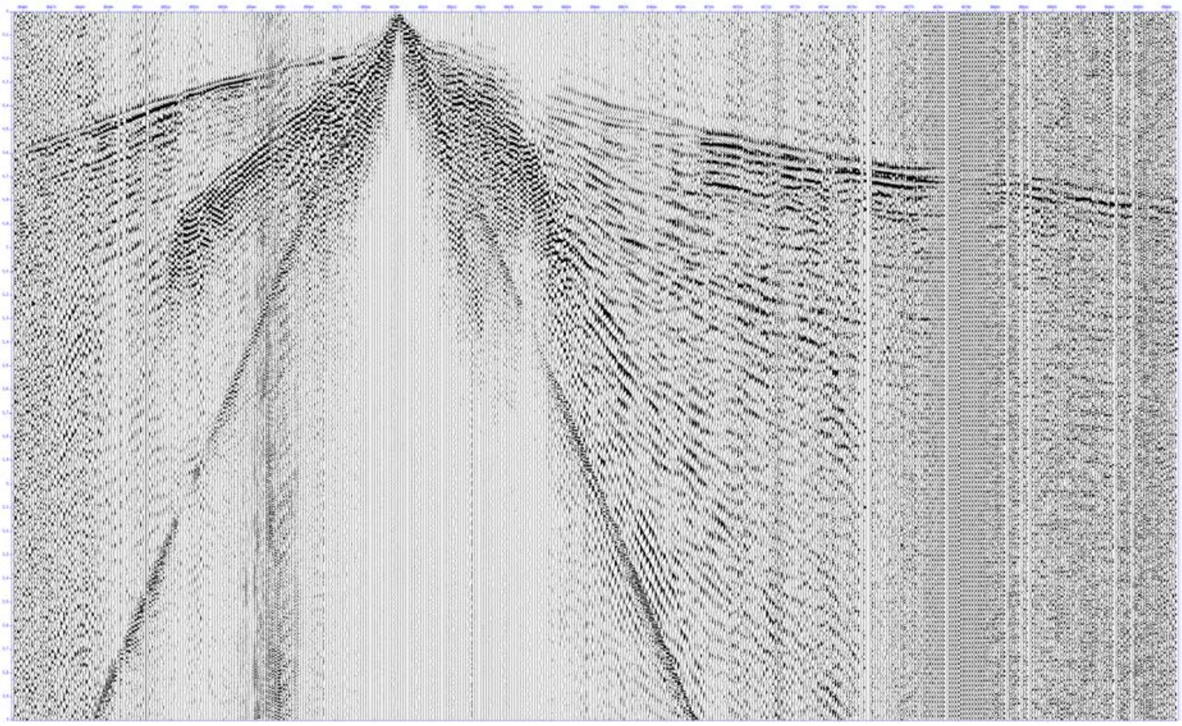

Figure 3: Raw seismic record of a shot at full offset corresponding to profile FP1 (see Fig. 1 and Table 1) once the effect of the seismic source has been removed. The record is cut to 3 s of double time.

INQUA Focus Group Terrestrial Processes Perturbed by Tectonics (TPPT)

paleoseismicity.org

Unveiling the Upper Quaternary earthquake history on a large submarine strike-slip fault: The Yusuf Fault System (Alboran Sea)

Perea, Hector (1,2), Sara Martínez-Loriente (2), Jaume Llopart (2), Ariadna Canari (2), Stefanie Almeida (2), Eulàlia Gràcia (2)

(1) Departamento de Geodinámica, Estratigrafía y Paleontología, Facultad de Ciencias Geológicas -Universidad Complutense de Madrid, 28040 – Madrid, Spain. Corresponding author: hperea@icm.csic.es.
(2) Barcelona-CSI, Institut de Ciències del Mar, CSIC, 08003 Barcelona, Spain

Abstract: *The NW-SE convergence (4-5 mm/yr) between Africa and Iberia controls the present-day crustal deformation in the Alboran Sea (westernmost Mediterranean). Although seismic activity is mainly characterized by low to moderate magnitude events, large and destructive earthquakes have occurred in this region. The Yusuf Fault (YF), which is a right-lateral strike-slip fault, is one of the largest active structures in the area. The analysis of ultra-high resolution geophysical data acquired with an autonomous underwater vehicle (AUV) shows that the YF offsets the upper Pleistocene to Holocene sedimentary units reaching up the seafloor and producing topographic scarps. The results of the on-fault sub-aqueous paleoseismological analyses reveal that the YF may have generated at least 8 earthquakes in the last 200 ka. The estimated average vertical offset is about 0.64 m; however, this value needs to be considered as a minimum since YF is predominantly a strike-slip fault.*

Key words: *Offshore active faults, ultra-high resolution geophysical data, sub-aqueous paleoseismology, Alboran Sea, Western Mediterranean.*

INTRODUCTION

The NW-SE convergence (4-5 mm/yr) between the African and Eurasian plates controls the present-day crustal deformation along the southern Iberian and northern African margins (Argus et al., 2011; Palano et al., 2015; Sparacino et al., 2020). The strain due to this convergence is accommodated over a deformation zone with significant seismic activity across the Alboran Sea (Buforn et al., 1995; Stich et al., 2010), which is interpreted as a Neogene back-arc basin generated by subduction-related extension in the Gibraltar Arc (Booth-Rea et al., 2007; Comas et al., 1999). Although seismicity is mainly characterized by low to moderate magnitude events (Figure 1), large and destructive earthquakes (Intensity > IX) have occurred in the region, as shown by the historical and instrumental earthquake catalogues (i.e., 1522 Almeria, 1790 Oran, 1910 Adra, 1994 and 2004 Al-

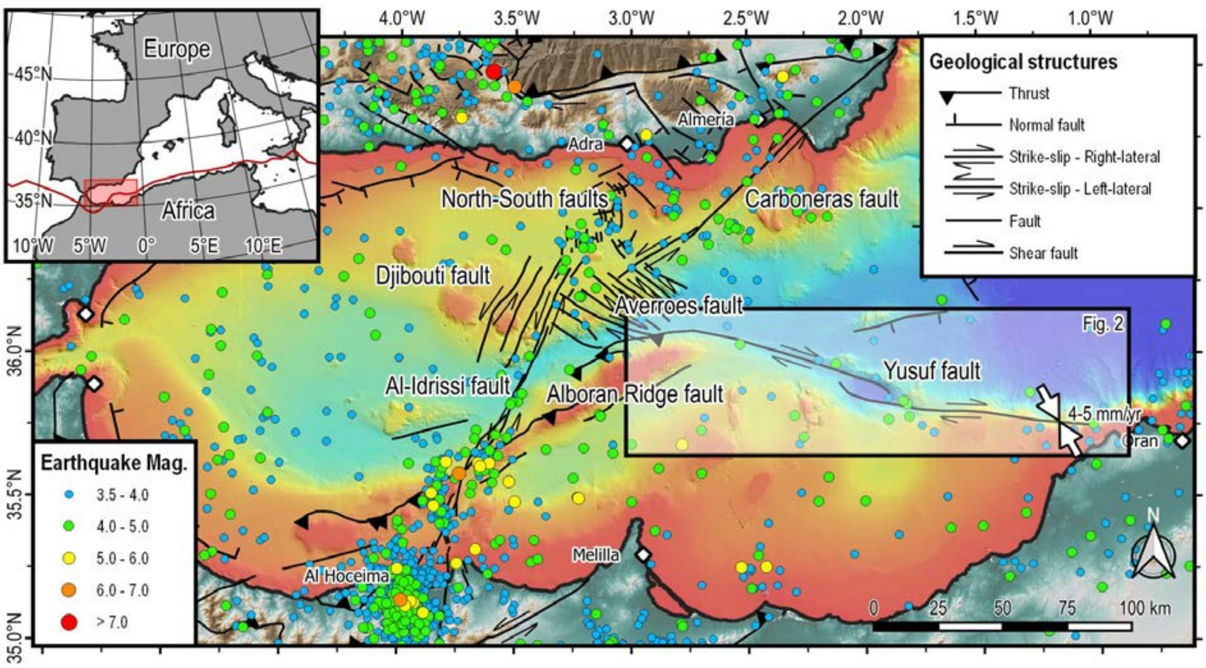

Figure 1: Map of the Alboran Sea (western Mediterranean) with the location of the main active fault systems (Gràcia et al., 2019) and the earthquakes above magnitude 3.5 that have occurred in the area obtained from the Instituto Geográfico Nacional (Spain) instrumental earthquake catalogue (https://www.ign.es/web/ign/portal/sis-catalogo-terremotos). The black and transparent white rectangle shows the location of Figure 2. The inset map of the Western Mediterranean shows the location of the main map.

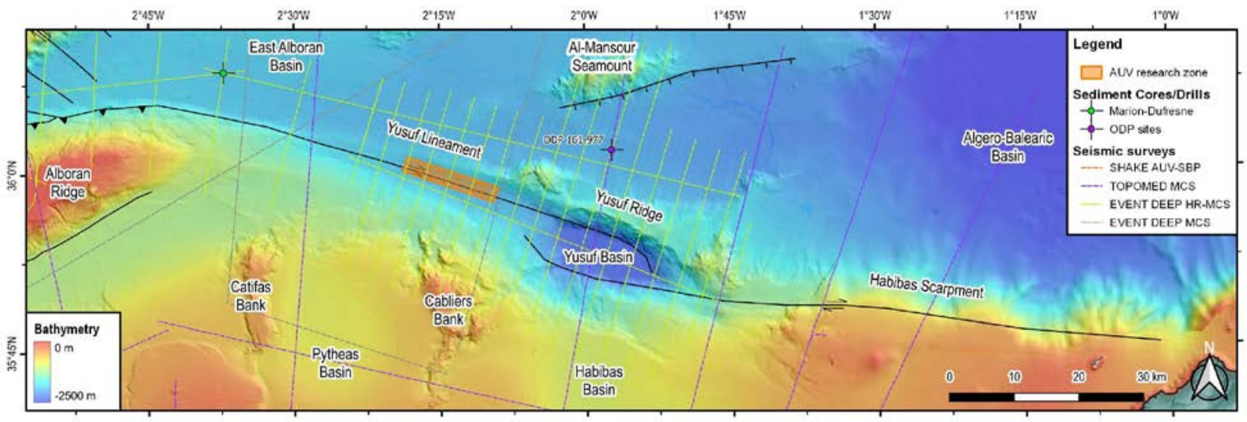

Figure 2: Bathymetric map centered in the Yusuf fault identifying the main physiographic features in the area and showing the different data used in the study of the fault (i.e., sediment cores, AUV data and seismic profiles). The location of this area in the Alboran Sea is shown in Figure 1.

Hoceima or 2016 Al-Idrissi earthquakes) (Buforn et al., 1995; Martínez Solares & Mezcua, 2002; Stich et al., 2010).

During the last two decades, different investigations have focused in the identification and location of the active structures in the Alboran Sea through the acquisition of bathymetric and seismic data at different resolution (Gómez de la Peña et al., 2022; Gràcia et al., 2019; Moreno et al., 2016; Perea et al., 2018). However, there is a lack of knowledge about the seismogenic potential of these faults, which is essential to improve our knowledge about earthquake and tsunami hazards along the coasts of South Iberia and North Africa. Accordingly, the aim of the present study is to characterize the seismic cycle of the Yusuf fault, one of the main geological structures in the Alboran Sea, using the sub-aqueous active tectonics and paleoseismological existing methods.

GEOLOCICAL SETTING: THE YUSUF FAULT

The Yusuf fault, localized between the Eastern and Southern Alboran basins, is one of the main active faults in the area and represents the boundary between two different crustal regions (Gómez de la Peña et al., 2018, 2022; Perea et al., 2018). It is a right-lateral strike-slip fault that trends WNW-ESE and has a length of ~150 km. The fault has been divided into two main segments, the western segment with ~87 km and trending N100 and the eastern segment with ~105 km and trending N095. Both segments overlap in the Yusuf pull-apart basin (Figure 2).

Some geodetic kinematic models have used the Yusuf fault as a block boundary and the results suggest that the fault could be absorbing between 2 to 4 mm/yr in a right lateral movement with some reverse component (Asensio et al., 2014; Vernant et al., 2010). More recently, using forward numerical modelling, it has been estimated that the minimum slip in the extensional faults related to the Yusuf pull-apart basin would be 12 km accommodated during the Plio-Holocene (Gómez de la Peña et al., 2022). This might result in a minimum fault slip rate of 2.3 mm/yr for the last 5.3 Ma. This slip rate is in agreement with the rates obtained from the geodetic kinematic models. Accordingly, the Yusuf fault might be absorbing an important part of the convergence between the African and Iberian plates.

DATA AND METHODS

The available geophysical dataset imaging the Yusuf fault includes bathymetry of high (30m) and ultra-high resolution (1m, acquired with Autonomous Underwater Vehicles or AUV), parametric sub-bottom and CHIRP (with cm vertical resolution acquired with AUV) profiles, and medium and high penetration multichannel seismic profiles (MCS) acquired during the EVENT-DEEP and SHAKE cruises.

Sub-aqueous paleoseismological studies aim to identify individual vertical movements in the fault plane related to large earthquakes and for this we use very high resolution seismic profiles, at the centimetre level. The used methodology assumes that when a fault produce seafloor rupture, it generates a scarp and, therefore, space for sediment accommodation (Barnes & Pondard, 2010; Brothers et al., 2011). Due to the presence or the scarp, the units that correspond to the same age on both sides of the fault and deposited after the earthquake do not have the same thickness. On the downthrown block, units will be thicker because there is more accommodation space. These units correspond to growth sequences. Once the escarpment is covered, the units of the same age on both sides of the fault have the same thickness and correspond to equivalent sequences. Representing in a graph the age of the reflectors and the accumulated vertical displacement on either side of the fault, equivalent sequences are represented by a horizontal line segments, there is no vertical displacement, while the growth sequences correspond to inclined line segments. Then, the passage from an equivalent sequence to a growth sequence marks the moment of occurrence of the earthquake, and the vertical distance between two equivalent sequences corresponds to the vertical event slip.

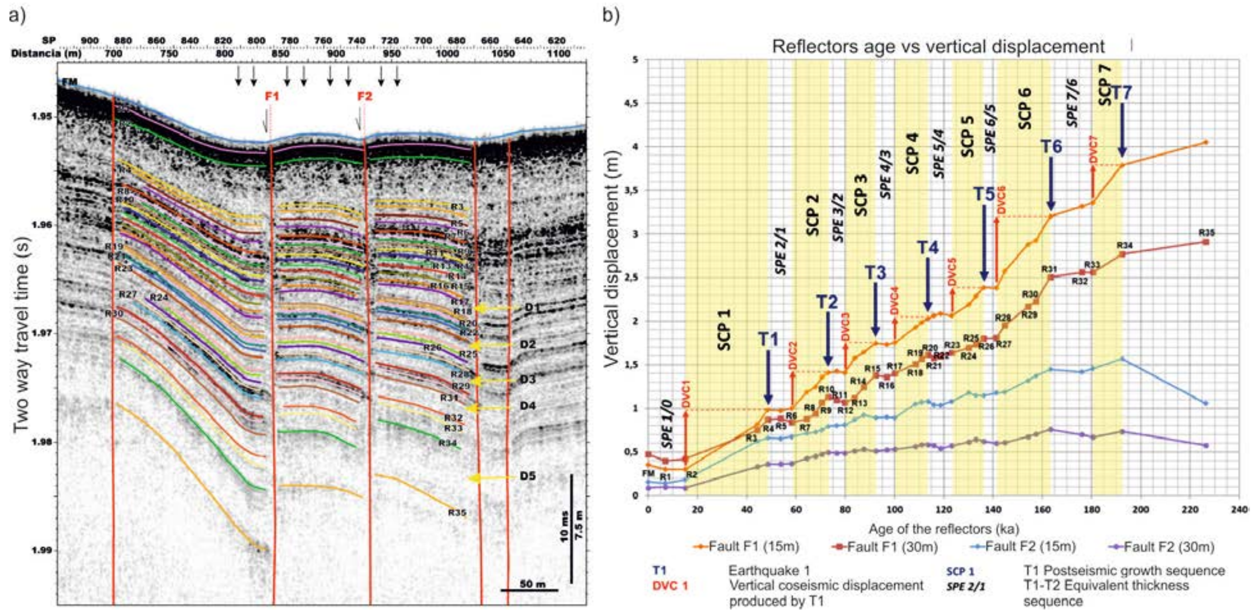

Figure 3: a) Zoom on the faulted area of the ultra-high resolution sub-bottom seismic profile FY-AUV011; this profile shows the presence of several faults offsetting the seismic reflectors corresponding to sedimentary units deposited during the last 220 ka (see text for further explanations about the ages). Colored reflectors identified by R(num) correspond to the units where vertical displacements along faults F1 and F2 have been measured. Arrows on top indicate the position (15 and 30 m at both sides of the faults) where reflectors depth has been measured. b) Graph plotting the measured vertical displacement and estimated age for each of the 38 reflectors interpreted in the seismic profile. The different curves correspond to measurements done form F1 and F2 at 15 and 30 m at each side of the fault. R(num) identify the specific reflector. Horizontal sections of the graph indicate the presence of equivalent thickness sequences (SPE) and inclined sections correspond to growth sequences (see text for more information). D(num) and a yellow arrow identify different interpreted submarine wasting deposits.

RESULTS

The analysis of the acquired ultra-high resolution sub-bottom seismic profiles reveal the presence of faults, that are quite steep and offset all the seismostratigraphic units and, in most of the cases, also the seafloor producing geomorphological scarps. These observations imply Quaternary activity on the fault system and suggest the occurrence of a quite recent earthquake in the fault.

The centimetre resolution of the profiles has allowed us to carry out an on-fault sub-aqueous paleoseismological study on the Yusuf fault. To carry out the analysis we marked up to 35 different reflectors across two different faults (F1 and F2; Figure 3a). To date the different reflectors, we used a sedimentary rate calculated along a high-resolution multichannel profile were the ages of the reflectors were calibrated with an IODP well. The obtained sedimentary rate was 0.1 mm/yr, which allowed estimating that the deeper marked reflector would have deposited approximately 220 ka ago.

According to the paleoseismological analysis (Figure 3b), the fault may have generated at least 8 earthquakes during the last 200 ka, the last one occurred in a quite recent time, maybe in historical times, with an average recurrence interval of 27.5 ka. The estimated average vertical offset would be 0.64 m. However, this has to be considered as a minimum offset since this is a dextral strike-slip fault and the lateral slip must be much larger than the vertical. According to different empirical relationships the fault could produce earthquakes larger than 7.0.

Even with some uncertainties, our results show that sub-aqueous paleoseismological studies are also feasible in low slip-rate faults, as the ones in the Alboran Sea, and essential to improve our knowledge of their seismic potential and, then, to characterize better the seismic and tsunami hazards in surrounding coastal areas.

Acknowledgements: This research was supported by EVENT (CGL2006-12861-C02-02), SHAKE (CGL2011-30005-C02-02), UNrIDDLE (2018-T1/AMB-11039), THREAT (PID2021-128513OA-I00) and STRENGTH (PID2019-104668RB-I00) projects. This project acknowledges the 'Severo Ochoa Centre of Excellence' accreditation (CEX2019-000928-S) and the grant 2018-T1/AMB-11039 funded by MCIN/AEI/ 10.13039/501100011033. Grateful thanks are also due to the captain, crew, scientific party and UTM-CSIC technical staff on board the R/V Hespérides during the IMPULS 2006 and R/V Sarmiento de Gamboa during the EVENT-DEEP 2010 cruise. H. Perea was a fellow postdoctoral researcher under the Marie Sklodowska-Curie Actions funded by the European Commission (H2020-MSCA-IF-2014 657769) and the "Atracción de Talento" program funded by the Community of Madrid (2018-T1/AMB-11039).

REFERENCES

Argus, D. F., Gordon, R. G., & DeMets, C. (2011). Geologically current motion of 56 plates relative to the no-net-rotation reference frame. *Geochemistry, Geophysics, Geosystems*, *12*(11), n/a-n/a. https://doi.org/10.1029/2011GC003751

Asensio, E., Khazaradze, G., & Echeverria, A. (2014). Modelos cinemático de bloques en la región Ibero-Magrebí a partir de datos geodésicos/Block kinematics of the Ibero-Maghrebian region from inversion of geodetic data. In J. A. Álvarez-Gómez & F. Martín-González (Eds.), *Una aproximación multidisciplinar al estudio de las fallas activas, los terremotos y el riesgo sísmico. 2ª reunión ibérica sobre fallas activas y paleosismología (Lorca, Spain)* (pp. 221–224). IGME.

Barnes, P. M., & Pondard, N. (2010). Derivation of direct on-fault submarine paleoearthquake records from high-resolution seismic reflection profiles: Wairau Fault, New Zealand. *Geochemistry, Geophysics, Geosystems*, *11*(11), n/a-n/a. https://doi.org/10.1029/2010GC003254

Booth-Rea, G., Ranero, C. R., Martínez-Martínez, J. M., & Grevemeyer, I. (2007). Crustal types and Tertiary tectonic evolution of the Alborán sea, western Mediterranean. *Geochemistry, Geophysics, Geosystems*, *8*(10), n/a-n/a. https://doi.org/10.1029/2007GC001639

Brothers, D., Kilb, D., Luttrell, K., Driscoll, N., & Kent, G. (2011). Loading of the San Andreas fault by flood-induced rupture of faults beneath the Salton Sea. *Nature Geoscience*, *4*(7), 486–492. https://doi.org/10.1038/ngeo1184

Buforn, E., Sanz de Galdeano, C., & Udías, A. (1995). Seismotectonics of the Ibero-Maghrebian region. *Tectonophysics*, *248*, 247–261.

Comas, M. C., Platt, J. P., Soto, J. I., & Watts, A. B. (1999). The origin and tectonic history of the Alboran Basin: Insights from Leg 161 results. In R. Zahn, M. C. Comas, & A. Klaus (Eds.), *Proceedings of the Ocean Drilling Program, Scientific Results, Vol. 161* (Vol. 161, pp. 555–580).

Gómez de la Peña, L., Ranero, C. R., & Gràcia, E. (2018). The Crustal Domains of the Alboran Basin (Western Mediterranean). *Tectonics*, *37*(10), 3352–3377. https://doi.org/10.1029/2017TC004946

Gómez de la Peña, L., R. Ranero, C., Gràcia, E., Booth-Rea, G., Azañón, J. M., Tinivella, U., & Yelles-Chaouche, A. (2022). Evidence for a developing plate boundary in the western Mediterranean. *Nature Communications*, *13*(1), 4786. https://doi.org/10.1038/s41467-022-31895-z

Gràcia, E., Grevemeyer, I., Bartolomé, R., Perea, H., Martínez-Loriente, S., Gómez de la Peña, L., et al. (2019). Earthquake crisis unveils the growth of an incipient continental fault system. *Nature Communications*, *10*(1), 3482. https://doi.org/10.1038/s41467-019-11064-5

Martínez Solares, J. M., & Mezcua, J. (2002). *Catálogo sísmico de la Península Ibérica (880 a.C.-1900) (Monografía núm.18)*. Dirección General del Instituto Geográfico Nacional.

Moreno, X., Gràcia, E., Bartolomé, R., Martínez-Loriente, S., Perea, H., de la Peña, L. G., et al. (2016). Seismostratigraphy and tectonic architecture of the Carboneras Fault offshore based on multiscale seismic imaging: Implications for the Neogene evolution of the NE Alboran Sea. *Tectonophysics*, *689*, 115–132. https://doi.org/10.1016/j.tecto.2016.02.018

Palano, M., González, P. J., & Fernández, J. (2015). The Diffuse Plate boundary of Nubia and Iberia in the Western Mediterranean: Crustal deformation evidence for viscous coupling and fragmented lithosphere. *Earth and Planetary Science Letters*, *430*, 439–447. https://doi.org/10.1016/j.epsl.2015.08.040

Perea, H., Gràcia, E., Martínez-Loriente, S., Bartolome, R., de la Peña, L. G., de Mol, B., et al. (2018). Kinematic analysis of secondary faults within a distributed shear-zone reveals fault linkage and increased seismic hazard. *Marine Geology*, *399*(October 2017), 23–33. https://doi.org/10.1016/j.margeo.2018.02.002

Sparacino, F., Palano, M., Peláez, J. A., & Fernández, J. (2020). Geodetic Deformation versus Seismic Crustal Moment-Rates: Insights from the Ibero-Maghrebian Region. *Remote Sensing*, *12*(6), 952. https://doi.org/10.3390/rs12060952

Stich, D., Martín, R., & Morales, J. (2010). Moment tensor inversion for Iberia–Maghreb earthquakes 2005–2008. *Tectonophysics*, *483*(3–4), 390–398. https://doi.org/10.1016/j.tecto.2009.11.006

Vernant, P., Fadil, A., Mourabit, T., Ouazar, D., Koulali, A., Davila, J. M., et al. (2010). Geodetic constraints on active tectonics of the Western Mediterranean: Implications for the kinematics and dynamics of the Nubia-Eurasia plate boundary zone. *Journal of Geodynamics*, *49*(3–4), 123–129. https://doi.org/10.1016/j.jog.2009.10.007

Likelihood of primary surface faulting: a sequel

Marco Pizza (1), M. Francesca Ferrario (1), Frank Thomas (1), Giorgio Tringali (1), Franz Livio (1)

(1) Università degli Studi dell'Insubria, Como, Italy. Email: m.pizza@uninsubria.it

Abstract: *Surface faulting is a common phenomenon for crustal earthquakes and is an important source of localized hazard to buildings and infrastructures. When the avoidance criterion cannot be pursued, a probabilistic approach is used to assess fault displacement hazard. The likelihood of primary surface faulting is defined based on empirical datasets. The reference dataset was created almost 30 years ago (Wells & Coppersmith, 1993): therefore, we considered it appropriate to update the dataset itself and the derived regression. The analysis of 915 global earthquakes is currently underway; the events have any type of kinematics, M_w 5.5-7.9, hypocentral depth <20 km, and occurred between 1992 and 2018. We constructed a homogeneous dataset including, for each earthquake, Mw values, hypocentral depth, fault geometry and kinematics, and especially evidence of primary surface faulting. The input data are derived from the ISC-GEM earthquake catalogue, and compilation of the dataset was accomplished through analysis of published literature. The purpose of this work is to create a homogeneous database of recent earthquakes, classified according to the occurrence or non-occurrence of primary surface faulting. Preliminary results show that, for a given magnitude, the likelihood of primary surface faulting in our dataset is slightly lower than what is expected from extant equations; this is possibly due to technological improvements achieved in the last 30 years in the realm of surface faulting documentation (e.g., InSAR, optical image correlation). We will derive updated regressions on the likelihood of primary surface faulting, which can be used for probabilistic hazard analysis.*

Key words*: earthquake, surface faulting, fault, seismic hazard*

INTRODUCTION

Surface faulting is one of the most important and impactful cosismic effects. The IAEA guidelines (SSG-9: IAEA, 2010; DS507: IAEA, 2021a; Tecdoc-1987: IAEA, 2021b), differentiate surface faulting into primary, i.e. concerning the main seismogenic structure, and distributed faulting. Our work investigated the evidence of primary surface faulting effects induced by earthquakes over the past 30 years. This phenomenon can cause significant damage to buildings and infrastructure located on or near the "capable fault". Therefore, the proper definition of the surface faulting hazard is essential to mitigate its future effects.

For high-risk plants, probabilistic models are usually recommended to define the hazard associated with surface faulting. This approach has been introduced by Youngs et al. (2003), who analyzed a database of 345 historical earthquakes, occurred in 1847-1992 and with M_w >5 (Wells & Coppersmith, 1993). Considering that this database is about 30 years old, the purpose of this work is to create a new updated dataset that will allow analysis on the surface faulting phenomenon with more recent data.

DATASET

The dataset contains 915 worldwide earthquakes that occurred in the last 30 years (Figure 1). We gathered data from the ISC-GEM Earthquake Catalogue (International Seismological Center, 2022), an instrument that homogeneously collects information on thousands of earthquakes worldwide. Then, we filtered the earthquakes considering earthquakes with epicenters onshore and applying the following thresholds:

- Earthquake occurrence between 1992 and 2018;
- Moment magnitude M_w ≥5.5;
- Hypocentral depth <20 km.

These numerical thresholds assure an unbiased data selection and the repeteability of the procedure. Additionally, the selection of parameters is coherent with the choices made in the previous reference database and other similar works (Wells & Coppersmith, 1993; Pezzopane & Dawson, 1996; Lettis et al., 1997).

The definition of minimum moment magnitude is a critical choice: in fact, it is commonly assumed that surface faulting occurs from a "threshold magnitude". In the work of Wells & Coppersmith (1993) the minimum magnitude was set at M_w >5, in our work we decided to set the minimum value at M_w≥5.5, as in the work of Pezzopane & Dawson (1996) and similar to the value of M_w ≥5.4 adopted by Lettis et al. (1997). The "threshold" M_w ≥5.5 is based on the fact that from this value an appreciable increase in surface faulting events occurs. The strongest event contained in our dataset has M_w 7.9 (2008 Wenchuan). Figure 1b shows the frequency-magnitude distribution of the dataset: 379 earthquakes have M_w between 5.5 and 6.0 and 148 have M_w between 6.1 and 6.5, thus 527 earthquakes (86%) have a magnitude M_w between 5.5 and 6.5.

During the dataset implementation, we added specific fields (Figure 2), related to fault kinematics and occurrence of surface faulting. The fault kinematic is a categorical field, defined as "reverse", "normal", "strike-slip", "transpressive" and "transtensive". This information is obtained from the analyzed literature or from the focal mechanism rake.

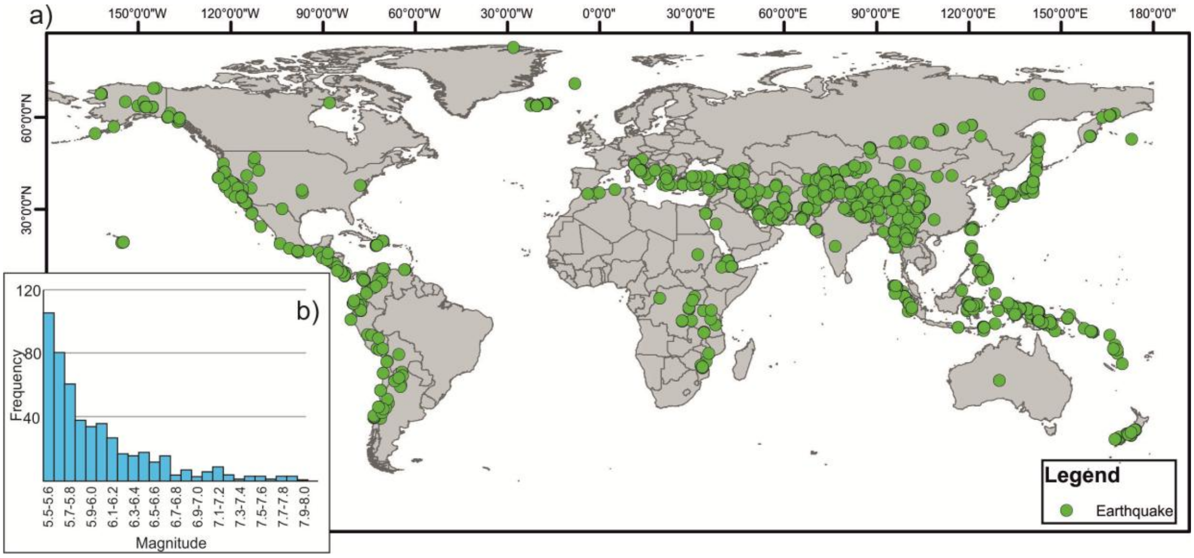

Figure 1: a) Map with location of earthquakes included in the dataset; b) frequency-magnitude distribution.

date	lat	lon	depth	Mw	Fault kinematic	Surface faulting	Reference
1992-01-23 04:24:16,24	38,335	20,542	15	**5,59**	Reverse	**No info**	
1992-02-06 03:35:16,41	29,597	95,638	13,4	**5,73**		**No info**	
1992-02-11 10:25:40,58	-9,327	124,741	18,4	**5,7**		**No info**	
1992-03-05 08:55:09,69	11,474	42,862	15	**6,22**	Strike-slip	**No rupture**	Foster & Jackson 1998
1992-03-13 17:18:41,47	39,706	39,6	20	**6,65**	Strike-slip	**Yes faulting**	Fuenzalida et al 1997
1992-03-15 16:16:26,80	39,543	39,873	20	**5,86**	Strike-slip	**No info**	Fuenzalida et al 1997
1992-03-19 06:34:28,72	17,238	120,91	18,9	**6,02**		**No info**	
1992-04-05 07:47:49,53	35,838	80,696	10	**5,68**		**No info**	
1992-04-08 13:36:58,43	-16,766	168,339	15	**5,93**		**No info**	
1992-04-23 04:50:25,58	33,866	-116,416	10	**6,16**	Strike-slip	**No rupture**	Sieh et al., 1992
1992-04-23 14:18:37,57	22,47	98,996	10	**6,07**		**No info**	Lian et al., 2019
1992-04-23 15:32:51,29	22,441	98,905	10	**6,13**		**No info**	Lian et al., 2019
1992-04-24 07:07:26,05	27,547	66,235	20	**6,01**		**No info**	
1992-04-25 18:06:06,66	40,387	-124,101	15	**7,16**	Reverse	**No rupture**	Oppenheimer et al., 1992
1992-05-10 04:04:33,11	37,162	72,922	20	**5,78**		**No info**	
1992-05-20 12:20:34,58	33,341	71,331	15	**6,04**	Reverse	**No rupture**	Lettis et al., 1997
1992-06-15 02:48:58,44	24,042	95,961	15,7	**6,27**		**No info**	
1992-06-28 11:57:38,46	34,188	-116,557	10	**7,29**	Strike-slip	**Yes faulting**	Sieh et al., 1993
1992-06-28 15:05:33,82	34,196	-116,802	10,9	**6,49**	Strike-slip	**No rupture**	Sieh et al., 1993

Figure 2: Informations contained in the dataset

The “surface faulting” is a categorical field as well, defined as:

- *Yes faulting*: the information found unequivocally mentions the occurrence of surface faulting;
- *No rupture*: we found unequivocal information on the absence of surface faulting;
- *Debated faulting*: in this case the presence of surface faulting is debated within the literature related to that earthquake;
- *No info*: this voice was entered when no information on the occurrence of surface faulting is available. In the case of earthquake sequences, if it was not possible to discriminate the event that generated surface faulting, the voice "Yes faulting" was assigned to the strongest event, while the others were categorized as "No info."

RESULTS AND DISCUSSION

The compilation of the new dataset is still in progress, currently we have analyzed 611 earthquakes out of the 915 events. This permits us to make an analysis, however preliminary, of the data obtained.

A total of 76 earthquakes caused surface faulting, 191 did not, 18 are debated, and for 326 we have no information. Figure 3 shows the data distribution according to magnitude. For most of the earthquakes we have no information: out of the 326 earthquakes catalogued with “No info”, 309 (95%) belong to the range M_w 5.5-6.5; the “No info” percentage decreases with increasing magnitude. This is arguably due to a more widespread attention of the scientific communtiy, and thus a higher number of publications dealing with it, toward surface faulting in the more recent years. It must be recalled that our dataset is not declustered, i.e., several entries may be related to a seismic sequences: in these cases, if surface faulting has been observed, we attributed it to the main event and the other events were catalogued with “No info”. On the contrary, if the main event is categorized as “No rupture”, all the foreshocks/aftershocks are categorized as “No rupture” as well.

Examples of seismic sequences in our dataset include the 2005 Kashmir events: there are 15 earthquakes, but

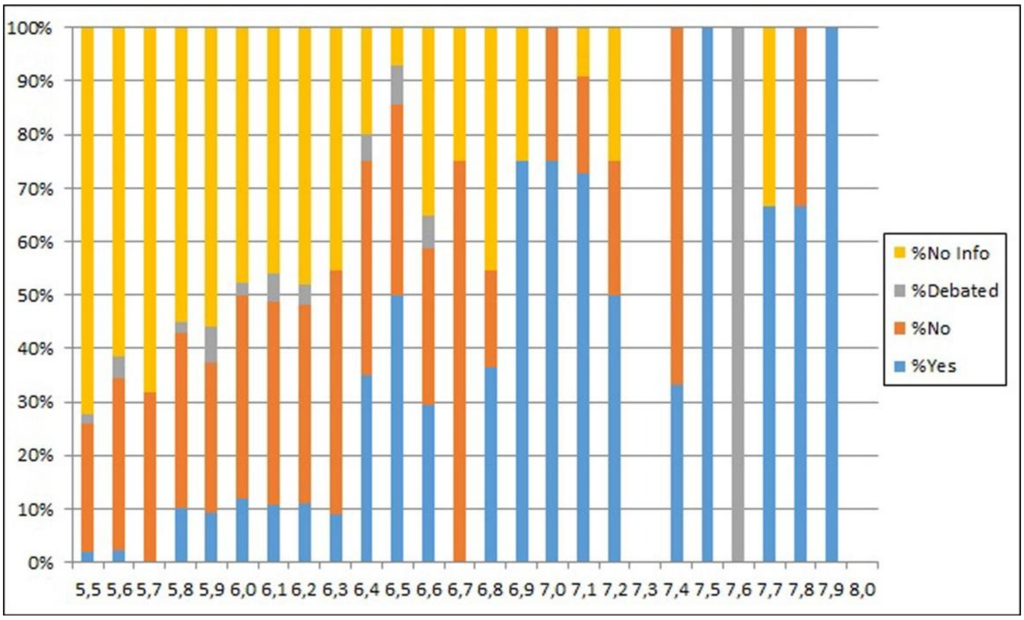

Figure 3: Percentage of events, that caused ("Yes"), did not cause ("No"), is "debated" or we have no information ("No info") about surface faulting. Data are plotted according to magnitude, bin width is 0.1 magnitude units.

surface faulting effects were attributed only to the main event (M_w 7.6). Other seismic sequences with numerous events included in our dataset are those of 2004 Niigata Prefecture, Japan (10 events, main event M_w 6.6), 2008 Sichuan, China (10 events, main event M_w 7.9), 2018 Porgera, Papua New Guinea (10 events, main event M_w 7.5), in which there was surface faulting but it was attributed to the main event only.

We now focus our attention on the data with certain occurrence/non-occurrence of the surface faulting phenomenon: as for now, there are 76 “Yes faulting” and 191 “No rupture” events.

The percentage of surface-rupturing earthquakes increases with magnitude, as expected: in the magnitude range Mw 5.5-5.9, 10.5% of the events ruptured the surface, while this figure increases to 26.6% in the Mw range 6.0-6.4; to 55.9% in the Mw range 6.5-6.9; to 70% in the Mw range 7.0-7.4; and to 90% in the Mw range 7.5-7.9 (Figure 4, orange dots). It is evident that the greatest increase in “Yes faulting” earthquakes occurs between Mw 6.5 and 6.9.

The next step will be to calculate a regression fit of our data, applying a similar approach to the one adopted by Wells & Coppersmith (1993). They used a "logistic regression" model to evaluate the conditional probability of surface faulting rupture. This model is generally used to evaluate the outcome of a dichotomous variable: if an earthquake happens, surface faulting will or will not occur. The probability of occurrence of principal surface faulting given the occurrence of an earthquake is given by the expression (Wells & Coppersmith 1993):

$$\boldsymbol{P}\ (principal\ surface\ rupture) = \frac{\boldsymbol{e\,f(x)}}{\boldsymbol{1 + e\,f(x)}}$$

Equation 1*: With f (x) = a + bm*

Where *m* is the magnitude of the earthquake and the parameters a and b are estimated from the data.

Figure 4 presents Equation 1 as proposed by Wells & Coppersmith (1993), and the percentage of “Yes faulting” in our dataset, with a bin width of 0.1 magnitude units. In accordance with the work of Youngs et al. (2003), the coefficients for Equation 1 are: a = -12.51; b =2.053.

The earthquakes included in the new dataset show a lower tendency to create surface faulting than those contained in the Wells & Coppersmith (1993) dataset (Figure 4). As a first approximation, we can propose several hypotheses to explain such behavior, mainly dealing with the role of epistemic uncertainty: our dataset covers the period 1992-2018, while the Wells & Coppersmith dataset cover the time period 1847-1992. We argue that in the last 30 years or so the documentation of surface faulting gained an increased attention in the scientific community; this has been fostered by the acknowledgment of the critical role posed by fault displacement hazard for high-risk plants or engineering infrastructures, and subsequent guidelines and best practices (e.g., IAEA technical documents). Additionally, the last decades have seen tremoendous technological improvements (e.g., InSAR, optical image correlation), which allow to investigate the seismogenic source and whether or not it caused surface faulting.

CONCLUSION AND PERSPECTIVES

The preliminary data presented here will provide the grounds to update previous databases and to derive updated regressions on the probability of primary surface faulting. We will explore the likelihood of faulting at the global, localized, or kinematic type level. We envisage that the new regressions that we will develop could be used in probabilistic assessments, for instance building alternative branches of logic trees.

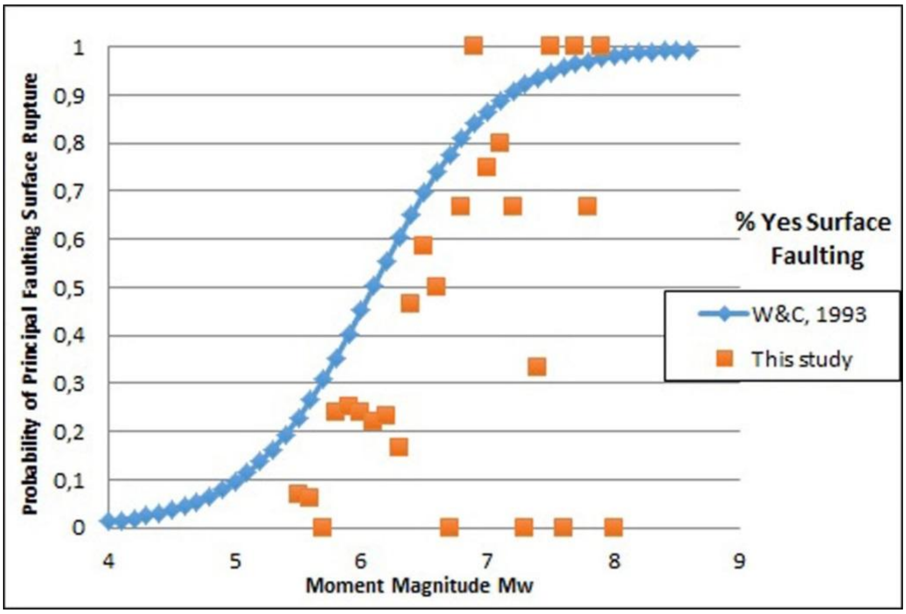

Figure 4: Empirical models for Conditional probability of surface rupture by principal faulting, as proposed comparison of values obtained by Wells & Coppersmith (1993). The coefficients for Equation 1 are a = -12.51, b = 2.053 (Youngs et al., 2003).

REFERENCES

IAEA, 2010. Seismic hazards in site evaluation for nuclear installations, *IAEA Safety Standards Series, Specific Safety Guide*, SSG-9, IAEA, Vienna, Austria.

IAEA, 2021a. Seismic hazards in site evaluation for nuclear installations no. DS507, Revision of Safety Guide SSG-9, IAEA, Vienna, Austria (in publication).

IAEA, 2021b. An Introduction to probabilistic Fault Displacement Hazard analysis in site evaluation for existing nuclear installations, IAEA, Vienna.

International Seismological Center, 2022. ISC-GEM Earthquake Catalogue, Version 9.0, https://doi.org/10.31905/d808b825

Lettis, W. R., Wells, D. L., & Baldwin, J. N., 1997. Empirical observations regarding reverse earthquakes, blind thrust faults, and quaternary deformation: Are blind thrust faults truly blind?. *Bulletin of the Seismological Society of America*, *87*(5), 1171-1198.

Pezzopane, S. K., & Dawson, T. E., 1996. Fault displacement hazard: a summary of issues and information. *Seismotectonic Frame work and Characterization of Faulting at Yucca Mountain, Nevada*.

Wells, D. L., & K. J. Coppersmith, 1993. Likelihood of surface rupture as a function of magnitude, *Seismol. Res. Lett.* 64, no. 1, 54.

Youngs, R. R., W. J. Arabasz, R. E. Anderson, A. R. Ramelli, J. P. Ake, D. B. Slemmons, J. P. McCalpin, D. I. Doser, C. J. Fridrich, F. H. Swan, et al., 2003. A methodology for probabilistic fault displacement hazard analysis (PFDHA), *Earthq. Spectra* 19, no. 1, 191– 219, doi: 10.1193/1.1542891.

INQUA Focus Group Terrestrial Processes Perturbed by Tectonics (TPPT)

paleoseismicity.org

Characterization of normal fault scarp using convolutional neural network: application to Mexico

Lea, Pousse-Beltran (1), Sophie, Giffard-Roisin (1), Laurence, Audin (1), Pierre, Lacan (2), Théo, Lallemand (1), Glenn, Cougoulat (3), Andres, Nuñez Meneses (2)

(1) Univ. Grenoble Alpes, Univ. Savoie Mont Blanc, CNRS, IRD, Univ. Gustave Eiffel, ISTerre, 38000 Grenoble, France. Email address of corresponding author: lea.pousse@univ-grenoble-alpes.fr

(2) Centro de Geociencias, Universidad Nacional Autónoma de México

(3) LJK - Laboratoire Jean Kuntzmann, Université Grenoble Alpes, France

Abstract: *Fault markers in the landscape (scarps, offset rivers) are records of fault activity. The geomorphological characterization of these markers is currently a time-consuming step with expert-dependent results, often qualitative and with uncertainties that are difficult to estimate. To overcome those issues, we are developing a bayesian supervised machine learning method using convolutional neural networks (CNN) trained on a database of simulated topographic profiles across normal fault scarps, called ScLearn. From a topographic profile the implemented, ScLearn is able to automatically give the scarp heigth with an uncertainty, and to show the area of the profile containing the scarp. We apply ScLearn for the characterization of normal active faults in the Trans-Mexican Volcanic Belt. From this specific case study, we will explore the progress (computation time, accuracy, uncertainties) that machine learning methods bring to the field of morphotectonics, as well as the current limits (such as bias).*

Key words*: machine learning, normal fault scarp*

Introduction

Fault marker characterization is necessary to understand past fault activity, the physical processes that govern fault rupture, and hence to improve seismic hazard estimates. Among the examples of characterization, the estimation of marker offset by ruptures that have reached the surface is a parameter directly used to estimate fault rates, or the spatial pattern of past ruptures, or the number of ruptures. Currently the estimation of this offset is done by empirical or semi-automatic approaches (i.e. Hodge et al. 2019; Wolfe et al. 2020). These methods are often time consuming and user dependent.

Today, AI techniques have proven to be efficient in performing automatic tasks in geosciences (i.e. Ren et al. 2020), and in particular Convolutional Neural Networks (CNN), a deep learning architecture specifically designed for processing image or series, have made it possible to perform automatic mapping of fractures (Mattéo et al. 2021). Here we propose to automatize the following fundamental task in morphotectonics analyses by evaluating the ability of a CNN to characterize a normal fault scarp (surface offset, position).

Scope

The CNN ScLearn presented is applied to normal fault scarp on topographic profiles perpendicular to the fault (see *Figure 1*). The profiles are first extracted by the user from terrain elevation models, each one consisting in a series of 500 spatial points. We also assume that the fault is crossing in the middle of the topographic profile, and that the area is only sparsely anthropized. The ScLearn CNN estimates the total surface offset with a model uncertainty. Furthermore, to explain the results, we produce a visualization of the ScLearn CNN intermediate steps, providing insights of where the ScLearn CNN focuses its attention (i.e. the scarp area).

ScLearn is trained on realistic synthetic topographic profile catalogs. Those synthetic are created by a simulator developed here. Synthetic profiles characteristics are therefore based on the choices made to simulate (see details in the methodological section). Here the simulator create only one fault branch in the middle of the topographic profile, this fault branch ruptures several times creating fault scarp. At each inter-seismic period, the scarp is subjected to some diffuse erosion (*Figure 1*), and random perturbations are also added to produce a realistic profile.

After training on the synthetic data, ScLearn is tested on Mexico in the Trans-Mexican Volcanic Belt *(Figure 2). Th*is region is affected by more than 600 potentially active faults yet less than 5% have been correctly characterized by paleoseismological studies (Núñez Meneses et al. 2021). In this context, a robust and automatic method to characterize the normal fault active scarp in a global, reproducible, robust (not expert-dependent) quantitative way is very valuable and a great step towards a better characterization of the region seismic hazard. To do so, we sampled real data across Ameca-Ahuisculco fault system *(Figure 2)*. We will compare the ScLearn's results with existing empirical and semi-automatic methods: MCSST (Monte Carlo Slip Statistics Toolkit of Wolfe et al. 2020) and SPARTA (Scarp PARameTer Algorithm of Hodge et al. 2019).

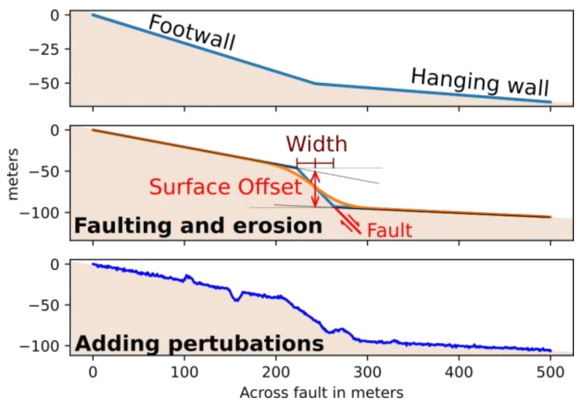

Figure 1: Synthetic normal fault scarp produced by our simulator pipeline to train ScLearn. The total surface offset (in meters) is used as the ground truth label.

Methodology

The scarp "simulator" pipeline:

To train the CNN, we simulate 1000 different topographic profiles with random parameters (*Figure 3*). They have two slopes, one for the hanging wall and one for the footwall (uniform distribution between 0° and 20°). The simulator breaks a single fault branch, with a dip randomly set between 30° and 50° (unif. distribution). The rupture location is randomly set to ± 5% from the profile center (Gaussian distribution). At each rupture, a fault scarp is created (for a total cumulative throw in an uniform distribution between 0 and 50m). Then, between each rupture a diffusive erosion (Avouac et Peltzer 1993) following Smith et Bretherton (1972)'s equation is simulated with a random constant diffusion (uniform distribution between 0.5 and 10 m^2/kyr). The seismic recurrence is also random, but is constrained by a throw velocity between 0.05 and 20 mm/yr. Once the ruptures are produced, we add perturbations to create a realistic morphology using random hyperbolas such as in Hodge et al., (2020) to represent trees, narrow drainage, wide rivers, hills. Finally, we add a Gaussian noise. The resolution of the profile is 500 points. Here we use 1m resolution.

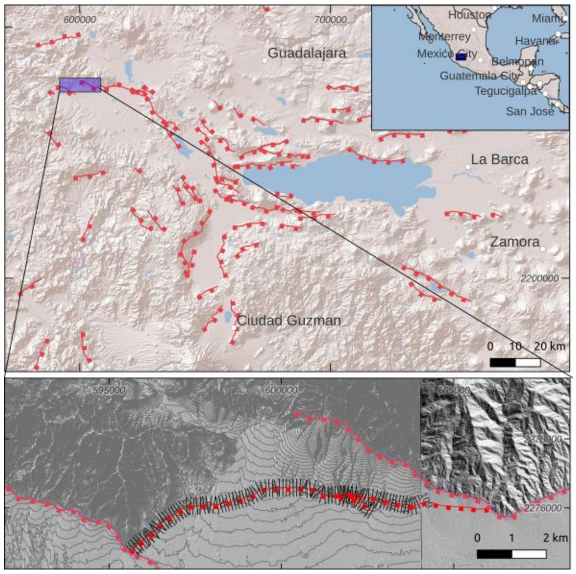

Figure 2: Topographic profile locations across the Ameca-Ahuisculco fault system in the Trans-Mexican Volcanic Belt. Red lines are active faults from Núñez Meneses et al. (2021), light gray lines are 10m elevations contours, black lines are topographic profiles.

The CNN ScLearn :

In order to weight the final assessments of morphotectonic analyses, uncertainty quantification is crucial, in particular for the scope of probabilistic seismic hazard models. To address it, we estimate the model uncertainty in the CNN using variational Bayesian learning inference (*Figure 3)*. We follow the method of Blundell et al. (2015) which assigns probability distribution on the weights of a neural network. The CNN training then consists in reducing the error between predicted and real offsets while estimating consistent uncertainties. In addition, we also show a visualization of the intermediate steps of the CNN processing (in intermediate feature maps) to understand better how the CNN identifies the fault scarp (Zeiler et al. 2014). The visualization on a processed profile allows making sure that the prediction of the surface offset has been calculated from the fault scarp area. This can be useful in complex areas that are at the limits of the application requirements.

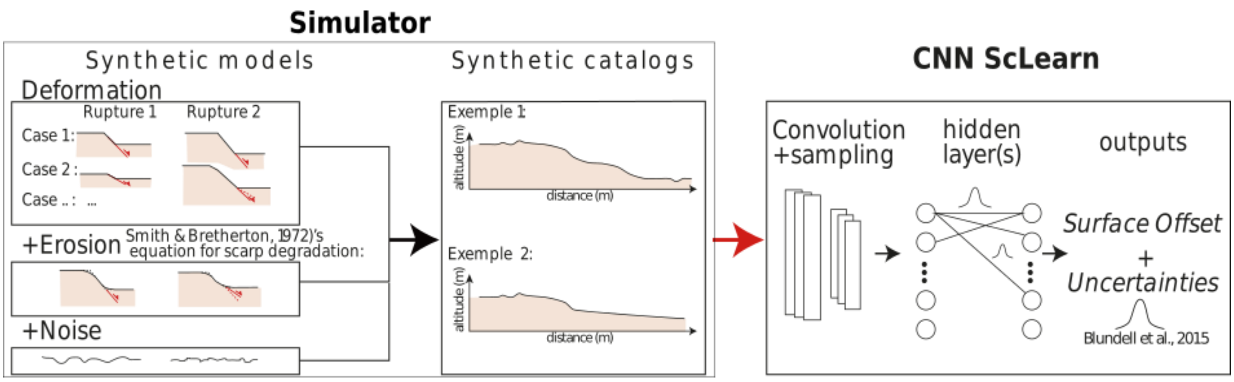

Figure 3: Synthetic normal fault scarp produced by the simulator pipeline to train ScLearn. The total surface offset is fixed as the ground truth.

Results

We first test our CNN model on a second simulated dataset: 1000 profiles created using the same simulator pipeline. Training the CNN on the synthetic data yields a mean accuracy of 4.1 m. Furthermore, we observe that where the predictions are correct the uncertainty bars (*3σ*) are reduced, while the distant predictions have larger errors allowing encompassing the actual values (*Figure 4*).

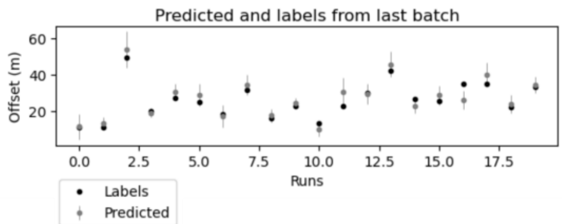

Figure 4: Validation of ScLearn. Labels (ground truth) and predictions of the last batch of validation using synthetic data. Here uncertainty bars show 3σ.

For validation on real data; we apply ScLearn, SPARTA and MCSST to 110 topographic profiles (*Table 1 and Figure 5*) extracted along the Ameca-Ahuisculco fault system. Empirical and semi-automatic methods are time-consuming (several days), do not always produce results and the estimates depend on the user (several choices to make). The ScLearn CNN allows obtaining results within a second, for every profile, independent of the user and therefore reproducible. Compared to the MCSST result, the ScLearn gives a mean residual of 1.9m (median 0.5m) (and a mean 3.0m and a median 1.5m using absolute residual). The residual standard deviation is 4.6m. In addition, there is a constant variance at every level of scarp height. Finally, the CNN predictions overlaps MCSST results at 66.6 % at 3-sigma.

	Average surface offset	*Mean residual (from the MCSST value)*	*Proportion of profiles with overlapping uncertainty bars for CNN and MCSST (3σ)*
	Comparison for all 110 profiles		
MCSST	9.0 m	/	66.6 %
CNN	6.6 m	3.0 m	
	Comparison for the subset of profiles (22) estimated by SPARTA*		
MCSST	17.3 m	/	50 %
SPARTA	12.2 m	4.9 m	
CNN	11,4 m	5.6 m	

*Table 1: Comparison between ScLearn, SPARTA and MCSST from 110 topographic profiles sampled across the Ameca-Ahuisculco fault system. * SPARTA does not give a prediction when the profile is too complicated.*

Discussions and conclusions

ScLearn is comparable with semi-automatic methods and overlaps the MCSST results on 66.6% of the cases. Although the distribution of residuals is centered around 0.5m (median 0.5 m and mode is 0.5 m), there are complicated profiles where the CNN differs from the MCSST, such as in Figure 6. This is due to the fact that the CNN has been trained by synthetic data that does not take into account this type of configuration: antropized area, with high slope in hanging wall. Although the CNN is automatic, it is always necessary to have an expert overview on the context in which the CNN can be applied or not. Here it depends on the fault scarp model: one fault branch, sparsely anthropized, hanging and footwall slope between 0 and 20°. However, once these conditions are fulfilled, the ScLearn allows gaining considerable expert time, to obtain reproducible results, not depending on the user, and to make many measurements with uncertainties. This provides therefore a reliable database on which to perform further fault analysis. This abstract thus shows the potential of the proof of concept of CNN for scarp characterization. Moreover, a future development will consider a larger variety of profiles in order to be able to estimate the scarp in much more contexts. A future study will also estimate other scarp parameters such as two fault branchs, antropized area,…

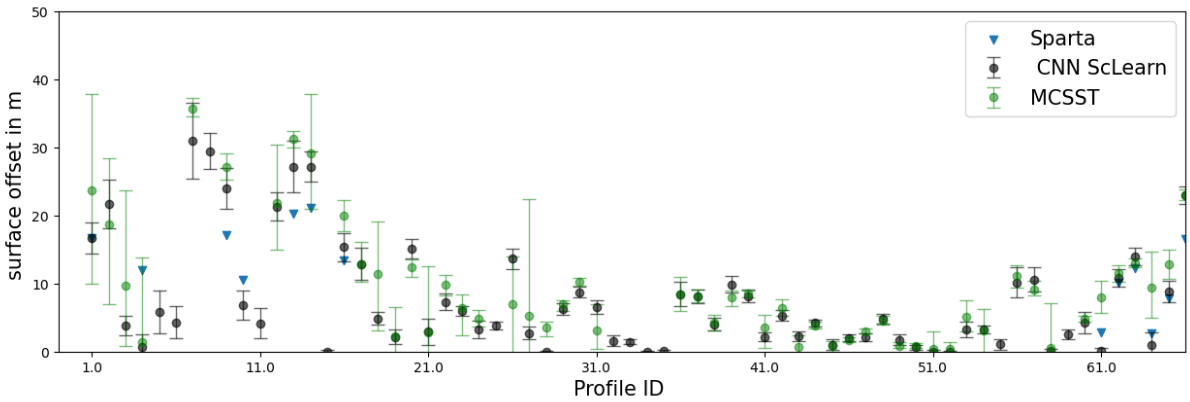

Figure 5: Comparison with ScLearn predictions, SPARTA and MCSST estimations for the first 65 profiles of the 110 topographic profiles across one segment of the Ameca-Ahuisculco fault system. Bars uncertainties show 3σ.

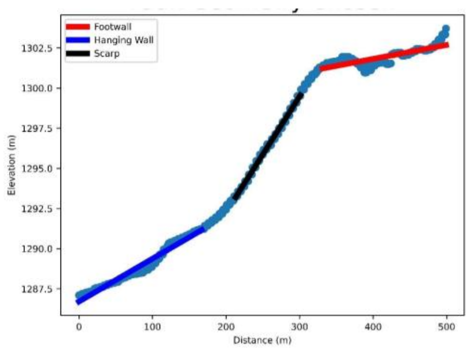

Figure 6: Characterization of the topographic profile 29 through MCSST which allows to estimate a surface offset of 7 ± 0.54 m (2σ) meters, while the CNN predicts a value of 5.6 ± 0,59 m (2σ).

Acknowledgments:

This work has been partially supported by the MIAI@ Grenoble Alpes, (ANR-19-P3IA-0003). Thanks to GRICAD infrastructure (gricad.univ-grenoble- alpes.fr), which is supported by the Grenoble research communities, for the computations. ISTerre is part of Labex OSUG@2020 (ANR10 LABX56). We also thank ISTerre for funding the master internship of Théo Lallemand. We thank the CNES for providing high-resolution optical images. Access to topographic data was granted through the DINAMIS program (https://dinamis.teledetection.fr/).

REFERENCES

Avouac, J., et G. Peltzer. 1993. « Active Tectonics in Southern Xinjiang, China: Analysis of Terrace Riser and Normal Fault Scarp Degradation along the Hotan-Qira Fault System ». *Journal of Geophysical Research: Solid Earth* 98 (B12): 21773-807.

Blundell, C., J. Cornebise, K. Kavukcuoglu, et D. Wierstra, 2015. « Weight uncertainty in neural network ». In International conference on machine learning, 1613-22. PMLR.

Hodge, M., J. Biggs, Å. Fagereng, A. Elliott, H. Mdala, et F. Mphepo. 2019. « A Semi-Automated Algorithm to Quantify Scarp Morphology (SPARTA): Application to Normal Faults in Southern Malawi ». Solid Earth 10 (1): 27-57.

Hodge, M., J. Biggs, Å. Fagereng, H. Mdala, L. N. J. Wedmore, et J. N. Williams. 2020. « Evidence From High-Resolution Topography for Multiple Earthquakes on High Slip-to-Length Fault Scarps: The Bilila-Mtakataka Fault, Malawi ». *Tectonics* 39 (2)

Mattéo, L., I. Manighetti, Y. Tarabalka, J.-M. Gaucel, M. van den Ende, A. Mercier, O. Tasar, et al. 2021. « Automatic Fault Mapping in Remote Optical Images and Topographic Data With Deep Learning ». Journal of Geophysical Research: Solid Earth 126 (4).

Núñez Meneses, A., P. Lacan, F. R. Zúñiga, L. Audin, M. Ortuño, J. Rosas Elguera, R. León-Loya, et V. Márquez. 2021. « First Paleoseismological Results in the Epicentral Area of the Sixteenth Century Ameca Earthquake, Jalisco – México ». *Journal of South American Earth Sciences* 107

Ren, C., C. Hulbert, P. A. Johnson, et B. Rouet-Leduc. 2020. « Chapter Two - Machine Learning and Fault Rupture: A Review ». In *Advances in Geophysics*, édité par Ben Moseley et Lion Krischer, 61:57-107. Machine Learning in Geosciences. Elsevier.

Smith, T. R., et F.. Bretherton. 1972. « Stability and the Conservation of Mass in Drainage Basin Evolution ». *Water Resources Research* 8 (6): 1506-29.

Wolfe, F. D., T. A. Stahl, P. Villamor, et B. Lukovic. 2020. « Short Communication: A Semiautomated Method for Bulk Fault Slip Analysis from Topographic Scarp Profiles ». Earth Surface Dynamics 8 (1): 211-19.

Zeiler, M. D., & Fergus, R. 2014. Visualizing and understanding convolutional networks. In D. Fleet, T. Pajdla, B. Schiele, & T. Tuytelaars (Eds.), Computer vision – eccv 2014 (pp. 818–833). Cham: Springer International Publishing.

INQUA Focus Group Terrestrial Processes Perturbed by Tectonics (TPPT)

paleoseismicity.org

Fault-based seismic hazard assessment for the west of the Trans Mexican Volcanic Belt (TMVB), Central Mexico

Fabien Ramel (1), Pierre Lacan (2), Laurence Audin (3), Ramón Zúñiga (4), Mario Ordaz (4)

(1) Université de Montpellier. fabien.ramel@etu.umontpellier.fr
(2) Centro de Geociencias, Universidad Nacional Autónoma de México. placan@geociencias.unam.mx
(3) IRD-ISTerre, Université Grenoble Alpes. laurence.audin@ird.fr
(4) - Centro de Geociencias, Universidad Nacional Autónoma de México. ramon@geociencias.unam.mx
- Instituto de Ingeniería, Universidad Nacional Autónoma de México. MOrdazS@iingen.unam.mx

Abstract: *In the central part of Mexico, the Trans Mexican Volcanic Belt (TMVB) is affected by extensive tectonic deformation along numerous continental faults. Despite an important historical seismicity and the high population density of this region the hazard associated with these faults is still poorly characterized. Recently, paleoseismological studies highlighted long return periods and slow slip rates (< 1mm/year) for a dozen of these faults. Hence, the classic approach consisting in estimating the hazard from catalogs of seismicity is limited in this context in which the return time of earthquakes is significantly greater than the period covered by the catalogs. A probabilistic assessment of the seismic hazard is presented here for the West of the TMVB based on a source model including all known active faults and using assumptions and extrapolation on the geometry and activity for poorly known faults. Accelerations of 0.2 g and up to 0.5 g (475 years return period) in highly populated areas are calculated and a retro-analysis of the modeling show that a better characterization of the fault segmentation, slip rates and seismogenic depth appears critical for a better hazard assessment.*

Key words*: Continental faults, Probabilistic Seismic Hazard Assesment, TMVB*

INTRODUCTION

Crossing Central Mexican from east to west over more than 1000 km, the Trans-Mexican Volcanic Belt (TMVB) is an active volcanic arc, affected by N-S extensive intra-arc tectonic deformation (Ferrari et al., 2011; Fig. 1). This extension is accommodated along continental faults that are the source of several destructive historical and instrumental earthquakes (Suárez et al., 2019). Approximately 600 potentially active faults have been

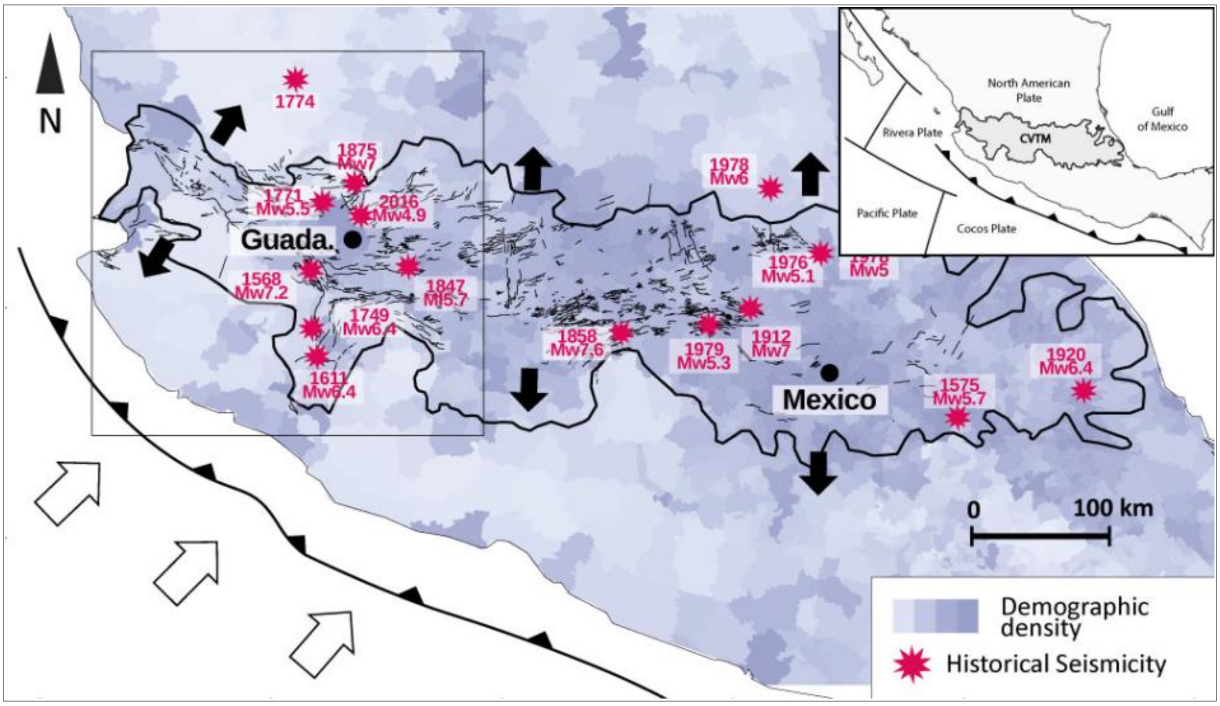

Figure 1. General map of the CVTM showing faults, historical seismicity and population density. Left rectangle : limits of the study area

identified along the TMVB and paleoseismology studies conducted on some of them indicate a return period for Mw>6 earthquake of several thousand years (e.g. Langridge et al., 2000; 2013; Sunye-Puchol et al., 2015; Lacan et al., 2018). These results indicate that the seismic cycle of these faults exceeds the periods covered by instrumental and historical seismicity catalogs by several orders of magnitude. However, studies aiming to characterize the seismic hazard in central Mexico have used only on these seismicity catalogs, which cover only the last 400 to 500 years. Until now, geological fault data such as location, trace, segmentation, kinematics or geometry have never been considered. Consider such data sources is however critical for a better evaluation of the seismic hazard, especially in an area that gathers more than 50% of the mexican population and constitutes the economic and industrial heart of the country.

OBJECTIVES AND METHOD

In order to evaluate the relevance of the integration of fault data in the evaluation of the seismic hazard, we focus on a set of active fault systems affecting the west of the TMVB, around the city of Guadalajara. The Metropolitan Zone of Guadalajara (MZG), with more than 5 million inhabitants, is the second largest city in the country after Mexico City.

The ambition of the present study is to initiate a new approach to overcome the lack of data through a modeling work able to provide a representation of the hazard associated with these faults (Fig.2). In this way, the objective is twofold: (1) provide a preliminary estimate of the hazard for several sites of interest and (2) identify, during the modeling process, the main critical data that we should complete or specify for a better assessment of the seismic hazard in the future. All existing data on fault activity and characteristics are compiled to construct a PSHA (Probabilistic Seismic Hazard Analysis) based on the method of Cornell (1968). The data available for the best studied faults are extrapolated to other structures of the same fault system identified as potentially active and sharing a set of common characteristics (orientation, dip, kinematics, slip velocities...). At each step of the model construction and for each component of the PSHA, a critical discussion mobilizing different experts

Figure 2. Source model map showing source faults and associated slip rates.

(seismologist, paleoseismologist, engineer - seismologist, PSHA expert) allows to convert the bibliographic data into exploitable parameters. The resulting source model, integrating the geometry and activity of the faults, is then used through the R-CRISIS software to calculate the hazard.

Finally, a retro-analysis of the modeling and tests of the impact of the variability of the different parameters used, led to identify the principal missing data requested to improve the model in the future, the limits of the model and the possible sources of improvement.

buildings, which are in the majority within the MZG, are most likely to be affected by the highest acceleration values.

The hazard map completes the analysis by providing a representation of the hazard distribution at the scale of the western TMVB. The hazard distribution directly reflects the location and activity of the faults considered in the source model. The highest hazard levels are concentrated along the major rifts that structure the western TMVB (Tepic, Colima, Chapala). Values up to 0.5 g are reached in densely populated areas at the level of cities of more than 50,000 inhabitants highlighting the

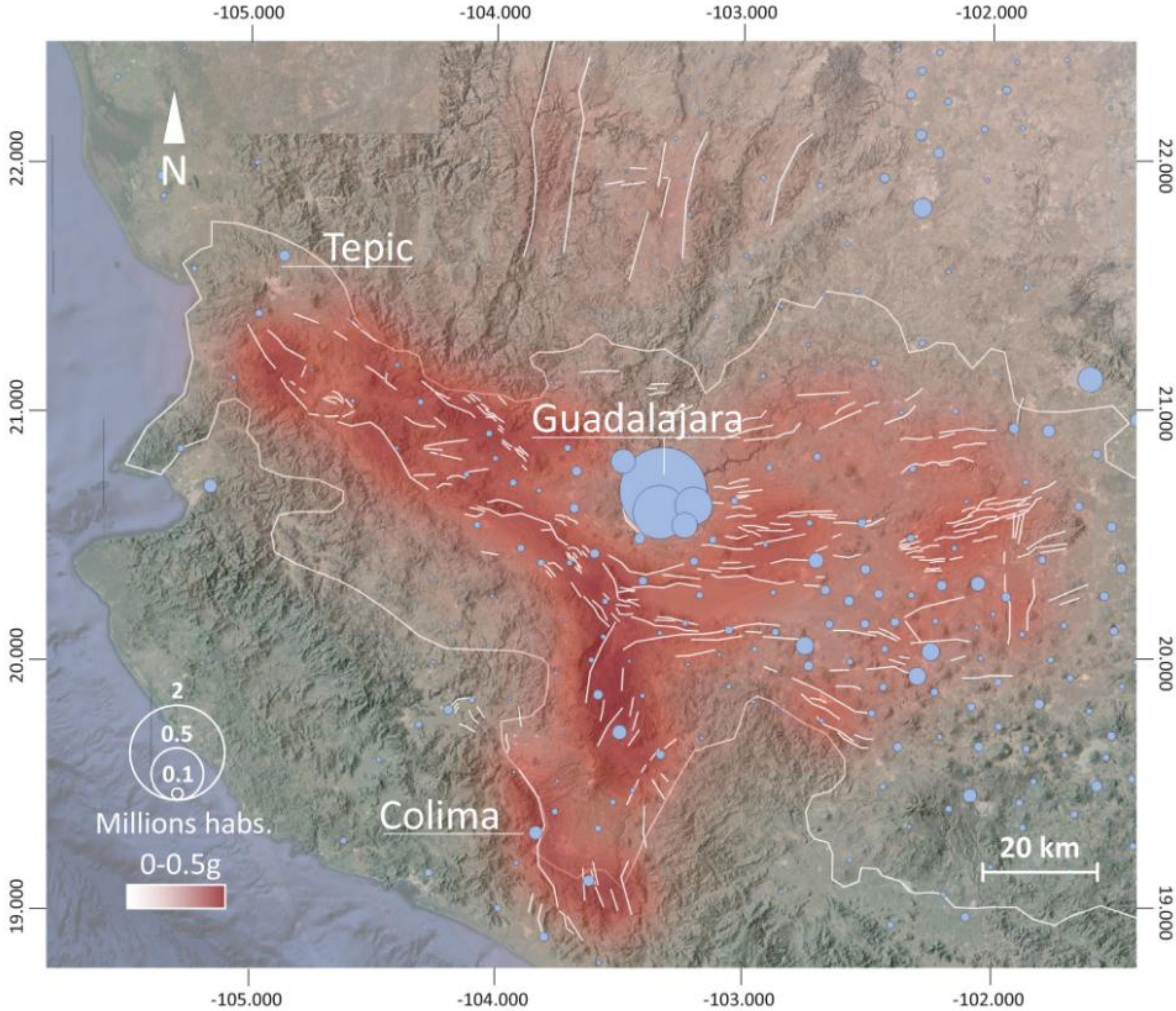

Figure 3: Map of spectral accelerations (period: 0.1s) for a 475-year return period and demography.

RESULTS

Expressed as spectral accelerations for a return period of 475 years, the highest hazard levels for the MZG site are encountered for a period of 0.1s (Fig.3). These values range from 0.15 g to 0.2 g in the city and reach up to 0.4 g at 20 km to the southeast and south east of the city. Considering that infrastructure can suffer significant damage for acceleration greater that 0.05, these hazard levels are significant for the city of Guadalajara. The study of the response spectrum also indicates that small

high hazard represented by the faults.

The impact of the variability of the parameter values on the calculated hazard levels also highlighted the importance of better characterizing some geological parameters. The slip rates and seismogenic depth assigned to the faults as well as the choice of ground motion prediction models appear to be the sources of the greatest variability in hazard levels. The identification of these sources of uncertainty is used here to point out the potential priority for future research, necessary for a better characterization of the seismic hazard.

DISCUSSION AND CONCLUSION

The importance of considering faults as the sources of seismicity in PSHA type analyses is recognized. The UCERF 3 model used in California is an example of the advanced development of this approach. Nevertheless, the traditional approach of representing seismic sources as simple areas of seismicity and using seismicity recurrence models based on the historical and instrumental seismic record is erroneous in slow fault zones such as the TMVB. Generally, the difficulty in identifying potentially active faults and characterizing their activity partly explains the choice of considering only the historical and instrumental seismic record among practitioners, even in a context of slow-moving faults.

The TMVB is traversed by numerous potentially active faults for which the seismic record is limited and not necessary representative of the seismic cycle. In this context, the known seismicity cannot serve as a satisfactory basis for seismic hazard analysis.

By integrating fault data for seismic hazard analysis, the main problem concerns the completeness of the active fault catalog. Exclude the poorly studied faults from the analysis and only considered faults with enough data, as is done in previous studies in central Mexico (GEM,2022), artificially reduces a significant part of the seismogenic potential.

On the contrary, the approach followed in this work, extrapolating fault source data, allows to propose a first source model integrating all the known potentially active faults for the western part of the TMVB and to calculate the hazard for a set of strategic sites. This strategy involves a potentially large margin of error, sometimes difficult to assess, but this one will gradually decrease when more faults in the region will be studied.

The preliminary results obtained suggest that the representation of the distribution and levels of hazard is more realistic than that presented in previous studies (GEM,2022). While the previous models do not show any spatial variation in hazard related to the location of the few faults considered, the hazard distribution of the western TMVB provided in this new model, directly reflects the location and activity of the active faults. Relatively high hazard levels of up to 0.5 g are encountered along the most active structures, some of them are of particular interest since they fit with densely populated areas.

Finally, the analysis of the parameters having the strongest impact on the hazard levels constitutes an integral component of this alternative approach. The key parameters requiring more data acquisition are identified and priority research areas can be defined. This approach aims to better structure the research and to rapidly improve the knowledge of the hazard associated with faults in a region where the human stake is major and requires a particular effort to be engaged.

Acknowledgements: Thanks to Stéphane Mazzotti and Céline Beauval for their expert advice on PSHA.

REFERENCES

Cornell C.A., (1968). Engineering seismic risk analysis. Bulletin of the Seismological Society of America, 58, 5, 1583-1606.

Ferrari, L., Orozco, E.T., Manea, V.C., Manea, M., 2011. The dynamic history of the Trans-Mexican Volcanic Belt and the Mexico subduction zone. Tectonophysics. 522-523. 122-149. 10.1016/j. Tecto.2011.09.018.

GEM, 2022. https://hazard.openquake.org/gem/models/MEX/. (Consulted on 10/02/2022).

Lacan, P., Ortuño, M., Audin, L., Perea, H., Baize, S., Aguirre-Díaz, G., Zúñiga, F.R., 2018. Sedimentary evidence of historical and prehistorical earthquakes along the venta de Bravo fault system, Acambay graben (Central Mexico). Sediment. Geol. 365, 62–77. https://doi.org/10.1016/j.sedgeo.2017.12.008.

Langridge, R.M., Weldon, R.J., Moya, J.C., Suárez, G., 2000. Paleoseismology of the 1912 Acambay earthquake and the acambay-tixmadejé fault, trans-Mexican volcanic belt. J. Geophys. Res. 105, 3019–3037.

Langridge, R.M., Persaud, M., Zúñiga, F.R., Aguirre-Díaz, G.J., Villamor, P., Lacan, P., 2013. Preliminary paleoseismic results from the Pastores fault and its role in the seismic hazard of the Acambay graben, Trans-Mexican Volcanic Belt, Mexico. Rev. Mex. Ciencias Geol. 30 (3), 463–481.

Suárez, G., Caballero-Jiménez, G.V., Novelo-Casanova, D.A, 2019. Active crustal deformation in the trans-Mexican volcanic belt as evidenced by historical earthquakes during the last 450 years. Tectonics 38. https://doi.org/10.1029/ 2019TC005601.

Sunyé-Puchol, I., Lacan, P., Ortuño, M., Villamor, P., Audin, L., Zúñiga, F.R., Langridge, R.M., Aguirre-Díaz, G.J., Lawton, T.F., 2015. La falla San Mateo: nuevas evidencias paleosismologicas de fallamiento activo en el graben de Acambay. Mexico. Rev. Mexicana Ciencias Geol. 32 (3), 361–375. https://doi.org/10.22201/ cgeo.20072902e.2015.3.589.

INQUA Focus Group Terrestrial Processes Perturbed by Tectonics (TPPT)

paleoseismicity.org

The largest earthquake and tsunami of the last five centuries in Mexico uncovered in historical and geological records

María-Teresa Ramírez-Herrera (1), Néstor Corona (2), Rocío Castillo-Aja (3), Jan Cerny (1), Marcelo Lagos (4), Avto Goguitchaichvili(1), M. Luisa Machain (5), María Ortuño (6)

(1) Instituto de Geofísica, Unidad Michoacán, Laboratorio de Tsunamis y Paleosismología, Universidad Nacional Autónoma de México, México. Email: teresar@igeofisica.unam.mx
(2) COLMICH, Centro de Estudios de Geografía Humana, Michoacán, México
(3) Depto. de Geografía y Ord. Territorial, CUCSH. Universidad de Guadalajara, Mexico, México
(4) Instituto de Geografía, Laboratorio de Tsunamis, Pontificia Universidad Católica de Chile, Santiago, Chile
(5) Instituto de Ciencias del Mar y Limnología, Universidad Nacional Autónoma de México, Mexico, Mexico
(6) Ciencias de La Tierra, Universidad de Barcelona, Barcelona, Spain

Abstract: *Instrumental seismic records provide a short timespan to understand earthquake recurrence of large and great events, and to assess earthquake hazard. Historical and geological investigations enlarge the earthquake record and provide data of several hundreds to thousands of years. However, incomplete records due to poor preservation of documents and/or geologic evidence might have less precision. The Mexican Pacific coast is one of the most seismically active regions, where the interaction of the North American and the subduction of Cocos and Rivera plate produces large tsunamigenic earthquakes . The largest instrumentally recorded tsunamigenic earthquakes took place along the subduction boundary. We present here results of historical documents and maps, and geologic evidence of the largest ever recorded earthquake, M8.6, and its tsunami in Mexico in 1787. Our results on tsunami and earthquake modeling confirm a large earthquake that produced coastal coseismic subsidence and a tsunami that flooded more than ~3 km inland.*

Key words*: Tsunami, earthquake, history, geologic record, Mexico .*

THE LARGEST EARTHQUAKE AND TSUNAMI OF THE LAST FIVE CENTURIES IN MEXICO UNCOVERED IN HISTORICAL AND GEOLOGICAL RECORDS

Tectonic setting

The study area sits on the Oaxaca coast, a segment of the Mexican subduction with frequent earthquakes (every +/- 40 yr) and magnitudes ranging from 7.3 to 7.7 (Figure 1).

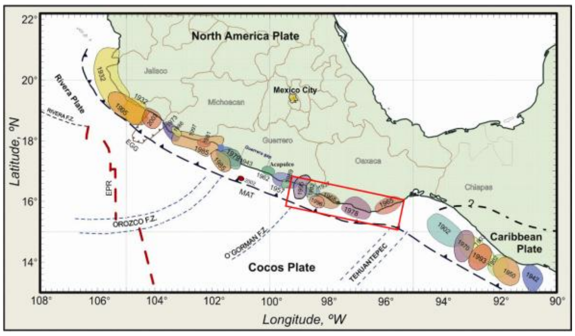

Figure 1. Mexican Subduction zone and most important registered earthquakes. The 1787 earthquake inferred Rupture Length 450 km long and Magnitude 8.6 (Suárez & Albini,2009)

Original Historical Accounts

The 1787 great earthquake (M 8.6) triggered a deadly tsunami that poured over the coast of Oaxaca, Guerrero, and Chiapas, along more than 500 km of the Mexican Pacific coast and up to 6 km inland (Orozco y Berra, 1887, 1888). This tsunami, according with historical documents, destroyed mostly farmlands and livestock, and damaged few villages since the density of population was sparse at the time (Figure 2).

"On Wednesday, 28 March, between 11 am and pm 12 local time, the first of a series of earthquakes was felt on the southeast coast of the Mexican Pacific, in central Mexico and even in the Gulf of Mexico. The most intense of the earthquakes occurred on the 28 March (M = 8.6 according to Suarez & Albini2009) and on April 3 (M = 7.3) during the morning (Orozco y Berra, 1888) (Figure 1).

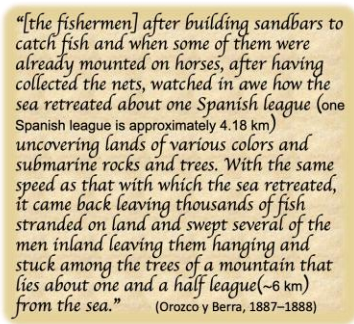

"[the fishermen] after building sandbars to catch fish and when some of them were already mounted on horses, after having collected the nets, watched in awe how the sea retreated about one Spanish league (one Spanish league is approximately 4.18 km) uncovering lands of various colors and submarine rocks and trees. With the same speed as that with which the sea retreated, it came back leaving thousands of fish stranded on land and swept several of the men inland leaving them hanging and stuck among the trees of a mountain that lies about one and a half league(~6 km) from the sea." (Orozco y Berra, 1887–1888)

Figure 2. Description of the 1787 tsunami in the Alotengo Lagoon (today renamed as the Corralero Lagoon), translated to English from old Spanish (Orozco y Berra, 1888).

Mexico´s recorded history of earthquakes goes back to the Aztecs civilization. We uncovered an earthquake and likely associated tsunami dating back to 1537. “"*This year Six Houses and from 1537, the Black people in Mexico City wanted to rise [...] The star was smoking and there was an earthquake, the greatest of which I (*Pedro de los Ríos, Dominican monk*) have seen, although I have seen many from these parts*” (Source: Codice Telleriano-Remensis. Universitätsbibliothek Rostock—Codex Telleriano-Remensis (Loubat 1901) (Figure 3).

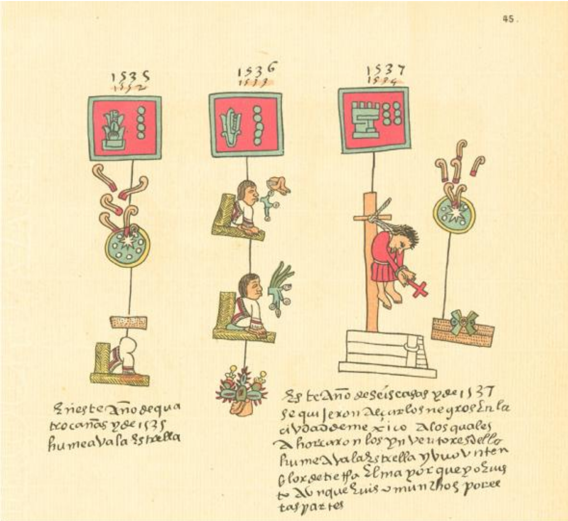

Figure 3. Codex Telleriano-Remensis with description of year 1537 earthquake. Codice Telleriano-Remensis. Universitätsbibliothek Rostock—Codex Telleriano-Remensis (Loubat 1901).

Geologic record of earthquakes and tsunamis

We report first on historical and geological evidence from the Corralero lagoon and adjacent coastal plain that corroborate these historical accounts. The evidence of the 1787 tsunami can be traced along a transect of cores and test pits from the coastline and up to 1.6 km inland (Figure 4).

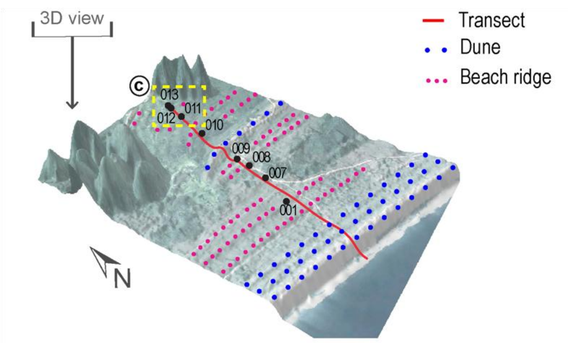

Figure 4. Tsunami deposits in swales. Transect 1.5 km long.

The test pits showed an anomalous sand layer apparently deposited in a single event in the swales of a series of beach ridges. The anomalous layer is continuous along the transect, about a 1000 m-long, and is formed of coarse to medium sand, at depths from 36 to 64 cm depth, with variable thickness, reaching about 28 cm and pinching with the distance from the coastline. We used stratigraphy, grain size, microfossils (foraminifera and diatoms), magnetic susceptibility and anisotropy of magnetic susceptibility proxies to reveal the nature of this anomalous sand layer. These proxies support a sudden and rapid event, consisting of sands transported by an extreme sea-wave far inland. Furthermore, based on the accounts of the 1787 earthquake (M 8.6) and tsunami, and Pb210 dates, we unravel this unit as the tsunami deposit left by this event (Figure 5).

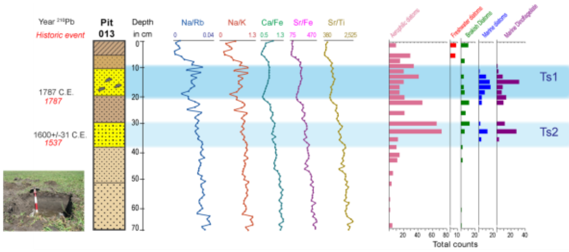

Figure 5. Stratigraphic, geochemical, diatoms proxies and ^{210}Pb and ^{14}C dates of tsunami deposits from 1787 and 1537 earthquakes. (Modified from Ramirez-Herrera et al., 2020).

Acknowledgements: M.T.R. acknowledges research support by grant numbers UNAM-PAPIIT-IN107721, CONACYT-SEP 284365, and CTIC-Intercambio Académico. J.C. was supported as a postdoctoral research assistant on UNAM-DGAPA-CTIC grant.

REFERENCES

Silva, P.G., Rodríguez-Pascua, M.A., Pérez-López, R., Giner-Robles, J.L., Lario, J., Bardají, T., Goy, J.L., & Zazo, C., 2009. Geological and archaeological record of the 1504 AD Carmona earthquake (Guadalquivir Basin, South Spain): a review after Bonsor, 1918. In: *Archaeoseismology and Palaeoseismology in the Alpine-Himalayan Collisional Zone* (Pérez-López, R., Grützner, C., Lario, J., Reicherter, K., Silva, P.G. eds). Baelo Claudia, Spain, 139-142.

Suarez, G. & Albini, P., 2009. Evidence for Great Tsunamigenic Earthquakes (M 8.6) along the Mexican Subduction Zone. *Bulleting of the Seismological Society of America* **99**, 892–896. https://doi.org/10.1785/0120080201

Orozco y Berra, J., 1888.Efemérides Sísmicas Mexicanas. *Memorias de la Sociedad Científica 'Antonio Alzate'* **I**, 303–541

Loubat, J. F. Facsimilies of the Codex Telleriano-Remensis, 2006. http://www.famsi.org/research/loubat/Telleriano-Remensis/thumbs0.html, last access: 31/Mar/2020

Ramírez-Herrera, MT., Corona, N., Cerny, J. *et al.*. 2020. Sand deposits reveal great earthquakes and tsunamis at Mexican Pacific Coast. *Sci Rep* **10**, 11452. https://doi.org/10.1038/s41598-020-68237-2

Paleoseismological investigations of the La Rouvière fault, unexpected source of the 11-11-2019, Mw4.9 Le Teil surface rupturing earthquake (Cévennes fault system, France)

J-F Ritz (1), S. Baize (2), N. Cathelin (1,2) , C. Thomasset (1, 3), M. Riesner (4, 7), E. Hannouz (5), M. Ferry (1), C. Larroque (6), L. Audin (5), L. Bollinger (4), K. Manchuel (3), C. Sue (5), M. Rizza (7), H. Jomard (2), C. Vergniault (3), P. Arroucau (3), R. Le Roux-Mallouf (3)

(1) Geosciences Montpellier, Univ. Montpellier, CNRS, Univ. Antilles, Montpellier, France. Jean-francois.ritz@umontpellier.fr
(2) Institut de Radioprotection et de Sûreté Nucléaire (IRSN), Fontenay-aux-roses, France.
(3) EDF-DIPNN-DI-TEGG, Aix-en-Provence, France
(4) Département Analyse Surveillance Environnement, CEA, DAM, DIF, 91297 Arpajon, France
(5) ISTerre, Université de Grenoble Alpes, Université Savoie Mont Blanc, CNRS, IRD, IFSTTAR, Grenoble, France
(6) Université Côte d'Azur, CNRS, Observatoire de la Côte d'Azur, IRD, Géoazur, 250 rue A. Einstein, Sophia Antipolis 06560 Valbonne, France
(7) Aix Marseille Univ., CNRS, IRD, INRAE, Collège De France, CEREGE, Aix-en-Provence, France

Abstract: *The 2019-11-1, Mw4.9 Le Teil earthquake occurred within the NE termination of the Cévennes faults system (CFS) in southern France, along the La Rouvière fault (LRF), an Oligocene normal fault which was not assessed to be potentially active. This shallow moderate magnitude reverse-faulting event produced a 5 km-long surface rupture and strong ground shaking. No evidence of previous quaternary activity was observed in the morphology, raising the question whether the LRF had been reactivated for the first time since the Oligocene or had broken the surface in the past without being detected in the morphology. To answer this question, we carried out paleoseismological investigations along the LRF to analyze and characterize evidences of paleo-ruptures in Quaternary deposits.*

Key words*: Cévennes faults system, La Rouvière fault, shallow fault reactivation, moderate magnitude, reverse-faulting*

INTRODUCTION AND TECTONIC SETTING

The Mw 4.9 Le Teil earthquake occurred in southern France, in the Rhône river valley near Montélimar, on November 11, 2019 (Fig. 1a). It corresponds to a historically unprecedented event in several ways. This was the first time in France that a surface rupture associated with an earthquake was observed and comprehensively measured on live (Fig. 1c), and it was the first time that an earthquake was clearly associated with the inversion of an ancient fault– i.e La Rouvière Fault - inherited from the Oligocene extensional period (Ritz et al., 2020; Cornou et al., 2021). The La Rouvière Fault belongs to the Cevennes Faults system (CFS) a major crustal structure, inherited from a rich polyphased tectonic history that began during the Variscan orogeny. This NE-SW trending, 120 km-long fault system is located at the boundary between the Massif Central crystalline basement and the sedimentary basin of southeastern France (Fig.1b).

Several authors stated that this fault system could have been active, either normal (Bishop and Bousquet, 1989) or transcurrent (Lacassin et al., 1998a) during recent times, based on geomorphological analyses. However, definitive evidence of past surface-rupturing events was missing, leading to intense debates (Ambert et al., 1998, Sébrier et al., 1998; Lacassin et al., 1998b). As for the LRF strictly speaking, no Quaternary evidence of tectonic activity had been collected so far, so that this fault is not reported as a potentially active one in the existing database (Jomard et al., 2017). The rupture, with a focal depth estimated at 1.5 ± 0.5 km (Delouis et al., 2021), generated strong ground motion in the epicentral zone, with maximum accelerations exceeding the gravity acceleration near the fault (Causse et al., 2021). The heaviest damage was observed in the villages of Le Teil and Viviers, with EMS98 macroseismic intensities of VII, or even locally VIII (Schlupp et al., 2021), a level of damage never reached in metropolitan France since the earthquake of Arette in 1967.

This significant earthquake raises important questions in terms of seismic hazard: Had the La Rouvière fault already broken in the past? Could other faults of the NE termination of the Cévennes fault system also produce this type of event? To answer these questions, a collaborative research program (FREMTEIL 2021-2023: “Faults, Ruptures and Strong Movements: What consequences for the seismic hazard in the TEIL region") involving several academic laboratories as well as several institutes has been launched, with the support of the CNRS-INSU and the numerous institutional collaborators. In this paper, we present some of our paleoseismological investigations, which allow us to show that the Rouvière fault had already ruptured in the past.

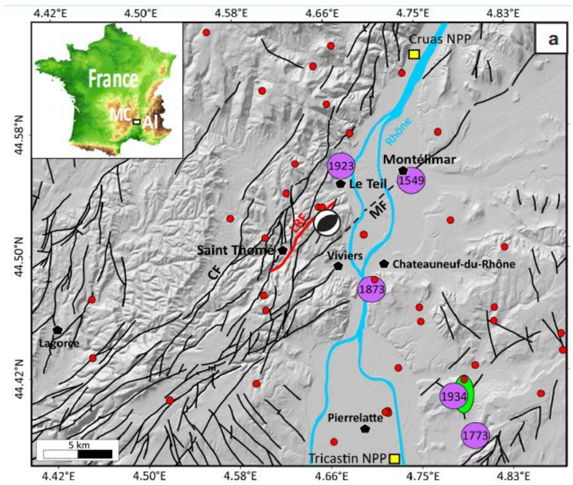

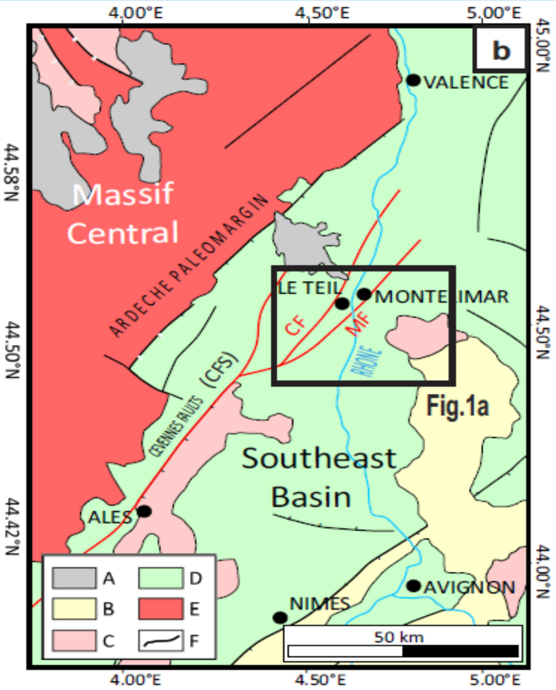

Figure 1 (a et b, [after Ritz et al., 2020): (a) Seismotectonic map of the Rhône River Valley where the November 11th, 2019 Mw4.9 Le Teil earthquake (44.518°N and 4.671°E) occurred. The black and white sphere indicates the reverse faulting focal mechanism; red and purple circles are instrumental and historical seismicity, respectively; the green ellipse corresponds to the Tricastin swarm; black lines are faults from the Aubenas geological map [Elmi et al. 1996] with the La Rouvière Fault (LRF) in red; CF: Cévennes Fault, MF: Marsanne Fault; the shaded DTM is from BD ALTI 25 m (IGN); MC and Al in the inset are Massif Central and Alps, respectively. (b) Simplified geological map of the western boundary of the South-eastern Basin [Roure et a., 1992; Chantraine et al., 1996] A, Plio-Quaternary volcanism; B, Miocene-Pliocene sediments; C: Oligocene sediments; D: Mesozoic sediments; E: Paleozoic crystalline basement (Massif Central); F, major faults (NE termination of the Cevennes fault system (CFS) in red, CF and MF for Cévennes Fault and Marsanne Fault, respectively). Black dots indicate main population centres. From Ritz et al. (2020). (c) One of the example of surface rupture associated with the 2019 Mw4.9 Le Teil earthquake.

PALEOSEISMOLOGICAL INVESTIGATIONS ALONG THE LA ROUVIÈRE FAULT

We carried out paleoseismic investigations along the La Rouvière Fault to analyse and characterize evidences of paleo-ruptures in Quaternary deposits. Thirteen trenches were dug along the section that broke the ground surface in 2019 (Fig.2). Several trenches within 2 sites (LR4 and LR1) yielded favourable Quaternary deposits (slope colluvium and eolian deposits) lying against the ancient LRF normal fault mirror carved in the Barremian limestones to document past-coseismic deformations.

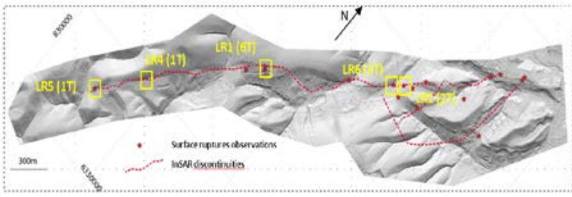

Figure 2: Location of the 5 sites (number of trenches per site in parenthesis) where 13 trenches were dug across the La Rouvière Fault and/or traces of 2019 earthquake surface effects. The 25-cm-resolution shaded relief topographic map with the surface ruptures observations (red stars) are from [Ritz et al., 2020].

The AMS radiocarbon and OSL dates (from "bulks" collected into colluvium clayey-silty matrices) within 3 trenches located in the central and southern parts of the LRF (LR6-TB, LR6-TD, LR4-TA) suggest that at least one event prior 2019, occurred after ~13 ka [Ritz et al., 2021]. In the trench LR1-TB, where we obtained the more age constraints, the age of this previous event is bracketed between 13.5 and 3.3 ka (Fig.3 up) [Ritz et al., 2022].

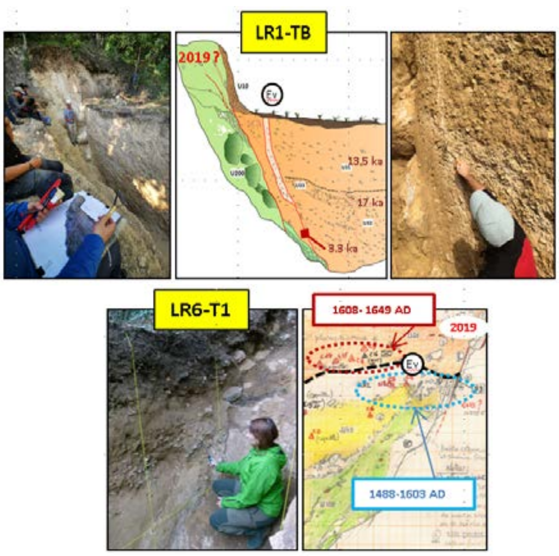

Fig. 3 [after Ritz et al., 2021, 2022]: Summary of the age constraints obtained within trenches LR1-TB (up) and LR6-T1 (down) dug across the central segment of the La Rouvière Fault that broke on 11-11-2019 during the Le Teil surface rupturing earthquake.

Within the northern part of the 2019 rupture, the radiocarbon dates of charcoals collected within trench LR6-T1 dug in younger deposits suggest that a younger event occurred between the end of the 15th century and the beginning of the 17th century with kinematic characteristics similar to the 2019 event (sense of movement, amount of displacement (Fig.3 down)

CONCLUSIONS AND PERSPECTIVES

Our study demonstrates that the LRF have had previous surface rupturing earthquakes prior to the 2019 event, without any clear consistent morphological imprint. We thus infer that, in a plate interiors such as metropolitan France, active faults capable of producing such earthquakes are not necessary detectable in the morphology. Concerning the La Rouvière Fault example, this can be explained by the small amount of displacement and a long return period, consistent with the low strain rate (0.5–1.0 x 10-9 yrs-1) measured by GPS in the region (Masson et al., 2019), easily balanced or even exceeded by erosion processes. To go further in the characterization of potential active faulting along the other faults segments of the Cévennes fault system - in order to be able to best determine where to set up trench sites - we are now performing detailed geophysical surveys at the intersection areas between the different faults and the Quaternary markers. Figure 4 shows an example of such an approach within the Marsanne fault, which bounds the northeastern termination of the Cévennes fault system along its southeastern border (see “MF” in Fig.1B).

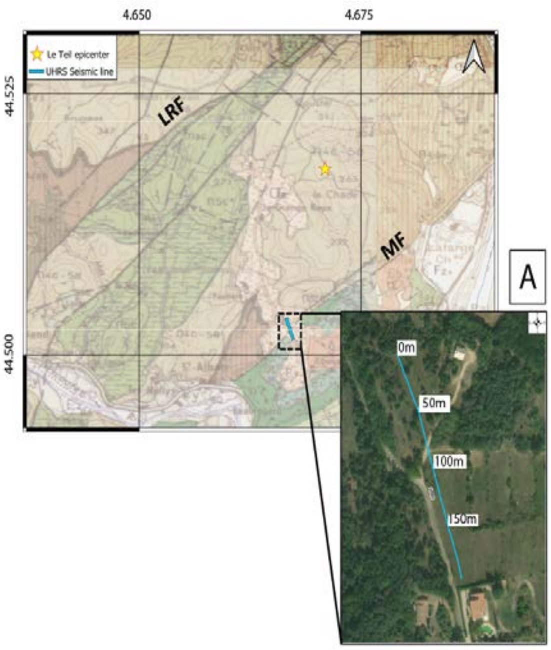

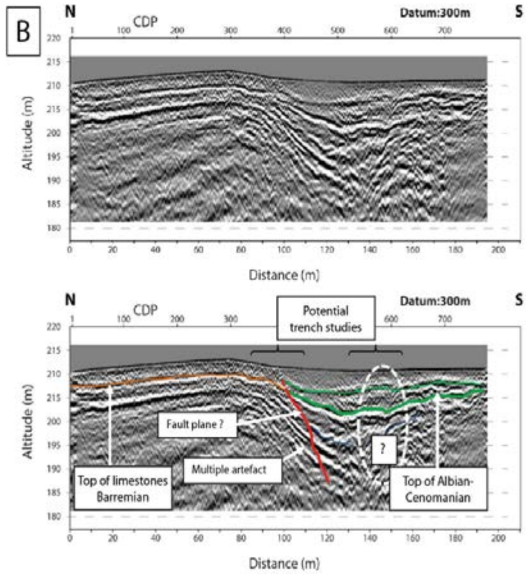

Figure 4 [after Ritz et al., 2021; Manchuel et al., 2022]: (A) Location of UHRS profile across the Marsanne fault (MF) LRF= La Rouvière Fault. (B) Seismic line (lower section = potential interpretation).

The UHRS (Ultra High Resolution Seismic) survey [e.g. Vergniault et al., 2019] was performed at a site where the Marsanne fault is mapped below Plio-Quaternary deposits (Fig. 4A). It shows an interruption of the horizontal continuity of some reflectors that are interpreted as the occurrence of the fault bellow the young deposits (Fig.4B). In 2022, we opened a new trench within these deposits in order to analyze the Quaternary activity of the Marsanne fault. Results are in progress.

Acknowledgements: Authors thanks the INSU-CNRS, the IRSN, EDF, the CEA as well as the academic laboratories Geosciences Montpellier, Isterre and Géoazur for their supports.

REFERENCES

Ambert P., H. Philip And J-F. Ritz, 1998, Geomorphic evidence for Quaternary sinistral slip on the Cevennes fault (Languedoc, France) – Comment, C. R. Acad. Sci. Paris, 327, 855-859Bishop, P., Bousquet, J.-C., 1989. The Quaternary terraces of the Lergue River and activity of the Cévennes Fault in the lower Hérault valley (Languedoc), southern France. zfg 33, 405–415.

Causse, M., Cornou, C., Maufroy, E., Grasso, J. R., Baillet, L., and El Haber, 2021, Exceptional ground motion during the shallow M w 4.9 2019 Le Teil earthquake, France. Commun. Earth Environ., 2(1), 1-9.

Chantraine J., Autran A., Cavelier C., 1996, Carte géologique de la France, 6ème édition, 1:1 000 000, BRGM, Orléans.

Cornou, C., and 90 co-authors, 2021, Rapid Response to The Mw 4.9 Earthquake Of November 11, 2019 In Le Teil, Lower Rhône Valley, France. Comptes Rendus. Géoscience, Académie des sciences (Paris), 353 (S1), pp.1-23.

Delouis, B., Oral, E., Menager, M., Ampuero, J. P., Trilla, A. G., Régnier, M., and Deschamps, A., 2021, Constraining the point source parameters of the 11 November 2019 Mw 4.9 Le Teil earthquake using multiple relocation approaches, first motion and full waveform inversions. Comptes Rendus. Géoscience, 353(S1), 1-24.

Elmi, S., Busnardo, R., Clavel, B., Camus, G., Kieffer, G., Bérard, P. and B. Michaëly, 1996, Notice 53 explicative, Carte géologique de France (1/50 000), Feuille Aubenas (865). Orléans : BRGM, 170 p. 54 Carte géologique par Y. Kerrien (coord.), S. Elmi, R. Busnardo, G. Camus, G. Kieffer, J. Moinereau, 55 A. Weisbrod (1989)

Jomard, H., Cushing, E. M., Palumbo, L., Baize, S., David, C., & Chartier, T., 2017, Transposing an active fault database into a seismic hazard fault model for nuclear facilities–Part 1: Building a database of potentially active faults (BDFA) for metropolitan France. Natural Hazards and Earth System Sciences, 17(9), 1573-1584.

Lacassin, R., meyer, B., benedetti, L., armijo, R., tapponnier, P., 1998a. Signature morphologique de l'activité de la faille des Cévennes (Languedoc, France). Comptes Rendus de l'Académie des Sciences - Series IIA - Earth and Planetary Science 326, 807–815.

Lacassin, R., Meyer, B., Benedetti, L., Armijo, R., Tapponnier, P., 1998b. Réponse aux commentaires de Ambert et al., Mattauer et Sébrier et al. à la note. Comptes Rendus de l'Académie des Sciences - Series IIA - Earth and Planetary Science 327, 861–866.

Manchuel K, Pouliquen S., Vergniault C., Arroucau P., Le Roux Mallouf R., Ritz J-F., 2022, Quelle place pour l'imagerie sismique dans la caractérisation des failles en domaine intraplaque ? How to use seismic imagery for fault characterization in intraplate domain ? Journées AGAP, March 2022, Numéro spécial de la collection E3S Web of Conferences – Journées Scientifiques AGAP Qualité 2022, publié par EDP Sciences (proceeding 04002).

Masson, C., Mazzotti, S., Vernant, P., and Doerflinger, E., 2019, Extracting small deformation beyond individual station precision from dense Global Navigation Satellite System (GNSS) networks in France and Western Europe. Solid Earth, 10: 1905–1920.

Ritz, J.-F., Baize, S., Ferry, M., Larroque, C., Audin, L., Delouis, B., and Mathot, E., 2020, Surface rupture and shallow fault reactivation during the 2019 Mw 4.9 Le Teil earthquake, France, Commun. Earth Environ., 1:10.

Ritz, J-F., S. Baize, M. Ferry, E. Hannouz, M. Riesner, L. Bollinger, C. Larroque, L. Audin, K. Manchuel, M. Rizza, H. Jomard, C. Sue, P. Arroucau, J. Billant, 2021, Analyzing the paleoseismic history of the La Rouvière fault, unexpected source of the 11-11-2019, Mw4.9 Le Teil surface rupturing earthquake (Cévennes fault system, France), EGU General Assembly 2021, EGU21-13044.

Ritz J-F, Baize S., Ferry M, Hannouz E., Riesner M., Cathelin N., Thomasset C., Bollinger L., Larroque C., Audin L., Manchuel K., Rizza M., Jomard H., Sue C., Arroucau P., Le Roux-Mallouf R., 2022, Paleoseismological investigations of the La Rouvière fault, unexpected source of the 11-11-2019, Mw4.9 Le Teil surface rupturing earthquake (Cévennes fault system, France), AFEQ workshop, Strasbourg March 14-18.

Ritz J-F., Baize S., Audin L., Authemayou C., Graveleau F., Kaub C., Lacan P., Leclerc F., Larroque C., Antoine P., Manchuel K., Mugnier J-L., Ortuño M., Rizza M., Vassallo R. Arroucau P., Billant J., Bollinger L., Ferry M., Fillon C., Geoffroy L., Jomard H., Le Roy P., Migeon S., Perrin C., Perrot J., Ratzov G., Reicherter K., Soubigou O., Vergniault C., Viaplana M., Van Der Woerd J., 2021, New perspectives in studying active faults in metropolitan France: the "Active faults France" (FACT/ATS) research axis from the Resif-Epos consortium, Comptes Rendus Géoscience, 353, S1, 381-412.

Roure, F., Brun, J.P., Colletta, B. and J. Van den Driessche, 1992, Geometry and kinematics of extensional structures in the Alpine Foreland Basin of southeastern France. Journal of Structural Geology, 14,503-519.

Sébrier, M., Bellier, O., Peulvast, J.-P., Vergély, P., Ambert, P., Philip, H., Ritz, J.-F., Mattauer, M., 1998. Commentaires à la note de Robin Lacassin, Bertrand Meyer, Lucilla Benedetti, Rolando Armijo et Paul Tapponnier. Comptes Rendus de l'Académie des Sciences - Series IIA - Earth and Planetary Science 327, 855–859.

Schlupp, A., Sira, C., Maufroy, E., Provost, L., Dretzen, R., Bertrand, E., Beck E. and Schaming, M., 2021, EMS98 intensities distribution of the "Le Teil" earthquake, France, 11 November 2019 (Mw 4.9) based on macroseismic surveys and field investigations. Comptes Rendus. Géoscience, 353(S1), 1-28.

Vergniault, C., Strobbia, C., Deida, G-P., and Dupuy, D., 2019, Surface seismic methods comparison to image the near surface basement. Journées scientifiques de l'AGAP Qualité, 28-30 Oct. 2019.

Inheritance of Detrital Charcoal: Implications for Age Estimates on Paleoearthquakes

Thomas Rockwell (1), Aron Meltzner (2)

(1) Geological Sciences, San Diego State University, San Diego, CA 92182 USA. Email: trockwell@sdsu.edu
(2) Earth Observatory of Singapore and Asian School of the Environment, Nanyang Technological University, Singapore 639798. Email: meltzner@ntu.edu.sg

Abstract: We have compiled nearly 800 stratigraphically constrained radiocarbon dates from five stratigraphic sequences to determine the extent to which detrital charcoal is either reworked or carries inherited age. The 120 stratigraphically inconsistent dates (out of 284) from Lake Cahuilla show that nearly half (41%) of all dates are older than underlying strata, indicating significant age inheritance. Similarly, inheritance ranges between 30% for the Old Town site along the Rose Canyon fault to 41% at the Mystic Lake site along the San Jacinto fault, to 46% at the Beteiha site along the Dead Sea Transform. In contrast, 111 dates from Hog Lake show that only about 15% of dates there exhibit ages older than underlying strata, but at that site most dates were on seeds contained in thin organic mat layers, all of which were in stratigraphic order. Hence, it is clear that chronologies constructed from single year growth samples substantially improve the accuracy of the ages of individual strata. The percentage of reworked or older charcoal indicates that paleoseismic studies should consider dating twice as many samples as are expected to define an age sequence. Further, whenever possible, single-year growth samples, such as seeds, pine cones, and grass blades, should be dated to help constrain and anchor a chronologic model. These statistics have broad implications not only for paleoseismic studies, but for fire frequency and slip rate studies. Reliance on a single date to quantify processes or events appears to be quite risky.

Key words: *^{14}C age inheritance, earthquake age resolution*

Introduction

Geochronology underpins most subdisciplines in geology, and this is particularly the case in paleoseismic studies where quantitative ages of faulted strata are critical to resolve the timing of prehistorical ruptures. Radiocarbon (^{14}C) is the oldest and most broadly applied technique to date past earthquakes when organic materials are present in the faulted stratigraphy. In early studies, ^{14}C dating relied on the collection of large amounts of carbon-bearing material, commonly in excess of a gram, for gas-proportional counting. This commonly required collecting numerous smaller fragments of charcoal and combing them to amass enough material for a date, resulting in an age that represented the average age of charcoal pieces. This is somewhat equivalent to applying the central age model in OSL dating.

Modern ^{14}C dating using accelerator mass spectrometry (AMS) on charcoal and other organic materials now requires very little material, on the order of only one to a few milligrams, and the best practice is to date individual fragments so as not to mix ages. In so doing, many dates can be acquired from individual strata to test the age distribution of charcoal and other organics (leaves, twigs, grass blades, etc.) within a deposit.

Charcoal and other burned organic substances are, by their very nature, maximum ages for a host deposit because most subaerial vascular plants incorporate atmospheric carbon on an annual basis, and vegetation that grows annual rings, such as deciduous and conifer trees, lock in the year that the ring grew in. As there must be some time lag between the growth of individual rings and the time of deposition to allow for the burning of the wood and its subsequent transport, the host sediments must be younger. If old trees are burned in a range fire, or if humans burn wood for cooking and heating (in which case, most people opt for dead wood), this leads to the long-known "old wood problem" (Erlandson and Rockwell, 1987). The focus of this paper is to explore the percentage of "old wood" in the system by studying several well-constrained stratigraphic sequences with at least 50 radiocarbon dates.

Methods

We chose five published coherent stratigraphic sequences to assess the amount of older charcoal with a depositional system (Wechsler et al., 2014, 2018; Rockwell et al., 2015; Onderdonk et al., 2013; 2018; Singleton et al., 2018; Rockwell et al., 2022). All radiocarbon ages from a sequence were placed in OxCal regardless of whether they appeared out of sequence. The resulting plots were analyzed in terms of the agreement index in OxCal, as well as obvious outliers. Plots are presented in Figures 1 through 5.

Results

Of the five sites studied, dating at four sites is dominated by ages on detrital charcoal and exhibit evidence of the "old wood effect" ranging from 30 to 46% of all samples. In contrast, the one site dominated by single-year growth

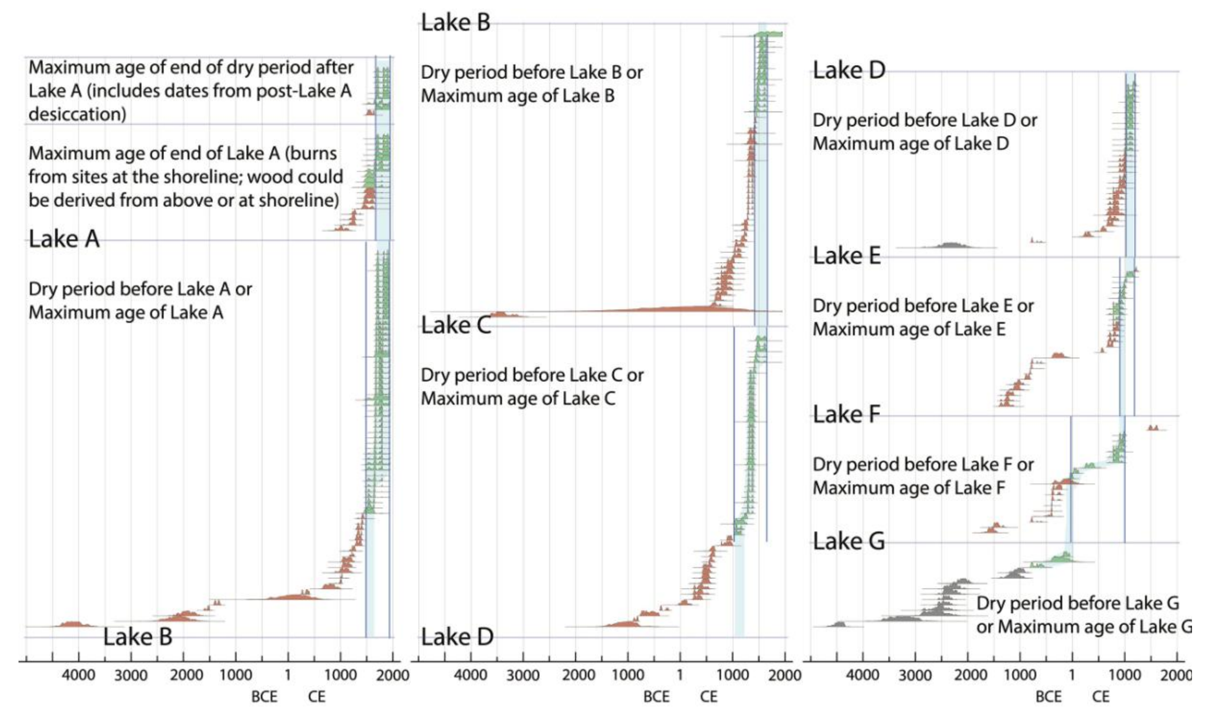

Figure 1: Radiocarbon ages from prehistoric Lake Cahuilla in the Salton Trough of Southern California. From left to right, Lake A is the youngest and Lake G is the oldest. The ages shown in green run in OxCal with agreement indices greater than 60. Those in red have poor agreement indices or violate stratigraphic ordering altogether. About 40 % of all dates exhibit the "old wood effect" and date older than underlying strata (from Rockwell et al., 2022). The blue band captures all of the stratigraphically reliable dates and must always slope down and to the left.

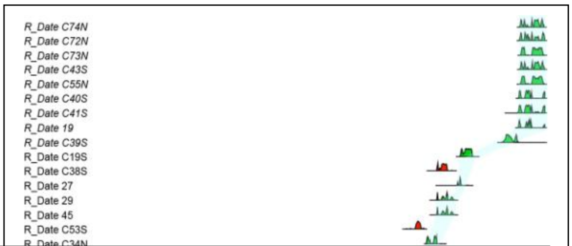

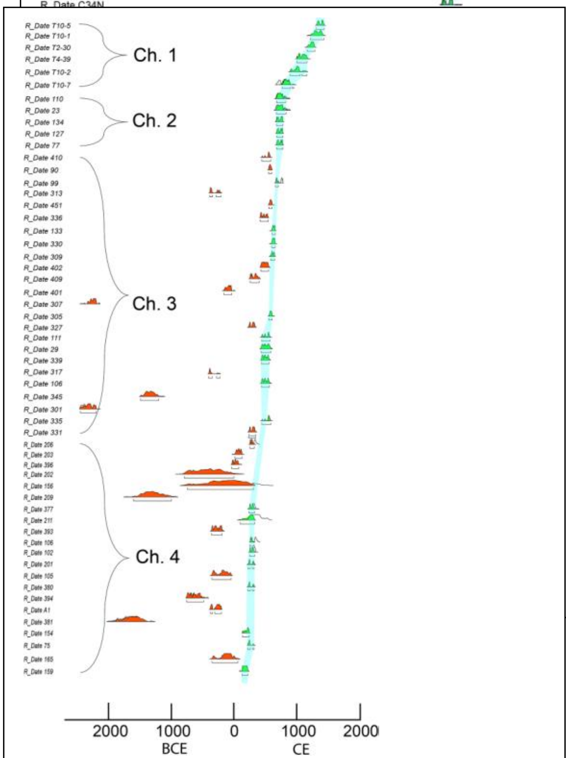

Figure 3: Plot of radiocarbon ages by stratigraphic order for the Beteiha paleoseismic site in Israel (Wechsler et al., 2014, 2018). Dates from channels are treated as phases. About 46% of dates exhibit age inheritance.

samples, mostly seeds but some reed charcoal, exhibits a much lower percentage of samples with age inheritance, only about 10-15%, depending on where the agreement index is cut. All or nearly all samples exhibiting age inheritance were analyzed on detrital charcoal whereas most of the samples that line up stratigraphically were seeds and marsh reed charcoal. This is a clear demonstration that single-year growths, such as seeds, pine cones, grass blades and leaves are demonstrably more reliable than detrital charcoal for age constraints.

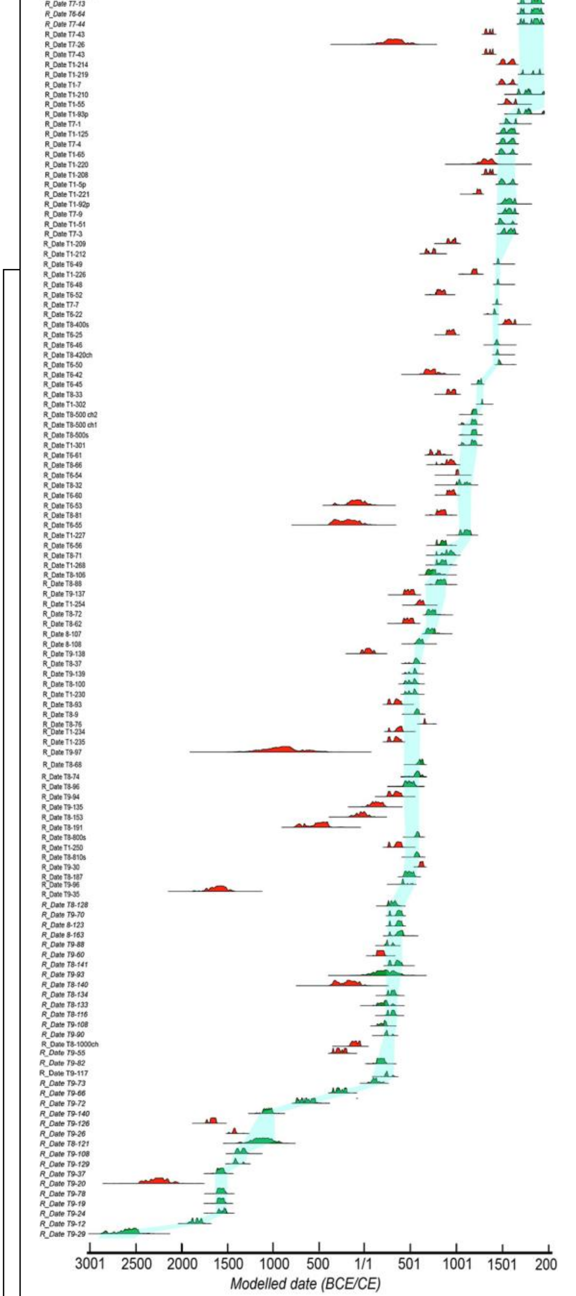

Figure 4: Plot of radiocarbon ages from the Mystic Lake paleoseismic site (Onderdonk et al., 2013, 2018). About 40% of samples exhibit age inheritance.

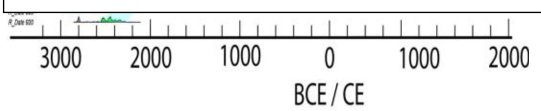

Figure 5. Radiocarbon ages from the Hog Lake paleoseismic site (Rockwell et al., 2015). Note the sparseness of samples with age inheritance. Most samples were on seeds in organic layers. Some were on marsh reed charcoal. All "red" samples are on detrital charcoal.

Discussion

It is interesting to speculate on the effects of humans on the source of charcoal in these environments. For the samples from Lake Cahuilla in the Salton Trough, most or all are likely derived from Native American fires because the region is hyper-arid and vegetation is so sparse that wildfires are unlikely. As most people would prefer to burn dead wood, of which there is plenty on the desert floor, the most likely explanation for the abundant number of samples exhibiting the "old wood" effect is that most of the wood was scavenged from dead vegetation. Similarly, the samples from the Beteiha site along the Dead Sea fault in Israel extensively exhibit the "old wood" effect, and as people have lived there for thousands of years in the semi-arid Holocene climate, and likely preferred dead wood for cooking, the 46% of "old" radiocarbon ages is not a surprise. The Mystic Lake site along the northern San Jacinto fault also lies in a semi-arid environment and exhibited about 40% old wood. Both the Beteiha and Mystic Lake sites do, however, have sufficient vegetation for a range fire, so some of the charcoal is expected to be close to the age of the sediments.

In contrast, The Hog Lake stratigraphic section was commonly below surface water (hence, Hog Lake), although it periodically dried out as the "lake" was only 1.5 m deep at its deepest. The site hosted marsh vegetation that produced abundant seeds, and when the lake completely dried out during drought periods, the surface could burn as demonstrated by fire-oxidized layers that contained abundant charcoal. Many of these oxidized layers graded laterally into organic layers in the lowest parts of the lake, indicating that the lake was not completely dry when the burn occurred. In any case, it was the accumulation of seeds on the marsh bottom, along with other organics, which led to the more than 40 dense organic layers in about 6.5 m of section.

Another question could be asked: what if some dates are selectively tossed to try to improve the agreement index? A common assumption is that when a slightly younger sample lies below a slightly older sample, the older sample likely exhibits age inheritance. While this is normally true, about 5% of all radiocarbon ages are expected to be outside of the 95% confidence limits, so large datasets should have some dates that are just wrong. The Mystic Lake sequence is a good example to test for this as there are some dates that are younger

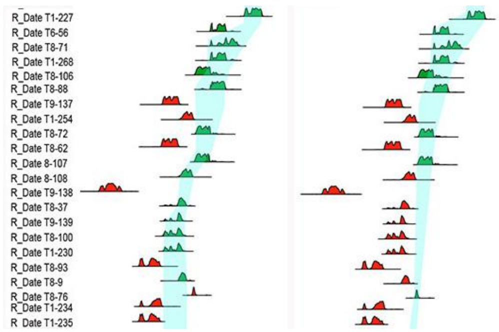

Figure 6: Two alternative models for a section of the Mystic Lake sequence. In Alt 1, sample T6-76 was treated as an outlier, even though it was younger than overlying ages, whereas in Alt 2, simple T6-76 was assumed to be correct, which resulted in several overlying samples turning red.

than several overlying dates. Figure 6 shows two models: model Alt 1 treats sample T6-76 as an outlier because there are several older sample ages immediately above it. In contrast, model Alt 2 assumes this sample to read true, which then makes the five overlying "green" samples turn red. In the final analysis, this has about a 1% effect on the percentage of samples with inherited age, but it could be critical if the earthquake event that is to be dated falls within this sequence of ages.

In the end, judgement is called on to correctly place radiocarbon ages in their correct sequence and to decide which are in or out of a model. At the first order, it is clear that dating many more samples than one initially thinks is necessary is important to better constrain event ages.

Conclusions

The percentage of reworked or older charcoal indicates that paleoseismic studies should consider dating at least twice as many samples as are expected to be needed to define an age sequence. Further, whenever possible, single-year growth samples, such as seeds and pine cones, should be dated to help constrain and anchor a chronologic model as this will substantially improve the accuracy of the ages of individual strata. These statistics have broad implications not only for paleoseismic studies, but for fire frequency and slip rate studies. Reliance on a single date to quantify processes or events appears to be quite risky.

Acknowledgements: This worked is underpinned by several grants to TKR, and by the National Research Foundation Singapore and the Singapore Ministry of Education under the Research Centres of Excellence initiative. We thank the USGS NEHRP program and NSF for earlier support.

References

Onderdonk, N., S. McGill and T. Rockwell, 2018. A 3700-year paleoseismic record for the northern San Jacinto fault and implications for joint rupture of the San Jacinto and San Andreas faults. *Geosphere*, 14, 2447-2468. doi:10.1130/GES01687.1

Rockwell, T.K., T.E. Dawson, J.Y. Ben-Horin, and G. Seitz, 2015. A 21-event, 4,000-year history of surface ruptures in the Anza Seismic Gap, San Jacinto Fault and implications for long-term earthquake production on a major plate boundary fault. *Pure Appl Geophys.*, 172, 1143-1165. doi:10.1007/s00024-014-0955-z

Rockwell, T.K., Meltzner, A.J., Haaker, E., Madugo, D., 2022. The Late Holocene History of Lake Cahuilla: Two Thousand Years of Repeated Fillings Within the Salton Trough, Imperial Valley, California. *Quat. Sci. Rev.,* 282, 107456. doi:10.1016/j.quascirev.2022.107456

Singleton, D.M., T.K. Rockwell, D. Murbach, M. Murbach, J.M. Maloney, T. Freeman, and Y. Levy, 2019. Late-Holocene Rupture History of the Rose Canyon Fault in Old Town, San Diego: Implications for cascading earthquakes on the Newport-Inglewood-Rose Canyon Fault System. *Bull. Seismol. Soc Am*., 109, 855-874. doi:10.1785/0120180236

Wechsler, N., T.K. Rockwell, Y. Klinger, 2018. Variable slip-rate and slip-per-event on a plate boundary fault: The Dead Sea Fault in northern Israel. *Tectonophysics*, 722, 210-226. doi:10.1016/j.tecto.2017.10.017

Contributions of lithospheric strength, mantle hydration and slab flexure to seismic localization in the southern Central Andes

Rodriguez Piceda, Constanza (1), Scheck-Wenderoth, Magdalena (2), Cacace, Mauro (3), Bott, Judith (4), Gao, Ya-Jian (5), Tilmann, Frederik (6), Strecker, Manfred (7)

(1) University of Plymouth, Portland Square, Drake Circus, PL4 8AA United Kingdom. Email: constanza.rodriguezpiceda@plymouth.ac.uk
GFZ German Research Centre for Geosciences, Telegrafenberg, 14473, Germany.
University of Potsdam, Karl-Liebknecht-Str. 24-25, 14476 Germany.
(2) GFZ German Research Centre for Geosciences, Telegrafenberg, 14473, Germany. Email: magdalena.scheckwenderoth@gfz-potsdam.de
RWTH Aachen, Germany
(3) GFZ German Research Centre for Geosciences, Telegrafenberg, 14473, Germany. Email: cacace@gfz-potsdam.de
(4) GFZ German Research Centre for Geosciences, Germany. Email: bott@gfz-potsdam.de
(5) Karlsruhe Institute of Technology, Herstrasse 16, 76187, Germany. Email: gao@kit.edu
(6) GFZ German Research Centre for Geosciences, Telegrafenberg, 14473, Germany. Email: tilmann@gfz-potsdam.de
(7) University of Potsdam, Karl-Liebknecht-Str. 24-25, 14476 Germany. Email: Manfred.Strecker@geo.uni-potsdam.de

Abstract: *We investigated the effects of the long-term yield strength of the lithosphere on the active seismic deformation of the subduction zone bordering the southern central Andes (29°S-39°S). We present a rheological model that accounts for the heterogeneities in thickness, composition and temperature of the upper and lower plates based on 3D structural and thermal models of the region. We found that most of the upper-plate deformation spatially correlates with the steepest strength gradients. To address the effects of dehydration reactions within the oceanic plate on slab seismicity, we map the hydration state of the mantle using a recent seismic tomography model. We propose that slab seismicity in regions of hydrated mantle below a hydrated mantle wedge is principally caused by fluid-mediated reactions. In contrast, slab seismicity in areas of inferred lower fluid content in the overriding plate above is facilitated by enhanced flexural stresses due to changes in the subduction angle of the Nazca plate.*

***Key words**: subduction, lithosphere, rheology*

Introduction

In the subduction zone along the southern Central Andes (SCA, 29°S-39°S), the oceanic Nazca Plate changes its dip angle underneath the continental south American Plate from almost horizontal (< 5° dip) in the north (in the area known as the Pampean Flat Slab) to a steeper angle (~30° dip) in the south (Fig. 1). This whole region is characterized by widespread seismic activity in the subducting slab, the overriding plate and along the subduction interface.

Previous research has attributed the occurrence of seismicity to the reactivation of discrete faults and fabrics at a local-crustal scale (e.g., Alvarado et al., 2005). However, the role of the long-term strength of the lithosphere (i.e., maximum differential stress that a rock is able to withstand before breaking or creeping), which depends on its bulk structure, composition and temperature has not been inquired in detail yet.

This contribution aims at providing an integrative view on the influences of the lithospheric strength on the seismic localization in the SCA by calculating the mechanical strength of the area on the basis of existing 3D models of the thickness, composition and temperature of the layers that form the subducting and overriding plates (Rodriguez Piceda et al., 2021, 2022a). Additionally, we explore a full waveform-inversion tomography of the region (Gao et al., 2021) and potential effects of flexural stresses arising from changes in the subduction angle of the oceanic plate.

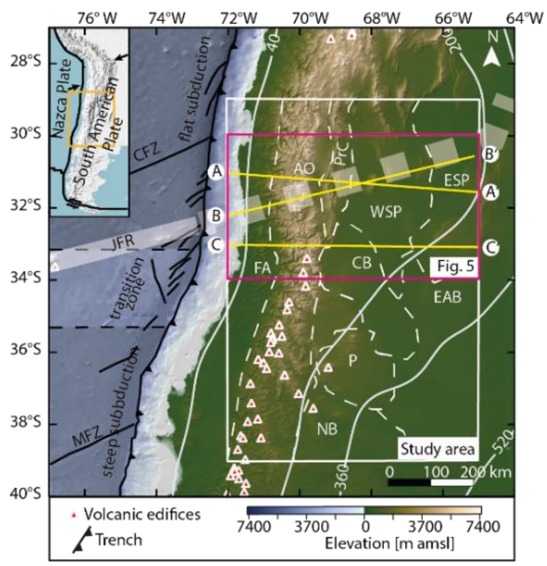

Figure 1: (a) Topography and bathymetry of the southern central Andes taken from ETOPO1 (Amante & Eakins, 2009). *The white rectangle encloses the area of this study. Black dashes in the oceanic domain show the boundaries between subduction segments. White lines show the isodepth contours (km) of the top of the oceanic crust from Slab2* (Hayes et al., 2018)*. The thick and dashed white lines show the offshore and onshore projected track of the Juan Fernandez Ridge* (JFR, Yáñez et al., 2001)*. The white rectangle encloses the area of study. The magenta rectangle shows the area of Figure 5. Red triangles depict the active volcanoes. Yellow lines show the locations of the profiles in Figures 3 and 4. Dashed lines mark the limits between morphotectonic provinces. Abbreviations of main*

morphotectonic provinces: AO = Andean orogen, CB = Cuyo Basin, ESP = Eastern Sierras Pampeanas, EAB = extra-Andean basins, FA = forearc, NB = Neuquén Basin, P = Payenia volcanic province, Prc = Precordillera, WSP = Western Sierras Pampeanas

Discussion

We constructed a 3D rheological model of the present-day lithospheric strength of the SCA orogen and adjacent forearc and foreland regions (Rodriguez Piceda et al, 2022b) using as input: (i) a structural and density model built based on seismic models from the literature and by fitting gravity(Rodriguez Piceda et al., 2021) and (ii) a thermal model (Rodriguez Piceda et al., 2022a) based on a mantle temperature field constructed by conversion of S-wave velocities and application of steady-state conductive computations. Figure 2 shows key characteristics of the structural and thermal models (modified from Rodriguez Piceda et al., 2021, 2002a). For the rheological calculations, we assumed: (i) brittle behaviour at shallow depths according to Byerlee's Law (Byerlee, 1968) and ductile behaviour as described by dislocation creep and low-temperature plasticity (e.g., Goetze & Evans, 1979).

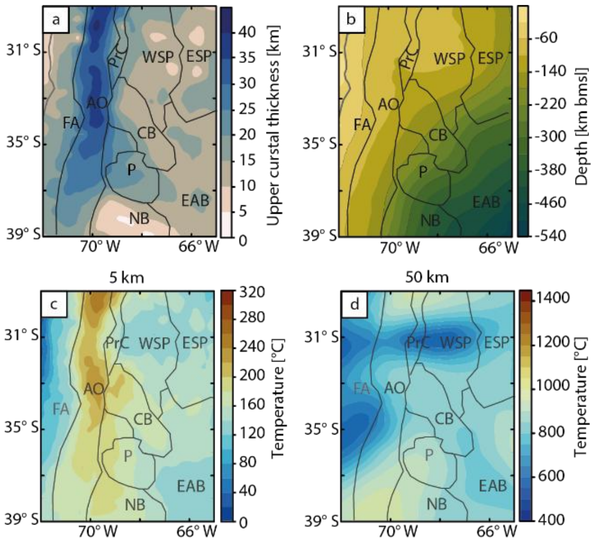

Figure 2: (a) thickness of the continental upper crust (Rodriguez Piceda et al., 2021). (b) depth below sea level to the top of the oceanic crust from the "Slab2" model (Hayes et al., 2018). (c) and (d) are temperature slices at 5 and 50 km, respectively, from the thermal model of Rodriguez Piceda et al. (2022a).

Figure 3 shows the calculated integrated strength of the continental crust. Figure 4 is a cross-section perpendicular to the strike of the oceanic plate at the latitudes of the Pampean Flat Slab region displaying the calculated strength distribution. We identified a heterogeneous distribution of temperature and lithospheric strength: cold and mechanically strong regions are found in the forearc, the central-western part of the orogen and the northern foreland areas; on the contrary, most parts of the orogen display warmer temperatures and weaker rheology (Figs. 3 and 4). This variable thermomechanical configuration is controlled by different factors at different depths. At depths shallower than 50 km, the thermomechanical field varies as function of the heterogeneous composition of the overriding plate. Higher temperatures (Fig. 2c) and weaker lithosphere (Fig. 3) are encountered within the orogenic domain, where the more radiogenic upper crust is thick (Fig. 2a). The oceanic plate conspicuously counteracts this warming effect where the slab is located at shallower than ~85 km depth and the radiogenic crust is thin, resulting in lower temperature (Fig. 2c) and higher strength (Fig. 3) than in regions where the slab dips more steeply (Fig. 2b) and the radiogenic crust is thicker (i.e., forearc and northern part of the foreland, Fig. 2a). Conversely, the deep thermomechanical field (> 50 km) is mainly controlled by the mantle heat input and the subducting plate geometry. Areas with low temperatures at 50 km (bmsl) spatially correlate with the areas where the cold subducting plate is encountered (Fig. 2d; Rodriguez Piceda et al., 2022a).

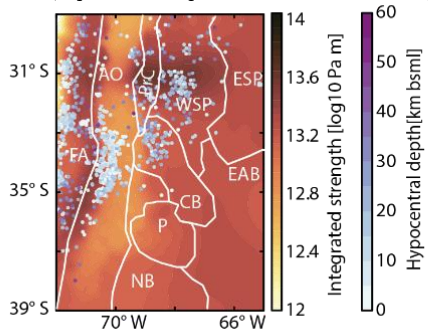

Figure 3: Crustal integrated strength overlain with upper-plate seismicity (International Seismological Centre, 2021) color-coded by depth. See Figure 1 for abbreviations of morphotectonic provinces. Figure was modified from Rodriguez Piceda et al., 2022b

We find that modeled variations in lithospheric strength correlate with the spatial distribution of upper-plate seismicity (International Seismological Centre, 2021): first, these seismic events are bounded to the brittle domain of the lithosphere (Fig. 4), which indicates that the brittle-ductile transition (BDT) provides a conservative estimate of the lower seismogenic depth. Where the lithosphere is cold and strong (i.e., in the forearc and northern parts of the foreland), the BDT is deeper, so are the seismic events. On the contrary, the warm and weak lithosphere of the orogen displays a shallower BDT and seismogenic depth. Second, most of the upper-plate seismicity (Fig. 3) is recorded at the transitions from strong to weak domains, implying that stresses related to the plate convergence can be effectively transmitted from mechanically strong to weak regions, where they are released and seismic rupture occurs.

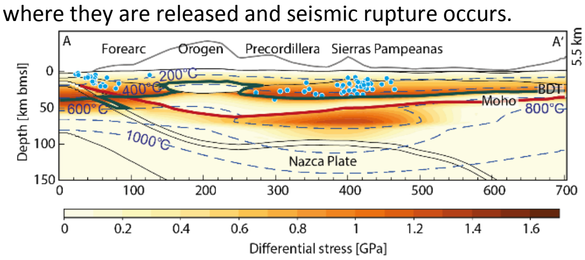

Figure 4: Differential stress along cross-section A-A' representative of the flat slab segment (see Figure 1 for profile location). Light blue dots show the locations of seismic activity within 5 km from the profile. Modeled isotherms are depicted as dashed blue lines. The modeled brittle ductile transition is shown by a thick green line. Black likes show the structural interfaces between model layers.

An exception to these spatial correlations between integrated strength and seismicity is observed in the cold and strong northern foreland (Fig. 3), which is characterized by active seismicity in spite of the modelled strength (1.6 GPa) exceeding typical plate-driving stresses (100-600 MPa; e.g., Burov, 2011). In this region, where deformation could be expected to be inhibited, the actual weakening could be related to structures inherited from pre-Andean events of terrane amalgamation and rifting (while not being integrated in our models). Alternatively, increased slab pull where the plate transitions from flat to steep subduction could provide the additional stresses needed to enhance seismic localization.

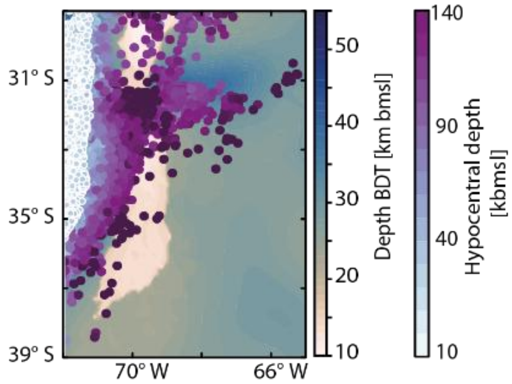

Figure 5: Depth of the brittle ductile transition(Rodriguez Piceda et al.; 2022b) overlain with earthquakes on the plate interface or within the slab (International Seismological Centre, 2021), color-coded by depth. Events in the brittle part of the lithosphere are marked with white outlines/contours, while events in the ductile domain are shown without edges

Apart from the upper-plate seismic events, seismicity also occurs below the calculated BDT where energy should be more effectively dissipated by viscous creep rather than brittle failure, such as along the subduction interface (inter-plate events) and within the oceanic slab (intra-slab events), (Fig. 5). Past research has stressed the role of fluids released during dehydration reactions (i.e. metamorphic reactions of the crust and mantle) for the intermediate-depth (intra-slab) earthquakes (50-300 km; e.g., Hacker et al., 2003). An increase in fluid content is thought to increase the pore-fluid pressure, decreasing the effective normal stress, weakening the rock and facilitating brittle failure. To investigate the potential effects of fluids in the occurrence of slab seismicity in the SCA, we analyzed the ratio between P- and S-wave velocity (Vp/Vs) from the (full waveform) seismic tomography model of Gao et al. (2021) (Rodriguez Piceda et al., under review). Vp/Vs can be used to infer the respective hydration states of the lithospheric mantle, oceanic mantle and subduction interface. Low Vp/Vs (1.65-1.8) suggests anhydrous mantle (Christensen, 2004), while high Vp/Vs (>1.9) is indicative of hydrous composition with free-fluids (Bloch et al., 2018). Intermediate values between 1.8 and 1.9 suggest serpentinization (Bezacier et al., 2010). High Vp/Vs may also indicate fluids ascending from the subducting slab and causing partial melting in the mantle wedge (Hirschmann, 2000).

The Vp/Vs distribution overlain with the slab seismicity is shown across two profiles representative of the flat slab segment (Fig. 6a) and the transition zone (Fig. 6b). We observe a progressive eastward dehydration of the subducting plate mantle as indicated by a decrease in the Vp/Vs ratio from around or greater than 1.9 below the forearc and the orogen (70°W-72°W) to lower values below the foreland east of 70°W. This region of hydrated mantle is characterized by active slab seismicity. In the transition zone segment, the part of the slab below 100 km that is likely dehydrated (indicated by Vp/Vs < 1.8) is devoid of seismic events (Fig. 6b). The detected spatial relationships between regions of hydrated mantle and slab seismicity suggest that triggering of seismic events is caused by dehydration reactions in the subducting slab. While this holds for the transition zone segment, in the flat slab segment (Fig. 6a), seismic activity is also detected in areas of the subducting plate with intermediate to low Vp/Vs (<1.8, 68°W-69.5°W). This suggests that where the slab lies subhorizontally and low temperatures persist at relatively shallow depths (~100 km), metamorphic reactions are slowed down, such that fluid release is impeded. The low fluid content implies that there should be an alternative mechanism to explain this seismic cluster.

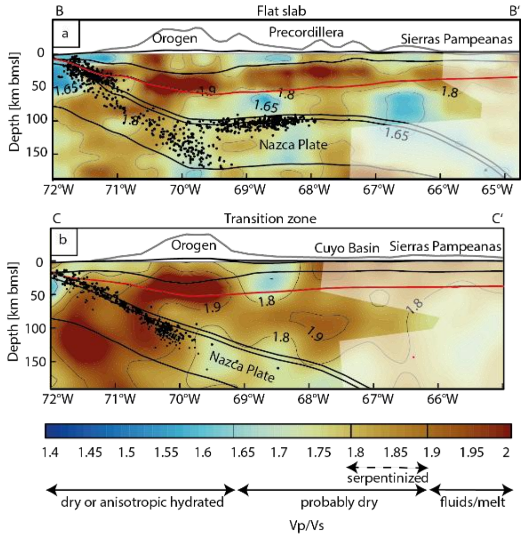

Figure 6: Vp/Vs ratio along cross-sections (see Figure 1 for profile locations). White-shaded areas with transparency denote areas with insufficient resolution. Dots show the locations of hypocentres of slab seismic events (International Seismological Centre, 2021) *within 5 km distance from each profile. The interfaces of the lithospheric model units are marked by black lines, except for the Moho discontinuity, which is shown by red lines. On top of each profile, surface topography is displayed with a vertical exaggeration of 10:1.*

Previous studies have shown that flexural stresses associated to changes in the subduction angle of the slab provide additional forces to facilitate seismic rupture if effective strain rates related to flexure surpass stresses related to slab pull (e.g., Engdahl & Scholz, 1977). This hypothesis has been derived for different subduction zones from the observed spatial correlation between slab curvature and the orientation of earthquake moments tensors. For the top of the slab, they found that bending segments with positive (concave-down) curvature gradients are characterized by focal mechanisms with downdip extensional axis, while unbending segments with negative curvature gradients (concave-up) show focal mechanisms with downdip compressional axis. We tested this hypothesis for the case of the SCA, by comparing the curvature gradient of the top slab with the orientation of the main axes of the focal mechanisms (GCMT catalog, Ekström et al., 2012) in the southern part of the flat slab segment (Fig. 7). Indeed, we observed an overall switch in the orientation of the main axes from downdip compressional (71°W-72°W) to downdip extensional (67°W-69.5°W) and back to downdip compressional (65°W-66°W); this change spatially correlates with the transition between unbending segments with negative curvature gradient and the bending segment with positive curvature gradient. These observations suggest that seismicity in this part of the flat slab subduction segment is additionally assisted by enhanced flexural stresses of the oceanic slab when the slab flattens and re-steepens to the east and to the south.

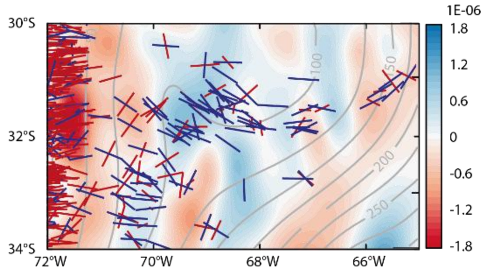

Figure 7: Curvature gradient of the top of the oceanic plate in the region of the flat-slab to steep-dip subduction transition, overlain with P-(red) and T-(blue) axes projected horizontally from slab focal mechanisms (Ekström et al., 2012). Only the sub-horizontal axes (plunge < 45°) are shown. The isodepth contours of the top of the slab (Hayes et al., 2018) are depicted in grey lines.

In summary, this contribution brings together geophysical and geological observations into a comprehensive framework by integrating the compositional, thermal and rheological fields of the plates with their 3D geometrical configuration which allows us to better quantify the relative importance of different factors influencing the distribution of upper- and lower-plate seismicity.

Acknowledgements: This research was funded by the DeutscheForschungsgemeinschaft (DFG) and the Federal State of Brandenburg under the auspices of the International Research Training Group IGK2018 STRATEGy (DFG 373/34-1). Yajian Gao was sponsored by Freie Universität Berlin - China Scholarship Council Programm. The seismic tomography processing was supported by the Swiss National Supercomputing Center (CSCS) in the form of computing time grants s868 and s1040.

REFERENCES

Alvarado, P., Beck, S., Zandt, G., Araujo, M., & Triep, E. (2005). Crustal deformation in the south-central Andes backarc terranes as viewed from regional broad-band seismic waveform modelling. *Geophysical Journal International*, *163*(2), 580–598. https://doi.org/10.1111/j.1365-246X.2005.02759.x

Amante, C., & Eakins, B. (2009). *ETOPO1 1 Arc-Minute Global Relief Model: Procedures, Data Sources and Analysis* (NOAA Technical Memorandum NESDIS NGDC-24). National Geophysical Data Center, NOAA. Retrieved from doi:10.7289/V5C8276M

Bezacier, L., Reynard, B., Bass, J. D., Sanchez-Valle, C., & Van de Moortèle, B. (2010). Elasticity of antigorite, seismic detection of serpentinites, and anisotropy in subduction zones. *Earth and Planetary Science Letters*, *289*(1), 198–208. https://doi.org/10.1016/j.epsl.2009.11.009

Bloch, W., John, T., Kummerow, J., Salazar, P., Krüger, O. S., & Shapiro, S. A. (2018). Watching Dehydration: Seismic Indication for Transient Fluid Pathways in the Oceanic Mantle of the Subducting Nazca Slab. *Geochemistry, Geophysics, Geosystems*, *19*(9), 3189–3207. https://doi.org/10.1029/2018GC007703

Burov, E. B. (2011). Rheology and strength of the lithosphere. *Marine and Petroleum Geology*, *28*(8), 1402–1443. https://doi.org/10.1016/j.marpetgeo.2011.05.008

Byerlee, J. D. (1968). Brittle-ductile transition in rocks. *Journal of Geophysical Research (1896-1977)*, *73*(14), 4741–4750. https://doi.org/10.1029/JB073i014p04741

Christensen, N. I. (2004). Serpentinites, Peridotites, and Seismology. *International Geology Review*, *46*(9), 795–816. https://doi.org/10.2747/0020-6814.46.9.795

Ekström, G., Nettles, M., & Dziewoński, A. M. (2012). The global CMT project 2004–2010: Centroid-moment tensors for 13,017 earthquakes. *Physics of the Earth and Planetary Interiors*, *200–201*, 1–9. https://doi.org/10.1016/j.pepi.2012.04.002

Engdahl, E. R., & Scholz, C. H. (1977). A double Benioff Zone beneath the central Aleutians: An unbending of the lithosphere. *Geophysical Research Letters*, *4*(10), 473–476. https://doi.org/10.1029/GL004i010p00473

Gao, Y., Yuan, X., Heit, B., Tilmann, F., van Herwaarden, D.-P., Thrastarson, S., et al. (2021). Impact of the Juan Fernandez Ridge on the Pampean Flat Subduction Inferred From Full Waveform Inversion. *Geophysical Research Letters*, *48*(21), e2021GL095509. https://doi.org/10.1029/2021GL095509

Goetze, C., & Evans, B. (1979). Stress and temperature in the bending lithosphere as constrained by experimental rock mechanics. *Geophysical Journal International*, *59*(3), 463–478. https://doi.org/10.1111/j.1365-246X.1979.tb02567.x

Hacker, B. R., Peacock, S. M., Abers, G. A., & Holloway, S. D. (2003). Subduction factory 2. Are intermediate-depth earthquakes in subducting slabs linked to metamorphic dehydration reactions? *Journal of Geophysical Research: Solid Earth*, *108*(B1). https://doi.org/10.1029/2001JB001129

Hayes, G. P., Moore, G. L., Portner, D. E., Hearne, M., Flamme, H., Furtney, M., & Smoczyk, G. M. (2018). Slab2, a comprehensive subduction zone geometry model. *Science*, *362*(6410), 58. https://doi.org/10.1126/science.aat4723

Hirschmann, M. M. (2000). Mantle solidus: Experimental constraints and the effects of peridotite composition. *Geochemistry, Geophysics, Geosystems*, *1*(10). https://doi.org/10.1029/2000GC000070

International Seismological Centre. (2021). *On-line Bulletin*. Retrieved from https://doi.org/10.31905/D808B830

Rodriguez Piceda, C., Scheck-Wenderoth, M., Bott, J., Gomez Dacal, M. L., Cacace, M., Pons, M., et al. (2022). Controls of the Lithospheric Thermal Field of an Ocean-Continent Subduction Zone: The Southern Central Andes. *Lithosphere*, *2022*(1), 2237272. https://doi.org/10.2113/2022/2237272

Rodriguez Piceda, C., Scheck-Wenderoth, M., Cacace, M., Bott, J., & Strecker, M. R. (2022). Long-Term Lithospheric Strength and Upper-Plate Seismicity in the Southern Central Andes, 29°–39°S. *Geochemistry, Geophysics, Geosystems*, *23*(3), 22. https://doi.org/10.1029/2021GC010171

Rodriguez Piceda, Constanza, Scheck Wenderoth, M., Gomez Dacal, M. L., Bott, J., Prezzi, C. B., & Strecker, M. R. (2021). Lithospheric density structure of the southern Central Andes constrained by 3D data-integrative gravity modelling. *International Journal of Earth Sciences*, *110*(7), 2333–2359. https://doi.org/10.1007/s00531-020-01962-1

Yáñez, G. A., Ranero, C. R., von Huene, R., & Díaz, J. (2001). Magnetic anomaly interpretation across the southern central Andes (32°–34°S): The role of the Juan Fernández Ridge in the late Tertiary evolution of the margin. *Journal of Geophysical Research: Solid Earth*, *106*(B4), 6325–6345. https://doi.org/10.1029/2000JB900337

INQUA Focus Group Terrestrial Processes Perturbed by Tectonics (TPPT)

paleoseismicity.org

First palaeoseismological constraints on the Anghiari normal fault (Upper Tiber Valley, Northern Apennines)

Testa Alessio[1], Boncio Paolo[2], Baize Stephane[3], Mirabella Francesco[4], Pucci Stefano[5], Pauselli Cristina[4], Ercoli Maurizio[4], Magali Riesner[6], Pace Bruno[2], Benedetti Lucilla[6], Anita Di Chiara[5].

(1) DiSPUTer Department, Università degli Studi G. d'Annunzio Chieti e Pescara, Italy. E-mail: alessio.testa@unich.it
(2) InGEO Department, Università degli Studi G. d'Annunzio Chieti e Pescara, Italy
(3) Institut de Radioprotection et Sûreť e Nucľ eaire, Fontenay-aux-Roses, France
(4) Dipartimento di Fisica e Geologia, Università di Perugia, Italy
(5) Istituto Vazionale di Geofisica e Vulcanologia (INGV), Rome, Italy
(6) Aix-Marseille Université, CEREGE CNRS-IRD UMR 34, Aix-en-Provence, France

Abstract: *The Anghiari fault (AF) is a 11 km-long NE-dipping normal fault which bounds the western side of the Quaternary fluvio-lacustrine Upper Tiber Valley in the Northern Apennines of Italy, and which belongs to the 22 km long Anghiari-Città di Castello main normal fault, a synthetic splay of the low-angle Altotiberina normal fault system.*

The AF is composed of at least two splays. The eastern splay runs at the base of the Pleistocene Anghiari ridge, juxtaposing late Quaternary alluvial deposits of the Tiber Valley against Middle Pleistocene continental deposits. The western splay is located within the Middle Pleistocene continental units of the Anghiari ridge.

Detailed geomorphological analysis, geological mapping and near-surface geophysical survey performed on the western splay enabled us to select two sites for palaeoseismological trenching. Radiocarbon dating of faulted sediments provides constraints for Late Pleistocene to historical surface faulting events, significantly contributing to constrain the seismic hazard of the region.

Key words*: Active normal fault, Northern Apennines, palaeoseismology, seismic hazard.*

INTRODUCTION

The Upper Tiber Valley is a system of three main fluvio-lacustrine basins in the Northern Apennines of Italy, resulting from the extensional processes which have affected this sector of the chain since the Late Pliocene. Extension in the Northern Apennines is accommodated by the Altotiberina low-angle normal fault (ATF), well known in literature

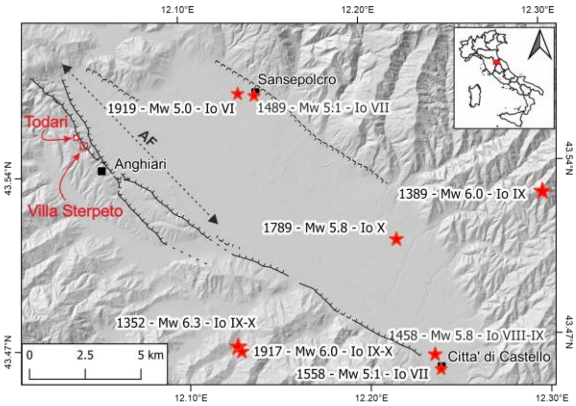

Figure 1 Structural map of the Sansepolcro Basin with normal faults and epicentres (stars) of the largest historical earthquakes.

thanks to deep seismic surveys and instrumental seismicity (Barchi et al, 1998a, b; Boncio et al, 1998; Brozzetti et al 2009). The ATF is a 70 km-long, NE-dipping low-angle normal fault with a staircase geometry and an average dip of 30°, reaching the surface along the western side of the Upper Tiber Valley, (Boncio et al, 2000). The Sansepolcro basin, located in the northernmost part of the Upper Tiber Valley, is bounded by synthetic and antithetic splays of the ATF (Pucci et al., 2014). This work focuses on the Anghiari fault (AF), in the western side of the Sansepolcro basin, which is supposed to be the youngest synthetic splay of the ATF (e.g., Brozzetti et al., 2009). However, there are not field outcrops of the AF documented in the literature, and chronologic constraint on its activity, and on its capability of producing surface faulting earthquakes are lacking. We performed tectonic geomorphology analysis, field mapping, near-surface geophysical prospecting and paleoseismologic trenching to constrain the geometry, kinematics, and activity of the AF.

We present for the first-time proofs of repeated surface faulting episodes along the AF, demonstrating its capability of generating surface faulting earthquakes.

GEOLOGIC SETTING

The AF bounds the eastern side of the Anghiari ridge, a NW-SE elongated hill made of Pleistocene gravel and sands exhumed by the fault activity. This fault is made of at least 2 different splays (Fig.1). The western one is located within the Pleistocene deposits of the Anghiari ridge. The eastern one runs at the base of the ridge, juxtaposing the Pleistocene units of the Anghiari ridge, in the footwall, against late Quaternary fluvial sediments of Tiber River, and colluvial and alluvial fan deposits
In the hanging wall (Testa et al, 2020).

The eastern splay is completely buried or hidden by colluvial deposits and alluvial fans and anthropogenic modifications. The upper splay is easily recognizable thanks to its geomorphological expression. In fact, the eastern side of the Anghiari ridge is featured by triangular facets and deep incised gullies. Beside the morphological evidence, there are displaced geological markers, such us the depositional unit outcropping in the Anghiari ridge (Citerna and Monterchi units) and an overlying palaeosol. These units are commonly attributed to the Middle Pleistocene (Cattuto et al, 1995; Pucci et al, 2014; Benvenuti et al, 2016), but their ages are poorly constrained.

Moreover, in correspondence of the northern termination of the Anghiari ridge, the upper splay also affects the outcropping Jurassic Ophiolite rocks belonging to the Ligurian tectonic unit.

The capability of the ATF and of its splays, including the AF studied in this work, to nucleate strong earthquakes is debated in the literature. The Sansepolcro basin was struck by several moderate to strong historical earthquakes, such as the 1352 (Mw 6.3, MCS epicentral Intensity I_0 IX-X), 1389 (Mw 6.0, I0(MCS) IX), 1458 (Mw 5.8, I0(MCS) VIII-IX), 1489 (Mw 5.1, I0(MCS) VII), 1558 (Mw 5.1, I0(MCS) VII), 1789 (Mw 5.8, I0(MCS) X), 1917 (Mw 6.0, I0(MCS) IX-X) and 1919 (Mw 5.0, I0(MCS) VI) earthquakes (Rovida et al, 2020).

On the other hand, the seismicity recorded instrumentally in the Sansepolcro basin during the past 40 years is relatively low. A nearly opposite behaviour is observed along the Upper Tiber Valley SE of the Sansepolcro basin, with very high background and microseismic activity and almost no strong historical earthquakes. The microseismicity is confined in the hanging wall of the ATF and concentrates along the down-dip trace of the ATF (Boncio et al, 2000; Piccinini et al, 2003; Chiaraluce et al, 2007, Brozzetti et al, 2009). This allowed previous authors to hypothesize different seismogenic behaviours of the ATF in the Sansepolcro basin and south of it. For example, Brozzetti et al (2009) suggested that the ATF could be: i) creeping, accompanied by microseismicity, in the southern sector; and ii) locked for most of its tectonic history and able to nucleate large earthquakes in the northern sector. According to the damage distribution, these authors suggest that the 1389, 1458 and 1789 earthquakes could have nucleated along the Città di Castello seismogenic source, which include the AF. However, there is no palaeoseismological evidence to support these assumptions.

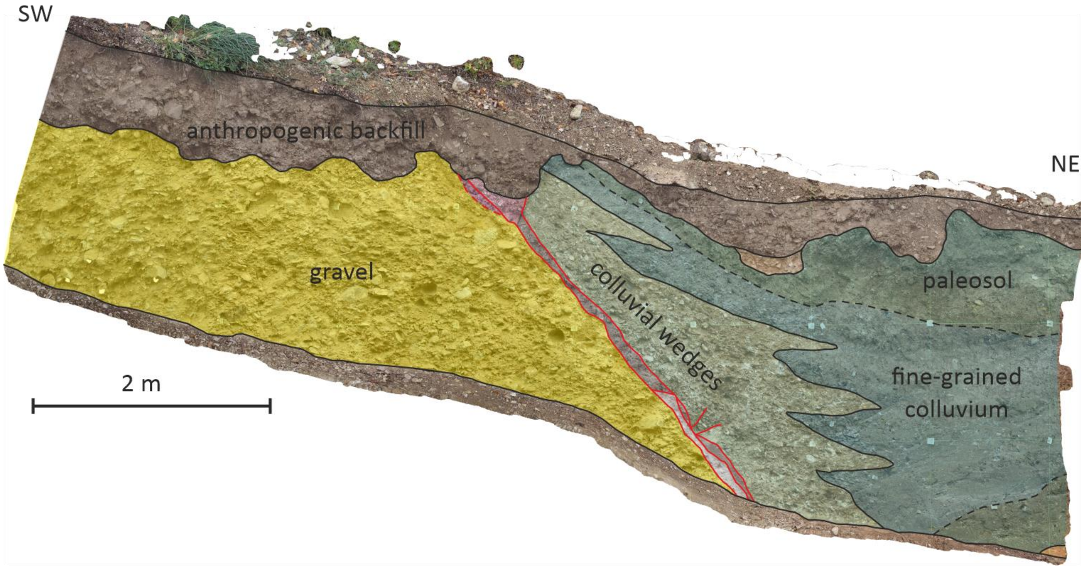

Fig. 2 Ortophotomosaic of the Villa sterpeto trench, limited to the fault zone.

RESULTS

We mapped the fault using a 1 m DSM from Pleiades images, and we selected several sites suitable for geophysical surveys and paleoseismologic trenching.

Two high-resolution seismic reflections lines were acquired across the upper splay of the AF. The most suitable site was identified across a scarp between the Citerna unit, at the footwall, and a flat paleo-surface carved on the Monterchi unit, at the hanging wall (Villa Sterpeto site, Fig. 1).

Here, the data show displaced high-amplitude reflections interpreted as the surface expression of the fault. A GPR survey additionally confirmed the possible presence of a fault in the very shallow subsurface. Therefore, we selected the Villa Sterpeto site for paleoseismologic trenching.

Moreover, during the geological survey we spotted a nearby outcrop of a normal fault affecting the gravels and sands of the Cirerna unit and several younger, fine-grained, palustrine and colluvial units. This outcrop was selected as the second site for the palaeoseismologic investigation (Todari road-cut site, Fig. 1).

The paleoseismic survey started in autumn 2021.

The Villa Sterpeto site.

We dug a 50 m-long, N60°-oriented trench across the fault. The northern wall of the trench was cleaned, gridded, and analysed for paleoseismology. The ortophotomosaic of the trench, obtained by photogrammetric survey, limited to the fault zone exposure, is shown in fig. 2.

A narrow fault zone (≥ 15 cm thick) separates the Citerna unit, at the footwall, from a colluvial unit, at the hanging wall, overlaying the Monterchi unit. The average fault attitude is 052/51.

The colluvial unit is made up of a sequence of stacked coarse-grained colluvial wedges overlapped each other and interfingered with fine-grained colluvium. We mapped at least 4 clear coarse-grained colluvial wedges. A fifth possible colluvial wedge is partially visible in the lower part of the trench wall. The maximum vertical thickness of the wedges is 45 cm on average.

We interpreted these wedges as scarp-derived colluvial units sourced by surface faulting earthquake fault scarps. In order to bracket the ages of the earthquakes, we sampled the fine-grained colluvium beneath and above each wedge. Only the radiocarbon dating of the bulk organic fraction of the sediments was possible due to the absence of charcoals. It was not possible to constrain the age of the sediment layer beneath the lowermost wedge since it is deeper than the trench floor.

According to the results of the radiocarbon dating the colluvial wedges are between 23 and 4 ky BCE.

The minimum vertical displacement in the last 27ky is 2.7 m.

The chronology of the events has been modelled using OxCal (V4.4 Bronk Ramsey, 2021).

The earthquakes ages are:

- E1 VS : between 22-15 ka BCE;
- E2 VS: between 15 and 13 ka BCE;
- E3 VS: between 13 and 11 ka BCE;
- E4 VS: between 11 abd 4 ka BCE.

Since the youngest unit is faulted, the recent most earthquake is younger than the E1 and older than a colluvial deposit trapped inside the fault zone.

Another important finding related to the excavation is the stratigraphy of the Monterchi unit, for which there is not an exhaustive description in the literature. In fact, two thirds of the Villa Sterpeto trench are curved within this unit.

Starting from the top, the Monterchi unit is made up of reddish to brownish 5 m-thick paleosol; yellowish sands with interbedded black chert clasts; grey clay and deeply altered yellowish to orange gravel; for a total thickens of at least 15 meters.

The dip of the bedding gradually increases toward the fault, indicating back-tilting.

In order to understand the relations between these units and the fault activity, we analysed the anisotropy of the magnetic susceptibility (AMS) of clay layers, the paleosol and the colluvial edge. In general, in compressive tectonic settings, the magnetic lineation (the maximum susceptibility axis) is commonly parallel to fold axes and thrust faults, while in extensional regimes, it is perpendicular to normal faults and parallel to bedding dip directions (e.g., Borradaile and Jackson 2004; Maffione et al., 2012). The mean susceptibility on the sites collected on clays varies from 139 to 217 e-6 SI, while the sites collected on the paleosol and on the colluvial unit containing the wedges have higher susceptibility, from 888 to 7162 e-6 SI. The degree of anisotropy, Pj, varies from weakly anisotropic (4% of the clay layers) to strongly anisotropic (43% of the colluvial edge) approaching the fault trace. The anisotropy data suggest that a primary sedimentary fabric has been overprinted by an incipient tectonic fabric. The orientation of magnetic lineation is mostly shallowly oriented NE-SW, thus parallel to the fault plane, consistent with a compressive tectonic regime. These results are comparable to the conclusions of Maffione et al. (2012) which correlated the AMS data with a compressive tectonic regime related of the Alto Tiberina fault to local effects in a regional extensional tectonic regime.

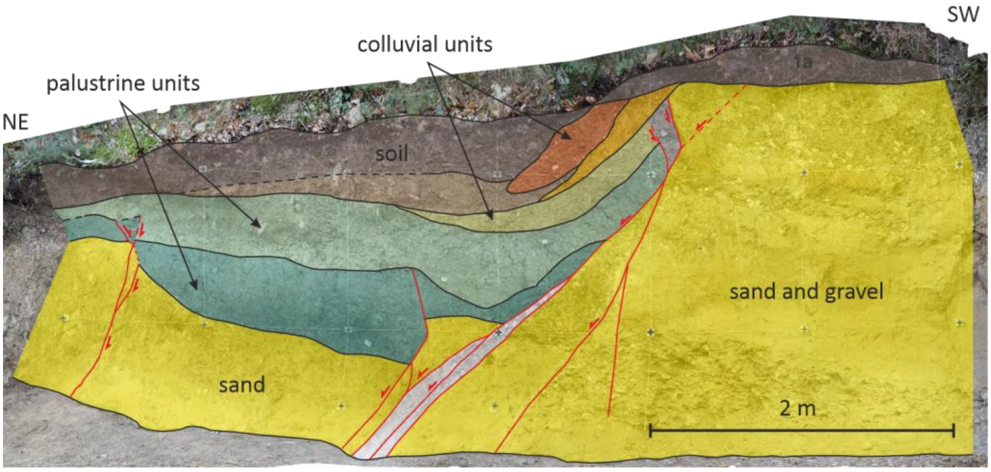

Fig. 3 Ortophotomosaic of the Toradi road-cut.

The Todari road-cut site.

We widened with a digger, cleaned, gridded and analysed a pre-existing NW-facing outcrop. The Orto-photomosaic of the Todari road-cut is shown in fig. 3.

Here the fault zone is wider than the Villa Sterpeto site and it is characterized by antithetic and synthetic fault strands. The main fault of the outcrop, which is a synthetic splay of the fault trenched in the Villa Sterpeto site, is dipping 40° toward north-east.

The footwall of the main fault, and the bottom of the hanging wall are featured by sand and gravel belonging to the Citerna unit. A palustrine depositional sequence is faulted and dragged against the fault and overlayed by younger, fault-related, colluvial deposits. Another important tectonic feature that helps to constrain the interpretation of the outcrop history is a filled fissure located at the hanging wall of the main fault. Even in this case we collected samples for radiocarbon dating of the bulk sediment, and we modelled the earthquakes ages using OxCal. According to our interpretation it is possible to recognize at least three surface faulting earthquakes. The earthquakes ages are:

- E1 T: between 5 and 3 ka BCE;
- E2 T: between 0,8 ka BCE and 967 CE;
- E3 T: between 0,3 ka BCE and 1450 CE.

The cumulative net slip of the last three earthquakes is larger than 1 m.

DISCUSSION AND CONCLUSIONS

Putting together the novel data achieved on the two paleosismological trenches we rebuilt the slip history of the AF during the last 22 ka BCE, which includes seven surface faulting earthquakes.

The resulting recurrence time ranges between 3200 and 2500 years and the vertical slip rate ranges from 0.12 and 0.2 mm/yr.

At the Villa Sterpeto site, the minimum displacement of each faulting event can be estimated thanks to the maximum vertical thickness of the wedges, which is on average, up to 45 cm.

Moreover, the age of the youngest earthquake derived by this study is close to the age of two historical earthquakes in the Sansepolcro basin: the 1458 (Mw 5.8, I_0(MCS) VIII-IX) and the 1489 (Mw 5.1, I_0MCS VII) earthquakes (red stars in fig. 1).

In conclusion we proved that the AF experienced repeated surface faulting events in the last 20 ka, demonstrating its capability to generate surface faulting earthquakes.

Is the AF the surface expression of a seismogenic LANF? Further investigations are needed to answer this question.

Acknowledgements:

These are results of the Ph.D. project of Alessio Testa (Scuola Superiore G. D'Annunzio - University of Chieti, Italy). This work is funded by "Ente Acque Umbre Toscane (EAUT), Arezzo, Italy", which is warmly acknowledged (Conventions 2019 and 2020 between EAUT and Universities of Chieti and Perugia; Resp.: P. Boncio). This work is also partially funded by the EQTIME ANR-project (Resp.: L. Benedetti).

REFERENCES

Barchi, M.R., Minelli, G. & Pialli, G. 1998 (a). The CROP 03 Profile: a synthesis of results on deep structures of the Norther Apennines. Mem. Soc. Geol. It., 52, 383-400.

Barchi, M.R., De Feyter, A., Magnani, M.B., Minellig., Pialli, G. & Sotera, B.M. 1998 (b). Extensional tectonics in the Northern Apennines(Italy): Evidence from the CROP03 deep seismic reflection line.Mem. Soc. Geol. It., 52, 527-538.

Benvenuti, M., Bonini, M. & Moroni, A. 2016. Tectonic control on the Late Quaternary hydrography of the Upper Tiber Basin (Northern Apennines, Italy). Geomorphology, 269, 85-103.

Boncio, P., Brozzetti, F., Ponziani, F., Barchi, M., Lavecchia, G. & Pialli, G. 1998. Seismicity and extensional tectonics in the northern Umbria–Marche Apennines. Mem. Soc. Geol. It., 52, 539-555.

Boncio, P., Brozzetti, F. & Lavecchia, G. 2000. Architecture and seismotectonics of a regional low-angle normal fault zone in central Italy. Tectonics, 19, 1038-1055.

Borradaile GJ, Jackson M (2004) Anisotropy of magnetic susceptibility (AMS): magnetic petrofabrics of deformed rocks. In: Martın-Hernandez F, Luneburg C, Aubourg C, Jackson M (eds) Magnetic Fabric methods and applications. Geol Soc Lond Spec Publ 238:299–360

Brozzetti, F., Boncio, P., Lavecchia, G. & Pace, B. 2009. Present activity and seismogenic potential of a low-angle normal fault system (Città di Castello, Italy): Constraints from surface geology, seismic reflection data and seismicity. Tectonophysics, 463, 31-46.

Cattuto, C., Cencetti, C., Fisauli, M. & Gregori, L. 1995. I Bacini Pleistocenici di Anghiari e Sansepolcro nell'alta Valle del F. Tevere. Il Quaternario, 8, 119-128.

Chiaraluce, L., Chiarabba, C., Collettini, C., Piccinini, D. & Cocco, M. 2007. Architecture and mechanics of an active low-angle normal fault: Alto Tiberina Fault, northern Apennines, Italy. J. Geoph. Res., 112, B10310. https://doi.org/10.1029/2007JB005015.

Maffione, M., Pucci, S., Sagnotti, L., & Speranza, F. (2012). Magnetic fabric of Pleistocene continental clays from the hanging-wall of an active low-angle normal fault (Altotiberina Fault, Italy). International Journal of Earth Sciences, 101(3), 849-861.

Piccinini, D., Cattaneo, M., Chiarabba, C., Chiaraluce, L., De Martin, M., Di Bona, M., Moretti, M., Selvaggi, G., Augliera, P., Spallarossa, D., Ferretti, G., Michelini, A., Govoni, A., Di Bartolomeo, P., Romanelli, M. & Fabbri, J. 2003. A microseismic study in a low seismicity area of Italy: the Città di Castello 2000–2001 experiment. Ann. Geophys., 46(6), 1315-1324.

Pucci, S., Mirabella, F., Pazzaglia, F., Barchi, M.R., Melelli, L., Tuccimei, P., Soligo, M. & Saccucci, L. 2014. Interaction between regional and local tectonic forcing along a complex Quaternary extensional basin: Upper Tiber Valley, Northern Apennines. Quat. Sci. Rev., 102, 111-132.

Rovida, A., Locati, M., Camassi, R., Lolli, B. & Gasperini, P. 2020. The Italian earthquake catalogue CPTI15. Bulletin of Earthquake Engineering, 18, 2953-2984 https://doi.org/10.1007/s10518-020-00818-y.

Testa, A., Valentini, A., Boncio, P., Pace. B, Visini. F, Mirabella, F., Pauselli, C., 2021. Probabilistic fault displacement hazard analysis of the Anghiari-Città di Castello normal fault (Italy). Ital. J. Geosci., Vol. 140, No. 3 (2021), pp. 327-346, 13 figs., 1 tab. (https://doi.org/10.3301/IJG.2021.07)

INQUA Focus Group Terrestrial Processes Perturbed by Tectonics (TPPT)

paleoseismicity.org

Site selection for creepmeter fault monitoring in a complex volcano-tectonic framework: the Mt. Etna eastern flank as an example

Tringali, Giorgio (1), Pia Victor (2), Raffaele Azzaro (3), Domenico Bella (4), Alessandro Bonforte (3), Silvia Crosetto (2), Gianluca Groppelli (5), Alessandro Maria Michetti (1, 6), Rosario Pettinato (4), Morelia Urlaub (7)

(1) Università degli Studi dell'Insubria, Dipartimento di Scienza e Alta Tecnologia, Como, Italy. Email: gtringali@uninsubria.it
(2) Helmholtz-Zentrum Potsdam, Deutsches GeoForschungs Zentrum (GFZ) Potsdam, Potsdam, Germany.
(3) INGV – Istituto Nazionale di Geofisica e Vulcanologia, Osservatorio Etneo, Catania, Italy
(4) Studio di Geologia Domenico Bella, Acireale, Italy.
(5) CNR – Consiglio Nazionale delle Ricerche, Istituto di Geologia e Geoingegneria, sezione di Milano, Milano, Italy.
(6) INGV – Istituto Nazionale di Geofisica e Vulcanologia, Osservatorio Vesuviano, Napoli, Italy.
(7) GEOMAR Helmholtz Centre for Ocean Research Kiel, Kiel, Germany

Abstract: *Mt. Etna is one of the most active volcanoes representing an exceptional natural laboratory for in-depth studies on volcano-tectonic processes. The volcano is monitored by the INGV-OE geophysical networks onshore given the high population density along its slopes, which have been affected not only by volcanic eruptions but also by damaging earthquakes. Seismicity and aseismic creep are more common in the eastern slope which is involved in flank instability processes resulting in slow gravitational sliding toward the sea with an active deformation also offshore. Thus, it is important to complement the actual monitoring system with creepmeters providing time series of displacement across active faults with continuous and high-resolution measurements. In this work we provide the first results of the geological and geophysical investigations in the Etna eastern flank and we present the methodology to characterize best suited sites for future installation.*

Key words*: creepmeter, fault monitoring, Mt. Etna, creep, earthquake*

INTRODUCTION

Mt. Etna is one of the most active volcanoes in the world with a well-developed monitoring system due to the high urbanization and population density in the lower slopes. The complex-volcano tectonic framework is the result of an interaction between regional tectonic, magmatic processes and flank instability. Several active fault segments affect the eastern flank with normal and transtensive kinematics (Azzaro et al., 2012; ITHACA Working Group, 2019), and surface faulting is produced by moderate magnitude earthquakes (Mw 4 to 5) and aseismic creep events (Rasà et. al, 1996; Azzaro et al., 2012). Creepmeter installation can provide new time series of displacement accumulation across monitored fault segments with high resolution (1 µm), as already observed in other tectonic environments (Bilham et al., 2004; Victor et al., 2018). In this work we show the first results of field investigations and geophysical surveys to find suitable sites for the installation of the creepmeters in this highly urbanized area. With these results, we were able to install already two instruments in the Etna complex volcano-tectonic environment in July 2022.

GEOLOGICAL AND SEISMOTECTONIC SETTING

Mt. Etna is located on the Appeninic-Maghrebian thrust and fold belt with effusive and explosive activity from 4 summit craters and also from flank fissures opened temporarily along the slopes. The seismicity is often related to dyke intrusions with the strongest earthquakes that occur typically along the faults of the eastern flank (Fig. 1), causing damage of grade VIII-IX of the EMS scale (Azzaro et al., 2012).

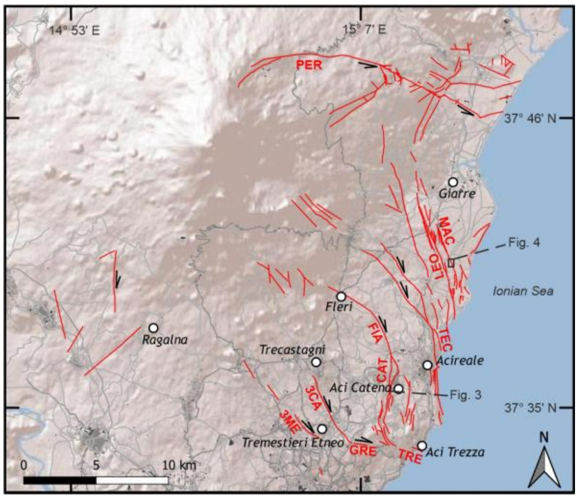

Figure 1: Mt. Etna general map focused on the eastern flank; in grey roads and urbanized area; capable faults in red. PER: Pernicana; 3ME: Tremestieri; 3CA: Trecastagni; GRE: San Gregorio; TRE: Aci Trezza; FIA: Fiandaca; CAT: Aci Catena; TEC: Santa Tecla; LEO: San Leonardello; MAC: Macchia.

These faults are strictly related to the gravitational collapse (Azzaro et al., 2013) which also involves the offshore sector as revealed by multibeam and seismic reflection investigations and seafloor geodesy (Urlaub et al., 2018, 2022). The onshore flank sliding is bounded to the north by the left lateral Pernicana Fault, and to the south by the right lateral Tremestieri – Trecastagni - Aci Trezza faults system (Fig. 1). Surface deformation along the Etna slopes is constantly monitored by the INGV seismic and geodetic networks. The Trecastagni Fault is accurately monitored by two extensometers held by INGV-OE, while offshore monitoring has been recently improved with five GEOMAR transponders along the Aci Trezza Fault offshore extension. In particular, the first offshore creep event has been recorded in 2016 with 4 cm of slip (Urlaub et al., 2018).

CREEPMETER FAULT MONITORING SYSTEM

The creepmeter used in our project measures the fault displacements along a 12 mm thick Invar rods, which passes through a PVC pipe, attached to concrete foundations on both sides of the fault (Fig. 2). The creepmeters are generally buried at a depth of 30-70 cm. The measurement process is performed by an LVDT (linear variable differential transformer) with a range depending on long term slip rates (50-150 mm) that monitors the relative displacement of the free end of the rod with respect to the fixed endpoint (Fig. 2). Displacement is recorded as voltage change and stored on a data logger with a sampling rate of 2/min. The length of the instrument depends on the characteristics of each site and varies between 3 and 9 m. Site can be equipped with a meteorological station to monitor potential effects of temperature, humidity and air pressure changes. The data is stored locally and sent to the GFZ via modem.

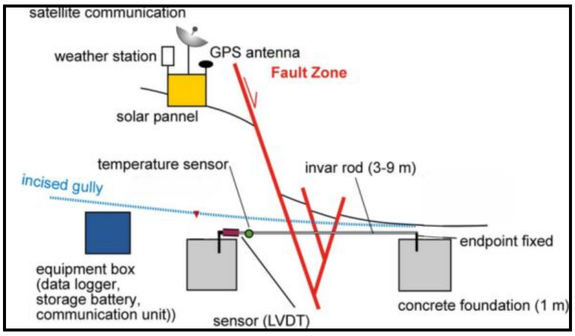

Figure 2: Sketch of creepmeter setup across a normal fault.

SITE SELECTION FOR CREEPMETER INSTALLATION

The main challenge in this type of environmental setting is to have access in a suitable site in areas generally characterized by (1) high urbanization; (2) private properties; and (3) unprotected public places (e.g., squares and parking areas).

We started by analysing published data with a focus on a) ITHACA capable faults catalogue (ITHACA Working Group, 2019); b) the volcano-tectonic map of Etna volcano 1:100.000 scale (Azzaro et al., 2012); c) a pilot GIS database of active faults of Mt. Etna (Barreca et al., 2013). Afterwards, we preliminarily selected 16 potential sites suitable for the creepmeters installation (Table 1). Most of the sites are located along creeping faults (e.g., the Aci Catena, Tremestieri, San Gregorio, Santa Tecla, San Leonardello, and Macchia faults). Some sites are also located along the Fiandaca Fault that showed coseismic surface ruptures in 2018, and the extensive surface faulting is mapped in great detail (Civico et al., 2019; Tringali et al., 2022). We also acquired and analysed refraction seismic profiles (seismic tomography) from previous studies performed along the faults.


Figure 3: Ruptures on the ground and a wall along the Aci Catena Fault.

Considering the parameters that need to be fulfilled for the installation of a creepmeter, we performed a field survey to detect ground ruptures (Fig. 4) and deformations related to tectonic activity. In particular, for each site we evaluated: if displacement is well localized, the geometrical parameters of the fault plane, if gravitational effects can be avoided, the amount of distributed displacement, the possibility of obtaining permission as well as possible logistical problems during creepmeter installation and anthropogenic noise.

To comply the above points, in addition to detailed field investigations we performed seismic refraction surveys along some faults to better identify the width and localization of the tectonic deformation zone. Seismic refraction is a geophysical methodology that uses the velocity contrasts generated by the propagation of elastic waves in the subsurface. The seismic wave velocity depends on the lithological contrast of the underground layers.

N	Locality	Municipality	Fault	Surface litology	Latitude and Longitude	Ownership
1	Santa Tecla	Acireale	Santa Tecla	Alluvial deposit	37°38'1.73"N 15°10'20.93"E	Private
2	Pozzillo	Acireale	San Leonardello	Lava flow	37°40'7.18"N 15°10'55.32"E	Private
3	Pozzillo	Acireale	San Leonardello	Lava flow	37°40'16.20"N 15°10'49.10"E	Private
4	San Leonardello	Riposto	San Leonardello	Chiancone/Lava flow	37°41'1.75"N 15°10'26.28"E	Private
5	Macchia	Giarre	San Leonardello	Lava flow	37°42'40.12"N 15° 9'32.28"E	Private
6	Malpassoti	Riposto	Macchia	Chiancone	37°40'37.78"N 15°11'4.10"E	Private
7	Malpassoti	Riposto	Macchia	Chiancone	37°40'43.67"N 15°11'2.12"E	Private
8	San Leonardello	Giarre	Macchia	Chiancone	37°41'51.93"N 15°10'28.76"E	Private
9	Santa Maria La Stella	Acireale	Fiandaca	Lava flow	37°37'33.10"N 15° 8'6.72"E	Private
10	Fiandaca	Aci Sant'Antonio	Fiandaca	Lava flow	37°38'10.82"N 15° 7'47.34"E	Private
11	Pennisi	Acireale	Fiandaca	Lava flow	37°38'38.74"N 15° 7'26.73"E	Private
12	San Giacomo	Aci Catena	Acicatena	Lava flow	37°36'16.52"N 15° 8'20.05"E	Public
13	San Giovanni la punta	San Giovanni la punta	Trecastagni	Lava flow	37°34'42.60"N 15° 5'29.62"E	Public
14	San Giovanni la punta	San Giovanni la punta	Trecastagni	Lava flow	37°33'57.73"N 15° 6'6.35"E	CAS
15	Tremestieri Etneo	Tremestieri Etneo	Tremestieri	Lava flow	37°34'9.34"N 15° 4'38.44"E	Public
16	San Gregorio	San Gregorio	San Gregorio	Lava flow	37°33'51.18"N 15° 6'43.33"E	Public

Table 1: Preliminarily sites information for creepmeters installation.

The aim of the tomographic survey used for this study is to identify the fault zone and provide a well-determined location of the deformation in the subsurface. The instrumentation used for the survey consists of a multi-channel seismograph (MAE sysmatrack with 24 channels), two seismic cables with 12 sockets each, 22 geophones with a frequency of 4.5 Hz and one 8 kg hammer. SmartTomo 2020 is the software used for the processing of the acquired seismic data where the inversion is performed with GRM (General Reciprocal Method). In order to carry out processing using the GRM method, it is necessary to have two reciprocal energisation points where the refractor is visible and for each geophone are calculated the travel times.

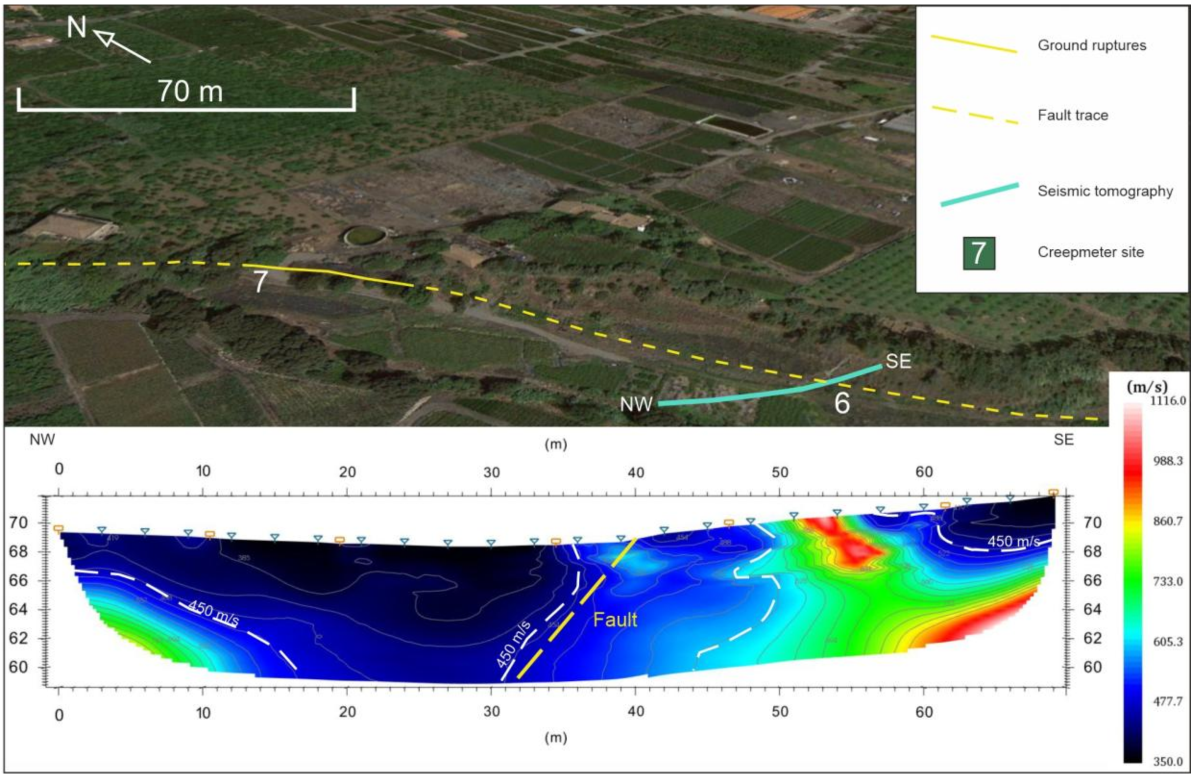

Figure 4: Seismic tomography along the Macchia Fault.

RESULTS

According to the field surveys, we observed that the range of deformation inferred from ground ruptures varies according to kinematics. Faults with strike-slip kinematics, such as the Tremestieri Fault and especially the San Gregorio Fault, show a wider deformation zone up to about 20 m due to the formation of Riedel fractures along the shear zone. Conversely, predominantly normal, east-dipping faults, such as the Aci Catena Fault and the San Leonardello Fault, show a narrower deformation zone, averaging less than 10 m (Fig. 3).

We conducted seismic profile along the normal west dipping Macchia Fault, which is an antithetic fault to the San Leonardello Fault. The seismic profile has an NW-SE direction (Fig. 4), the geophones were positioned with a 3 m interval for a final length of 57m. In order to have a good number of seismic data, 7 total energisations were performed with various iterations to increase the signal-to-noise ratio, 2 outside the spread (3 m from the last geophone) and 5 inside (4 intermediate and one central). The tomographic survey (Fig. 4) allowed us to investigate an underground area up to a maximum depth of approximately 10 m from the topographic surface. The seismostratigraphic profile revealed an area between 20 and 32 m with Vp velocity values of ≈ 450 m/s. This low velocity area could be ascribed to a damaged fault zone or loose fluvial sediments. The area delimited by low Vp values tends to decrease as the maximum depth is reached. Laterally seismic layers with different thicknesses and velocities are present with a maximum Vp of 1000/ m/s is reached in the SE part.

DISCUSSION AND CONCLUSION

Knowledge on fault zones is additionally complemented with subsurface studies to determine best suited sites for creepmeter installations. This approach is necessary due to the bad accessibility of many sites. The number of sites could be lowered from 16 to 5 options due to this methodology and we were already able to install 2 creepmeters in optimal positions along the Macchia Fault, in the sites number 6 and 7.

Volcanic processes at Mt. Etna can cause stress variations along faults triggering earthquakes and fault creep, often in the framework of flank instability events. Monitoring these faults with creepmeters could provide us new data to better understand these complex interactions in a volcano-tectonic setting.

Acknowledgements: We are deeply grateful to the local people who allowed us to enter their properties and install the instruments. We also thank the local authorities for their willingness to implement the current Etna monitoring system. Part of the fieldwork and the creepmeters assembly has been supported by M. Urlaub HGF funds.

REFERENCES

Azzaro, R., Branca, S., Gwinner, K., Coltelli, M., 2012. The volcano-tectonic map of Etna volcano, 1:100.000 scale: an integrated approach based on a morphotectonic analysis from high-resolution DEM constrained by geologic, active faulting and seismotectonic data. Italian Journal of Geosciences. 2012; 131 (1): 153–170. https://doi.org/10.3301/IJG.2011.29

Azzaro, R., Bonforte, A., Branca, S. & Guglielmino, F., 2013. Geometry and kinematics of the fault systems controlling the unstable flank of Etna volcano (Sicily). Journal of Volcanology and Geothermal Research 251, 5–15.

Barreca, G., Bonforte, A., Neri, M., 2013. A pilot GIS database of active faults of Mt. Etna (Sicily): A tool for integrated hazard evaluation, Journal of Volcanology and Geothermal Research, Volume 251, Pages 170-186, ISSN 0377-0273, https://doi.org/10.1016/j.jvolgeores.2012.08.013.

Bilham, R., Suszek, N., Pinkney, S., 2004. California Creepmeters. Seismological Research Letters 2004; 75 (4): 481–492. https://doi.org/10.1785/gssrl.75.4.481

Civico, R., et al., 2019. Surface ruptures following the 26 December 2018, Mw 4.9, Mt. Etna earthquake, Sicily (Italy). J. Maps 15 (2), 831–837.

ITHACA Working Group, 2019. ITHACA (ITaly HAzard from CApable faulting), A database of active capable faults of the Italian territory. Version December 2019. http://sgi2.isprambiente.it/ithacaweb/Mappatura.aspx ISPRA Geological Survey of Italy.

Rasà, R., Azzaro, R. & Leonardi, O., 1996. Aseismic creep on faults and flank instability at Mount Etna volcano, Sicily. Geological Society, London, Special Publications 110, 179–192.

Urlaub, M. et al., 2018. Gravitational collapse of Mount Etna's southeastern flank. Science Advances 4, eaat9700.

Urlaub, M., Geersen, J., Petersen, F., Gross, F., Bonforte, A., Krastel, S., Kopp, H., 2022. The Submarine Boundaries of Mount Etna's Unstable Southeastern Flank. Front. Earth Sci. 10:810790. doi: 0.3389/feart.2022.810790

Victor, P., Oncken, O., Sobiesiak, M., Kemter, M., Gonzalez, G., Ziegenhagen, T., 2018. Dynamic triggering of shallow slip on forearc faults constrained by monitoring surface displacement with the IPOC Creepmeter Array. Earth and Planetary Science Letters, Volume 502, 2018, Pages 57-73, ISSN 0012-821X, https://doi.org/10.1016/j.epsl.2018.08.046

Tringali, G., Bella, D., Livio, F.A., Ferrario, M.F., Groppelli, G., Blumetti, A.M., Di Manna, P., Vittori, E., Guerrieri, L., Porfido, S., Boso, D., Pettinato, R., Paradiso, G., & Michetti, A.M. (2022). Fault rupture and aseismic creep accompanying the December 26, 2018, Mw 4.9 Fleri earthquake (Mt. Etna, Italy): Factors affecting the surface faulting in a volcano-tectonic environment. Quaternary International. ISSN 1040-6182, https://doi.org/10.1016/j.quaint.2021.12.019

Geological and Geodetic Slip Rates of the Dzhungarian Fault, Northern Tien Shan

Chia-Hsin Tsai (1), Christoph Grützner (2), Simon Daout (3), Kanatbek Abdrakhmatov (4), Aidyn Mukambayev (5), Kathryn Fitzsimmons (6), Andrew S. Carr (7), Ed Rhodes (8), Andrew Ivester (8), Anna H. Rood (9), Dylan H. Rood (10), Roberta Wilkinson (1), Richard Walker (1)

(1) COMET, Dept. of Earth Sciences, University of Oxford, South Parks Rd, Oxford, OX 1 4AN, UK. Email: chia-hsin.tsai@earth.ox.ac.uk
(2) Institute of Geological Sciences, Friedrich Schiller University Jena, Jena, Germany
(3) CRPG, University of Lorraine, Vandœuvre-lès-Nancy, France
(4) Institute of Seismology, National Academy of Sciences, Bishkek, Kyrgyz Republic
(5) Data Center of the Institute of Geophysical Researches, Almaty, Kazakhstan
(6) Department of Geosciences, University of Tübingen, Tübingen, Germany
(7) School of Geography, Geology and the Environment, University of Leicester, Leicester, UK
(8) Department of Geography, University of Sheffield, Sheffield, UK
(9) Department of Civil and Environmental Engineering, Imperial College London, London, UK
(10) Department of Earth Science and Engineering, Imperial College London, London, UK

Abstract: *Cities and infrastructures within and around the Tien Shan are exposed to seismic hazards due to the existence of large active faults, but little is understood in terms of earthquake occurrence and fault slip rates. Here we present both geological and geodetic slip rates of the Dzhungarian Fault, which is a major structure bounding the northern Tien Shan. High-resolution topographic imagery and various Quaternary dating approaches were used to measure and date offset geomorphic features. We also used Interferometric Synthetic-Aperture Radar (InSAR) data with time-series analysis to reveal the geodetic slip rates. We provide the very first geological uplift rates of the Dzhungarian Fault, which is 0.4 – 1.0 mm/yr averaged over 60 kyr timescales. For the lateral slip rates, we estimated the geological rate to be 1.5 – 4.7 mm/yr averaged over 14 kyr timescales and the preliminary modern geodetic rates to be 1 – 2 mm/yr.*

Key words: *Dzhungarian Fault, Slip rate, Tien Shan, Shortening, Strike-slip*

INTRODUCTION

Slip rates of faults are essential information for understanding fault activity and regional crustal deformation which are important for seismic hazard assessment. In the interior of Tien Shan, Global Navigation Satellite System (GNSS) velocities show that the ~N-S India-Eurasia convergence rate is 15 – 22 mm/yr but the rate drops to only 1 – 3 mm/yr around the Dzhungarian Alatau (Abdrakhmatov et al., 1996; Zubovich et al., 2010). This shortening is accommodated by E-W trending reverse structures and block rotations between large right-lateral strike-slip faults in the Tien Shan. Despite the slow deformation rate across the Dzhungarian Alatau, prominent palaeo-earthquake ruptures in this region show the faults are potential to cause earthquakes with magnitudes up to Mw 8.4 (Tsai et al., 2022), which could be the upper-end of earthquake magnitude in continental interior settings. The major fault bounding at the edge of the Dzhungarian Alatau is the Dzhungarian Fault (fig. 1), which is a strike-slip fault with a reverse component and a length of over 300 km along the route of the Eurasia Railway. However, large historical earthquakes are absent in the historical records in the Dzhungarian region and only the strike-slip rates at the southern part of the Dzhungarian Fault were investigated using modern Quaternary dating approaches. These rates are 1.4 – 4.6 mm/yr (Campbell et al., 2013; Hu et al., 2021). Since the Dzhungarian Fault is important in building understanding for large-magnitude intra-continental earthquakes, in this study, we further collected samples from uplifted river terraces at the northern parts of the fault, which provide the first uplift-rate data. We also collected samples for estimating the exposure ages of the laterally-offset fan surfaces to validate the strike-slip rates from previous studies that had limited age constraint. InSAR time-series analysis is further applied for estimating the geodetic strike-slip rate of the Dzhungarian Fault.

METHODS

To calculate the geological slip rates of the Dzhungarian Fault, we first used optical images and high-resolution digital elevation models (DEMs) by structure-from-motion from drone photos and the Pléiades satellite images to recognize and to measure displaced geomorphic features. When defining the vertical displacements for uplifted features such as river terraces, we assumed no post-uplift deposition on the footwall since it is barely possible to reveal the depth of corresponding terrace surfaces prior to uplift on the footwall. Thus, the uplift rates estimated in this study should all be the minimum rates. Since radiocarbon samples are rare in this region, we collected fluvial samples for quartz/feldspar optically/infrared stimulated luminescence dating (OSL/IRSL) (Rhodes et al., 2010; Rhodes, 2015), and quartz-rich samples for terrestrial cosmogenic nuclides (TCN) dating (Schaefer et al., 2022) to constrain the ages of those displaced features. To calculate the geodetic slip rate, we did the time-series analysis on the two tracks of Sentinel-1 SAR data from 2014-2020 using the New Small Baseline Subset (NSBAS) processing chain (Doin et al., 2010).

RESULTS

The Dzhungarian Fault (DZF) has been separated into eight sections, mainly based on fault geomorphology: the northern sections S0 – S3 show oblique slip; the southern sections S4 – S7 are characterised by pure strike-slip (fig. 1) (Tsai et al., 2022).

Section S0: Shynzhyly River

On S0 at the northern Shynzhyly River bank, a river terrace abandoned after 44.9 ± 4.5 ka (OSL) has been uplifted for 26.7 ± 1.4 m, which yields an uplift rate of 0.6 ± 0.1 mm/yr. At the southern river bank, a young but abandoned fan has been uplifted for about 3 m with an abandonment age of 5.3 – 6.4 ka, yielding an uplift rate of 0.5 – 0.6 mm/yr which is consistent with the one at the northern bank (fig. 2).

Section S2: site 1 & site 2

Sampling sites on S2 are about 30 km SE of the Shynzhyly River. At site 1, two levels of uplifted river terraces are recognized with displacements of 29.6 ± 2.0 m and 13.8 ± 0.3 m for the older and younger ones respectively with their abandoned ages dated by OSL as 59.1 ± 7.6 ka and 20.9 ± 2.2 ka (fig. 3a). These yield an uplift rate of 0.6 ± 0.2 mm/yr. At site 2, we only have one sample pit on the oldest terrace abandoned after 20.4 ± 1.9 ka (OSL) with 18.7 ± 0.5 m of vertical displacement, which yields an uplift rate of 0.9 ± 0.1 mm/yr (fig. 3b).

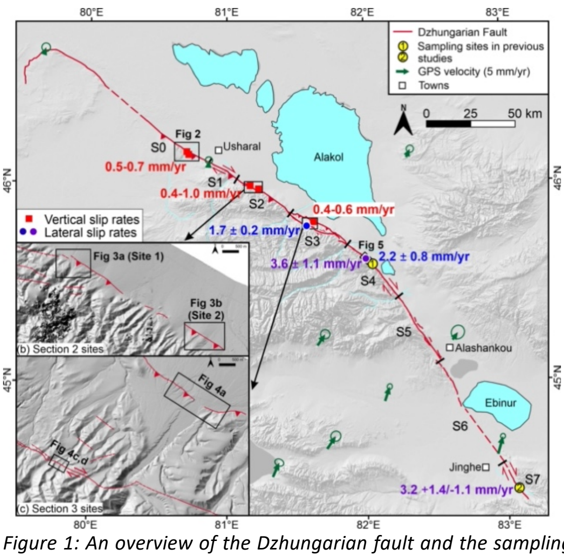

Figure 1: An overview of the Dzhungarian fault and the sampling sites in this study and previous work with geological slip rates annotated. GPS velocity vectors are from Zheng et al. (2017). Panels on the left are demonstrated in the DEMs made from Pléiades imagery.

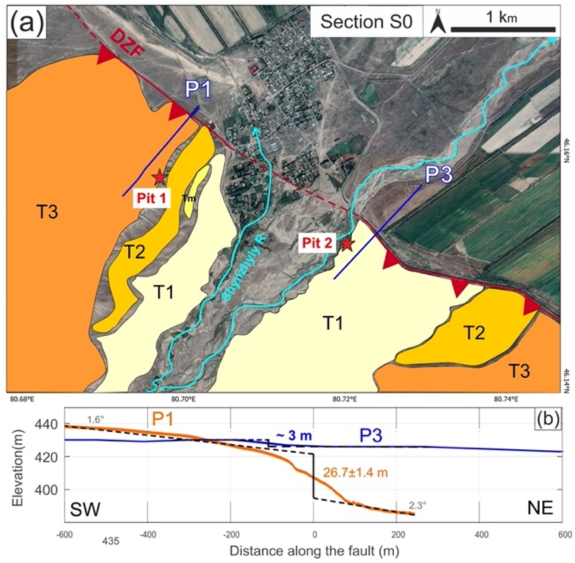

Figure 2: (a) Uplifted river terraces on both sides of the Shynzhyly River on Section S0. Red stars are the sample pits from where OSL samples were collected. (b) Fault scarp profiles for P1 (orange) and P3 (blue) with the heights annotated.

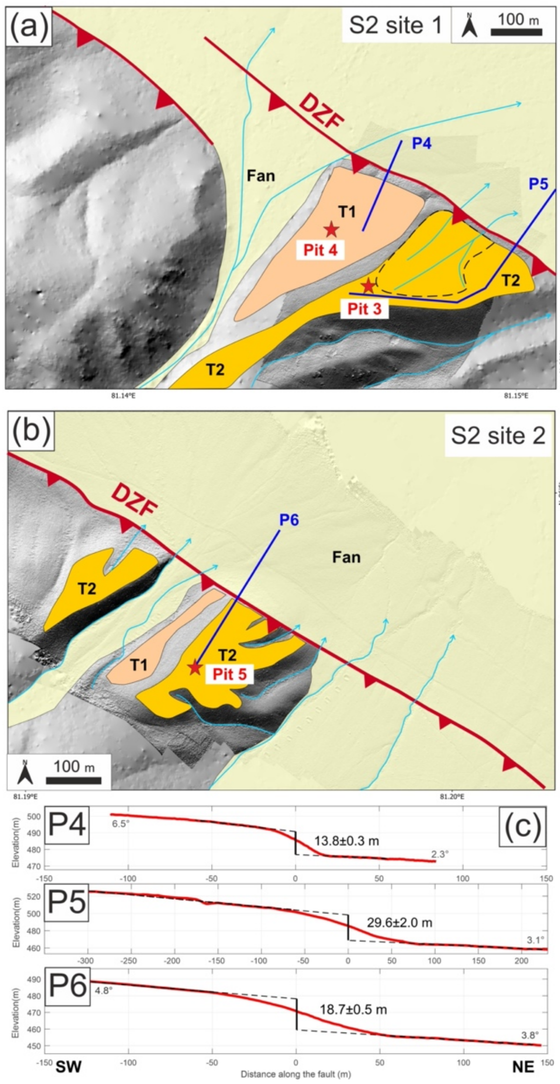

Figure 3: Uplifted river terraces at site 1 (a) and site 2 (b) on Section S2. Red stars are the pits from where OSL samples were collected. (c) Fault scarp profiles for P4, P5 and P6 with the heights annotated.

Section S3: Northern & Southern Branch

S3 of the DZF is a slip-partitioning zone with two main branches: the northern branch shows prominent reverse components whereas the southern branch is dominated by strike-slip movements. On the northern branch, an old river terrace has been uplifted for 14.6 ± 1 m with an abandoned age of 29.6 ± 2.8 ka (IRSL), yielding an uplift rate of 0.5 ± 0.1 mm/yr (fig. 4a,b).

On the southern branch, we found two ridges laterally-offset by about 30 m and one river channel, between the two ridges, laterally-offset by 19.2 ± 0.6 m. One sample of likely aeolian loess was collected next to the offset channel and dated as 11.2 ± 0.8 ka (IRSL). Considering this aeolian sample should post-date the channel, we could estimate a maximum lateral-slip rate of 1.7 ± 0.2 mm/yr (fig. 4c-f).

Section S4

S4 of the DZF is a pure strike-slip section. A minimum slip rate of 2.2 ± 0.8 mm/yr has been reported based on a ~ 50 m-displaced alluvial fan and a ~ 26 ka fan age derived from a single OSL sample (Campbell et al., 2013). We collected quartz cobbles along the 49.4 ± 8.0 m-offset channel levees, which is 2.5 km NW of the previous OSL sample site, and they yield an average age of 14.3 ± 2.0 ka (TCN) (fig. 5). This indicates a minimum lateral-slip rate of 3.6 ± 1.1 mm/yr, which is consistent with the previous result.

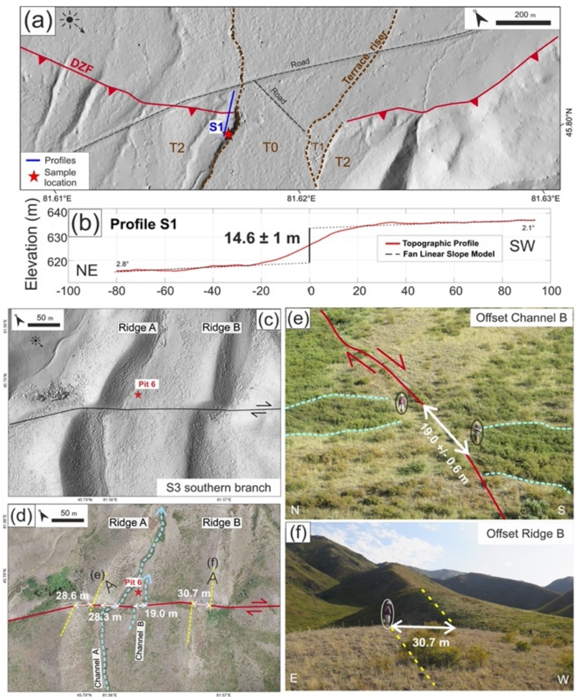

Figure 4: (a) Uplifted river terraces on the northern branch of Section S3 with the fault scarp of Profile S1 shown in (b). (c)-(d) Laterally-offset ridges and channels with the amounts of displacements annotated and field photos shown in (e) and (f).

Section S4 & S5: Geodetic slip rates

S5 of the DZF is also a pure strike-slip section. We did InSAR time-series analysis for one descending (D063) and one ascending (A012) tracks and found that the massive regional moisture and high topographic relief pose great challenges for the unwrapping process. We managed to get Line of Sight (LOS) velocity profiles across S4 and S5, which show about 1 – 2 mm/yr LOS velocity change across the DZF (fig. 6).

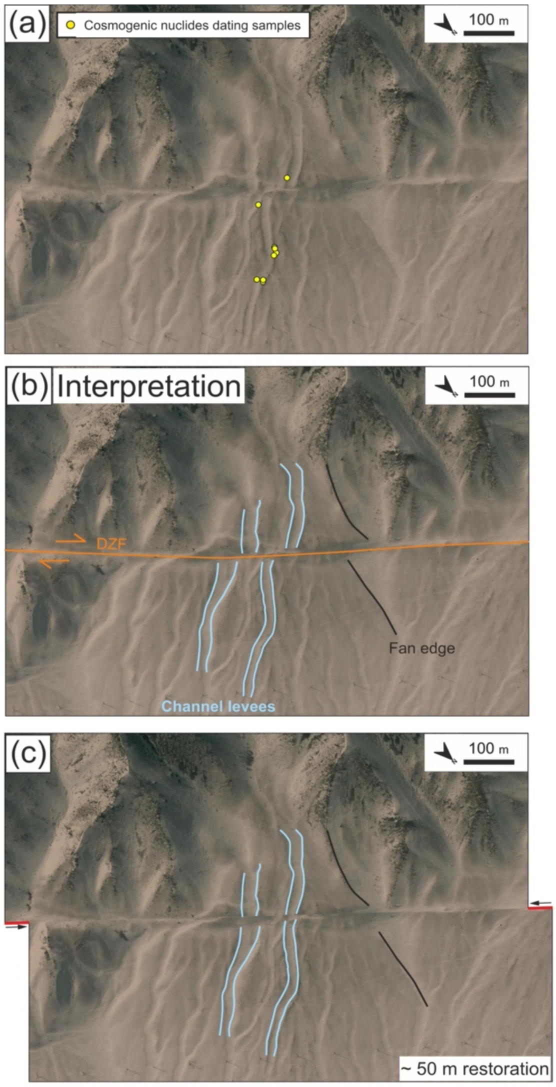

Figure 5: (a) the right-laterally offset fan and channels on Section S4 with the locations of the nine samples (yellow) collected for TCN. (b) Interpretation for the geomorphic features with displaced channels (blue) and fan (black) marked. (d) Restoration of the displaced features for ~ 50 m

DISCUSSION & CONCLUSIONS

The vertical slip rates of 0.4 – 1.0 mm/yr along the northern DZF estimated from the uplifted terraces at different sections fit well with each other. This does not cover the total convergence rates (1 – 3 mm/yr) across the Dzhungarian Alatau, which indicates block rotation and other reverse faults in the northern Alatau are actively accommodating the shortening as well. The strike-slip rates from this and previous studies are also consistent with each other (in the range of 1.4 – 4.7 mm/yr). The preliminary InSAR results fit well with the GNSS velocity change across the DZF (Zheng et al., 2017), too. This means block rotation is dominating in the southern DZF region. Combining the likely coseismic slip of 6 – 9 m on the southern DZF (Tsai et al., 2022) with the strike-slip rates, we get a mean recurrence interval for major earthquakes of ~2500 years.

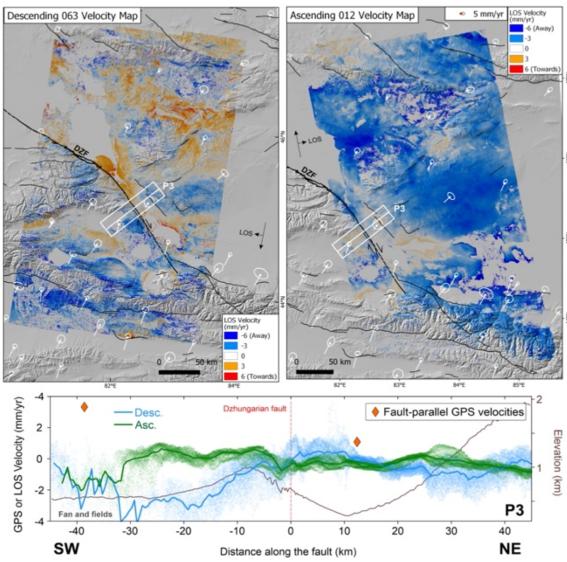

Figure 6: InSAR LOS velocity maps from the two tracks with a profile below showing the oppsite velocity change across the DZF from the two tracks, indicating it is tectonic signal. There are LOS velocity steps of ~2 mm/yr and ~1 mm/yr across the fault in the desc. and asc. tracks respectively. The velocity step in the desc. track is greater as expected due to the optimal fault orientation to the track. GPS velocity vectors are from Zheng et al. (2017).

Acknowledgements: This work was funded and supported by the NERC-ESRC Increasing Resilience to Natural Hazards program 'Earthquakes without Frontiers' (NE/J02001X/1) and the NERC-funded the Centre for the Observation and Modelling of Earthquakes, Volcanoes and Tectonics (COMET). We thank those involved in the 2016 and 2017 field seasons, and in the laboratory sample processing.

REFERENCES

Abdrakhmatov, K. E., Aldazhanov, S. A., Hager, B. H., Hamburger, M. W., Herring, T. A., Kalabaev, K. B., Makarov, V. I., Molnar, P., Panasyuk, S. V., Prilepin, M. T., Reilinger, R. E., Sadybakasov, I. S., Souter, B. J., Trapeznikov, Y. A., Tsurkov, V. Y., & Zubovich, A. V. (1996). Relatively recent construction of the Tien Shan inferred from GPS measurements of present-day crustal deformation rates. Nature, 384(6608), 450–453. https://doi.org/10.1038/384450a0

Campbell, G. E., Walker, R. T., Abdrakhmatov, K. E., Schwenninger, J., Jackson, J. A., Elliott, J. R., & Copley, A. (2013). The Dzhungarian fault: Late Quaternary tectonics and slip rate of a major right-lateral strike-slip fault in the northern Tien Shan region. Journal of Geophysical Research: Solid Earth, 118(10), 5681–5698. https://doi.org/10.1002/jgrb.50367

Doin, M. P., Twardzik, C., Ducret, G., Lasserre, C., Guillaso, S., & Sun, J. (2015). InSAR measurement of the deformation around Siling Co Lake: Inferences on the lower crust viscosity in central Tibet. Journal of Geophysical Research: Solid Earth, 120(7), 5290–5310. https://doi.org/10.1002/2014JB011768.

Hu, Z., Yang, X., Yang, H., Huang, W., Wu, G., Miao, S., & Zhang, L. (2021). Slip Rate and Paleoseismology of the Bolokenu-Aqikekuduk (Dzhungarian) Right-Lateral Strike-Slip Fault in the Northern Tian Shan, NW China. Tectonics, 40(8), e2020TC006604. https://doi.org/https://doi.org/10.1029/2020TC006604.

Rhodes, E. J., Fanning, P. C., & Holdaway, S. J. (2010). Developments in optically stimulated luminescence age control for geoarchaeological sediments and hearths in western New South Wales, Australia. Quaternary Geochronology, 5(2–3), 348–352. https://doi.org/10.1016/j.quageo.2009.04.001

Rhodes, E. J. (2015). Dating sediments using potassium feldspar single-grain IRSL: Initial methodological considerations. Quaternary International, 362, 14–22. https://doi.org/10.1016/j.quaint.2014.12.012

Schaefer, J. M., Codilean, A. T., Willenbring, J. K., Lu, Z.-T., Keisling, B., Fülöp, R.-H., & Val, P. (2022). Cosmogenic nuclide techniques. Nature Reviews Methods Primers, 2(1). https://doi.org/10.1038/s43586-022-00096-9

Tsai, C. H., Abdrakhmatov, K., Mukambayev, A., Elliott, A., Elliott, J., Grützner, C., Rhodes, E., Ivester, A., Walker, R. & Wilkinson, R. (2022). Probing the upper end of intra-continental earthquake magnitude: a prehistoric example from the dzhungarian and lepsy faults of Kazakhstan. Tectonics. (in press)

Zheng, G., Wang, H., Wright, T. J., Lou, Y., Zhang, R., Zhang, W., Shi, C., Huang, J., & Wei, N. (2017). Crustal Deformation in the India-Eurasia Collision Zone From 25 Years of GPS Measurements. Journal of Geophysical Research: Solid Earth, 122(11), 9290–9312. https://doi.org/10.1002/2017JB014465.

Zubovich, A. V., Wang, X. Q., Scherba, Y. G., Schelochkov, G. G., Reilinger, R. E., Reigber, C., Mosienko, O. I., Molnar, P., Michajljow, W., Makarov, V. I., Li, J., Kuzikov, S. I., Herring, T. A., Hamburger, M. W., Hager, B. H., Dang, Y. M., Bragin, V. D., & Beisenbaev, R. T. (2010). GPS velocity field for the Tien Shan and surrounding regions. Tectonics, 29(6), 1–23. https://doi.org/10.1029/2010TC002772

Late Cenozoic reactivation of a trench parallel strike- slip system and tectonic forcing of drainages close to the Oroclinal Bend, Andean forearc of N-Chile

Ambrosio Vega Ruiz (1), Pia Victor (1), Vanessa Steinritz (2), Arianne Binnie (3), Gabriel Gonzalez (4,5), Kathrin Lampert (6), Klaus Reicherter (2), Steven Binnie (3)

(1) Deutsches GeoForschungsZentrum GFZ, Telegrafenberg 14473 Potsdam, Germany. Email: vegaruiz@gfz-potsdam.de
(2) Neotectonics and Natural Hazards, RWTH Aachen University, Lochnerstrasse 4-20 D – 52056 Aachen, Germany.
(3) Institute of Geology and Mineralogy, University of Cologne, Zülpicher Str. 49a 50674 Köln, Germany.
(4) Departamento de Ciencias Geológicas, Universidad Católica del Norte, Casa Central, Angamos 0610 Antofagasta, Chile.
(5) Centro de Investigación para la Gestión Integrada del Riesgo de Desastres (CIGIDEN), Edificio Hernán Briones, Av. Vicuña Mackenna 4860 Santiago, Chile.
(6) Institute of Zoology, University of Cologne, Zülpicher Str. 47b 50674 Köln, Germany.

Abstract: *The forearc of northernmost Chile forearc presents important latitudinal changes in its tectogeomorphologic setting: to the north (18°30' – 19°30'S), the forearc is dissected by exoreic drainages and main coastal forearc structures are clear-traced NE – SW sinistral strike-slip faults. South of 19°30', drainages are little incised and endorheic while large W – E reverse faults are the dominant coastal forearc structures. Thick Neogene infill of the Longitudinal Valley mask continuity of fault structures and hinders remote and field structural mapping. However, preservation of multigenerational fluvial landforms due to long-term hyperaridity set an optimal scenario to detect subtle morphological changes indicative of recent fault activity and unravel the so far not well understood tectonic evolution of this area. Detailed geomorphic evidence from an exhaustive fault mapping combined with morphological analysis of drainage networks suggests a Late Cenozoic reactivation of a ~100 km long Mesozoic inherited trench-parallel dextral strike-slip fault system along the forearc.*

Key words*: Strike-slip, Orocline bend, Quaternary, tectonic forcing, lowlands.*

INTRODUCTION

Crustal deformation induced by plate convergence is well known to be capable to drive changes in topography and climate, directly influencing drainage pattern development (e.g., Royden et al., 1997). Thus, drainage patterns may be used not only to detect the presence of previous and active blind faults (e.g., Keller et al., 1999), but also to unveil aspects of the intricate landscape evolution.

At 13 – 27°S, the Central Andes stands out for the Altiplano-Puna region (Allmendinger et al., 1997). Its western front, better known as the Western Flank of the Altiplano (e.g., Farías et al., 2005; Jordan et al., 2010; Victor et al., 2004), compromises the forearc along northern Chile and southern Perú (Figure 1a, d). Here, an arid to hyperarid clime has been developed during the Cenozoic, leading to the million years-existent Atacama Desert (Hartley et al., 2005) (Figure 1b). Stability of landscape against denudation was achieved by long-lasting dominant hyperaridity conditions (0.1 – 1m Myr-1 at the Longitudinal Valley since ~6 Ma, Kober et al., 2007). Under these given conditions, gross topography and distribution of landforms of the forearc are dictated mainly by multi-scale crustal tectonic structures (Binnie et al., 2020; Evenstar et al., 2017) related to a still-active convergence margin. This hyperarid tectonically active region offers a unique scenario to observe how incremental crustal deformation interacts with long-term drainage network development, where water is virtually absent, and landscape is apparently unalterable against erosion.

In this study we demonstrate how subtle, but widespread geomorphological markers can be used to detect evidence of recent active faulting along the Longitudinal Valley, where the lack of rock outcrops and the preserved thick Neogene continental infill hinders classical remote and field structural mapping. An exhaustive fault mapping was carried out based on high resolution DEMs, satellite, UAV imagery data and literature, combined with the analysis of orientation and patterns of lowlands drainages, windgaps, and longitudinal profiles of major rivers. A compilation of cosmogenic exposure ages of paleosurfaces (Evenstar et al., 2017) was used to constrain ages of geomorphic markers and for interpretation of the incremental tectonic evolution across the forearc close to the Oroclinal Bend (Figure 1c).

DISCUSSSION

Results of the detailed fault mapping reveals the presence of a ~100 km long NW – SE major fault zone along the eastern Longitudinal Valley and NW – SE, N – S and NE – SW branch structures (Figure 2a). Geomorphic analysis of windgaps and lowland drainages, and fieldwork observations suggest that NW – SE and N – S faults form broad compressive horsetail structures with principal subvertical east-vergent faults. These reversed the piedmont along the western Longitudinal Valley, uplifting and preserving the oldest paleosurface generation (~20.2 – 18.4 Ma) (Figure 3a). The paleosurface presents southward increasing numbers of E – W oriented windgaps (Figure 3b) as the overall magnitude and accumulative relative vertical offsets of their frontal scarp reduce.

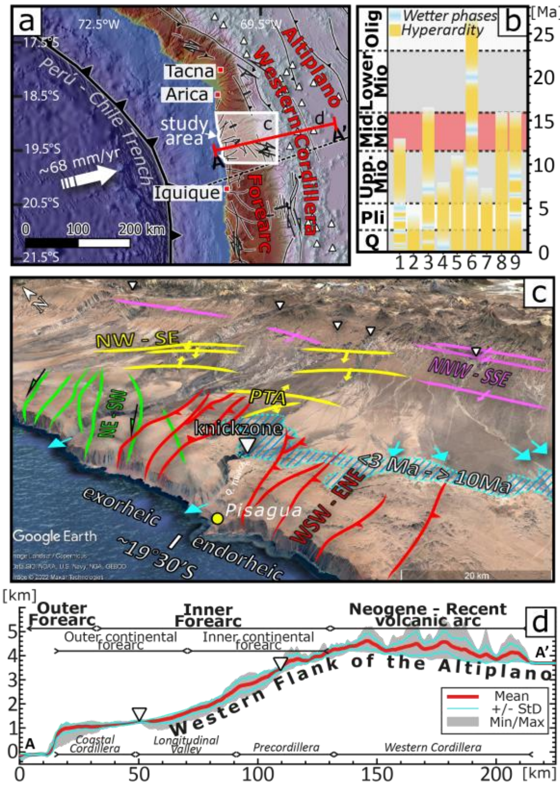

Figure 1: Overall tectonic and climatic setting of the Western Flank of the Altiplano. (a) Andean forearc along the Arica Bend and its main morpho-structural regions and tectonic features. Whitish polygon corresponds to the study area. Current convergence vector from (Norabuena et al., 1998). DEM correspond to GEBCO Bathymetric Compilation Group 2022 topographic and bathymetric data. (b) Proposed Cenozoic climate fluctuations across the Atacama Desert according to 1= Jordan et al. (2014); 2= Amundson et al. (2012); 3= Evenstar et al. (2009); 4= Kober et al. (2007); 5= Arancibia et al. (2006); 6= Dunai et al. (2005); 7= Hartley & Chong (2002); 8= Sillitoe & McKee (1996); 9= Alpers & Brimhall (1988). (c) Summary of main structural and fluvial features within the study area shown by previous works. Satellite image from Digital Globe (Google Earth). (d) Swath profile of the physiographic units of the Western Flank of the Altiplano of Northernmost Chile across the study area. Location in (a).

Younger El Diablo Formation surface (~16 – 11.3 Ma) is mainly preserved along the eastern Longitudinal Valley – Precordillera (Figure 3a). Here, windgaps show opposite north-westward and south-westward orientations in the northern and southern half of the study zone, respectively (Figure 3b). Both anticlockwise (Farías et al., 2005) and clockwise rotation of the forearc with a transitional limit along the Pampa de Tana interfluve, coeval or later than the main deposition of the El Diablo Formation can be suggested.

Yet, crustal faulting has enhanced local drainage reorganization by tectonic deviation, deflection and beheading of drainages: along the eastern Longitudinal Valley, El Diablo Formation paleosurface is disrupted by. NW – SE oriented duplex type structures that transition to a southern Riedel shear zone, (Figure 2a – f). Alluvial surfaces with cosmogenic exposure ages ranging from ~7.8 – 2.4 Ma stacked in en echelon tectonic basins within duplex structures and then disrupted by the Riedel shear zone can be observed (Figure 3a). Northward, continuation of systematic faulting, anticlockwise rotation and right-lateral deflection of windgaps up to ~140 m along principal faults suggests that these structures conform a NW – SE dextral strike-slip principal displacement zone.

Incremental – strike slip faulting of NW – SE branching structures facilitated deviation of paleostreams and consequent abandonment of alluvial surfaces related to Quebrada Pinonave drainage network at ~6.8 – 2.5 Ma. Further south, restraining bends acted as water division and may be responsible from Quebrada Soga drainage network disconnection from northern exoreic ones (Kirk-Lawlor et al., 2013) by tectonic isolation (Figure 3a – b).

Geometric arrangement of faults, observed subvertical fault planes, and discussed kinematics suggest that faulting along the Longitudinal Valley correspond to a reactivated Mesozoic inherited complex strike-slip fault system compromising both Coastal Cordillera and the Longitudinal Valley. This agrees and complements previous structural observations and interpretations regarding the tectonic evolution of outer continental forearc fault structures (e.g., García & Fuentes, 2012). We suggest that strike – slip faulting at the Longitudinal Valley is likely to have an activity onset >11.3 Ma, contemporaneous to oblique Pliocene convergence, regional tilting, and onset of strike-slip kinematics along the Precordillera (Farías et al., 2005). Added to beheading of >2 Ma streams crossing Pampa de Tana horsetail (Binnie et al., 2020), right-lateral deflection of active lowlands drainages along both principal displacement zone and NW – SE branching structures suggest that strike-slip faulting has been active during the Quaternary. Nevertheless, a more comprehensive sampling of cosmogenic nuclides in each of the hanging walls, related beheaded streams and in surfaces stacked within local tectonic basins at the footwalls are needed to bring enough insights for a much higher resolution chronology of faulting and local evolution of drainages.

Morphometric analysis of longitudinal profiles of major rivers shows clustered knickpoints and high k_{sn} anomalies at the Precordillera in all profiles and a low-retreated knickzone within the western slope of the Coastal Cordillera at the lower segment of the Quebrada Retamilla river, (Figure 2a). This agrees with the location of major knickzones shown in previous geomorphic analysis (Kirk-Lawlor et al., 2013 and reference therein). Second minor knickpoints clusters are observed along the trace of the trench-perpendicular Atajaña and Pisagua reverse faults, matching high k_{sn} anomalies (Figure 2a). These large faults are suspected and known to be active, respectively (e.g., González et al., 2015). Slope-area log plot suggest that all knickpoints are strong related to tectonic uplift. However, no exoreic river has a significant k_{sn} anomaly or knickpoints related to the principal strike-slip fault zone nor Coastal Cordillera NE – SW sinistral faults.

The fact that the even the analysed endoreic river present a major knickzone within the Precordillera support the idea that development of exoreism – endorheism and the formation of the coastal knickzone are not related to the uplift along the Western Flank of the Altiplano, but rather to long-term coastal tectonic processes (Kirk-Lawlor et al., 2013; Madella et al., 2018) segmentate along trench due the establishment of the Arica Bend since ~25 Ma (Madella et al., 2018). Distribution of active crustal faults also have been related to long-term tectonic behavior of the forearc (e.g., González et al. 2021). Fault pattern and incremental fault activity shown in this work spatially correlates with the proposed along-trench segmentation tectonic behaviour and strength this hypothesis.

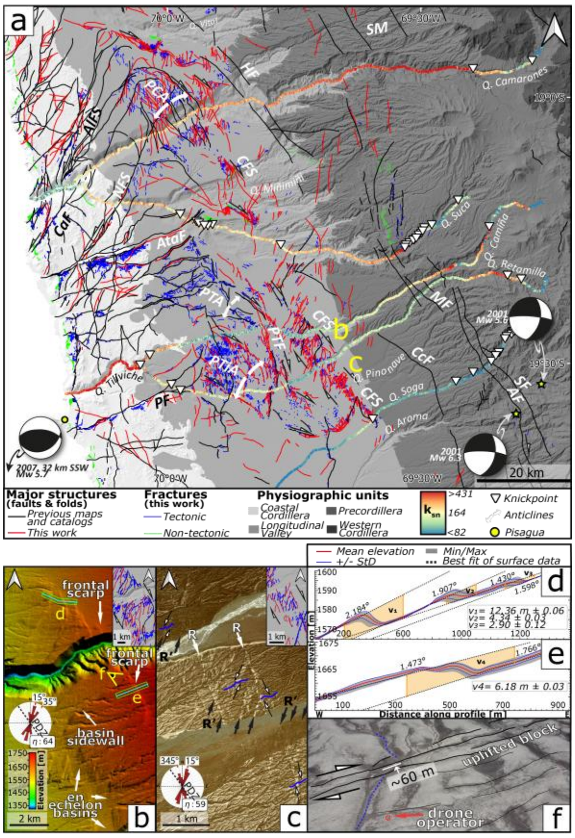

Figure 2: Results of fault mapping and examples of applied analysis and observations along the best surface expression of the principal NW – SE strike-slip fault zone, here called Camiña Fault System (CFS). (a) Resulting fault mapping and large crustal earthquakes. Notice fault density and arrangement of faults along the Longitudinal Valley. Hillshade is from a TerraSAR-X (12.5 m) DEM (Pitz & Miller, 2010). (b) Close-up a transtensional duplex structure show in the coloured shaded relief; frontal scarp and the occurrence of en echelon tectonic basins at the backslope of the structure are highlighted. Light blue lines with green polygons correspond to 200 m width swath profiles on (d) and (e). Small map shows mapped structures with colour palette according to (a). (c) Close-up of Bing satellite image (+50% contrast) showing a portion of the Riedel shear zone; R and R' structures and deflection of streams (black and white arrows) are highlighted. Small map shows mapped structures with colour palette according to (a). (d & e) 200 m width swath profiles shown in map view in (b) with relative vertical offsets and slopes of displaced surfaces. (f) Drone photography of right-lateral deflected and beheaded windgaps across the frontal fault zone of the transtensional duplex. Location and orientation of photography are shown in (b). Structures: AF= Aroma Flexure; AlF= Alejo Fault System; AtaF= Atajaña Fault; CcF= Calacala Flexure; CFS= Camiña Fault System; HF= Humayani Flexure; LSF= Low Quebrada Soga Fault; NFS= Negrito Fault System; PF= Pisagua Fault; SF= Soga Flexure; SM= Sucuna Monocline

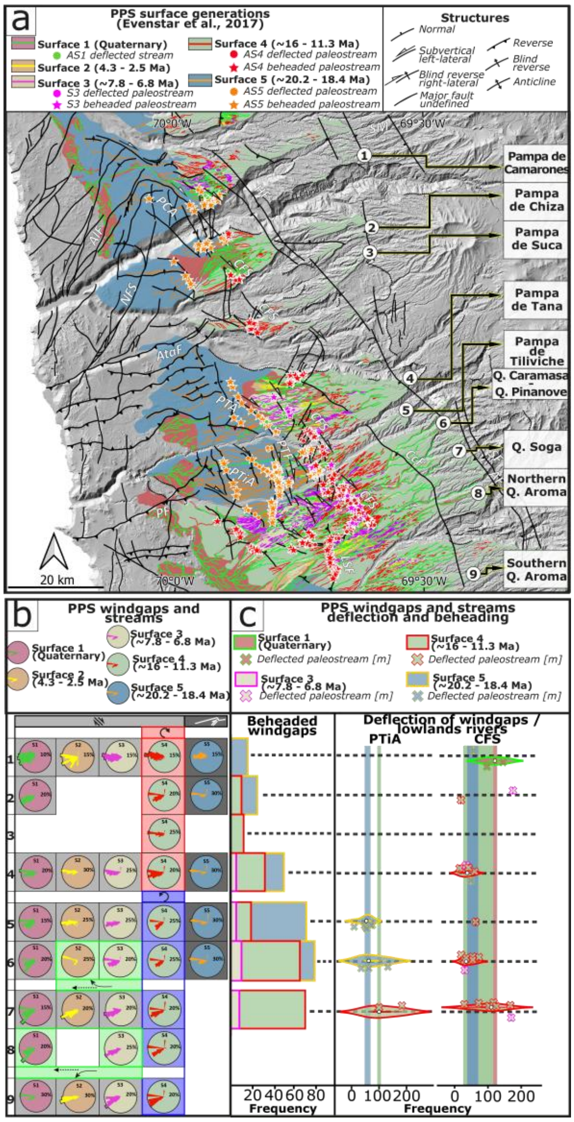

Figure 3: Distribution and tectonic disturbance of windgaps of the PPS paleosurfaces and lowlands drainage networks. (a) Detail remapped PPS windgaps and lowlands rivers within the study area and simplified structural mapping. (b) Main tectonic processes controlling orientation of windgaps and lowlands rivers within each interfluve. Black shading= east-vergent reverse faulting; blue shading= anticlockwise rotation; grey shading= strike-slip faulting; green shading= local tectonic deviation; red shading= anticlockwise rotation (c) Magnitude of the tectonic

disturbance of the different generation of windgaps and lowland rivers along a NW – SE branch (PTiA) structure and the principal displacement zone (CFS). Both magnitude of deflection and beheading increases with younger generations and southward.

Acknowledgements: We are grateful to Damian Lopez and Eduardo Campos for crucial logistic support and to Ricardo Aguilera for assistance in field This work was funded in part by the Deutsche Forschungsgemeinschaft (DFG, German Research Foundation) – Projektnummer 268236062 –SFB 1211.

REFERENCES

Allmendinger, R. W., Jordan, T. E., Kay, S. M., & Isacks, B. L. (1997). The evolution of the Altiplano-Puna plateau of the central Andes. *Annual Review of Earth and Planetary Sciences*, *25*(1), 139–174. https://doi.org/10.1146/annurev.earth.25.1.139

Alpers, C. N., & Brimhall, G. H. (1988). Middle Miocene climatic change in the Atacama Desert, northern Chile: Evidence from supergene mineralization at La Escondida. *Geological Society of America Bulletin*, *100*(10), 1640–1656. https://doi.org/10.1130/0016-7606(1988)100<1640:MMCCIT>2.3.CO;2

Amundson, R., Dietrich, W., Bellugi, D., Ewing, S., Nishiizumi, K., Chong, G., Owen, J., Finkel, R., Heimsath, A., Stewart, B., & Caffee, M. (2012). Geomorphologic evidence for the late Pliocene onset of hyperaridity in the Atacama Desert. *Geological Society of America Bulletin*, *124*(7–8), 1048–1070. https://doi.org/10.1130/B30445.1

Arancibia, G., Matthews, S. J., & Pérez de Arce, C. (2006). K–Ar and 40Ar/39Ar geochronology of supergene processes in the Atacama Desert, Northern Chile: tectonic and climatic relations. *Journal of the Geological Society*, *163*(1), 107–118. https://doi.org/10.1144/0016-764904-161

Binnie, S. A., Reicherter, K. R., Victor, P., González, G., Binnie, A., Niemann, K., Stuart, F. M., Lenting, C., Heinze, S., Freeman, S. P. H. T., & Dunai, T. J. (2020). The origins and implications of paleochannels in hyperarid, tectonically active regions: The northern Atacama Desert, Chile. *Global and Planetary Change*, *185*, 103083. https://doi.org/10.1016/j.gloplacha.2019.103083

Dunai, T. J., González López, G. A., & Juez-Larré, J. (2005). Oligocene–Miocene age of aridity in the Atacama Desert revealed by exposure dating of erosion-sensitive landforms. *Geology*, *33*(4), 321. https://doi.org/10.1130/G21184.1

Evenstar, L. A., Hartley, A. J., Stuart, F. M., Mather, A. E., Rice, C. M., & Chong, G. (2009). Multiphase development of the Atacama Planation Surface recorded by cosmogenic 3He exposure ages: Implications for uplift and Cenozoic climate change in western South America. *Geology*, *37*(1), 27–30. https://doi.org/10.1130/G25437A.1

Evenstar, L. A., Mather, A. E., Hartley, A. J., Stuart, F. M., Sparks, R. S. J., & Cooper, F. J. (2017). Geomorphology on geologic timescales: Evolution of the late Cenozoic Pacific paleosurface in Northern Chile and Southern Peru. *Earth-Science Reviews*, *171*, 1–27. https://doi.org/10.1016/j.earscirev.2017.04.004

Farías, M., Charrier, R., Comte, D., Martinod, J., & Hérail, G. (2005). Late Cenozoic deformation and uplift of the western flank of the Altiplano: Evidence from the depositional, tectonic, and geomorphologic evolution and shallow seismic activity (northern Chile at 19°30'S). *Tectonics*, *24*(4). https://doi.org/10.1029/2004TC001667

García, M., & Fuentes, G. (2012). *Carta Cuya, regiones de Arica y Parinacota y de Tarapacá, Escala 1: 100.000*.

González, G., Pasten-Araya, F., Victor, P., González, Y., Valenzuela, J., & Shrivastava, M. (2021). The role of interplate locking on the seismic reactivation of upper plate faults on the subduction margin of northern Chile. *Scientific Reports*, *11*(1), 21444. https://doi.org/10.1038/s41598-021-00875-6

Hartley, A. J., & Chong, G. (2002). Late Pliocene age for the Atacama Desert: Implications for the desertification of western South America. *Geology*, *30*(1), 43. https://doi.org/10.1130/0091-7613(2002)030<0043:LPAFTA>2.0.CO;2

Hartley, A. J., Chong, G., Houston, J., & Marther, A. E. (2005). 150 million years of climatic stability: evidence from the Atacama Desert, northern Chile. *Journal of the Geological Society*, *162*(3), 421–424. https://doi.org/10.1144/0016-764904-071

Jordan, T. E., Kirk-Lawlor, N. E., Blanco, N. P., Rech, J. A., & Cosentino, N. J. (2014). Landscape modification in response to repeated onset of hyperarid paleoclimate states since 14 Ma, Atacama Desert, Chile. *Geological Society of America Bulletin*, *126*(7–8), 1016–1046. https://doi.org/10.1130/B30978.1

Jordan, T. E., Nester, P. L., Blanco, N., Hoke, G. D., Dávila, F., & Tomlinson, A. J. (2010). Uplift of the Altiplano-Puna plateau: A view from the west. *Tectonics*, *29*(5). https://doi.org/10.1029/2010TC002661

Keller, E. A., Gurrola, L., & Tierney, T. E. (1999). Geomorphic criteria to determine direction of lateral propagation of reverse faulting and folding. *Geology*, *27*(6), 515–518. https://doi.org/10.1130/0091-7613(1999)027<0515:GCTDDO>2.3.CO;2

Kirk-Lawlor, N. E., Jordan, T. E., Rech, J. A., & Lehmann, S. B. (2013). Late Miocene to Early Pliocene paleohydrology and landscape evolution of Northern Chile, 19° to 20° S. *Palaeogeography, Palaeoclimatology, Palaeoecology*, *387*, 76–90. https://doi.org/10.1016/j.palaeo.2013.07.011

Kober, F., Ivy-Ochs, S., Schlunegger, F., Baur, H., Kubik, P. W., & Wieler, R. (2007). Denudation rates and a topography-driven rainfall threshold in northern Chile: Multiple cosmogenic nuclide data and sediment yield budgets. *Geomorphology*, *83*(1–2), 97–120. https://doi.org/10.1016/j.geomorph.2006.06.029

Madella, A., Delunel, R., Audin, L., & Schlunegger, F. (2018). Why is there no Coastal Cordillera at the Arica Bend (Western Central Andes)? *Basin Research*, *30*, 248–268. https://doi.org/10.1111/bre.12218

Norabuena, E., Leffler-Griffin, L., Mao, A., Dixon, T., Stein, S., Sacks, I. S., Ocola, L., & Ellis, M. (1998). Space Geodetic Observations of Nazca-South America Convergence Across the Central Andes. *Science*, *279*(5349), 358–362. https://doi.org/10.1126/science.279.5349.358

Pitz, W., & Miller, D. (2010). The TerraSAR-X Satellite. *IEEE Transactions on Geoscience and Remote Sensing*, *48*(2), 615–622. https://doi.org/10.1109/TGRS.2009.2037432

Royden, L. H., Burchfiel, B. C., King, R. W., Wang, E., Chen, Z., Shen, F., & Liu, Y. (1997). Surface deformation and lower crustal flow in eastern Tibet. *Science*, *276*(5313), 788–790. https://doi.org/10.1126/science.276.5313.788

Sillitoe, R. H., & McKee, E. H. (1996). Age of supergene oxidation and enrichment in the Chilean porphyry copper province. *Economic Geology*, *91*(1), 164–179. https://doi.org/10.2113/gsecongeo.91.1.164

Victor, P., Oncken, O., & Glodny, J. (2004). Uplift of the western Altiplano plateau: Evidence from the Precordillera between 20° and 21°S (northern Chile). *Tectonics*, *23*(4), n/a-n/a. https://doi.org/10.1029/2003TC001519

The IPOC Creepemter Array: Deciphering the imprint of seismic and aseismic deformation on shallow fault zones and the potential for a future natural fault observatory

Victor, Pia (1), Schleicher, Anja (1), Mona Lüder (1), Salazar, Pablo (2) & Gonzalez, Gabriel (2)

(1) GFZ Potsdam, Telegrafenberg, D-14473 Potsdam, Germany. email: pvictor@gfz-potsdam.de
(2) Departamento de Ciencias Geologicas, Universidad Catolica del Norte, Avenida Angamos 0610, Antofagasta, Chile

***Abstract:**. The partitioning of seismic and aseismic behavior in active faults is key for seismic hazard assessment. Often there is a distinction between locked and creeping fault segments. In recent years it became evident, that faults can transiently change their slip behavior. The IPOC Creepmeter array in N-Chile is a unique fault monitoring network to record this transient behavior. We have detected the accumulation of numerous triggered shallow slip events, as well as creep. We report on the different behaviors through time for a 10 year monitoring period. We demonstrate, how the instrumentally observed behavior matches fault gouge properties of the specific fault segments. In the final section we give an outlook, how the IPOC Creepmeter array can be transformed into a natural fault observatory for the on-site exploration of fault properties in relation to the instrumental records and with this to work towards understanding the physics of fault slip.*

***Key words**: fault monitoring, creepmeter, fault gouge, natural fault observatory*

INTRODUCTION

The mode of fault slip behavior for shallow slip is an important parameter to define potential hazard on active fault zones. Faults fail in a continuous spectrum of modes ranging from seismic failure as one endmember of slip behavior to aseismic creep as the second endmember, including slow slip phenomena (e.g. Marone & Richardson, 2010, Peng & Gomberg 2010). The slip behavior of the shallow fault zone in the uppermost levels of the crust appears to be extremely complex and is not well understood. From the geological record, Fagereng & Toy (2018) describe how the seismological character of a fault is highly dependent on fault geology. Distinguishing seismic and aseismic behavior from the fault rock record of shallow near-surface sediments is also possible but even more challenging (Cashman et al. , 2007).

On the other hand long-term monitoring can reveal fault behavior on instrumental time-scales that is important to understand the distribution of seismic and aseismic behavior on faults (e.g. Lienkaemper et al., 1997). Besides levelling lines and InSAR observations, creepmeters provide important high resolution insights in slip accumulation patterns along active faults through time (Bilham et al., 2016; Bilham et al., 2004). Especially high resolution creepmeter arrays can detect triggered seismic slip events on active faults and distinguish near-field or remote sources for these events (Victor et al., 2018). More recent efforts of time-series decomposition of creepmeters in N-Chile result in the quantification of seismic vs. aseismic slip on different fault segments that correlate with fault gouge thickness and mineral composition (Victor et al., 2019).

With the IPOC Creepmeter array (https://www.ipoc-network.org/observatory/creepmeter/creepmeter-at-ipoc/) we have the unique opportunity to investigate the shallow fault zone in terms of frictional properties and slip behavior, not only on instrumental time scales but additionally complemented by field observations. We jointly interpret the time-series of slip accumulation with field observations of fault cross sections and compare the instrumentally monitored fault slip behavior with fault zone properties covering the paleoseismological past.

This unique setup at IPOC Creep is now ready to move to the next level of monitoring, using the knowledge acquired through the past years to equip selected stations with additional monitoring technology to capture multiparameter datasets and develop a holistic understanding of the faulting process.

Seismotectonic Setting

The IPOC Creepmeter array monitors four active segments of the Atacama Fault System (AFS) a highly segmented trench-parallel fault system that extends for almost 1000km in the continental forearc of the Nazca-Chile subduction zone (Fig.1). Since the Miocene, branches of the AFS have been reactivated mainly as normal faults with a minor component of reverse reactivation (Allmendinger and Gonzalez, 2010). The normal faulting leads to exposure of linear bedrock fault scarps with vertical offsets of up to 400m generating significant alluvial fan deposits in half graben settings. A younger set of normal faults subparallel to the bedrock fault scarps again offsets this alluvial fan generation with up to 10m of vertical throw (Gonzalez et al., 2006) generated during multiple reactivations (Ewiak et al., 2015) during the past 10 – 100ky (Cortés et al., 2012; Gonzalez et al., 2006). Surface ruptures along individual segments of the main fault scarp unambiguously reveal that the AFS has seismically ruptured several times during the Late Quaternary [Cortés et al., 2012; Ewiak et al., 2015;]. Paleoseismological studies reveal recurrence intervals of earthquakes with magnitudes up to M < 7 on the order of 1000 – 3000 years [Cortés et al., 2012; Robinson et al., 2011].

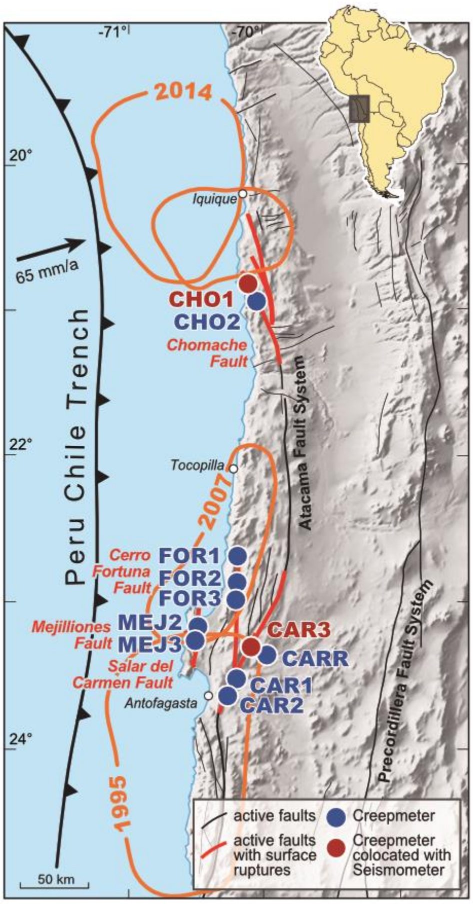

Figure 1: Distribution of Creepmeter sites along the four segments of the Atacama Fault System (AFS) in the N-Chilean Forearc. Sites with collocated seismometers are marked in red.

INSTRUMENTAL SET UP

All the installed instruments use 12 mm thick invar rods as length standards, which are firmly attached to a concrete foundation on one side of the fault and pass through a PVC pipe to the far side of the fault. The creepmeters are buried at a depth of 30 - 70 cm, to increase the signal-to-noise ratio. We use a LVDT (linear variable differential transformer) with a linear range of 50mm to monitor the relative displacement of the free end of the rod relative to the fixation point. Displacement is converted to voltage change and stored on a data logger with a sampling rate of 2/min. One pilot station (MEJ3) is run at 100Hz. The length of the instrument is dependent on the geometry at each site and ranges between 3 and 9 m. One station per target fault is also equipped with a weather station to control effects of humidity and air pressure changes. All instruments are equipped with a satellite link and data is sent directly to GFZ. Collocated with three of the creepmeters, we operate broadband seismometers.

Figure 2: Set-up of the CAR3 Creepmeter. In the foreground is the LVDT sensor and the broadband seismometer. In the background the localized fault scarp is visible. Trench for installation is later closed to minimize external influence.

FAULT ROCK SAMPLING

To bridge timescales of fault slip observations and to investigate if and how fault zone properties compare to the instrumentally monitored dataset, we sampled the fault gouges exposed at the creepmeter sites. Before sampling the fault core in the field, its fault structure, grain size distribution and lithological composition were investigated on outcrop scale. The thickness and structure of secondary faults were also described. Thin sections were prepared from suitable samples and mineral fractions have been separated and analyzed with XRD methodology.

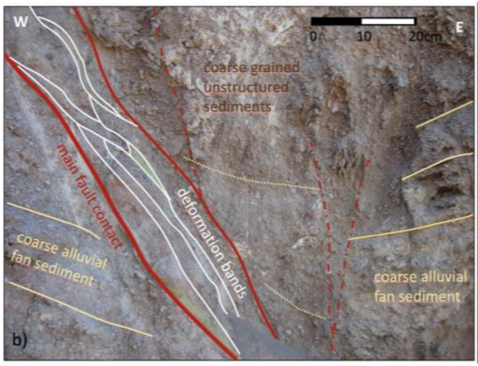

Figure 3: Example of one of the sampled fault gouges, outcropping along the Salar del Carmen fault segment, close to the CAR1 creepmeter. Fine grained material in the gouge is gypsum rich and shows nicely developed deformation bands.

DECOMPOSITION OF CREEPMETER TIME SERIES

To differentiate between the slip components, we decompose the time-series after applying correction techniques to improve the signal to noise ratio of the creepmeter time series as described in (Victor et al., 2018). Besides detection of the obvious signal contribution by **S**hallow Sip **E**vents (SSE), we use the time series decomposition to detect a potential trend component in the original time series that is superposed by a seasonal component. After performing all steps of decomposition, we are able to quantify the ratio of aseismic vs. seismic slip component through time for each fault segment (Fig.4.).

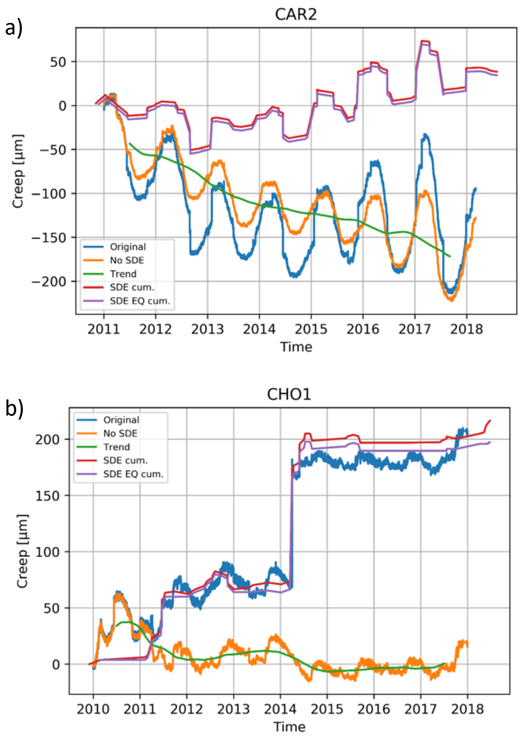

Figure 4: Creepmeter time-series of two different sites on the Salar del Carmen Fault (a) and Chomache Fault (b). The original time-series is shown in blue, shallow slip events in red and the creep component in green. Both fault segments are endmember examples of slip behavior. CAR2 is creeping and CHO1 accumulates slip by seismic displacement events.

SLIP VELOCITIES

We resolve the slip velocities of slip events picking onset and end of the event to determine the event duration, as well as calculating the fault parallel slip magnitude for the specific event. For the 30sec sampling rate this gives us a minimum velocity which is a good estimate of the velocity spectrum, especially for the events lasting longer than 1 min. For the 100Hz station at the MEJ3 site we get highly resolved velocities (Fig.5).

RESULTS

In the past years we have detected the accumulation of numerous triggered shallow slip events, as well as transient creep events. Most of the shallow slip events are dynamically triggered with durations ranging from 10^2sec to up to 3 minutes. Creep events can be dynamically triggered as well and have event durations up to 12 hours, or they can be climatically triggered by rainfall events and have much longer durations of up to 1,5 years.

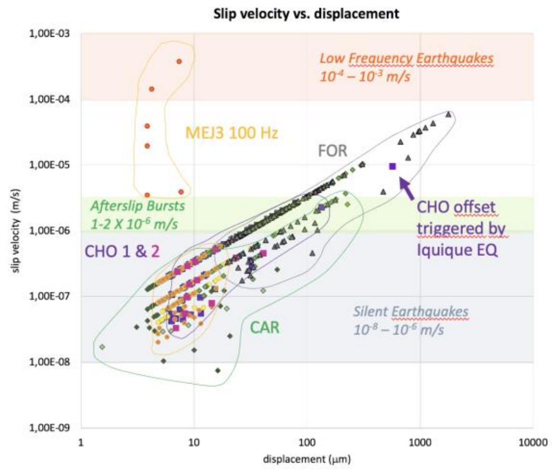

Figure 5: Slip velocities plotted with displacement magnitude. The compilation shows, that slip velocities cover the spectrum of slow slip events, ranging from silent earthquakes to low frequency earthquakes. It seems, as if larger slip events like the one triggered by the Iquique EQ on the CHO1 station tend to have higher velocities. Nevertheless highest velocities occur, when the 100Hz dataset is used, because it allows calculation of highly resolved velocities and not the minimum velocity for a specific event.

We observe all types of slip accumulations patterns in the >10-year long time series recorded on the 4 different fault segments. We can specify the type of slip events in terms of their seismogenic nature according to slip velocities, demonstrating that the whole spectrum of velocities between 10^{-9}m/sec up to 10^{-3}m/sec occurs in the monitoring period (Fig. 5).

Time series decomposition additionally allows us to extract a trend component representing the creep signal of the monitored segments, indicating a slow creep component (<2mm/year) especially for the Salar del Carmen fault (Fig. 4a). All four fault segments have a homogeneous behavior along strike but each fault segment has a distinct behavior with respect to the other segments. The Salar del Carmen fault is creeping at all three stations (Fig.4a). The Chomache fault is accumulating its slip only via shallow slip events (Fig. 4b). The Fortuna fault exhibits a long lasting contractional creep, whereas the Mejillones fault is in general accumulating seismic slip events through time, but after an unusual rainfall event the fault started creeping for 1,5 years. Today the fault accumulation pattern is again dominated by accumulation of seismic slip events.

To understand if the pattern of displacement accumulation is related to the properties of the fault zone at the sites, we directly correlated specific fault structural and mineralogical properties of rock samples from the sites, with specific instrumentally monitored slip modes. We found that the creeping fault behavior (Fig. 4a) of the Salar del Carmen Fault segment correlates well with the more mature, at least 10cm thick, gypsum bearing fault gouge (Fig.2). The Chomache fault exhibits a wealth of seismically triggered displacement events, especially the offset triggered by the Iquique earthquake and it's aftershocks. This behavior seems to be tightly correlated to the immature fault zone developed in andesitic bedrock. Only densely fractured host rock can be identified, but there is no fault gouge developed. The Mejillones fault is mostly seismogenically accumulating displacement, which is in close correspondence with the extremely thin incipient fault zone rupturing alluvial fan material. Nevertheless the Smectite bearing mm thin coating on the fault planes allows the fault to transiently creep during and after a rain event.

CONCLUSION AND OUTLOOK

After 1 decade of fault observation with IPOC Creep we have collected a set of time-series of fault displacement across the 4 target segments of the AFS at 11 stations. With the >10 year long time series we can now decompose the time-series into a seismic and an aseismic component and calculate their contribution to the cumulative offset. Correlating these findings with fault zone properties, we find an extremely good correlation with the different parameters of the 4 fault segments including mineralogy and structure.

With this background knowledge provided by a successful network it is time to rethink IPOC Creep. It now provides the potential to understand fault processes in a natural environment, which is densely instrumented. In future we will enforce exploration of the fault gouge composition and structure, together with soil moisture sensing, to investigate the impact of environmental changes on fault triggering. Sampling the fault cores we are able to determine fault core frictional parameters and correlate those to the seismic/aseismic slip accumulation pattern of each fault segment. Thinking further ahead IPOC Creep is the ideal setting for a natural fault observatory, gathering several temporary experiments to better understand the shallow slip process on these seismogenic faults.

Acknowledgements: This work was only possible in the framework of IPOC and associated GFZ observatory funds. Field assistance by Chilean colleagues was crucial for the success of the project.

REFERENCES

Allmendinger, R. W., and Gonzalez, G., 2010, Neogene to Quaternary tectonics of the coastal Cordillera, northern Chile: *Tectonophysics*, v. 495, p. 93-110.

Bilham, R., Suszek , N., and Pinkney, S., 2004, California Creepmeters: *Seism. Res. Lett*., v. 75, no. 4, p. 481-492.

Binnie, A., Dunai, T., Binnie, S., Victor, P., González, G., and Bolten, A., 2016, Accelerated late quaternary uplift revealed by 10Be exposure dating of marine terraces, Mejillones Peninsula, northern Chile. *Quaternary Geochronology,* v. 36, p. 12-27.

Cashman, S. M., Baldwin, J. N., Cashman, K. V., Swanson, K., and Crawford, R., 2007, Microstructures developed by coseismic and aseismic faulting in near-surface sediments, San Andreas fault, California. *Geology*, v. 35, no. 7.

Cortés, J., González, G., Binnie, S., Robinson, R., Freeman, S. P. H. T., and Vargas, G., 2012, Paleoseismology of the Mejillones Fault, northern Chile: Insights from cosmogenic 10Be and optically stimulated luminescence determinations: *Tectonics*, v. 31.

Ewiak, O., Victor, P., and Oncken, O., 2015, Investigating multiple fault rupture at the Salar del Carmen segment of the Atacama Fault System (northern Chile): Fault scarp morphology and knickpoint analysis: *Tectonics*, v. 34, no. 2, p. 187-212.

Fagereng, Å., and Toy, V. G., 2018, Geology of the earthquake source: an introduction, *Geological Society, London, Special Publications*, Volume 359, p. 1-16.

Gonzalez, G., Dunai, T. J., Carizo, D., and Allmendinger, R. W., 2006, Young displacements on the Atacama Fault System, northern Chile from field observations and cosmogenic 21Ne concentrations: *Tectonics*, v. 25, p. doi:10.1029/2005TC001846.

Lienkaemper, J. J., Galehouse, J. S., and Simpson, R. W., 1997, Creep Response of the Hayward Fault to Stress Changes Caused by the Loma Prieta Earthquake: *Science*, v. 276, no. 5321, p. 2014-2016.

Marone, C., and Richardson, E., 2010, Learning to read fault-slip behavior from fault-zone structur: *Geology*, v. 38, no. 8, p. 767-768.

Peng, Z., and Gomberg, J., 2010, An integrated perspective of the continuum between earthquakes and slow-slip phenomena: *Nature geoscience,* v. 3, no. 9, p. 599-607.

Robinson, R. A., Binnie, S., González, G., and Cortés, J., 2011, Dating upper plate normal fault slip events in Late Pleistocene and Holocene sediments of northern Chile, , AGU Fall Meeting: San Francisco.

Victor, P., Müting , A., Gonzalez, G., and Oncken, O., 2019a, Exploring the properties of shallow slip on surface rupturing faults: Evidence from instrumental monitoring and fault gouge thickness: *Geophysical Research Abstracts,* v. 21, p. EGU2019-15915, 12019, EGU General Assembly 12019.

Victor, P., Oncken, O., Sobiesiak, M., Kemter, M., Gonzalez, G., and Ziegenhagen, T., 2018, Dynamic triggering of shallow slip on forearc faults constrained by monitoring surface displacement with the IPOC Creepmeter Array: *Earth and Planetary Science Letters*, v. 502, p. 57-73.

Paleoseismological trenching and tectonic geomorphology reveal an active fault with evidence for repeated large Holocene earthquakes in Papua New Guinea

Whitney, Beau (1, 2), Rossi, Frédéric (2), Duvail, Cédric (2), Yönlü, Önder (3) Labidi, Manel (2), Hengesh, James (4)

(1) Whitney Geologic, 7 Rue Baudin, Montpellier, 34000 France, Email: beau@whitneygeologic.com
(2) Fugro France SAS, 115 av. de la Capelado, Castries, 34160 France
(3) Fugro House, Hithercroft Road, Wallingford, Oxfordshire, OX10 9RB, United Kingdom
(4) Interface Geohazard Consulting, 20 Plumeria Pl., Lahaina, HI, 96761 USA

Abstract:
Papua New Guinea (PNG) occupies one of the most active and tectonically complex plate boundary collisions on Earth, and experiences frequent large-magnitude earthquakes and rapid rates of subduction and mountain building. The fundamental geology of the region has been studied for over a century, but little is known about the earthquake history prior to ~1900. We present new geological and geomorphological data that constrain the magnitude and frequency of paleo-earthquakes on a previously unconstrained plate boundary thrust fault near the Purari River in the Gulf Province of southern PNG. A paleoseismological investigation of this fault identified evidence for repeated earthquakes of ~Mw 7.3 to 8.1. Based on radiometric dating and oral histories from villages along the fault, the most recent earthquake occurred approximately 450 years ago. This event ruptured the ground surface and caused coastal uplift of a Holocene strandplain complex. The timing of the event coincides with village re-settlement and re-initiation of the regionally important Hiri trading voyages. The results shed light on what may have caused abrupt changes in trading activities and village movements in the region over the past few thousand years.

Key words: *tectonic geomorphology; marine terraces; surface rupture*

INTRODUCTION

Papua New Guinea occupies a complex deformation zone between the Australian and Pacific plates. The regional geodynamics are controlled by a number of microplates interacting through several subduction zone and transform fault systems (De Mets et al., 1994; Wallace et al., 2004; Bird, 2003; Baldwin et al., 2012; *Figure 1*). Within the resolution of the geodetic data, most of this deformation appears to be concentrated on major structures that bound relatively coherent or stable crustal blocks (Koulali et al, 2015). However, the magnitude and frequency of earthquakes on these major crustal structures are not geologically constrained.

A combination of factors (high uplift, precipitation and erosion rates, dense vegetation, and limited access) have inhibited the ability to identify specific active faults and access research sites. Active tectonic features have been mapped at regional rather than outcrop scale and their locations are inferred based on the distribution of large tectono-stratigraphic terranes, as well as broad tectonic geomorphological indicators such as mountain ridgelines, variations in topographic relief, or river patterns (e.g., Cooper, 1987; Van Ufford and Cloos, 2005).

In this paper, we present results of a paleoseismological investigation that was carried-out on a major thrust fault we identified using airborne light detection and ranging (LiDAR) derived DTMs in southern Papua New Guinea (PNG). The investigation area lies along the southern margin of the Aure fold and thrust belt (AFTB) where it emerges from the low relief deltaic swampland of the Purari River near the coast at Orokolo Bay (*Figure 1*). The AFTB trends in a north-south direction for about 70 km along the eastern margin of the Purari River. Near *Arehava* village, the trend of the thrust belt turns approximately 80^{o} from north-south to northwest-southeast for a distance of 40 km before continuing offshore and structurally connecting with the Moresby Trough. We refer to this change in structural trend as the "Arehava bend". The earthquake history of the Arehava bend is the focus of this short paper.

Our results constrain the earthquake history using tectonic geomorphology and fault trenching techniques coupled with oral histories and a review of regional archeological literature. This newly-discovered fault last ruptured approximately 450 years ago and is accommodating at least 2.2 mm yr^{-1} of crustal shortening between the Australian and Pacific Plates. The timing of the most recent earthquake (MRE) is corroborated by oral histories of three nearby villages and numerical dating techniques. The oral histories provide information on past sea-level changes and village settlement patterns which align with the numerical dating constraints on the timing of the most recent event. The results of this study suggest that previously undocumented large magnitude earthquakes may have directly influenced human occupations, migration patterns, and cultural phenomena in this region during the latest Holocene

TECTONIC GEOMORPHOLOGY

LiDAR data collected in the vicinity of the Arehava bend were used to develop a 1m resolution bare-earth digital terrain model (DTM). The DTM provides a detailed topographic image of the area and was used to identify and map geomorphological

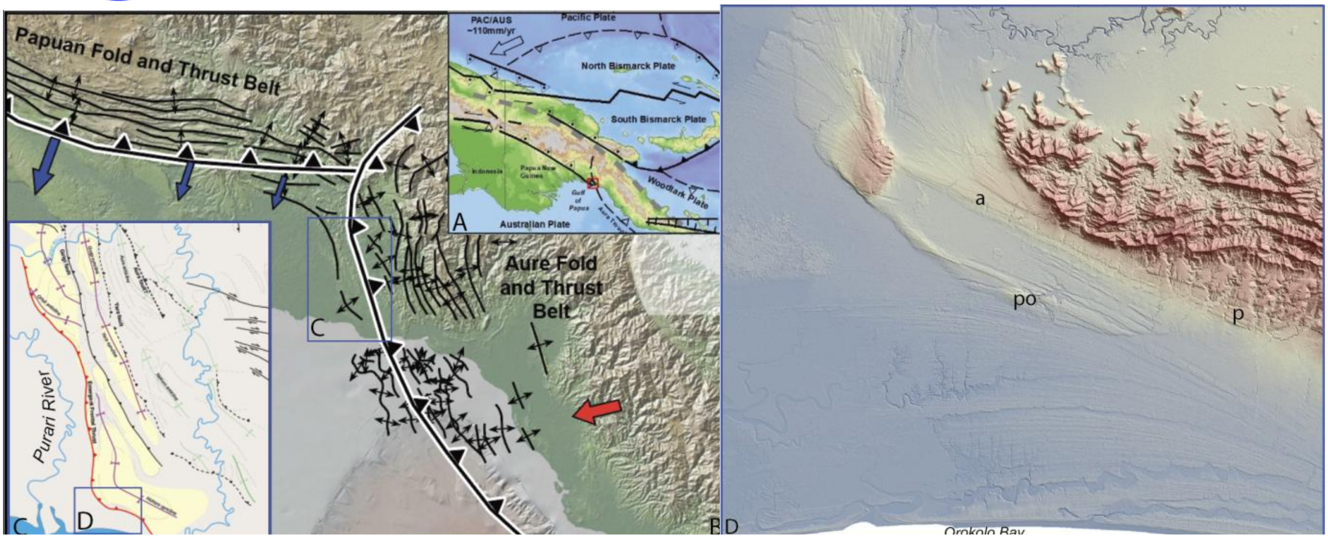

Figure 1: A: Inset showing major plate boundary crustal units after Cooper (1987) and Van Ufford and Cloos (2005). B: Regional scale structural map of the Aure and Papuan fold and thrust belts. Red and blue arrows show relative plate motions with respect to a stable Australian plate (from Koulali et al. 2015). C: Map of the study area showing the structural bend (D)—the Arehava Bend—that is the focus of this paper. D: Lidar derived digital terrain model of the Arehava Bend showing village locations (a, Arehava; p, Paevara; po, Popo). Popo village is no longer occupied.

features including a flight of marine terraces and a series of strandlines on the coastal plain between the base of the AFTB range-front and the coastline. This area lies on the estuarine delta of the Purari River and has experienced long-lived beach aggradation driven by abundant sediment supply delivered to the coast by the river system. This is evidenced by a sequence of marine strandlines (beach ridges) that arcuately stripe the coastal plain (*Figure 1D*). The rate of beach progradation is estimated as high as 3 m yr^{-1} over the past 500 years (Skelly et al., 2014).

Topographic profiles constructed across the transition from the coastal plain to the range-front show the presence of four uplifted marine-terrace treads and risers, that form a stair-stepped morphology leading up the base of the range-front (*Figure 2*). Their morphology consists of a terrace tread backed by a riser, relict back-edge, or sea cliff; the intersection of the terrace tread and riser approximates the paleo-shoreline angle. The paleo-shoreline angle provides a time-stratigraphic land-level datum that can be used to measure elevation changes over time (e.g., Lajoie, 1986).

The marine terraces occupy a zone that is less than 1 km-wide and occur with elevations less than ~20 meters above mean sea level (MSL). Each successive terrace tread is separated by an approximately 1.5-3 m high riser. The lowest elevation marine terraces are covered by an ~3 km-wide zone of regressive strandlines below 7 m elevation. The strandlines are subparallel positive relief features (beach ridges) on the gently seaward sloping terrace surfaces (sloping <0.1 degrees). The beach ridges have been deposited with little net elevation change from one side of the ridge crest to the other. The ridge elevations vary, but are consistent along their longitudinal crests, except where crossed by the Paevera fault.

The Paevera fault (named after a nearby village) forms a south-facing arcuate scarp that is up to 4-metres high and has clear geomorphic expression where it crosses the coastal plain (*Figure 1*). The flight of marine terraces is well preserved on the upslope, hanging wall, side of the Paevera fault (*Figure 2*).

FAULT TRENCHING

We excavated a trench across the Paevera fault scarp near Paevera village (black star on *Figure 2*). The stratigraphy exposed in the trench consisted of an overall fining upward sequence of sedimentary units. The lowest exposed units consisted of interbedded, fine- to medium-grained, well-rounded quartz-rich sand. Abundant primary sedimentary structures, and layers rich with crushed shell fragments, indicative of beach and tidally influenced depositional environments. Black crystalline sand is interbedded within the quartz-dominated layers. The thickest black sand observed in the foot-wall exposure is just below a transition from beach to back-beach or dune facies.

The Paevera fault was identified in the trench. It is a low angle thrust fault that approaches the ground surface (*Figure 3*) and is overlain by a thin scarp-derived colluvial wedge composed of re-worked sand and organic-rich topsoil. The fault zone consists of multiple anastomosing strands within a ~2 m wide deformation zone. The individual shear zones along each fault plane are less than a centimetre wide. The main fault displaces sedimentary units, 3.2 m along a 24^{o} dipping fault plane. A secondary splay displaces units an additional 0.4 m along a 47^{o} fault plane. Smaller fault splays dipping between 47^{o} and 10^{o} collectively displace additional units ~0.4 m. The cumulative dip-slip fault displacement across all strands is 4.0 m. The secondary deformation zone associated with broader fault-related folding observed in the trench is ~17 m wide. There are 4 m of total vertical uplift of the hanging-wall as a result of the thrusting event along the low angle fault plane (*Figure 3*).

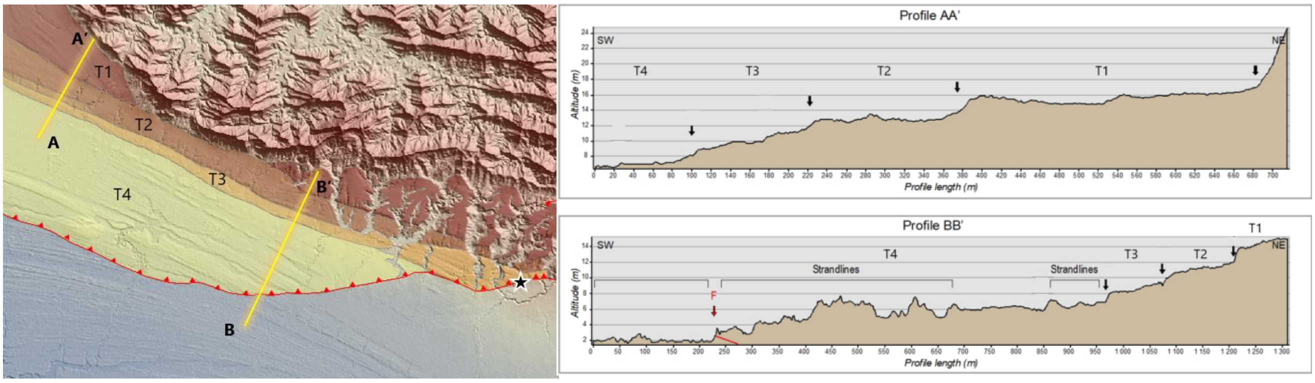

Figure 2: Topographic profiles across progressively older marine terrace surfaces and strandplain. Black star is trench location. Arrows on profiles point to terrace risers. Red F shows the location of the Paevera fault.

The fault exhibits pure dip-slip displacement in this location. No oblique component of motion was inferred from the trench exposure (e.g. block rotation, slickensides) or from the geomorphology (e.g. laterally displaced drainages or ridge crests). Based on consistent offset of stratigraphic markers, no evidence for progressive deformation was observed. A single scarp-derived colluvial wedge was the only un-faulted unit exposed in the trench wall. These observations suggest that all of the deformation observed in the trench is attributable to one displacement event.

Five samples were collected for ^{14}C analysis to constrain the age of the fault displacement observed in the trench wall. The youngest sediments deformed by faulting yield an age of ~514 cal yrs BP. The oldest un-faulted sediments from the colluvial wedge yield an age of ~394 cal. yrs BP. We consider these as constraining ages on the most recent event (MRE) which therefore occurred between ~400-500 years ago.

ORAL HISTORY and ARCHEOLOGY

Discussions with local residents from Paevera, Arehava, and Huruta villages provides insight into the earthquake history of the region. None of the villagers have a specific earthquake story in their oral history. However Paevera and Arehava villagers have similar, independent, stories about the origins of their villages that we relate to the earthquake history on the fault. Based on stories told by village elders, twenty-two generations have lived in Paevera and Arehava villages. A common thread in the stories is that sea-level dropped, as an event, just prior to 22 generations ago, and this event allowed for settlement of the village sites. The event demarcated a historical division between the time before and the time after village settlement, whereas the coastline migration that has occurred since was described as a continuum. These descriptions are consistent with the geomorphology that indicate punctuated sea-level change followed by slower continuous beach progradation. We interpret this event as coinciding with the most recent earthquake.

Archaeological studies in the area indicate that village of Popo was settled around 455 cal. BP (Urwin et al., 2018) (*Figure 1*). Popo became a hub for the long-distance *Hiri* trading voyages between the Port Moresby region and the Gulf Province. The *Hiri* traders would sail many hundreds of kilometers to exchange pottery for local sago and canoe hulls (Urwin et al., 2019). Pottery sherds found in the archaeological record at village sites along a few hundred kilometres of the coast between Orokolo Bay and Port Moresby suggest the *Hiri* trade restarted after an hiatus ~500 cal. BP (Urwin, 2019).

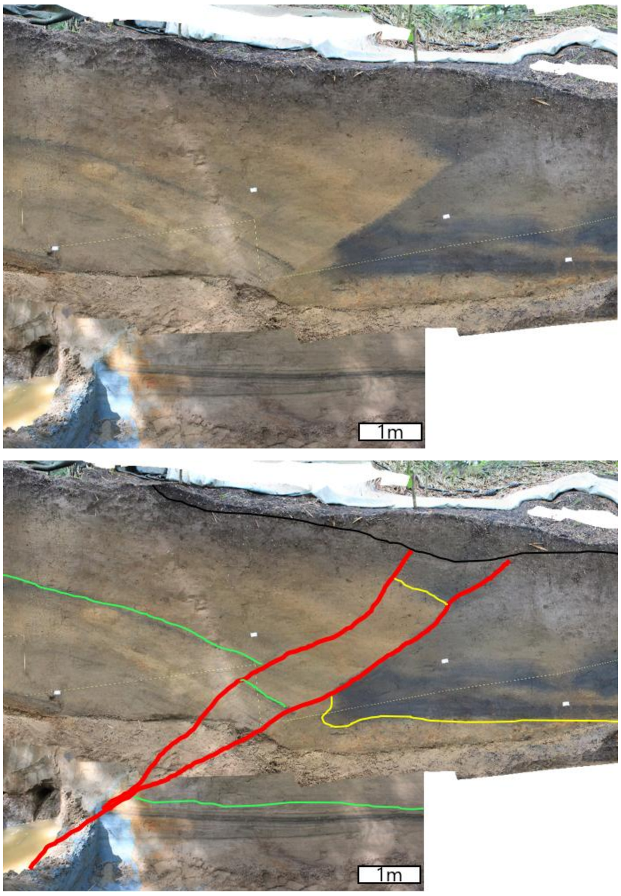

Figure 3: Interpreted and uninterpreted photo of east trench wall. Black line demarcates erosional contact at base of colluvial wedge. Yellow contact is base of black sand. Green contact is base of distinct sand stringer.

The mass production of sago, perhaps up to 600 tons (Allen, 1977), would have needed coordinated effort and planning requiring the existence of well-established village settlements and local community networks (David, 2008). Along this stretch of coast, earlier trade involving pottery began nearly 2500 years ago and steadily increased until a marked disruption occurred around 1200 years ago (Allen, 1982; Kirch, 1991). Indeed, David (2008) comments that the causes of repeated time gaps in the archaeological evidence of the Gulf Province, three in the past 2000 years, are a mystery. The community and social infrastructure required to sustain this trade would have been susceptible to intermittent disruption due to great earthquakes on the Paevera fault, the emergent frontal thrust of the Aure fold and thrust belt.

INTERPRETATION

Sea-level rose rapidly after the last glacial maximum. By ~6.5 ka eustatic levels were within a few meters of current levels (Fleming et al., 1998; Lambeck et al., 2019). Therefore, based on their elevations, the Holocene marine terraces could only have formed more recently than ~6.5 ka. We interpret the marine terraces as coseismic morphological features formed during repeated large earthquakes on the Paevera fault (*Figure 4*). The elevation differences between each successive terrace treads suggest between 2 to 4 m of vertical uplift occurred on the hanging-wall side of the fault during each of the earthquake events.

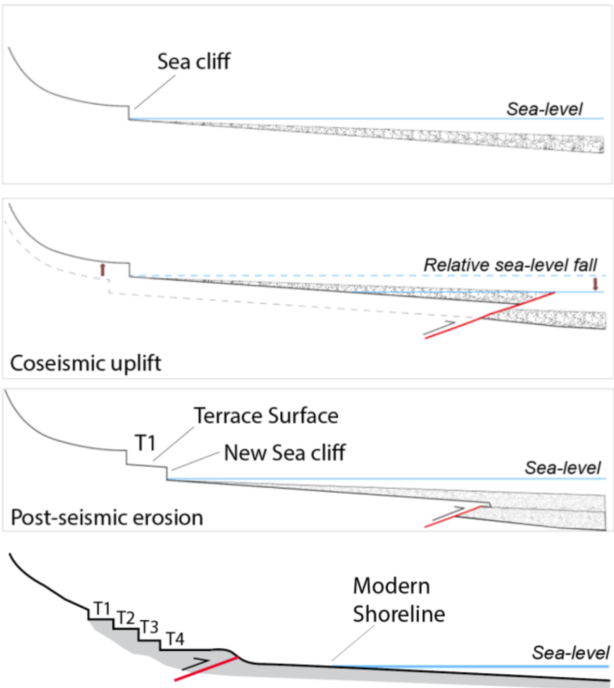

Figure 4: Schematic elevation profiles over time showing repeated marine terrace formation due to coseismic displacements. T1 coincides with marine terrace 1. Sequence is repeated forming terraces T1-T4.

This interpretation requires four large earthquakes to have occurred on the fault in the past 6,500 years or less. The most recent earthquake ruptured the surface and formed the Paevera scarp that displaces the late Holocene strandplain. The trenching results indicate that the most recent event occurred between 514 ±28 and 394 ±80 cal yrs BP. The trench exposed four meters of dip-slip displacement across a faulted sedimentary unit. This displacement resulted in 3.6 meters of shortening and 4.0 meters of uplift across the fault and hanging-wall fold. This displacement, if characteristic, would produce 14.4 m of shortening and 16 meters of uplift during four events in the last 6500 years; this equates to a *minimum* Holocene crustal shortening rate of 2.2 mm yr^{-1}, a minimum fault slip rate of 2.5 mm yr^{-1} and an uplift rate of 2.5 mm yr^{-1}. This shortening rate is roughly a third of the 6-7 mm yr^{-1} of shortening inferred across this zone based on geodetic modelling (Koulali et al., 2015). Using multiple published regressions we estimate the earthquake magnitude associated with the 4 m dip-slip displacement event identified in the trench to be on the order of Mw 7.3 to 8.1 (Wells and Coppersmith, 1994; Dowrick and Rhoads, 2004; Wesnousky, 2008; Leonard, 2010).

We have estimated the coseismic displacement, earthquake magnitude, slip rate and recurrence intervals for the Paevera fault based on the stratigraphic and structural relations observed in the trench, the characteristics of the marine terraces, and constraints provided by the eustatic sea-level curve. These data indicate that the Paevera fault has the capability to produce frequent very large earthquakes up to Mw~8.0. These events changed the coastal morphology and may have triggered changes in living patterns of local communities. Our trenching results are consistent with the oral histories of nearby villages and the archeological record that indicate significant changes to village settlements and trade activities occurred approximately 450 years ago.

The Paevera fault is part of an emergent frontal thrust that defines the southern limit of a broad collision zone that accommodates Australian-Pacific Plate convergence in Papua New Guinea. Earlier settlements in Papua New Guinea's Gulf Province from ~3000 BP (e.g., Rhoads, 1982; McNiven et al., 2012) may have experienced multiple great earthquakes on this fault. These earthquakes may have significantly affected local settlements and community organization - potentially disrupting trade, and may directly relate to regional archaeological hiatuses. The MRE coincides with the end of Irwin's (1991) "ceramic hiccup" and the most recent onset of the long distance *Hiri* trading voyages. The "ceramic hiccup" is demarcated by an hiatus in trade along the coast as suggested by a lack of pottery observed at archeological sites that were otherwise occupied during this time. We anticipate that the discovery of the Paevera fault, which this study demonstrates has generated repeated large magnitude earthquakes, will provide new insights into the causes of village migrations and commencement or cessation of cultural or economical phenomena in the Gulf Province during the late Holocene.

Acknowledgements:

Many thanks to the local support teams and villagers who provided access to their lands and shared their oral histories.

REFERENCES

ALLEN, J. 1982. Pre-contact trade in Papua New Guinea. In Melanesia: Beyond Diversity, Vol. 1, ed. R. J. May, H. Nelson, pp. 193-205. Canberra: Aust. Natl. Univ.

BIRD, P. (2003), An updated digital model of plate boundaries: Geochemistry, Geophysics, Geosystems, v.4, p 1027

BALDWIN, S.L., FITZGERALD, P.G. & WEBB, L.E., (2012). Tectonics of the New Guinea region, Annu. Rev. Earth Planet. Sci., 40, 495–520.

COOPER, P., TAYLOR, B., (1987), Seismotectonics of New Guinea: A model for Arc Reversal Following Arc-Continent Collision, Tectonics, V. 6, No. 1, p. 53-67.

DAVID, B. 2008. Rethinking cultural chronologies and past landscape engagement in the Kopi region, Gulf Province, Papua New Guinea. The Holocene, 18, 3, pp. 463-479.

DE METS C, GORDON RG, ARGUS DF, STEIN S. (1994). Events of recent revisions to the geomagnetic reversal time scale on estimates of current plate motions. Geophys. Res. Lett. 21:2191–94.

DOWRICK, D.J., and RHOADS, D.A., 2004. Relations between earthquake magnitude and fault rupture dimensions: How regionally variable are they? Bulletin of the Seismological Society of America, vol 94. N 3., p 776-788.

FLEMING, K., JOHNSTON, P., ZWARTZ, D., YOKOYAMA, Y., LAMBECK, K., CHAPPELL, J., 1998. Refining the eustatic sea-level curve since the Last Glacial Maximum using far- and intermediate-field sites. Earth and planetary science letters, 163. Pp. 327-342.

IRWIN, G.R., 1991. Themes in prehistory of the coastal Papua and the Massim. In A. Pawley (ed.), Man and a half: essays in Pacific anthropology and ethnobiology in honour of Ralph Bulmer, pp. 503-511. Auckland: Polynesian Society.

KOULALI, A., TREGONING, P., MCCLUSKY, S., STANAWAY, R., WALLACE, L., & LISTER, G. (2015). New Insights into the present-day kinematics of the central and western Papua New Guinea from GPS. Geophysical Journal International, 202(2), 993-1004.

KIRCH, P. 1991. Prehistoric exchange in Western Melanesia. Annual review of anthropology, vol. 20, pp. 141-165.

LAJOIE, K., 1986. Coastal Tectonics. In: Wallace, R.E. (Ed), Active Tectonics, National Academy Press, Washington, D.C., 95-124.

LAMBECK, K., ROUBY, H., PURCELL, A., SUN, Y., SAMBRIDGE, M., 2014. Sea level and global ice volumes from the Last Glacial Maximum to the Holocene. PNAS, vol. 111, no. 43. Pp. 15296-15303.

LEONARD, M., 2010. Earthquake fault scaling: self-consistent of rupture length, width, average displacement, and moment release. Bulletin of the Seismological Society of America, Vol. 100, No. 5A, pp. 1971–1988, October 2010, doi: 10.1785/0120090189

McNIVEN, I.J., B. DAVID, T. RICHARDS, C. ROWE, M. LEAVESLEY, J. MIALANES, S.P. CONNAUGHTON, B., BARKER, K. APLIN, B. ASMUSSEN, P. FAULKNER & S. ULM. 2012. Lapita on the south coast of Papua New Guinea: challenging new horizons in Pacific archaeology. Australian Archaeology 75: 16–22.

RHOADS, J.W. 1982. Prehistoric Papuan exchange systems: the hiri and its antecedents, in T.E. Dutton (ed.) The hiri in history: further aspects of long distance Motu trade in central Papua (Pacific Research Monograph 8): 131–51. Canberra: Research School of Pacific Studies, Australian National University.

SKELLEY, R., DAVID, B., PETCHEY, F., LEAVESLEY, M. 2014. Tracking ancient beach-lines inland: 2600-year-old dentate-stamped ceramics at Hopo, Vailala River region, Papua New Guinea. Antiquity, vol. 88, pp. 470-487.

URWIN, C., HUA, Q., SKELLY, R., ARIFEAE, H. 2018. The chronology of Popo, an ancestral village site in Orokolo Bay, Gulf Province, Papua New Guinea. Australian Archaeology, 9 pp, https://doi.org/10.1080/03122417.2018.1443900

URWIN, C., 2019. Excavating and interpreting ancestral action: stories from the subsurface of Orokolo Bay, Papua New Guinea. Journal of Social Archaelogy, vol. 19(3) pp. 279-306.

VAN UFFORD, Q. A., and M. Cloos, 2005. Cenozoic tectonics of New Guinea, Am. Assoc. Petrol. Geol. Bull., 89, 119–140.

WALLACE, L. M., et al., 2004. GPS and seismological constraints on active tectonics and arc-continent collision in Papua New Guinea: Implications for mechanics of microplate rotations in a plate boundary zone, J. Geophys. Res., 109, B05404, doi:10.1029/2003JB002481.

WELLS, D.L., AND COPPERSMITH, K.J., 1994. New empirical relationships among magnitude, rupture length, rupture width, rupture area, and surface displacement: Bulletin of the Seismological Society of America, v. 84, p. 974-1002.

WESNOUSKY, S. G., 2008. Displacement and geometrical characteristics of earthquake surface ruptures: Issues and implications for seismic hazard analysis and the process of earthquake rupture, Bulletin of the Seismological Society of America. 98, no. 4, 1609–1632.